

Universidade Federal de Santa Catarina
Centro de Ciências Físicas e Matemáticas
Curso de Pós-Graduação em Física

Espectroscopia 3-D de galáxias: síntese de populações estelares e morfologia

André Luiz de Amorim

Orientadores:

Dr. Roberto Cid Fernandes Jr. (UFSC)
Dra. Rosa María González Delgado (IAA)

Tese submetida ao Programa de Pós-Graduação em Física da Universidade Federal de Santa Catarina para a obtenção do título de Doutor em Física. Trabalho financiado por CNPq e CAPES.

Florianópolis, 2015

Ficha de identificação da obra elaborada pelo autor,
através do Programa de Geração Automática da Biblioteca Universitária da UFSC.

Amorim , André Luiz de
Espectroscopia 3-D de galáxias : síntese de populações
estelares e morfologia / André Luiz de Amorim ;
orientador, Roberto Cid Fernandes Junior ; coorientadora,
Rosa María González Delgado. - Florianópolis, SC, 2015.
321 p.

Tese (doutorado) - Universidade Federal de Santa
Catarina, Centro de Ciências Físicas e Matemáticas.
Programa de Pós-Graduação em Física.

Inclui referências

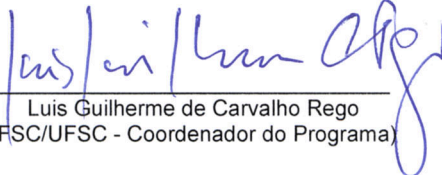
1. Física. 2. Galáxias: espectroscopia. 3. Galáxias:
populações estelares. 4. Galáxias: morfologia. I. Cid
Fernandes Junior, Roberto. II. González Delgado, Rosa
María. III. Universidade Federal de Santa Catarina.
Programa de Pós-Graduação em Física. IV. Título.

ESPECTROSCOPIA 3-D DE GALÁXIAS: SÍNTESE DE POPULAÇÕES ESTELARES E MORFOLOGIA


André Luiz de Amorim

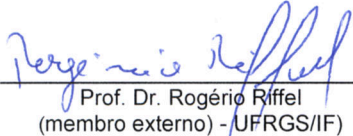
Esta Tese foi julgada adequada para a obtenção do título de **DOUTOR EM FÍSICA**, na área de concentração **Astrofísica** e aprovada em sua forma final pelo Programa de Pós-Graduação em Física.



Prof. Dr. Roberto Cid Fernandes Junior
(UFSC - orientador)

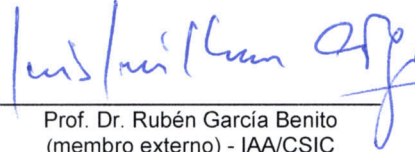

Luis Guilherme de Carvalho Rego
(FSC/UFSC - Coordenador do Programa)

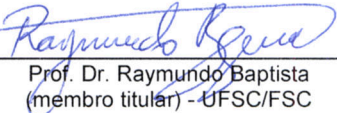

Prof. Dr. Roberto Cid Fernandes Junior
(UFSC - Presidente)


Prof^a. Dr^a. Natalia Vale Asari
(membro titular) - UFSC/FSC


Prof. Dr. Rogério Riffel
(membro externo) - UFRGS/IF


Prof. Dr. Abílio Mateus Junior
(membro titular) - UFSC/FSC


Prof. Dr. Rubén García Benito
(membro externo) - IAA/CSIC


Prof. Dr. Raymundo Baptista
(membro titular) - UFSC/FSC

Para Marilize e nosso pequeno mais-que-tudo.

Agradecimentos

Agradeço primeiro à minha esposa Marilize, que tanto me apoiou nesta aventura, e com quem terei junto a maior aventura de todas, que vai chegar logo, logo. Agradeço também aos meus pais e irmãos pelo amor e companheirismo, e por eu sempre poder contar com eles.

Ao meu orientador e grande amigo Cid, por todas as oportunidades, e pelas infindáveis discussões, às vezes sobre esta tese, e muitas vezes muito bem regadas. À Rosa, minha orientadora no IAA, que nos recebeu, eu e Marilize, com tanto carinho tão longe de casa. E principalmente por dar um norte científico a alguém que costumava pensar primeiro nos aspectos técnicos do trabalho.

Também ao Enrique, à Natalia e ao Rubén, sempre com ideias geniais, muitas das quais encontrando o seu caminho para esta tese. Se há resultados bons nestes trabalho, seus conselhos, dicas e sugestões tiveram um papel fundamental.

Aos colegas de estudos, William, Eduardo, Fábio, Rafa, Clara e todo o pessoal do Grupo de Astrofísica e do IAA, pelo ambiente agradável de trabalho; muitas amizades que devo levar pro resto da vida.

Este trabalho não seria possível sem os recursos financeiros da Coordenação de Aperfeiçoamento de Pessoal do Nível Superior, CAPES; do Conselho Nacional de Desenvolvimento Científico e Tecnológico, CNPq; do Instituto Nacional de Ciência e Tecnologia de Astrofísica, INCT-A; do programa Ciência sem Fronteiras; e do Instituto de Astrofísica de Andalucía, IAA/CSIC. Também sou grato ao Curso de Pós Graduação em Física, tanto pelo apoio financeiro quanto pela estrutura e instalações adequadas.

Finalmente, agradeço à colaboração do CALIFA, pelas inúmeras discussões e sugestões, especialmente nas *Busy Weeks*, sempre produtivas. E principalmente à equipe de observação e redução por produzir os dados com tanto capricho e dedicação, fundações sobre as quais este trabalho se ergueu.

Resumo

Neste trabalho foram desenvolvidas ferramentas para trabalhar com espectros de campo integral (IFS) do *survey* CALIFA. Os espectros dos *spaxels* são preprocessados e em seguida analisados com o uso do programa STARLIGHT. Uma das ferramentas principais discutidas aqui, PYCASSO, organiza os arquivos de saída do STARLIGHT em cubos de dados de produtos da síntese de população estelar. Ele também permite uma programação interativa e exploratória, dando acesso de forma prática e simples aos dados multidimensionais.

Através do uso destas ferramentas, foi desenvolvido um método que obtém e analisa as populações estelares das componentes morfológicas (bojo e disco) de galáxias, a partir de dados de IFS. A decomposição morfológica é feita utilizando o programa IMFIT, com um *wrapper* em Python. Uma amostra de 43 galáxias classificadas como S0 e com baixa inclinação foi escolhida para aplicação do método. O modelo morfológico utilizado foi um bojo com perfil de Sérsic e um disco exponencial. A decomposição morfológica é feita a cada comprimento de onda, de tal forma que se obtém ao final um espectro para cada *pixel* do bojo e do disco. Uma boa medida da PSF é essencial neste procedimento, então foi feita a caracterização da PSF do CALIFA utilizando as estrelas de calibração do *survey*. Os parâmetros morfológicos (r_e , n , P.A. e ϵ para o bojo, h , P.A. e ϵ para o disco), na maioria dos casos, depende linearmente, em média, do comprimento de onda, mas o seu comportamento a cada λ ainda não é bem compreendido. Foi feita a síntese espectral de populações estelares das componentes morfológicas de 9 galáxias da amostra, que tiveram um bom resultado na decomposição. Apenas duas destas produziram ajustes do STARLIGHT com pouco resíduo, CALIFA 0592 (NGC 4874) e CALIFA 0858 (UGC 10905). Em ambos os casos se obtém um bojo mais velho e menos metálico e um disco mais jovem e mais metálico do que o resultado da síntese do espectro observado. A síntese de populações estelares utilizando os espectros integrados produziram resultados mais robustos. Os espectros espacialmente resolvidos do bojo e do disco parecem ter artefatos que interferem no ajuste do STARLIGHT, sendo interpretados como poeira, entre outras coisas, levando a resultados equivocados.

Abstract

In this work we have developed some tools to work with Integral Field Spectroscopy (IFS) spectra from the CALIFA survey. The spectra from the spaxels are preprocessed, and then analyzed using the software `STARLIGHT`. One of the main tools discussed here, `PYCASSO`, organizes the output from `STARLIGHT` into datacubes of stellar population synthesis products. It also allows for interactive exploratory programming, giving easy access to the multi-dimensional data.

Using these tools, we developed a method for recovering and analyzing the stellar populations of the different morphological components of galaxies using IFS data. Using the software `IMFIT`, wrapped in Python, we perform the decomposition of a sample of 43 candidate S0 galaxies from the CALIFA Survey into a Sérsic bulge and an exponential disk. The decomposition is made wavelength-wise, so that at the end we get the bulge and disk spectra for each pixel. A good PSF measurement is critical to this process, so we perform a characterization of the PSF using the calibration stars from the survey. The morphological parameters (r_e , n , P.A. and ϵ for bulge, h , P.A. and ϵ for disk) in most cases depend linearly on the wavelength, on average, but their behavior at each λ are not yet fully understood. Using the decomposed spectra from the 9 best decompositions from the sample we apply a stellar population synthesis using `STARLIGHT`, in order to recover the stellar populations of bulge and disk. Only two of those galaxies produced `STARLIGHT` fits with a small residual, CALIFA 0592 (NGC 4874) and CALIFA 0858 (UGC 10905). In both cases we recover an older and lower-metallicity bulge and a younger and higher-metallicity disk (in comparison to the whole galaxy). The stellar synthesis produces more robust results using the integrated spectra. The spatially resolved spectra from bulge and disk seem to have artifacts that get interpreted as dust, among other things, thus leading to wrong results.

Sumário

Sumário	11
Lista de Figuras	14
Lista de Tabelas	19
1 Introdução	21
1.1 Espectroscopia de campo integral	21
1.2 Síntese de população estelar espacialmente resolvida	22
1.3 O nascimento do PYCASSO	24
1.4 Decomposição morfológica de galáxias	25
2 Síntese de populações estelares em espectroscopia de campo integral	27
2.1 O <i>survey</i> CALIFA	27
2.1.1 Instrumentação	28
2.1.2 Amostra	31
2.1.3 <i>Data Releases</i>	31
2.2 Síntese de população estelar	34
2.2.1 QBICK	34
2.2.2 STARLIGHT	37
3 PYCASSO	41
3.1 A ferramenta de manipulação de cubos de dados PYCASSO	42
3.2 Artigos publicados	45
3.2.1 Artigo: <i>Resolving galaxies in time and space. I. Applying STARLIGHT to CALIFA datacubes</i>	46
3.2.2 Artigo: <i>Resolving galaxies in time and space: II: Uncertainties in the spectral synthesis of datacubes</i>	48

3.2.3	Artigo: <i>The Evolution of Galaxies Resolved in Space and Time: A View of Inside-out Growth from the CALIFA Survey</i>	52
3.2.4	Artigo: <i>The star formation history of CALIFA galaxies: Radial structures</i>	53
4	Morfologia de galáxias	57
4.1	Classificação de Hubble	57
4.2	Componentes estruturais	60
4.2.1	Bojos e discos	60
4.2.2	Dependência dos modelos com o comprimento de onda	62
4.2.3	Ajuste de modelos	65
5	Caracterizando a PSF do CALIFA	71
5.1	Efeitos instrumentais e atmosféricos	71
5.2	Medindo a PSF	73
6	Testes da decomposição morfológica espectral	81
6.1	Construindo uma galáxia	82
6.2	Decompondo a galáxia sintética	85
6.3	Efeitos da PSF no ajuste	92
7	Decomposição morfológica espectral de galáxias	101
7.1	O procedimento de decomposição morfológica espectral	101
7.1.1	Cinemática	102
7.1.2	Propagação de erros nos espectros	104
7.1.3	Modelos iniciais e ajuste a cada comprimento de onda	105
7.2	Seleção da amostra de galáxias	108
7.3	Aplicação da decomposição na amostra final	110
7.4	Síntese espectral de populações estelares	113
8	Conclusões e perspectivas	121
A	Amostra para decomposição morfológica espectral	125
B	Decomposição morfológica espectral e síntese de populações estelares da amostra final	127
B.1	K0018 (NGC 0155)	127
B.2	K0127 (NGC 1349)	135
B.3	K0592 (NGC 4874)	142

B.4	K0602 (NGC 4956)	149
B.5	K0832 (NGC 6146)	156
B.6	K0846 (UGC 10695)	163
B.7	K0851 (NGC 6338)	170
B.8	K0858 (UGC 10905)	177
B.9	K0912 (NGC 7623)	184
C	Manual do <i>software</i> PyCASSO	191
D	Artigos publicados	239
D.1	Resolving galaxies in time and space. I. Applying STAR- LIGHT to CALIFA datacubes	239
D.2	Resolving galaxies in time and space. II. Uncertainties in the spectral synthesis of datacubes	257
D.3	The Evolution of Galaxies Resolved in Space and Time: A View of Inside-out Growth from the CALIFA Survey	279
D.4	The star formation history of CALIFA galaxies: Radial struc- tures	287
	Referências Bibliográficas	315

Lista de Figuras

1.1	Comparação entre <i>surveys</i> espectroscópicos de campo integral	23
2.1	Distribuição das fibras no instrumento PMAS/PPAK	29
2.2	Exemplos de espectros V500 e V1200 do CALIFA	30
2.3	Distribuição de magnitude r contra <i>redshift</i> da amostra mãe do CALIFA	32
2.4	Diagrama cor–magnitude da amostra mãe do CALIFA	33
2.5	Distribuição de massa das galáxias no DR2 do CALIFA	34
2.6	Caracterização da PSF do CALIFA DR2	35
2.7	Exemplo processamento com QWICK, galáxia K0277	36
2.8	Exemplos de ajuste de espectro com o STARLIGHT	39
3.1	Mapa da idade estelar média da galáxia IC 5376	44
3.2	Perfil radial da idade estelar média da galáxia IC 5376	45
3.3	Propriedades físicas espacialmente resolvidas para a galáxia NGC 2916	47
3.4	Idade estelar e metalidade espacialmente resolvidas para a galáxia NGC 2916	48
3.5	Diagramas $R \times t$ para luz, massa e SFR	49
3.6	Incerteza nos perfis radiais	50
3.7	Comparação dos ajustes com bases de SSP diferentes	51
3.8	Crescimento da massa estelar de galáxias de dentro para fora	53
3.9	Correlação entre idade, desidade superficial e massa estelar total	54
3.10	Relação entre a_{50}^M/a_{50}^L e a massa estelar total	55
3.11	Perfis radiais para várias caixas de massa estelar	56
4.1	Classificação de Wolf	58
4.2	Classificação de Hubble	59
4.3	Perfis empíricos de Sérsic	62

4.4	Ajuste morfológico de bandas fotométricas	63
4.5	Espectros das componentes morfológicas	65
4.6	Idade e metalicidade de bojos e discos de galáxias S0	66
4.7	Ajuste morfológico em uma dimensão	67
4.8	Ajuste morfológico em duas dimensões	68
5.1	Ajuste de perfil de Moffat ao modelo de PSF de Kolmogorov	72
5.2	Exemplo de ajuste de PSF para estrela de calibração	75
5.3	PSF do CALIFA – estrelas de calibração	76
5.4	PSF do CALIFA – estrelas de campo	77
6.1	Modelo morfológico inicial da galáxia sintética	83
6.2	Modelos de populações estelares da galáxia sintética	84
6.3	Modelo morfológico inicial do ajuste da galáxia sintética	86
6.4	Parâmetros morfológicos da galáxia sintética	88
6.5	Espectros ajustados à galáxia sintética	89
6.6	Razão ajuste–original dos espectros ajustados à galáxia sintética	91
6.7	Parâmetros morfológicos (teste com PSF FWHM = 2,6'')	93
6.8	Parâmetros morfológicos (teste com PSF FWHM = 3,3'')	94
6.9	Espectros ajustados (teste com PSF FWHM = 2,6'')	96
6.10	Espectros ajustados (teste com PSF FWHM = 3,3'')	97
6.11	Razão ajuste–original (teste com PSF FWHM = 2,6'')	98
6.12	Razão ajuste–original (teste com PSF FWHM = 3,3'')	99
7.1	Correção de efeitos da cinemática	103
7.2	Programa gráfico para encontrar o modelo inicial	107
7.3	Ajuste morfológico em 5635 Å para K0858 (UGC 10905)	111
7.4	Parâmetros morfológicos em função do comprimento de onda para K0858 (UGC 10905)	112
7.5	Espectro das componentes morfológicas de K0858 (UGC 10905). Acima, espectros	114
7.6	Espectros ajustados com STARLIGHT das componentes morfológicas de K0858 (UGC 10905)	115
7.7	Propriedades físicas das componentes morfológicas de K0858 (UGC 10905)	116
7.8	Idade e metalicidade médios das componentes morfológicas	118
7.9	A mesma Figura que 4.6	119
B.1	Ajuste morfológico em 5635 Å de K0018 (NGC 0155)	128

B.2	Parâmetros morfológicos em função do comprimento de onda de K0018 (NGC 0155)	129
B.3	Imagens em 5635 Å das componentes morfológicas de K0018 (NGC 0155)	130
B.4	Espectro das componentes morfológicas de K0018 (NGC 0155)	131
B.5	Perfis radiais para diversos comprimentos de onda de K0018 (NGC 0155)	132
B.6	Espectros ajustados com STARLIGHT das componentes morfológicas de K0018 (NGC 0155)	133
B.7	Propriedades físicas das componentes morfológicas de K0018 (NGC 0155)	134
B.8	Ajuste morfológico em 5635 Å de K0127 (NGC 1349)	135
B.9	Parâmetros morfológicos em função do comprimento de onda de K0127 (NGC 1349)	136
B.10	Imagens em 5635 Å das componentes morfológicas de K0127 (NGC 1349)	137
B.11	Espectro das componentes morfológicas de K0127 (NGC 1349)	138
B.12	Perfis radiais para diversos comprimentos de onda de K0127 (NGC 1349)	139
B.13	Espectros ajustados com STARLIGHT das componentes morfológicas de K0127 (NGC 1349)	140
B.14	Propriedades físicas das componentes morfológicas de K0127 (NGC 1349)	141
B.15	Ajuste morfológico em 5635 Å de K0592 (NGC 4874)	142
B.16	Parâmetros morfológicos em função do comprimento de onda de K0592 (NGC 4874)	143
B.17	Imagens em 5635 Å das componentes morfológicas de K0592 (NGC 4874)	144
B.18	Espectro das componentes morfológicas de K0592 (NGC 4874)	145
B.19	Perfis radiais para diversos comprimentos de onda de K0592 (NGC 4874)	146
B.20	Espectros ajustados com STARLIGHT das componentes morfológicas de K0592 (NGC 4874)	147
B.21	Propriedades físicas das componentes morfológicas de K0592 (NGC 4874)	148
B.22	Ajuste morfológico em 5635 Å de K0602 (NGC 4956)	149
B.23	Parâmetros morfológicos em função do comprimento de onda de K0602 (NGC 4956)	150

B.24	Imagens em 5635 Å das componentes morfológicas de K0602 (NGC 4956)	151
B.25	Espectro das componentes morfológicas de K0602 (NGC 4956)	152
B.26	Perfis radiais para diversos comprimentos de onda de K0602 (NGC 4956)	153
B.27	Espectros ajustados com STARLIGHT das componentes morfológicas de K0602 (NGC 4956)	154
B.28	Propriedades físicas das componentes morfológicas de K0602 (NGC 4956)	155
B.29	Ajuste morfológico em 5635 Å de K0832 (NGC 6146)	156
B.30	Parâmetros morfológicos em função do comprimento de onda de K0832 (NGC 6146)	157
B.31	Imagens em 5635 Å das componentes morfológicas de K0832 (NGC 6146)	158
B.32	Espectro das componentes morfológicas de K0832 (NGC 6146)	159
B.33	Perfis radiais para diversos comprimentos de onda de K0832 (NGC 6146)	160
B.34	Espectros ajustados com STARLIGHT das componentes morfológicas de K0832 (NGC 6146)	161
B.35	Propriedades físicas das componentes morfológicas de K0832 (NGC 6146)	162
B.36	Ajuste morfológico em 5635 Å de K0846 (UGC 10695)	163
B.37	Parâmetros morfológicos em função do comprimento de onda de K0846 (UGC 10695)	164
B.38	Imagens em 5635 Å das componentes morfológicas de K0846 (UGC 10695)	165
B.39	Espectro das componentes morfológicas de K0846 (UGC 10695)	166
B.40	Perfis radiais para diversos comprimentos de onda de K0846 (UGC 10695)	167
B.41	Espectros ajustados com STARLIGHT das componentes morfológicas de K0846 (UGC 10695)	168
B.42	Propriedades físicas das componentes morfológicas de K0846 (UGC 10695)	169
B.43	Ajuste morfológico em 5635 Å de K0851 (NGC 6338)	170
B.44	Parâmetros morfológicos em função do comprimento de onda de K0851 (NGC 6338)	171
B.45	Imagens em 5635 Å das componentes morfológicas de K0851 (NGC 6338)	172
B.46	Espectro das componentes morfológicas de K0851 (NGC 6338)	173

Lista de Figuras

B.47 Perfis radiais para diversos comprimentos de onda de K0851 (NGC 6338)	174
B.48 Espectros ajustados com STARLIGHT das componentes morfológicas de K0851 (NGC 6338)	175
B.49 Propriedades físicas das componentes morfológicas de K0851 (NGC 6338)	176
B.50 Ajuste morfológico em 5635 Å de K0858 (UGC 10905)	177
B.51 Parâmetros morfológicos em função do comprimento de onda de K0858 (UGC 10905)	178
B.52 Imagens em 5635 Å das componentes morfológicas de K0858 (UGC 10905)	179
B.53 Espectro das componentes morfológicas de K0858 (UGC 10905)	180
B.54 Perfis radiais para diversos comprimentos de onda de K0858 (UGC 10905)	181
B.55 Espectros ajustados com STARLIGHT das componentes morfológicas de K0858 (UGC 10905)	182
B.56 Propriedades físicas das componentes morfológicas de K0858 (UGC 10905)	183
B.57 Ajuste morfológico em 5635 Å de K0912 (NGC 7623)	184
B.58 Parâmetros morfológicos em função do comprimento de onda de K0912 (NGC 7623)	185
B.59 Imagens em 5635 Å das componentes morfológicas de K0912 (NGC 7623)	186
B.60 Espectro das componentes morfológicas de K0912 (NGC 7623)	187
B.61 Perfis radiais para diversos comprimentos de onda de K0912 (NGC 7623)	188
B.62 Espectros ajustados com STARLIGHT das componentes morfológicas de K0912 (NGC 7623)	189
B.63 Propriedades físicas das componentes morfológicas de K0912 (NGC 7623)	190

Lista de Tabelas

6.1	Modelo morfológico original da galáxia sintética	82
6.2	Modelo inicial ajustado à galáxia sintética	87
6.3	Ajuste morfológico espectral – média dos parâmetros	90
6.4	Parâmetros do ajuste morfológico espectral com PSF diferente .	95
7.1	Amostra final para decomposição morfológica espectral	109
A.1	Amostra selecionada para decomposição morfológica espectral .	126

Introdução

1.1 Espectroscopia de campo integral

Na última década presenciamos uma proliferação de *surveys* de imageamento e espectroscopia. *Surveys* como o SDSS (York et al. 2000), ALHAMBRA (Moles et al. 2008) e COSMOS (Scoville et al. 2007), para citar alguns exemplos, permitem explorar a distribuição espectral de energia (SED¹) de centenas de milhares a milhões de galáxias. Entretanto, da forma como estes *surveys* são executados, há sempre um compromisso entre a resolução espacial e a espectral. As imagens obtidas pelo SDSS têm uma boa resolução espacial, mas mapeiam a SED de forma grosseira, com apenas 5 filtros de banda larga (*ugriz*). Já os espectros obtidos pelo mesmo *survey* possuem uma excelente resolução e cobertura espectral, mas apenas sobre a superfície integrada da região central das galáxias.

O melhor dos dois mundos pode ser alcançado com instrumentos que fazem espectroscopia de campo integral (IFS²). Instrumentos que realizam este tipo de espectroscopia consistem em geral de um amontoado de fibras óticas, as quais alimentam um espectrógrafo comum. Assim, depois de um processo relativamente complicado de redução de dados, obtêm-se espectros espacialmente resolvidos com uma boa resolução espectral e espacial. O *survey* CALIFA (*Calar Alto Legacy Integral Field Area survey*³) está utilizando o instrumento PMAS/PPAK do observatório Calar Alto para obter IFS de 600 galáxias (Sánchez et al. 2012). Destas, 100 foram disponibilizadas no primeiro *Data Release* (Husemann et al. 2013, DR1), e 200 no segundo (García-Benito et al. 2015), afirmando o caráter de legado deste *survey*.

Quando completado, o CALIFA terá obtido da ordem de 10⁶ espectros, quase o mesmo que o SDSS. Porém, este não será apenas mais um

¹*Spectral Energy Distribution.*

²*Integral Field Spectroscopy.*

³<http://www.caha.es/CALIFA/>

1. Introdução

survey espectroscópico. A riqueza do CALIFA está nas informações espacialmente resolvidas, em uma amostra representativa do universo local ($0,005 < z < 0,03$, limitada em diâmetro angular) cobrindo a distribuição de galáxias no diagrama cor–magnitude da nuvem azul à sequência vermelha, amostrando galáxias de todos os tipos morfológicos (espirais, elípticas, irregulares e até mesmo alguns sistemas em interação).

Comparado a outros *surveys* já realizados, como o Atlas3D (Cappellari et al. 2011) ou o *Disk Mass Survey* (DMS) (Bershady et al. 2010), o CALIFA cobre uma faixa muito maior de tipos morfológicos e massas. Outros *surveys* que estão em andamento são o SAMI (Croom et al. 2012; Bryant et al. 2015) e o MaNGA (Bundy et al. 2015). Estes também buscam obter uma amostra grande de galáxias, bem maior do que a do CALIFA. Entretanto, a vantagem do CALIFA está na cobertura e amostragem espacial, observando uma maior porção de cada galáxia com mais riqueza de detalhes. A Figura 1.1, mostra uma comparação simplificada do tamanho do campo e cobertura espectral destes *surveys*. A Seção 2.1 apresenta o *survey* CALIFA em mais detalhes.

1.2 Síntese de população estelar espacialmente resolvida

Espectros espacialmente resolvidos podem ser descritos como um cubo de dados, com as duas primeiras dimensões sendo a posição x e y (ascensão reta e declinação) e a terceira sendo o comprimento de onda. Nestes cubos, planos com comprimento de onda constante são imagens, enquanto colunas definidas por um par (x, y) constante são espectros. Podem-se tratar estes espectros individualmente, embora na verdade nos cubos do CALIFA os *spaxels*⁴ vizinhos estejam correlacionados devido ao *seeing* do céu e ao processo de observação e redução. Há a queda na relação sinal/ruído (S/N) nas regiões mais afastadas do núcleo da galáxia, onde o brilho superficial é muito menor. Algumas galáxias possuem outros objetos “intrusivos” que precisam ser mascarados. Linhas telúricas⁵ também precisam ser mascaradas. Assim, em geral, é necessário um pré-processamento visando manter um S/N mínimo e garantir um espectro livre de contaminação. Os detalhes sobre o pré-processamento utilizado neste trabalho estão descritos na seção 3 do Apêndice D.1.

⁴A palavra *spaxel* é uma mistura de *space* e *pixel*, se referindo ao espectro proveniente da região espacial representada por um *pixel*.

⁵Linhas de absorção causadas pela atmosfera.

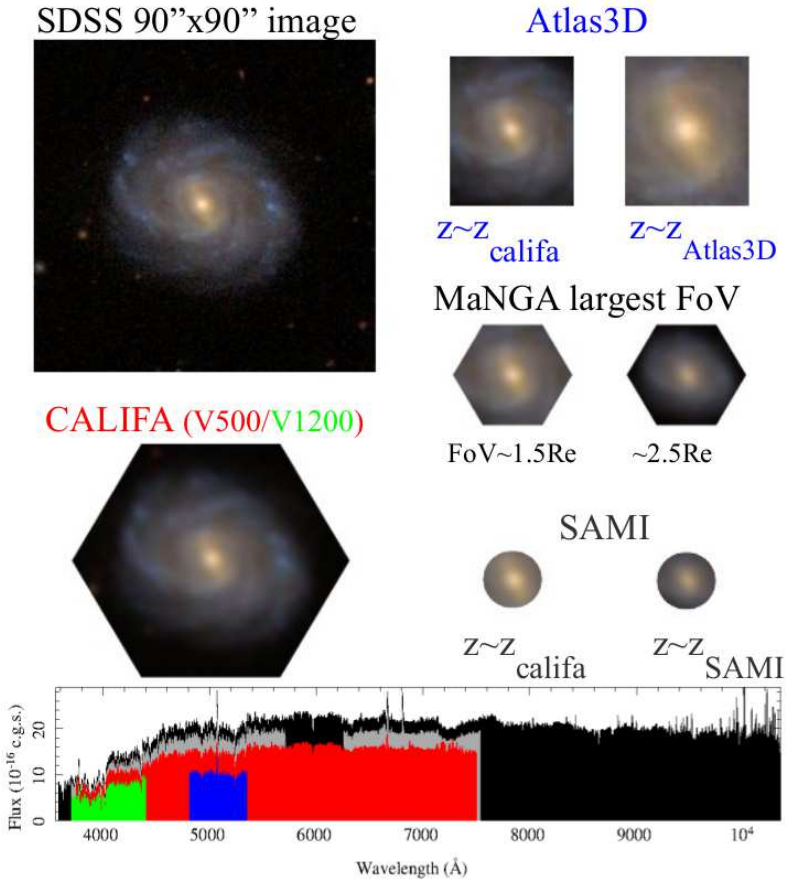


Figura 1.1: Comparação entre *surveys* espectroscópicas de campo integral em execução atualmente. A figura superior à esquerda mostra um recorte de $90 \times 90''$ de NGC 5947, extraída do SDSS. Ao redor, como esta galáxia seria observada pelos *surveys* ATLAS3D, MaNGA, SAMI e CALIFA a diferentes *redshifts* típicos de cada amostra. Abaixo a faixa de comprimento de onda coberta por cada *survey* (CALIFA em verde e vermelho, ATLAS3D em azul, SAMI em cinza, MaNGA em preto). Retirado de Sánchez (2014).

1. Introdução

Um aspecto importante do pré-processamento utilizado é que o cubo de dados é dividido em zonas de Voronoi, onde regiões com baixo S/N são combinadas, formando efetivamente “*spaxels* maiores”. Desta forma, o cubo original é transformado numa matriz de zonas e comprimento de onda, onde fatias de zona constante são espectros. Com isso, os espectros, e as máscaras e erros que os acompanham, estão prontos para serem usados pelo próximo passo.

A síntese de população estelar consiste em obter a história de formação estelar (SFH⁶) de uma galáxia utilizando modelos de população estelar simples (SSP⁷). Ajusta-se o espectro de uma galáxia como a soma de espectros de SSPs com idades e composições químicas distintas (levando em conta a atenuação por poeira e a cinemática). O resultado é um vetor de frações de luz e massa destas SSPs, que podem ser facilmente convertidos a uma SFH conforme a prescrição de Asari et al. (2007). O programa utilizado é o STARLIGHT, desenvolvido por Cid Fernandes et al. (2005).

Como apresentado na Seção 2.2.1, todos os espectros das zonas foram passados pelo STARLIGHT, obtendo-se o resultado da síntese como um arquivo de saída separado para cada zona. Entretanto, para visualizar ou mesmo tentar entender estes resultados, é preciso organizar e converter estes arquivos para um formato mais adequado.

1.3 O nascimento do PYCASSO

Dada a grande quantidade de dados espalhados em diversos formatos, a análise dos resultados da síntese de populações estelares para uma determinada galáxia pode se tornar um grande e complexo quebra-cabeças computacional. Trabalhar com todas as galáxias do *survey* fica virtualmente impossível desta forma. Assim, da necessidade de manipular os resultados da síntese dos cubos de dados das galáxias do CALIFA, nasceu o software PYCASSO.

PYCASSO (*Python CALIFA STARLIGHT Synthesis Organizer*) é um software desenvolvido em Python com o objetivo de organizar e gerenciar os dados produzidos pelo STARLIGHT com base nos dados do CALIFA. O *survey* CALIFA é apresentado no Capítulo 2, que também discute os softwares QBICK e STARLIGHT, ferramentas básicas em nossa análise de cubos de dados. O Capítulo 3 apresenta a documentação do PYCASSO, e em seguida discute alguns dos artigos publicados que o utilizam intensivamente.

⁶Star Formation History.

⁷Simple Stellar Population.

1.4 Decomposição morfológica de galáxias

Utilizando PYCASSO para trabalhar com cubos do CALIFA, buscou-se um problema onde se pudesse utilizar a natureza multidimensional dos dados. Com o STARLIGHT se obtêm informações sobre a história das populações estelares, ou seja, transforma-se comprimento de onda em tempo e luminosidade em massa. Porém, isto é feito de forma individual, para cada *spaxel*. Adicionando uma análise na distribuição de brilho da galáxia, pode-se tentar decompor o seu espectro em componentes morfológicas, e em seguida estudar a história das populações estelares de cada componente.

O processo de fazer a decomposição morfológica em cubos de dados espectrais de galáxias, tal que se toma imagens de fatias em comprimento de onda (λ -a- λ), é chamado neste trabalho de decomposição morfológica espectral. Dele resulta um conjunto de modelos morfológicos, que podem ser manejados de forma a obter cubos de dados espectrais das componentes morfológicas. O modelo morfológico de interesse aqui consiste em um bojo e um disco. O Capítulo 4 apresenta um breve histórico de morfologia.

A decomposição morfológica depende de uma boa caracterização da PSF (*Point Spread Function*). Como parte deste trabalho, a PSF do CALIFA foi determinada (Capítulo 5), com os resultados sendo aproveitados pela colaboração do CALIFA, e publicados em García-Benito et al. (2015). Foram feitos testes do algoritmo de decomposição, descritos no Capítulo 6, utilizando uma galáxia sintética. Estes testes não foram exaustivos, eles apenas indicam que a decomposição pode funcionar. Os testes incluem populações estelares compostas, variáveis com a posição no modelo. Outro teste importante, apresentado no mesmo capítulo, foi o efeito de usar uma PSF mal dimensionada na decomposição, com largura diferente da PSF do cubo de dados.

O Capítulo 7 descreve em detalhes o algoritmo de decomposição morfológica espectral. O pré-processamento dos dados inclui (mas não se limita a) regularizar a cinemática da galáxia, combinar espectros em imagens, calcular erros correlacionados. O ajuste das imagens ao modelo bojo–disco é feito utilizando o programa IMFIT (Erwin 2015), descrito na seção 4.2.3. Foi escolhida uma amostra de galáxias que potencialmente podem ser decompostas em bojos e discos, resultando num conjunto de cubos espectrais de componentes bojo e disco de cada galáxia desta amostra. Os cubos destas componentes são tratados exatamente da mesma forma que uma galáxia ao serem passados pelo STARLIGHT. Utilizando PYCASSO, os resultados da síntese espectral foram analisados e comparados com a síntese da galáxia original.

Síntese de populações estelares em espectroscopia de campo integral

2.1 O *survey* CALIFA

O *Centro Astronómico Hispano Alemán* (CAHA) se localiza na *Sierra de los Filabres*, na Comunidade Autónoma de Andaluzia, Espanha. Ele é operado pelo *Max-Planck-Institut für Astronomie* (MPIA), em Heidelberg, Alemanha, e pelo *Instituto de Astrofísica de Andalucía* (IAA/CSIC), em Granada, Espanha. O *survey* CALIFA foi agraciado com 210 noites pelo Comitê Executivo do Calar Alto, espalhadas por 6 semestres, iniciando em junho de 2010 (na prática, as observações se estenderam até o final de 2014). O instrumento utilizado foi a unidade de campo integral PPAK¹ (Kelz et al. 2006), do Espectrógrafo PMAS² (Roth et al. 2005; Roth et al. 2010), no telescópio de 3,5 m do CAHA.

A intenção do *survey* é caracterizar a população local de galáxias, que pode ser resumida nos seguintes aspectos científicos principais (Sánchez et al. 2012):

- Amostra cobrindo uma fração substancial da função de luminosidade.
- Amostra grande o suficiente para obter conclusões com uma estatística significativa para todas as classes de galáxias do *survey*.
- Caracterização das galáxias sobre toda a sua extensão, evitando bias de abertura.

¹*PMAS fiber PAcK*.

²*Potsdam Multi-Aperture Spectrophotometer*.

2. Síntese de populações estelares em espectroscopia de campo integral

- Determinação de mecanismos de ionização do gás: formação estelar, choques, AGN.
- Medição de abundâncias de oxigênio e nitrogênio no gás ionizado (regiões H II).
- Medição de propriedades de populações estelares: idades, razões massa-luminosidade, metalicidades e (de forma limitada) padrões de abundâncias.
- Medição de cinemática galáctica em gás em estrelas, campos de velocidade para todas as galáxias e dispersão de velocidades para as mais massivas.

A arquitetura do *survey* foi então desenhada levando em conta os requerimentos acima, junto com as limitações instrumentais e de tempo disponível. Ela está descrita nas seções a seguir.

2.1.1 Instrumentação

À época do início do CALIFA³, o PPAK/PMAS era o instrumento de sua classe com o maior tamanho de campo, $> 1 \text{ arcmin}^2$. Ele consiste em um maço de 331 fibras ópticas cobrindo o campo de observação, direcionado a um espectrógrafo de fenda longa que espalha a luz sobre um detector CCD⁴. A Figura 2.1 ilustra a montagem esquemática do instrumento. Desta forma, de cada fibra se obtém um espectro. Através de um programa de computador, os espectros podem ser reorganizados de modo a formar um cubo de dados, onde há duas dimensões espaciais e uma dimensão espectral. Todavia, pode-se notar na Figura 2.1 que as fibras não cobrem totalmente o campo de observação. Na verdade, apenas em torno de 60% da luz proveniente do campo cai dentro das fibras. O restante se perde nos espaços entre elas. Para mitigar este problema utiliza-se uma técnica chamada *dithering*, observando-se o mesmo campo 3 vezes, a cada vez deslocando o telescópio uma fração do diâmetro de uma fibra em direções diferentes formando um triângulo, tal que as 3 exposições cobrem toda a área a ser observada. O cubo de dados é reconstruído utilizando os programas de computador da *pipeline* de observação (Sánchez et al. 2012).

³Hoje em dia o MUSE (<https://www.eso.org/sci/facilities/develop/instruments/muse.html>) é o detentor do recorde.

⁴*Charge Coupled Device*.

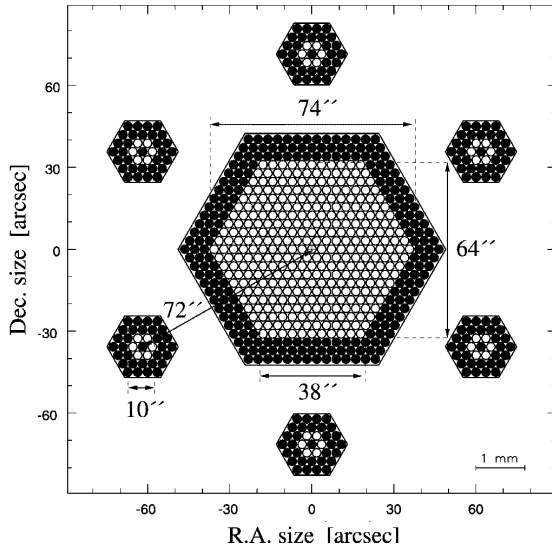


Figura 2.1: Distribuição espacial das fibras e dimensões do IFU do instrumento PMAS/PPAK. Círculos brancos representam fibras ativas, e círculos pretos fibras espaçadoras, que têm apenas papel estrutural e não obtêm espectros. Os 6 conjuntos de fibras ao redor do IFU são utilizados para medir o céu. O tamanho físico é de 4 mm e a largura do campo é maior que 1''. Retirado de Kelz et al. (2006).

A estratégia inicial do *survey* foi observar todos os objetos utilizando duas configurações diferentes e complementares do instrumento. A primeira utiliza a grade de difração V500, com resolução $\lambda/\Delta\lambda \approx 850$ em $\lambda = 5000 \text{ \AA}$ e uma largura a meia altura FWHM $\approx 6 \text{ \AA}$, cobrindo a maior faixa espectral possível, tal que as linhas [O II] $\lambda 3727$ e [S II] $\lambda 6731$ sejam observadas para todos os objetos da amostra. A segunda utiliza a grade de difração V1200, com resolução $\lambda/\Delta\lambda \approx 1650$ em $\lambda = 4500 \text{ \AA}$ e uma largura a meia altura FWHM $\approx 2,7 \text{ \AA}$, cobrindo a faixa azul do espectro, para incluir a descontinuidade de Balmer, H δ , H γ e [O III] $\lambda 4363$. Estas duas configurações são chamadas daqui em diante de V500 e V1200 respectivamente. A principal motivação para as observações com a V1200 é medir a cinemática estelar,

2. Síntese de populações estelares em espectroscopia de campo integral

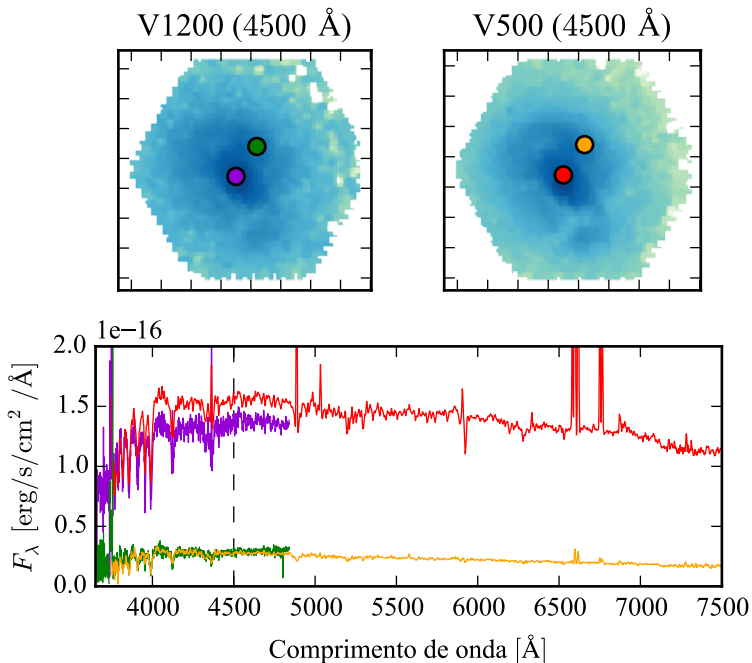


Figura 2.2: Espectros V500 e V1200 da galáxia NGC 7625, publicada no DR2 do CALIFA (García-Benito et al. 2015). Nos painéis superiores são mostradas imagens em 4500 Å nas duas configurações. Os espectros referentes aos pontos de cores violeta e vermelho, localizados no núcleo, e aos pontos de cores verde e laranja, a 12'' do núcleo, são mostrados no painel inferior, com as mesmas cores. A linha tracejada mostra o comprimento de onda utilizado nas imagens.

explorando a maior resolução espectral dessa grade ($\sigma_{\text{instrumental}} \sim 78$ km/s). Exemplos de espectros obtidos com as duas configurações, para a galáxia NGC 7625, são mostrados na Figura 2.2.

2.1.2 Amostra

A amostra obtida pelo CALIFA deve satisfazer os requerimentos científicos descritos anteriormente, levando em conta as limitações técnicas e instrumentais. Assim, uma amostra foi inicialmente selecionada a partir do catálogo DR7 do SDSS (Abazajian et al. 2009), garantindo a disponibilidade de imagens de boa qualidade em múltiplas bandas espectrais, e, em muitos casos, espectros nucleares. Sobre esta amostra inicial foram feitos cortes referentes ao tamanho aparente e o *redshift* da galáxia. O tamanho aparente da galáxia deve ser compatível com o instrumento, por isso escolheu-se limitar a amostra em diâmetro da isofota de brilho superficial 25 mag/arcsec^2 (D_{25}), tal que $45'' < D_{25} < 80''$ na banda *r* do SDSS. O *redshift* deve ser $0,005 < z < 0,03$, para manter a cobertura espectral consistente, e também descartar objetos do catálogo que são na verdade estrelas classificadas como galáxias de forma equivocada. O resultado é uma amostra de 939 galáxias, denominada *amostra mãe*, descrita e estudada em detalhes por Walcher et al. (2014). O conteúdo da amostra, junto com tabelas auxiliares, está disponível no *website* do CALIFA⁵. Todas as galáxias da amostra têm imagens obtidas nas bandas óptica (SDSS), infravermelha próxima (WISE) e rádio (NVSS); 655 delas têm fotometria em ultravioleta (GALEX) e 42 têm imagens em raios-X (Chandra). Espectros ópticos do SDSS DR7 (obtidos a menos de $15''$ do núcleo) estão disponíveis para 622 galáxias da amostra.

A amostra final observada deve conter aproximadamente 2/3 da amostra mãe, em torno de 600 galáxias, a serem selecionadas conforme a visibilidade, num padrão quase aleatório. A Figura 2.3 mostra a distribuição de magnitude aparente na banda *r* contra o *redshift* da amostra mãe. O diagrama cor–magnitude pode ser visto na Figura 2.4.

2.1.3 Data Releases

A primeira liberação pública de dados (em inglês, *data release*), denominada DR1 (Husemann et al. 2013), ocorreu em outubro de 2013. Foram escolhidas 100 galáxias nas duas configurações, V500 e V1200, que passaram por um

⁵<http://www.caha.es/CALIFA/>

2. Síntese de populações estelares em espectroscopia de campo integral

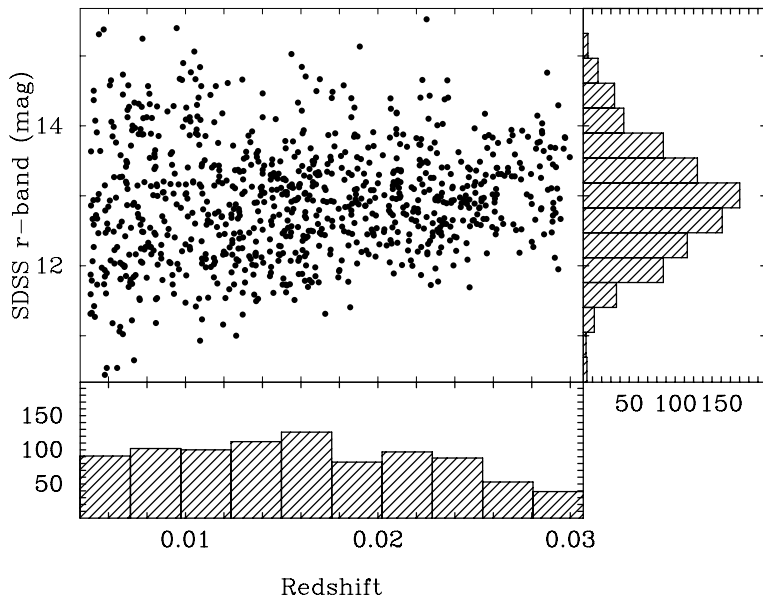


Figura 2.3: Distribuição de magnitude aparente na banda r contra o $redshift$ da amostra mãe do CALIFA. Retirado de Sánchez et al. (2012).

controle de qualidade do *survey*, num total de 200 cubos de dados. As características da amostra do DR1 reproduzem bem as da amostra mãe, dentro do que é esperado estatisticamente para uma amostra menor.

O *data release* seguinte, DR2 (García-Benito et al. 2015), dobra a quantidade de cubos de dados, com 200 galáxias nas duas configurações. Todos os cubos de dados do DR2 foram reduzidos com uma versão aprimorada do *pipeline* de redução de dados, apresentando melhor calibração espectrofotométrica, registro de imagem e resolução espacial. A massa das galáxias obtidas através de síntese espectral de populações estelares foi utilizada para caracterizar a amostra do DR1 e do DR2 (painel inferior da Figura 2.5). A PSF (*Point Spread Function*) típica dos cubos de dados (Figura 2.6) do *survey* foi determinada utilizando as mesmas técnicas de ajuste de imagem apresentadas no Capítulo 7. Mais detalhes sobre a medição da PSF no Capítulo 5.

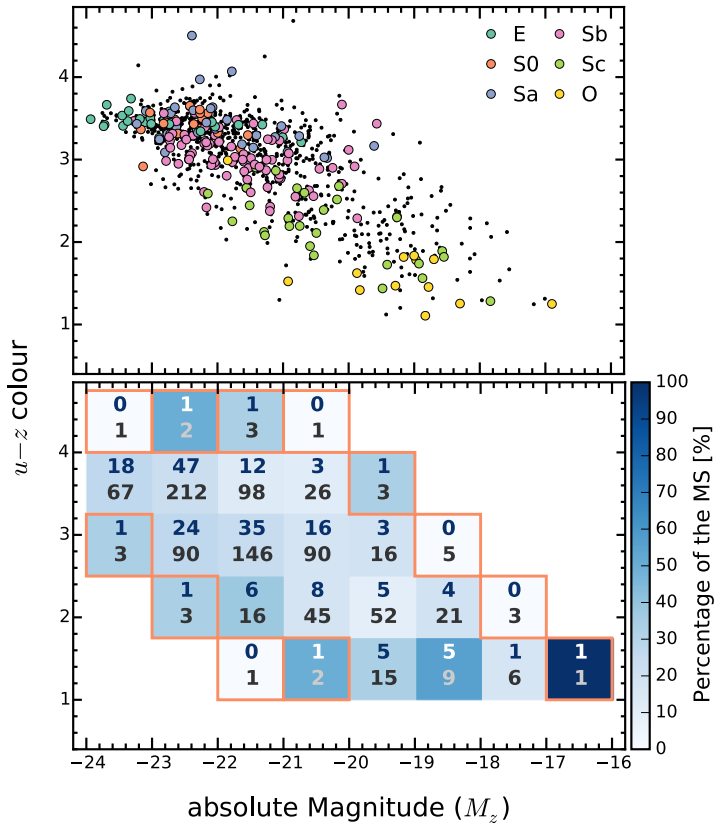


Figura 2.4: Painel superior: diagrama cor–magnitude ($u - z$ contra M_z) da amostra mãe do CALIFA. Os círculos coloridos indicam galáxias publicadas no DR2 (ver Seção 2.1.3), com a cor indicando o tipo morfológico. Painel inferior: percentual das galáxias publicadas no DR2 com respeito à amostra mãe. Os números indicam a quantidade observada (cima) e a quantidade na amostra mãe (baixo) em cada caixa. Caixas com contornos laranja contém poucas galáxias da amostra. Retirado de García-Benito et al. (2015).

2. Síntese de populações estelares em espectroscopia de campo integral

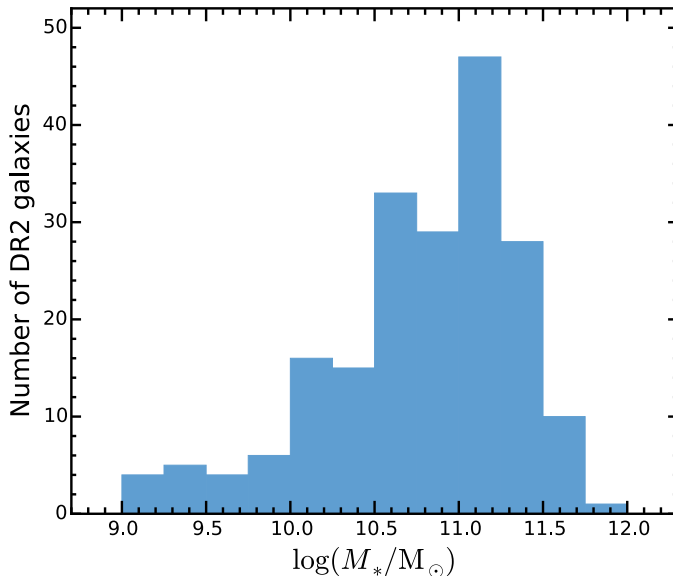


Figura 2.5: Distribuição de massa estelar das galáxias no DR2 do CALIFA. As massas foram determinadas através de síntese espectral de populações estelares com o STARLIGHT. Retirado de García-Benito et al. (2015).

Um *data release* final está programado para o final de 2015.

2.2 Síntese de população estelar

2.2.1 QBICK

O programa QBICK foi desenvolvido por Rubén García Benito para fazer o mascaramento e tesselação dos cubos de dados descrito a seguir. Para mais detalhes sobre o processo completo, ver o artigo por Cid Fernandes et al. (2013), reproduzido no Apêndice D.1.

É preciso preparar os espectros para passarem pelo STARLIGHT. Isto envolve principalmente remover medidas não confiáveis, além de deixar todos os espectros e cubos de dados num formato comum, para executar o STAR-

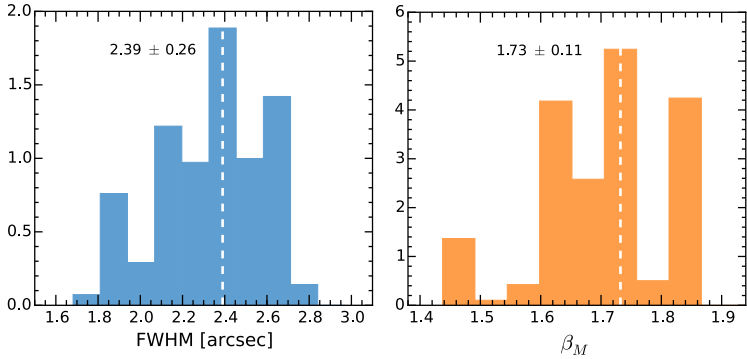


Figura 2.6: Caracterização da PSF do CALIFA DR2. À esquerda, distribuição da largura a meia altura (FWHM), e à direita, de β de um perfil de Moffat. Ver mais detalhes na Seção 5.2. Retirado de García-Benito et al. (2015).

LIGHT em modo *pipeline*. Antes de tudo, todos os *spaxels* que contêm luz não proveniente da galáxia, como estrelas de campo ou galáxias de fundo, foram mascarados. Também foram mascarados artefatos da observação e regiões de baixo sinal–ruído. Este é um procedimento quase artesanal, e necessita de um bom par de vistas humanas bem treinadas. Para um *survey* do porte do CALIFA, com cerca de 600 galáxias, isto ainda é factível. Após o mascaramento espacial, foram mascaradas as linhas espectrais causadas pela atmosfera terrestre. Os espectros foram em seguida postos no referencial de repouso utilizando o *redshift* obtido pela *pipeline*, medido nos 5'' centrais da galáxia. Foi escolhida uma janela espectral de 5590 a 5680 Å para fazer a medida do sinal–ruído dos espectros. Espectros com sinal–ruído baixo, em geral nas regiões menos brilhantes da galáxia, podem gerar resultados espúrios no STARLIGHT. Estes espectros foram combinados de modo a obter um melhor sinal–ruído utilizando uma técnica conhecida como tesselação de Voronoi. Foi escolhido um sinal–ruído de 20 como alvo para o agrupamento dos *spaxels*. O código utilizado para a tesselação de Voronoi foi implementado por Cappellari & Copin (2003) e modificado para levar em conta erros correlacionados. Um exemplo de aplicação do QBICK é mostrado na Figura 2.7.

2. Síntese de populações estelares em espectroscopia de campo integral

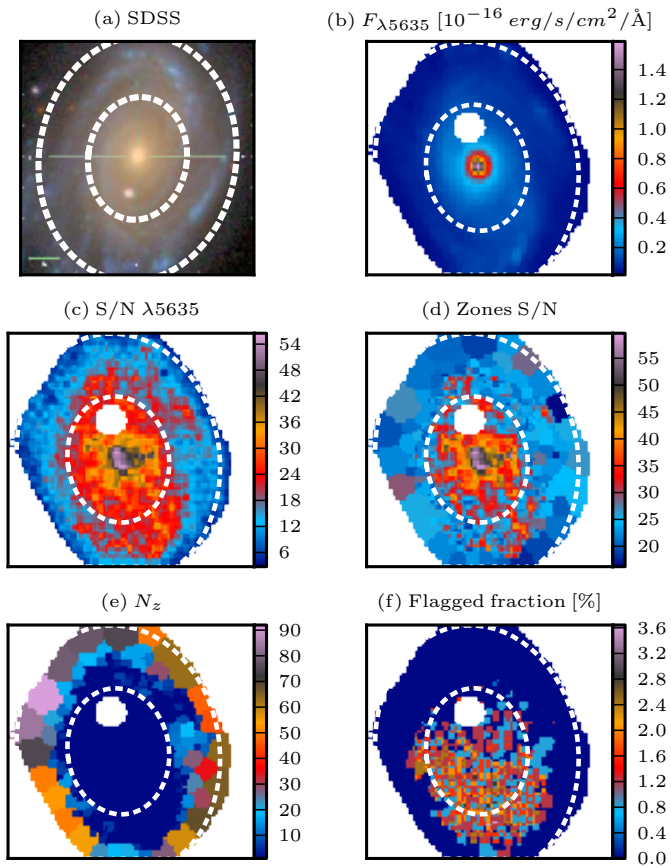


Figura 2.7: Exemplo processamento com `qwick` da galáxia NGC 2916 (CALIFA 0277). (a) Imagem do SDSS na banda r . (b) Imagem do CALIFA em 5635 \AA com máscara espacial. (c) Mapa de sinal–ruído em 5635 \AA . (d) Sinal–ruído após a segmentação em zonas de Voronoi. (e) Número de $spaxels$ em cada zona. (f) Percentual de $pixels$ ruins na faixa de $3800\text{--}6850 \text{ \AA}$. Retirado de Cid Fernandes et al. (2013).

2.2.2 STARLIGHT

O STARLIGHT é um código de síntese espectral desenvolvido por Cid Fernandes et al. (2005). Nele, o espectro observado de uma galáxia é modelado como uma combinação linear de espectros de uma base, um modelo de atenuação por poeira, e efeitos cinemáticos (*redshift* e dispersão gaussiana de velocidades). Esta base é composta por uma grade de populações estelares simples (SSP), onde cada SSP consiste em um conjunto de estrelas formadas ao mesmo tempo com a mesma metalicidade, com espectros proveniente de alguma biblioteca de modelos. O STARLIGHT busca neste espaço de parâmetros (que pode ser imenso, com quase 300 dimensões no caso do presente estudo) qual conjunto de frações de luz, atenuação e cinemática que melhor ajusta o espectro observado, que toma a forma

$$F_{\lambda}^{\text{modelo}} = \sum_{j=1}^{N_{\star}} F_{\lambda}^{\star}(t_j, Z_j) 10^{-0.4A_{\lambda}} \otimes G(v_{\star}, \sigma_{\star}).$$

Nesta equação, $F_{\lambda}^{\text{modelo}}$ é o fluxo em cada comprimento de onda. O termo $10^{-0.4A_{\lambda}}$ corrige o espectro pelo efeito de atenuação interestelar, que pode ser por exemplo do tipo CCM (Cardelli, Clayton, & Mathis 1989) ou CAL (Calzetti, Kinney, & Storchi-Bergmann 1994). $G(v_{\star}, \sigma_{\star})$ denota uma função gaussiana (centrada em v_{\star} e com dispersão σ_{\star}) utilizada para modelar os efeitos da cinemática estelar. Na prática a equação acima é implementada após um procedimento de normalização a um comprimento de onda de referência λ_N , isto é,

$$F_{\lambda}^{\text{modelo}} = F_{\lambda_N}^{\text{modelo}} \sum_{j=1}^{N_{\star}} x_j b_{\lambda}^{\star}(t_j, Z_j) 10^{-0.4(A_{\lambda} - A_{\lambda_N})} \otimes G(v_{\star}, \sigma_{\star}),$$

onde $b_{\lambda}^{\star}(t_j, Z_j) \equiv F_{\lambda}^{\star}(t_j, Z_j) / F_{\lambda_N}^{\star}(t_j, Z_j)$ denota o espectro do elemento j da base normalizado a seu valor em λ_N . A dada elemento j corresponde uma idade t_j e uma metalicidade Z_j , e a importância de cada elemento na soma total é dada pelo peso x_j . O conjunto $\{x_j, i = 1, 2, \dots, N_{\star}\}$ é chamado vetor de população (\vec{x}) da galáxia considerada. O melhor ajuste é escolhido minimizando

$$\chi^2 = \sum_{\lambda} \left[(F_{\lambda}^{\text{observado}} - F_{\lambda}^{\text{modelo}}) w_{\lambda} \right]^2$$

onde o peso w_{λ} é definido como o inverso da incerteza na medida de $F_{\lambda}^{\text{observado}}$.

2. Síntese de populações estelares em espectroscopia de campo integral

Os espectros da base provêm de modelos de síntese evolutiva de populações estelares. A maior parte dos resultados publicados do STARLIGHT usa os modelos de Bruzual & Charlot (2003, BC03). Em particular, em seus estudos de galáxias do SDSS o grupo da UFSC normalmente usa uma base composta de 150 SSPs cobrindo 25 idades (entre 0,001 e 18 Ga) e 6 metalicidades ($\log Z/Z_{\odot}$ entre $-2,3$ e $+0,4$; vide Mateus (2006)). A Figura 2.8 mostra ajustes feitos para 5 galáxias do SDSS utilizando esta base. A extinção é modelada com uma lei de avermelhamento de CCM. Neste trabalho usamos modelos mais atualizados de espectros de SSPs, extraídos dos modelos de Granada (González Delgado et al. 2005, para idades até 63 Ma) e os do projeto MILES (Vazdekis et al. 2010, para idades maiores que 63 Ma). No total esta nova base contém 235 elementos cobrindo idades de 0,001 a 14 Ga, e $\log Z/Z_{\odot}$ de $-2,3$ a $+0,33$. Para mais detalhes ver González Delgado et al. (2014a,b).

A aplicação mais imediata do resultado do STARLIGHT é a remoção do contínuo estelar para medir com maior precisão as linhas de emissão provenientes do gás, não incluídas no modelo. É possível também estudar o vetor de população \vec{x} , que representa a fração de luz proveniente de cada população estelar da base (como na coluna central de painéis da Figura 2.8). De forma alternativa, pode-se utilizar o vetor de fração de massa $\vec{\mu}$, que se relaciona ao \vec{x} através da relação massa–luminosidade de cada elemento da base. Individualmente os componentes x_j e μ_j dos vetores não são confiáveis, pois há muita degenerescência nos elementos da base (Cid Fernandes et al. 2005). Porém, a informação contida nos vetores pode ser condensada, gerando medidas físicas mais robustas. A idade estelar média ponderada pela luminosidade pode ser definida como $\langle \log t \rangle_L = \sum_j x_j \log t_j$, onde t_j é a idade de cada elemento da base. Pode-se substituir o vetor de população (\vec{x}) pelo vetor de fração de massa ($\vec{\mu}$) e assim obter a idade ponderada pela massa. Outra propriedade bastante utilizada é a metalicidade estelar média ponderada pela massa, definida como $\langle Z \rangle_M = \sum_j \mu_j Z_j$, onde Z_j é a metalicidade de cada elemento da base. Medidas como estas geram resultados muito mais confiáveis, como demonstrado por Cid Fernandes et al. (2014), reproduzido no Apêndice D.1.

Esta técnica foi utilizada em diversos artigos. Em particular a colaboração SEAGal (*Semi Empirical Analysis of Galaxies*), liderada pela UFSC, aplicou o STARLIGHT a 926246 espectros de galáxias do DR7 do SDSS. As propriedades físicas derivadas desta análise de populações estelares, junto com as medidas de linhas de emissão, foram disponibilizadas como um banco de dados no *website* <http://www.starlight.ufsc.br/>.

Os resultados foram utilizados em estudos varrendo desde a história

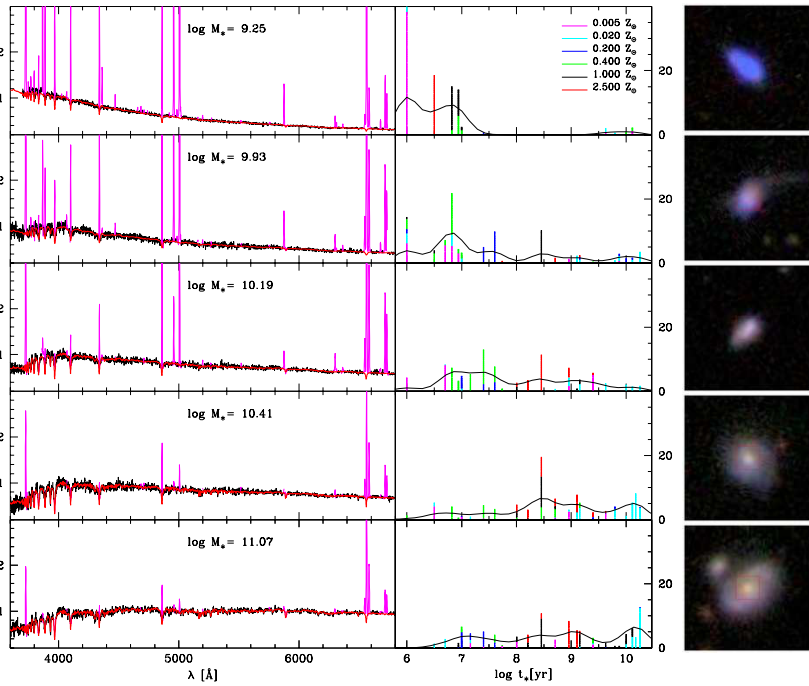


Figura 2.8: Exemplos de ajuste de espectros de galáxias com o STARLIGHT (Asari et al. 2007). À esquerda, espectros observados (preto), espectros modelados (vermelho), com regiões mascaradas em magenta. No meio, a fração da luz associada a cada uma das 25 idades das SSPs usadas na síntese, com a curva representando a versão suavizada do histórico de formação estelar. À direita, imagens do SDSS correspondentes às galáxias.

2. Síntese de populações estelares em espectroscopia de campo integral

de formação estelar de galáxias (Asari et al. 2007) a efeitos ambientais (Mateus et al. 2007) e a origem de linhas de emissão de galáxias “aposentadas” (Stasińska et al. 2008; Cid Fernandes et al. 2011). Além desses, pesquisadores em todo o mundo produziram artigos independentes (Bian et al. 2006; Liang et al. 2007; Peeples et al. 2009; Lara-López et al. 2009, 2010, para citar alguns) baseados nesse banco de dados.

Em todos esses estudos, cada galáxia é representada por apenas um espectro. A extensão desse tipo de estudo a dados IFS parece trivial, e em certa medida o é se considerarmos o espectro de cada zona (ou *spaxel*) como o espectro de uma galáxia inteira. No entanto, para tirar máximo proveito da informação sobre populações estelares e sua distribuição espacial é necessária uma ferramenta que organize os resultados do STARLIGHT para um dado cubo de dados. Dessa necessidade nasceu a plataforma PYCASSO, assunto do próximo capítulo.

PYCASSO

A fim de agilizar o desenvolvimento de ferramentas de manipulação de cubos de dados do CALIFA, alguns programas de computador foram desenvolvidos. Foi montado um “kit de ferramentas”, chamado PYCASSO (*Python CALIFA STARLIGHT Synthesis Organizer*), para organizar e analisar o resultado da síntese de populações sobre os dados do CALIFA. PYCASSO foi desenvolvido em sua maior parte pelo autor desta tese, utilizando a linguagem Python, e foi utilizado de forma extensiva pelo grupo de populações estelares (cerca de 10 pessoas), resultando em vários artigos, alguns deles descritos neste capítulo.

A grosso modo, PYCASSO é composto de três partes:

1. Conversor de tabelas. Com ele se converte a saída do STARLIGHT (arquivos ASCII para cada pixel de cada galáxia) para cubos de dados nos formatos FITS e HDF5, de forma a otimizar o acesso aos dados. Uma galáxia leva tipicamente 2 minutos para ser carregada em memória usando arquivos texto. Este tempo se reduz para menos de um segundo usando arquivo FITS. Há outra otimização para acessar dados de várias galáxias simultaneamente, utilizando o formato HDF5. Neste caso a carga dos dados em disco para a memória é “preguiçosa”, quer dizer, é feita somente quando os dados são efetivamente acessados. O capítulo 3 do manual (Apêndice C) demonstra como fazer a conversão.
2. Camada de entrada e saída. Os arquivos FITS e HDF5 foram montados de forma a serem facilmente acessados em qualquer ambiente. Ainda assim, há uma camada de abstração de armazenamento, onde as várias matrizes e cubos são acessadas com nomes próprios (por exemplo, `popx`, que designa a fração de luz distribuída pelas populações estelares), de forma a ser possível programar ferramentas de análise sem precisar se preocupar com as características de cada formato de armazenamento.

3. Camada de análise. Como foi mencionado na Seção 1.2, o resultado da síntese consiste em cubos indexados por zona. Os dados ficam armazenados no disco desta forma. Porém, na grande maioria das vezes se está interessado na informação espacialmente resolvida. Esta camada implementa uma rotina de conversão da notação de zonas para (x, y) . Boa parte das propriedades da síntese, como luminosidade, massa, atenuação por poeira, e idade estelar, já estão implementadas. Estes cubos espacialmente resolvidos são calculados dinamicamente, quer dizer, não ocupam memória do sistema até que sejam acessados. Existem outras rotinas para calcular geometria, perfis radiais e azimutais, e raio de escala. Outras rotinas podem ser adicionadas facilmente¹.

Este software está sendo utilizado pelo grupo de populações estelares da colaboração do CALIFA, do qual o autor faz parte. No total são aproximadamente 10 pessoas utilizando este software. Foram publicados 6 artigos que utilizam extensivamente PYCASSO, e mais alguns que utilizaram algum dado resultante de forma indireta, apresentados na Seção 3.2.

3.1 A ferramenta de manipulação de cubos de dados PYCASSO

PYCASSO é uma biblioteca desenvolvida em Python. Porém uma biblioteca não é nada sem uma boa documentação. Aqui se apresenta de forma breve as capacidades do PYCASSO. A documentação completa se encontra no Apêndice C.

O trabalho com a variedade e quantidade de dados gerados pela síntese espectral em 3-D tem em geral um caráter fortemente exploratório. Frequentemente não se sabe exatamente o que se está buscando, e o trabalho do pesquisador consiste em desenhar gráficos, realizar cálculos, determinar operações ou filtros nos dados com base nestes gráficos e cálculos, desenhar novamente, e assim sucessivamente. Assim se escolheu a linguagem Python, que possui ferramentas adequadas à programação exploratória², como o IPython³ e o matplotlib⁴. Foi feito um esforço para que o acesso aos dados de cada galáxia fosse feito de forma simples e direta. Um exemplo de código pode ser visto na listagem de código fonte abaixo.

¹Há um estudo de PCA (análise de componentes principais) sendo desenvolvido pelo estudante da UFSC Eduardo A. D. Lacerda, por exemplo.

²Além de estar se tornando uma espécie de *lingua franca* na Astrofísica computacional.

³<http://ipython.org/>

⁴<http://matplotlib.org/>

Código fonte 3.1: Exemplo de acesso aos dados. Todas as propriedades estão disponíveis diretamente pelo nome, inclusive utilizando a função autocompletar da maioria dos ambientes de desenvolvimento Python.

```
1 | # Carregar arquivo FITS com os dados.
2 | from pycasso import fitsQ3DataCube
3 | K = fitsQ3DataCube('K0001_synthesis.fits')
4 |
5 | # Acessar a idade média ponderada pela luminosidade.
6 | at = K.at_flux__z
7 |
8 | # Calcular a idade média da galaxia.
9 | at_total = (at * K.Lobn__z).sum() / K.Lobn__z.sum()
10 | print 'Idade média da galaxia: %.2f' % at_total
```

Para algumas operações, como o cálculo da idade estelar média feito na Figura 3.1, pode-se utilizar apenas o resultado para as zonas. Neste caso, a idade estelar média é calculada usando a expressão $\langle \log t \rangle_L^{\text{gal}} = \sum_z \langle \log t \rangle_{L,z} L_z / \sum_z L_z$, onde L_z é a luminosidade de cada zona e $\langle \log t \rangle_{L,z}$ é a idade estelar média de cada zona. Entretanto, para tirar vantagem das informações espaciais, é preciso converter as propriedades da notação de zona para imagem. Por exemplo, o programa a seguir calcula a idade estelar média espacialmente resolvida⁵, e em seguida desenha um gráfico da imagem gerada.

Código fonte 3.2: Programa para desenhar o mapa de idade estelar média ponderada pela luminosidade. O gráfico resultante é mostrado na Figura 3.1.

```
1 | # Carregar arquivo FITS com os dados.
2 | from pycasso import fitsQ3DataCube
3 | K = fitsQ3DataCube('K0001_synthesis.fits')
4 |
5 | # Converter zonas para imagem.
6 | at_image = K.zoneToYX(K.at_flux__z, extensive=False)
7 |
8 | # Desenhar o mapa.
9 | import matplotlib.pyplot as plt
10 | plt.imshow(at_image)
11 | plt.colorbar()
```

⁵O mapa de idade já está previamente calculado, disponível através da propriedade `at_flux__yx`. Esta conversão é feita explicitamente aqui para ilustrar como a conversão pode ser feita para qualquer propriedade.

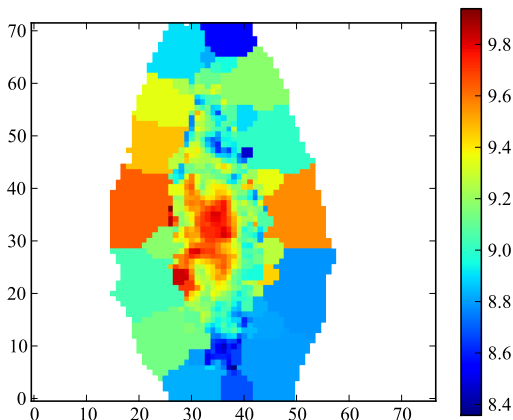


Figura 3.1: Mapa de idade estelar média ponderada pela luminosidade da galáxia IC 5376, desenhado pelo programa da Listagem de código fonte 3.2.

Enquanto um mapa é uma forma muito boa de visualizar informações em duas dimensões, há vezes em que uma visualização resumida é mais adequada. Galáxias em geral têm simetria aproximadamente axial, logo poder medir perfil radial das propriedades das galáxias é fundamental para estudá-las. Com o PYCASSO, o cálculo do perfil radial é bastante simples, como pode ser visto na Listagem de código fonte 3.3, que calcula o perfil radial da idade estelar média. O resultado está na Figura 3.2.

Código fonte 3.3: Programa para desenharm o perfil radial da idade estelar média ponderada pela luminosidade.

```

1 # Carregar arquivo FITS com os dados.
2 from pycasso import fitsQ3DataCube
3 K = fitsQ3DataCube('K0001_synthesis.fits')
4
5 # Converter zonas para imagem.
6 at_image = K.zoneToYX(K.at_flux__z, extensive=False)
7
8 # Calcular o perfil radial.
9 bins = np.arange(0, 26, 1)
10 bin_center = (bins[1:] + bins[:-1]) / 2.0

```

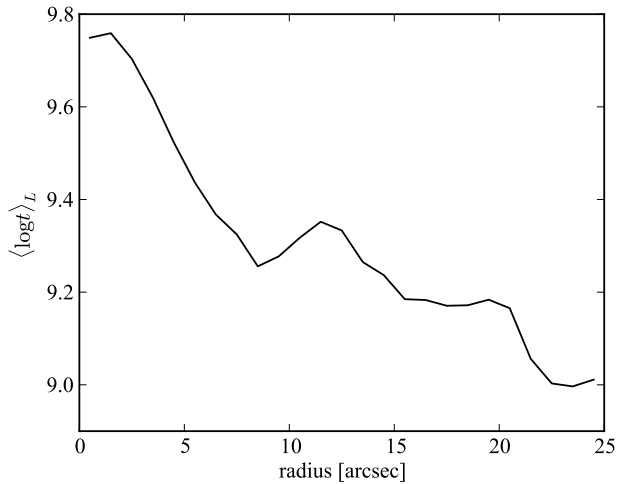


Figura 3.2: Perfil radial da idade estelar média ponderada pela luminosidade da galáxia IC 5376, desenhado pelo programa da Listagem de código fonte 3.3.

```

11 | at_rad = K.radialProfile(at_image, bins, rad_scale=1.0)
12 |
13 | # Desenhar o perfil radial.
14 | import matplotlib.pyplot as plt
15 | plt.plot(bin_center, at_rad)

```

Esta é só uma pequena demonstração das ferramentas existentes no `pycasso`. Também é possível trabalhar com espectros, calcular perfis azimutais, lidar com *pixels* mascarados, entre outras coisas. Tudo isto está descrito em detalhes no manual do programa (Apêndice C).

3.2 Artigos publicados

Nesta seção discutem-se os artigos onde se utilizou `pycasso` e nos quais o autor desta tese teve uma colaboração importante. Além destes artigos, Husemann et al. (2013), no artigo apresentando o DR1 do CALIFA, utiliza as

massas estelares determinadas pelo STARLIGHT e disponibilizadas pelo PYCASSO para caracterizar a amostra do CALIFA. O artigo que apresenta o DR2, de García-Benito et al. (2015), também utiliza as massas da mesma forma (ver Figura 2.5). O mesmo artigo inclui a medição da PSF do CALIFA (ver Figura 2.6), apresentado neste trabalho na Seção 5.2.

González Delgado et al. (2014a) explora a relação massa–metallicidade estelar em 300 galáxias do CALIFA, utilizando PYCASSO. Em González Delgado et al. (2015) se utiliza, além do PYCASSO, a decomposição bojo–disco (ver Seção 4.2.1) em uma amostra de galáxias, realizada pelo autor desta tese, adaptando técnicas discutidas no Capítulo 7.

3.2.1 Artigo: *Resolving galaxies in time and space. I. Applying STARLIGHT to CALIFA datacubes*

Este artigo por Cid Fernandes et al. (2013) descreve todo o processo de síntese espectral dos cubos de dados do CALIFA, mencionados no Capítulo 1, e serve como uma demonstração da capacidade do PYCASSO. O artigo está reproduzido na íntegra no Apêndice D.1. O pré-processamento dos cubos de espectros é feito através do programa QWICK, desenvolvido por Rubén García Benito especialmente para o CALIFA, mas é genérico o bastante para ser usado em outros cubos de dados. Após explicar em detalhes todos os passos envolvidos desde o pré-processamento, passando pela descrição do STARLIGHT até a importação dos dados pelo PYCASSO, o artigo apresenta um caso de estudo com a galáxia NGC 2916.

As Figuras 3.3 e 3.4 mostram mapas de propriedades físicas obtidas pela síntese espectral. Propriedades como a massa (Figura 3.3d) e luminosidade (Figuras 3.3a e 3.3c) são quantidades extensivas, e são proporcionais à escala. Já a atenuação por poeira (Figura 3.3b), idade e metalicidade estelar são quantidades intensivas, independentes de escala. Na prática isto significa que as quantidades extensivas podem ser divididas entre os *pixels* que compõem uma zona, enquanto as intensivas são uma propriedade comum a todos os *pixels* desta zona. Esta diferença pode ser notada nas zonas mais externas dos mapas, onde aparecem platôs nas quantidades intensivas. As quantidades extensivas passam por um processo apelidado de “dezonificação”, onde uma medida referente a uma zona é dividida entre os *pixels* com base em um peso, normalmente dado pelo fluxo na janela de normalização. Isto faz com que as imagens não tenham um aspecto segmentado, com patamares nas zonas periféricas.

Um dos desafios de se trabalhar com cubos multidimensionais é como

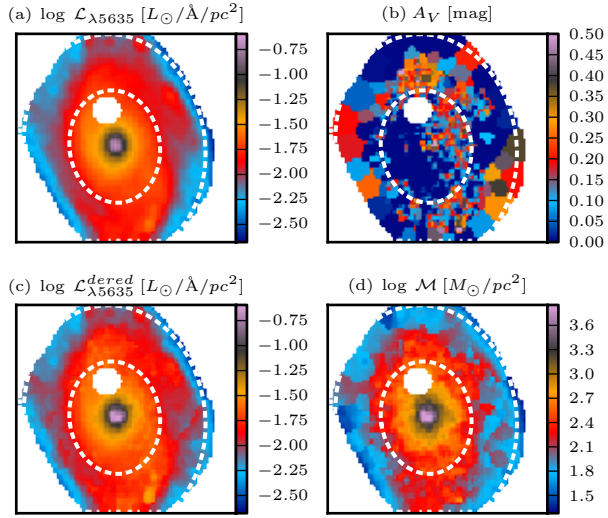


Figura 3.3: Propriedades físicas espacialmente resolvidas para a galáxia NGC 2916. (a) Luminosidade em 5635 \AA por unidade de área. (b) Atenuação por poeira na banda V. (c) Luminosidade em 5635 \AA por unidade de área, corrigido de extinção. (d) Densidade superficial de massa estelar. Retirado de Cid Fernandes et al. (2013, figura 4), Apêndice D.1.

visualizar esta informação. Uma alternativa é comprimir determinadas dimensões. Para ilustrar esta capacidade do `pycasso`, a Figura 3.5 mostra diagramas de luz, massa e taxa de formação estelar (SFR) em função do tempo, onde as dimensões x e y foram transformadas em distância radial. Diagramas como este, junto com perfis 1-D radiais e temporais ajudam a visualizar e interpretar o resultado da síntese espectral, oferecendo novas ferramentas para estudar a estrutura e evolução de galáxias.

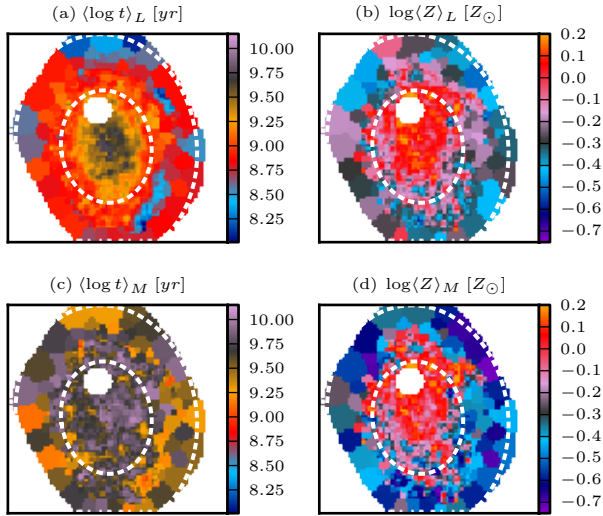


Figura 3.4: Idade e metalicidade estelar média, espacialmente resolvidas, para a galáxia NGC 2916. (a) Idade estelar média pesada pela luminosidade. (b) metalicidade estelar média pesada pela luminosidade. (c) Idade estelar média pesada pela massa. (d) metalicidade estelar média pesada pela massa. Retirado de Cid Fernandes et al. (2013, figura 6), Apêndice D.1.

3.2.2 Artigo: *Resolving galaxies in time and space: II: Uncertainties in the spectral synthesis of datacubes*

Uma crítica bastante comum aos métodos de ajuste é que eles não provêm a incerteza associada aos valores ajustados. A forma mais simples de determinar esta incerteza é refazer o ajuste várias vezes, perturbando as medidas levando em conta os erros de forma realista. Este artigo por Cid Fernandes et al. (2013) investiga a incerteza nos ajustes feitos no artigo discutido na seção anterior. O artigo está reproduzido na íntegra no Apêndice D.2.

Quando se injetam erros aleatórios, obtém-se incertezas de $\sim 0,08$ dex em idades e metalicidades pesadas pela luminosidade, e de $\sim 0,15$ dex quando pesadas pela massa. A massa estelar teve uma incerteza de $\sim 0,08$ dex, e

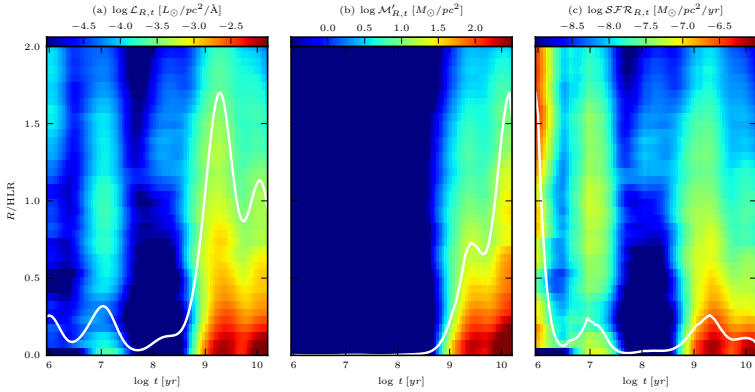


Figura 3.5: Diagramas $R \times t$ para luz, massa e taxa de formação estelar (SFR). (a) Luminosidade em 5635 \AA por unidade de área. (b) Massa transformada em estrelas por unidade de área. (c) Taxa de formação estelar por unidade de área. A linha sólida representa o gráfico colapsado na direção vertical, apenas para ilustrar a variação temporal das quantidades mapeadas. Retirado de Cid Fernandes et al. (2013, figura 12), Apêndice D.1.

A_V de $\sim 0,06$ mag. Injetando erros sistemáticos em cor^6 as incertezas são similares, exceto para A_V , que recebe um desvio sistemático de $+0,05$ mag e uma incerteza de $\sim 0,16$ mag.

Embora haja uma incerteza considerável analisando-se as propriedades da galáxia pixel a pixel, os perfis radiais em geral são bastante robustos. Propriedades diretas como a luminosidade, massa, idade e metalicidade estelar, quando vistas em perfil radial (Figura 3.6), mantêm o mesmo formato com pouca dispersão, exceto nas regiões mais afastadas do núcleo, onde há poucas zonas. Na verdade, qualquer forma de média espacial que envolva *pixels* (ou zonas) suficientes deverá levar a uma diminuição na incerteza.

O artigo também explora os efeitos da escolha da base de SSPs nos resultados do ajuste. Em geral, bases diferentes levam a resultados consistentes. Pode-se ver na Figura 3.7 que a idade estelar média ponderada pela luminosidade, a atenuação e a massa estelar inicial têm uma concordância

⁶Adicionando componentes lineares em comprimento de onda, a fim de emular uma má calibração de fluxo.

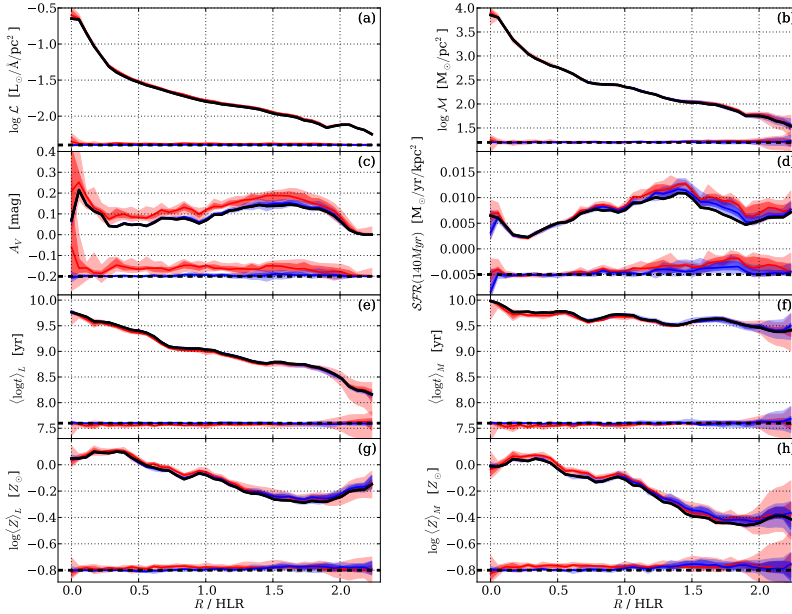


Figura 3.6: Incerteza nos perfis radiais de algumas propriedades. (a) Luminosidade superficial a 5635 \AA , corrigida de extinção. (b) Densidade superficial de massa. (c) Atenuação na banda V. (d) Taxa de formação estelar (últimos 140 Ma) por unidade de área. (e) Idade estelar média ponderada pela luminosidade. (f) Idade estelar média ponderada pela massa. (g) Metalicidade estelar média ponderada pela luminosidade. (h) Metalicidade estelar média ponderada pela massa. As linhas em preto marcam a solução original. Em faixas azuis e vermelhas, as distribuições das realizações com ruído aleatório, e sistemático em cor, respectivamente. A diferença entre as simulações e o original está desenhada abaixo de cada painel, com o zero marcado pela linha tracejada. Retirado de Cid Fernandes et al. (2014, figura 4), Apêndice D.2.

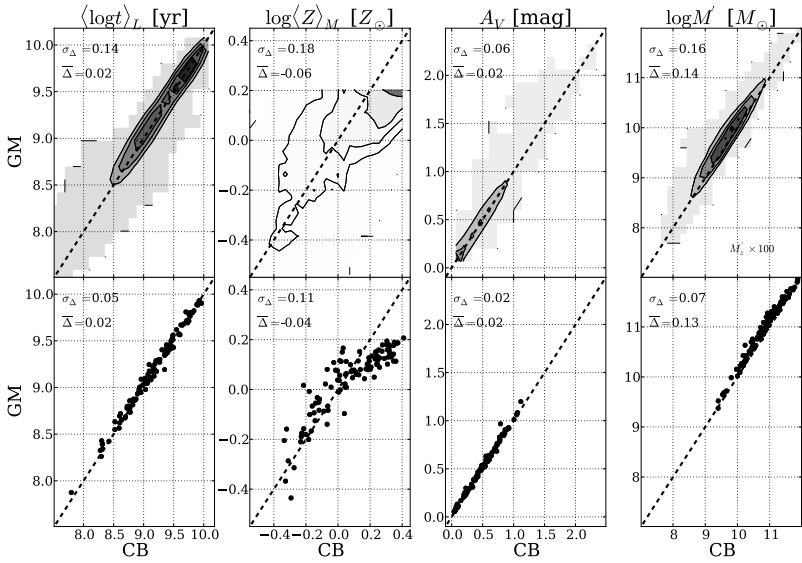


Figura 3.7: Comparação de propriedades obtidas com o ajuste utilizando as bases GM (eixo vertical) CB (eixo horizontal). Os painéis superiores mostram um histograma 2-D com contornos para propriedades de cada pixel de 107 galáxias do CALIFA. Da esquerda para a direita: idade estelar ponderada pela luminosidade, metalicidade estelar ponderada pela massa, atenuação na banda V, massa estelar inicial. Os painéis inferiores mostram a distribuição das mesmas propriedades, porém calculadas para o espectro integradas das galáxias. Retirado de Cid Fernandes et al. (2014, figura 9), Apêndice D.2.

muito boa entre as bases. As metalicidades médias mostram uma correlação, mas com uma dispersão muito grande, certamente devido a diferenças nas trajetórias evolucionárias dos modelos, poucos valores de metalicidade na base, e diferenças na metalicidade máxima da base. A incerteza nestas propriedades mencionadas acima é cerca de 2 vezes maior do que as calculadas adicionando ruído aleatório. Claramente a escolha de uma base adequada é de grande importância para a análise.

3.2.3 Artigo: *The Evolution of Galaxies Resolved in Space and Time: A View of Inside-out Growth from the CALIFA Survey*

Em Pérez et al. (2013) se estuda o crescimento de dentro para fora de 105 galáxias do CALIFA. O estudo se baseia na síntese espectral com o STARLIGHT, e segue exatamente a mesma prescrição de Cid Fernandes et al. (2014), descrita na Seção 3.2.1. O artigo está reproduzido na íntegra no Apêndice D.3.

Galáxias vêm em todos os tamanhos. Para determinar o crescimento, as distâncias são normalizadas utilizando o raio onde a luminosidade cumulativa (em 5635 \AA) alcança 50% da luminosidade total da galáxia, denominado R_{50} (ou HLR⁷). As galáxias da amostra são separadas em caixas com 15 galáxias cada, segundo a sua massa. O crescimento em massa em função do tempo é calculado para cada pixel de cada galáxia e somado em cada caixa de massa.

A Figura 3.8 ilustra o crescimento de massa em anéis crescentes em raio ($0,1 R_{50}$, $0,5 R_{50}$, $1 R_{50}$ e $> 1 R_{50}$). Em cada painel, o tempo passa da direita para a esquerda, e a massa estelar, normalizada, cresce desde zero (direita, em preto) até 1 (esquerda, em branco). Se vê claramente que galáxias menos massivas, na parte inferior das figuras, têm um crescimento gradual mais ou menos constante em todos os raios. As galáxias mais massivas, na parte superior das figuras, apresentam um crescimento muito rápido nas regiões centrais, enquanto as regiões externas crescem mais gradualmente. As linhas azul, verde e vermelha, em cada painel, representam cortes horizontais na caixa de mais baixa massa, no intermediário e no de mais alta massa, respectivamente, para facilitar a visualização. A mudança de regime ocorre em $\log M_{\star} = 10,83$, ou seja, uma massa de $\sim 7 \times 10^{10} M_{\odot}$. Vários estudos indicam esta faixa como uma “massa especial”, onde a taxa de formação estelar alcança valores altos muito rapidamente. De qualquer forma, esta é uma

⁷Half Light Radius.

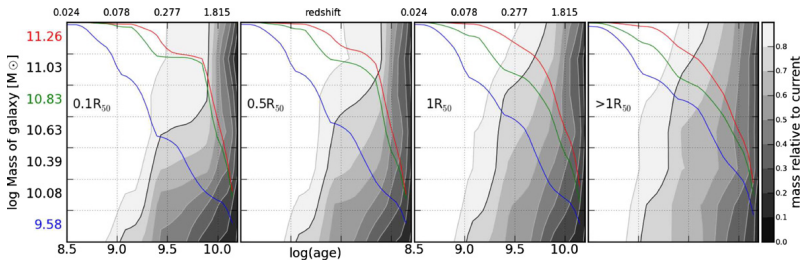


Figura 3.8: Crescimento de massa estelar de dentro para fora. As 105 galáxias foram separadas em grupos de 15, em massa, formando as caixas do eixo vertical. Os painéis mostram o crescimento da massa em escala de cinza, normalizado, em função do tempo e da massa das galáxias. O contorno em preto marca 80%. Da direita para a esquerda se vê as regiões em raio $r < 0,1 R_{50}$, $0,1 < r \leq 0,5 R_{50}$, $0,5 < r \leq 1 R_{50}$ e $r > 1 R_{50}$. Para facilitar a visualização da forma da variação temporal, as linhas azuis, verdes e vermelhas em cada painel mostram um corte horizontal nas caixas inferior, intermediário e superior, com escala de 0 a 1. Retirado de Pérez et al. (2013, figura 9), Apêndice D.3.

evidência observacional de algo que já se suspeita há muito tempo: que as galáxias massivas se formaram de dentro para fora.

3.2.4 Artigo: *The star formation history of CALIFA galaxies: Radial structures*

O artigo por González Delgado et al. (2014b) faz um estudo detalhado da estrutura radial de diversas propriedades de 107 galáxias do CALIFA. O artigo está reproduzido na íntegra no Apêndice D.4. Um dos resultados mais importantes é que a densidade superficial de massa estelar e idade estelar média ponderada por luminosidade, medidas a $1 R_{50}$, são representativos das médias da galáxia como um todo. A Figura 3.9 mostra a correlação entre os valores em três raios distintos e o global para a idade estelar média ponderada pela luminosidade (esquerda) e a densidade superficial de massa estelar (centro). Valores a $1 R_{50}$, marcado como HLR nas figuras, coincidem em geral com a média global da galáxia. Ainda na mesma figura pode-se ver a correlação entre a densidade superficial de massa estelar média da galáxia e a massa estelar total da galáxia. Este resultado está de acordo com Kauffmann et al. (2003),

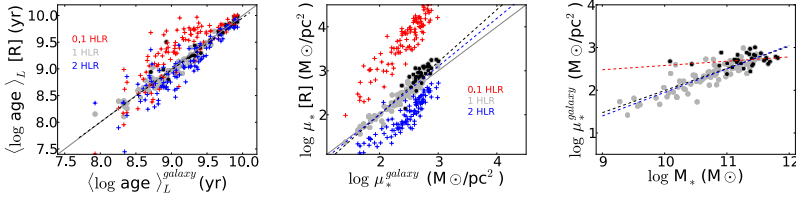


Figura 3.9: Esquerda: correlação entre a idade estelar média ponderada pela luminosidade em $1 R_{50}$ (círculos cinza), $0,1 R_{50}$ (cruzes azuis), $2 R_{50}$ (cruzes vermelhas) e a média da galáxia. Pontos em preto marcam galáxias esferoidais, com $C \geq 2,8$. Meio: o mesmo gráfico para a densidade superficial de massa estelar. Direita: correlação entre a densidade superficial de massa média da galáxia e a massa estelar total da galáxia. As linhas tracejadas mostram o ajuste linear total (preto), apenas discos (azul), e apenas para esferoidais (vermelho). Retirado de González Delgado et al. (2014b, figura 6), Apêndice D.4.

usando a amostra do SDSS.

O raio contendo metade da massa estelar (HMR⁸) é em média 20% menor que R_{50} (HLR). A razão entre HMR e HLR tem correlação com a massa total da galáxia e o tipo morfológico. Na Figura 3.10 pode-se ver que a relação HMR/HLR diminui com a massa estelar para galáxias com massa menor que $10^{11} M_{\odot}$, enquanto permanece constante para galáxias mais massivas. Um comportamento similar ocorre com o tipo morfológico: em galáxias com disco a relação HMR/HLR diminui com a massa, e em galáxias esferoidais a relação é aproximadamente constante.

Para galáxias esferoidais, o gradiente de idade depende mais da massa estelar total da galáxia do que da densidade superficial de massa estelar, que, conforme o painel inferior esquerdo da Figura 3.11, é aproximadamente constante. A massa total da galáxia é a propriedade mais fundamental para galáxias esferoidais, enquanto a densidade superficial de massa é mais importante para as galáxias com disco.

⁸Half Mass Radius.

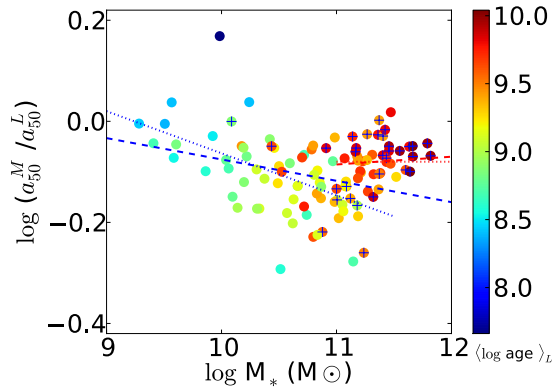


Figura 3.10: Relação entre a_{50}^M/a_{50}^L e a massa estelar total. A cor dos pontos reflete a idade estelar média ponderada pela luminosidade, em $0,5 a_{50}^L$. Galáxias com índice de concentração $C \geq 2,8$ estão marcadas com uma cruz. A linha azul mostra o ajuste linear para galáxias com massa estelar. Retirado de González Delgado et al. (2014b, figura 10), Apêndice D.4.

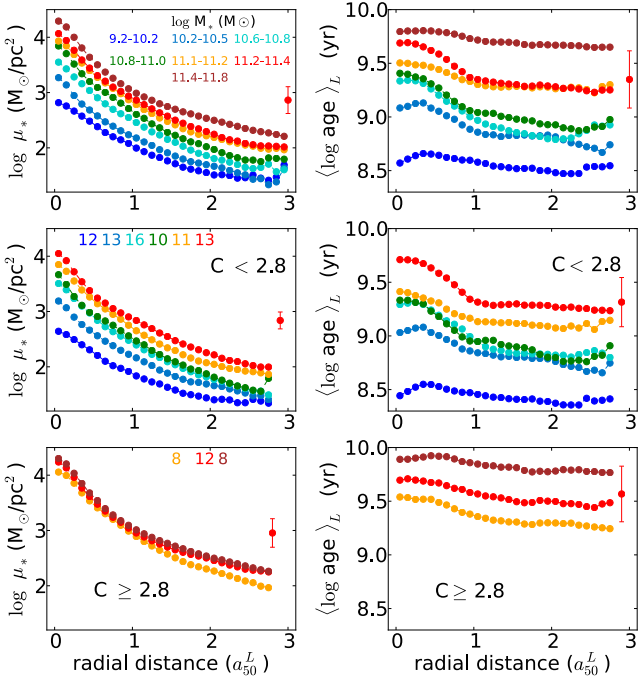


Figura 3.11: Perfis radiais da densidade superficial de massa estelar (esquerda) e idade estelar média ponderada pela luminosidade (direita), para caixas de massa estelar contendo 15 galáxias cada. Cima: todas as galáxias. As caixas em massa estão codificadas em cores. Meio: galáxias dominadas por disco. Baixo: galáxias esferoidais ($C \geq 2,8$). Retirado de González Delgado et al. (2014b, figura 13), Apêndice D.4.

Morfologia de galáxias

A descoberta das formas das galáxias, e a sua separação em classes segundo a sua morfologia, somente se tornou uma ciência séria quando *surveys* fotográficos extensos começaram a ser realizados (Sandage et al. 1975). Pode-se considerar o ano de 1845 como um marco inicial no estudo da forma das galáxias, quando Lord Rosse, observando com o telescópio refletor de 72 polegadas no Castelo de Birr, descobriu estruturas espirais em M51 (Galáxia do Redemoinho, no catálogo de Messier). À época, pouco se sabia sobre a natureza das “nebulosas espirais” e os esquemas de classificação eram puramente descritivos como o de Wolf (1908), mostrado na Figura 4.1. Knox-Shaw (1915), entre outros, chamou a atenção para nebulosas sem braços espirais, que viam a ser chamadas mais tarde de elípticas. Curtis (1918) foi o primeiro a identificar espirais com barra. Em meados de 1940 já se havia descoberto a maioria dos tipos mais comuns das “nebulosas extragaláticas”, termo que já começava a cair em desuso em favor do nome mais glamouroso, segundo o próprio Hubble (1936): “galáxias”.

Neste capítulo é feita uma breve introdução sobre a morfologia de galáxias. O objetivo é compreender e descrever quantitativamente uma galáxia segundo a sua forma. Daqui saem as ferramentas e a motivação para a decomposição morfológica espectral, estudada nos Capítulos 6 e 7. A decomposição, conforme será visto na Seção 4.2.3, requer uma boa PSF¹. Por isso, é feito pequeno desvio no Capítulo 5 para caracterizar a PSF do CALIFA.

4.1 Classificação de Hubble

O primeiro sistema amplamente utilizado de classificação de galáxias segundo a sua morfologia foi o de Hubble (1926). Neste sistema, as galáxias são separadas nas classes elíptica, espiral, espiral com barra e irregular. As

¹*Point Spread Function.*

4. Morfologia de galáxias

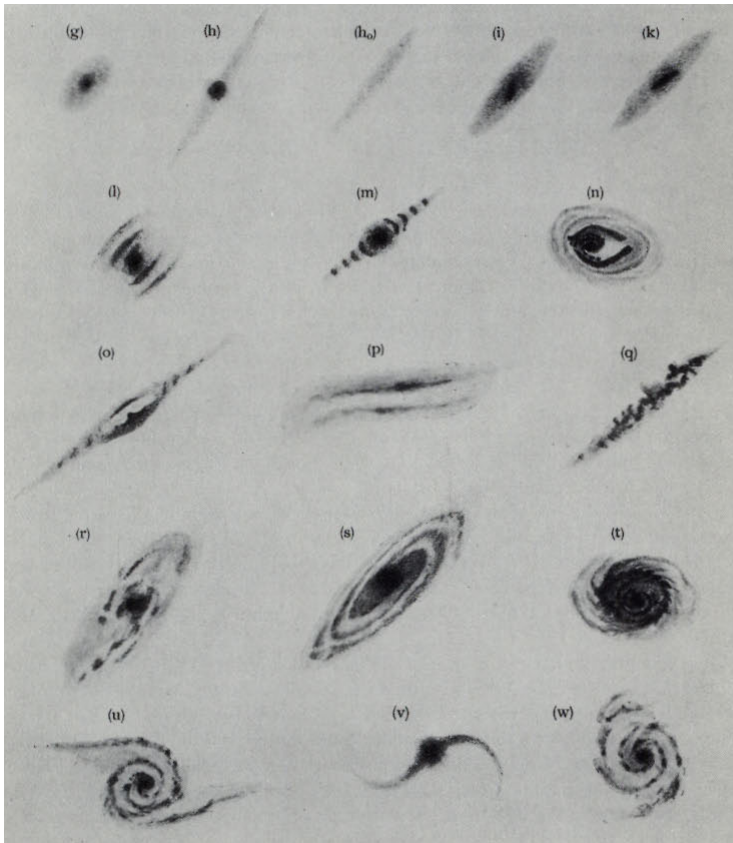


Figura 4.1: Sistema de classificação descritivo de nebulosas por Wolf (1908), apresentava também nebulosas galácticas (na primeira linha, que foi removida). Reproduzido de Sandage et al. (1975).

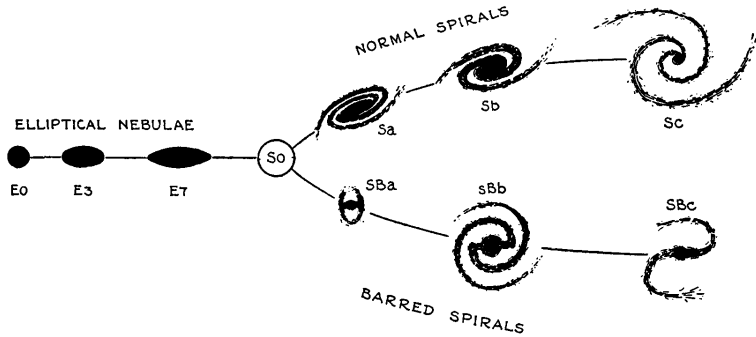


Figura 4.2: Sistema de classificação de Hubble (1936), também conhecido como “diagrama diapasão de Hubble”. Foi atualizado por Sandage et al. (1975), de onde se reproduz a figura, para incluir a classe S0 na intersecção dos ramos das espirais.

elípticas são classificadas segundo o seu formato, desde esférico até mais alongado. As espirais são classificadas conforme o tamanho relativo do bojo e as características dos braços (quantidade, grau de espiralamento e granularidade). A forma final de classificação de Hubble é frequentemente ilustrada pelo “diagrama diapasão”, apresentado na Figura 4.2, do clássico *The Realm of the Nebulae* de Hubble (1936), e atualizado (incluindo a classe S0 na intersecção dos ramos das espirais) por Sandage et al. (1975).

O sistema de Hubble parece ser mais do que um simples “catálogo botânico” de galáxias. Muitas das propriedades observadas das galáxias, como índices de cor, tipo espectral e densidade de hidrogênio gasoso, variam sistematicamente na sequência de formas. De algum modo, parece haver algo de fundamental escondido nesta classificação baseada apenas na forma, que talvez indique uma relação com as condições iniciais e subsequente evolução temporal das galáxias (Sandage et al. 1975). Estas correlações fizeram com que, durante muito tempo, a sequência de Hubble fosse considerada uma sequência evolutiva, onde as galáxias eram inicialmente elípticas, passavam a ser lenticulares e depois espirais. Isto sobrevive até hoje na nomenclatura “*early type*” (tipo jovem, ou primeiras galáxias) para elípticas e lenticulares, e “*late type*” (tipo tardio, ou galáxias recentes) para espirais e irregulares.

4. Morfologia de galáxias

Entretanto, Hubble (1927) enfatizou desde o início que a classificação era puramente empírica, e que interpretações de natureza evolutiva deveriam ser tomadas com cautela.

4.2 Componentes estruturais

Os sistemas de classificação descritos na seção anterior são baseados em inspeção visual, com natureza evidentemente qualitativa. Levando tal forma de classificação a um extremo, como o projeto *GalaxyZoo* (Lintott et al. 2008; Willett et al. 2013), chegam-se a conclusões estatísticas, mas ainda não se obtêm medidas quantitativas de objetos individuais. Para descrever mais precisamente a estrutura de uma galáxia, normalmente é necessário decompô-la em subestruturas. Estas subestruturas são em geral modeladas como funções analíticas, as quais permitem derivar medidas quantitativas. De forma simplificada, podemos considerar que galáxias são compostas de duas componentes principais: bojo e disco. Os próprios discos podem conter barras, braços espirais e anéis, para citar algumas subcomponentes mais comuns.

4.2.1 Bojos e discos

Do ponto de vista fotométrico (medindo o perfil de brilho superficial), galáxias lenticulares (S0) e espirais *early type* (Sa-Sb) podem ser bem descritas como uma combinação de duas componentes: um bojo e um disco. Neste modelo, o disco é delgado enquanto o bojo é quase esférico (embora haja casos em que ele seja um elipsoide triaxial), ambos observados projetados no plano do céu.

Levando em consideração apenas o perfil de brilho superficial, a separação em componentes baseado no aspecto visual parecer arbitraria. Afinal, pode-se inventar algum modelo empírico onde uma só componente descreva as imagens observadas tão bem quanto a soma de um bojo e um disco. Porém, estas componentes parecem ter outras propriedades distintas, como índices de cor, conteúdo de gás e poeira, cinemática e populações estelares, o que confere uma certa confiança no conjunto de componentes escolhido.

King (1966) descreve um modelo derivado para aglomerados globulares, assumindo velocidades estelares isotérmicas e isotrópicas. Muito embora este modelo tenha motivações físicas, ele não possui uma forma funcional simples. Leis como as de Hubble-Reynolds (Binney & Tremaine 2011, equação 2.55) e de Vaucouleurs (1948, 1977), mesmo sendo puramente empíricas,

descrevem bem bojos de galáxias. Suas formas funcionais são:

$$I(r) = \frac{I_0}{[1 + (r/r_H)^2]} \text{ (Hubble-Reynolds)}$$

$$I(r) = I_e \exp \left\{ -7,67 \left[\left(\frac{r}{r_e} \right)^{1/4} - 1 \right] \right\} \text{ (de Vaucouleurs)}$$

Os termos r_e e r_H são os parâmetros de escala radial, I_0 é o brilho para $r=0$ na lei de Hubble-Reynolds e I_e é o brilho para $r = r_e$ na lei de de Vaucouleurs. Estas formas funcionais se ajustam bem à maioria dos bojos e galáxias elípticas. Para sistemas que não são esféricos, deve-se ainda introduzir uma elipticidade e uma orientação. Adicionalmente, a elipticidade e a orientação podem variar com o raio.

Discos, por outro lado, são facilmente modelados como um perfil exponencial (Freeman 1970) dado por

$$I(r) = I_0 \exp \left(-\frac{r}{h} \right),$$

com h sendo o parâmetro de escala radial, e I_0 o brilho em $r=0$.

Sérsic (1963) mostra que os perfis de de Vaucouleurs e exponencial podem ser tomados como casos particulares da equação

$$I(r) = I_e \exp \left\{ -b_n \left[\left(\frac{r}{r_e} \right)^{1/n} - 1 \right] \right\},$$

que ficou conhecida como “lei de Sérsic”. Aqui, o parâmetro n é o índice de concentração, também chamado de “índice de Sérsic”, que pode variar continuamente. A Figura 4.3 mostra alguns exemplos. Com $n = 1$ obtém-se uma lei exponencial (linha azul), e com $n = 4$ a lei de de Vaucouleurs (linha vermelha). A maioria dos bojos de espirais e galáxias elípticas podem ter seus perfis de brilho ajustados com índices de Sérsic na faixa de $1 < n < 10$. Valores maiores de n mudam muito pouco a forma da curva. O termo b_n está definido em função de n , ver a seção 6.1.5 de Erwin (2015).

É preciso ter em mente que estas leis são empíricas, e dependem do bom senso de escolher o perfil (ou conjunto de perfis) certo para a galáxia em questão. Tentar ajustar um modelo inapropriado a uma galáxia pode levar a conclusões equivocadas, embora o ajuste possa parecer bem sucedido.

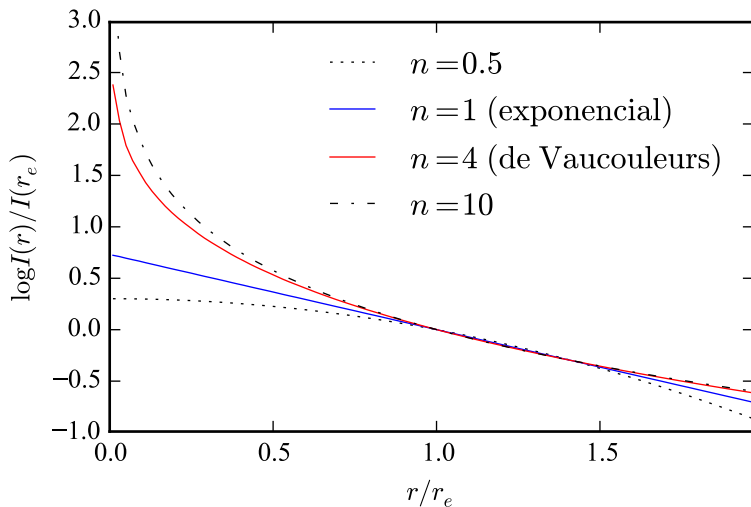


Figura 4.3: Perfis empíricos de Sérsic. O índice n controla a concentração do perfil. Com $n = 1$ obtém-se um perfil exponencial (azul), e com $n = 4$ um perfil de de Vaucouleurs (vermelho). Outros valores de n são mostrados em linhas descontínuas.

4.2.2 Dependência dos modelos com o comprimento de onda

Tudo o que se discutiu sobre classificação de galáxias quanto à sua forma, até agora, levou em conta imagens feitas na banda óptica do espectro. Basta olhar umas poucas galáxias em infravermelho ou ultravioleta para verificar que a forma de uma galáxia pode mudar dramaticamente dependendo do comprimento de onda em que se observa. Bojos normalmente desaparecem em ultravioleta por possuírem poucas estrelas jovens. Já em infravermelho, os bojos tendem a dominar, e discos podem ter uma forma bastante diferente por conta da menor profundidade óptica das estruturas de poeira. Claramente há uma dependência da morfologia das galáxias com o comprimento de onda.

Kelvin et al. (2012) utilizou imagens de galáxias do projeto GAMA (Driver et al. 2009) em 9 bandas espectrais, do óptico (Abazajian et al. 2009, bandas *ugriz* do SDSS DR7) ao infravermelho (Lawrence et al. 2007, bandas

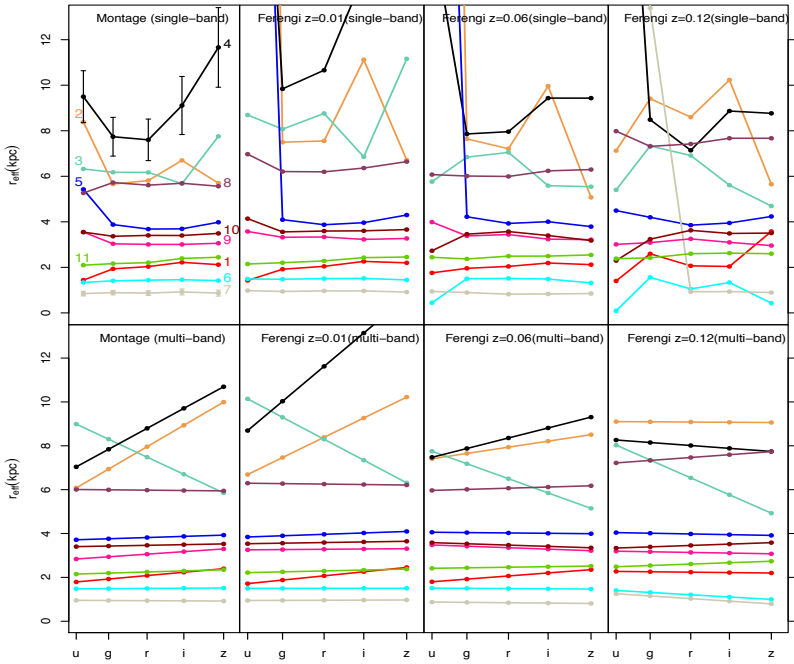


Figura 4.4: Ajuste morfológico de 11 galáxias, utilizando as bandas fotométricas do SDSS. Os gráficos mostram o raio efetivo (r_e neste trabalho) ajustado livremente a cada banda (painéis superiores), e com uma dependência linear em comprimento de onda (painéis inferiores). À esquerda estão os ajustes com as imagens originais, as colunas seguintes são para imagens com *redshift* artificiais. Retirado de Vika et al. (2013).

YJHK do UKIDSS), para ajustar perfis de Sérsic a mais de 160.000 galáxias, encontrando gradientes leves no índice de Sérsic em função do comprimento de onda. Os ajustes para cada comprimento de onda foram feitos individualmente. O projeto MegaMorph (Häußler et al. 2013) faz o mesmo de uma forma um pouco mais refinada. Utilizando as bandas fotométricas do SDSS, eles ajustam a variação dos parâmetros morfológicos com o comprimento de onda através de um polinômio (Vika et al. 2013, Figura 4.4). Todos os comprimentos de onda são ajustados de uma vez. Aí se pode ver que em grande escala (em comprimento de onda), há galáxias com um comportamento linear (ou até razoavelmente constante) em r_e . Nestes casos, utilizar um modelo linear em função do comprimento de onda, segundo os autores, melhora a qualidade do ajuste.

Além de efeitos causados pelo método de ajuste, como má escolha do modelo, mudança no sinal-ruído nas várias bandas espectrais, ou mínimos locais, parece haver motivos reais para levar a sério a variação dos parâmetros morfológicos com o comprimento de onda. Populações estelares diferentes emitem mais intensamente em comprimentos de onda distintos, com populações mais jovens dominando em comprimentos de onda menores. Isto parece causar um leve gradiente no índice de Sérsic em galáxias *early type* (La Barbera & de Carvalho 2009). Poeira parece afetar a medida do tamanho e forma de discos (Möllenhoff et al. 2006). O conteúdo e a distribuição de poeira pode variar significativamente de galáxia a galáxia, dificultando uma conclusão global sobre o seu efeito nos parâmetros morfológicos.

Johnston et al. (2012) obtiveram espectros de fenda longa de galáxias lenticulares (S0), gerando assim perfis de brilho unidimensionais das galáxias para cada comprimento de onda. Ajustando um perfil de de Vaucouleurs e um exponencial ao perfil de brilho de cada uma das galáxias (em ambos os lados do núcleo), eles obtêm os espectros separados de cada um dos seus dois componentes morfológicos, como mostrado na Figura 4.5. Com os espectros, pode-se tentar entender que populações estelares compõem o bojo e o disco destas galáxias. Os autores estimam a idade e a metalicidade estelar das componentes utilizando a intensidade da linha H β e do tripleto de magnésio, comparando com uma grade de modelos sintéticos de populações estelares. A conclusão que chegam é que os bojos são sistematicamente mais jovens e mais metálicos do que os discos (Figura 4.6). Inspirado neste estudo, os Capítulos 6 e 7 descrevem a decomposição de espectros de galáxias em espectros de bojos e discos, mas utilizando cubos de dados do CALIFA.

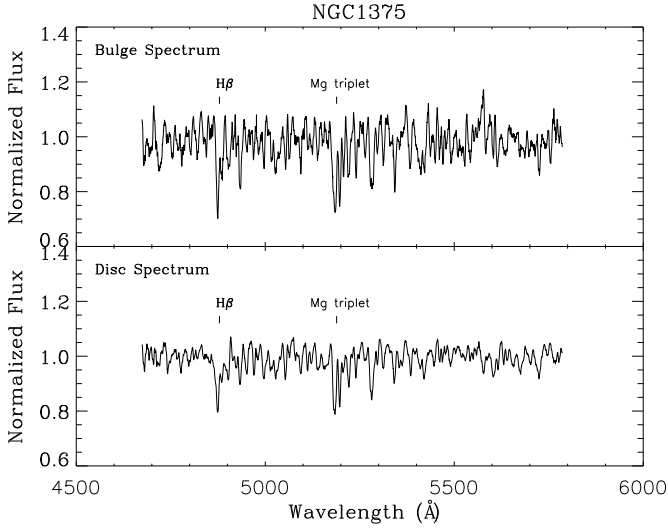


Figura 4.5: Espectros unidimensionais de bojo (acima) e disco (abaixo) de NGC 1375. É possível reconhecer a linha espectral H β e o tripleto de magnésio, em absorção. Retirado de Johnston et al. (2012).

4.2.3 Ajuste de modelos

Utilizam-se geralmente algoritmos de minimização para encontrar os modelos que melhor ajustam o perfil de brilho de uma galáxia. A abordagem usual é baseada no princípio de máxima verossimilhança (\mathcal{L}). Se a estatística das medidas é gaussiana (que é aproximadamente verdade na maioria das imagens astronômicas relevantes ao ajuste de modelos), o logaritmo da verossimilhança se assemelha à familiar soma de χ^2 (Erwin 2015, seção 4.1.2). Isto significa que o problema passa a ser a minimização da equação

$$-2 \ln \mathcal{L} = \chi^2 = \sum_i^N \frac{(d_i - m_i)^2}{\sigma_i^2},$$

onde d_i é o valor medido, m_i é o valor do modelo, e σ_i é o erro gaussiano na medida. O modo como se procura o mínimo χ^2 vai depender de como se aborda o problema.

4. Morfologia de galáxias

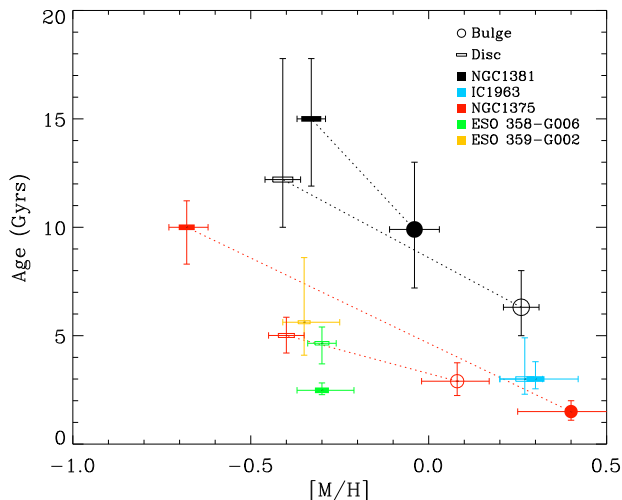


Figura 4.6: Idade (eixo vertical) e metalicidade (eixo horizontal) estelares de bojos (marcadores redondos) e discos (marcadores retangulares) de uma amostra de galáxias S0 observadas com espectrógrafo de fenda longa. As linhas pontilhadas ligam componentes de uma mesma galáxia. Retirado de Johnston et al. (2012).

A Figura 4.7 mostra um exemplo de ajuste de bojo e disco em um perfil de brilho unidimensional. Pode-se fazer o ajuste diretamente na imagem, em duas dimensões (Figura 4.8), utilizando modelos com perfis elipsoidais. Independente da escolha do modelo, há um aspecto importante do ajuste da morfologia que foi negligenciado até agora: efeitos instrumentais e atmosféricos. Estes efeitos são representados pela figura da PSF, tratada em detalhes no Capítulo 5. A grosso modo, levar em conta a PSF significa considerar que a luz que atinge determinada posição no detector não é proveniente apenas de uma região pontual no céu, e sim de uma região extensa que depende dos instrumentos e da turbulência atmosférica. Efetivamente, objetos pontuais tornam-se “borrões” na imagem observada.

Pode-se evitar tocar neste ponto quando se faz o ajuste em uma dimensão. Se as dimensões da PSF forem muito menores do que as da galáxia,

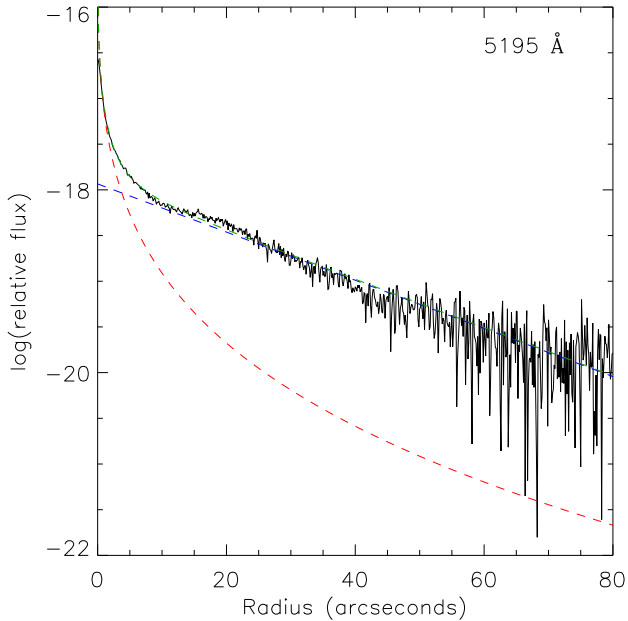


Figura 4.7: Ajuste morfológico em uma dimensão, utilizando modelos de bojo e disco. A linha preta mostra o perfil de brilho da galáxia NGC 1375 em 5195 Å, obtido através de espectroscopia de fenda longa. Em azul um perfil exponencial e em vermelho um perfil de De Vaucouleurs (Sérsic com $n = 4$), que somados são o melhor ajuste, em verde. Retirado de Johnston et al. (2012).

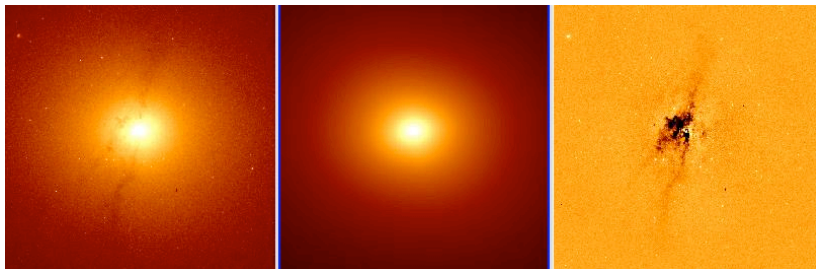


Figura 4.8: Ajuste morfológico em duas dimensões, feito com o programa GALFIT. Retirado de (Peng et al. 2002).

e esta tiver uma imagem suave, a forma da galáxia muda muito pouco devido à PSF, exceto exatamente sobre o núcleo. Isto é especialmente problemático em *early types*, onde um perfil de Sérsic pode gerar um pico de várias ordens de magnitude, concentrado em uns poucos em *pixels*. A forma mais simples de se escapar da PSF, em uma dimensão, é “varrê-la para baixo do tapete”, isto é, não tentar ajustar pontos muito próximos ao núcleo (mascarando alguns segundos de arco, dependendo do tamanho da PSF). O ajuste de um perfil de Sérsic pode ficar comprometido em casos onde a PSF é muito grande e se descarta uma fração considerável do bojo.

Em duas dimensões o mais adequado é adotar a PSF como parte do problema. Uma boa caracterização da PSF é crucial para se obter resultados satisfatórios no ajuste. Mas trabalhar com a PSF traz um custo computacional enorme, uma vez que é preciso efetuar um cálculo de convolução (ver Seção 5.1) cada vez que se avalia o modelo para um determinado conjunto de parâmetros. O problema de minimização, que já é de natureza não linear para modelos de componentes de galáxia, torna-se ainda mais complicado.

Diversos algoritmos foram desenvolvidos para tratar do problema de minimização não linear. O método Levenberg-Marquardt (Levenberg 1944; Marquardt 1963, daqui em diante L-M), com sua busca através do gradiente no espaço de parâmetros, tem a vantagem de ser muito rápido. Mas sua própria natureza de gradiente faz com que seja necessário um bom “chute inicial”, com a possibilidade de ficar preso em mínimos locais. Pode-se reduzir a chance de ser pego em mínimos locais utilizando algoritmos mais complexos, como o Nelder-Mead *simplex* (Nelder & Mead 1965, daqui em diante

N-M). A desvantagem é que, conforme se vai aumentando a complexidade do algoritmo, o tempo necessário para encontrar o mínimo tende a crescer drasticamente. De qualquer modo, tanto o L-M quanto o N-M sofrem de um problema comum: é preciso especificar um valor inicial, e o algoritmo segue um ou mais caminhos até encontrar o mínimo. O algoritmo de Metropolis (Metropolis et al. 1953; Saha & Williams 1994) adota uma abordagem Bayesiana, e o problema de minimização se torna análogo a um problema de mecânica estatística, onde, combinado com uma técnica de *Simulated Annealing* (Kirkpatrick et al. 1983), baixa-se a temperatura até encontrar o estado de menor energia. São necessários apenas os limites do espaço de parâmetros, uma grande vantagem em casos onde não se sabe de antemão o modelo aproximado. Novamente troca-se velocidade por robustez, este algoritmo é significativamente mais lento do que L-M e N-M. *Differential Evolution* (Storn & Price 1997, daqui em diante DE) aborda o problema de forma completamente distinta. Nele, a busca através do espaço de parâmetros é feita com uma população de modelos. Os modelos sofrem “mutações” e “recombinações” em cada iteração, e somente os modelos que se saem melhor são mantidos. Algoritmos desta natureza são chamados genéticos. Como o algoritmo de Metropolis, apenas são necessários os limites do espaço de parâmetros. Outra vantagem é que é muito mais improvável que este algoritmo fique preso num mínimo local do que o L-M, o N-M ou mesmo o de Metropolis. Tudo isto cobra um grande preço: ele é o algoritmo mais lento considerado aqui, cerca de duas ordens de magnitude mais lento do que o L-M para este problema.

Existem diversas ferramentas utilizadas em astrofísica que implementam algum destes algoritmos para fazer o ajuste de modelos em imagens. Vale citar, por exemplo, *GALFIT3* (Peng et al. 2010) e *GASP2D* (Méndez-Abreu et al. 2008) utilizando L-M, *BUDDA* (de Souza et al. 2004) utilizando N-M, *GIM2D* (Simard et al. 2002) utilizando o algoritmo de Metropolis, e *IMFIT*² Erwin (2015), que utiliza L-M, N-M ou DE. O programa escolhido para o presente trabalho foi o *IMFIT*, em grande parte por ter seu código livre, e também por ter sido desenvolvido tendo em mente a facilidade de modificação. Entretanto, como a versão original foi feita em forma de um programa executado em linha de comando, não é muito prático utilizá-la em seu formato original para implementar as tarefas deste trabalho.

Foi feita uma versão modificada do *IMFIT* em forma de biblioteca dinâmica. Em seguida foi feito um código *wrapper*, em Python, que acessa todas as funções do *IMFIT*. Esta biblioteca, junto com o código *wrapper* foi

²<http://www.mpe.mpg.de/~erwin/code/imfit/index.html>

4. Morfologia de galáxias

chamada `PYTHON-IMFIT`³. Com ela pode-se fazer tudo que o `IMFIT` permite, mas em *arrays* numéricos do Python. Esta biblioteca é bastante genérica, e pode ser utilizada para qualquer aplicação de ajuste de imagem. Contudo, o mais importante é que a manipulação de modelos e o ajuste para múltiplas imagens deixa de ser um exercício tedioso de organização de *shell scripts*, passando a ser um programa de computador propriamente dito, com toda a maquinaria do Python a sua disposição. O programa resultante, que faz a decomposição em bojo e disco em um cubo de dados do CALIFA, é apresentado no Capítulo 7.

³<https://github.com/streeto/python-imfit>

Caracterizando a PSF do CALIFA

5.1 Efeitos instrumentais e atmosféricos

A PSF (sigla para *Point Spread Function*, em inglês) descreve a resposta de um sistema de imageamento a uma fonte pontual. Observando uma fonte pontual no infinito, que emite no comprimento de onda λ com uma lente ideal de diâmetro de abertura D , obtém-se uma imagem de diâmetro (em radianos) $\theta \approx 1,22 \frac{\lambda}{D}$. Esta imagem, conhecida como Disco de Airy, é a figura de interferência causada por uma abertura circular, e limita a resolução espacial teórica que se pode obter com um telescópio de uma dada abertura. Isto vale para desde câmeras e pequenos telescópios, até telescópios espaciais.

Para um telescópio suficientemente grande, na superfície terrestre, a figura de difração torna-se desprezível se comparada ao efeito causado pela turbulência atmosférica, conhecida como *seeing*. Telescópios com diâmetro a partir de ~ 20 cm já têm sua resolução espacial (no óptico) limitada pelo *seeing*¹. O modelo de Kolmogorov, baseado em estudos de turbulência e desenvolvido por Tatarskii (1961), descreve como as frentes de onda são perturbadas durante a passagem por células de turbulência atmosférica. Uma excelente revisão sobre a teoria da PSF é feita por Racine (1996). O perfil de Kolmogorov é dado pela transformada de Bessel da função de transferência de modulação atmosférica dado pelo modelo de Kolmogorov, e fica definido em função de uma integral sem forma fechada, devendo ser resolvida numericamente. Costumam-se utilizar formas funcionais que se aproximam do perfil de Kolmogorov. Gaussianas são usadas muito frequentemente, mesmo não sendo adequadas. O perfil de Moffat (1969) se ajusta bem ao perfil de Kolmogorov numa faixa de ~ 7 magnitudes em brilho superficial, muito além do que a maioria dos casos de uso requer, e tem uma forma bastante simples,

¹Desconsiderando telescópios que aplicam técnicas de óptica adaptativa, que não fazem parte do escopo deste trabalho.

5. Caracterizando a PSF do CALIFA

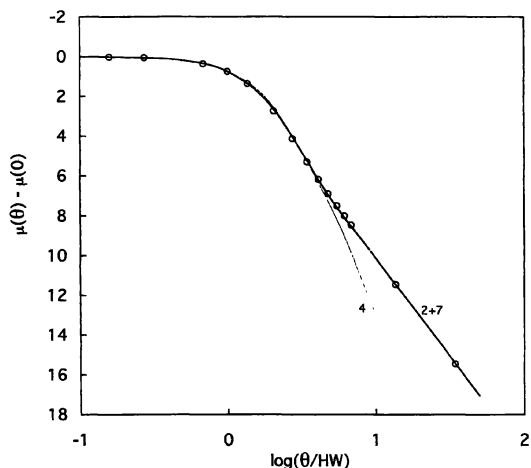


Figura 5.1: Ajuste de perfil de Moffat (linhas sólidas) ao modelo de PSF de Kolmogorov (círculos abertos). A linha fina, é um perfil de Moffat com $\beta=4$, e a linha espessa é a soma de dois perfis de Moffat, com $\beta=7$ (80 % do fluxo) e $\beta=2$ (20 % do fluxo). Retirado de Racine (1996).

dada por

$$I(r) = \frac{I_0}{\left[1 + \left(\frac{r}{\alpha}\right)^2\right]^\beta}, \quad \alpha = \frac{\text{FWHM}}{2\sqrt{2^{1/\beta} - 1}}.$$

Dois parâmetros controlam a forma da PSF neste perfil: a largura a meia altura (FWHM) e o índice β , que controla a intensidade das “asas” da PSF. Com $\beta \rightarrow \infty$, o perfil de Moffat torna-se uma gaussiana. O melhor ajuste ao perfil de Kolmogorov se obtém quando $\beta=4$ (Figura 5.1).

Se a PSF é constante em todo o campo, seu efeito na imagem pode ser calculado como a convolução entre a imagem da PSF e a imagem original. Isto tem um custo computacional extremamente elevado, especialmente quando se utiliza algum procedimento iterativo como um ajuste de modelo. Uma convolução, em cálculo numérico, significa calcular uma integral em duas dimensões para cada *pixel*, ou seja, escala com $O(n^2)$. Um truque bastante comum é utilizar transformadas de Fourier para simplificar este cálculo e transformá-lo num algoritmo que escala com $O(n \log n)$. Se I é a imagem

original e I^{PSF} a imagem da PSF, a imagem final I^* é dada por

$$I^* = I \otimes I^{\text{PSF}}.$$

Aplicando a transformada de Fourier,

$$\begin{aligned}\mathcal{F}\{I^*\} &= \mathcal{F}\{I \otimes I^{\text{PSF}}\} \\ &= \mathcal{F}\{I\} \cdot \mathcal{F}\{I^{\text{PSF}}\},\end{aligned}$$

ou seja, troca-se uma convolução por uma multiplicação. Para obter a imagem final, basta aplicar a transformada de Fourier inversa sobre o produto. A transformada de Fourier da PSF é sempre a mesma, logo a cada iteração apenas duas integrais numéricas em duas dimensões são necessárias: a transformada da imagem original e a transformada inversa para a imagem final. O ganho é tão significativo que praticamente todos os programas de ajuste de imagens astronômicas utilizam transformadas de Fourier para convoluir a imagem.

5.2 Medindo a PSF

Para determinar as características da PSF, idealmente é preciso observar um objeto pontual brilhante, em várias regiões do campo do detector, e com as mesmas condições atmosféricas que as observações. Raramente estas condições são preenchidas, mesmo para fotometria CCD com campos muito grandes. Assim, conhecer a PSF em instrumentos IFU não é uma tarefa trivial. Ainda há o fato de que as imagens são reconstruídas através de técnicas de *dithering* (ver Seção 2.1.1), e, dependendo o algoritmo utilizado, a PSF pode nem sequer ser analítica. Entretanto, é preciso de algum modo obter uma aproximação da forma da PSF para poder modelar a morfologia de uma galáxia (Capítulo 4), especialmente o seu bojo. O procedimento descrito a seguir é mais um esforço para entender a PSF e poder realizar a decomposição morfológica do que um estudo aprofundado sobre o tema.

Para o CALIFA, observar campos estelares para caracterizar a PSF significaria a redução no número de galáxias na amostra final do *survey*. Dadas as restrições de tempo de telescópio e de significância estatística da amostra, além do fato de a PSF não ser fundamental para os casos científicos alvo do *survey*, estas observações não foram realizadas. Porém, sendo um *survey* espectroscópico, o CALIFA necessita de observações de “velas padrão” para calibrar o fluxo das galáxias. Foram observadas 45 estrelas para este fim,

5. Caracterizando a PSF do CALIFA

as quais foram reaproveitadas aqui para análise da PSF. Estas estrelas se encontram no centro no campo de observação do instrumento, com um tempo de exposição muito menor do que o das galáxias (120 s contra 900 s). Esta amostra foi denominada “estrelas de calibração”. Alternativamente, pode-se procurar estrelas que apareçam na frente das galáxias do *survey*. Neste caso a vantagem é que as estrelas têm o mesmo tempo de exposição das galáxias, e são observadas nas mesmas condições atmosféricas. Porém, não se encontram estas estrelas intronmetidas em todos os cubos, logo obter uma PSF para cada um deles está descartado. Outro problema em potencial é que elas em geral, por construção do *survey*, são fracas e se localizam na periferia do campo de observação. Esta amostra foi denominada “estrelas de campo”, com 9 estrelas suficientemente brilhantes escolhidas em cubos de galáxias *early type*. As duas amostras de estrelas reaproveitadas foram usadas para caracterizar a PSF do CALIFA com o procedimento descrito a seguir.

O modelo utilizado foi um perfil de Moffat 2-D elipsoidal, com $\beta=4$, conforme visto na Seção 5.1. Os cubos foram combinados em caixas de 400 Å de largura, gerando 10 imagens de fluxo e incerteza para cada estrela. Estas imagens foram ajustadas aos modelos através de um programa desenvolvido utilizando a biblioteca PYTHON-IMFIT². O resultado do ajuste são os parâmetros do perfil de Moffat e a estatística χ^2 do melhor modelo. A Figura 5.2 ilustra o ajuste feito para uma estrela de calibração, numa faixa espectral próxima a 5000 Å.

Este procedimento foi realizado para as 45 estrelas de calibração, e o resultado pode ser visto na Figura 5.3. Praticamente não há dependência da PSF com o comprimento de onda, como se pode verificar no painel superior da figura. Na mesma figura, no painel inferior, mostra-se um histograma ponderado pela verossimilhança ($e^{-\chi^2/2}$) de todos os ajustes (todas as estrelas em todas as caixas de comprimento de onda). Desta distribuição obtém-se uma largura a meia altura média de $\text{FWHM} = 2,888 \pm 0,332''$. A elipticidade ($\epsilon = 1 - b/a$) média encontrada é de $\epsilon = 0,097 \pm 0,065$, ou seja, a PSF é praticamente circular. A incerteza nos dois casos representa o desvio padrão (1σ) da média ponderada. O mesmo vale para todas as incertezas obtidas no resto desta seção.

O mesmo procedimento foi realizado para as 9 estrelas de campo, presentes nos cubos de galáxias do *survey* e normalmente mascarados por não serem de interesse no estudo do espectro das galáxias. As estrelas desta amos-

²PYTHON-IMFIT é uma biblioteca baseada no programa IMFIT de Erwin (2015), a mesma utilizada no programa de decomposição morfológica, ver Seção 4.2.2.

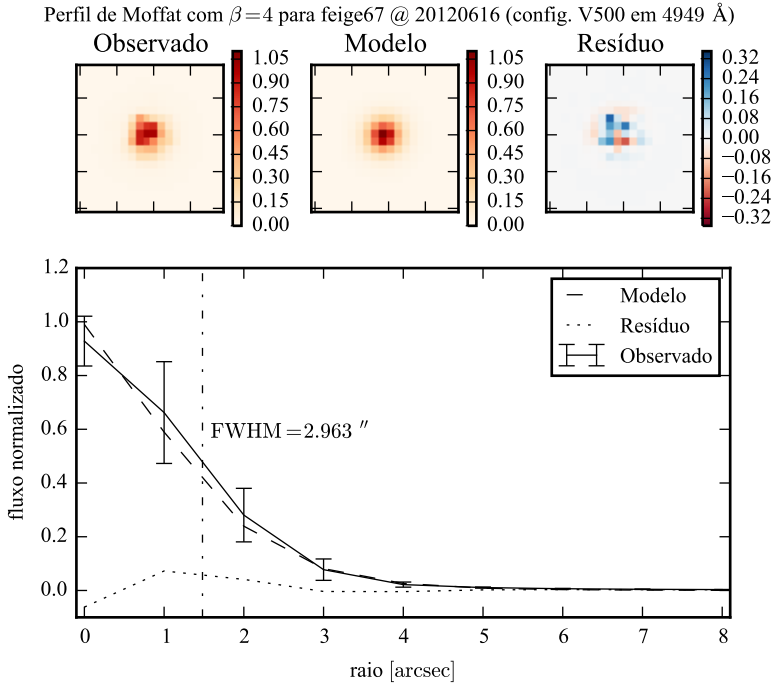


Figura 5.2: Exemplo de ajuste de PSF para a estrela de calibração Feige67, observada em 16/06/2012, com a configuração V500. O modelo ajustado foi um perfil de Moffat elipsoidal com $\beta = 4$. Nos painéis superiores estão imagens do fluxo observado numa caixa de 400 \AA centrada em 4949 \AA , do modelo ajustado e do resíduo do ajuste. No painel inferior mostra-se o perfil de brilho radial médio: observado (linha sólida, onde as barras de erro são $\pm 1 \sigma$ da média), modelo (linha tracejada, e a linha traço-ponto marca a largura a meia altura FWHM = $2,963''$) e resíduo (linha pontilhada).

5. Caracterizando a PSF do CALIFA

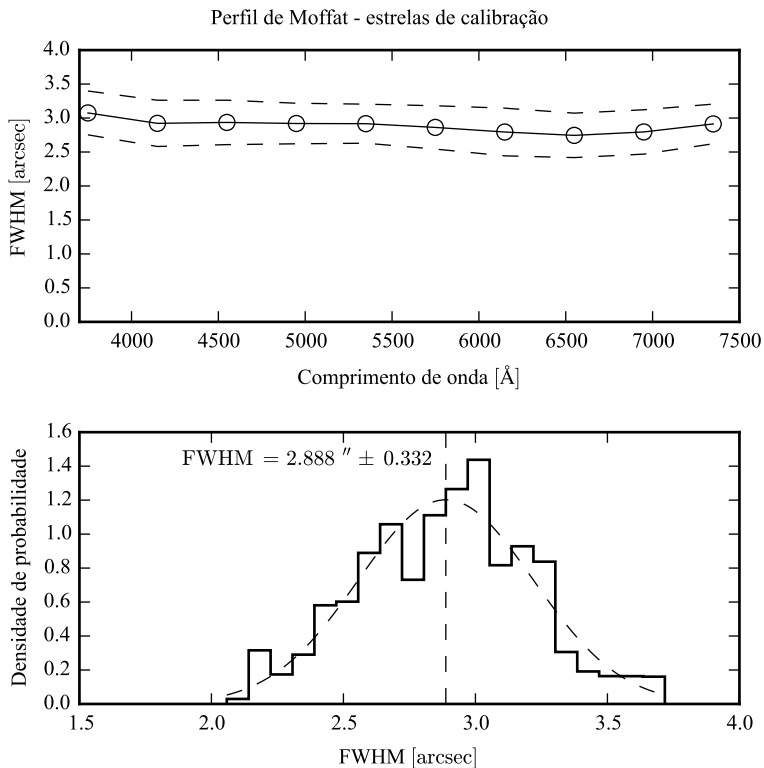


Figura 5.3: PSF do CALIFA modelada como um perfil de Moffat com $\beta = 4$, utilizando 45 estrelas de calibração. *Acima*: FWHM da PSF em função do comprimento de onda (caixas de 400 \AA). As linhas tracejadas indicam a distribuição em 1σ . *Abaixo*: Histograma da FWHM da PSF, ponderado pela verossimilhança do modelo em todos os comprimentos de onda de todas as estrelas, com $\text{FWHM} = 2,888 \pm 0,332''$.

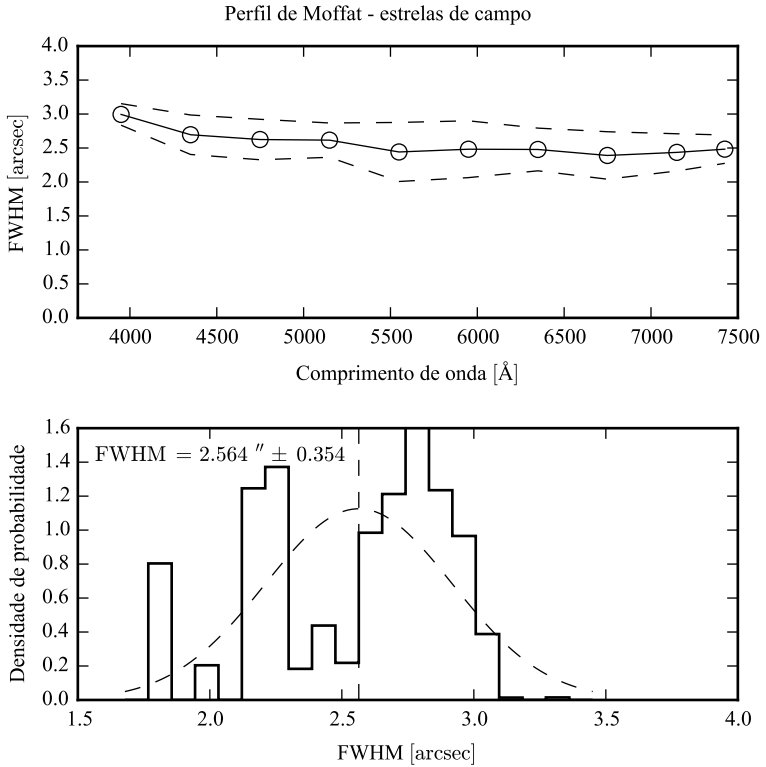


Figura 5.4: PSF do CALIFA modelada como um perfil de Moffat com $\beta = 4$, utilizando 9 estrelas de campo, na frente das galáxias observadas. *Acima*: FWHM da PSF em função do comprimento de onda (caixas de 400 Å). As linhas tracejadas indicam a distribuição em 1σ . *Abaixo*: Histograma da FWHM da PSF, ponderada pela verossimilhança do modelo em todos os comprimentos de onda de todas as estrelas, com $FWHM = 2,564 \pm 0,354''$.

5. Caracterizando a PSF do CALIFA

tra estão na frente de galáxias com simetria axial (elípticas e S0). Dado um cubo de uma galáxia, recortaram-se 7 *spaxels* ao redor da estrela, gerando dois cubos: um da galáxia, com a estrela mascarada, e outro da estrela. Neste ponto o cubo da estrela ainda está contaminado pela luz da galáxia. Então, considerando que a galáxia tem simetria axial, calculou-se um perfil de brilho radial médio da galáxia (ver Seção 3.1, Figura 3.2), para cada comprimento de onda. Com este perfil, é possível estimar quanto a galáxia está contribuindo para a luz de cada *spaxel* do cubo da estrela, pois a distância de cada *spaxel* ao centro da galáxia é conhecido. Criou-se assim um cubo de “luz de fundo” para a mesma região que contém a estrela. Subtraindo o cubo de fundo do cubo da estrela, obteve-se um cubo com apenas a luz proveniente da estrela. Este cubo foi então analisado da mesma forma que os cubos de estrelas de calibração, com os resultados mostrados na Figura 5.4. Da mesma forma, não há dependência da FWHM da PSF com o comprimento de onda, com $\text{FWHM} = 2,564 \pm 0,354''$ e elipticidade $\epsilon = 0,093 \pm 0,059$.

Há uma diferença considerável no valor obtido para a FWHM da PSF nos dois casos, embora eles estejam a cerca de 1σ de separação. Isto poderia indicar uma diferença sistemática entre a PSF das estrelas de calibração e a PSF das estrelas de campo. Todavia, observando atentamente o histograma de FWHM das estrelas de campo (painel inferior da Figura 5.4), pode-se notar que o valor mais frequente da distribuição (moda) é aproximadamente $2,8''$, muito próximo do valor obtido para as estrelas de calibração. A distribuição se desvia de uma gaussiana, com a média ponderada da FWHM da PSF das estrelas de campo menor do que o valor mais frequente. Isto, aliado ao fato de que o tamanho da amostra de estrelas de calibração (45) é maior do que o das estrelas de campo (9), fez com que se escolhesse a medida da primeira amostra como a mais confiável.

Já com os valores de elipticidade (ϵ) obtidos nos dois casos, os semi-eixos maior e menor da FWHM estão dentro da faixa de 1σ um do outro. E, em ambos os casos, ϵ é muito próximo a zero, dentro da incerteza. Levar a elipticidade em conta seria adicionar uma complexidade desnecessária (e possivelmente artificial) ao modelo de PSF.

Assim, a PSF adotada neste trabalho é um perfil de Moffat com simetria axial, $\beta = 4$ e $\text{FWHM} = 2,9 \pm 0,3''$. Este foi o mesmo procedimento para fazer a caracterização da PSF publicada no DR2 do CALIFA (García-Benito et al. 2015), mas com uma diferença. Naquele caso, ajustaram-se tanto FWHM quanto β , obtendo-se $\text{FWHM} = 2,39 \pm 0,26''$ e $\beta = 1,73 \pm 0,11$. A diferença está basicamente em qual região da PSF se está interessado em modelar mais precisamente. Por uma questão geométrica, há mais *pixels* longe

do centro do perfil, o que acaba causando mais peso destas regiões periféricas no modelo escolhido pelo ajuste (ver as barras de erro cada vez menores com a distância, na Figura 5.2, que são a grosso modo inversamente proporcionais ao peso). Porém, na maioria destes *pixels* periféricos o fluxo proveniente da estrela já está submerso no ruído, achatando o perfil (isto é, diminuindo β). O ajuste resultante é então pior nas regiões centrais, com peso menor. No caso do ajuste morfológico de uma galáxia, em particular utilizando um perfil centrado como o de Sérsic para o bojo, requer uma forma precisa da PSF nas regiões centrais. Qualquer erro sistemático na forma da PSF pode causar problemas na determinação dos parâmetros morfológicos do bojo. Desta forma, optou-se por refazer a análise da PSF para esta tese com β fixo.

Testes da decomposição morfológica espectral

A decomposição morfológica espectral, aplicada ao cubo de dados de uma galáxia, resulta numa sequência de modelos morfológicos em função do comprimento de onda. Avaliando os modelos como imagens, é possível montar cubos de dados espectrais para as componentes do modelo. Ou seja, com um modelo bojo e disco, a decomposição de um cubo de dados de uma galáxia gera dois cubos, um para o bojo e outro para o disco.

De posse destes cubos de dados espectrais das duas componentes, pode-se começar a ponderar o significado de um de seus *spaxels*. Intuitivamente, espera-se que, espectroscopicamente, ele se pareça a um *spaxel* da galáxia original. No entanto, nada garante que ele deva ser parecido com espectro algum, afinal o cubo espectral da componente morfológica é resultado de um processo computacional bastante complexo, que leva em conta apenas informações espaciais. Também, como se comentou na Seção 4.2.1, é preciso ter cuidado ao interpretar o resultado de um ajuste de modelo empírico. Isto é ainda mais importante em casos onde se faz este ajuste de forma automatizada, sem inspecionar cada imagem e seus modelos de forma individual, como é o caso da decomposição morfológica espectral.

O próximo Capítulo descreve em detalhes a decomposição morfológica espectral de cubos de dados do CALIFA. A fim de determinar se o método funciona, neste capítulo foi construído um modelo de galáxia simples, com parâmetros morfológicos e espectros das componentes conhecidos. A decomposição foi aplicada a esta galáxia sintética, com o resultado apresentado a seguir.

6. Testes da decomposição morfológica espectral

Modelo original			
Bojo		Disco	
I_e	2,0	I_0	1,0
r_e	5,0''	h	15,0''
n	4		
P.A.	60°	P.A.	45°
ϵ	0,1	ϵ	0,1

Tabela 6.1: Parâmetros do modelo morfológico original da galáxia sintética.

6.1 Construindo uma galáxia

Não é objetivo deste exercício modelar uma galáxia realista. Os parâmetros foram escolhidos apenas para que o modelo que se assemelhe a uma galáxia real, sem qualquer necessidade de ser fisicamente possível tal galáxia existir. O modelo utilizado foi um bojo com uma lei de de Vaucouleurs (Sérsic com $n = 4$) e um disco com uma lei exponencial (ver Seção 4.2.1), cada componente com um perfil elipsoidal distinto dado por uma elipticidade ($\epsilon = 1 - b/a$, onde a e b são os semieixos maior e menor) e um ângulo de posição (P.A.) medido em sentido anti-horário a partir do eixo horizontal. Os parâmetros do modelo original são listados na Tabela 6.1.

Este modelo original, mostrado na Figura 6.1, descreve o brilho superficial da galáxia no comprimento de onda de normalização escolhido, 5635 Å.

Para transformar este modelo num cubo de dados espectral, deve-se estendê-lo na direção de comprimento de onda. Utilizando espectros de populações estelares simples (SSP) de uma base e históricos de formação estelar (SFH) sintéticos para cada componente, obteve-se espectros para cada *pixel* da galáxia. Neste teste, o SFH do disco é sempre o mesmo, independente da posição na componente. Isto significa que todos os espectros do disco têm a mesma forma, modulados pela distribuição espacial de brilho dado pelo modelo morfológico (Figura 6.1). Já o SFH do bojo varia com a posição, ou seja, os espectros variam tanto em forma quanto em intensidade. A forma exata dos SFH do bojo e do disco não é relevante, basta que representem populações suficientemente diferentes uma da outra. O modelo de populações é mostrado na Figura 6.2.

Escolheu-se modelar o SFH do bojo como um surto de decaimento exponencial de formação estelar com início há 14 Ga, com a taxa de formação

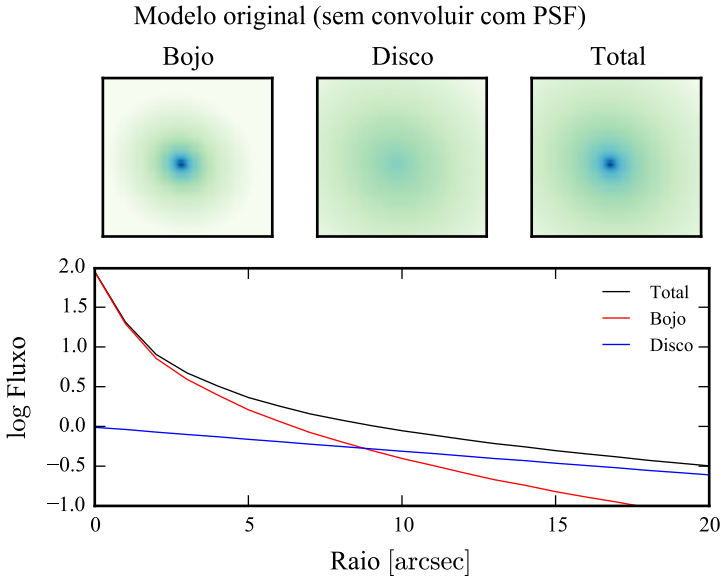


Figura 6.1: Modelo morfológico da galáxia sintética utilizada para testar a decomposição morfológica espectral. A este modelo ainda não foi aplicada a convolução com a PSF. Acima, a imagem referente às componentes bojo e disco, e total (bojo + disco). Abaixo, o perfil radial de brilho, calculado em isofotas da imagem total.

estelar em função do tempo (SFR) dada por $\Psi(t) = A \exp(-t/\tau)$, normalizada de tal forma que $\int \Psi(t) dt = 1 M_{\odot}$. O SFH do disco consiste numa SFR constante. A escala de tempo de decaimento τ tem a sua dependência espacial, no bojo, dada pela lei linear $\tau = \tau_0 + \alpha r$, onde τ_0 é o seu valor no núcleo da galáxia e α o seu gradiente. Foram escolhidos $\tau_0 = 2 \text{ Ga}$ e $\alpha = 0,2 \text{ Ga}''$, com um τ resultante mostrado no o painel superior da Figura 6.2. Para o disco, a SFR constante é obtida com $\tau \rightarrow \infty$. Estas SFR sintéticas foram discretizadas para aplicar a uma base de modelos de SSP. A base utilizada foi a de Granada–MILES, explicada na Seção 2.2.2. A SFR do bojo e do disco estão mostrados no painel central da mesma figura, respectivamente em vermelho e

6. Testes da decomposição morfológica espectral

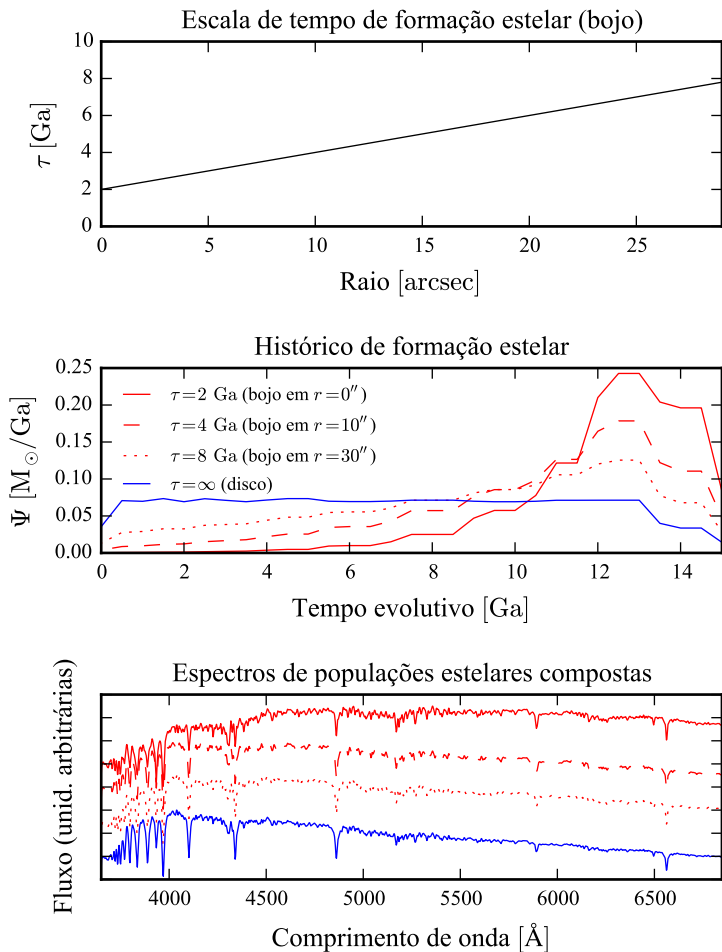


Figura 6.2: Populações estelares das componentes bojo (em vermelho) e disco (em azul) da galáxia sintética. No painel superior, a dependência espacial do tempo de escala do decaimento, τ , da SFR do bojo. No painel central taxas de formação estelar (SFR), modelados como $\Psi(t) = A \exp(-t/\tau)$. A SFR do disco é constante, com $\tau \rightarrow \infty$. Abaixo, os espectros resultantes, utilizando a base Granada–MILES.

azul. A forma das SFR foge um pouco de uma exponencial devido ao fato de a base de modelos não ser homogeneamente espaçada em idade. Os espectros finais são obtidos somando os espectros da base, com o peso dado pelo vetor de população obtido das SFR sintéticas. O painel inferior da Figura 6.2 mostra os espectros do bojo para $r = 0, 10$ e $30''$ com o mesmo código de cores das SFR. O espectro do bojo tem um aspecto de populações velhas no centro da galáxia ($\tau = 2$ Ga), e vai ficando cada vez mais jovem à medida que se afasta do centro. O espectro do disco é sempre mais jovem do que o do bojo.

Nenhuma outra propriedade física foi modelada. Adicionar poeira, por exemplo, modificaria os espectros, mas isto não faria diferença no teste. O importante aqui é que bojo e disco tenham espectros diferentes, e que os espectros possam variar de forma com a posição. Por outro lado, a cinemática mereceria um teste dedicado. Modelar (e levar em conta no ajuste morfológico) o efeito da cinemática não é uma tarefa trivial, já que bojos e discos têm cinemáticas completamente distintas. Este é certamente um problema que deve ser visitado no futuro.

Multiplicando a imagem do modelo pelo conjunto de espectros de cada componente, obteve-se um cubo de dados espectral para bojo e disco. Para obter o cubo da galáxia sintética, somaram-se as duas componentes, convolveu-se com a PSF de $\text{FWHM} = 2,9''$, e adicionou-se ruído gaussiano de 5% (para um sinal-ruído de 20). Para deixar o cubo em dimensões parecidas à do CALIFA, os *spaxels* a uma distância $r > 32''$ foram mascarados, como aparece nos painéis superiores da Figura 6.3, descrita na próxima seção.

6.2 Decompondo a galáxia sintética

O algoritmo da decomposição morfológica espectral é tratado em detalhes no Capítulo 7, sendo descrito apenas superficialmente nesta seção.

Como o objetivo é fazer a decomposição λ -a- λ , o algoritmo escolhido foi o de L-M (Seção 4.2.3). Ele pode ser extremamente rápido, mas requer um bom chute inicial. Então, o primeiro passo na decomposição é encontrar um modelo com valores aproximado das propriedades das componentes. Para tanto, pode-se utilizar um algoritmo mais complexo, como o DE, que requer apenas uma faixa de valores para os parâmetros do modelo. O procedimento de ajuste inicial é descrito em detalhes é descrito na Seção 7.1.3. A decomposição foi feita com a mesma PSF utilizada para criar o cubo, $\text{FWHM} = 2,9''$. Na Seção 6.3 discute-se o que acontece quando se utiliza uma PSF diferente

6. Testes da decomposição morfológica espectral

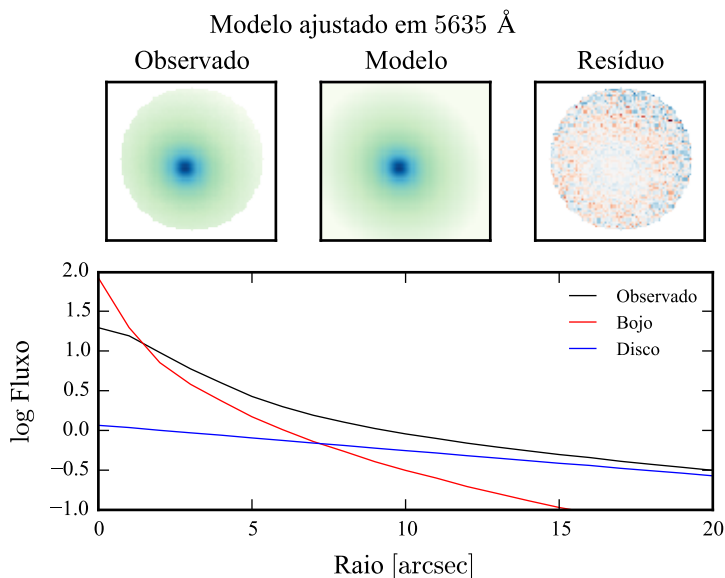


Figura 6.3: Modelo morfológico ajustado à galáxia sintética em 5635 Å utilizando o algoritmo DE. A imagem de resíduo é a diferença entre observado e modelo, dividida pelo observado, nos painéis superiores. O perfil radial de brilho, no painel inferior, pode ser comparado ao perfil da Figura 6.1. Note que o perfil para o fluxo observado, aqui, está convoluído com a PSF.

da ideal.

A Figura 6.3 mostra o modelo ajustado inicial. O ajuste foi feito numa faixa de 90 Å ao redor de 5635 Å (a mesma utilizada para normalizar os espectros antes de rodar o STARLIGHT). O ajuste foi suficientemente bom, próximo ao modelo original (comparar com a Figura 6.1). Os parâmetros do modelo inicial ajustado estão listados na Tabela 6.2.

Este ajuste não precisa ser perfeito, ele será refinado no primeiro passo do ajuste espectral. Espera-se que os parâmetros morfológicos variem com o comprimento de onda, logo o valor inicial deve variar de acordo. O cubo espectral é então quebrado em caixas de 200 Å, cada fatia sendo somada em

	Modelo inicial				
	Bojo		Disco		
	Ajuste	Original		Ajuste	Original
I_e	3,0	2	I_0	1,2	1
r_e	3,9''	5''	h	14,3''	15''
n	3,4	4			
P.A.	60,3°	60°	P.A.	46,5°	45°
ϵ	0,1	0,1	ϵ	0,1	0,1

Tabela 6.2: Parâmetros do modelo inicial ajustado à galáxia sintética, utilizando o algoritmo DE.

comprimento de onda, formando várias imagens. Cada imagem é ajustada agora com algoritmo de L-M, e os parâmetros são, independentemente, ajustados a uma reta em função do comprimento de onda. Estas retas, uma para cada parâmetro, formam os modelos iniciais para o segundo passo, a decomposição λ -a- λ do cubo de dados espectral da galáxia sintética.

Os parâmetros morfológicos ajustados são mostrados em função do comprimento de onda na Figura 6.4. Os ajustes individuais dos parâmetros, λ -a- λ (linhas pretas), não se afastam muito dos parâmetros iniciais (pontos vermelhos), e concordam bem com o modelo original (linhas pontilhadas), praticamente escondidas atrás das linhas de ajuste na maioria dos gráficos. Os parâmetros r_e e n , do bojo, parecem crescer um pouco na região abaixo de 4000 Å, o que pode indicar uma dependência destes valores com as características da população estelar do bojo. O ajuste do disco, por outro lado, é praticamente constante em comprimento de onda. Os parâmetros morfológicos médios, ponderados pela verossimilhança do ajuste, são listados na Tabela 6.3.

Estes valores não necessariamente precisam ser iguais aos do modelo original. Aquele foi usado para definir o modelo em 5635 Å, e se a média espectral se desvia dele, claramente é devido à dependência dos parâmetros morfológicos com o comprimento de onda. Isto é, se a decomposição realmente encontra os cubos espectrais do bojo e do disco. É preciso examinar os espectros ajustados.

A Figura 6.5 mostra os espectros em *spaxels* escolhidos (núcleo, acima, e $r = r_e$, no centro), e os espectros integrados. Os ajustes parecem muito bons, com os espectros originais (linhas pontilhadas) praticamente indistin-

6. Testes da decomposição morfológica espectral

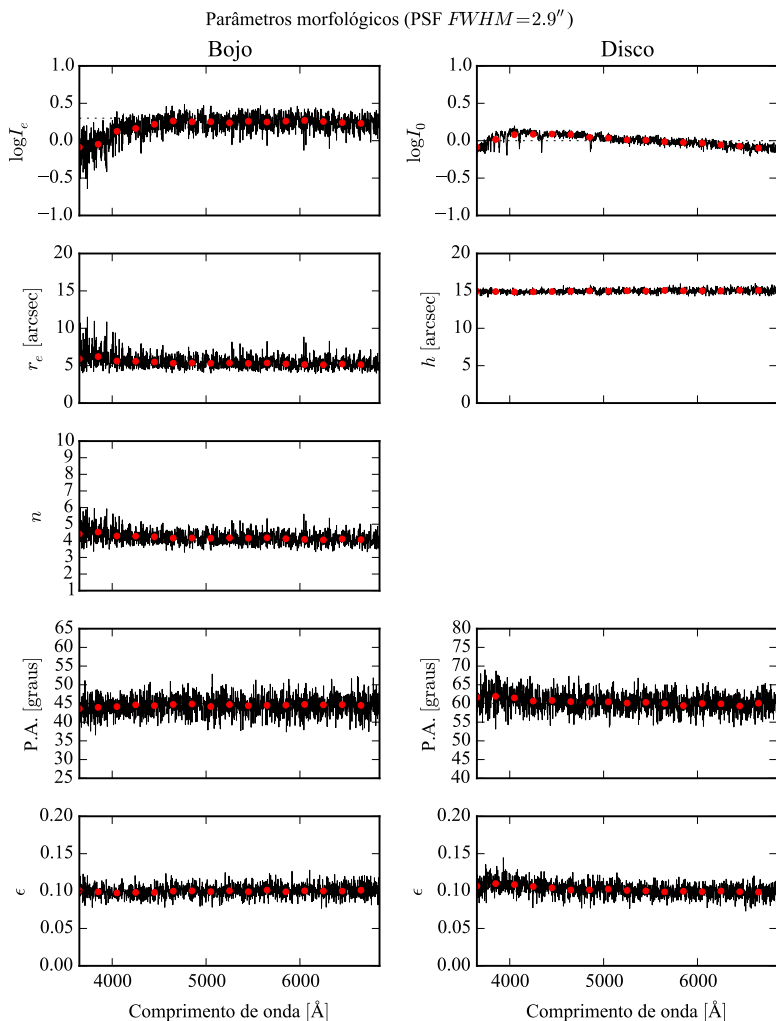


Figura 6.4: Parâmetros morfológicos da galáxia sintética, em função do comprimento de onda. Pontos vermelhos: ajuste feito em caixas de 200 \AA . Linhas pretas: ajuste feito λ -a- λ . Linhas pontilhadas, que praticamente não aparecem por trás dos ajustes, são os parâmetros originais em 5635 \AA . Os painéis à esquerda são referentes ao bojo, e os à direita ao disco. Ajuste feito com uma PSF de $FWHM = 2,9''$.

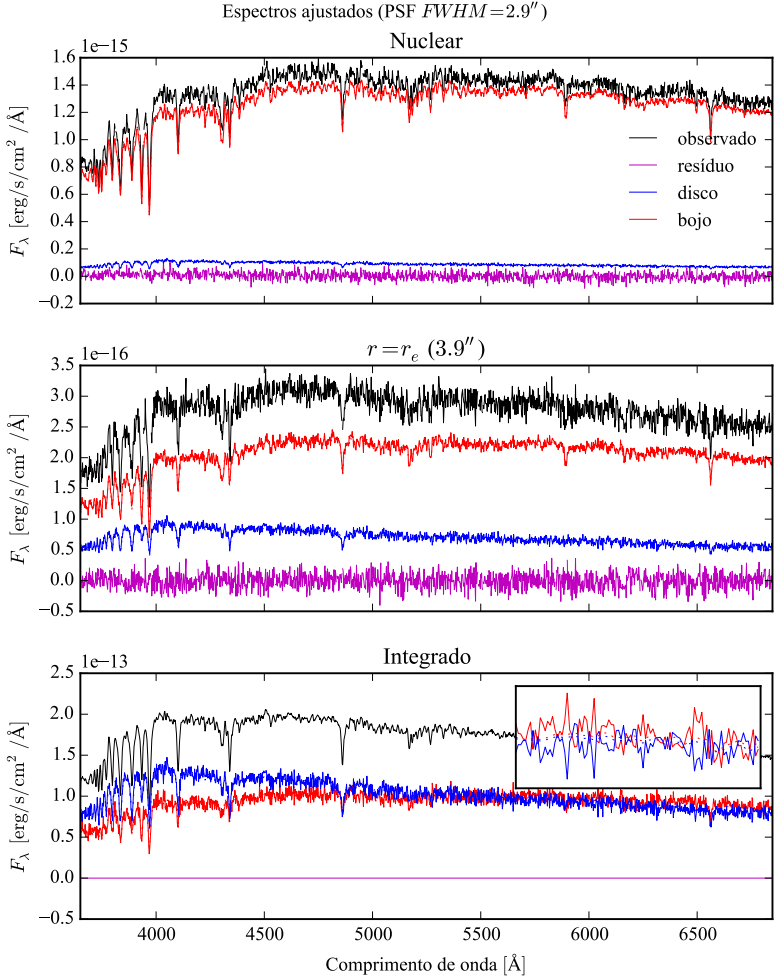


Figura 6.5: Espectros ajustados à galáxia sintética. Em preto o espectro observado, em vermelho o bojo, em azul o disco, e em magenta o resíduo. Os espectros dos componentes originais são as linhas pontilhadas, praticamente cobertas pelos ajustes. Os dois painéis superiores mostram a decomposição no *spaxels* nuclear e em $r = r_e$. Os espectros integrados espacialmente são mostrados no painel inferior, com um *zoom* entre 6000 e 6200 \AA para mostrar a anti-correlação entre os ajustes de bojo e disco.

6. Testes da decomposição morfológica espectral

Média espectral dos modelos					
	Bojo			Disco	
	Ajuste	Original		Ajuste	Original
r_e	$5,50 \pm 0,88''$	$5''$	h	$14,97 \pm 0,27''$	$15''$
n	$4,21 \pm 0,39$	4			
P.A.	$60,4 \pm 2,4^\circ$	60°	P.A.	$44,5 \pm 2,5^\circ$	45°
ϵ	$0,10 \pm 0,01$	0,1	ϵ	$0,10 \pm 0,01$	0,1

Tabela 6.3: Média espectral dos parâmetros morfológicos ajustados à galáxia sintética, ponderada pela verossimilhança dos ajustes.

guíveis dos espectros ajustados (linhas contínuas). No caso integrado, os espectros ajustados parecem ruidosos, mas o resíduo é praticamente nulo. Isto quer dizer que aquilo que parece ruído nos espectros é na verdade causada por degenerescência no ajuste. As variações nas duas componentes estão anti-correlacionadas, como se pode verificar no painel de *zoom* nos espectros integrados. Esta degenerescência precisa ser estudada mais a fundo no futuro.

Mesmo verificando visualmente que os espectros ajustados são parecidos com os originais, é preciso quantificar a qualidade do ajuste. Calculando a média da razão entre o ajuste e o original, obtém-se para o bojo um valor de $1,00 \pm 0,03$. Ou seja, o ajuste tem um desvio médio de menos de 1%, e um desvio padrão de 3%. Para o disco a razão média é $0,99 \pm 0,05$, isto é, um desvio médio de 1%, e um desvio padrão de 5%. A ordem de magnitude destes desvios não é nenhuma surpresa, levando em conta que foram adicionados 5% de ruído gaussiano aos dados. Mesmo assim, deve-se explorar melhor a razão ajuste–original, para determinar se existe algum efeito sistemático nestes desvios. A Figura 6.6 mostra a razão média em anéis de raio constante, para que seja possível fazer uma análise visual em termos de espaço e comprimento de onda simultaneamente. O ajuste do bojo, mostrado no painel superior, tem um desvio menor no centro, e vai aumentando conforme se afasta do núcleo. Isto é esperado, já que o brilho superficial do bojo cai muito rapidamente com o raio. O ajuste do disco, no painel inferior, parece não ter desvios espaciais significativos. Não há tampouco um gradiente espectral apreciável, isto é, uma cor, nas duas componentes. Entretanto, ambas mostram o surgimento de “linhas espectrais artificiais”, que parecem estar anti-correlacionadas, conforme foi visto nos espectros integrados.

Em linhas gerais, o resultado do teste é promissor. Idealmente, é ne-

6.2. Decompondo a galáxia sintética

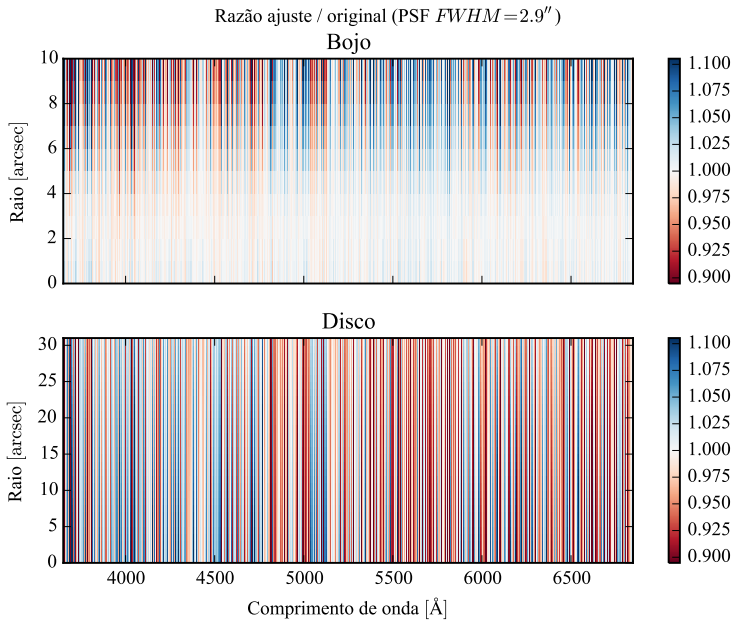


Figura 6.6: Razão ajuste–original média dos espectros ajustados à galáxia sintética, em função do comprimento de onda e da distância ao centro da galáxia, tomada em anéis de raio constante. Valores desviando de 1 indicam erro no ajuste. Acima a razão para o bojo, e abaixo para o disco. A escala radial é diferente nos dois casos.

6. Testes da decomposição morfológica espectral

cessário testar todas as configurações possíveis de morfologia, para mapear em quais delas a decomposição espectral é válida. Mas é preciso lembrar que o modelo morfológico tem 7 parâmetros livres. Se cada um deles puder tomar n valores diferentes, a quantidade de modelos a serem testados é n^7 . Com somente 4 valores por parâmetro, são mais de 16 mil modelos possíveis, o que, com cada decomposição levando cerca de 5 minutos em um computador de 24 núcleos, leva mais de 50 dias, sem contar o tempo necessário para análise dos resultados. Isso sem incluir populações estelares variáveis, e diferentes PSFs (ver a Seção seguinte). Esgotar toda a gama de modelos possíveis não é uma estratégia viável. É preciso buscar uma abordagem mais inteligente. Também é preciso determinar se as populações estelares das componentes modeladas, ajustadas com *STARLIGHT*, são compatíveis com as originais. Os espectros são parecidos, o que indica populações semelhantes, mas pode haver efeitos sistemáticos. Este teste preliminar apenas serviu para verificar que o algoritmo pode funcionar, e justificar o seu uso em galáxias reais, do CALIFA, no próximo Capítulo.

6.3 Efeitos da PSF no ajuste

A PSF do CALIFA foi caracterizada no Capítulo 5. Lá se verificou que a PSF segue um perfil de Moffat com $\beta = 4$ e $\text{FWHM} = 2,9 \pm 0,3''$. Os testes da Seção anterior foram feitos utilizando esta PSF, tanto nos dados originais quanto no ajuste morfológico. Mas, dado que a FWHM da PSF tem uma certa distribuição de valores, é justo levantar a questão: o que acontece quando a PSF original e a utilizada na decomposição são diferentes? Em outras palavras, como se comporta a decomposição morfológica espectral quando não temos um conhecimento perfeito da PSF?

Para tentar compreender o efeito de uma PSF inadequada aos dados na decomposição, o teste foi refeito, porém com a galáxia original sintética convoluída com PSFs de $\text{FWHM} = 2,6''$ e $\text{FWHM} = 3,3''$. Com isto tem-se valores próximos aos limites dados pela incerteza na medida da PSF do CALIFA. A mesma PSF de $\text{FWHM} = 2,9''$ foi utilizada na decomposição morfológica espectral. No caso da galáxia sintética com a PSF de $2,6''$, o ajuste está sobre-estimando o valor da FWHM real, enquanto no caso da galáxia com $3,3''$ a FWHM é subestimada.

As Figuras 6.7 e 6.8 mostram os parâmetros morfológicos obtidos para os dois casos. Pode-se ver que os parâmetros obtidos para o disco são muito próximos dos parâmetros do teste anterior. Não é de se estranhar, pois o disco

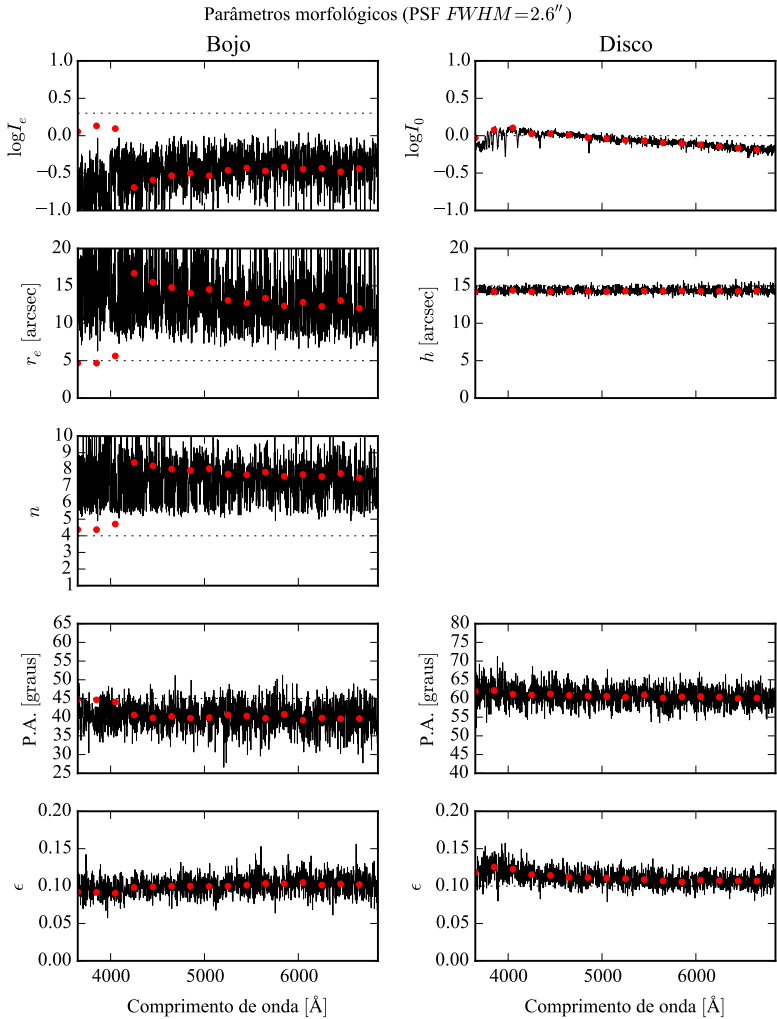


Figura 6.7: Parâmetros morfológicos da galáxia sintética, em função do comprimento de onda. Ajuste feito com uma PSF de $FWHM = 2,9''$ sobre dados com $FWHM = 2,6''$. Ver legenda da Figura 6.4.

6. Testes da decomposição morfológica espectral

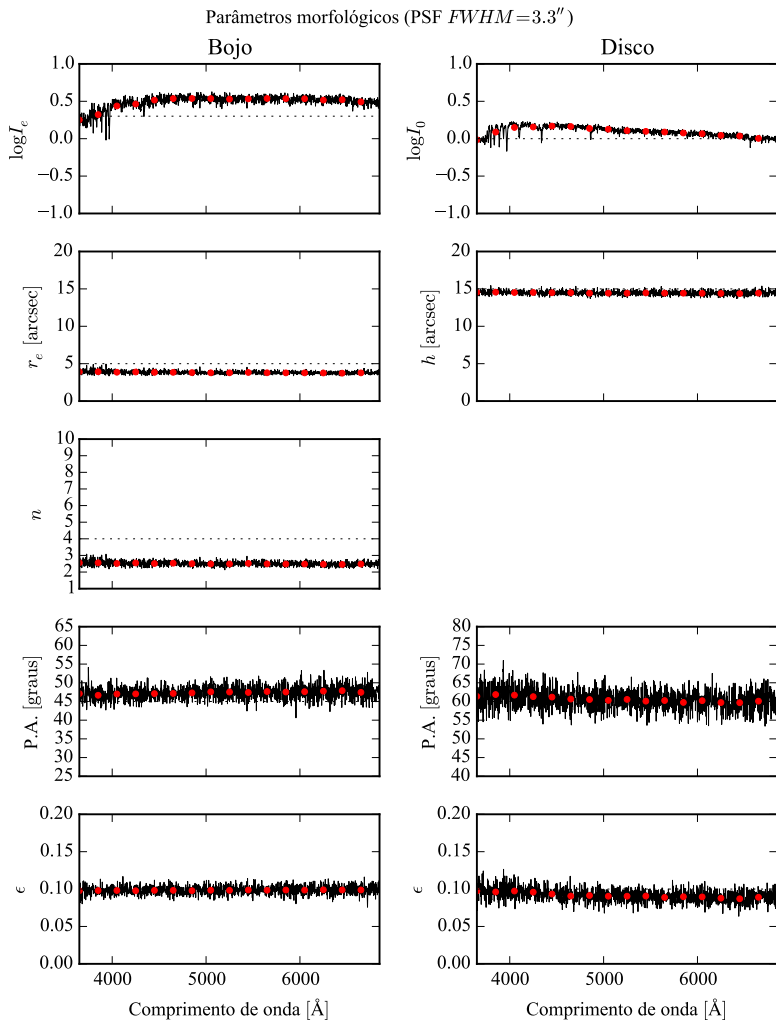


Figura 6.8: Parâmetros morfológicos da galáxia sintética, em função do comprimento de onda. Ajuste feito com uma PSF de $FWHM = 2,9''$ sobre dados com $FWHM = 3,3''$. Ver legenda da Figura 6.4.

Média espectral dos modelos (PSF diferente)					
	Bojo			Disco	
	FWHM = 2,6''	FWHM = 3,3''		FWHM = 2,6''	FWHM = 3,3''
r_e	$13,64 \pm 5,22''$	$3,83 \pm 0,22''$	h	$14,40 \pm 0,38''$	$14,47 \pm 0,27''$
n	$7,38 \pm 1,25$	$2,51 \pm 0,13$			
P.A.	$60,7 \pm 2,6^\circ$	$60,5 \pm 2,6^\circ$	P.A.	$40,2 \pm 3,6^\circ$	$47,4 \pm 1,7^\circ$
ϵ	$0,11 \pm 0,01$	$0,09 \pm 0,01$	ϵ	$0,10 \pm 0,01$	$0,099 \pm 0,01$

Tabela 6.4: Média espectral dos parâmetros morfológicos ajustados à galáxia sintética, ponderada pela verossimilhança dos ajustes, com a PSF do ajuste (FWHM = 2,9'') diferente da PSF dos dados.

é muito suave e não tem estruturas na escala de tamanho da PSF. O bojo, por outro lado, é muito afetado pela má escolha da PSF. *Sobre-estimar* a FWHM da PSF (2,9'' > 2,6'') faz os valores de r_e e n aumentarem muito, de 5'' e 4 para cerca de 13'' e 7, respectivamente. Também aumenta a dispersão nos dois parâmetros, provavelmente causado por degenerescência no ajuste. Com a FWHM *subestimada* (2,9'' < 3,3''), os valores destes parâmetros diminuí, com $r_e \sim 4''$ e $n \sim 2,5$. O disco muda pouco, como no outro caso. Os parâmetros médios das duas decomposições são listados na Tabela 6.4.

A dispersão nos parâmetros do bojo, no caso sobre-estimado, parece um problema em potencial. Percebe-se, porém, que a dispersão nos parâmetros não se reflete tanto nos espectros, como mostra a Figura 6.9. Os espectros são parecidos com os originais, com diferenças sistemáticas e um “ruído” maior do que o ajuste com a PSF correta. No caso subestimado, os espectros parecem melhor ajustados (Figura 6.10), mas também com diferenças sistemáticas.

Fazendo a razão ajuste–original (Figura 6.11), percebe-se que espectro ajustado do bojo torna-se maior do que o original conforme se afasta do centro, enquanto o disco apresenta um gradiente espectral, ficando mais azul, quando se sobre-estima a FWHM. As “linhas espectrais artificiais” neste caso são bem pronunciadas. A razão média para o bojo é de $1,06 \pm 0,06$, e para o disco de $0,77 \pm 0,08$. Quando se subestima a FWHM (Figura 6.12), o espectro ajustado do bojo é mais fraco e do que o original, e diminui com o raio. O disco não parece ter gradiente radial, e, em ambos os casos, não há um gradiente espectral perceptível, com “linhas espectrais artificiais” menos intensas do que no outro caso. A razão média neste caso é $0,94 \pm 0,05$ para o bojo e

6. Testes da decomposição morfológica espectral

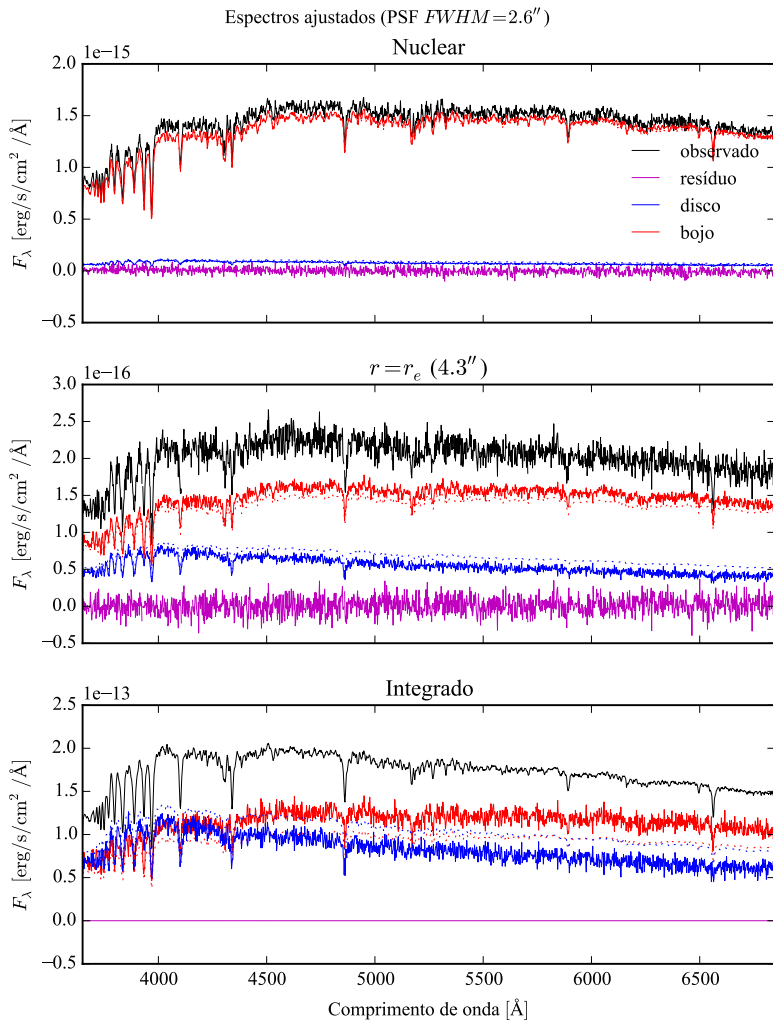


Figura 6.9: Espectros ajustados à galáxia sintética. Ajuste feito com uma PSF de $FWHM = 2,9''$ sobre dados com $FWHM = 2,6''$. Ver legenda da Figura 6.5.

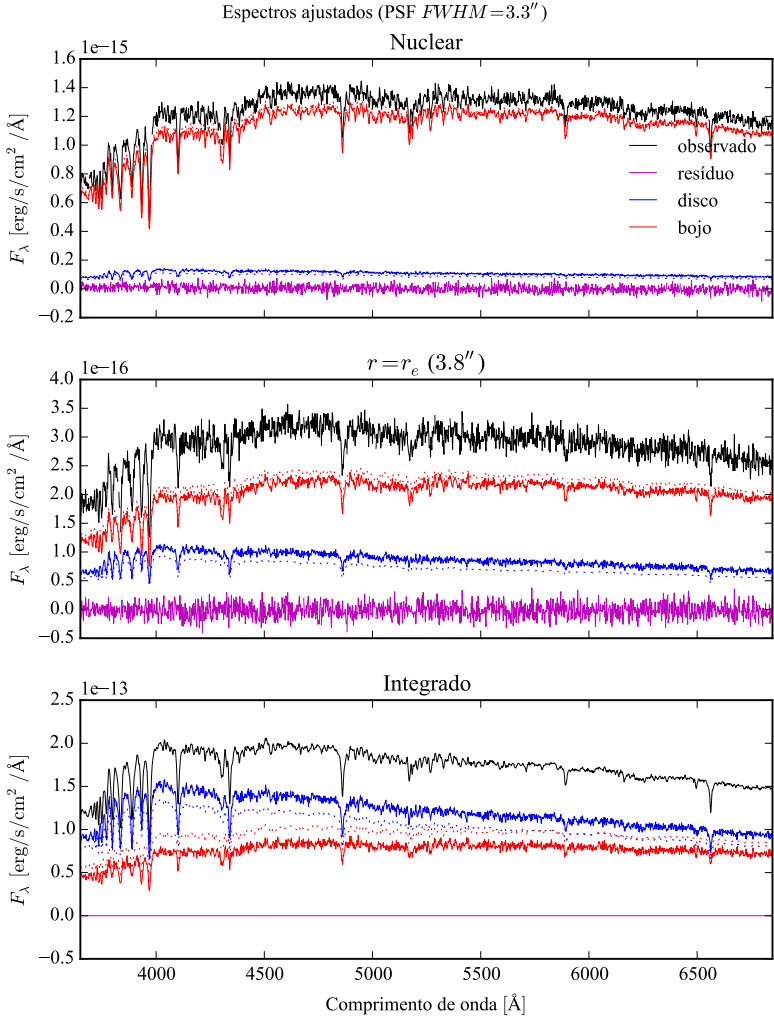


Figura 6.10: Espectros ajustados à galáxia sintética. Ajuste feito com uma PSF de $FWHM = 2,9''$ sobre dados com $FWHM = 3,3''$. Ver legenda da Figura 6.5.

6. Testes da decomposição morfológica espectral

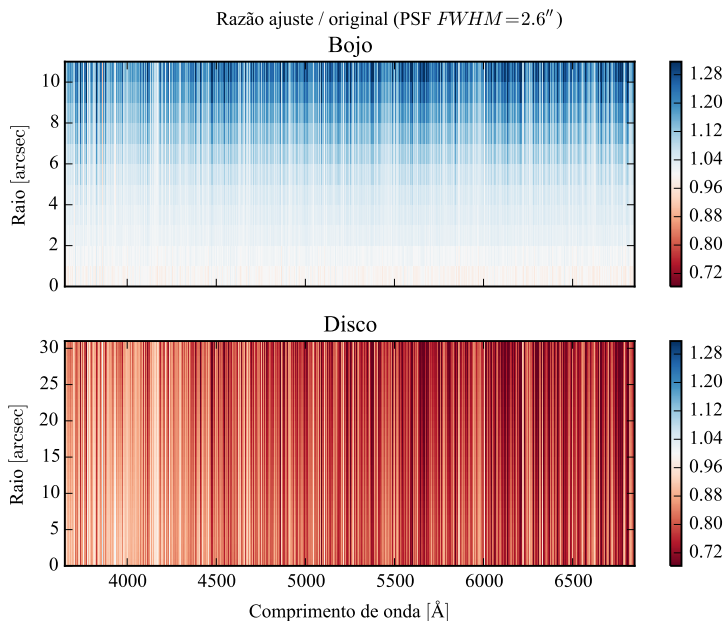


Figura 6.11: Razão ajuste–original média dos espectros ajustados à galáxia sintética. Ajuste feito com uma PSF de $FWHM = 2,9''$ sobre dados com $FWHM = 2,6''$. Ver legenda da Figura 6.6.

$1,13 \pm 0,04$ para o disco.

Ao se utilizar, na decomposição morfológica, uma PSF com $FWHM$ maior do que a real (superestimando), é impossível criar um modelo com um bojo tão concentrado quanto o observado. O que acontece então é que o algoritmo chega aos modelos mais próximos, que não representam exatamente a galáxia. O mesmo não ocorre quando se utiliza uma $FWHM$ menor. Neste caso, basta fazer um bojo menos concentrado (r_c e/ou n menor). Pelo teste, este caso é mais estável, isto é, possui menos degenerescência.

Assim, pode-se ficar tentado a utilizar a PSF com $FWHM$ menor na decomposição morfológica espectral das galáxias do CALIFA, a fim de evitar os casos onde se superestima a PSF. Utilizando uma PSF menor pode-se

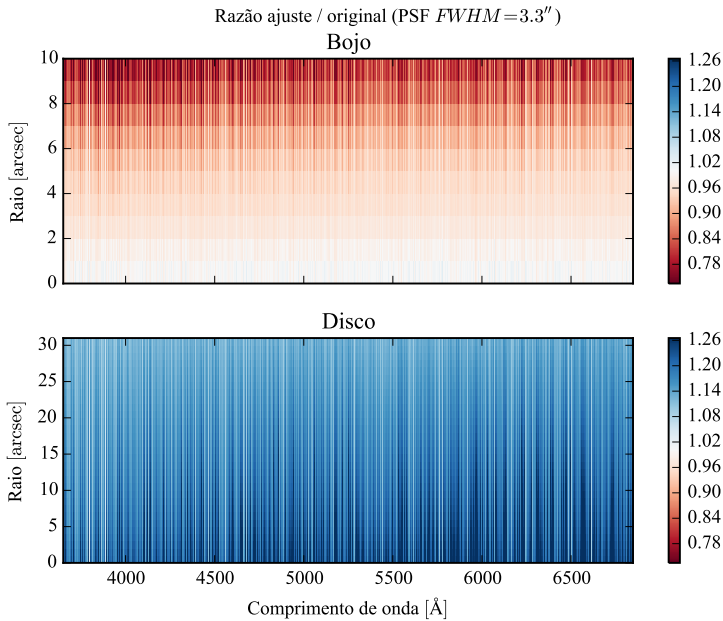


Figura 6.12: Razão ajuste–original média dos espectros ajustados à galáxia sintética. Ajuste feito com uma PSF de $FWHM = 2,9''$ sobre dados com $FWHM = 3,3''$. Ver legenda da Figura 6.6.

ter a ilusão de obter o resultado da decomposição para mais galáxias. Entretanto, deve-se lembrar que o ajuste é significativamente melhor quando se usa a PSF correta, e apresentando menos artefatos na dependência dos parâmetros morfológicos com o comprimento de onda. Com uma PSF menor, conforme visto na distribuição da Figura 5.3, a probabilidade é muito pequena de que algumas das galáxias tenham sido observadas com aquela PSF. Como a decomposição morfológica espectral é um método experimental, o melhor é utilizar a PSF mais frequente da distribuição, de $FWHM = 2,9''$, e selecionar somente as galáxias onde a decomposição parece ter um menor espalhamento no ajuste dos parâmetros em função do comprimento de onda. A decomposição é, provavelmente, mais confiável nestes casos.

Decomposição morfológica espectral de galáxias

7.1 O procedimento de decomposição morfológica espectral

A decomposição morfológica espectral apresentada neste capítulo foi desenvolvida para trabalhar com galáxias lenticulares (S0), que podem ser decompostas em um bojo e um disco. Conforme a Seção 4.2.1, o perfil de brilho do bojo é modelado como uma lei de Sérsic, e o perfil do disco como uma lei exponencial, conforme as equações

$$I_{\text{bojo}}(r) = I_e \exp \left\{ -b_n \left[\left(\frac{r}{r_e} \right)^{1/n} - 1 \right] \right\},$$
$$I_{\text{disco}}(r) = I_0 \exp \left(-\frac{r}{h} \right).$$

Diferente do método de Johnston et al. (2012), os perfis do bojo e do disco são tratados em duas dimensões como elipsoides, cada qual com uma elipticidade (ϵ) e um ângulo de posição (P.A.) independentes. O ângulo de posição é medido em sentido anti-horário a partir do eixo horizontal positivo. Estes modelos são ajustados a imagens em cada comprimento de onda, utilizando o programa `IMFIT`, conforme descrito na seção a seguir. A decomposição é realizada sobre os espectros observados. As linhas de emissão são mascaradas, pois estamos interessados apenas na distribuição de populações estelares. O ajuste morfológico é feito deixando livres todos os parâmetros das equações acima (I_e , r_e , n , I_0 , h) e a geometria de cada componente (P.A. e ϵ), sem fazer hipótese alguma sobre como os parâmetros morfológicos variam a cada comprimento de onda.

Conforme descrito na Seção 5.2, convoluem-se as imagens do modelo com uma PSF de perfil de Moffat com $\beta = 4$ e FWHM = 2,9". Possíveis efeitos causados por uma PSF mal dimensionada foram vistos na Seção 6.3.

7. Decomposição morfológica espectral de galáxias

Esta é uma preocupação muito relevante no caso do CALIFA, pois em geral os bojos estão mal resolvidos.

7.1.1 Cinemática

Antes de começar a decomposição, é preciso refletir um pouco sobre a cinemática das estrelas da galáxia. As estrelas estão distribuídas em bojos e discos, e a cinemática em cada um dos casos é diferente. A estrutura plana dos discos é causada por um alto momento angular, com um campo de velocidades sistêmico projetado na linha de visada. Isto faz com que uma dada linha espectral tenha um *redshift* diferente, dependendo da sua posição no disco. Já os bojos são normalmente caracterizados por baixa rotação, mas uma grande dispersão de velocidades, crescendo à medida que se aproxima do centro. Ou seja, as linhas são mais alargadas nas regiões centrais.

Para que a decomposição morfológica espectral faça sentido, é preciso ter certeza que, em uma imagem em uma dada janela espectral, se estejam observando os mesmos processos físicos em todos os *spaxels*. Por exemplo, não se pode ter um *spaxel* que contenha fluxo proveniente do fundo de uma linha de absorção, enquanto outro *spaxel* contém fluxo do contínuo adjacente. Chega-se então num problema cíclico. É preciso saber as características das componentes morfológicas para que se conheça a cinemática de cada uma delas. Porém, sem compensar os efeitos da cinemática, não se pode fazer a decomposição de forma confiável.

O que se faz aqui é obter uma medida aproximada da cinemática, medindo apenas uma velocidade sistêmica (v_0) e uma dispersão (v_d) assumindo uma distribuição de velocidades gaussiana para cada *spaxel*. Isto não é o ideal, pois bojos podem ter alguma rotação e discos podem ter alguma dispersão de velocidades. A cinemática pode até ser diferente para cada população estelar em uma mesma componente. Entretanto, isto é uma boa primeira aproximação. A medida de v_0 e v_d foi obtida utilizando o STARLIGHT, que ajusta a cinemática juntamente às populações estelares.

Corrigir efeitos de v_0 é simples, basta aplicar um *redshift* (ou *blueshift*) de mesma velocidade, na direção oposta, tal que os espectros fiquem todos em *rest frame*. Já v_d requer um pouco mais de consideração, pois não é possível “desalargar” as linhas espectrais. O que se faz então é tentar deixar todos os *spaxels* com a mesma dispersão de velocidades, degradando a resolução do espectro. Se a distribuição de velocidades na linha de visada segue uma distribuição gaussiana, isto é obtido convoluindo (em espaço de velocidades) o fluxo de cada *spaxel* com uma gaussiana de largura dada por um $v_{d,*}$ ade-

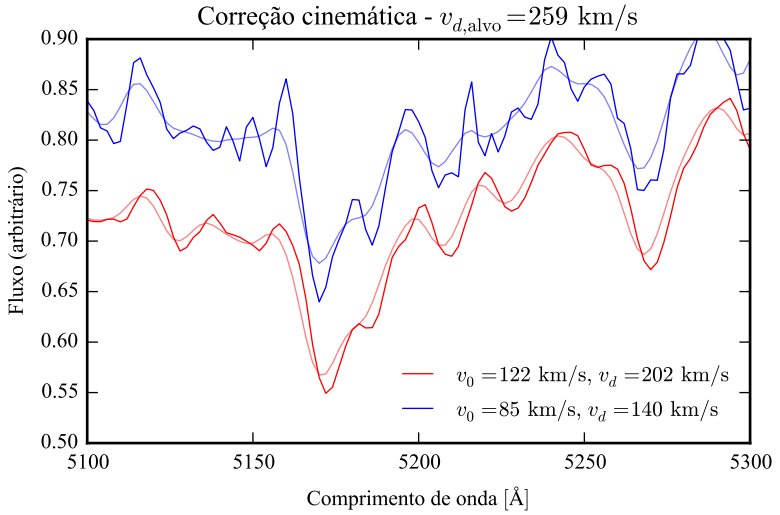


Figura 7.1: Correção de efeitos da cinemática. Linhas escuras: dois espectros com cinemática diferente. Linhas claras: espectros deslocados para *rest frame*, com as linhas alargadas para uma dispersão de velocidades $v_{d,alvo} = 259$ km/s. O fluxo está em unidades arbitrárias para melhor visualização.

quado, isto é

$$F_{\lambda,*} = \frac{1}{v_{d,*} \sqrt{2\pi}} \int_{-\infty}^{+\infty} F_{\lambda} \left(\lambda' = \frac{\lambda}{1 + v/c} \right) \exp \left[-\frac{1}{2} (v/v_{d,*})^2 \right] dv.$$

Quando se convolui duas gaussianas, suas dispersões se somam em quadratura. Portanto, $v_{d,*}$ deve ser tal que o fluxo final tenha a dispersão alvo $v_{d,alvo}$:

$$v_{d,*} = \sqrt{v_{d,alvo}^2 - v_d^2}.$$

Deve-se escolher $v_{d,alvo}$ de modo que $v_{d,*}$ seja sempre um número real, ou seja, $v_{d,alvo} > v_d$, para todos os *spaxels*. Na prática, alguns cubos podem ter uns poucos *spaxels* com v_d anômalo (tanto por ajuste ruim pelo STARLIGHT quanto por uma dispersão realmente grande). Neste caso, a resolução espectral seria degradada enormemente por conta de um punhado de *spaxels*. A

7. Decomposição morfológica espectral de galáxias

solução encontrada foi usar um $v_{d,\text{alvo}}$ maior do que 95% dos v_d , e não fazendo a convolução nos poucos casos onde $v_d > v_{d,\text{alvo}}$. A Figura 7.1 ilustra o efeito da correção de cinemática em *spaxels* com cinemática distinta. Pode-se ver que as linhas espectrais tendem a ficar coerentes após a correção.

7.1.2 Propagação de erros nos espectros

Em alguns passos da decomposição, são tomadas imagens dos cubos espectrais em caixas com uma determinada largura em comprimento de onda. Os espectros são empilhados formando uma imagem, e os erros devem ser propagados de acordo. Os espectros do CALIFA, na configuração V500, têm uma PSF espectral gaussiana de $\text{FWHM} = 6 \text{ \AA}$. Porém, a amostragem é feita em caixas de 2 \AA . Isto quer dizer que fluxos estão correlacionados, logo deveria-se trabalhar com a matriz de covariância, ao invés de um espectro de erros (ou incerteza). Entretanto, somente o espectro de erros está disponível nos cubos de dados do CALIFA (e na maioria dos espectros astronômicos). Note que o mesmo raciocínio de propagação de erros se aplica à correção de cinemática descrita anteriormente, com a gaussiana da dispersão de velocidades fazendo o papel de um peso na soma dos espectros.

Sem a matriz de covariância, há duas alternativas. Se erros nos fluxos estão correlacionados com dependência na distância espectral de forma a depender apenas da distância, isto é, uma função $p(\lambda' - \lambda'')$, pode-se calcular a correção que a covariância causaria numa soma ponderada de fluxo. O fluxo médio F ponderado pelos pesos w_λ é dado por

$$F = \frac{\sum_{\lambda} w_{\lambda} F_{\lambda}}{\sum_{\lambda} w_{\lambda}}.$$

Geralmente se normalizam os erros tal que $\sum_{\lambda} w_{\lambda} = 1$, para simplificar os cálculos. O erro σ_F sobre o fluxo médio F é, levando em conta a correlação,

$$\sigma_F^2 = \sum_{\lambda} w_{\lambda}^2 \sigma_{\lambda}^2 + \sum_{\lambda'} \sum_{\lambda''}^{\lambda' \neq \lambda''} p(\lambda' - \lambda'') w_{\lambda'} w_{\lambda''} \sigma_{\lambda'} \sigma_{\lambda''}.$$

Para erros gaussianos, $p(\Delta\lambda) \sim \exp[-1/2(\Delta\lambda/c_{\text{FWHM}})^2]$, normalizado. A distância de covariância é dada por $\text{FWHM} = 2\sqrt{2\ln 2} c_{\text{FWHM}}$. Se os erros não estiverem correlacionados (isto é, se $\text{FWHM} \rightarrow 0$), $p(\Delta\lambda) = 0$, a segunda soma desaparece e o erro é dado pela soma ponderada usual.

A segunda alternativa é estimar o erro a partir dos dados. Isto só funciona quando a soma é feita sobre uma caixa espectral com um grande número de medidas. Neste caso, o erro é dado pela covariância amostral,

$$\sigma_F^2 = \frac{\sum_{\lambda} w_{\lambda}}{\left(\sum_{\lambda} w_{\lambda}\right)^2 - \sum_{\lambda} w_{\lambda}^2} \sum_{\lambda} w_{\lambda} (F_{\lambda} - F)^2.$$

A primeira alternativa é utilizada na convolução de velocidades, pois em geral cada elemento do espectro convoluído contém fluxo proveniente de poucas medidas. A segunda é utilizada ao se empilhar espectros em caixas de comprimento de onda de largura maior que 100 Å, para uma estimativa mais realista do erro. Quando se calcula a imagem média numa caixa, neste trabalho, o peso na soma ponderada dos fluxos é dado por $w_{\lambda} = \sigma_{\lambda}^{-2}$, ou seja, o inverso dos erros provenientes dos cubos de dados, ao quadrado.

7.1.3 Modelos iniciais e ajuste a cada comprimento de onda

A decomposição morfológica espectral requer, nesta implementação, um número de ajustes morfológicos igual ao número de amostras de comprimento de onda. Para cubos com a configuração V500, são 1600 amostras de largura 2 Å. Isto requer que se utilize um algoritmo rápido para fazer o ajuste. Para o programa `IMFIT` (Erwin 2015), este algoritmo é o L-M (ver a descrição dos algoritmos na Seção 4.2.3). Para fazer um ajuste utilizando L-M, é preciso ter um bom chute inicial, visto que este algoritmo é muito propenso a cair em mínimos locais. Este chute inicial é determinado utilizando os outros algoritmos mais lentos, N-M e DE.

Como primeira aproximação, toma-se uma caixa de 100 Å ao redor de 5635 Å (comprimento de onda de normalização) e calculam-se as imagens de fluxo e erro conforme visto na seção anterior. Esta imagem é utilizada para calcular o chute inicial nos parâmetros morfológicos, utilizando as seguintes heurísticas:

1. Encontrar o raio que contém metade da luz (HLR), que é, em primeira aproximação, o local mais provável para que a componente dominante deixe de ser o bojo e passe a ser o disco (González Delgado et al. 2015);
2. Mascarar a região central ($r < \text{HLR}$);
3. Criar um modelo de disco de $h = 1,5 \text{ HLR}$ utilizando DE;

7. Decomposição morfológica espectral de galáxias

4. Ajustar o disco à imagem mascarada;
5. Criar um modelo de bojo com $n = 4$ e $r_e = 0,5$ HLR;
6. Ajustar os modelo de bojo e disco (já ajustado anteriormente) à imagem completa utilizando DE;
7. Refinar o ajuste utilizando N-M, depois L-M.

Este procedimento é computacionalmente intensivo, e o conjunto de heurísticas foi determinado de forma empírica. Ainda assim, ele falha em muitos casos, geralmente precisando ser modificado caso a caso. O tempo típico, em um computador atual, de ajuste do modelo inicial é de 10 minutos. É possível fazer este ajuste de forma interativa, utilizando uma ferramenta gráfica, numa fração deste tempo. Com este objetivo foi desenvolvido o programa mostrado na Figura 7.2. Com ele podem-se escolher modelos iniciais, limites, e fazer um ajuste de teste, tudo em tempo real. Como a amostra é pequena, um programa interativo ainda é uma abordagem viável.

Como visto na Seção 4.2.2, os parâmetros morfológicos podem depender do comprimento de onda. Logo, um único modelo inicial pode não ser suficiente para escapar dos mínimos locais. Assim, utiliza-se imagens em caixas de 100 \AA , e espaçadas em intervalos também de 100 \AA , para fazer ajustes utilizando o algoritmo N-M. Obtém-se desta forma modelos iniciais para cada comprimento de onda. Os parâmetros destes modelos são, de forma independente, ajustados a polinômios em função de λ . Em nenhum caso (da amostra final deste trabalho) houve necessidade de ajuste de um polinômio de ordem maior que 1, isto é, uma reta.

O ajuste morfológico final se dá utilizando os chutes iniciais dados pelos polinômios dos parâmetros. As imagens são tomadas λ -a- λ , sem combinar imagens. O ajuste é feito utilizando L-M. Caso não haja convergência do algoritmo, ou o melhor ajuste fique preso em algum limite dos parâmetros, o ajuste é marcado como falho.

Ao final do ajuste morfológico, cria-se uma imagem para o bojo e para o disco em cada comprimento de onda. Os cubos de dados espectrais são montados apenas armazenando estas imagens em ordem de comprimento de onda. Os cubos de dados espectrais das componentes morfológicas estão prontos para serem analisados como espectros.

7.1. O procedimento de decomposição morfológica espectral

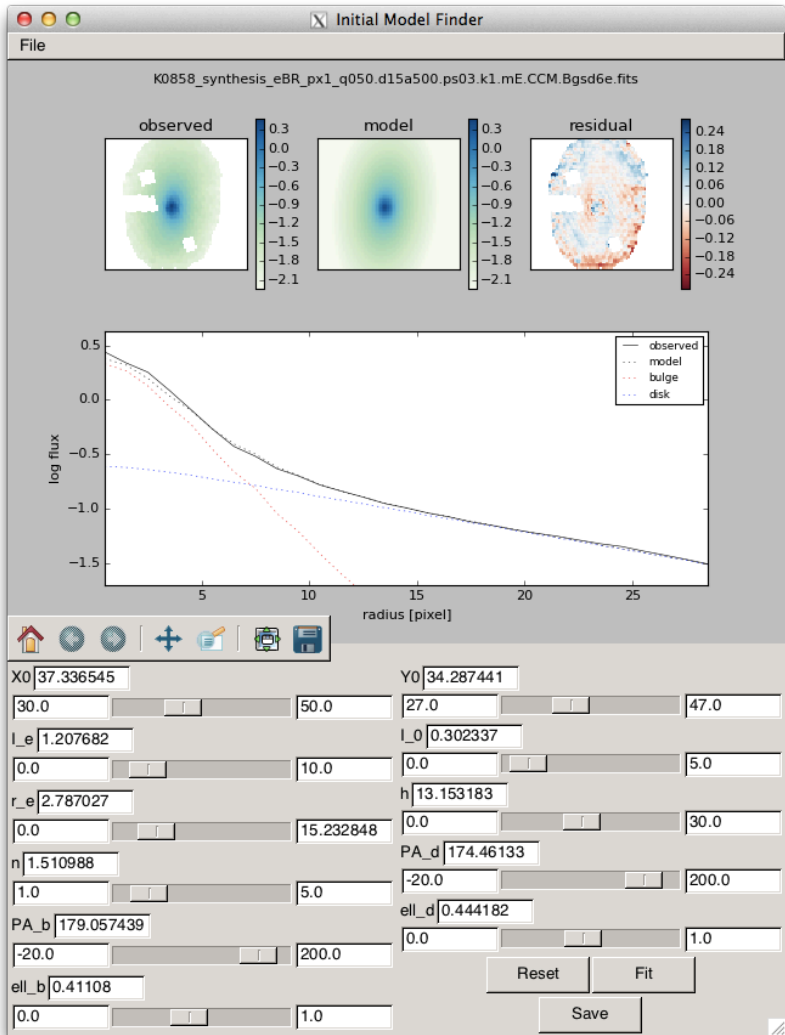


Figura 7.2: Programa gráfico para encontrar o modelo inicial de forma interativa.

7.2 Seleção da amostra de galáxias

A amostra para candidatos à decomposição morfológica espectral foi selecionada a partir de 331 galáxias observadas com a configuração V500, as quais passaram pelo QBICK e tiveram os espectros passados pelo STARLIGHT, sem segmentação em zonas de Voronoi (ver Seções 2.2.1 e 2.2.2). Isto é necessário para que se tenham medidas da cinemática da galáxia, utilizadas para preparar os dados antes da decomposição.

O passo seguinte foi selecionar as galáxias conforme seu tipo morfológico. A classificação morfológica das galáxias da amostra mãe do CALIFA foi feita visualmente por 5 voluntários, utilizando imagens do SDSS nas bandas r e i (Walcher et al. 2014). Os critérios foram:

- Elíptica (E), com subclasse 0–7.
- Espiral (S), com subclasses 0, 0a, a, ab, b, bc, c, cd, d, m;
- Irregular (I);
- Em qualquer classe, barra (B), sem barra (A), ou indefinida (AB);
- Características de *merger* (sim ou não).

Os três primeiros itens formam uma sequência numérica segundo a classificação de Hubble, de 0 a 18. As 5 classificações independentes foram combinadas, calculando a média (descartando valores atípicos, distante mais de 4 classes da média). Os valores máximos e mínimos, para dar uma ideia da incerteza, são calculados utilizando todas as 5 classificações. Foi feita uma filtragem na lista de galáxias observadas, baseada na tabela de classificação morfológica. Dada a natureza subjetiva da classificação visual, optou-se por utilizar as classificações máxima e mínima, de tal forma que seja possível que galáxia em questão seja da classe S0. Isto é, se a galáxia for classificada como elíptica ($< S0$), mas a classificação máxima for, por exemplo, Sa ($> S0$), a galáxia entra na amostra. O inverso também vale, uma galáxia Sa tiver uma classificação mínima E7, também entra na amostra. As galáxias também têm que ser sem barra (A), e sem características de *merger*.

Adicionalmente, as galáxias precisam ter uma elipticidade máxima $\epsilon < 0,5$, medida nas imagens do SDSS na banda r . Isto é necessário para evitar problemas na decomposição morfológica, pois o modelo bojo–disco não funciona bem em sistemas muito inclinados. A amostra inicial é listada na Tabela A.1 (Anexo A).

ID	Nome	Classe	Classe (mín.)	Classe (máx.)	ϵ
K0018	NGC 0155	1 (E1)	0 (E0)	8 (S0)	0,22
K0127	NGC 1349	6 (E6)	0 (E0)	10 (Sa)	0,11
K0592	NGC 4874	0 (E0)	0 (E0)	8 (S0)	0,12
K0602	NGC 4956	1 (E1)	0 (E0)	8 (S0)	0,14
K0832	NGC 6146	5 (E5)	3 (E3)	8 (S0)	0,23
K0846	UGC 10695	5 (E5)	2 (E2)	8 (S0)	0,33
K0851	NGC 6338	5 (E5)	1 (E1)	8 (S0)	0,34
K0858	UGC 10905	9 (S0a)	7 (E7)	11 (Sab)	0,47
K0912	NGC 7623	8 (S0)	8 (S0)	8 (S0)	0,29

Tabela 7.1: Amostra final para decomposição morfológica espectral.

O programa interativo de ajuste foi utilizado nas 43 galáxias da amostra. O ajuste não pode ser feito em 19 delas, pois apresentaram características que não permitem fazer a decomposição morfológica em bojo e disco, como faixas de poeira ou disco muito fraco. Outras 15 apresentam problemas no ajuste, como mínimos locais intermitentes ou ausência de alguma componente. A coluna de observações na Tabela A.1 informa os problemas encontrados em cada caso. O sumário dos descartes é o seguinte:

- Ajuste ruim: 15
- Faixa de poeira: 9
- Disco fraco: 5
- Inclinada: 2
- Braço espiral: 1
- Irregular: 1
- Poucos *spaxels*: 1

A identificação dos ajustes ditos ruins foi feita através de inspeção visual, com um grau considerável de subjetividade. Os critérios incluem, por exemplo, a presença de mínimos locais intermitentes e degenerados (parâmetros saltando entre dois patamares com mudança imperceptível no aspecto dos perfis e no χ^2). Esta seleção foi feita de forma fortemente conservadora.

7. Decomposição morfológica espectral de galáxias

A amostra final deste trabalho (listada na Tabela 7.1) consiste em 9 galáxias que tiveram uma decomposição boa segundo estes critérios.

7.3 Aplicação da decomposição na amostra final

A decomposição morfológica espectral foi realizada nas 9 galáxias da amostra final. Figuras mostrando o resultado da decomposição de todas as galáxias podem ser vistas no Apêndice B. Nesta seção é discutido o resultado apenas para a galáxia em que se obteve a melhor decomposição, K0858 (UGC 10905). Recomenda-se comparar as figuras das outras galáxias com o que está exposto a seguir.

A Figura 7.3 permite uma visualização bidimensional, nos painéis superiores, do fluxo observado, modelo e resíduo em 5635 Å. No resíduo se observam efeitos de borda próximos às regiões externas mascaradas, além de artefatos seguindo um padrão quase regular¹. Pode-se observar também uma estrutura que parece ser um braço espiral, em excesso (azul) no resíduo. Isto não é surpresa, dado que esta galáxia é classificada como S0a. Outra forma de visualizar a qualidade do ajuste é através do perfil de brilho radial, no painel inferior. O perfil é calculado utilizando anéis elípticos, com a elipticidade calculada a partir da imagem observada.

A dependência em λ dos parâmetros morfológicos obtidos para K0858 é mostrada na Figura 7.4. As linhas pretas representam a decomposição final, feita λ -a- λ , e os pontos azuis a decomposição feita no primeiro passo da decomposição, em caixas de 100 Å. Regiões espectrais mascaradas antes de iniciar a decomposição (onde pode haver emissão de gás) estão marcadas em cinza. Marcadas em rosa estão regiões espectrais onde a decomposição falhou, quando o algoritmo não convergiu ou ficou preso nos limites dos parâmetros.

A primeira coisa que chama a atenção na Figura 7.4 é a diferença entre os parâmetros morfológicos obtidos em caixas de 100 Å e os obtidos a cada comprimento de onda. Isto pode ser devido à correção da cinemática (Seção 7.1.1), que praticamente não tem efeito numa imagem de banda espectral larga. Pode também estar relacionado ao sinal-ruído das imagens, que aumenta quando se soma imagens. De qualquer forma, estamos interessados apenas no espectro; sendo assim, leva-se em conta apenas a decomposição final.

¹O padrão hexagonal que aparece nas imagens (sobretudo nas de resíduo) está relacionado com a forma como os cubos são reconstruídos.

7.3. Aplicação da decomposição na amostra final

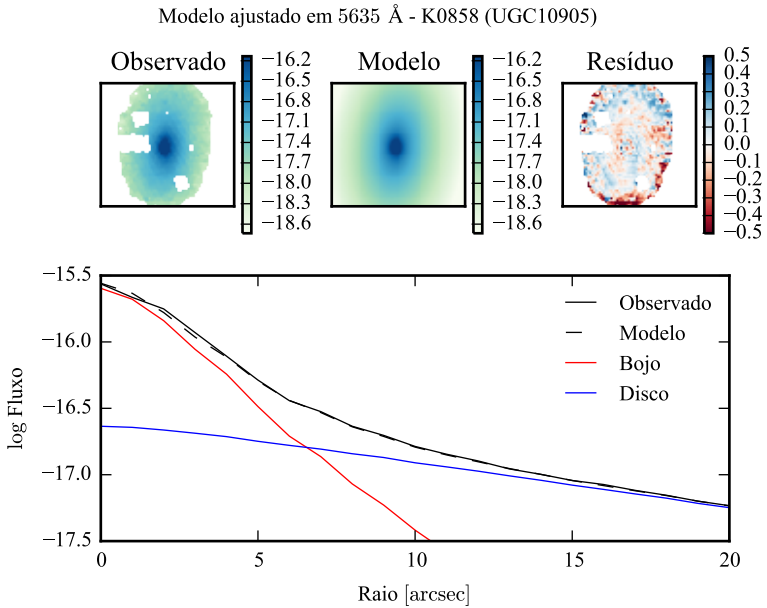


Figura 7.3: Acima: imagens observada, modelada e resíduo do fluxo em 5635 Å para K0858 (UGC 10905). Abaixo: perfis radiais, obtidos pela média do fluxo em anéis elípticos nas imagens. O fluxo observado é representado pela linha preta sólida. O melhor ajuste é representado pela linha preta tracejada. O bojo e o disco que compõem o modelo são mostrados em vermelho e azul, respectivamente.

7. Decomposição morfológica espectral de galáxias

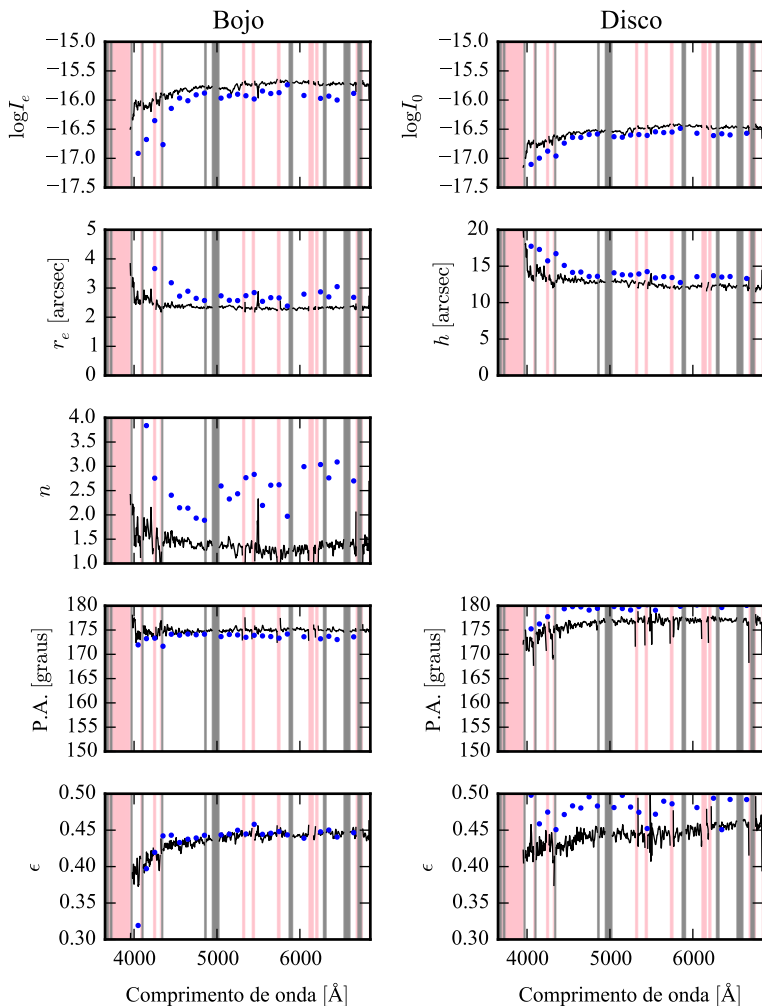


Figura 7.4: Parâmetros morfológicos em função do comprimento de onda para K0858 (UGC 10905). Regiões em rosa representam comprimentos de onda onde a decomposição falhou. Regiões em cinza foram mascaradas antes de iniciar a decomposição. Pontos azuis indicam o primeiro passo da decomposição, em caixas de 100 Å.

Pode-se observar um gradiente espectral no comprimento de escala do disco (h). Já o raio efetivo do bojo (r_e) e o índice de Sérsic (n) não apresentam um gradiente apreciável. Todos os parâmetros parecem ter um salto em 4000 Å. O ajuste falha em comprimentos de onda menores, ficando difícil determinar se isto é um resultado espúrio. Na verdade, qualquer tentativa de interpretação, observando apenas a dependência dos parâmetros morfológicos com o comprimento de onda, deve ser feita com cuidado. É esperado que os parâmetros variem com o comprimento de onda, quando são medidos em bandas espectrais largas e distantes, como mencionado na Seção 4.2.2. Entretanto, estas são evidências empíricas, sem um modelo que as suportem. Tirar conclusões da variação λ -a- λ dos parâmetros pode ser precipitado.

Os espectros de galáxias, por outro lado, são melhor compreendidos. Mesmo as menores características dos espectros, como linhas fracas de absorção, podem ser razoavelmente bem explicadas com modelos de populações estelares. Então, se um espectro de bojo ou disco tiver o aspecto de um espectro de galáxia, pode-se começar a levar o resultado da decomposição a sério. A Figura 7.5 mostra os espectros dos modelos (bojo em vermelho e disco em azul), no *spaxel* nuclear, a r_e de distância do núcleo, e o espectro integrado dos modelos. O espectro observado é mostrado em preto, e o resíduo em magenta.

Com uma análise visual, os espectros parecem galáticos. Nos piores casos os bojos parecem ter um ajuste pior do que os discos, e costumam ter dimensões comparáveis à largura da PSF. A má resolução dos bojos pode comprometer a decomposição, nestes casos. Pode-se observar que o resíduo geralmente apresenta um gradiente nos *spaxels*, e praticamente desaparece no espectro integrado. Este gradiente no resíduo indica que os modelos somados são mais vermelhos do que o espectro observado. Isto certamente irá afetar o resultado da síntese de populações estelares, analisada na seção a seguir. Os espectros integrados dos modelos, se tiverem tal gradiente de cor, devem ter uma forma tal que se cancelam no resíduo.

7.4 Síntese espectral de populações estelares

A síntese espectral de populações estelares utilizando STARLIGHT foi aplicada às componentes morfológicas e ao espectro original de todas as galáxias da amostra final. A base utilizada foi a de Granada–MILES. Dentre as galáxias da amostra, apenas duas tiveram um ajuste bom com o STARLIGHT: K0592 e K0858. Os espectros ajustados e as propriedades obtidas para toda a amostra

7. Decomposição morfológica espectral de galáxias

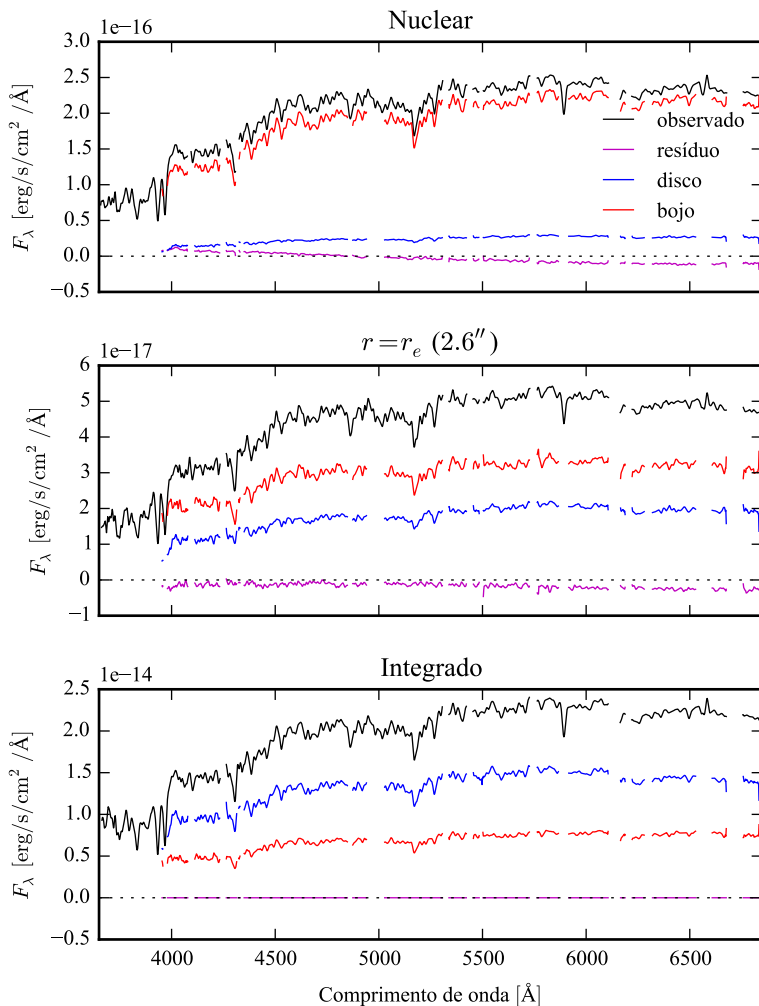


Figura 7.5: Espectro das componentes morfológicas de K0858 (UGC 10905), observado (preto), bojo (vermelho), disco (azul) e resíduo (magenta). Acima: Espectro do *spaxel* nuclear da galáxia. Meio: Espectro em um *spaxel* a uma distância de r_e do núcleo. Abaixo: Espectro integrado espacialmente.

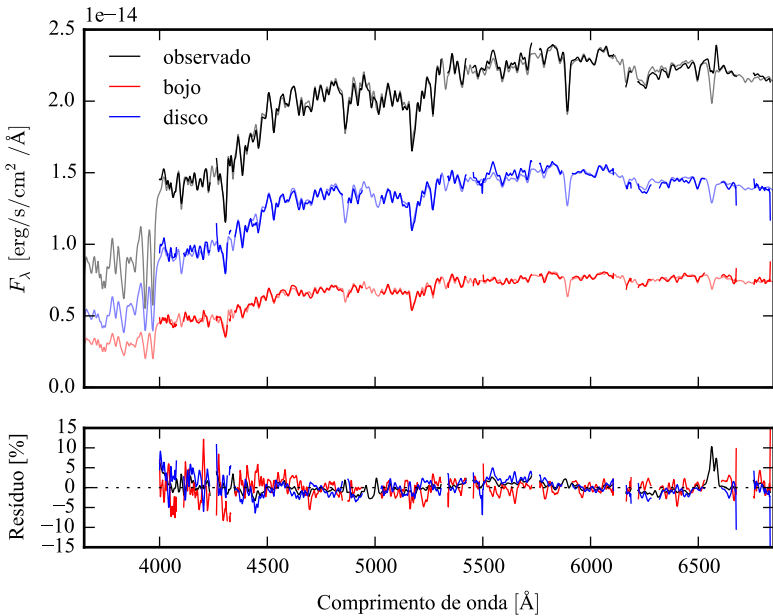


Figura 7.6: Acima: Espectros integrados das componentes morfológicas de K0858 (UGC 10905), ajustados com STARLIGHT. Em preto, espectro observado. Em vermelho, e azul, as componentes bojo e disco. Em linhas de cor clara, o espectro ajustado pelo STARLIGHT. Abaixo: Resíduo dos espectros (observado menos sintético, dividido pelo observado).

estão no Apêndice B. A seguir uma discussão sobre o resultado para K0858.

A Figura 7.6 mostra ajustes do STARLIGHT para os espectros integrados observado, do bojo e do disco. As linhas mais claras mostram o melhor ajuste. No painel inferior, tem-se o resíduo do ajuste em relação ao espectro de entrada. O ajuste é bom em linhas gerais, embora seja possível ver alguns pontos onde o resíduo do bojo e do disco estejam anti-correlacionados, devido à degenerescência do modelo.

As propriedades físicas derivadas da síntese de populações estelares é mostrada na Figura 7.7. Ali, pode-se ver um perfil radial das propriedades,

7. Decomposição morfológica espectral de galáxias

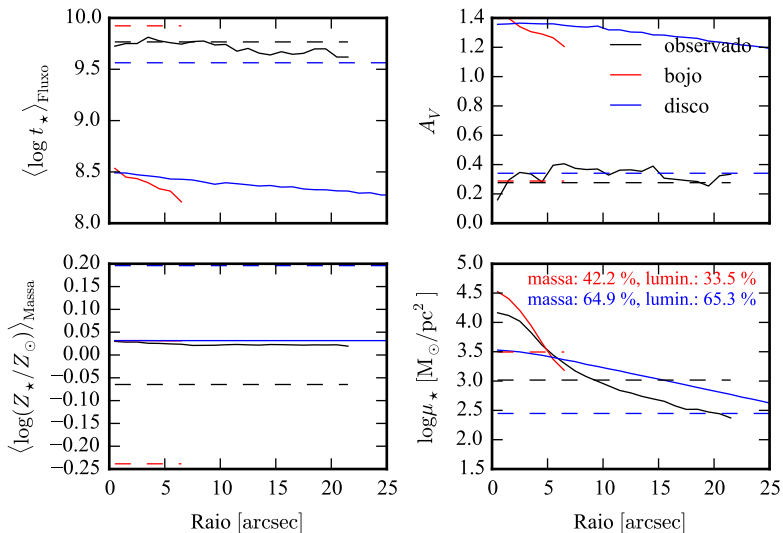


Figura 7.7: Perfil radial de propriedades físicas das componentes morfológicas de K0858 (UGC 10905), obtidos através do STARLIGHT. As linhas contínuas representam as propriedades obtidas utilizando espectros espacialmente resolvidos. As linhas tracejadas representam as propriedades obtidas utilizando os espectros integrados. Em preto, espectro observado. Em vermelho, e azul, as componentes bojo e disco. Acima, à esquerda: idade estelar média ponderada pela luminosidade. Acima, à direita: atenuação por poeira, na banda V. Abaixo, à esquerda: metalicidade estelar média, ponderada pela massa. Abaixo, à direita: densidade superficial de massa estelar. As frações de massa e luminosidade entre as componentes e a total (obtida do espectro observado) são indicadas no painel inferior, à direita.

ajustados nos espectros de cada *spaxel*, ou seja, espacialmente resolvidos, em linhas sólidas. As propriedades derivadas do espectro integrado são mostradas como linhas tracejadas. Pode-se notar que a atenuação por poeira A_V (painel superior direito), tanto no bojo quanto no disco, é muito diferente da atenuação para os espectros observados quando se utilizam os espectros espacialmente resolvidos. O mesmo se observa para a idade estelar média ponderada pela luminosidade (painel superior esquerdo). Estes dois fatos provavelmente têm relação com o gradiente de cor aparente no resíduo da decomposição morfológica espectral. A metalicidade estelar média ponderada pela massa (painel inferior esquerdo), quando espacialmente resolvida, é muito diferente da calculada no espectro integrado, para todos os casos. A densidade superficial de massa estelar é mostrada no painel inferior direito. A massa e a luminosidade das componentes morfológicas, em relação à massa da galáxia original, são mostrados no mesmo painel. Note que, devido à quantidade de poeira, a densidade de massa superficial espacialmente resolvida das componentes morfológicas é maior do que a calculada com o espectro observado. Estes problemas com a idade estelar e a atenuação por poeira, nos espectros espacialmente resolvidos, aparecem também nas outras galáxias da amostra, mesmo na outra galáxia com um bom ajuste de populações estelares, a K0592.

As propriedades obtidas com os espectros integrados, por outro lado, parecem melhor comportadas. A Figura 7.8 mostra um gráfico da idade contra metalicidade estelar, para as componentes morfológicas (bojo em vermelho e disco em azul) e para o espectro observado (em preto) de K0592 e K0858. A massa da galáxia (ou da componente morfológica) é representada pela área do círculo. As duas galáxias, neste gráfico, têm um comportamento similar. Ambas têm um bojo mais velho e de metalicidade mais baixa, e um disco mais jovem e de metalicidade mais alta, com relação à idade e metalicidade do espectro observado. Também é interessante notar que os pontos para uma mesma galáxia estão alinhados. Isto pode acontecer devido à degenerescência entre idade e metalicidade, comumente vista em sínteses de população estelar.

É interessante comparar a Figura 7.8 com o resultado de Johnston et al. (2012), reproduzido na Figura 7.9. Os resultados obtidos aqui, embora não tenham significância estatística, são contrários ao resultado de Johnston et al., que obtêm, para galáxias S0, bojos mais jovens e mais metálicos que seus discos. Tanto a idade quanto a metalicidade que eles utilizam foram obtidos através do ajuste de duas linhas de absorção, enquanto neste trabalho o espectro inteiro foi utilizado no ajuste de populações estelares.

7. Decomposição morfológica espectral de galáxias

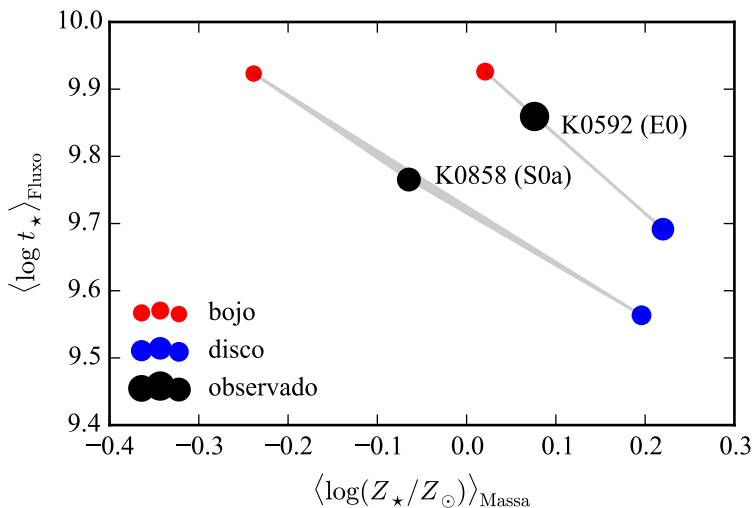


Figura 7.8: Idade estelar média ponderada pela luminosidade contra metalicidade estelar média ponderada pela massa, para as componentes morfológicas de duas galáxias do CALIFA: K0592 (NGC 4874, E0) e K0858 (UGC10905, S0a). Idades e metalicidades foram obtidas pelo STARLIGHT. Pontos em preto são referentes ao espectro observado, total da galáxia. Pontos em vermelho são referentes ao bojo, e em azul, ao disco. A área dos círculos indica a massa estelar.

Além disso, eles trabalham com perfis unidimensionais (espectros de fenda longa), enquanto análise feita aqui é toda em 2-D (imagens). Por fim, não é óbvio que as galáxias de nossa amostra sejam comparáveis à da amostra de Johnston et al.. De fato, apesar de ambas amostras selecionarem galáxias S0, as galáxias de Johnston et al. parecem ser menos massivas que as nossas. Enquanto K0858 tem magnitude absoluta na banda B de $M_B = -21$ (K0592 tem medida somente na banda V , com $M_V = -23,6$), as de Johnston et al. M_B entre -17 e -19 .

Todas essas diferenças complicam a comparação dos resultados obtidos neste trabalho com aqueles do artigo que inspirou todo esse estudo. De

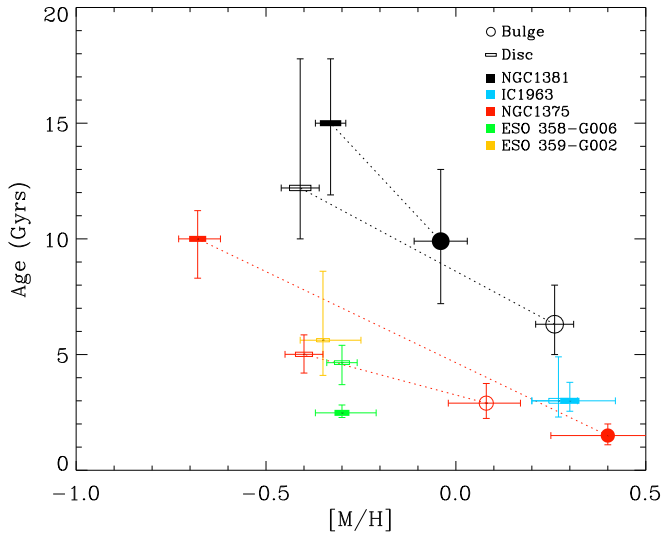


Figura 7.9: A mesma Figura que 4.6, mostrada novamente para comparar com a Figura 7.8.

qualquer modo, os experimentos aqui reportados mostram que a decomposição morfológica espectral é um problema bastante mais delicado do que se imaginava anteriormente.

Conclusões e perspectivas

O *survey* CALIFA observou cerca de 600 galáxias nas configurações V500 e V1200. Foram publicados cubos de 100 galáxias no primeiro *data release*, e de 200 galáxias no segundo. Os cubos das galáxias restantes ainda estão em processo de controle de qualidade e embargo da colaboração. Através do programa STARLIGHT, foram obtidos diversos parâmetros relacionados às populações estelares componentes de cada *spaxel*, formando cubos de dados adicionais aos observados, com as propriedades físicas espacialmente resolvidas obtidas a partir da saída do STARLIGHT.

Neste trabalho, foi desenvolvido um programa chamado PyCASSO para organizar e analisar estes cubos de dados. Este programa é utilizado por cerca de 10 pessoas que estudam populações estelares na colaboração do CALIFA. Bastante atenção foi dada à documentação (Seção 3.1, com o manual completo no Apêndice C). Foram publicados 6 artigos que se baseiam fortemente no uso de PyCASSO para análise e gráficos, resumidos na Seção 3.2 e presentes como apêndices deste trabalho (Apêndices D.1, D.2, D.3 e D.4).

Com o fim do *survey* CALIFA, e a liberação de todas as galáxias da amostra, os cubos de dados de propriedades físicas poderão ser publicados. Já tivemos uma boa experiência com a base de dados pública do STARLIGHT (<http://www.starlight.ufsc.br/>), com o resultado da síntese de população estelar de 926246 espectros de galáxias do SDSS. Será necessária uma abordagem diferente para o acesso aos cubos, algo que ainda precisa ser planejado e desenvolvido.

PyCASSO já foi usado com sucesso com dados de outros *surveys* como o PINGS (Rosales-Ortega et al. 2010), um precursor do CALIFA, porém com até 10 vezes mais espectros por galáxia. MaNGA (Bundy et al. 2015) está em andamento, e deverá obter IFS de 10.000 galáxias. Muito embora tenha um número muito maior de galáxias do que o CALIFA, sua cobertura espacial será menor. Assim, estes *surveys* deverão ser complementares

8. Conclusões e perspectivas

ao CALIFA. Testes com dados preliminares do MaNGA foram feitos com PyCASSO, requerendo apenas pequenas modificações para que funcionem normalmente.

É importante que PyCASSO se torne um programa modular, onde o usuário cria uma descrição do arquivo de IFS de forma que o programa saiba como ler os dados. Recentemente o autor deste trabalho, junto com pesquisadores do Grupo de Astrofísica da UFSC, começou a colaborar com um novo *survey* chamado Diving3D. Este *survey*, descrito em Ricci et al. (2014), vai obter IFS de quase 200 núcleos de galáxias utilizando o Telescópio Gemini. Os cubos de dados espectrais são de uma qualidade excepcional, e já iniciamos a adaptação de ferramentas como o PyCASSO e o STARLIGHT para trabalhar com esses dados. O objetivo, do ponto de vista ferramental, é que se crie uma *pipeline* onde dados como populações estelares, morfologia, etc, vão sendo adicionados de forma incremental aos cubos, mantendo uma interface comum para análise dos dados.

Foi desenvolvida uma técnica de síntese espectral aplicada às componentes morfológicas (bojo e disco) de galáxias. A decomposição morfológica do perfil de brilho em uma imagem de uma galáxia é um campo de estudo bem desenvolvido, com ferramentas bastante eficientes disponíveis na comunidade acadêmica (GALFIT, BUDDA e IMFIT, por exemplo). A ideia aqui foi se valer destas ferramentas, junto com PyCASSO, e realizar a decomposição para imagens em cada comprimento de onda dos cubos de dados espectrais.

Ao fazer a decomposição morfológica em janelas estreitas de comprimento de onda, os efeitos de cinemática precisaram ser levados em consideração. Em uma imagem de uma galáxia, em um determinado comprimento de onda, não se observam os mesmos processos físicos em todos os *pixels*. A luz de cada *pixel* é composta pela luz de diversas estrelas, cada uma com uma velocidade diferente em relação à linha de visada (e conseqüentemente um *redshift* ou *blueshift* diferente), com cada *pixel* contendo um conjunto distinto destas velocidades. Para mitigar este problema, a distribuição de velocidades de cada *spaxel* dos cubos de dados foi determinada, de forma aproximada, por uma velocidade sistêmica e uma dispersão de velocidades. Os *spaxels* foram colocados todos no *rest frame*, e com a mesma dispersão de velocidade (ver Seção 7.1.1 para detalhes). Isto fez com que a resolução fosse degradada, mas garante que se observa a luz da galáxia inteira de forma consistente.

A PSF é uma peça chave neste quebra-cabeças morfológico. Sem uma boa medida da forma da PSF, a decomposição morfológica pode não funcionar, ou pior, gerar resultados equivocados. No Capítulo 5, foi descrito como

a PSF do CALIFA foi medida, um resultado que acabou sendo adotado pela colaboração, publicado no segundo *data release* (García-Benito et al. 2015). A PSF obtida segue um perfil de Moffat, com $\beta = 4$ e $\text{FWHM} = 2,9 \pm 0,3''$. Com esta incerteza na estimativa da largura da PSF, testes foram feitos para determinar o efeito que um erro na PSF causa no resultado da decomposição morfológica, apresentados na Seção 6.3. Em via de regra, a decomposição dos espectros em componentes morfológicas, quando se utiliza a PSF errada, apresenta artefatos como gradientes de cores e linhas espectrais artificiais. Estes problemas parecem ser atenuados quando se utilizam os espectros integrados das componentes morfológicas.

No Capítulo 7 foi escolhida, dentre as galáxias do CALIFA observadas com a configuração V500, uma amostra de 43 galáxias que foram classificadas com boa possibilidade de serem da classe S0. O objetivo era ter galáxias que pudessem ser bem ajustadas a um modelo bojo–disco. Destas 43, 19 tinham características que não permitiam o uso deste modelo, seja por faixas de poeira, uma das componentes muito fraca, ou problema nos dados, entre outras coisas. Outras 15 tiveram problema no ajuste do modelo inicial. Somente 9 galáxias tiveram um relativo sucesso na decomposição morfológica espectral. O resultado da decomposição para todas as 9 galáxias da amostra final é mostrado nas figuras do Apêndice B. A galáxia K0858 (UGC 10905), classificada como S0a, foi escolhida para uma análise mais detalhada, em parte pela sua decomposição morfológica ter sido muito boa, e em parte por ter um bom ajuste com o STARLIGHT.

Em K0858 verificou-se que há um gradiente espectral em alguns dos parâmetros morfológicos, que foram ajustados levando em conta apenas informações espaciais. Entretanto, não se pode descartar que estes gradientes, e outras características menores observadas na dependência dos parâmetros com o comprimento de onda, não sejam artefatos da forma como a decomposição foi feita. O teste com os erros na PSF deixaram isto bem claro, assim como os resíduos nos espectros (vide Figura 7.5). É preciso estudar a forma como os parâmetros morfológicos deveriam variar com o comprimento de onda. Compreender a forma como as populações estelares se distribuem nas componentes morfológicas de uma galáxia, e como estas populações se refletem no espectro espacialmente resolvido da galáxia, é fundamental para poder fazer uma decomposição morfológica que leve em conta informações das regiões vizinhas no espectro.

A síntese de populações estelares foi realizada com sucesso apenas em K0592 (NGC 4874, classificada como E0), e K0858. O ajuste dos espectros e as propriedades físicas, para todas as 9 galáxias da amostra, estão disponí-

8. Conclusões e perspectivas

veis no Apêndice B. Apenas K0592 e K0858 tiveram um resíduo no ajuste do STARLIGHT pequeno o bastante para poderem ter as propriedades físicas obtidas para seus bojos e discos levadas a sério. A Figura 7.8 mostra idade e metalicidade estelar médias para as componentes das duas galáxias, calculados sobre os espectros integrados. Esta figura indica que os bojos apresentam populações mais velhas e menos metálicas, enquanto os discos apresentam populações mais jovens e mais metálicas, em relação ao espectro observado.

Um estudo que poderia ser feito com os resultados da síntese de populações aplicados à decomposição morfológica espectral é medir a densidade superficial de massa estelar do disco, que fica normalmente ofuscado pelo bojo nas regiões centrais. O objetivo é verificar previsão de Freeman (1970), que diz que a densidade superficial de massa do núcleo dos discos de galáxias é sempre o mesmo, independente do tipo morfológico e do perfil de massa que a galáxia tenha. Todavia, a síntese de populações espacialmente resolvida não é muito robusta da forma como é feita aqui, como visto na Figura 7.7. Entre as prováveis causas está a degenerescência no modelo bojo–disco, com 7 parâmetros livres. Deixar parâmetros como P.A. e ϵ fixos pode ajudar, mas isso requer testes.

Muitos problemas podem ter sido causados pela forma como se trata a cinemática. Talvez seja preciso fazer testes com modelos dinâmicos simples de galáxias para verificar se a abordagem utilizada é mesmo adequada. Outra alternativa seria fazer a decomposição de forma iterativa. Depois de ter determinado as componentes morfológicas, utilizar este conhecimento para tentar medir a cinemática das duas componentes nos dados originais, e tentar fazer uma correção melhor, repetindo a decomposição. Não é óbvio, entretanto, que esta abordagem vá realmente convergir, ou mesmo se é factível computacionalmente.

Mesmo com todos estes problemas em potencial, o passo lógico seguinte é tentar aplicar o ajuste a galáxias espirais. A própria K0858 apresenta um resíduo no ajuste morfológico que parece um braço espiral (ver Figura B.52). Os braços espirais têm um papel importante na formação estelar, e com esta abordagem pode-se tentar obter o histórico de formação estelar nestas regiões. Também pode-se tentar utilizar um outro modelo morfológico para ajustar galáxias com um grande ângulo de inclinação. Com mais galáxias, seria possível aplicar o estudo a uma boa fração da amostra do CALIFA, e obter uma melhor estatística.

Apêndice A

Amostra para decomposição morfológica espectral

Tabela A.1

ID	Nome	Classe	Mín.	Máx.	ε	Obs.
K0018	NGC 0155	1 (E1)	0 (E0)	8 (S0)	0,22	-
K0020	NGC 0160	10 (Sa)	8 (S0)	13 (Sbc)	0,37	Disco fraco
K0044	NGC 0499	5 (E5)	2 (E2)	8 (S0)	0,39	Ajuste ruim
K0046	NGC 0504	8 (S0)	7 (E7)	8 (S0)	0,47	Inclinada
K0051	NGC 0529	4 (E4)	3 (E3)	8 (S0)	0,14	Disco fraco
K0072	NGC 0774	8 (S0)	6 (E6)	8 (S0)	0,28	Disco fraco
K0087	NGC 0932	9 (S0a)	8 (S0)	10 (Sa)	0,04	Braço espiral
K0100	NGC 1056	10 (Sa)	8 (S0)	11 (Sab)	0,43	Faixa de poeira
K0119	NGC 1167	8 (S0)	7 (E7)	10 (Sa)	0,19	Ajuste ruim
K0127	NGC 1349	6 (E6)	0 (E0)	10 (Sa)	0,11	-
K0160	NGC 2476	6 (E6)	3 (E3)	8 (S0)	0,31	Ajuste ruim
K0279	NGC 2918	6 (E6)	4 (E4)	8 (S0)	0,29	Ajuste ruim
K0311	NGC 3106	11 (Sab)	8 (S0)	19 (Ir)	0,07	Ajuste ruim
K0341	UGC 05771	6 (E6)	4 (E4)	8 (S0)	0,29	Ajuste ruim
K0548	NGC 4470	14 (Sc)	5 (E5)	19 (Ir)	0,34	Irregular
K0592	NGC 4874	0 (E0)	0 (E0)	8 (S0)	0,12	-
K0602	NGC 4956	1 (E1)	0 (E0)	8 (S0)	0,14	-
K0607	UGC 08234	8 (S0)	6 (E6)	8 (S0)	0,37	Ajuste ruim
K0612	NGC 5029	6 (E6)	4 (E4)	8 (S0)	0,32	Ajuste ruim
K0633	NGC 5216	0 (E0)	0 (E0)	8 (S0)	0,09	Disco fraco
K0708	NGC 5485	5 (E5)	1 (E1)	8 (S0)	0,19	Faixa de poeira
K0744	NGC 5631	8 (S0)	1 (E1)	8 (S0)	0,11	Faixa de poeira
K0778	NGC 5784	8 (S0)	1 (E1)	8 (S0)	0,19	Faixa de poeira
K0780	NGC 5797	7 (E7)	4 (E4)	8 (S0)	0,35	Ajuste ruim
K0814	UGC 10097	5 (E5)	1 (E1)	8 (S0)	0,26	Ajuste ruim
K0816	NGC 6021	5 (E5)	3 (E3)	8 (S0)	0,22	Ajuste ruim
K0822	UGC 10205	9 (S0a)	8 (S0)	10 (Sa)	0,42	Faixa de poeira
K0832	NGC 6146	5 (E5)	3 (E3)	8 (S0)	0,23	-
K0840	NGC 6173	6 (E6)	3 (E3)	8 (S0)	0,35	Ajuste ruim

Continua na próxima página

A. Amostra para decomposição morfológica espectral

Tabela A.1 – continuada da página anterior

ID	Nome	Classe	Mín.	Máx.	€	Obs.
K0846	UGC 10695	5 (E5)	2 (E2)	8 (S0)	0,33	-
K0850	NGC 6314	11 (Sab)	8 (S0)	14 (Sc)	0,49	Faixa de poeira
K0851	NGC 6338	5 (E5)	1 (E1)	8 (S0)	0,34	-
K0858	UGC 10905	9 (S0a)	7 (E7)	11 (Sab)	0,47	-
K0874	NGC 7025	9 (S0a)	8 (S0)	10 (Sa)	0,28	Poucos <i>spaxels</i>
K0875	UGC 11694	9 (S0a)	8 (S0)	10 (Sa)	0,23	Faixa de poeira
K0900	NGC 7550	4 (E4)	0 (E0)	8 (S0)	0,08	Ajuste ruim
K0908	NGC 7611	8 (S0)	6 (E6)	8 (S0)	0,50	Inclinada
K0912	NGC 7623	8 (S0)	8 (S0)	8 (S0)	0,29	-
K0913	NGC 7625	10 (Sa)	0 (E0)	19 (Ir)	0,22	Faixa de poeira
K0916	NGC 7671	8 (S0)	7 (E7)	8 (S0)	0,35	Ajuste ruim
K0917	NGC 7683	8 (S0)	6 (E6)	8 (S0)	0,38	Ajuste ruim
K0923	NGC 7711	7 (E7)	4 (E4)	8 (S0)	0,47	Disco fraco
K0925	NGC 7722	11 (Sab)	3 (E3)	19 (Ir)	0,13	Faixa de poeira

Tabela A.1: Amostra selecionada para decomposição morfológica espectral.

Decomposição morfológica espectral e síntese de populações estelares da amostra final

B.1 K0018 (NGC 0155)

- Galáxia NGC 0155
- Tipo morfológico: E1 (mín. E0, máx. S0)
- Magnitude absoluta na banda r : $-21,85$
- Elipticidade: 0,22

B. Decomposição morfológica espectral e síntese de populações estelares da amostra final

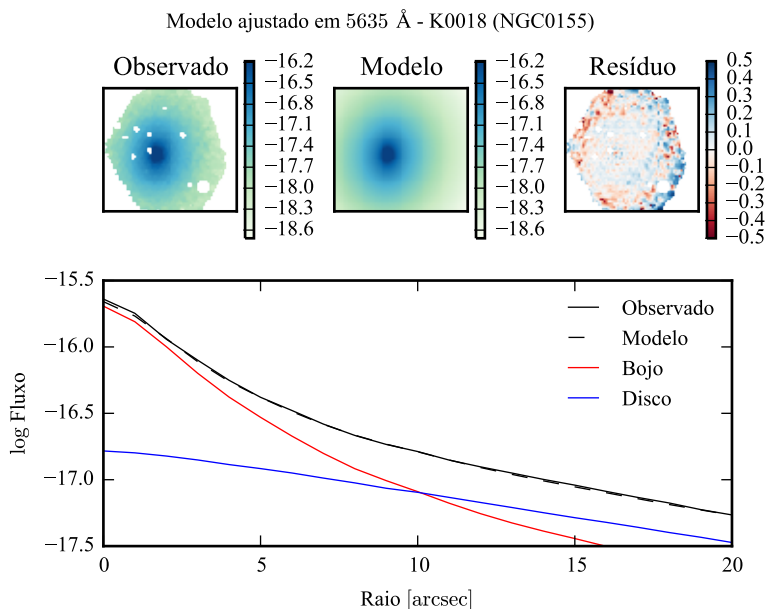


Figura B.1: Acima: imagens observada, modelada e resíduo, do fluxo em 5635 Å para K0018 (NGC 0155). Abaixo: perfis radiais, obtidos pela média do fluxo em anéis elípticos nas imagens. O fluxo observado é representado pela linha preta sólida. O melhor ajuste é representado pela linha preta tracejada. O bojo e o disco que compõe o modelo são mostrados em vermelho e azul, respectivamente.

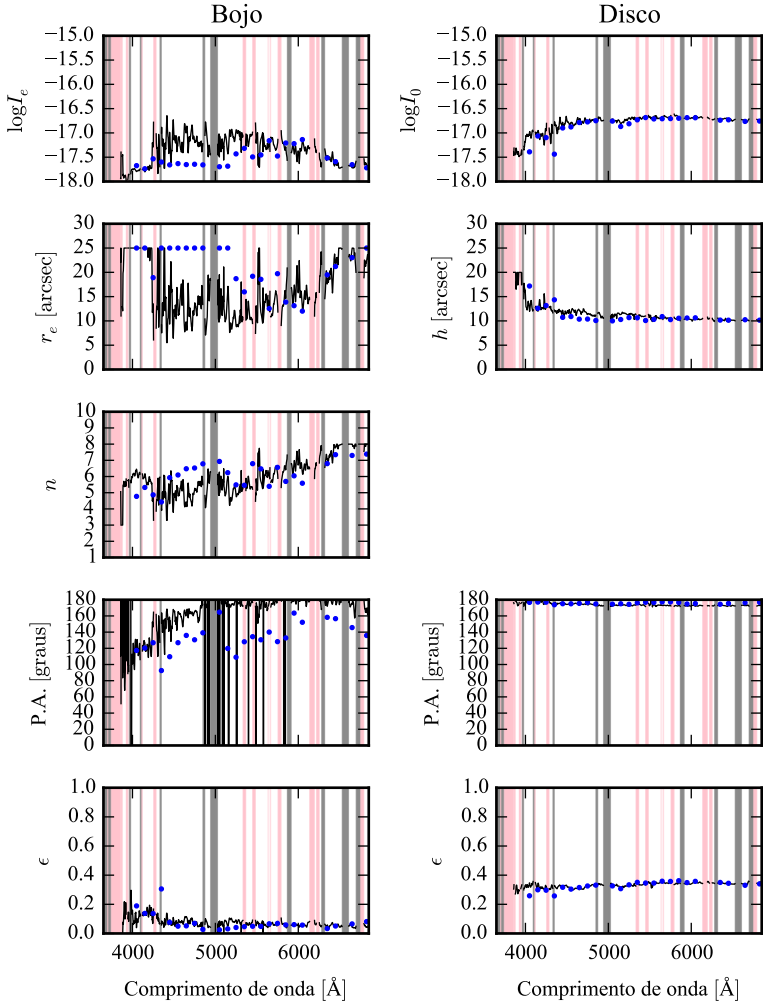


Figura B.2: Parâmetros morfológicos em função do comprimento de onda para K0018 (NGC 0155). Regiões em rosa representam comprimentos de onda onde a decomposição falhou. Regiões em cinza foram mascaradas antes de iniciar a decomposição. Pontos azuis indicam o primeiro passo da decomposição, em caixas de 100 Å.

B. Decomposição morfológica espectral e síntese de populações estelares da amostra final

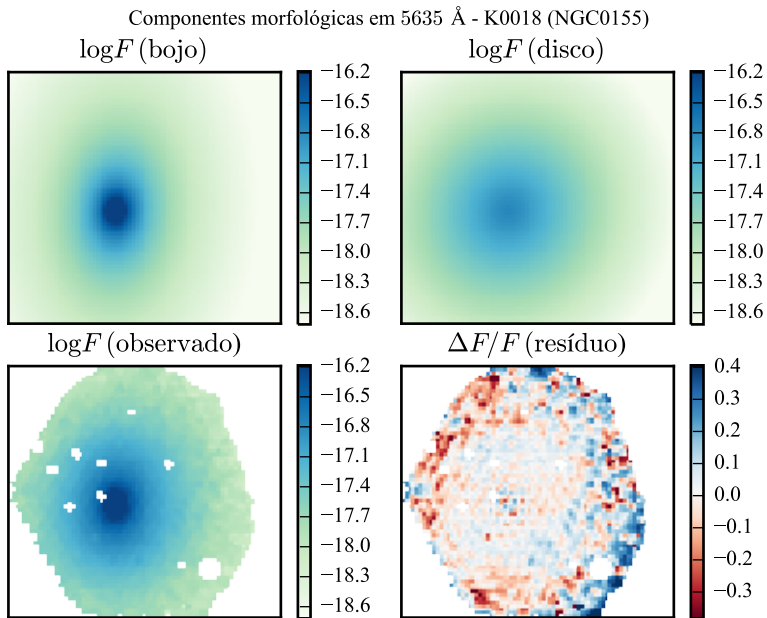


Figura B.3: Imagens em 5635 Å das componentes morfológicas de K0018 (NGC 0155).

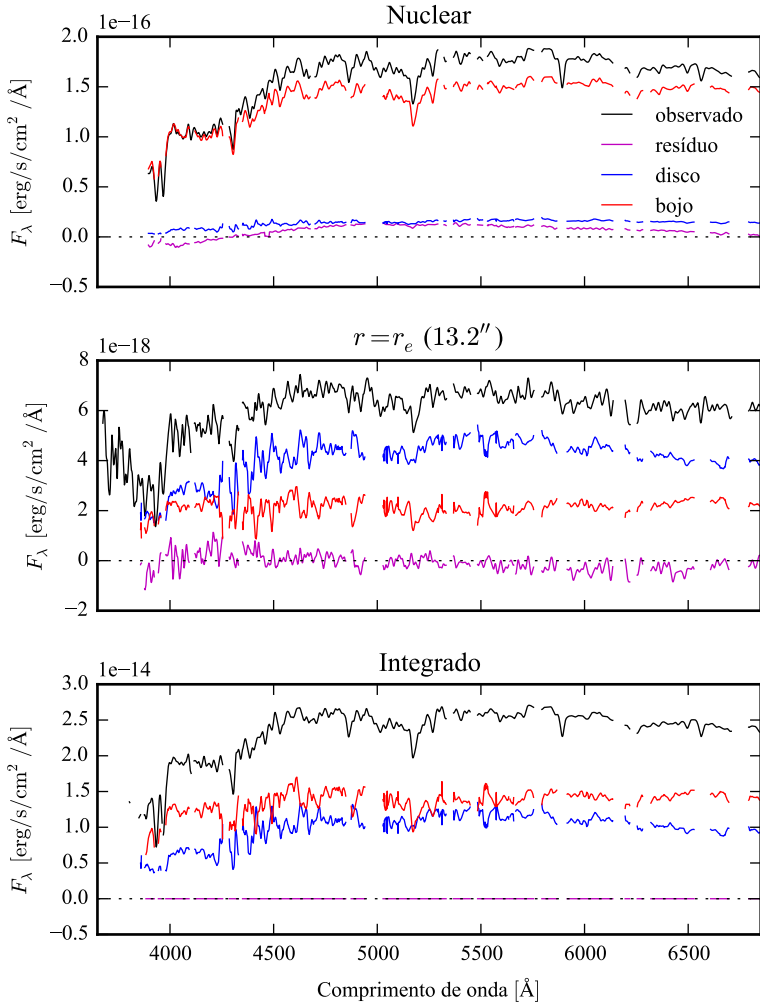


Figura B.4: Espectro das componentes morfológicas de K0018 (NGC 0155), observado (preto), bojo (vermelho), disco (azul) e resíduo (magenta). Acima: Espectro do *spaxel* nuclear da galáxia. Meio: Espectro em um *spaxel* a uma distância de r_e do núcleo. Abaixo: Espectro integrado espacialmente.

B. Decomposição morfológica espectral e síntese de populações estelares da amostra final

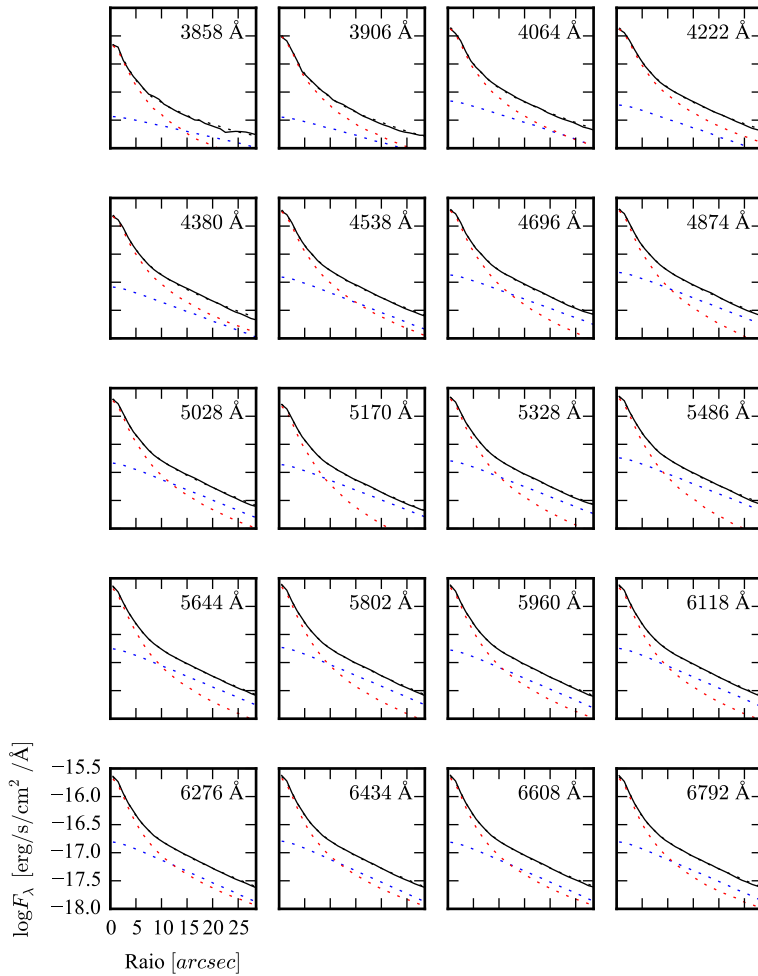


Figura B.5: Perfis radiais para diversos comprimentos de onda de K0018 (NGC 0155).

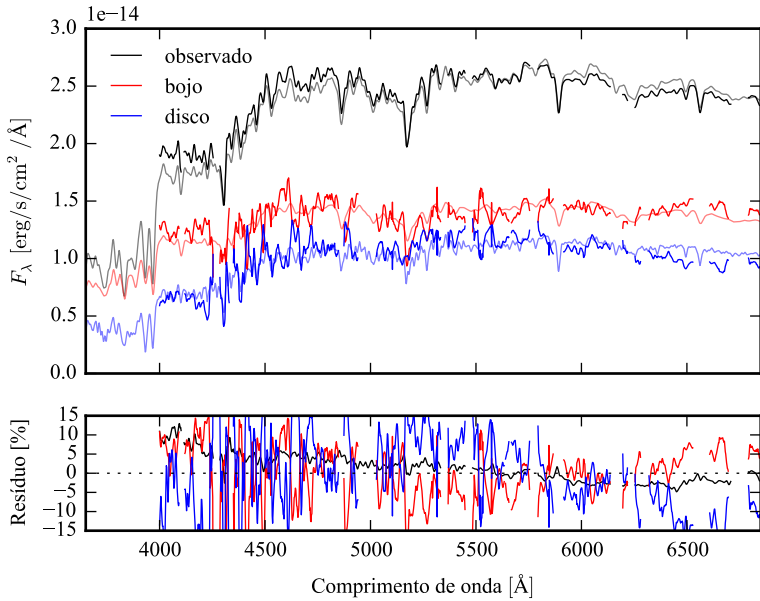


Figura B.6: Acima: Espectros integrados das componentes morfológicas de K0018 (NGC 0155), ajustados com STARLIGHT. Em preto, espectro observado. Em vermelho, e azul, as componentes bojo e disco. Em linhas de cor clara, o espectro ajustado pelo STARLIGHT. Abaixo: Resíduo dos espectros (observado menos sintético, divididos pelo observado).

B. Decomposição morfológica espectral e síntese de populações estelares da amostra final

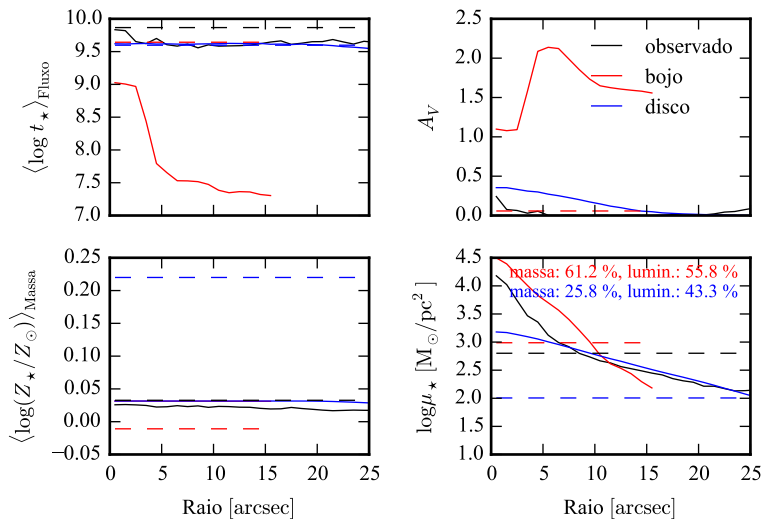


Figura B.7: Perfil radial de propriedades físicas das componentes morfológicas de K0018 (NGC 0155), obtidos através do STARLIGHT. As linhas contínuas representam as propriedades obtidas utilizando espectros espacialmente resolvidos. As linhas tracejadas representam as propriedades obtidas utilizando os espectros integrados. Em preto, espectro observado. Em vermelho, e azul, as componentes bojo e disco. Acima, à esquerda: idade estelar média ponderada pela luminosidade. Acima, à direita: atenuação por poeira, na banda V . Abaixo, à esquerda: metalicidade estelar média, ponderada pela massa. Abaixo, à direita: densidade superficial de massa estelar. As frações de massa e luminosidade entre as componentes e a total (obtida do espectro observado) é mostrada no painel inferior, à direita.

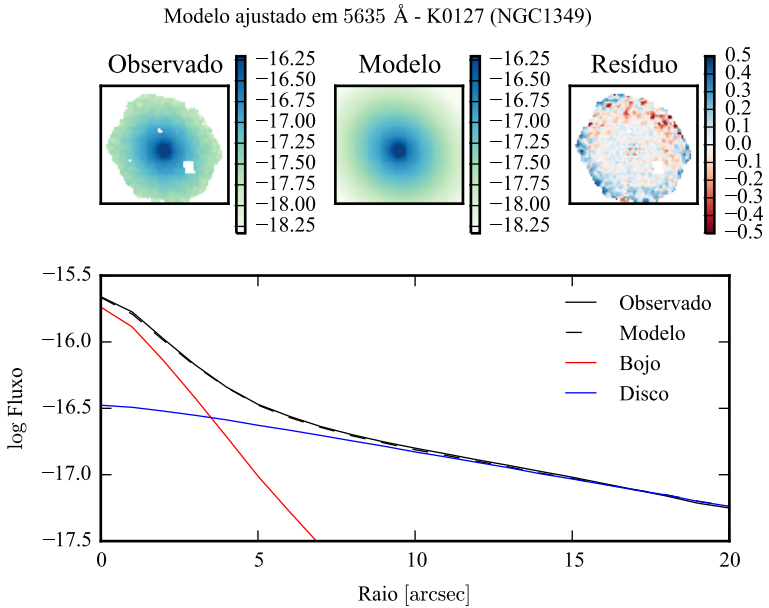


Figura B.8: Acima: imagens observada, modelada e resíduo, do fluxo em 5635 Å para K0127 (NGC 1349). Abaixo: perfis radiais, obtidos pela média do fluxo em anéis elípticos nas imagens. O fluxo observado é representado pela linha preta sólida. O melhor ajuste é representado pela linha preta tracejada. O bojo e o disco que compõe o modelo são mostrados em vermelho e azul, respectivamente.

B.2 K0127 (NGC 1349)

- Galáxia NGC 1349
- Tipo morfológico: E6 (mín. E0, máx. Sa)
- Magnitude absoluta na banda r : $-22,15$
- Elipticidade: 0,11

B. Decomposição morfológica espectral e síntese de populações estelares da amostra final

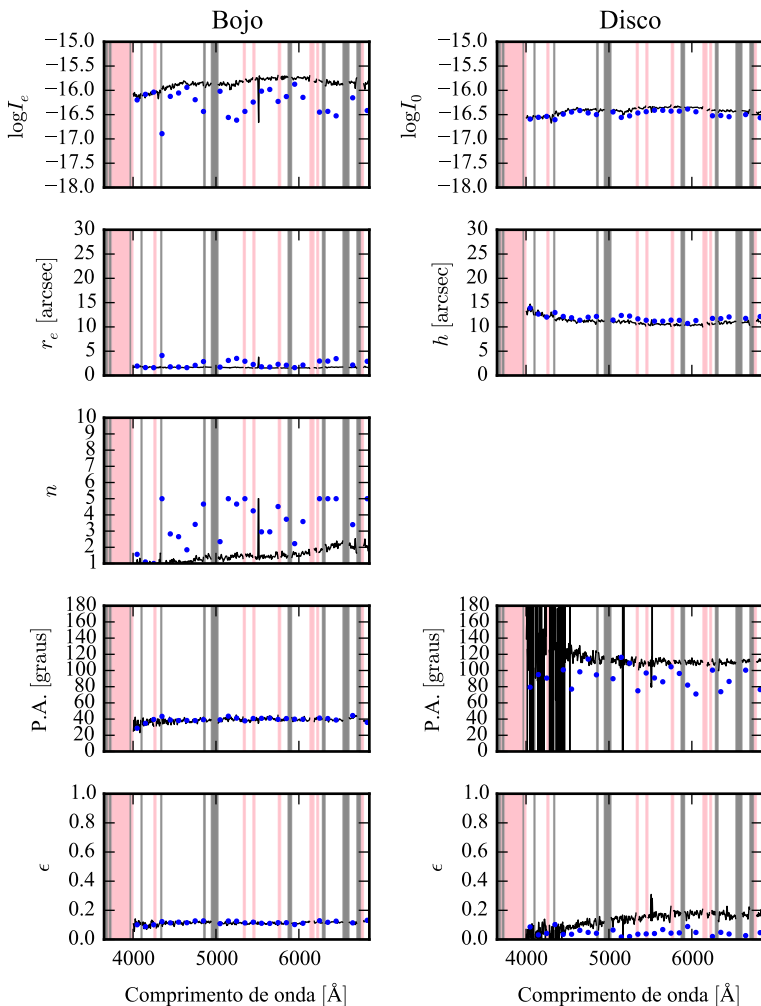


Figura B.9: Parâmetros morfológicos em função do comprimento de onda para K0127 (NGC 1349). Regiões em rosa representam comprimentos de onda onde a decomposição falhou. Regiões em cinza foram mascaradas antes de iniciar a decomposição. Pontos azuis indicam o primeiro passo da decomposição, em caixas de 100 Å.

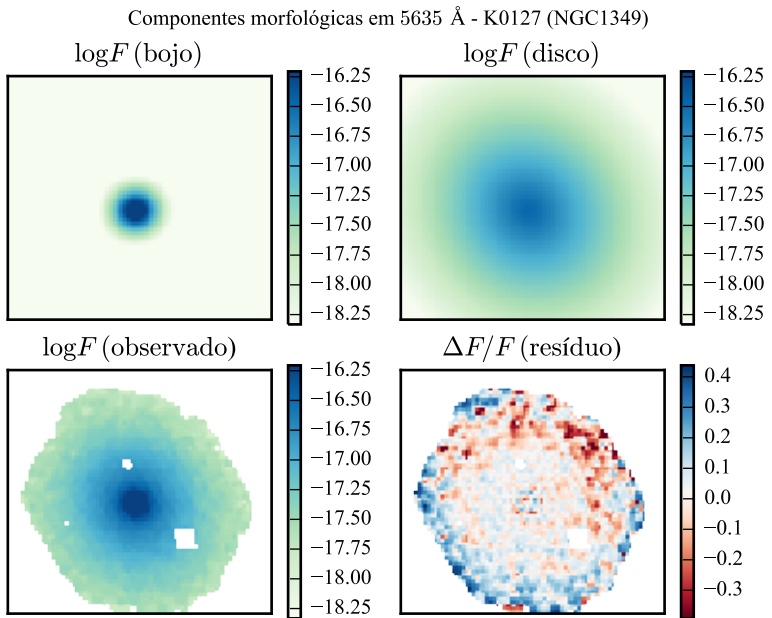


Figura B.10: Imagens em 5635 Å das componentes morfológicas de K0127 (NGC 1349).

B. Decomposição morfológica espectral e síntese de populações estelares da amostra final

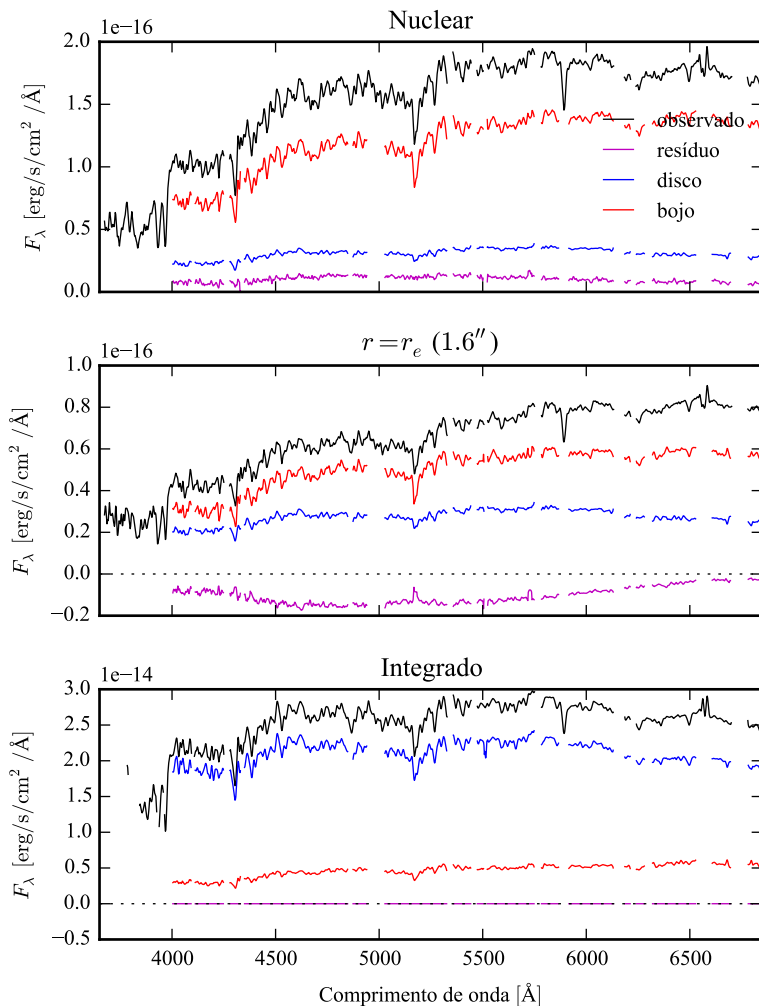


Figura B.11: Espectro das componentes morfológicas de K0127 (NGC 1349), observado (preto), bojo (vermelho), disco (azul) e resíduo (magenta). Acima: Espectro do *spaxel* nuclear da galáxia. Meio: Espectro em um *spaxel* a uma distância de r_e do núcleo. Abaixo: Espectro integrado espacialmente.

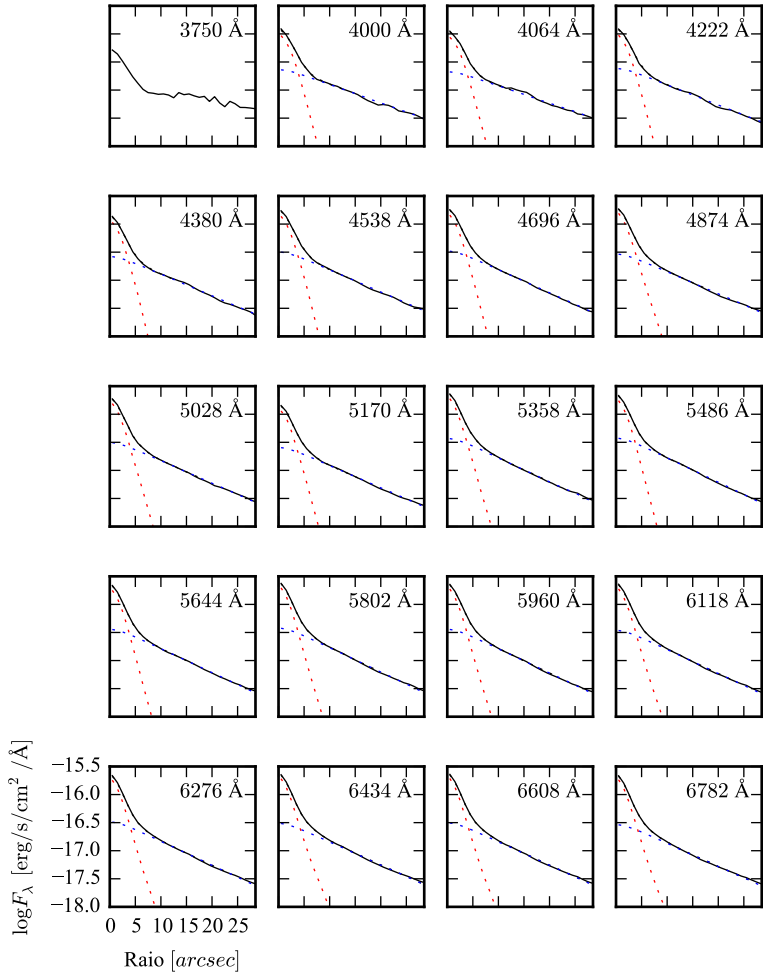


Figura B.12: Perfis radiais para diversos comprimentos de onda de K0127 (NGC 1349).

B. Decomposição morfológica espectral e síntese de populações estelares da amostra final

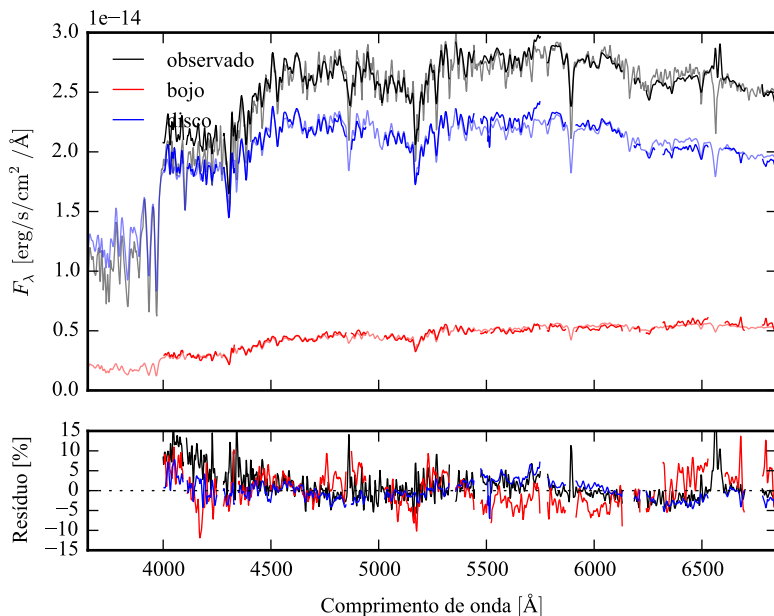


Figura B.13: Acima: Espectros integrados das componentes morfológicas de K0127 (NGC 1349), ajustados com STARLIGHT. Em preto, espectro observado. Em vermelho, e azul, as componentes bojo e disco. Em linhas de cor clara, o espectro ajustado pelo STARLIGHT. Abaixo: Resíduo dos espectros (observado menos sintético, divididos pelo observado).

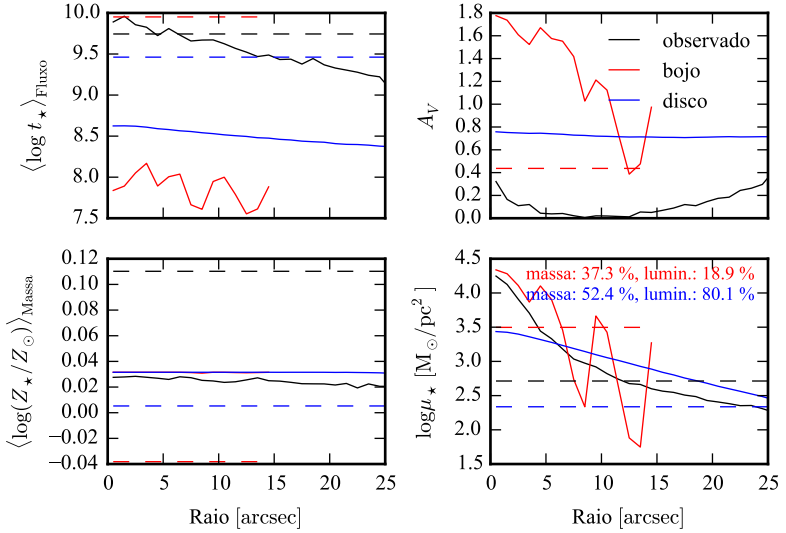


Figura B.14: Perfil radial de propriedades físicas das componentes morfológicas de K0127 (NGC 1349), obtidos através do STARLIGHT. As linhas contínuas representam as propriedades obtidas utilizando espectros espacialmente resolvidos. As linhas tracejadas representam as propriedades obtidas utilizando os espectros integrados. Em preto, espectro observado. Em vermelho, e azul, as componentes bojo e disco. Acima, à esquerda: idade estelar média ponderada pela luminosidade. Acima, à direita: atenuação por poeira, na banda V . Abaixo, à esquerda: metalicidade estelar média, ponderada pela massa. Abaixo, à direita: densidade superficial de massa estelar. As frações de massa e luminosidade entre as componentes e a total (obtida do espectro observado) é mostrada no painel inferior, à direita.

B. Decomposição morfológica espectral e síntese de populações estelares da amostra final

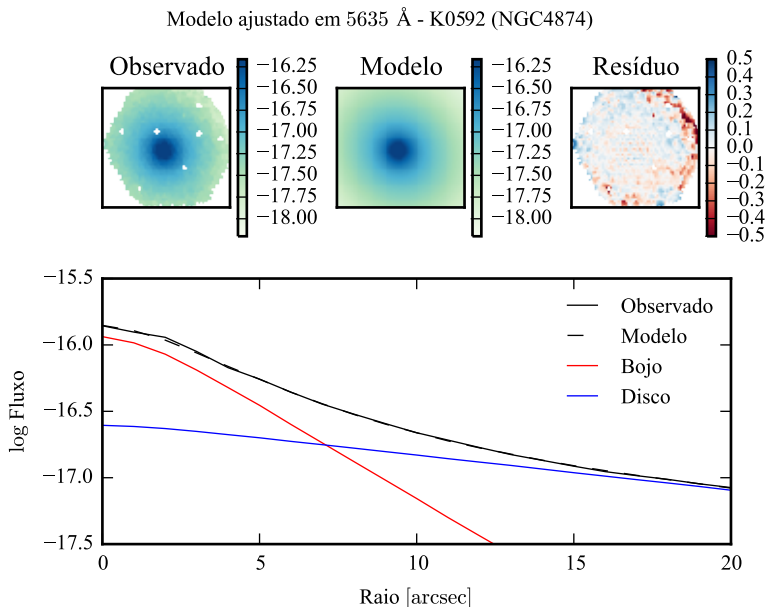


Figura B.15: Acima: imagens observada, modelada e resíduo, do fluxo em 5635 Å para K0592 (NGC 4874). Abaixo: perfis radiais, obtidos pela média do fluxo em anéis elípticos nas imagens. O fluxo observado é representado pela linha preta sólida. O melhor ajuste é representado pela linha preta tracejada. O bojo e o disco que compõe o modelo são mostrados em vermelho e azul, respectivamente.

B.3 K0592 (NGC 4874)

- Galáxia NGC 4874
- Tipo morfológico: E0 (mín. E0, máx. S0)
- Magnitude absoluta na banda r : $-22,67$
- Elipticidade: 0,12

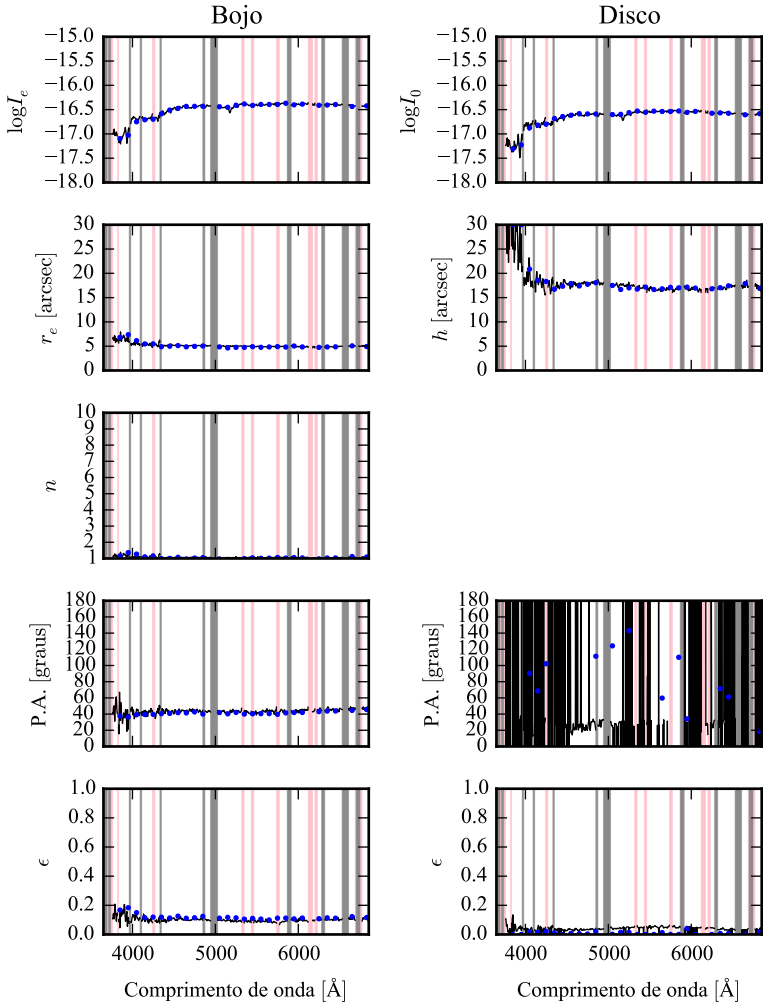


Figura B.16: Parâmetros morfológicos em função do comprimento de onda para K0592 (NGC 4874). Regiões em rosa representam comprimentos de onda onde a decomposição falhou. Regiões em cinza foram mascaradas antes de iniciar a decomposição. Pontos azuis indicam o primeiro passo da decomposição, em caixas de 100 Å.

B. Decomposição morfológica espectral e síntese de populações estelares da amostra final

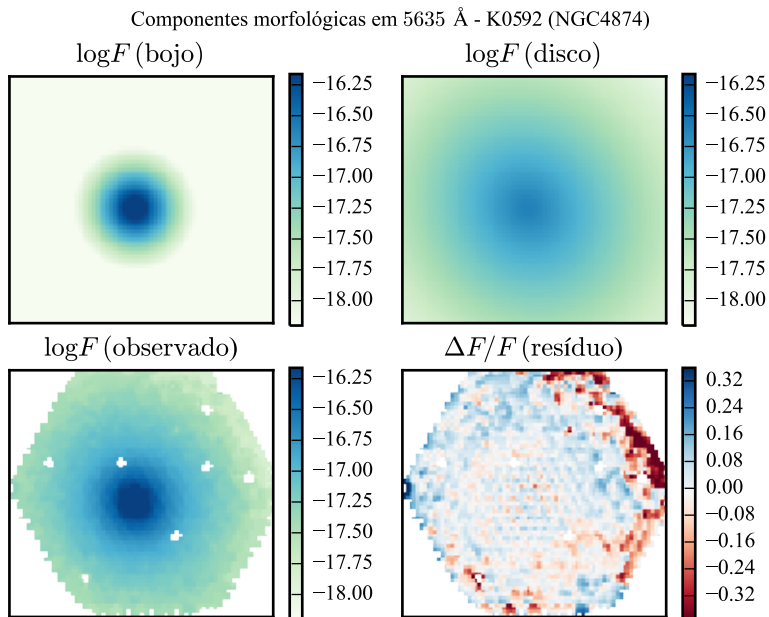


Figura B.17: Imagens em 5635 Å das componentes morfológicas de K0592 (NGC 4874).

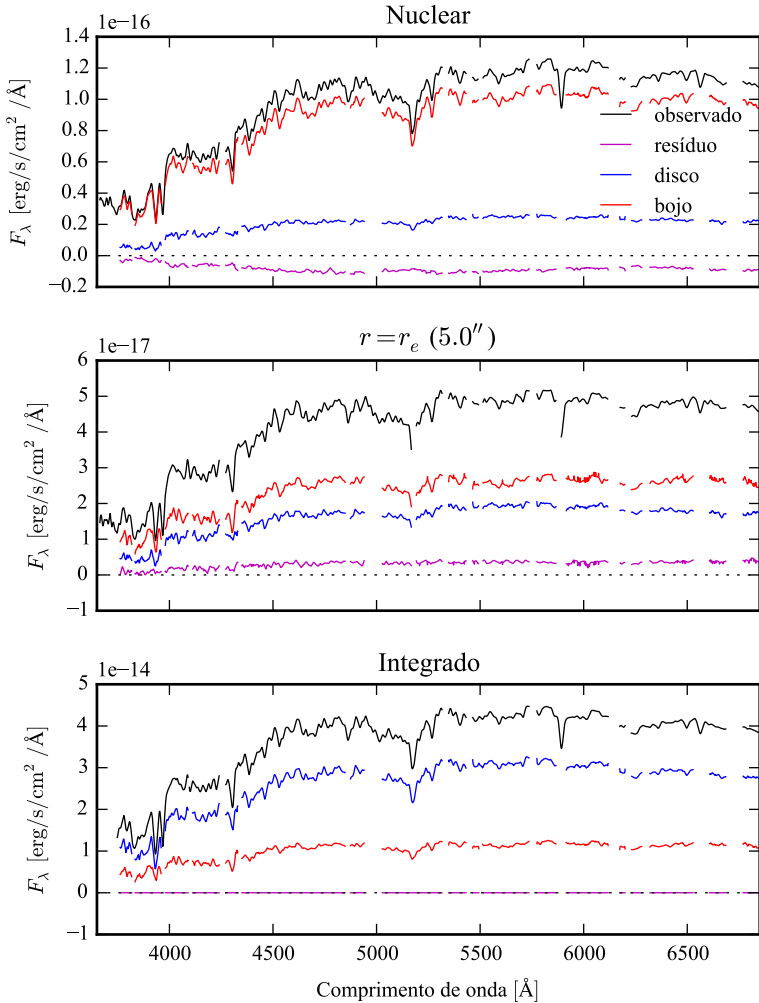


Figura B.18: Espectro das componentes morfológicas de K0592 (NGC 4874), observado (preto), bojo (vermelho), disco (azul) e resíduo (magenta). Acima: Espectro do *spaxel* nuclear da galáxia. Meio: Espectro em um *spaxel* a uma distância de r_e do núcleo. Abaixo: Espectro integrado espacialmente.

B. Decomposição morfológica espectral e síntese de populações estelares da amostra final

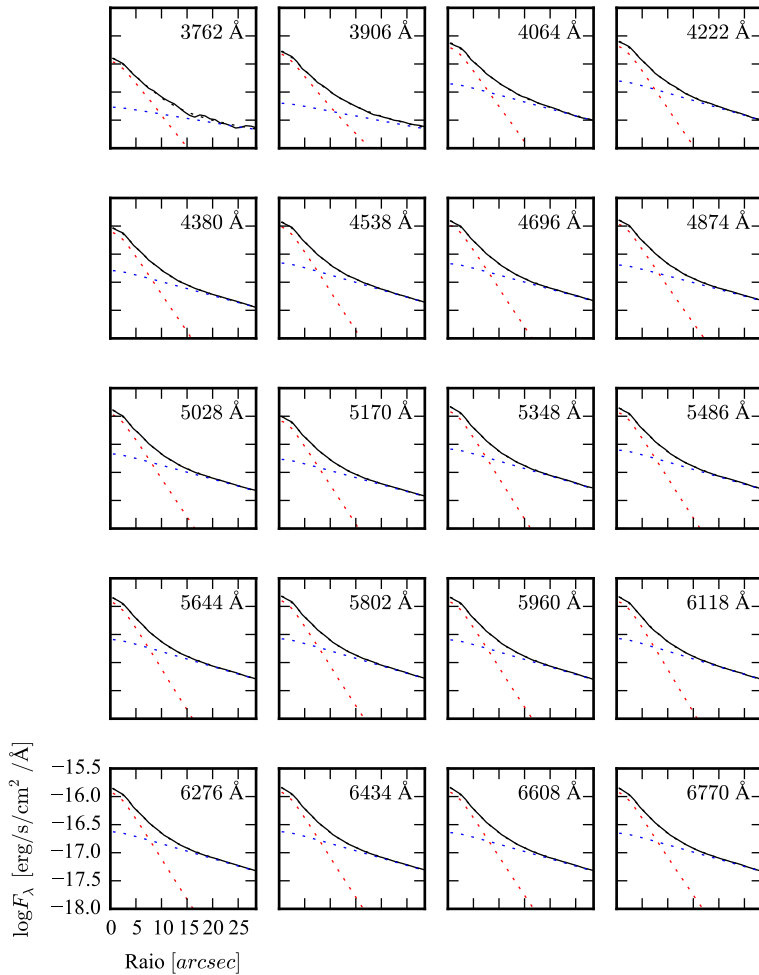


Figura B.19: Perfis radiais para diversos comprimentos de onda de K0592 (NGC 4874).

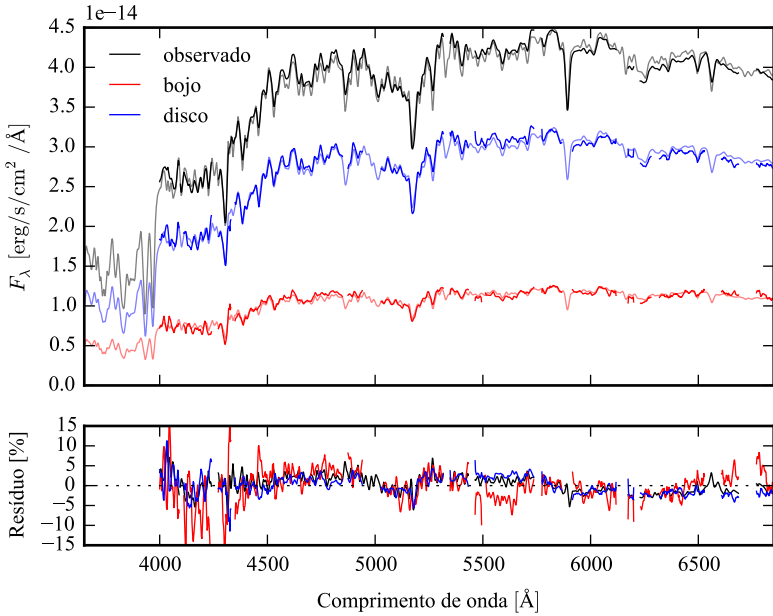


Figura B.20: Acima: Espectros integrados das componentes morfológicas de K0592 (NGC 4874), ajustados com STARLIGHT. Em preto, espectro observado. Em vermelho, e azul, as componentes bojo e disco. Em linhas de cor clara, o espectro ajustado pelo STARLIGHT. Abaixo: Resíduo dos espectros (observado menos sintético, divididos pelo observado).

B. Decomposição morfológica espectral e síntese de populações estelares da amostra final

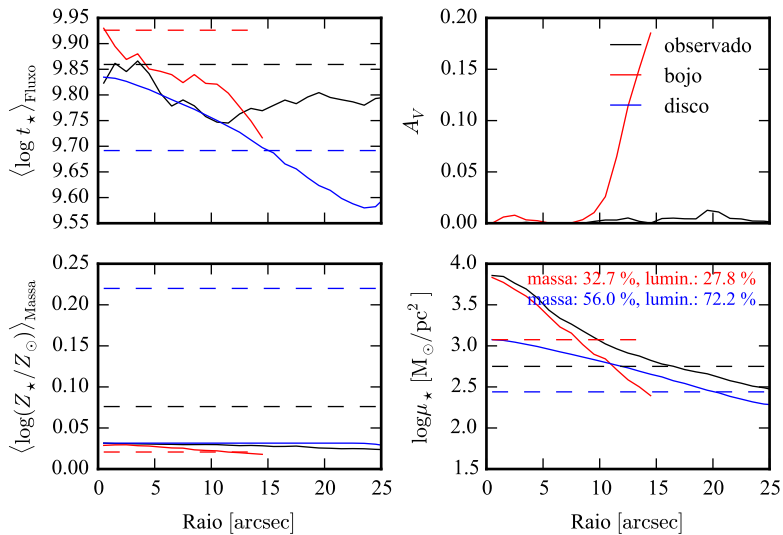


Figura B.21: Perfil radial de propriedades físicas das componentes morfológicas de K0592 (NGC 4874), obtidos através do STARLIGHT. As linhas contínuas representam as propriedades obtidas utilizando espectros espacialmente resolvidos. As linhas tracejadas representam as propriedades obtidas utilizando os espectros integrados. Em preto, espectro observado. Em vermelho, e azul, as componentes bojo e disco. Acima, à esquerda: idade estelar média ponderada pela luminosidade. Acima, à direita: atenuação por poeira, na banda V . Abaixo, à esquerda: metalicidade estelar média, ponderada pela massa. Abaixo, à direita: densidade superficial de massa estelar. As frações de massa e luminosidade entre as componentes e a total (obtida do espectro observado) é mostrada no painel inferior, à direita.

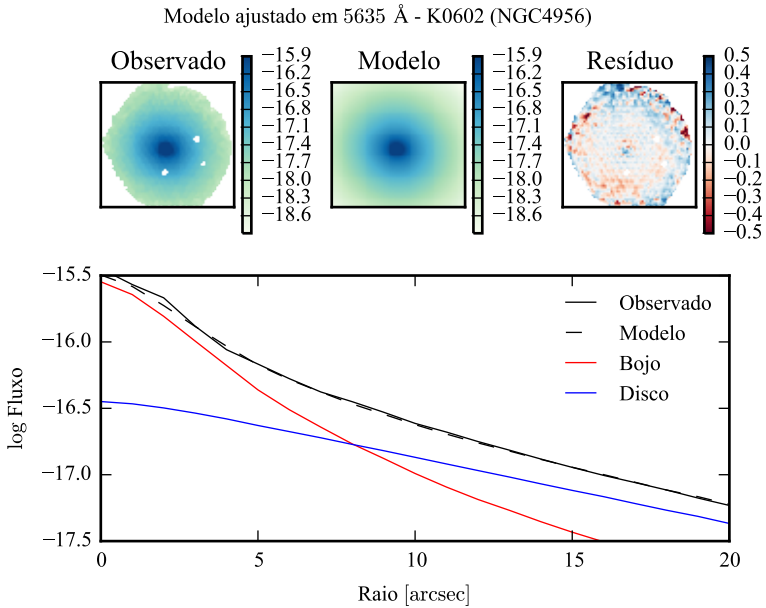


Figura B.22: Acima: imagens observada, modelada e resíduo, do fluxo em 5635 Å para K0602 (NGC 4956). Abaixo: perfis radiais, obtidos pela média do fluxo em anéis elípticos nas imagens. O fluxo observado é representado pela linha preta sólida. O melhor ajuste é representado pela linha preta tracejada. O bojo e o disco que compõe o modelo são mostrados em vermelho e azul, respectivamente.

B.4 K0602 (NGC 4956)

- Galáxia NGC 4956
- Tipo morfológico: E1 (mín. E0, máx. S0)
- Magnitude absoluta na banda r : $-21,97$
- Elipticidade: 0,14

B. Decomposição morfológica espectral e síntese de populações estelares da amostra final

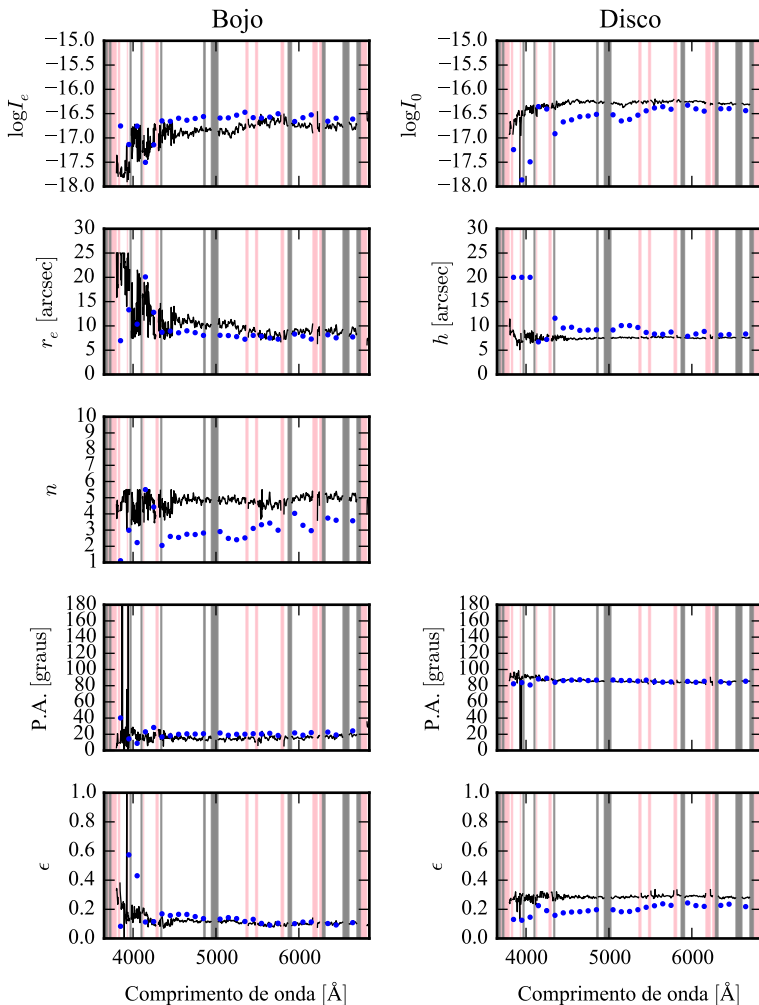


Figura B.23: Parâmetros morfológicos em função do comprimento de onda para K0602 (NGC 4956). Regiões em rosa representam comprimentos de onda onde a decomposição falhou. Regiões em cinza foram mascaradas antes de iniciar a decomposição. Pontos azuis indicam o primeiro passo da decomposição, em caixas de 100 Å.

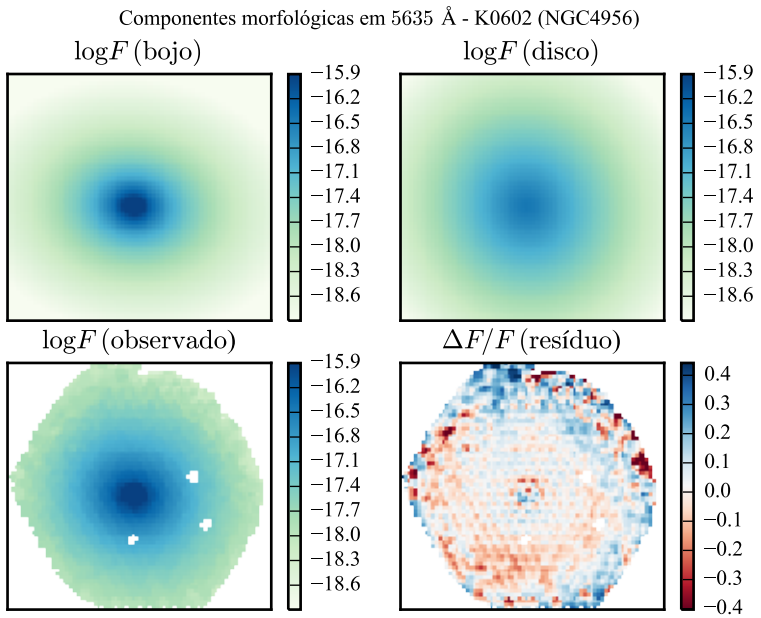


Figura B.24: Imagens em 5635 Å das componentes morfológicas de K0602 (NGC 4956).

B. Decomposição morfológica espectral e síntese de populações estelares da amostra final

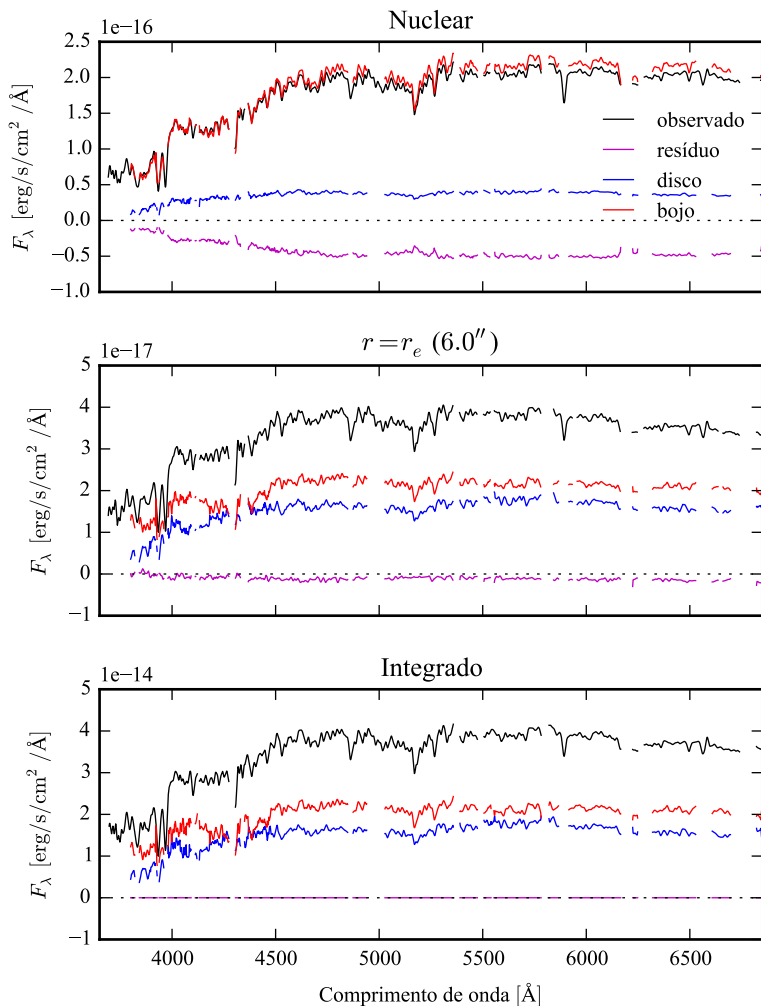


Figura B.25: Espectro das componentes morfológicas de K0602 (NGC 4956), observado (preto), bojo (vermelho), disco (azul) e resíduo (magenta). Acima: Espectro do *spaxel* nuclear da galáxia. Meio: Espectro em um *spaxel* a uma distância de r_e do núcleo. Abaixo: Espectro integrado espacialmente.

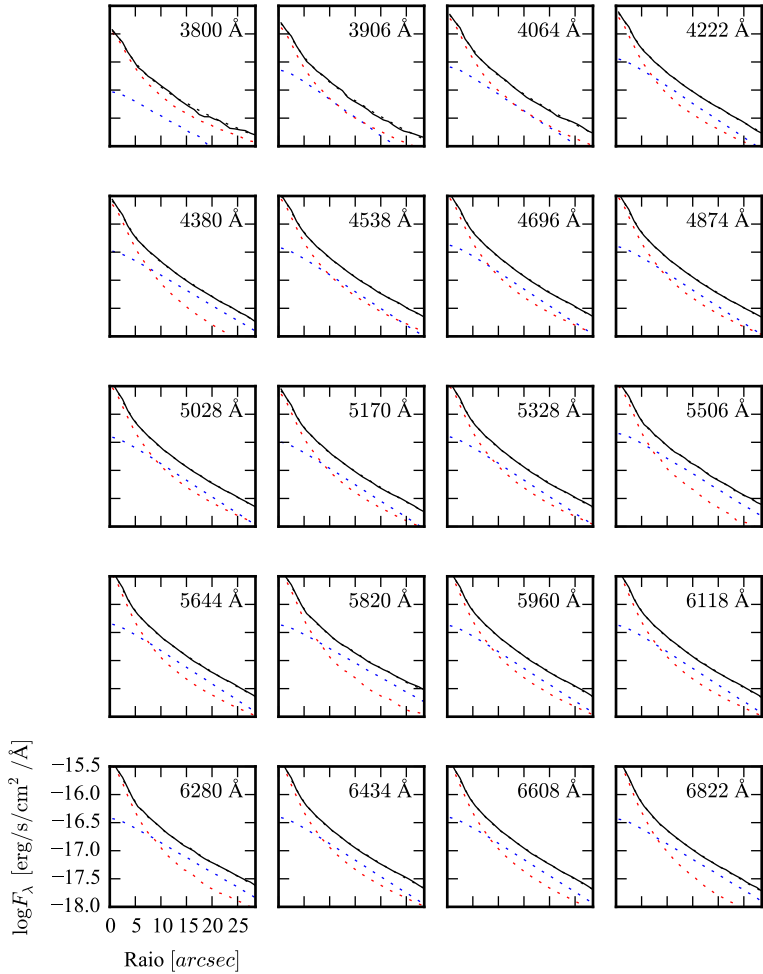


Figura B.26: Perfis radiais para diversos comprimentos de onda de K0602 (NGC 4956).

B. Decomposição morfológica espectral e síntese de populações estelares da amostra final

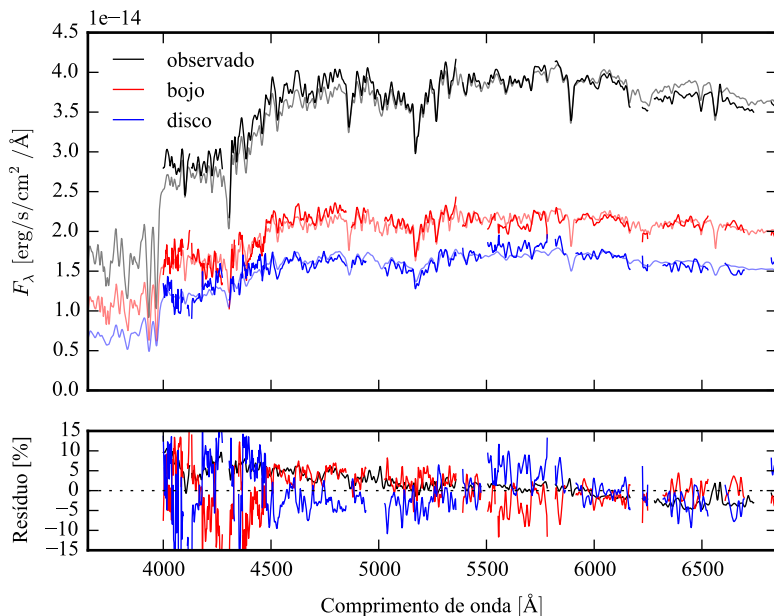


Figura B.27: Acima: Espectros integrados das componentes morfológicas de K0602 (NGC 4956), ajustados com STARLIGHT. Em preto, espectro observado. Em vermelho, e azul, as componentes bojo e disco. Em linhas de cor clara, o espectro ajustado pelo STARLIGHT. Abaixo: Resíduo dos espectros (observado menos sintético, divididos pelo observado).

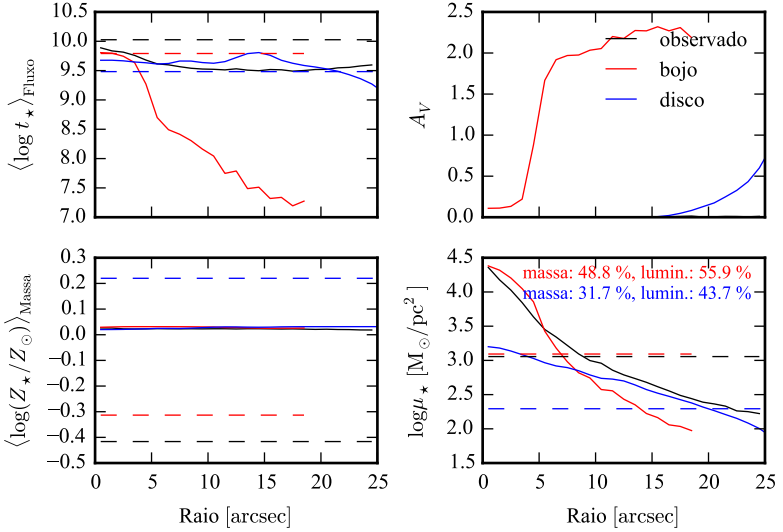


Figura B.28: Perfil radial de propriedades físicas das componentes morfológicas de K0602 (NGC 4956), obtidos através do STARLIGHT. As linhas contínuas representam as propriedades obtidas utilizando espectros espacialmente resolvidos. As linhas tracejadas representam as propriedades obtidas utilizando os espectros integrados. Em preto, espectro observado. Em vermelho, e azul, as componentes bojo e disco. Acima, à esquerda: idade estelar média ponderada pela luminosidade. Acima, à direita: atenuação por poeira, na banda V. Abaixo, à esquerda: metalicidade estelar média, ponderada pela massa. Abaixo, à direita: densidade superficial de massa estelar. As frações de massa e luminosidade entre as componentes e a total (obtida do espectro observado) é mostrada no painel inferior, à direita.

B. Decomposição morfológica espectral e síntese de populações estelares da amostra final

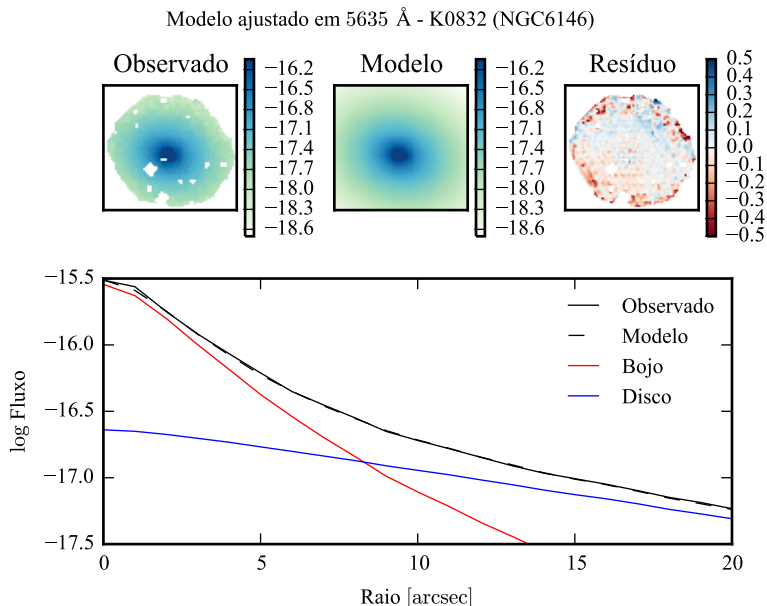


Figura B.29: Acima: imagens observada, modelada e resíduo, do fluxo em 5635 Å para K0832 (NGC 6146). Abaixo: perfis radiais, obtidos pela média do fluxo em anéis elípticos nas imagens. O fluxo observado é representado pela linha preta sólida. O melhor ajuste é representado pela linha preta tracejada. O bojo e o disco que compõe o modelo são mostrados em vermelho e azul, respectivamente.

B.5 K0832 (NGC 6146)

- Galáxia NGC 6146
- Tipo morfológico: E5 (mín. E3, máx. S0)
- Magnitude absoluta na banda r : $-22,94$
- Elipticidade: 0,23

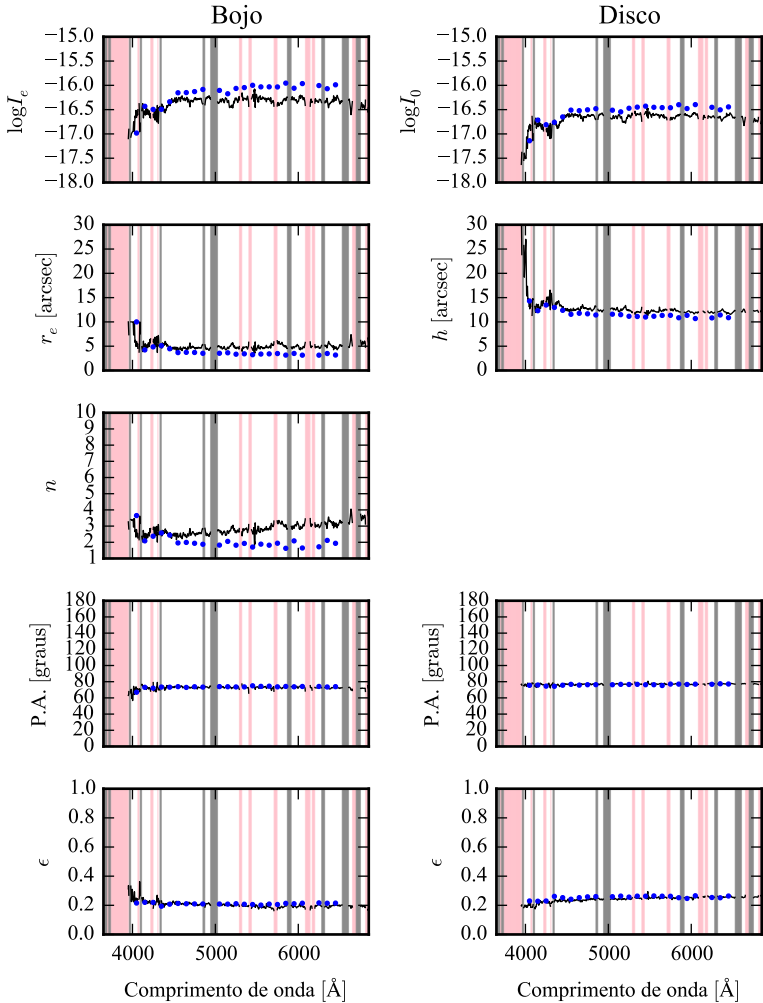


Figura B.30: Parâmetros morfológicos em função do comprimento de onda para K0832 (NGC 6146). Regiões em rosa representam comprimentos de onda onde a decomposição falhou. Regiões em cinza foram mascaradas antes de iniciar a decomposição. Pontos azuis indicam o primeiro passo da decomposição, em caixas de 100 Å.

B. Decomposição morfológica espectral e síntese de populações estelares da amostra final

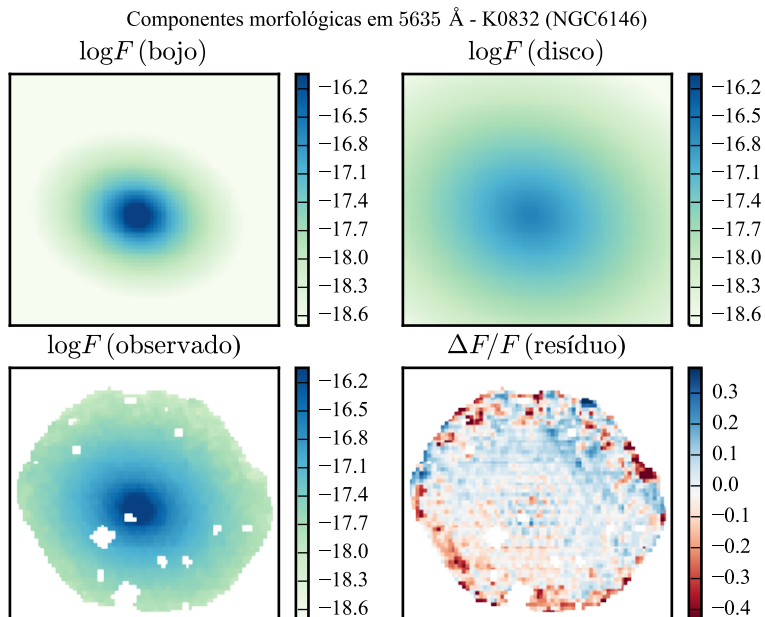


Figura B.31: Imagens em 5635 Å das componentes morfológicas de K0832 (NGC 6146).

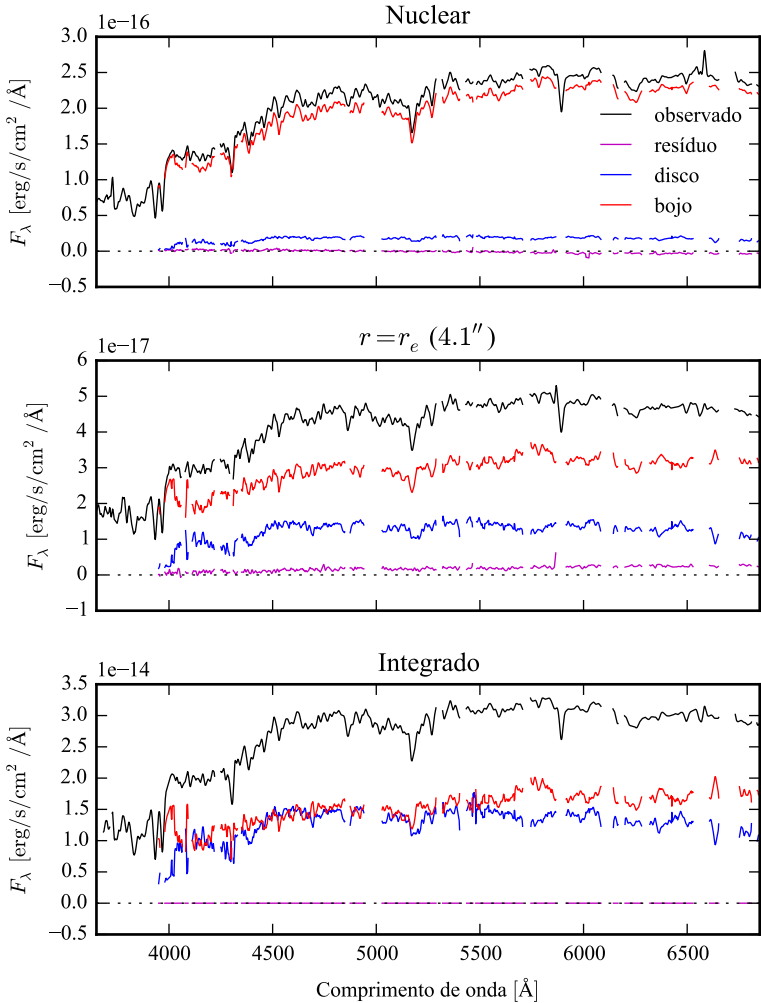


Figura B.32: Espectro das componentes morfológicas de K0832 (NGC 6146), observado (preto), bojo (vermelho), disco (azul) e resíduo (magenta). Acima: Espectro do *spaxel* nuclear da galáxia. Meio: Espectro em um *spaxel* a uma distância de r_e do núcleo. Abaixo: Espectro integrado espacialmente.

B. Decomposição morfológica espectral e síntese de populações estelares da amostra final

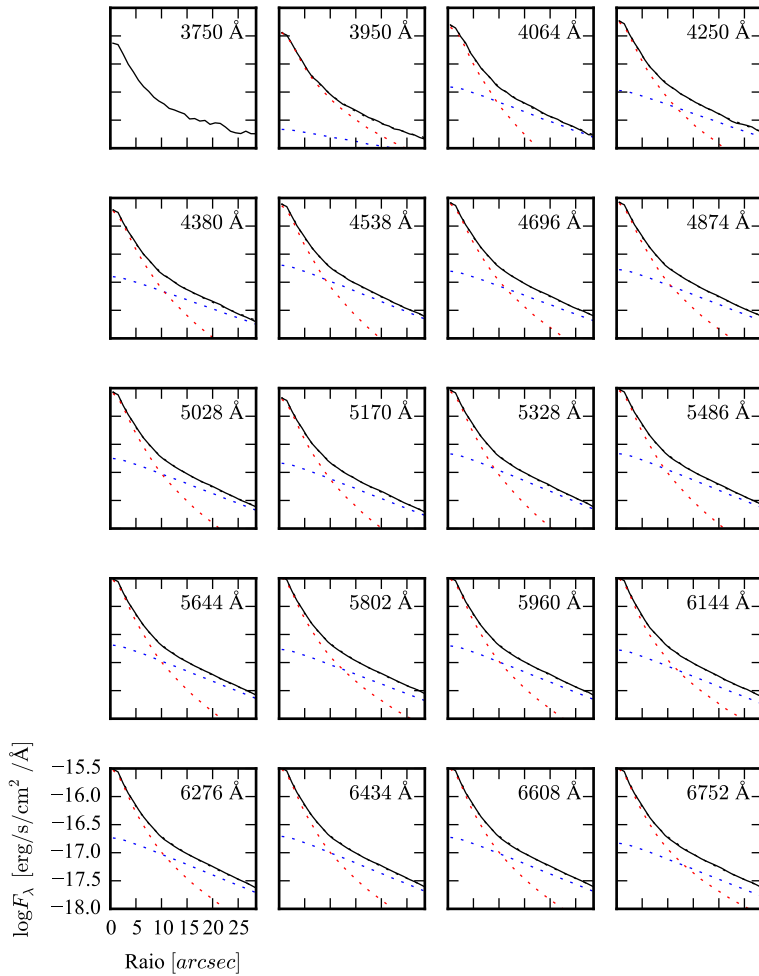


Figura B.33: Perfis radiais para diversos comprimentos de onda de K0832 (NGC 6146).

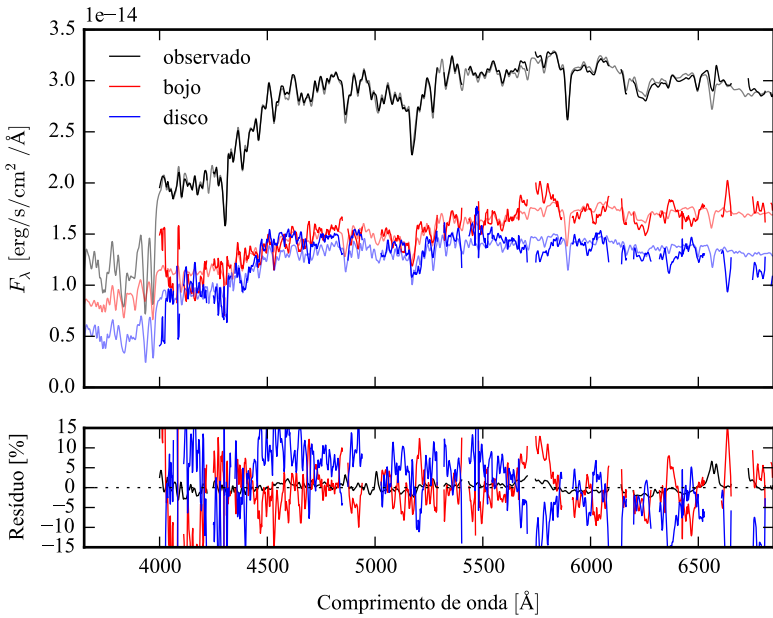


Figura B.34: Acima: Espectros integrados das componentes morfológicas de K0832 (NGC 6146), ajustados com STARLIGHT. Em preto, espectro observado. Em vermelho, e azul, as componentes bojo e disco. Em linhas de cor clara, o espectro ajustado pelo STARLIGHT. Abaixo: Resíduo dos espectros (observado menos sintético, divididos pelo observado).

B. Decomposição morfológica espectral e síntese de populações estelares da amostra final

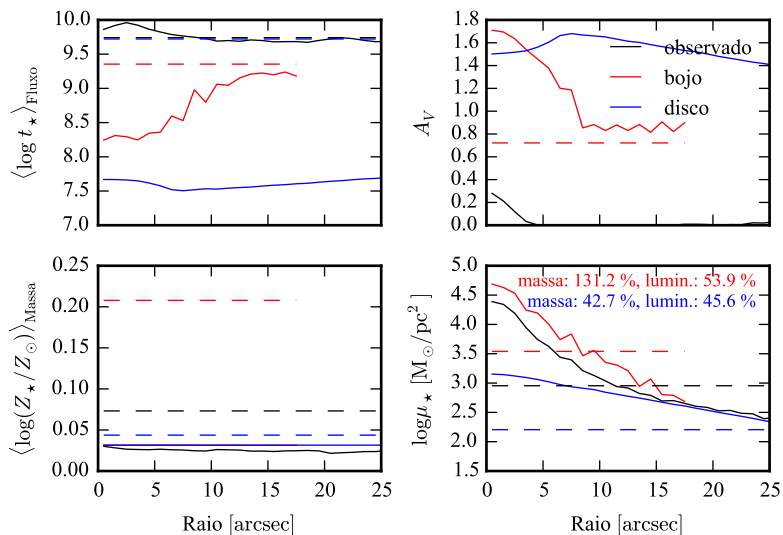


Figura B.35: Perfil radial de propriedades físicas das componentes morfológicas de K0832 (NGC 6146), obtidos através do STARLIGHT. As linhas contínuas representam as propriedades obtidas utilizando espectros espacialmente resolvidos. As linhas tracejadas representam as propriedades obtidas utilizando os espectros integrados. Em preto, espectro observado. Em vermelho, e azul, as componentes bojo e disco. Acima, à esquerda: idade estelar média ponderada pela luminosidade. Acima, à direita: atenuação por poeira, na banda V . Abaixo, à esquerda: metalicidade estelar média, ponderada pela massa. Abaixo, à direita: densidade superficial de massa estelar. As frações de massa e luminosidade entre as componentes e a total (obtida do espectro observado) é mostrada no painel inferior, à direita.

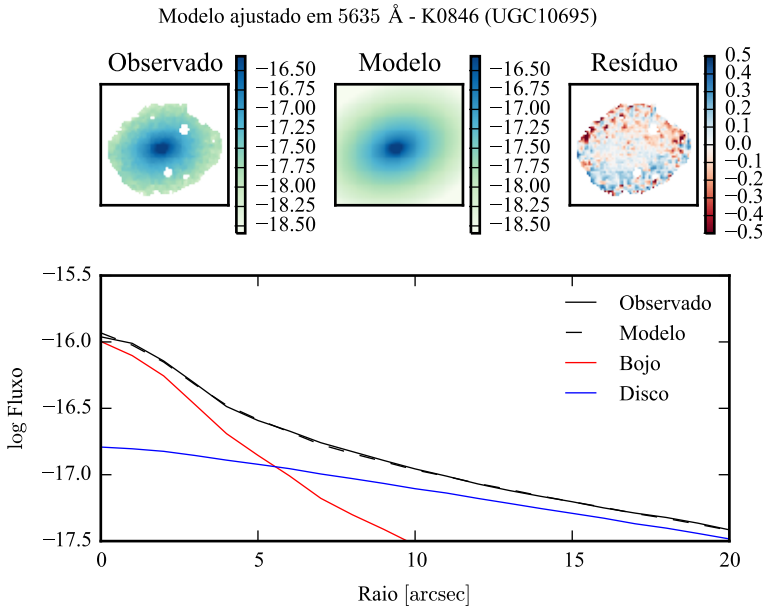


Figura B.36: Acima: imagens observada, modelada e resíduo, do fluxo em 5635 Å para K0846 (UGC 10695). Abaixo: perfis radiais, obtidos pela média do fluxo em anéis elípticos nas imagens. O fluxo observado é representado pela linha preta sólida. O melhor ajuste é representado pela linha preta tracejada. O bojo e o disco que compõe o modelo são mostrados em vermelho e azul, respectivamente.

B.6 K0846 (UGC 10695)

- Galáxia UGC 10695
- Tipo morfológico: E5 (mín. E2, máx. S0)
- Magnitude absoluta na banda r : $-22,09$
- Elipticidade: 0,33

B. Decomposição morfológica espectral e síntese de populações estelares da amostra final

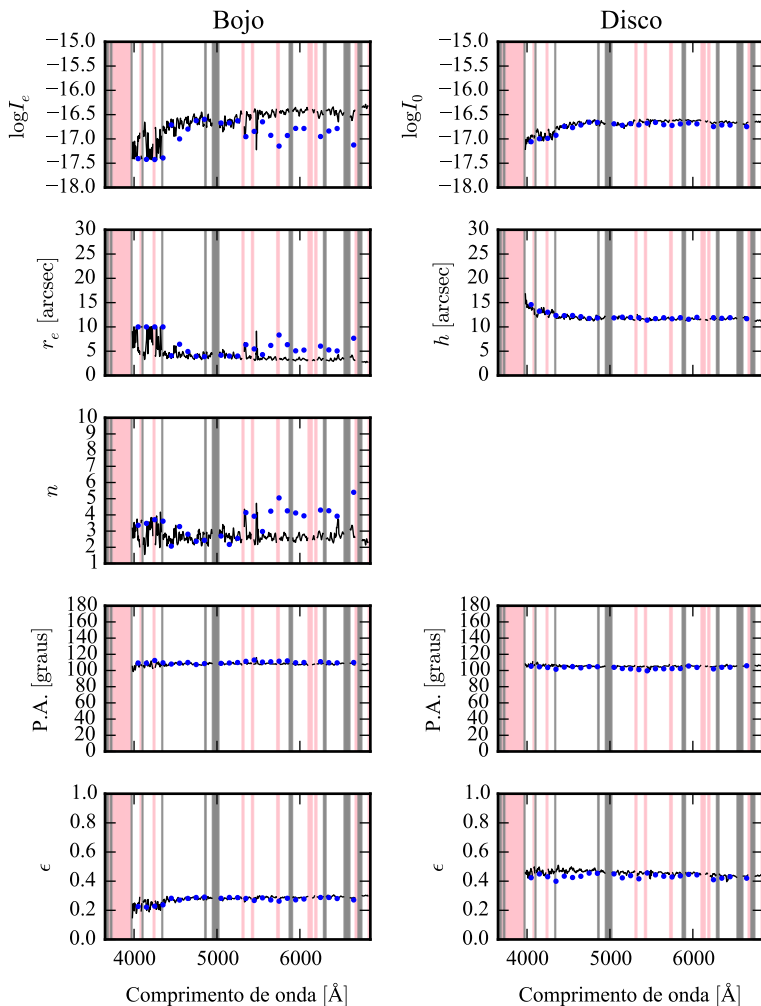


Figura B.37: Parâmetros morfológicos em função do comprimento de onda para K0846 (UGC 10695). Regiões em rosa representam comprimentos de onda onde a decomposição falhou. Regiões em cinza foram mascaradas antes de iniciar a decomposição. Pontos azuis indicam o primeiro passo da decomposição, em caixas de 100 Å.

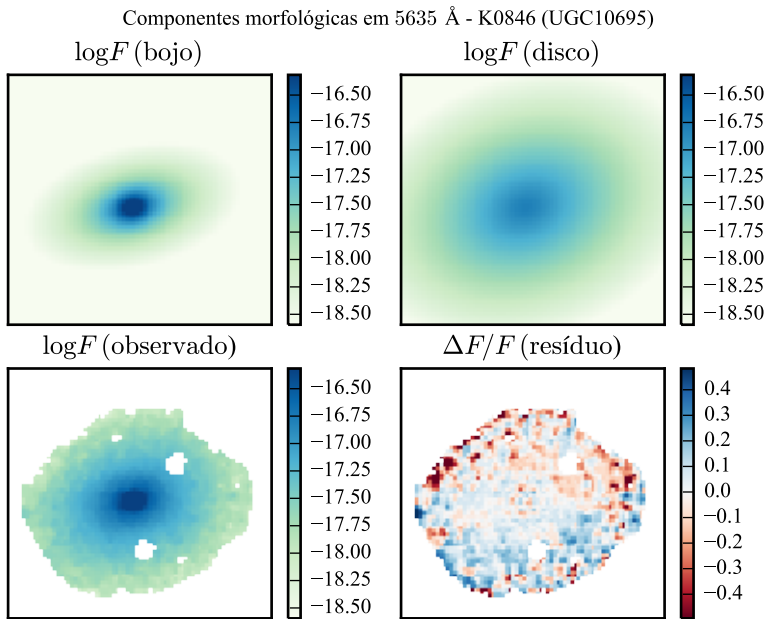


Figura B.38: Imagens em 5635 Å das componentes morfológicas de K0846 (UGC 10695).

B. Decomposição morfológica espectral e síntese de populações estelares da amostra final

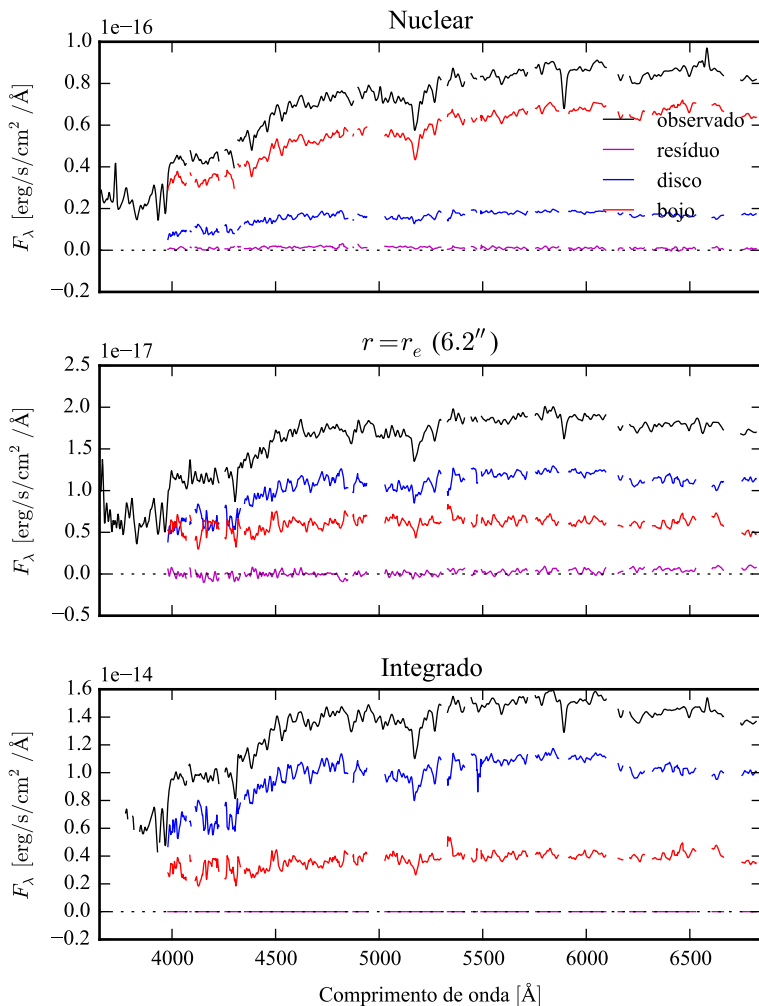


Figura B.39: Espectro das componentes morfológicas de K0846 (UGC 10695), observado (preto), bojo (vermelho), disco (azul) e resíduo (magenta). Acima: Espectro do *spaxel* nuclear da galáxia. Meio: Espectro em um *spaxel* a uma distância de r_e do núcleo. Abaixo: Espectro integrado espacialmente.

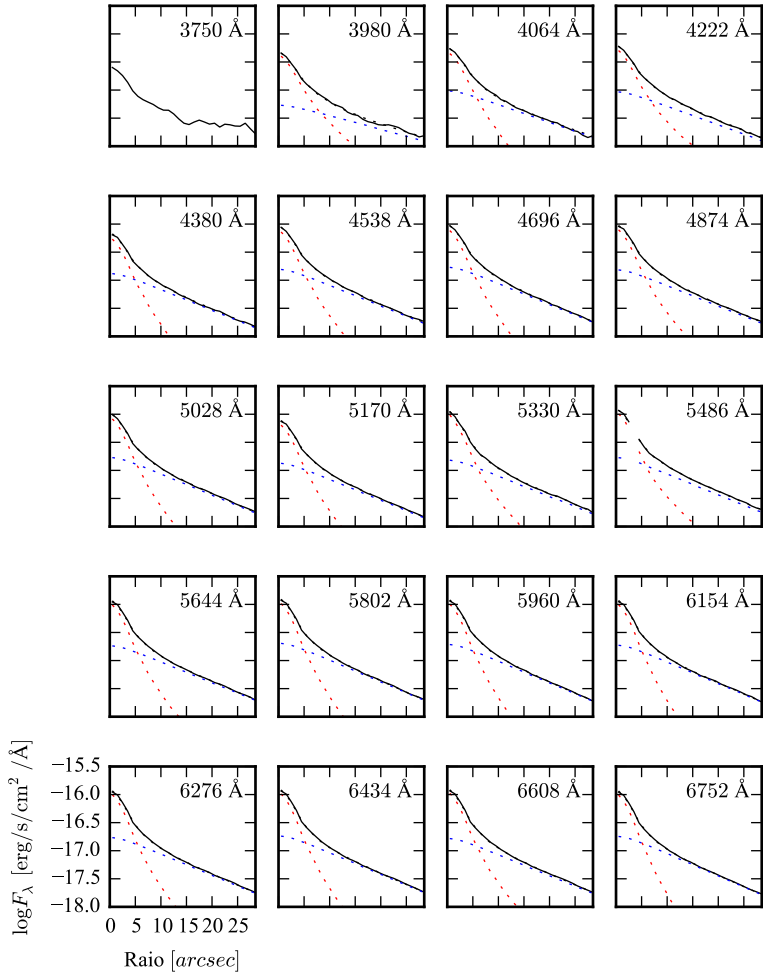


Figura B.40: Perfis radiais para diversos comprimentos de onda de K0846 (UGC 10695).

B. Decomposição morfológica espectral e síntese de populações estelares da amostra final

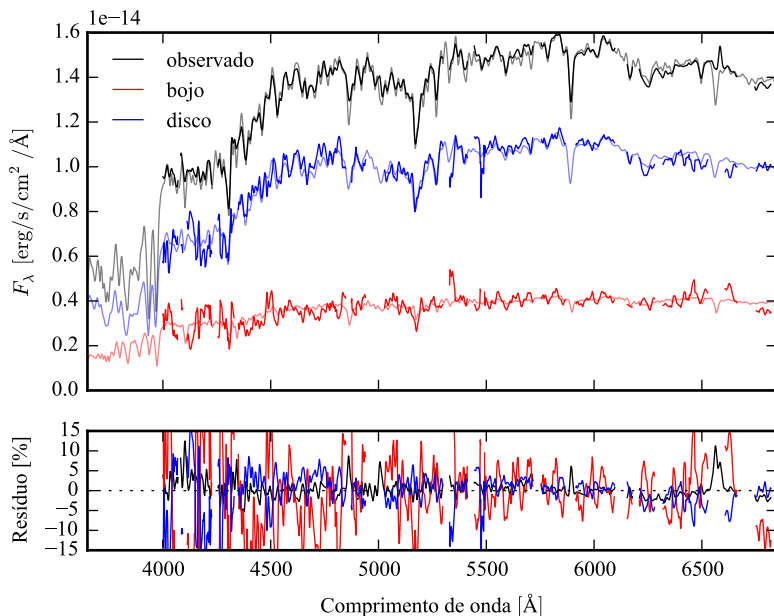


Figura B.41: Acima: Espectros integrados das componentes morfológicas de K0846 (UGC 10695), ajustados com STARLIGHT. Em preto, espectro observado. Em vermelho, e azul, as componentes bojo e disco. Em linhas de cor clara, o espectro ajustado pelo STARLIGHT. Abaixo: Resíduo dos espectros (observado menos sintético, divididos pelo observado).

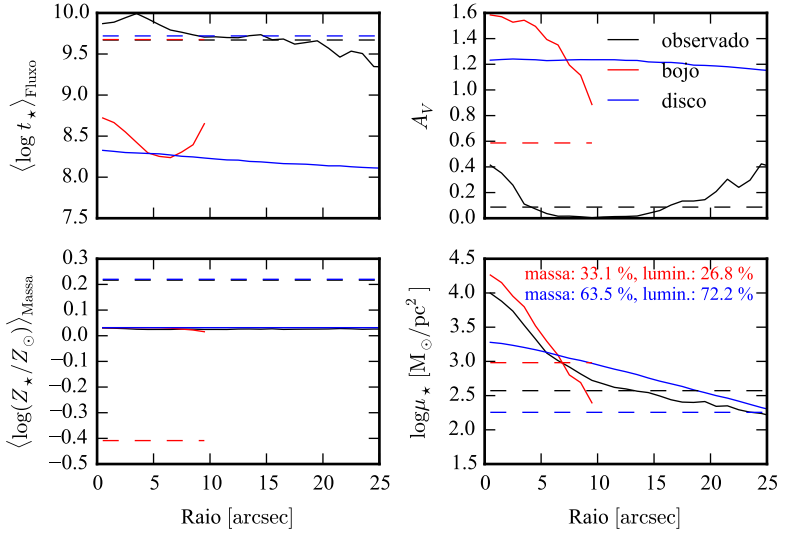


Figura B.42: Perfil radial de propriedades físicas das componentes morfológicas de K0846 (UGC 10695), obtidos através do STARLIGHT. As linhas contínuas representam as propriedades obtidas utilizando espectros espacialmente resolvidos. As linhas tracejadas representam as propriedades obtidas utilizando os espectros integrados. Em preto, espectro observado. Em vermelho, e azul, as componentes bojo e disco. Acima, à esquerda: idade estelar média ponderada pela luminosidade. Acima, à direita: atenuação por poeira, na banda V . Abaixo, à esquerda: metalicidade estelar média, ponderada pela massa. Abaixo, à direita: densidade superficial de massa estelar. As frações de massa e luminosidade entre as componentes e a total (obtida do espectro observado) é mostrada no painel inferior, à direita.

B. Decomposição morfológica espectral e síntese de populações estelares da amostra final

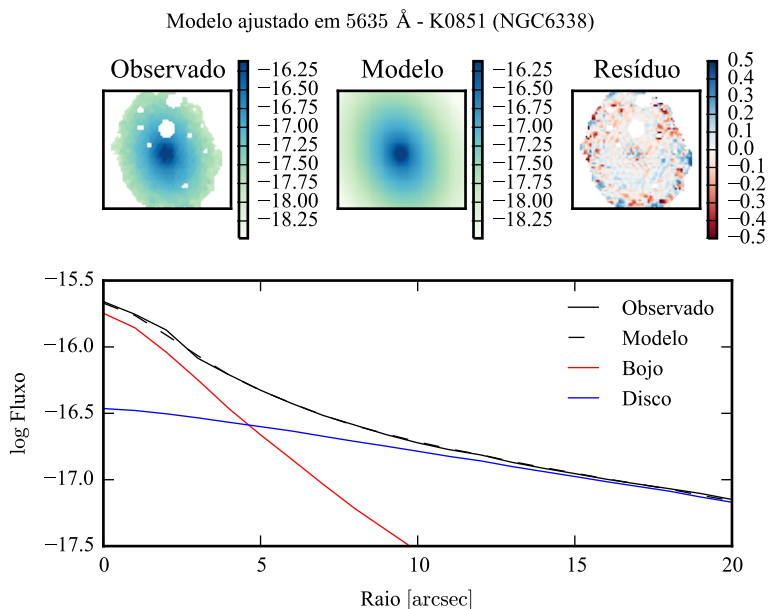


Figura B.43: Acima: imagens observada, modelada e resíduo, do fluxo em 5635 Å para K0851 (NGC 6338). Abaixo: perfis radiais, obtidos pela média do fluxo em anéis elípticos nas imagens. O fluxo observado é representado pela linha preta sólida. O melhor ajuste é representado pela linha preta tracejada. O bojo e o disco que compõe o modelo são mostrados em vermelho e azul, respectivamente.

B.7 K0851 (NGC 6338)

- Galáxia NGC 6338
- Tipo morfológico: E5 (mín. E1, máx. S0)
- Magnitude absoluta na banda r : $-22,75$
- Elipticidade: 0,34

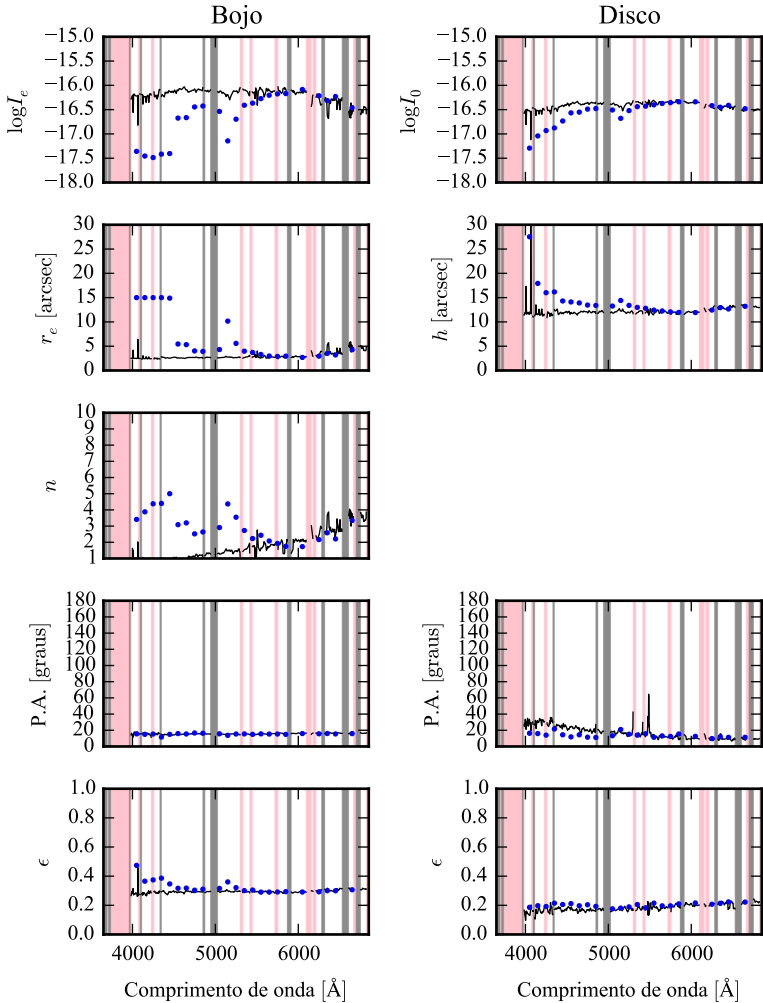


Figura B.44: Parâmetros morfológicos em função do comprimento de onda para K0851 (NGC 6338). Regiões em rosa representam comprimentos de onda onde a decomposição falhou. Regiões em cinza foram mascaradas antes de iniciar a decomposição. Pontos azuis indicam o primeiro passo da decomposição, em caixas de 100 Å.

B. Decomposição morfológica espectral e síntese de populações estelares da amostra final

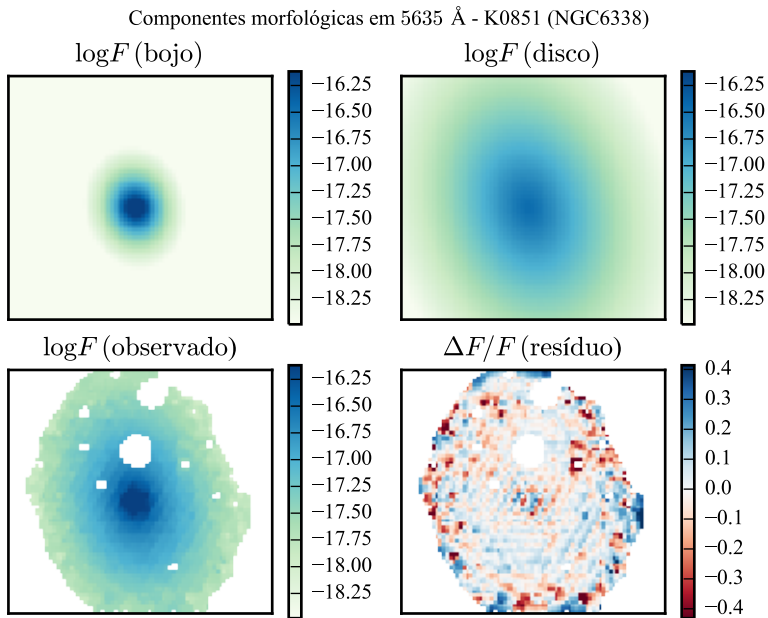


Figura B.45: Imagens em 5635 Å das componentes morfológicas de K0851 (NGC 6338).

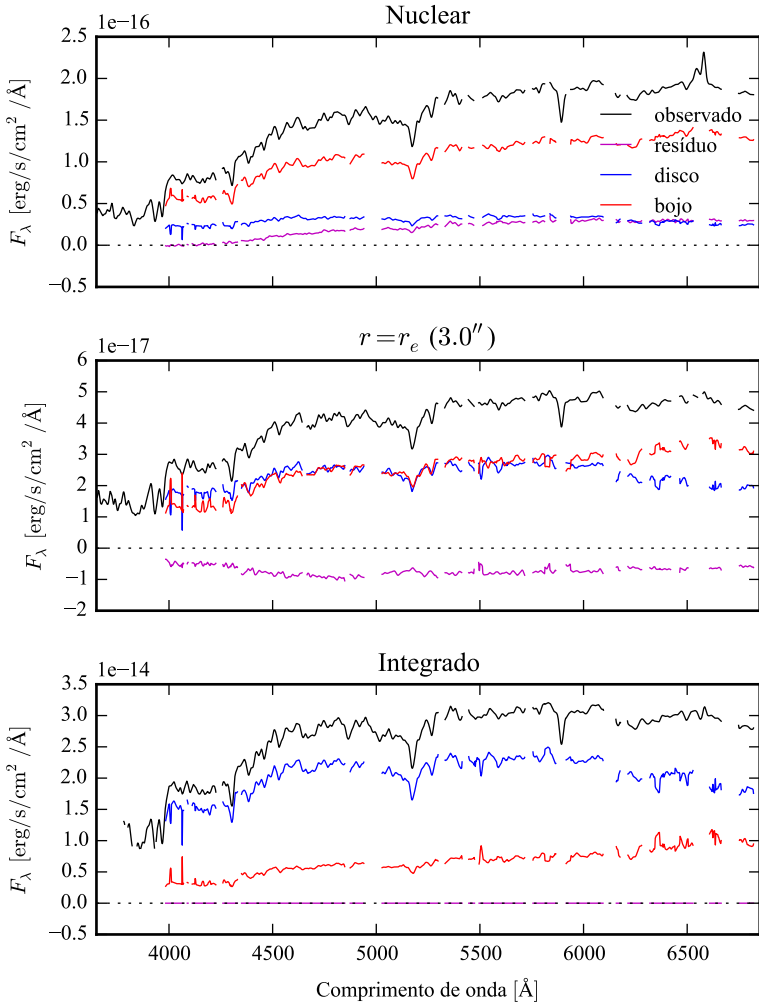


Figura B.46: Espectro das componentes morfológicas de K0851 (NGC 6338), observado (preto), bojo (vermelho), disco (azul) e resíduo (magenta). Acima: Espectro do *spaxel* nuclear da galáxia. Meio: Espectro em um *spaxel* a uma distância de r_e do núcleo. Abaixo: Espectro integrado espacialmente.

B. Decomposição morfológica espectral e síntese de populações estelares da amostra final

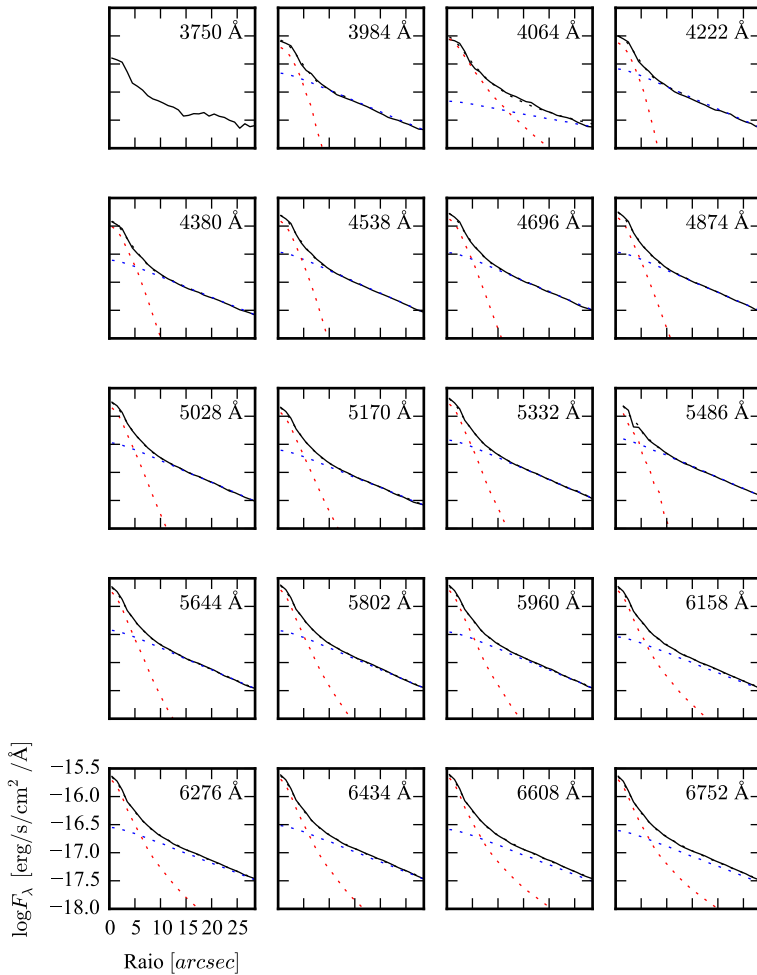


Figura B.47: Perfis radiais para diversos comprimentos de onda de K0851 (NGC 6338).

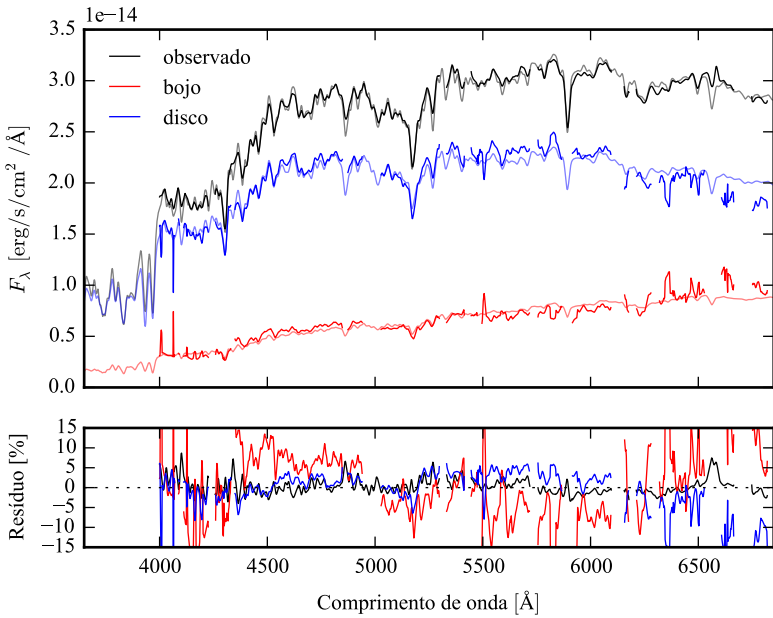


Figura B.48: Acima: Espectros integrados das componentes morfológicas de K0851 (NGC 6338), ajustados com STARLIGHT. Em preto, espectro observado. Em vermelho, e azul, as componentes bojo e disco. Em linhas de cor clara, o espectro ajustado pelo STARLIGHT. Abaixo: Resíduo dos espectros (observado menos sintético, divididos pelo observado).

B. Decomposição morfológica espectral e síntese de populações estelares da amostra final

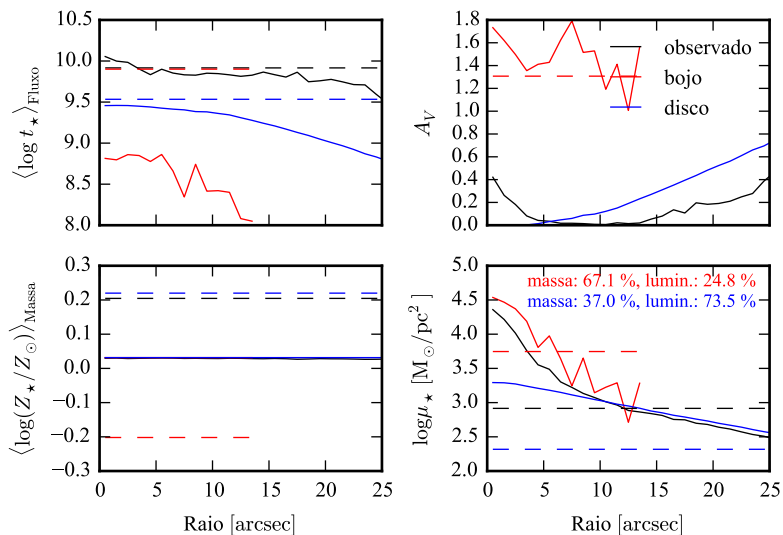


Figura B.49: Perfil radial de propriedades físicas das componentes morfológicas de K0851 (NGC 6338), obtidos através do STARLIGHT. As linhas contínuas representam as propriedades obtidas utilizando espectros espacialmente resolvidos. As linhas tracejadas representam as propriedades obtidas utilizando os espectros integrados. Em preto, espectro observado. Em vermelho, e azul, as componentes bojo e disco. Acima, à esquerda: idade estelar média ponderada pela luminosidade. Acima, à direita: atenuação por poeira, na banda V . Abaixo, à esquerda: metalicidade estelar média, ponderada pela massa. Abaixo, à direita: densidade superficial de massa estelar. As frações de massa e luminosidade entre as componentes e a total (obtida do espectro observado) é mostrada no painel inferior, à direita.

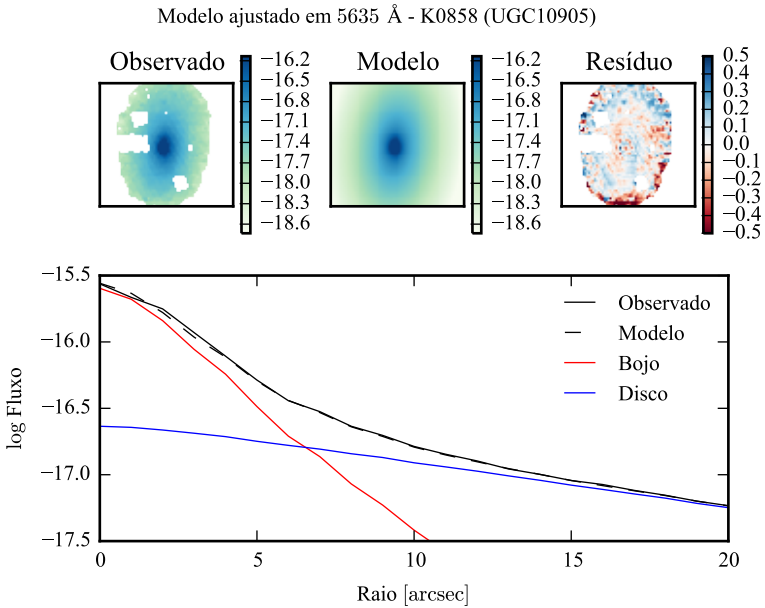


Figura B.50: Acima: imagens observada, modelada e resíduo, do fluxo em 5635 Å para K0858 (UGC 10905). Abaixo: perfis radiais, obtidos pela média do fluxo em anéis elípticos nas imagens. O fluxo observado é representado pela linha preta sólida. O melhor ajuste é representado pela linha preta tracejada. O bojo e o disco que compõe o modelo são mostrados em vermelho e azul, respectivamente.

B.8 K0858 (UGC 10905)

- Galáxia UGC 10905
- Tipo morfológico: S0a (mín. E7, máx. Sab)
- Magnitude absoluta na banda r : $-22,32$
- Elipticidade: 0,47

B. Decomposição morfológica espectral e síntese de populações estelares da amostra final

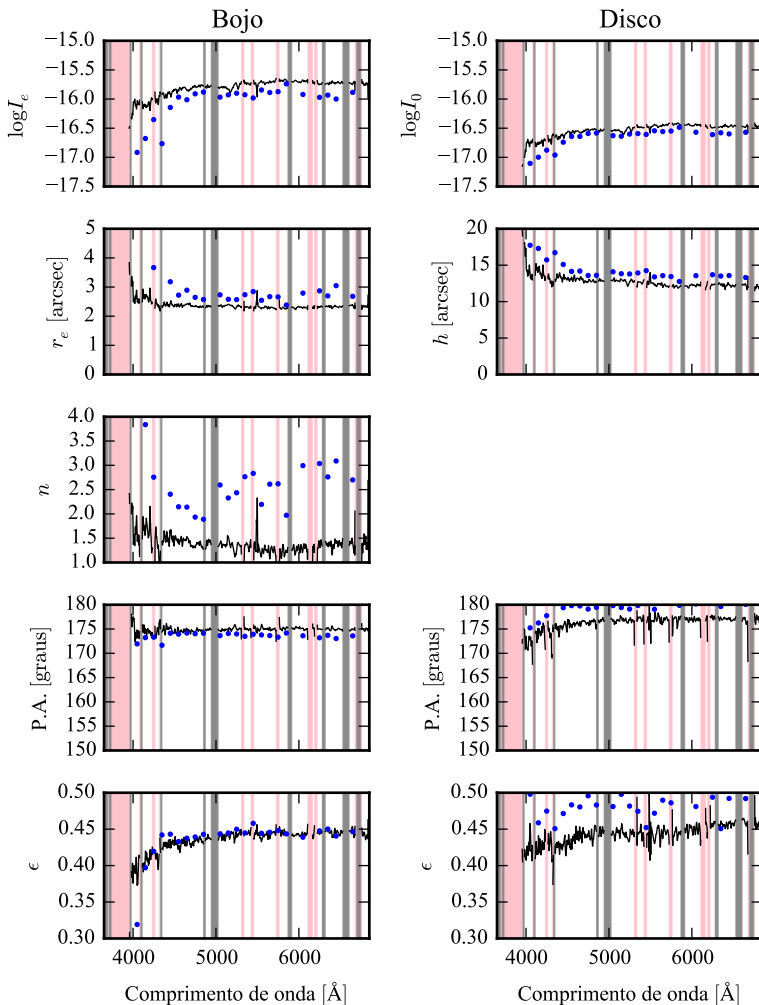


Figura B.51: Parâmetros morfológicos em função do comprimento de onda para K0858 (UGC 10905). Regiões em rosa representam comprimentos de onda onde a decomposição falhou. Regiões em cinza foram mascaradas antes de iniciar a decomposição. Pontos azuis indicam o primeiro passo da decomposição, em caixas de 100 Å.

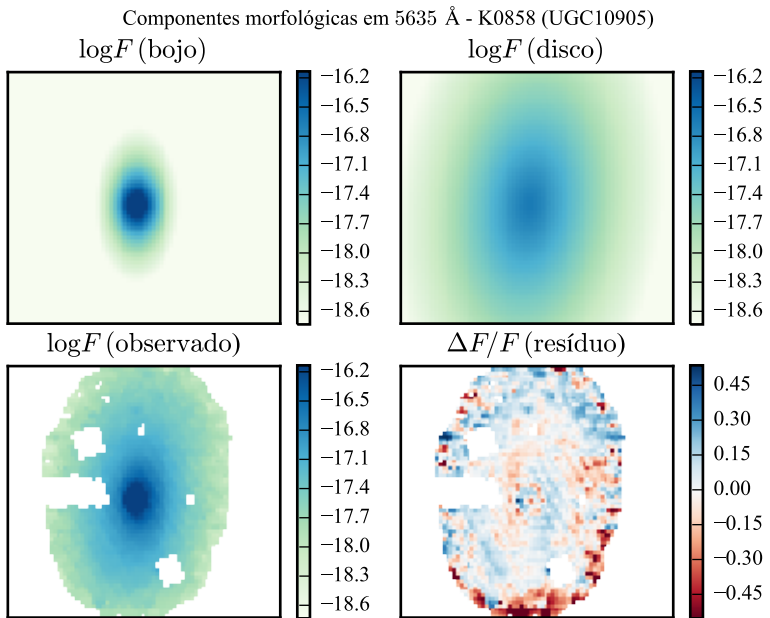


Figura B.52: Imagens em 5635 Å das componentes morfológicas de K0858 (UGC 10905).

B. Decomposição morfológica espectral e síntese de populações estelares da amostra final

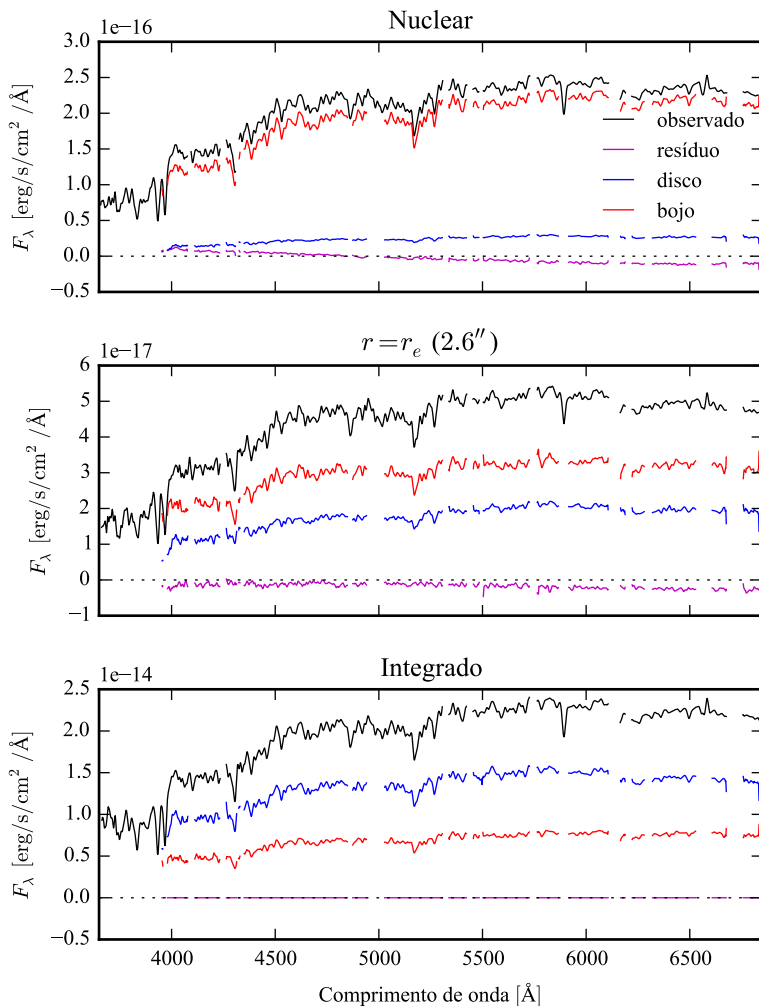


Figura B.53: Espectro das componentes morfológicas de K0858 (UGC 10905), observado (preto), bojo (vermelho), disco (azul) e resíduo (magenta). Acima: Espectro do *spaxel* nuclear da galáxia. Meio: Espectro em um *spaxel* a uma distância de r_e do núcleo. Abaixo: Espectro integrado espacialmente.

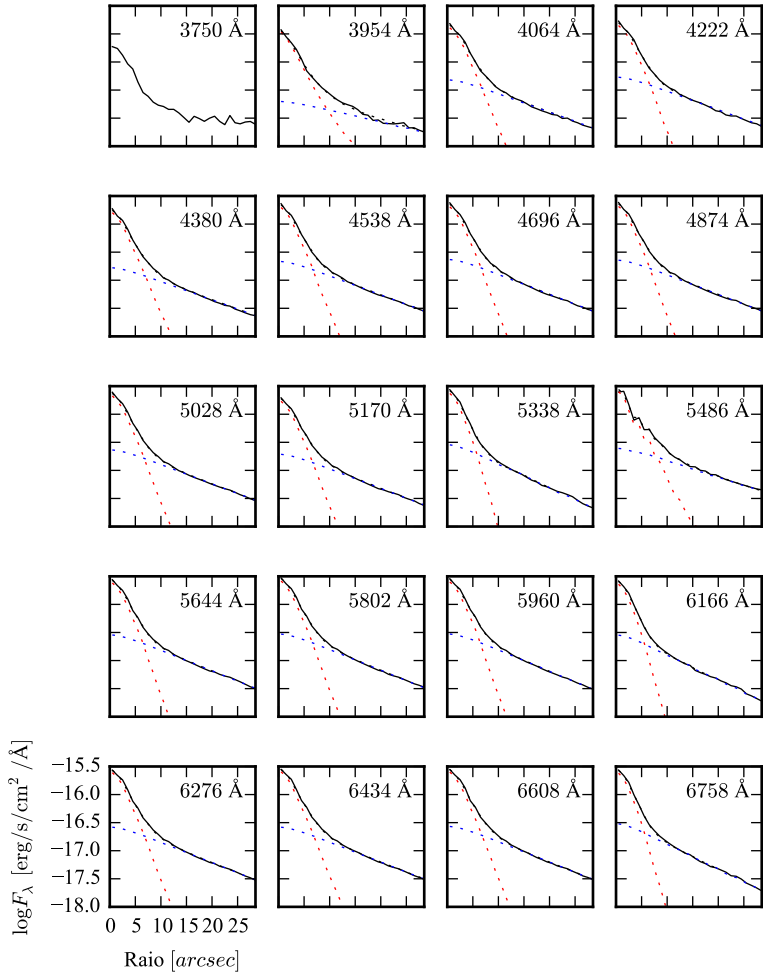


Figura B.54: Perfis radiais para diversos comprimentos de onda de K0858 (UGC 10905).

B. Decomposição morfológica espectral e síntese de populações estelares da amostra final

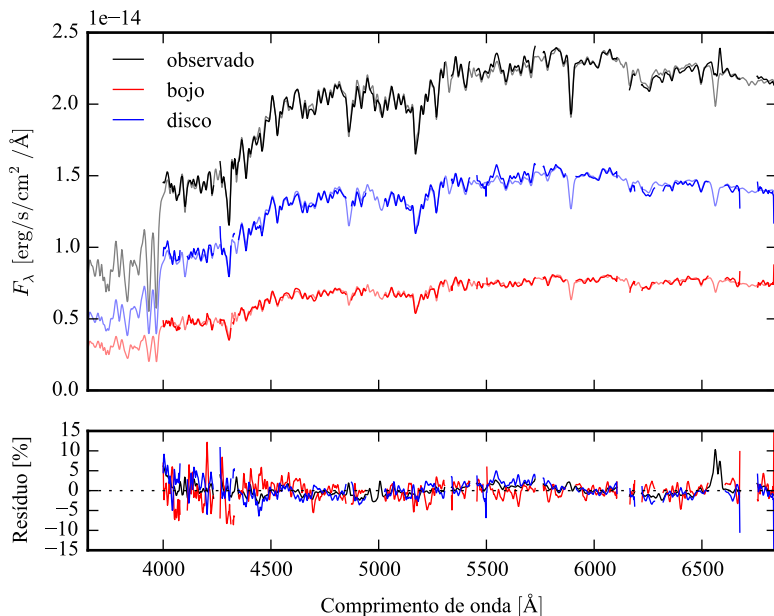


Figura B.55: Acima: Espectros integrados das componentes morfológicas de K0858 (UGC 10905), ajustados com STARLIGHT. Em preto, espectro observado. Em vermelho, e azul, as componentes bojo e disco. Em linhas de cor clara, o espectro ajustado pelo STARLIGHT. Abaixo: Resíduo dos espectros (observado menos sintético, dividido pelo observado).

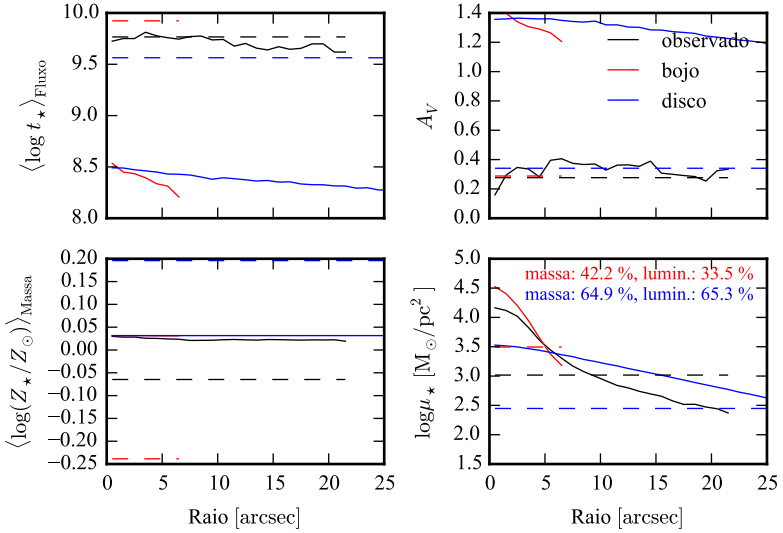


Figura B.56: Perfil radial de propriedades físicas das componentes morfológicas de K0858 (UGC 10905), obtidos através do STARLIGHT. As linhas contínuas representam as propriedades obtidas utilizando espectros espacialmente resolvidos. As linhas tracejadas representam as propriedades obtidas utilizando os espectros integrados. Em preto, espectro observado. Em vermelho, e azul, as componentes bojo e disco. Acima, à esquerda: idade estelar média ponderada pela luminosidade. Acima, à direita: atenuação por poeira, na banda V . Abaixo, à esquerda: metalicidade estelar média, ponderada pela massa. Abaixo, à direita: densidade superficial de massa estelar. As frações de massa e luminosidade entre as componentes e a total (obtida do espectro observado) é mostrada no painel inferior, à direita.

B. Decomposição morfológica espectral e síntese de populações estelares da amostra final

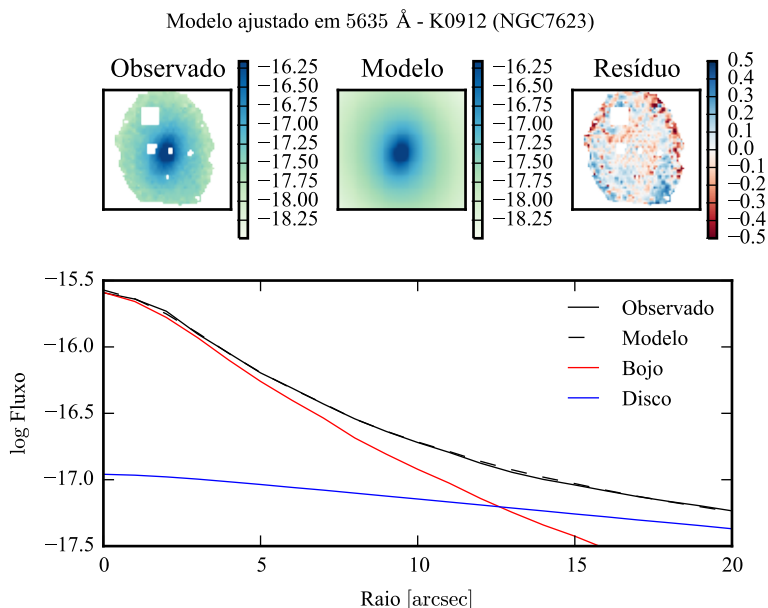


Figura B.57: Acima: imagens observada, modelada e resíduo, do fluxo em 5635 Å para K0912 (NGC 7623). Abaixo: perfis radiais, obtidos pela média do fluxo em anéis elípticos nas imagens. O fluxo observado é representado pela linha preta sólida. O melhor ajuste é representado pela linha preta tracejada. O bojo e o disco que compõe o modelo são mostrados em vermelho e azul, respectivamente.

B.9 K0912 (NGC 7623)

- Galáxia NGC 7623
- Tipo morfológico: S0 (mín. S0, máx. S0)
- Magnitude absoluta na banda r : $-21,97$
- Elipticidade: 0,14

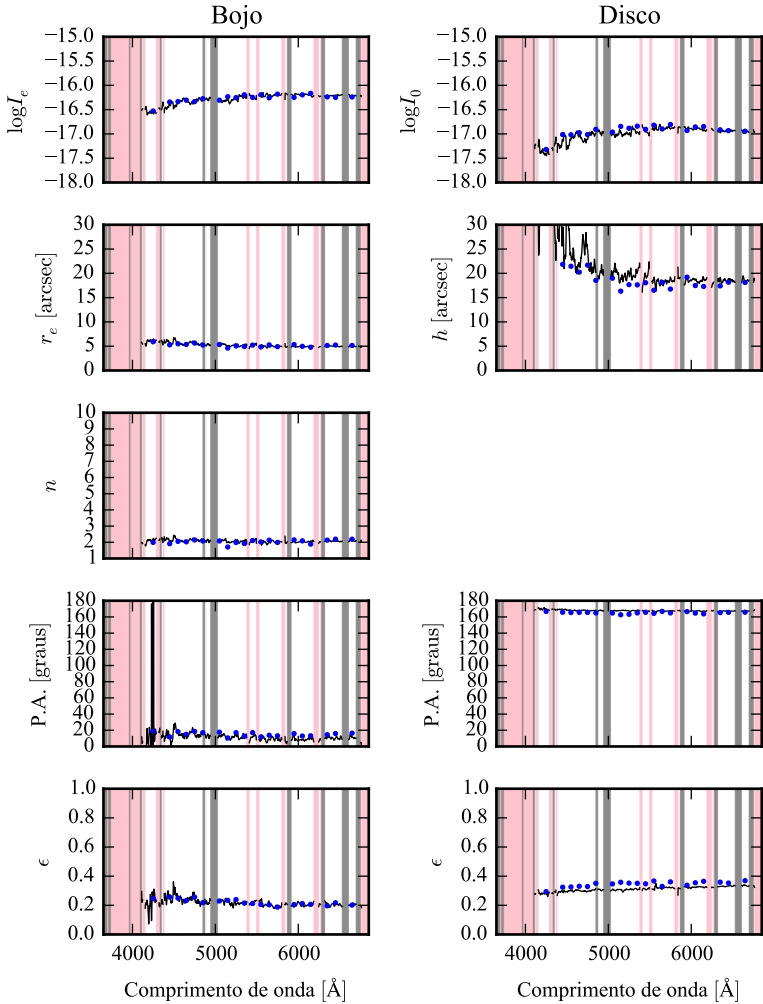


Figura B.58: Parâmetros morfológicos em função do comprimento de onda para K0912 (NGC 7623). Regiões em rosa representam comprimentos de onda onde a decomposição falhou. Regiões em cinza foram mascaradas antes de iniciar a decomposição. Pontos azuis indicam o primeiro passo da decomposição, em caixas de 100 Å.

B. Decomposição morfológica espectral e síntese de populações estelares da amostra final

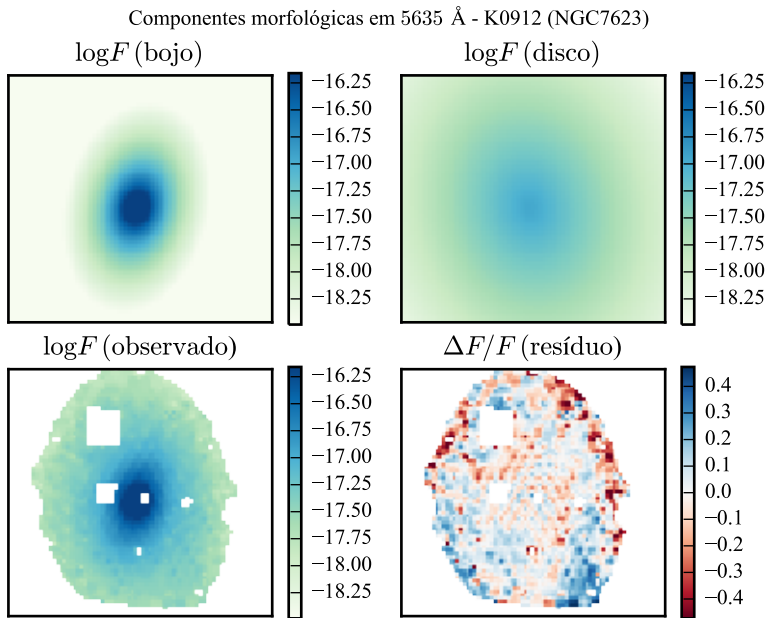


Figura B.59: Imagens em 5635 Å das componentes morfológicas de K0912 (NGC 7623).

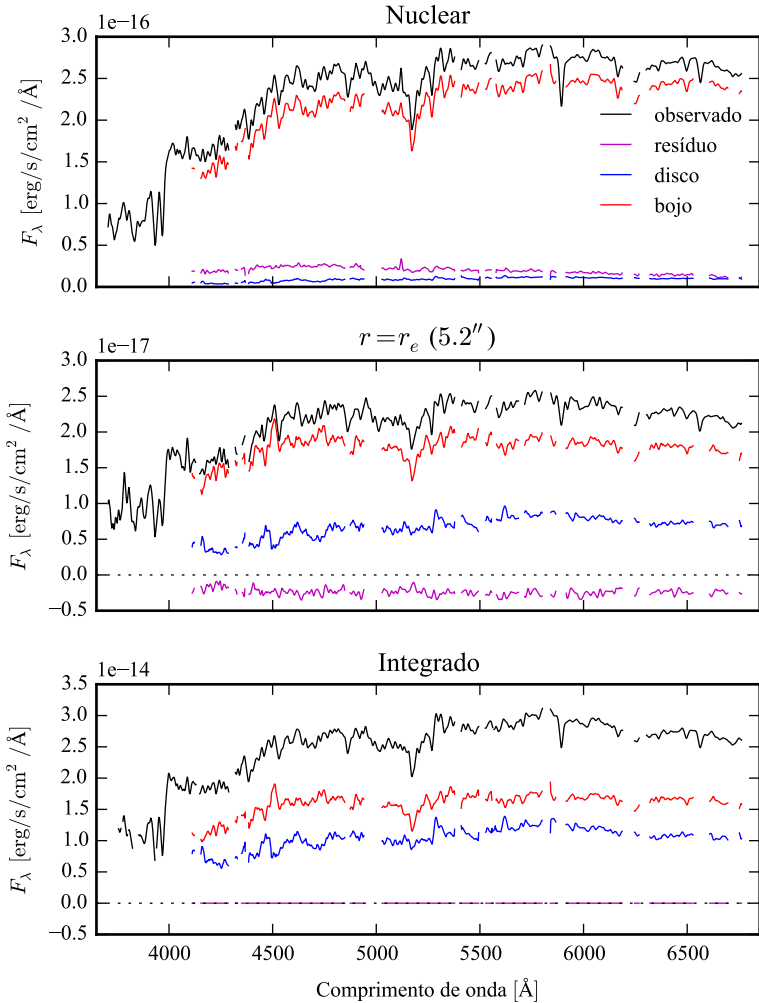


Figura B.60: Espectro das componentes morfológicas de K0912 (NGC 7623), observado (preto), bojo (vermelho), disco (azul) e resíduo (magenta). Acima: Espectro do *spaxel* nuclear da galáxia. Meio: Espectro em um *spaxel* a uma distância de r_e do núcleo. Abaixo: Espectro integrado espacialmente.

B. Decomposição morfológica espectral e síntese de populações estelares da amostra final

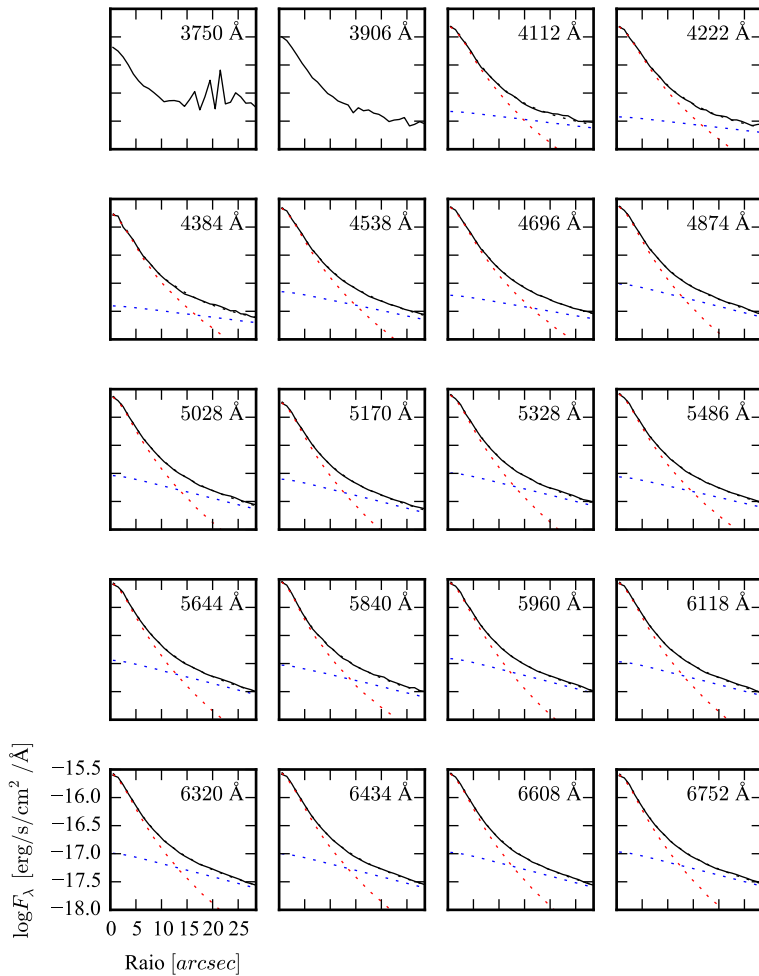


Figura B.61: Perfis radiais para diversos comprimentos de onda de K0912 (NGC 7623).

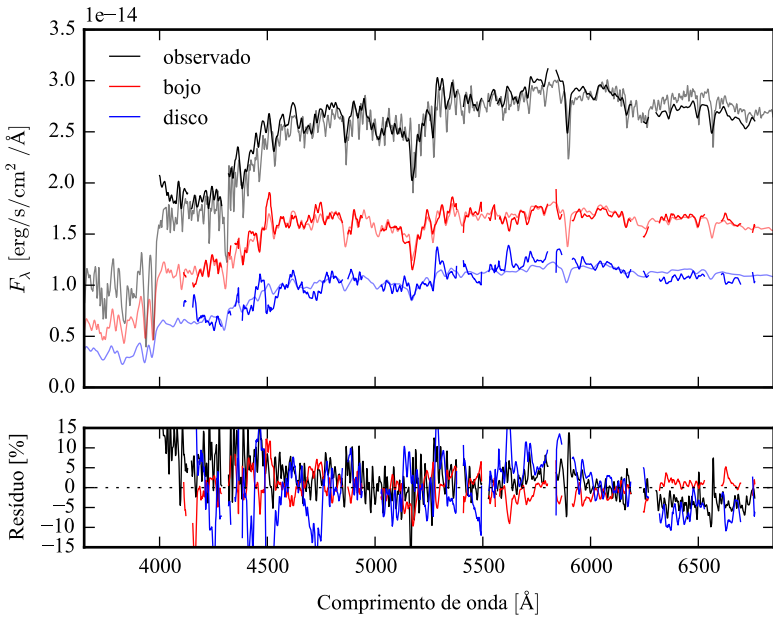


Figura B.62: Acima: Espectros integrados das componentes morfológicas de K0912 (NGC 7623), ajustados com STARLIGHT. Em preto, espectro observado. Em vermelho, e azul, as componentes bojo e disco. Em linhas de cor clara, o espectro ajustado pelo STARLIGHT. Abaixo: Resíduo dos espectros (observado menos sintético, divididos pelo observado).

B. Decomposição morfológica espectral e síntese de populações estelares da amostra final

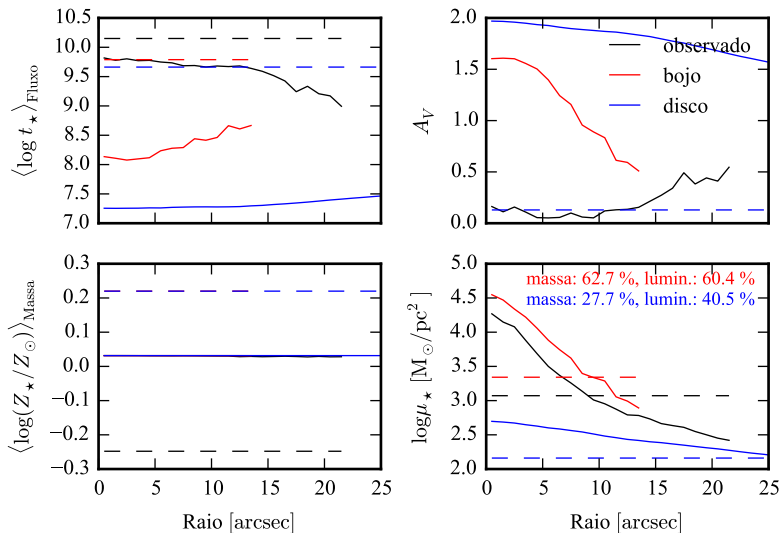


Figura B.63: Perfil radial de propriedades físicas das componentes morfológicas de K0912 (NGC 7623), obtidos através do STARLIGHT. As linhas contínuas representam as propriedades obtidas utilizando espectros espacialmente resolvidos. As linhas tracejadas representam as propriedades obtidas utilizando os espectros integrados. Em preto, espectro observado. Em vermelho, e azul, as componentes bojo e disco. Acima, à esquerda: idade estelar média ponderada pela luminosidade. Acima, à direita: atenuação por poeira, na banda V. Abaixo, à esquerda: metalicidade estelar média, ponderada pela massa. Abaixo, à direita: densidade superficial de massa estelar. As frações de massa e luminosidade entre as componentes e a total (obtida do espectro observado) é mostrada no painel inferior, à direita.

Manual do *software* PyCASSO

Versão impressa da documentação do *software* PyCASSO. Para uma melhor visualização e navegação entre as referências, acessar a versão completa deste manual se encontra no site:

<http://minerva.astro.ufsc.br/~andre/PyCASSO-0.9.3/>

Nota: a seção de referência foi removida por motivo de espaço.

PyCASSO Documentation

Release 0.9.3

André Luiz de Amorim

December 03, 2013

CONTENTS

1	Introduction	1
2	Getting started	3
2.1	Requirements	3
2.2	Stable version	3
2.3	Development version	4
3	Creating datasets	5
3.1	STARLIGHT data	5
3.2	The PyCASSO import tools	5
4	Usage	7
4.1	Listing synthesis runs	7
4.2	Loading galaxy data	7
4.3	Displaying property images	8
4.4	Radial and azimuthal profiles	10
4.5	Filling missing data	19
4.6	Working with spectra	21
4.7	Integrated properties	22
5	Legacy API	25
5.1	Loading from FITS files	25
5.2	Using very old scripts	25
5.3	Old API reference	26
6	Galaxy property list	31
6.1	Base	31
6.2	qbick planes	31
6.3	Population	33
6.4	Physical properties	35
6.5	Spectra	39
6.6	Synthesis fit diagnostics	41
7	Utility functions	43
7.1	Function list	43
8	Full data access API	49
8.1	HDF5 query functions	49
8.2	Synthesis data abstraction class	49
	Index	79

INTRODUCTION

PyCASSO stands for Python CALIFA Stellar Synthesis Organizer, and its main objective is to help handling stellar synthesis datacubes produced by [STARLIGHT](http://astro.ufsc.br/starlight/)¹ from integrated field spectra (IFS) produced by the [CALIFA survey](http://califa.caha.es/)².

This manual serves two purposes: it is a reference for the data cubes API, and a guide to the usage pattern of PyCASSO. The examples, when possible, contain real world data and perform common tasks when dealing with IFS data.

The CALIFA data cubes were preprocessed using a tool called QBICK to obtain spectra with a minimum signal-to-noise ratio using Voronoi binning. PyCASSO and QBICK may merge in the future.

¹<http://astro.ufsc.br/starlight/>

²<http://califa.caha.es/>

GETTING STARTED

2.1 Requirements

PyCASSO requires python 2.7. You also need these to use the data access modules.

- numpy/scipy
- pyfits
- h5py

These are probably available at your python package manager. For example, in Mac OSX using macports, use these commands to install python 2.7 and the dependencies, and then select this as your default python installation.

```
$ sudo port install python27 py27-h5py py27-numpy py27-scipy py27-pyfits
$ sudo port select --set python python27
```

You will also need PySTARLIGHT¹. The package is in the [python package index](#)², you may install it using `easy_install` or `pip` (*NOTE*: be sure that `pip` and `easy_install` are using the same python installation as you use for coding, or PySTARLIGHT will be installed at the wrong directory):

```
$ pip install PySTARLIGHT
```

or

```
$ easy_install PySTARLIGHT
```

If you want to create your own datasets, you'll also need `atpy`³. Refer to the site for installation instructions. In macports, install it using the command:

```
$ sudo port install py27-atpy
```

2.2 Stable version

The stable version of PyCASSO is 0.9.0⁴. Install using these commands:

```
$ tar xvzf PyCASSO-X.X.X.tar.gz
$ cd PyCASSO-X.X.X/
$ python setup.py install
```

¹https://bitbucket.org/astro_ufsc/pystarlight

²<https://pypi.python.org/pypi>

³<http://atpy.github.com/>

⁴https://bitbucket.org/astro_ufsc/pycasso/get/PyCASSO-0.9.0.tar.gz

2.3 Development version

Development version is hosted in bitbucket. Note that the development version may be broken or have half-implemented features. If you are feeling brave, clone it from the mercurial repository:

```
$ hg clone https://bitbucket.org/astro_ufsc/pycasso
```

To install it, run the commands:

```
$ cd pycasso
$ python setup.py install
```


CREATING DATASETS

3.1 STARLIGHT data

The main objective of PyCASSO is to organize the access to the stellar synthesis data provided by STARLIGHT. If you are reading this I assume you have the following files:

- QBICK segmentation FITS file (A.K.A. zone file)
- Input spectra for STARLIGHT
- STARLIGHT output

It is important to have the name of the files following the rules:

- Input spectra must have the format: `KNNNN_MMMM_suffix` where `KNNNN` is the CALIFA number and `MMMM` is the zone ID. The suffix can be anything and will be ignored.
- There can be only one input file starting with each pair `KNNNN_MMMM` in the same directory. Use different directories for different runs. This limitation will be fixed in later releases.
- STARLIGHT output files must have the format: `KNNNN_MMMM_runID`. These files can be gzipped or bziped, and the `.gz` or `.bz2` suffixes will be ignored.

3.2 The PyCASSO import tools

The import process is similar whether you want to use FITS or HDF5 files. Keep in mind that most of the effort will be towards the HDF5 storage, and the FITS support may be dropped in the future.

The import tools are `h5pycassoImport.py` and `pycassoImport.py` to import data to HDF5 and FITS, respectively. These scripts are located in the `tools` directory. Here is an example of a `h5pycassoImport.py` run:

```
$ h5pycassoImport.py --synthesis-dir=./sl_out/ --spectra-dir=./sl_in/ \  
> --base=Bgsd01 --base-description='Granada 01' \  
> --qbick-run=q027 --qbick-description='COMBO convex voronoi zones ver. 0.2.7' \  
> --run-id=eBR_v20_q027.d13c512.ps3b.k1.mC.CCM.Bgsd01.v01 \  
> --run-description='q027/Bgsd01 with default parameters' \  
> --zone-file=K0001_eBR_v20_q035.d13c512-planes.fits \  
> --database=qalifa-synthesis.h5 K0001
```

The arguments are the following:

- `--synthesis-dir`: Path to the synthesis output directory.
- `--spectra-dir`: Path to the synthesis input directory.
- `--base`: Identifier of the base used in the synthesis.
- `--base-description`: Description of the base used in the synthesis.

- `--qbick-run`: Identifier of the qbick run used in the synthesis.
- `--qbick-description`: Description of the qbick run used in the synthesis.
- `--run-id`: Identifier of the whole synthesis run.
- `--run-description`: Description of the whole synthesis run.
- `--zone-file`: Path to the FITS file containing the qbick planes.
- `--database`: Path to the HDF5 database file.
- CALIFAID: Califa name of the galaxy.

It is recommended to use a single database for everything.

The arguments for the FITS version are similar. For a complete list, run `h5pycassoImport.py --help` or `pycassoImport.py --help`.

For more information on the database structure, see [PyCASSO data model](#)¹.

¹<https://docs.google.com/document/d/1s3D8Ma-whWIZauMb9cMH7IISRfpuzTh5Tkhhm-zbbA>

USAGE

4.1 Listing synthesis runs

This section only applies to HDF5 datasets. If you are using the FITS format, you have one FITS file per galaxy per run.

Start a python shell. To list the synthesis runs present in the database *qalifa-synthesis.h5*, use the function `listRuns()` (page 49):

```
>>> from pycasso.h5datacube import
>>> listRuns('qalifa-synthesis.h5')
eBR_v20_q027.d13c512.ps3b.k1.mC.CCM.Bgsd01.v01
eBR_v20_q036.d13c512.ps03.k2.mC.CCM.Bgsd61
```

In this case, we have two runs, 'eBR_v20_q027.d13c512.ps3b.k1.mC.CCM.Bgsd01.v01' and 'eBR_v20_q036.d13c512.ps03.k2.mC.CCM.Bgsd61'. The other tools for listing the contents of a database are `listBases()` (page 49) and `listQbickRuns()` (page 49).

```
>>> listBases('qalifa-synthesis.h5')
Bgsd01 Bgsd61
>>> listQbickRuns('qalifa-synthesis.h5')
q027 q036
```

Now, we can search the runs that have specific bases or qbick runs using the keyword arguments `baseId` and `qbickRunId`. One can specify any one or both of these filter arguments.

```
>>> listRuns('qalifa-synthesis.h5', baseId='q036', qbickRunId='Bgsd61')
eBR_v20_q036.d13c512.ps03.k2.mC.CCM.Bgsd61
```

4.2 Loading galaxy data

To load the galaxy 'K0001' (IC5376), in the run 'eBR_v20_q036.d13c512.ps03.k2.mC.CCM.Bgsd61' from the database, do

```
>>> from pycasso.h5datacube import
>>> K = h5Q3DataCube('qalifa-synthesis.h5', \
'eBR_v20_q036.d13c512.ps03.k2.mC.CCM.Bgsd61', 'K0001')
```

The object `K` is a `h5Q3DataCube` (page 49), which implements `IQ3DataCube` (page 59). The latter defines high level algorithms like zone to spatial conversions and radial profiles, while the former contains the I/O related stuff. If you are using ipython, entering `K` followed by two tab keystrokes, you should see all the properties of the galaxy and all methods available to operate on those.

If you have FITS files with your data, please refer to *Loading from FITS files* (page 25).

4.2.1 Zone smoothing

The data from the galaxies are binned in spatial regions called voronoi bins. There is a procedure called “dezonification” which converts the data from voronoi bins back to spatial coordinates. When doing so, one can use the surface brightness of the image of the galaxy as a hint to smooth some of the properties.

This is enabled by default. To disable it, set the keyword argument `smooth` to `False` when loading the galaxy.

```
>>> K = h5Q3DataCube('galifa-synthesis.h5', \
'eBR_v20_q036.d13c512.ps03.k2.mC.CCM.Bgsd61', 'K0001', smooth=False)
```

For more information, see `getDezonificationWeight()` (page 59).

4.3 Displaying property images

In this section we explain how to obtain images of properties of the galaxy. Most of the properties of interest are already calculated, see the section *Galaxy property list* (page 31).

Here we assume the galaxy is loaded as `K`. Now, all the data is stored as voronoi zones, but we really want to see the spatial distribution of the galaxy properties. `K` has a method for converting data from voronoi zones to images, the method `zoneToYX()` (page 59).

Let’s see the property `popx` (page 54). It is a 3-dimensional array, containing the light fraction for every triplet (*age, metallicity, zone*).

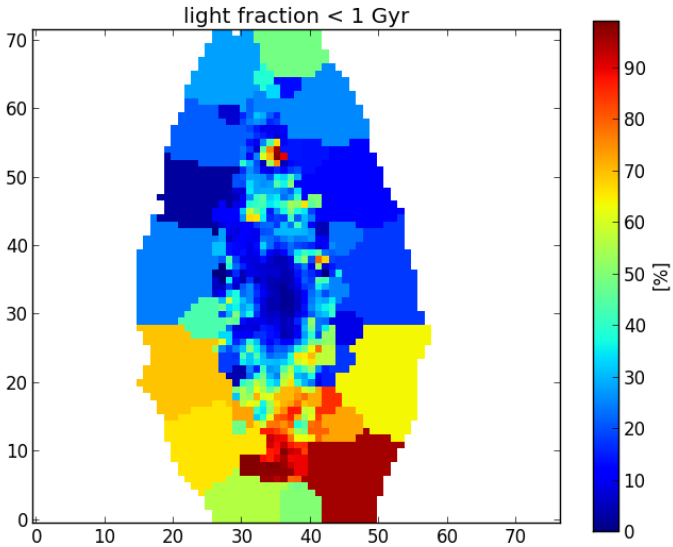
```
>>> K.popx.shape (39, 4, 649) >>> K.N_age, K.N_met, K.N_zone (39, 4, 649)
```

Now, we want to see how this is distributed in the galaxy. The fraction of light in each population is the same in every pixel of a zone. So, we call `popx` an **intensive** property. To inform `zoneToYX()` (page 59) that the property is intensive, we set `extensive=False`.

```
>>> popx = K.zoneToYX(K.popx, extensive=False) >>> popx.shape (39, 4, 72, 77)
```

In this case, the resulting `popx` is 4-dimensional, where the zone dimension has been replaced by the (x,y) plane. Let’s plot the young population (summing only the fractions for ages smaller than 1Gyr) as a function of the position in the galaxy plane.

```
>>> import matplotlib.pyplot as plt
>>> popY = popx[K.ageBase < 1e9].sum(axis=1).sum(axis=0)
>>> plt.imshow(popY, origin='lower', interpolation='nearest')
>>> cb = plt.colorbar()
>>> cb.set_label('%')
>>> plt.title('light fraction < 1 Gyr')
```



4.3.1 Masked pixels

The white pixels do not belong to any zone (*masked pixels*), and by default are set to `numpy.nan`. One might change the fill value for the masked pixels using the keyword `fill_value`. For example, to fill with zeros,

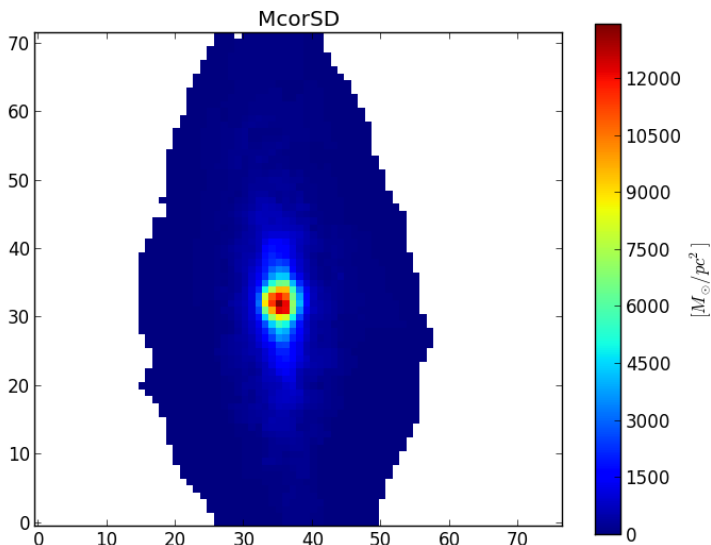
```
>>> popx_fill_zeros = K.zoneToYX(K.popx, extensive=False, fill_value=0.0)
```

It is recommended to use the fill values as `nan`, this way you know when you make a mistake and use values from regions where there's no data (`nan` is contagious, any operation containing a `nan` will yield `nan`).

4.3.2 Surface densities

When the property is extensive, such as mass or flux, it is more proper to work with surface densities of these properties, when working with images. The most easily acknowledged extensive properties are light and mass. The properties `Lobn__z` (page 73), `Mini__z` (page 74) and `Mcor__z` (page 74) are the total light and mass for the voronoi zones. When we convert these to images, setting `extensive=True`, the resulting image contains the surface density of these properties (for example, in units of M_{\odot}/pc^2).

```
>>> McorSD = K.zoneToYX(K.Mcor__z, extensive=True)
>>> plt.imshow(McorSD, origin='lower', interpolation='nearest')
>>> cb = plt.colorbar()
>>> cb.set_label('[M_\odot / pc^2]')
>>> plt.title('McorSD')
```



This is the same property as `McorSD__yx` (page 74), see the section below.

4.3.3 Predefined properties

The conversion from zones to images is perhaps the most common thing you will ever use from PyCASSO. To make things easier (and less verbose), most of the properties already have been converted to images. These predefined properties take care of the extensiveness or intensiveness nature of the physical property, and return a surface density when suitable. The full list of properties can be seen in the section *Galaxy property list* (page 31).

4.4 Radial and azimuthal profiles

Galaxy images are nice and all, but in the end you want to compare spatial information between galaxies, and it can not be done in a per pixel basis. One can think in polar coordinates and analyze only the radial variations of the properties. For this we have to think about what galaxy distances in these images really mean.

4.4.1 Image geometry

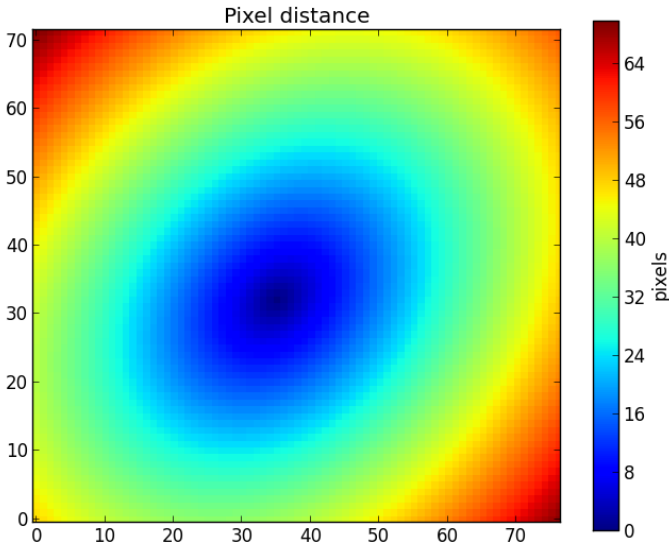
One fair approximation is to assume the galaxy has an axis-symmetric geometry. Therefore, if we see the galaxy as an elliptical shape, that is because of its inclination with respect to the line of sight. If we get all the points at a given distance a from the center of the galaxy, this will appear as an ellipse of semimajor axis equal to a .

To know the distance of each pixel to the center of the galaxy, we need to know the *ellipticity* (b/a (page 51)) of the galaxy, defined as $\frac{b}{a}$ (ratio between semiminor and semimajor axes), and the *position angle* (ρ_a (page 51), in radians, counter-clockwise from the X-axis) of the ellipse. These can be set using the method `setGeometry()` (page 60). The distance of each pixel is obtained using the property `pixelDistance__yx` (page 51).

```

>>> K.setGeometry(pa=45*np.pi/180.0, ba=0.75)
>>> dist = K.pixelDistance__yx
>>> plt.imshow(dist, origin='lower', interpolation='nearest')
>>> cb = plt.colorbar()
>>> cb.set_label('pixels')
>>> plt.title('Pixel distance')

```



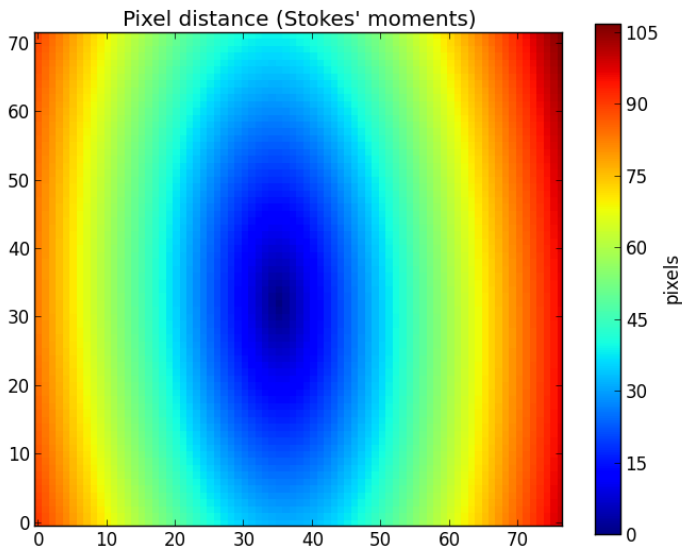
This example geometry clearly does not correspond to geometry of the galaxy, as seen in the previous figures. If we lack the values of ba and pa from other sources, we can use the method `getEllipseParams()` (page 68) to estimate these ellipse parameters using “Stokes’ moments” of the flux (actually, we use `qSignal` (page 52)) as explained in the paper Sloan Digital Sky Survey: Early Data Release¹.

```

>>> pa, ba = K.getEllipseParams()
>>> K.setGeometry(pa, ba)

```

¹<http://adsabs.harvard.edu/abs/2002AJ....123..485S>



Now the distances match the geometry of the galaxy assuming it has an elliptical distribution. Other parameters that may be set by `setGeometry()` (page 60) are the *Half Light Radius* (see below) and the center of the galaxy, by using respectively the keyword parameters `HLR_pix` and `center` (a tuple containing x and y).

4.4.2 Galaxy scales

We also need to take into account that galaxies exist in all sizes and distances. This means that using pixels as a distance scale is not satisfactory. Thus we have to convert distances to a “natural scale” to compare the radial profiles of distinct galaxies.

We define the *Half Light Radius* (`HLR_pix` (page 50)) as the semimajor axis of the ellipse centered at the galaxy center containing half of the flux in a certain band. In PyCASSO, we use `qSignal` (page 52), which is the flux in the normalization window (5635).

The HLR is updated whenever `setGeometry()` (page 60) is called. One can explicitly set the HLR using the `HLR_pix` parameter, or let it be determined automatically. Note that the HLR depends heavily on the ellipse parameters.

- Circular

```
>>> K.setGeometry(pa=0.0, ba=1.0)
>>> K.HLR_pix
9.334798311419563
```

- Ellipse

```
>>> pa, ba = K.getEllipseParams()
>>> K.setGeometry(pa, ba)
>>> K.HLR_pix
12.878480006876336
```



```
>>> K.HLR_pc
2545.9657503507078
```

In the last line we show the HLR in parsecs (`HLR_pc` (page 50)), which may be handy sometimes. It is based on `HLR_pix` (page 50) and `parsecPerPixel` (page 50).

Alternatively, one can think in terms of other property as a half-scale. This is achieved using the method `getHalfRadius()` (page 69). One alternate scale commonly used is the mass. To calculate the Half Mass Radius (HMR) use the following:

```
>>> K.getHalfRadius(K.McorSD__yx)
7.612629351561292
```

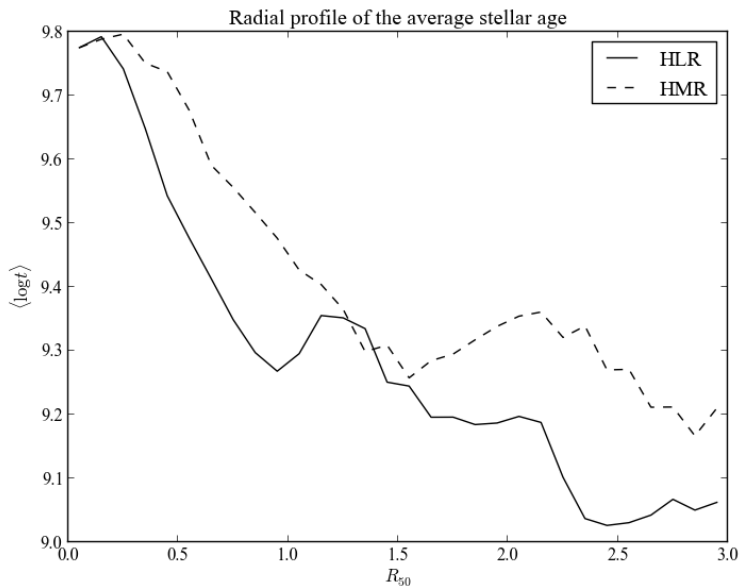
The input for this method must be a 2-D image.

Note: This uses the same computation as the HLR.

4.4.3 Calculating the radial profile of a 2-D image

Now that we have a scale to measure things in radial distance, it is useful to have a radial profile of things. First, let's assume we have a 2-D image we want to get the radial profile, for instance, `at_flux__yx` (page 75). The method `radialProfile()` (page 63) receives a 2-D image of a given property, a set of radial bins, an optional radial scale (it uses HLR by default) and returns the average values of the pixels inside each bin. Think of it as a fancy histogram.

```
>>> HMR = K.getHalfRadius(K.McorSD__yx)
>>> bin_r = np.arange(0, 3+0.1, 0.1)
>>> bin_center = (bin_r[1:] + bin_r[:-1]) / 2.0
>>> at_flux_HLR = K.radialProfile(K.at_flux__yx, bin_r)
>>> at_flux_HMR = K.radialProfile(K.at_flux__yx, bin_r, rad_scale=HMR)
>>> plt.plot(bin_center, at_flux_HLR, '--k', label='HLR')
>>> plt.plot(bin_center, at_flux_HMR, '--k', label='HMR')
>>> plt.ylabel(r'$\langle \log t \rangle$')
>>> plt.xlabel(r'$R_{50}$')
>>> plt.title('Radial profile of the mean stellar age')
>>> plt.legend()
```



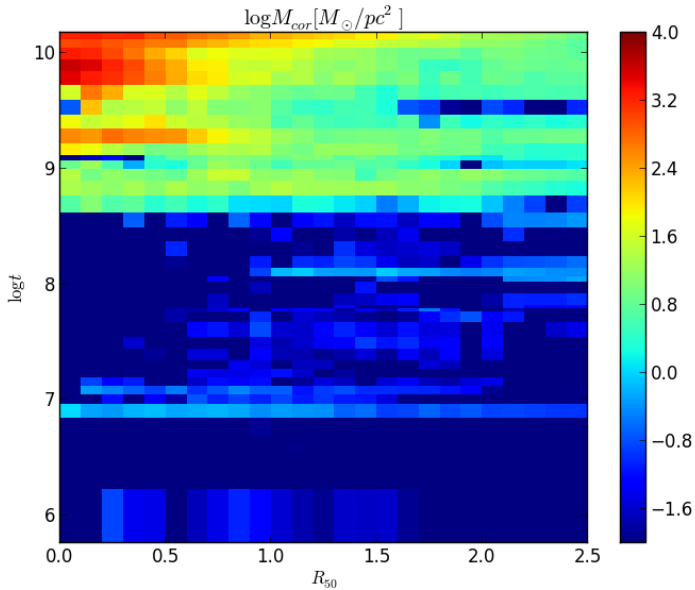
Now let's explain the procedure. `bin_r` represent the bin boundaries in which we want to calculate the mean value of the property. It is not suitable for plotting, as it contains one extra value (`len(bin_r) == len(at_flux__HLR) + 1`). So, we calculate the central points of the bins, `bin_center`. Then, we proceed to calculate the radial profile of `at_flux__yx`, which is the average log. of the age, weighted by flux. We do so using HLR and HMR as a distance scale. The mass is usually more concentrated in the center of the galaxy, so that in general $\text{HMR} < K \cdot \text{HLR}_{\text{pix}}$ and therefore the plots look similar, but stretched.

4.4.4 Calculating the radial profile of a N-D image

In the example above we compute the radial profile of a 2-D image. Now, the process is the same for higher-dimensional images. The presentation can be tricky, though. Let's see an example.

We have the surface distribution of mass in ages, `McorSD__tyx`, which is a 3-D array (age, y, x). One may be tempted to do a `for` loop for each age, but the method `radialProfile()` takes care of this, as it accepts properties with more than 2 dimensions, as long as the spatial dimensions are the rightmost (`[..., y, x]` in numpy slice notation). In this example, we want to plot a 2-D map of the mass as a function of radius and age. We will use the Half Light Radius as a radial scale, so we don't have to set the argument `rad_scale` as we did previously. We also don't need the bin centers, as the plot method used is fit for dealing with histogram-like data.

```
>>> bin_r = np.arange(0, 2.5+0.1, 0.1)
>>> McorSD__tyx = K.McorSD__tZyx.sum(axis=1)
>>> logMcorSD__tr = np.log10(K.radialProfile(McorSD__tyx, bin_r, mode='mean'))
>>> vmin = -2
>>> vmax = 4
>>> plt.pcolormesh(bin_r, K.logAgeBaseBins, logMcorSD__tr, vmin=-2, vmax=4)
>>> plt.colorbar()
>>> plt.ylim(K.logAgeBaseBins.min(), K.logAgeBaseBins.max())
>>> plt.ylabel(r'$\log t$')
>>> plt.xlabel(r'$R_{50}$')
>>> plt.title(r'$\log M_{\text{cor}} [M_{\odot} / \text{pc}^2]$')
```



As we said, the `meth:pseudocolor` method needs the bin edges, so we have to use the radial bin edges (provided by `bin_r`), and the age bin edges. The property called `logAgeBaseBins` returns the age bin edges in log space, see it's documentation for more details.

One can also compute the sum of the values (or the mean or median) inside a ring, using a pair of values as bins:

```
>>> Mcor_tot_ring = K.radialProfile(K.McorSD__yx, \
(0.5, 1.0), mode='sum') * K.parsecPerPixel**2
```

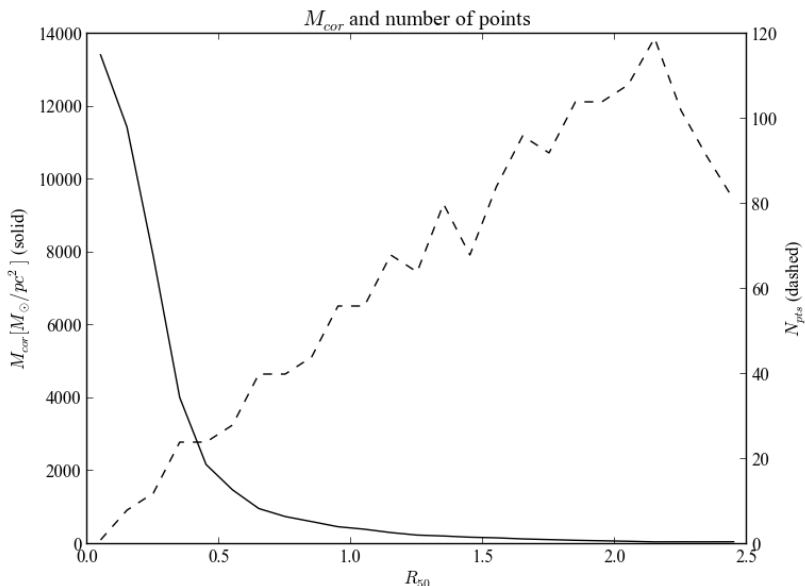
The rightmost term is the pixel area, to convert from surface density to absolute mass. The `mode` keyword indicates what to do inside the bins. By default, the mean is computed. The valid values for `mode` are:

- 'mean'
- 'mean_exact' (see below)
- 'sum'
- 'median'

If the number of pixels inside each radial bin is needed, the keyword argument `return_npts` may be set. In this case, the return value changes to a tuple containing the radial binned property and the number of points in each bin.

```
>>> bin_r = np.arange(0, 2.5+0.1, 0.1)
>>> bin_center = (bin_r[1:] + bin_r[:-1]) / 2.0
>>> McorSD__r, npts = K.radialProfile(K.McorSD__yx, bin_r, return_npts=True)
>>> fig = plt.figure()
>>> plt.title('$M_{cor}$ and number of points')
>>> ax1 = fig.add_subplot(111)
>>> ax1.plot(bin_center, McorSD__r, '-k')
>>> ax1.set_xlabel(r'$R_{50}$')
>>> ax1.set_ylabel(r'$M_{cor}$ [M_\odot / pc^2] (solid)')
>>> ax2 = ax1.twinx()
```

```
>>> ax2.plot(bin_center, npts, '--k')
>>> ax2.set_ylabel(r'$N_{pts}$ (dashed)')
```



4.4.5 Radial profiles using exact apertures

All the radial profiles calculated above suffer from a “jagginess” caused by the discrete method of assigning pixels to the radial bins (see the dashed line from the image above). When pixels fall in the boundaries of the bins, the whole pixel gets assigned to one or the other bin, based on the pixel center. Often this is harmless, but for small radii (or conversely, large pixels) this effect can be a problem. The solution in this case is to “split” the pixel between the bins, calculating the intersection of the bin boundaries and each pixel. Needless to say, this can be very slow. To use the exact apertures algorithm (shamelessly “stolen” from `photutils`²), change the mode parameter to ‘mean_exact’.

Here we can see a comparison between the exact and the discrete versions of the radial profile of the luminosity weighted mean stellar age.

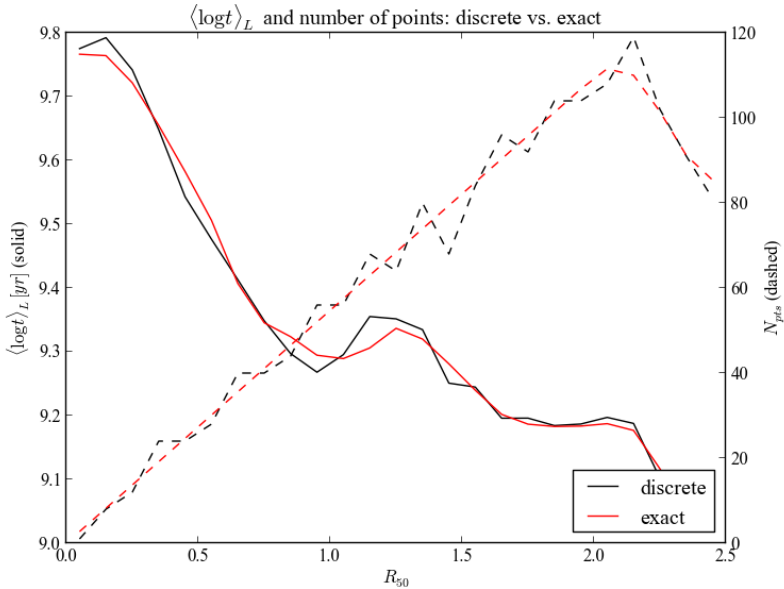
```
>>> bin_r = np.arange(0, 2.5+0.1, 0.1)
>>> bin_center = (bin_r[1:] + bin_r[:-1]) / 2.0
>>> atflux, npts = K.radialProfile(K.at_flux_yx, bin_r, \
mode='mean', return_npts=True)
>>> atflux_ex, npts_ex = K.radialProfile(K.at_flux_yx, bin_r, \
mode='mean_exact', return_npts=True)
>>> fig = plt.figure()
>>> plt.title(r'$\langle \log t \rangle$ and number of points: discrete vs. exact')
>>> ax1 = fig.add_subplot(111)
>>> ax1.plot(bin_center, atflux, '-k', label='discrete')
>>> ax1.plot(bin_center, atflux_ex, '-r', label='exact')
>>> ax1.set_xlabel(r'$R_{50}$')
```

²<https://github.com/astropy/photutils>

```

>>> ax1.set_ylabel(r'$\langle \log t \rangle_L$ (solid)')
>>> plt.legend(loc='lower right')
>>> ax2.plot(bin_center, npts_ex, '--r')
>>> ax2 = ax1.twinx()
>>> ax2.plot(bin_center, npts, '--k')
>>> ax2.set_ylabel(r'$N_{pts}$ (dashed)')

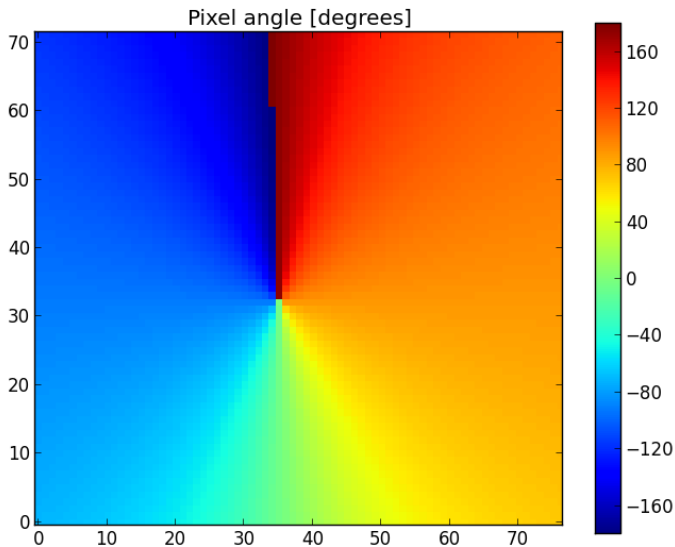
```



The bin area (dashed lines, right vertical axis) is much smoother when using the 'mean_exact' algorithm (in red), compared to the discrete 'mean' version (in black). As you can see, the age radial profile (solid lines, left vertical axis) becomes less noisy.

4.4.6 Azimuthal and radial profile of a N-D image

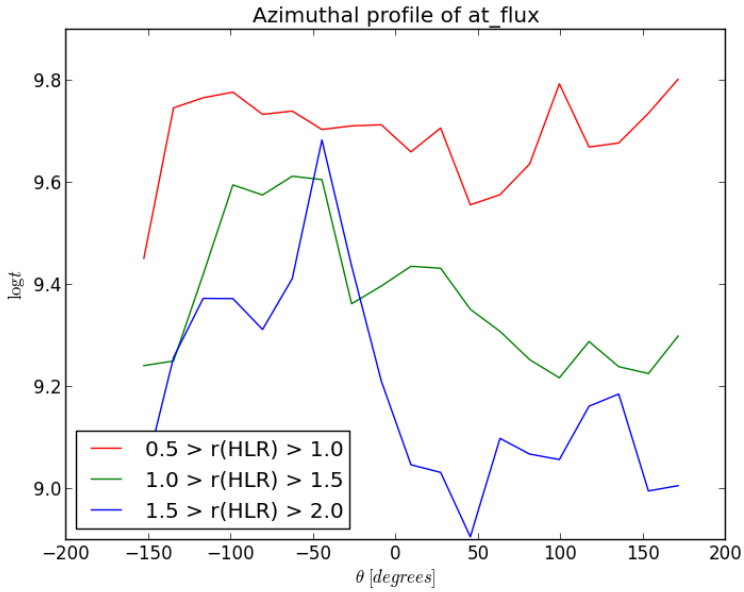
Still more generic than `radialProfile()` (page 63) is `azimuthalProfileNd()` (page 66). It adds the capability of azimuthal profiles, based on the angles associated with each pixel. This angle is accessible using `pixelAngle_yx` (page 51), in radians. The method `getPixelAngle()` (page 69) allows one to get the angle in degrees, or to get an arbitrary ellipse geometry, much like `getPixelDistance()` (page 68).



In PyCASSO the pixel angle is defined as the counter-clockwise angle between the pixel and the semimajor axis, taking the ellipse distortion into account. Please look at `getPixelAngle()` (page 69) for more details.

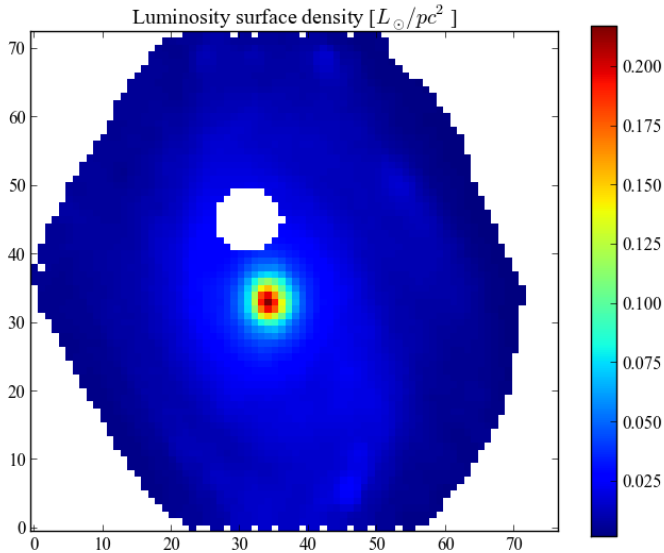
In the example below, we calculate the azimuthal profile of the log. age, averaged in flux, inside three rings between 0.5, 1.0, 1.5 and 2.0 HLR.

```
>>> bin_a = np.linspace(-np.pi, np.pi, 21)
>>> bin_a_center_deg = (bin_a[1:] + bin_a[:-1]) / 2.0 * 180 / np.pi
>>> bin_r = np.array((0.5, 1.0, 1.5, 2.0))
>>> at_flux__ar = K.azimuthalProfileNd(K.at_flux__yx, bin_a, bin_r)
>>> plt.plot(bin_a_center_deg, at_flux__ar[:,0], '-r', label='0.5 > r (HLR) > 1.0')
>>> plt.plot(bin_a_center_deg, at_flux__ar[:,1], '-g', label='1.0 > r (HLR) > 1.5')
>>> plt.plot(bin_a_center_deg, at_flux__ar[:,2], '-b', label='1.5 > r (HLR) > 2.0')
>>> plt.title('Azimuthal profile of mean stellar age')
>>> plt.ylabel(r'$\langle \log t \rangle_{\text{angle}_L}$')
>>> plt.xlabel(r'$\langle \theta \rangle$ [degrees]')
>>> plt.legend()
```

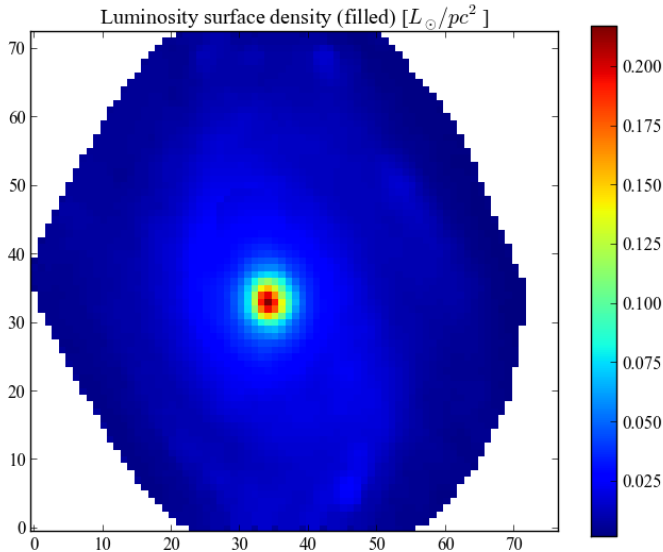


4.5 Filling missing data

The example galaxy used above does not have any masked foreground or background objects. This is not always the case. For example, galaxy K0277 (NGC2916) has a foreground star near its center, which was masked in the analysis pipeline.



This impacts some measurements like the total mass of the galaxy or the cumulative radial curves. The latter can have a big effect in properties like the half light radius. To take the hollow areas into account, we can use the method `fillImage()` (page 67). By default, it takes a property as input, calculates its radial profile and interpolates the missing data from the radial profile. This assumes the user already called `setGeometry()` (page 60) with proper values. Alternatively, one can calculate a radial profile and use it as parameter when filling, see the documentation. Also, there's two modes of filling: 'hollow' and 'convex'. The first one only fills the hollow pixels, while the second fills the complete convex hull of the image (that is, fills the edges making the image "roundy"). Here's the same image as above, filling the convex hull.



Note the barely visible artifact in the filled area. As an example, let's compare the values of the half light radius with and without filling. We will calculate the filling by hand to illustrate the usage. The methods `getHalfRadius()` (page 69) and `getHLR_pix()` (page 70) have a `fill` parameter, which when set to `True`, will perform the filling automatically.

```
>>> pa, ba = K.getEllipseParams()
>>> K.setGeometry(pa, ba)
>>> LobnSD_fill, mask = K.fillImage(K.LobnSD__yx, mode='hollow')
>>> K.getHalfRadius(LobnSD_fill, mask=mask)
19.43191121094409
>>> K.getHalfRadius(K.LobnSD__yx)
19.991108029801655
```

If one does not fill the hollow areas, the computed half light radius will be overestimated (in this case, by about 0.5 pixel, but it can be worse). The same applies to the total mass or luminosity of the galaxy.

4.6 Working with spectra

PyCASSO handles the stellar synthesis results from IFS data. One of the products of the stellar synthesis is a synthetic spectrum of each pixel (`f_syn_lyx` (page 77)), containing only the stellar contribution to the light. The observed spectra (`f_obs_lyx` (page 76)), errors (`f_err_lyx` (page 77)) and flags (`f_flag_lyx` (page 76)) are also available. Using these, one can easily, for example, obtain the residual spectra and measure emission lines.

```
>>> f_syn_nuc = K.f_syn_lyx[:, K.y0, K.x0]
>>> f_obs_nuc = K.f_obs_lyx[:, K.y0, K.x0]
>>> f_flag_nuc = K.f_flag_lyx[:, K.y0, K.x0]
>>> mask = f_flag_nuc < 1.0
>>> ax1 = plt.subplot(211)
```

```

>>> ax1.plot(K.l_obs[mask], f_obs_nuc[mask], '-k', label='Obs.')
```

```

>>> ax1.plot(K.l_syn_obs[mask], f_syn_nuc[mask], '-r', label='Syn.')
```

```

>>> ax1.set_xlabel(r'wavelength $\[AA]$')
```

```

>>> ax1.set_ylabel(r'Flux $\[erg / s / cm^2 / AA]$')
```

```

>>> ax1.set_title('Spectra')
```

```

>>> ax1.legend()
```

```

>>> ax2 = plt.subplot(212)
```

```

>>> ax2.plot(K.l_obs[mask], f_obs_nuc[mask] - f_syn_nuc[mask], '-k')
```

```

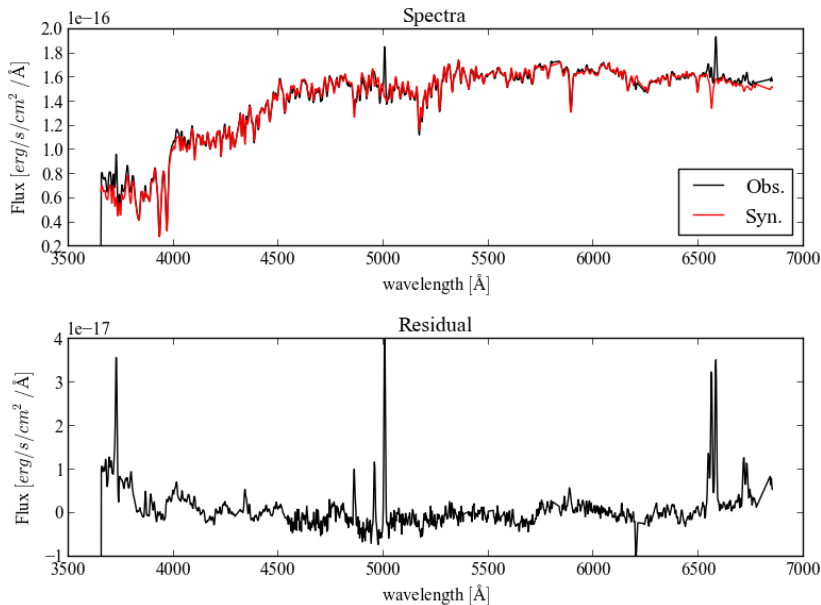
>>> ax2.set_xlabel(r'wavelength $\[AA]$')
```

```

>>> ax2.set_ylabel(r'Flux $\[erg / s / cm^2 / AA]$')
```

```

>>> ax2.set_title('Residual')
```



Notice the emission lines are more evident in the residual. Thus using PyCASSO it is possible to analyze the spatially resolved spectral features like the $D_n(4000)$ and Lick indices.

4.7 Integrated properties

In addition to the spatially stellar synthesis, we performed the stellar synthesis in the integrated spectra of the galaxies. This was one can check if the sum of the parts is equal to the whole. In general the properties in integrated form contain the prefix `integrated_`. Please take a look at the section *Galaxy property list* (page 31). Let's take a look in the mass of the galaxy.

```

>>> K.integrated_Mcor / 1e10
6.4588941491889695
>>> (K.McorSD_yx * K.parsecPerPixel**2).sum() / 1e10
6.7011924815290183
>>> K.integrated_Mcor / (K.McorSD_yx * K.parsecPerPixel**2).sum()
0.9638425051947227
```

That is, the total mass of the galaxy, calculated using the stellar synthesis of the integrated spectra

(`integrated_Mcor`) is 4% smaller than the sum of the masses of the pixels, calculated in the same way.

LEGACY API

5.1 Loading from FITS files

The process of loading data for a galaxy in a FITS file is similar to the HDF5 one. The main difference is that you only have to specify the path to the file. One should use sensible file names in this case. Using the same example, let's load the data from the file 'K0001_synthesis_eBR_v20_q036.d13c512.ps03.k2.mC.CCM.Bgsd61.fits'.

```
>>> from pycasso.fitsdatacube import fitsQ3DataCube
>>> K = fitsQ3DataCube('K0001_synthesis_eBR_v20_q036.d13c512.ps03.k2.mC.CCM.Bgsd61.fits')
```

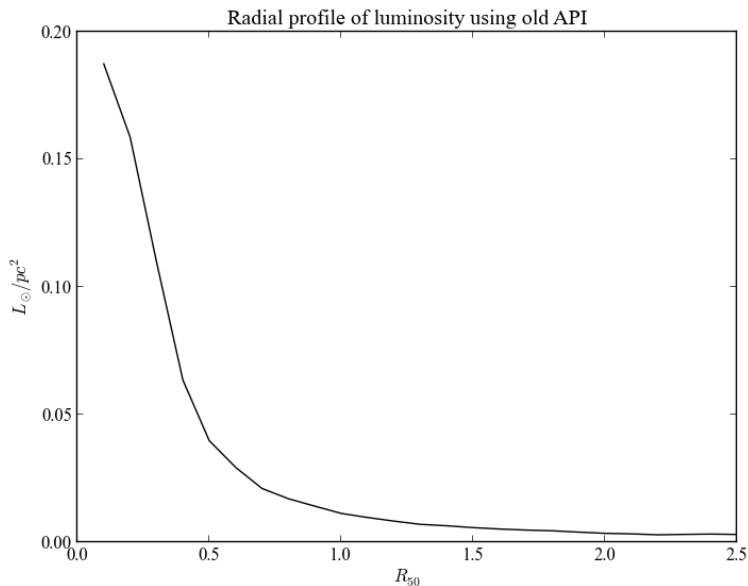
The object K is a `fitsQ3DataCube`, which quacks almost exactly like a `h5Q3DataCube` (page 49), except for the dynamic loading of data present in the HDF5 implementation. Your script should work just like before.

5.2 Using very old scripts

There were several prototype versions of PyCASSO containing features which were abandoned, or renamed, or had changes in functionality. The class `Q3DataCube` (page 26) is meant to be a backwards compatibility layer for older scripts that used these features.

The main use for the old API is to convert from zone to XY notation, and produce radial profiles using the older dialect.

```
>>> from califa.Q3DataCube import Q3DataCube
>>> K = Q3DataCube('K0001_synthesis_eBR_v20_q036.d13c512.ps03.k2.mC.CCM.Bgsd61.fits')
>>> zyx = K.getZoneToYXTensor(extensive=True, dezonification=True)
>>> LobnSD_yx = np.tensordot(K.Lobn_z, zyx, (0, 0))
>>> ryx, bin_r, bin_area = K.getYXToRadialBinsTensor(d_r=0.1, \
rad_bin_ini=0.0, rad_bin_fin=2.5)
>>> LobnSD_r = np.tensordot(LobnSD_yx, ryx, [(0, 1), (1, 2)])
>>> plt.plot(bin_r, LobnSD_r, '-k')
>>> plt.xlim(0, 2.5)
>>> plt.xlabel(r'$R_{50}$')
>>> plt.ylabel(r'$L_{\odot} / pc^2$')
>>> plt.title('Radial profile of luminosity using old API')
```



All that could be easily attained using the methods `zoneToYX()` (page 59) and `radialProfile()` (page 63) without the hassle intermediary matrices and the order of the dimensions in `tensorDot`.

5.3 Old API reference

`class califa.Q3DataCube.Q3DataCube` (*synthesisFile*, *circularProfile=True*, *runId=None*, *califald=None*, *smoothDezonification=True*)

`getZoneToYXTensor` (*extensive=True*, *dezonification=True*)

Returns a tensor to transform from zone notation to spatial notation, with shape (zone, y, x). The normalization of the pixels can take into account the area of the zones or the luminosity weight, using the following parameters:

Parameters `extensive` : boolean

A.K.A. “normalize by zone area”. Use surface density when calculating the transformation from zone to spatial coordinates.

`dezonification` : boolean

Use image at 5650AA to weight pixels in the zones. This is used only when `extensive=True`.

Returns `zoneToYX` : 3-D array

The transform tensor, shape (nZones, y, x).

See Also:

`getYXToRadialBinsTensor` (page 27), `getZoneToRadialBinsTensor` (page 27)

Examples

To transform a cube named `mycube`, with axes (age, zone), into a cube with axes (age, y, x), one can perform the operation

```
>>> K = Q3DataCube(filename)
>>> zyx = K.getZoneToYXTensor()
>>> numpy.tensordot(mycube, zyx, (1, 0))
```

where 1 is the number of the zone axis in `mycube`, and 0 is the zone axis number in `zyx`.

getYXToRadialBinsTensor (*d_r*, *rad_bin_ini*=0, *rad_bin_fin*=None, *use_HLR_units*=True, *normalize_area*=True)

Compute a tensor that transforms an array from zone binning notation to radial binning notation. Given the radial profile for this galaxy, this method calculates a tensor similar to the `zonesToYXTensor`, it transforms an image from spatial coordinates (x,y) to a radial profile.

Parameters **d_r** : float

Radial step of the rings, in units of HLR.

rad_bin_ini : float, defaults to 0.0

Initial value for rad bins, in units of HLR.

rad_bin_fin : float, defaults to infinity

Final value for rad bins, in units of HLR.

use_HLR_units : boolean

If True, use the bins in HLR units. If False, use pixels.

normalize_area : boolean

If True, divide the tensor by the bin area.

Returns **YXToRad** : array, shape (rad. bins, y, x).

The transform tensor.

bin_R : array of float

Radial bin outer edges.

bin_area : array of float

Radial bin area, in pixels.

See Also:

[getZoneToRadialBinsTensor](#) (page 27), [getZoneToYXTensor](#) (page 26)

Examples

```
>>> c = Q3DataCube(file)
>>> yxToRad, bins, unused = c.getYXToRadialBinsTensor(d_r=0.2)
```

`c.LobnSD__yx` is the luminosity surface density in each pixel. Compute the radial profile of the average luminosity surface density.

```
>>> radProf__R = np.tensordot(Lobn_tot__yx, yxToRad, [(0,1), (1,2)])
>>> plot(bins, radProf__R)
```

getZoneToRadialBinsTensor (*d_r*, *rad_bin_ini*=0, *rad_bin_fin*=None, *use_HLR_units*=True, *extensive*=True, *dezonification*=False)

Return a tensor that transforms an array from zone binning notation to radial binning notation. Given the radial profile for this galaxy, this method calculates a tensor similar to the `zonesToYXTensor`, it transforms an image from spatial coordinates (x,y) to a radial profile.

Parameters `d_r` : float

Radial step of the rings, in units of `HLR_pix`.

rad_bin_ini : float, defaults to 0.0

Initial value for rad bins, in units of `HLR_pix`.

rad_bin_fin : float, defaults to infinity

Final value for rad bins, in units of `HLR_pix`.

use_HLR_units : boolean

If True, use the bins in HLR units. If False, use pixels.

extensive : boolean

Use surface density when calculating the transformation from zone to spatial coordinates.

dezonification : boolean

Use image at 5650AA to weight pixels in the zones.

Returns `YXToRad` : array, shape (y, x, zone)

The transform tensor.

bin_R : array of float

Radial bin outer edges.

bin_area : array of float

Radial bin area, in pixels.

See Also:

`getYXToRadialBinsTensor` (page 27), `getZoneToYXTensor` (page 26)

Examples

```
>>> c = Q3DataCube(file)
>>> zoneToRad, bins, unused = c.getZoneToRadialBinsTensor(d_r=0.2)
```

`c.popx` is luminosity fraction per zone. `c.popx.shape` is (ageBase, metBase, zone). Get the flux per unit area (?) for each zone.

```
>>> Lobjn = c.popx / 100.0 * c.Lobs_norm
```

Total luminosity in each zone.

```
>>> Lobjn_tot = Lobjn.sum(axis=1).sum(axis=0)
>>> radProf = np.tensordot(Lobjn_tot, zoneToRad, (1,1))
>>> plot(bins, radProf)
```

findHLR_pix_CID()

TODO: Deprecated `findHLR_pix_CID()`. Find the half light radius using the image at 5650 Angstrom. Using radial bins of 1 pixel, calculate the cumulative sum of luminosity. The HLR is the radius where the cum. sum reaches 50% of its peak value.

Returns `HLR` : float

The half light radius, in pixels.

See Also:

`setGeometry`

Notes

This value should be close to $\frac{\text{HLR}_{\text{circular}}}{\sqrt{b/a}}$.

GALAXY PROPERTY LIST

These are most of the attributes for a galaxy. Refer to section *Full data access API* (page 49) for a complete (and very long) list.

Some properties have a suffix like `__tZyx`. This is a mnemonic to the dimensions of the property. The dimensions are as following:

- `t`: age - `N_age` (page 50)
- `Z` (capital): metallicity - `N_met` (page 50)
- `z` (small): zone - `N_zone` (page 50)
- `y`: Y-position - `N_y` (page 50)
- `x`: X-position - `N_x` (page 50)
- `l`: wavelength - `Nl_obs` (page 50)

6.1 Base

`h5Q3DataCube.ageBase`

Ages of the base.

- Units: $[Yr]$
- Shape: (N_zone)

`h5Q3DataCube.metBase`

Metallicities of the base.

- Units: dimensionless
- Shape: (N_zone)

`h5Q3DataCube.Mstars`

Fraction of the initial stellar mass for a given population that is still trapped inside stars.

- Units: dimensionless
- Shape: (N_age, N_met)

`h5Q3DataCube.fbase_norm`

TODO: Add description of cubes.

6.2 qbick planes

`h5Q3DataCube.qSignal`

Signal at wavelength WINDOWS.N.

- Units: $[erg/s/cm^2/\text{\AA}]$

- Shape: (N_y, N_x)

h5Q3DataCube.**qNoise**

TODO: Add description of cubes.

h5Q3DataCube.**qSn**

S/N at wavelength WINDOWS_N.

- Units: dimensionless

- Shape: (N_y, N_x)

h5Q3DataCube.**qSignalUnmasked**

Image at wavelength WINDOWS_N (quick, not masked).

- Units: $[erg/s/cm^2/\text{\AA}]$

- Shape: (N_y, N_x)

h5Q3DataCube.**qNoiseUnmasked**

TODO: Add description of qNoiseUnmasked.

h5Q3DataCube.**qPipeNoise**

TODO: Add description of qPipeNoise.

h5Q3DataCube.**qMask**

Boolean image mask used for data.

- Units: bool

- Shape: (N_y, N_x)

h5Q3DataCube.**qZones**

Voronoi/segmentation zones (bins).

- Units: index

- Shape: (N_y, N_x)

h5Q3DataCube.**qZonesSn**

S/N in Voronoi zones.

- Units: dimensionless

- Shape: (N_y, N_x)

h5Q3DataCube.**qZonesNoise**

Noise (RMS) in Voronoi zones.

- Units: $[erg/s/cm^2/\text{\AA}]$

- Shape: (N_y, N_x)

h5Q3DataCube.**qFlagRatio**

Ratio of flags in window at wavelength WINDOWS_N

- Units: [%]

- Shape: (N_y, N_x)

h5Q3DataCube.**qZonesSnOrig**

S/N in Voronoi zones (unresampled, beta).

- Units: dimensionless

- Shape: (N_y, N_x)

h5Q3DataCube.**qZonesNoiseOrig**

Noise (RMS) in Voronoi zones (unresampled, beta).

- Units: $[erg/s/cm^2/\overset{\circ}{A}]$
 - Shape: (N_y, N_x)
- h5Q3DataCube.**qSegmentationSn**
Voronoi program output S/N.
- Units: dimensionless
 - Shape: (N_y, N_x)
- h5Q3DataCube.**qPipeNoiseOrig**
Noise image derived from formal errors (unresampled).
- Units: $[erg/s/cm^2/\overset{\circ}{A}]$
 - Shape: (N_y, N_x)
- h5Q3DataCube.**qPipeZonesNoiseOrig**
Noise image derived from formal errors in Voronoi zones (unresampled).
- Units: $[erg/s/cm^2/\overset{\circ}{A}]$
 - Shape: (N_y, N_x)
- h5Q3DataCube.**qSpatialMask**
TODO: Add description of qSpatialMask.
- h5Q3DataCube.**qSnMask**
TODO: Add description of qSnMask.
- h5Q3DataCube.**qFilledMask**
TODO: Add description of qFilledMask.
- h5Q3DataCube.**qConvexHull**
Convex hull of data mask.
- Units: bool
 - Shape: (N_y, N_x)
- h5Q3DataCube.**qHollowPixels**
Masked (bad) pixels inside the data mask.
- Units: bool
 - Shape: (N_y, N_x)

6.3 Population

6.3.1 Zone

- h5Q3DataCube.**popx**
Light fractions for each population, in voronoi zones.
- -Units: [%]
 - Shape: (N_{age}, N_{met}, N_{zone})
- h5Q3DataCube.**popmu_ini**
Initial mass fractions for each population, in voronoi zones.
- Units: [%]
 - Shape: (N_{age}, N_{met}, N_{zone})
- h5Q3DataCube.**popmu_cor**
Current mass fractions for each population, in voronoi zones.

- Units: [%]
- Shape: (N_age, N_met, N_zone)

h5Q3DataCube.**popAV_tot**
Extinction for each population, in voronoi zones.

- Units: [mag]
- Shape: (N_age, N_met, N_zone)

h5Q3DataCube.**Lobs_norm**
Luminosity density in norm window, in voronoi zones.

- Units: [L_{\odot}/A°]
- Shape: (N_zone)

h5Q3DataCube.**Mini_tot**
Initial mass for each population, in voronoi zones.

- Units: [M_{\odot}]
- Shape: (N_zone)

h5Q3DataCube.**Mcor_tot**
Current mass for each population, in voronoi zones.

- Units: [M_{\odot}]
- Shape: (N_zone)

6.3.2 Spatially resolved

h5Q3DataCube.**popx_tZyx**
Spatially resolved light fractions for each population.

- Units: [%]
- Shape: (N_age, N_met, N_y, N_x)

h5Q3DataCube.**popmu_ini_tZyx**
Spatially resolved initial mass fractions for each population.

- Units: [%]
- Shape: (N_age, N_met, N_y, N_x)

h5Q3DataCube.**popmu_cor_tZyx**
Spatially resolved corrected mass fractions for each population.

- Units: [%]
- Shape: (N_age, N_met, N_y, N_x)

h5Q3DataCube.**popAV_tot_tZyx**
Spatially resolved extinction by dust for each population.

- Units: [mag]
- Shape: (N_age, N_met, N_y, N_x)

6.3.3 Integrated

h5Q3DataCube.**integrated_popmu_ini**
Current mass fractions for each population, in integrated spectrum.

- Units: [%]

- Shape: (N_age, N_met)

h5Q3DataCube.**integrated_popmu_cor**

Current mass fractions for each population, in integrated spectrum.

- Units: [%]

- Shape: (N_age, N_met)

h5Q3DataCube.**integrated_popAV_tot**

Extinction by dust for each population, in integrated spectrum.

- Units: [mag]

- Shape: (N_age, N_met)

6.4 Physical properties

See also [HLR_pix](#) (page 50), [HLR_pc](#) (page 50) and [q_norm](#) (page 50).

6.4.1 Zone

h5Q3DataCube.**Mini_tZz**

Initial mass of each population, in voronoi zones.

- Units: [M_{\odot}]

- Shape: (N_age, N_met, N_zone)

h5Q3DataCube.**Mcor_tZz**

Current mass of each population, in voronoi zones.

- Units: [M_{\odot}]

- Shape: (N_age, N_met, N_zone)

h5Q3DataCube.**Lobn_tZz**

Luminosity of each population in normalization window, in voronoi zones.

- Units: [L_{\odot}]

- Shape: (N_age, N_met, N_zone)

h5Q3DataCube.**DeRed_Lobn_tZz**

“Dereddened” luminosity of each population in normalization window, in voronoi zones.

- Units: [L_{\odot}]

- Shape: (N_age, N_met, N_zone)

h5Q3DataCube.**Mini_z**

Initial mass, in voronoi zones.

- Units: [M_{\odot}]

- Shape: (N_age, N_met, N_zone)

h5Q3DataCube.**Mcor_z**

Current mass, in voronoi zones.

- Units: [M_{\odot}]

- Shape: (N_age, N_met, N_zone)

h5Q3DataCube.**Lobn_z**

Luminosity in normalization window, in voronoi zones.

- Units: [L_{\odot}]

- Shape: (N_zone)

h5Q3DataCube.**DeRed_Lobn_z**

“Dereddened” luminosity in normalization window, in voronoi zones.

- Units: [L_{\odot}]

- Shape: (N_zone)

h5Q3DataCube.**A_v**

Extinction by dust, in voronoi zones.

- Units: [*mag*]

- Shape: (N_zone)

h5Q3DataCube.**v_0**

Velocity displacement, in voronoi zones.

- Units: [km/s]

- Shape: (N_zone)

h5Q3DataCube.**v_d**

Velocity dispersion, in voronoi zones.

- Units: [km/s]

- Shape: (N_zone)

6.4.2 Spatially resolved

h5Q3DataCube.**MiniSD_tZyx**

Spatially resolved initial mass surface density of each population.

- Units: [M_{\odot}/pc^2]

- Shape: (N_age, N_met, N_y, N_x)

h5Q3DataCube.**McorSD_tZyx**

Spatially resolved current mass surface density of each population.

- Units: [M_{\odot}/pc^2]

- Shape: (N_age, N_met, N_y, N_x)

h5Q3DataCube.**LobnSD_tZyx**

Spatially resolved luminosity surface density of each population in normalization window.

- Units: [L_{\odot}/pc^2]

- Shape: (N_age, N_met, N_y, N_x)

h5Q3DataCube.**DeRed_LobnSD_tZyx**

Spatially resolved “dereddened” luminosity surface density of each population in normalization window.

- Units: [L_{\odot}/pc^2]

- Shape: (N_age, N_met, N_y, N_x)

h5Q3DataCube.**MiniSD_yx**

Spatially resolved initial mass surface density.

- Units: [M_{\odot}/pc^2]

- Shape: (N_y, N_x)

h5Q3DataCube.**McorSD_yx**

Spatially resolved current mass surface density.

- Units: [M_{\odot}/pc^2]

- Shape: (N_y, N_x)
- h5Q3DataCube.**LobnSD_yx**
Luminosity surface density of each population in normalization window.
- Units: [L_{\odot}/pc^2]
 - Shape: (N_y, N_x)
- h5Q3DataCube.**DeRed_LobnSD_yx**
“Dereddened” luminosity surface density of each population in normalization window.
- Units: [L_{\odot}/pc^2]
 - Shape: (N_y, N_x)
- h5Q3DataCube.**M2L_yx**
Spatially resolved mass to light ratio.
- Units: [M_{\odot}/L_{\odot}]
 - Shape: (N_y, N_x)
- h5Q3DataCube.**DeRed_M2L_yx**
Spatially resolved “dereddened” mass to light ratio.
- Units: [M_{\odot}/L_{\odot}]
 - Shape: (N_y, N_x)
- h5Q3DataCube.**A_V_yx**
Spatially resolved extinction by dust.
- Units: [*mag*]
 - Shape: (N_y, N_x)
- h5Q3DataCube.**v_0_yx**
Spatially resolved velocity displacement.
- Units: [*km/s*]
 - Shape: (N_y, N_x)
- h5Q3DataCube.**v_d_yx**
Spatially resolved velocity dispersion.
- Units: [*km/s*]
 - Shape: (N_y, N_x)
- h5Q3DataCube.**at_flux_yx**
Spatially resolved, flux-weighted average log. age.
- Units: [*log Gyr*]
 - Shape: (N_y, N_x)
- h5Q3DataCube.**at_mass_yx**
Spatially resolved, mass-weighted average log. age.
- Units: [*log Gyr*]
 - Shape: (N_y, N_x)
- h5Q3DataCube.**az_flux_yx**
Spatially resolved, flux-weighted average metallicity.
- Units: dimensionless
 - Shape: (N_y, N_x)
- h5Q3DataCube.**az_mass_yx**
Spatially resolved, mass-weighted average metallicity.

- Units: dimensionless
- Shape: (N_y, N_x)

6.4.3 Integrated

h5Q3DataCube.**integrated_Lobn**

Luminosity in normalization window of the integrated spectrum.

- Units: [L_{\odot}]
- Type: float

h5Q3DataCube.**integrated_Lobn_tZ**

Luminosity of each population in normalization window of the integrated spectrum.

- Units: [L_{\odot}]
- Shape: (N_{age}, N_{met})

h5Q3DataCube.**integrated_DeRed_Lobn**

“Dereddened” luminosity in normalization window of the integrated spectrum.

- Units: [L_{\odot}]
- Type: float

h5Q3DataCube.**integrated_DeRed_Lobn_tZ**

“Dereddened” luminosity of each population in normalization window of the integrated spectrum.

- Units: [L_{\odot}]
- Shape: (N_{age}, N_{met})

h5Q3DataCube.**integrated_Mcor**

Current mass of the integrated spectrum.

- Units: [M_{\odot}]
- Type: float

h5Q3DataCube.**integrated_Mcor_tZ**

Current mass of each population of the integrated spectrum.

- Units: [M_{\odot}]
- Shape: (N_{age}, N_{met})

h5Q3DataCube.**integrated_Mini**

Initial mass of the integrated spectrum.

- Units: [M_{\odot}]
- Type: float

h5Q3DataCube.**integrated_Mini_tZ**

Initial mass of each population of the integrated spectrum.

- Units: [M_{\odot}]
- Shape: (N_{age}, N_{met})

h5Q3DataCube.**integrated_M2L**

Mass to light ratio of the integrated spectrum.

- Units: [M_{\odot}/L_{\odot}]
- Type: float

h5Q3DataCube.**integrated_DeRed_M2L**

“Dereddened” mass to light ratio of the integrated spectrum.

- Units: $[M_{\odot}/L_{\odot}]$

- Type: float

h5Q3DataCube.**integrated_at_flux**

Flux-weighted average log. age of the integrated spectrum.

- Units: $[\log Gyr]$

- Type: float

h5Q3DataCube.**integrated_at_mass**

Mass-weighted average log. age of the integrated spectrum.

- Units: $[\log Gyr]$

- Type: float

h5Q3DataCube.**integrated_az_flux**

Flux-weighted average metallicity of the integrated spectrum.

- Units: dimensionless

- Type: float

h5Q3DataCube.**integrated_az_mass**

Mass-weighted average metallicity of the integrated spectrum.

- Units: dimensionless

- Type: float

6.5 Spectra

6.5.1 Zone

h5Q3DataCube.**l_obs**

Wavelength array for the spectral.

- Units: $[\text{\AA}]$

- Shape: (N1_obs)

h5Q3DataCube.**f_obs**

Observed flux (input spectra for the synthesis), in voronoi zones.

- Units: $[erg/s/cm^2/\text{\AA}]$

- Shape: (N1_obs, N_zone)

h5Q3DataCube.**f_err**

Error in observed spectra, in voronoi zones.

- Units: $[erg/s/cm^2/\text{\AA}]$

- Shape: (N1_obs, N_zone)

h5Q3DataCube.**f_flag**

Flagged spaxels, in voronoi zones.

FIXME: describe flags.

- Units: dimensionless

- Shape: (N1_obs, N_zone)

h5Q3DataCube.**f_syn**

Synthetic spectra, in voronoi zones.

- Units: $[erg/s/cm^2/\text{\AA}]$
- Shape: (N1_obs, N_zone)

h5Q3DataCube.**f_wei**

Weight of the spaxels in the input spectra. This is the weight actually used by the synthesis, after clipping, etc. Values for voronoi zones.

FIXME: describe flags and weights.

- Units: dimensionless
- Shape: (N1_obs, N_zone)

6.5.2 Spatially resolved

h5Q3DataCube.**f_obs_lyx**

Spatially resolved observed flux (input spectra for the synthesis).

- Units: $[erg/s/cm^2/\text{\AA}]$
- Shape: (N1_obs, N_y, N_x)

h5Q3DataCube.**f_err_lyx**

Spatially resolved error in observed spectra.

- Units: $[erg/s/cm^2/\text{\AA}]$
- Shape: (N1_obs, N_y, N_x)

h5Q3DataCube.**f_flag_lyx**

Spatially resolved flagged spaxels.

FIXME: describe flags.

- Units: dimensionless
- Shape: (N1_obs, N_y, N_x)

h5Q3DataCube.**f_syn_lyx**

Spatially resolved synthetic spectra.

- Units: $[erg/s/cm^2/\text{\AA}]$
- Shape: (N1_obs, N_y, N_x)

h5Q3DataCube.**f_wei_lyx**

Spatially resolved weight of the spaxels in the input spectra. This is the weight actually used by the synthesis, after clipping, etc.

FIXME: describe flags and weights.

- Units: dimensionless
- Shape: (N1_obs, N_y, N_x)

6.5.3 Integrated

h5Q3DataCube.**integrated_f_obs**

Observed flux (input spectra for the synthesis), in integrated spectrum.

- Units: $[erg/s/cm^2/\text{\AA}]$
- Shape: (N1_obs)

h5Q3DataCube.**integrated_f_err**

Error in integrated observed spectrum.

- Units: [$erg/s/cm^2/\text{\AA}$]

- Shape: (N1_obs)

h5Q3DataCube.**integrated_f_flag**
Flagged spaxels, in integrated spectrum.

FIXME: describe flags.

- Units: dimensionless

- Shape: (N1_obs)

h5Q3DataCube.**integrated_f_syn**
Synthetic integrated spectrum.

- Units: [$erg/s/cm^2/\text{\AA}$]

- Shape: (N1_obs)

h5Q3DataCube.**integrated_f_wei**

Weight of the spaxels in the integrated input spectra. This is the weight actually used by the synthesis, after clipping, etc.

FIXME: describe flags and weights.

- Units: dimensionless

- Shape: (N1_obs, N_y, N_x)

6.6 Synthesis fit diagnostics

h5Q3DataCube.**adev**

Mean absolute relative deviation, in percent, only for the N1_eff points actually used in the synthesis.

- Units: [%]

- Shape: (N_zone)

h5Q3DataCube.**adevS**

From Cid @ 26/05/2012: Here's my request for pycasso reader: That it defines a new figure of merit analogous to adev, but which uses the synthetic flux in the denominator instead of the observed one. This is the adevS__z thing defined below in awful python. Why? Well, despite all our care there are still some non-flagged pixels with very low fluxes, which screws up adev, and this alternative definition fixes it.

Original code:

```
>>> adevS__z = np.zeros((self.nZones))
>>> for i_z in np.arange(self.nZones):
>>>     _a = np.abs(self.f_obs[:,i_z] - self.f_syn[:,i_z]) / self.f_syn[:,i_z]
>>>     _b = _a[self.f_wei[:,i_z] > 0]
>>>     adevS__z[i_z] = 100.0 * _b.mean()
>>> return adevS__z
```

Returns aDevS : array of length (nZones)

h5Q3DataCube.**NO1_eff**

Number of OK wavelengths in input spectrum, in voronoi zones.

- Units: dimensionless

- Shape: (N_zone)

h5Q3DataCube.**Nglobal_steps**

Number of steps in spectral fitting, in voronoi zones.

- Units: dimensionless

- Shape: (N_zone)

h5Q3DataCube.chi2

χ^2/N_{eff} of the fit, in voronoi zones.

- Units: dimensionless

- Shape: (N_zone)

Artigos publicados

D.1 Resolving galaxies in time and space. I. Applying
STARLIGHT to CALIFA datacubes

Artigo por Cid Fernandes et al. (2013) (doi : [10.1051/0004-6361/201220616](https://doi.org/10.1051/0004-6361/201220616)).
Também disponível em *preprint* (arXiv : [1304.5788](https://arxiv.org/abs/1304.5788)).

Resolving galaxies in time and space

I. Applying STARLIGHT to CALIFA datacubes

R. Cid Fernandes^{1,2}, E. Pérez¹, R. García Benito¹, R. M. González Delgado¹, A. L. de Amorim², S. F. Sánchez^{1,3},
B. Husemann⁴, J. Falcón Barroso^{5,6}, P. Sánchez-Blázquez⁷, C. J. Walcher⁴, and D. Mast^{1,3}

¹ Instituto de Astrofísica de Andalucía (CSIC), PO Box 3004, 18080 Granada, Spain
e-mail: cid@astro.ufrsc.br

² Departamento de Física, Universidade Federal de Santa Catarina, PO Box 476, 88040-900, Florianópolis, SC, Brazil

³ Centro Astronómico Hispano Alemán, Calar Alto, (CSIC-MPG), C/Jesús Durbán Remón 2-2, 04004 Almería, Spain

⁴ Leibniz-Institut für Astrophysik Potsdam, innoFSPEC Potsdam, An der Sternwarte 16, 14482 Potsdam, Germany

⁵ Instituto de Astrofísica de Canarias, Vía Lactea s/n, 38200 La Laguna, Tenerife, Spain

⁶ Departamento de Astrofísica, Universidad de La Laguna, 38205 Tenerife, Spain

⁷ Departamento de Física Teórica, Universidad Autónoma de Madrid, 28049 Madrid, Spain

Received 23 October 2012 / Accepted 16 April 2013

ABSTRACT

Aims. Fossil record methods based on spectral synthesis techniques have matured during the past decade, and their application to integrated galaxy spectra has fostered substantial advances in the understanding of galaxies and their evolution. Yet, because of the lack of spatial resolution, these studies are limited to a global view, providing no information about the internal physics of galaxies.

Methods. Motivated by the CALIFA survey, which is gathering integral field spectroscopy (IFS) over the full optical extent of 600 galaxies, we have developed an end-to-end pipeline that: (i) partitions the observed datacube into Voronoi zones in order to, when necessary and taking due account of correlated errors, increase the signal-to-noise ratio; (ii) extracts rest-framed spectra, including propagated errors and bad-pixel flags; (iii) feeds the spectra into the spectral synthesis code; (iv) packs the results for all galaxy zones into a single FITS or HDF5 file; (v) performs a series of post-processing operations, including zone-to-pixel image reconstruction and unpacking the spectral and stellar population properties derived by into multidimensional time, metallicity, and spatial coordinates. This paper provides an illustrated description of the whole pipeline and its many products. Using data for the nearby spiral NGC 2916 as a showcase, we go through each of the steps involved and present a series of ways of visualizing and analyzing this manifold. These include 2D maps of properties such as the velocity field, stellar extinction, mean ages and metallicities, mass surface densities, and star formation rates on different time scales and normalized in different ways, as well as 1D averages in the temporal and spatial dimensions, which lead to evolutionary curves and radial profiles of physical properties. Projections of the stellar light and mass growth onto radius-age diagrams are introduced as a means of visualizing galaxy evolution in time and space simultaneously, something which can also be achieved in 3D with snapshot cuts through the (x, y, t) cubes.

Results. The results vividly illustrate the richness both of the combination of IFS data with spectral synthesis and of the insights on galaxy physics provided by the variety of diagnostics and semi-empirical constraints obtained. Additionally, they give a glimpse of what is to come from CALIFA and future IFS surveys.

Key words. galaxies: general – galaxies: stellar content – galaxies: fundamental parameters

1. Introduction

Technology in the past decade has led to massive surveys either in imaging or spectroscopy modes that have been very successful in providing information of the spectral energy distribution or central/integrated spectra for a large number of galaxies (e.g., 2dF, Folkes et al. 1999; SDSS, York et al. 2000; COMBO-17, Bell et al. 2004; ALHAMBRA, Moles et al. 2008; COSMOS, Ilbert et al. 2009). These data have allowed significant insight into the integrated properties of galaxies, as well as into the evolution of global quantities such as the mass assembly (Pérez-González et al. 2008) and the star formation history (SFH) of the universe (Lilly et al. 1996; Madau et al. 1996). However, these surveys are limited in either spectral or spatial resolution. Imaging provides spatial information, but at the expense of coarse spectral coverage (typically broadband filters), limiting the amount of information on the stellar populations, and providing little or no information on the gas (emission lines)

or the kinematics of the galaxy. Surveys based on integrated spectra offer a richer list of diagnostics of the gaseous and stellar components but lack spatial resolution and suffer from aperture effects (one spectrum per object, centered at the nucleus and not covering the full galaxy). Moreover, integrated galaxy spectra do not allow, for example, the isolation of morphological components (bulge, disk, bars), the mapping of the effects of mergers, and the tracing of secular processes such as stellar migration and other features of galaxy formation and evolution, which can only be observationally tackled with a combination of imaging and spectroscopic capabilities.

The near future will see a proliferation of integral field spectroscopy (IFS) surveys, which will allow a detailed look at physics *within* galaxies, as opposed to the global view offered by integrated light surveys. The Calar Alto Legacy Integral Field Area survey (CALIFA) is a pioneer in this area (Sánchez et al. 2012), and others will follow soon, like SAMI (Croom et al. 2012), VENGA (Blanc et al. 2009), and MaNGA

(Bundy et al., in prep.). CALIFA is obtaining IFS for 600 nearby galaxies ($0.005 < z < 0.03$) of all types, mapping stellar populations, ionized gas and their kinematics across the full optical extent of the sources. The number of spectra to be generated is of the same order of the whole SDSS ($\sim 10^6$).

Clearly, however, these will not be “just another million galaxy spectra”. Processed through the machinery of fossil record methods, which recover the history of a stellar system out of the information encoded in its spectrum (Walcher et al. 2011 and references therein), CALIFA will provide valuable and hitherto unavailable information on the spatially resolved SFH of galaxies. An example of what can be done was presented by Pérez et al. (2012), where we used data on the first 105 galaxies observed by CALIFA in conjunction with the spectral synthesis code

(Cid Fernandes et al. 2005) to study the spatially resolved mass assembly history of galaxies. We find that the inner parts of massive galaxies grow faster than the outer ones, a clear signature of inside-out growth, and that the relative growth rate depends on the stellar mass of the galaxy, with a maximum relative growth efficiency for intermediate masses ($\sim 7 \times 10^{10} M_{\odot}$).

The application of spectral synthesis methods to IFS datacubes opens new ways of studying galaxies and their evolution. In practice, however, this apparently simple extension of work done for spatially integrated spectra involves a series of technical details and methodological issues, as well as challenges in the visualization and representation of the results.

The purpose of this paper is to present a detailed account of all steps in the processing of CALIFA (x, y, λ) datacubes to the multidimensional products derived from the analysis. We thus focus basically on methodology, leaving the exploration of results for subsequent studies. Paper II (Cid Fernandes et al. 2013) presents a thorough study of the uncertainties involved in these products, including the effects of random noise, spectral shape errors, and evolutionary synthesis models used in the analysis. Despite the emphasis on CALIFA and the issues discussed here and in Paper II are of direct interest to spectral synthesis analysis of IFS data in general.

The paper is organized as follows. Section 2 presents the data. Section 3 provides a detailed description of the pre-processing steps, which prepare the reduced data for a full spectral fitting analysis. Section 4 reviews the code and the ingredients used in our analysis. It also introduces the PyCASSO pipeline, used to pack and analyze the results of the synthesis. Our main results are presented in Sect. 5, which uses the nearby spiral NGC 2916 (galaxy 277 in the CALIFA mother sample) as a showcase. This long section starts with considerations on how to evaluate the quality of the spectral fits, and then proceeds to the presentation of the synthesis products in different ways, including 2D maps of the stellar light and mass, extinction, mean ages and metallicities, and star formation rate maps on different time scales; 1D maps on either the spatial or temporal dimensions, and attempts to visualize the evolution of galaxies in time and space simultaneously. The emphasis is always on methodological issues, but the examples naturally illustrate the richness of the multidimensional products of this analysis. Finally, our results are summarized in Sect. 6.

2. Data

The goals, observational strategy and overall characteristics of the survey were described in Sánchez et al. (2012). In summary, CALIFA’s mother sample comprises 939 galaxies in the 0.005–0.03 redshift range, which is extracted from the SDSS

imaging survey to span the full color–magnitude diagram down to $M_r < -18$ mag, with diameters selected to match the field of the IFU instrument ($\sim 1'$ in diameter). A thorough characterization of the sample will be presented in Walcher et al. (in prep). CALIFA will observe ~ 600 galaxies from this mother sample, applying purely visibility-based criteria at each observing night. The final sample will be representative of galaxies in the local universe, statistically significant, and well selected.

The data analyzed in this paper were reduced using the CALIFA pipeline version 1.3c, described in the Data Release 1 article (Husemann et al. 2013). Each galaxy is observed with PMAS (Roth et al. 2005, 2010) in the PPAK mode (Verheijen et al. 2004; Kelz et al. 2006) at the 3.5 m telescope of Calar Alto Observatory and with two grating setups: the V500, covering from ~ 3700 to 7500 \AA at $FWHM \sim 6 \text{ \AA}$ resolution, and the V1200 (~ 3650 – 4600 \AA , $FWHM \sim 2.3 \text{ \AA}$). The wide wavelength coverage of the V500 is ideal for our purposes, but the blue end of its spectra, which contains valuable stellar population tracers such as the 4000 \AA break and high-order Balmer lines, is affected by vignetting over a non-negligible part of the field of view. To circumvent this problem we worked with a combination of the two gratings, whereby the data for $\lambda < 4600 \text{ \AA}$ come from the V1200 (which does not suffer from this problem at this wavelength range) and the rest from the V500. The spectra were homogenized to the resolution of the V500.

For each galaxy the pipeline provides an (x, y, λ) cube with a final sampling of $(1'', 1'', 2 \text{ \AA})$. The cube comprises absolute calibrated flux densities at each spaxel ($F_{i,\lambda}$), corrected by Galactic extinction using the Schlegel et al. (1998) maps and the extinction law of Cardelli et al. (1989) law with $R_V = 3.1$. Besides fluxes, the reduced cubes contain carefully derived errors (ϵ_i) and a bad-pixel flag (b_i), which signals unreliable flux entries, due to bad columns, cosmic rays, and other artefacts (see Husemann et al. 2013, for details).

3. Pre-processing steps: from datacubes to STARLIGHT input

A series of pre-processing steps is applied to the reduced datacubes, with the general goal of extracting good quality spectra for a stellar population analysis with or any other similar code. These are:

1. definition of a spatial mask;
2. outer signal-to-noise ratio (S/N) mask;
3. refinements of the b_i (flag) and ϵ_i (error) spectra;
4. rest framing;
5. spatial binning;
6. resampling in λ .

This section describes each of these operations.

3.1. Spatial masks

The first step is to mask out foreground stars, artefacts, and low S/N regions. As a starting point, candidate spurious sources are identified applying SExtractor (Bertin & Arnouts 1996) to the SDSS r -band image. The masked image is then matched to the CALIFA field of view using the WCS information available in the headers to reproject the SDSS masks to the scale, orientation, and pixel size of the CALIFA cubes. To improve upon this first approximation, we perform a visual inspection of each galaxy, correcting its mask interactively whenever necessary. For instance, we manually fixed a few unmasked pixels that remained

in the borders of each masked object (probably due to a combination of the slightly better PSF of the SDSS images and the accuracy of the CALIFA WCS information used in the matching). Also, in a number of cases we found that the initial mask included bright H α regions, while in others very dim point-like sources can be distinguished in the SDSS image, but have no clear counterpart in the CALIFA image or spectra. In all cases, the masks were corrected by hand.

The resulting masks are free from spurious spaxels. Unlike the other operations described below, this step could not be fully automated. For the size of CALIFA, this is still a feasible, albeit laborious, task. A last step in defining the spatial mask is to impose a spectral quality threshold based on the S/N of the data. This step has been fully automated in the pipeline described next.

3.2. Flags, errors, and segmentation: the QWICK pipeline

The next steps (items ii to vi) were all packed in a fully automated package, built specifically for CALIFA but sufficiently general to handle any FITS format to pre-process databuces for a 3D spectral fitting analysis.

The b_1 flags produced by the reduction pipeline ($b_\lambda \equiv 0$ for good pixels and >0 for flagged ones) do a good job in identifying problematic pixels. For uniformity, we enforce $b_1 > 0$ around the strongest sky lines seen in the CALIFA data: HgI 4358 Å, HgI 5461 Å, OI 5577 Å, NaI D (around 5890 Å), OI-OH (6300 Å), OI 6364 Å, and the B-band atmospheric absorption (Sánchez et al. 2007). We have further set $b_1 > 0$ when the value of the error is very large (specifically, when $\epsilon_\lambda > 5F_\lambda$), but this is merely a cosmetic choice as these pixels would not influence the spectral fits anyway. Anomalously small ϵ_λ values, on the other hand, can have a disproportionately large weight on the analysis. In the very few cases where this happens, the pixels were flagged. These refinements are useful to circumvent potential problems in the spectral fitting analysis, specially when the whole data set is processed in “pipeline mode”.

After these fixes all spectra are rest-framed using the redshift derived by the reduction pipeline for the central 5” spectrum (Sánchez et al. 2012), which is included in the original headers. This step includes a $(1+z)^3$ correction for the energy, time, and bandwidth changes with redshift.

We used the (rest wavelength) window between 5590 and 5680 Å to estimate a S/N, defining the signal as the mean flux and the noise as the detrended standard deviation¹ of F_λ , both excluding flagged pixels². Regions outside the outer S/N = 5 iso-contour were added to the spatial mask and discarded from the analysis. In a few cases this threshold was lowered due to low surface brightness.

Figure 1b shows the 5635 ± 45 Å image of CALIFA 277, after the final spatial mask. The hole above the nucleus corresponds to the foreground source seen in the SDSS image (panel a). The hexagonal pattern of the fiber bundle is clearly visible since in this example S/N > 5 over most of the field of view (panel c).

The 5635 ± 45 Å image is also used to compute the galaxy’s half light radius (HLR), adding up fluxes in spaxels sorted by distance to the nucleus and picking the radius at which half of the total flux is reached. For CALIFA 277, HLR = 17.9”. This

¹ The detrended standard deviation is the rms variation with respect to a linear fit, which is useful to remove the effect of the spectral slope in the window.

² Note that this is an apparently superfluous definition since we already have the noise spectrum. This “empirical” S/N is nevertheless useful, as explained in Sect. 3.3.

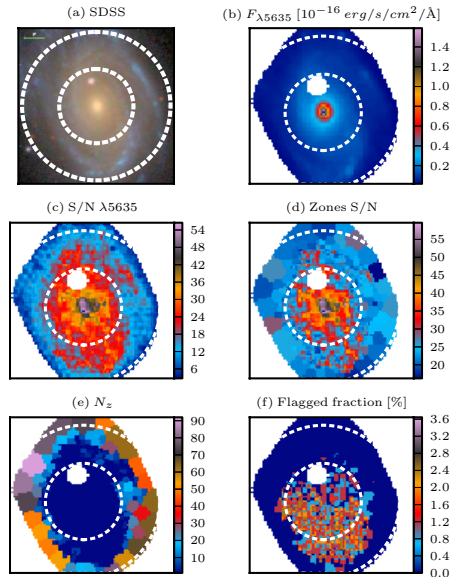


Fig. 1. a) SDSS stamp for NGC 2916 (CALIFA 277). As in other images throughout this paper, the circles mark $R = 1$ and 2 Half Light Radius (HLR). b) CALIFA image in the rest-frame 5635 ± 45 Å interval after applying the spatial mask. c) Map of the S/N at 5635 Å. d) S/N map after the Voronoi binning. e) Number of spaxels in each Voronoi zone. Note that no spatial binning ($N_z = 1$) was necessary throughout the inner ~ 1 HLR. f) Percentage of bad pixels in the 3800–6850 Å range. North is up and east is towards the left in all images.

datacube-based HLR may not be the ideal measure of the size of a galaxy, but it is the most convenient metric for the present analysis because it is based on the exact same data. In Fig. 1 and all images throughout this paper circles are drawn at $R = 1$ and 2 HLR to guide the eye.

The following step (item v in our list) consists of applying a segmentation structure to the data, grouping spaxels into spatial zones. All spaxels belonging to the same zone are assigned a common integer ID label, unique for each zone. This stores the zone-to- xy tensor needed to map zones to pixels and vice-versa. In this paper we use spatial binning to increase the S/N for the spectral analysis. Other applications may prefer to group spaxels according to, say, morphology or emission-line oriented criteria. This admits an externally provided segmentation map to allow for such choices.

The zoning scheme adopted here is based on the Voronoi tessellation technique, as implemented by Cappellari & Copin (2003), but with modifications to account for correlated errors (Sect. 3.3). The code is fed with the signal and noise images in the 5635 ± 45 Å range discussed above. The target S/N is set to 20. In practice, most individual spaxels inside 1 HLR satisfy this condition. Figure 1d shows the S/N map of CALIFA 277 after the spatial binning. For this galaxy, the 3649 non-masked spaxels were grouped into 1638 zones, the overwhelming majority (1527) of which are not binned at all. As seen in the map of the number of spaxels per zone (N_z , Fig. 1e), spatial binning

effectively starts at $R \sim 1$ HLR. Discounting the single spaxel zones, the median N_z is 10, but values up to 92 are reached in the outskirts.

Once the spatial binning map is defined, the flux, error, and flag spectra are computed for each zone. This operation must account for the flagged pixels. The total flux in zone z , which contains N_z spaxels whose fluxes are $F_{\lambda,k}$, is given by

$$F_{\lambda,z} = \frac{N_z}{\Phi_{\lambda,z}} \sum_{k=1}^{N_z} F_{\lambda,k} \phi_{\lambda,k}, \quad (1)$$

where $\phi_{\lambda,k} = 0$ for flagged pixels ($b_{\lambda,k} > 0$) or 1 otherwise ($b_{\lambda,k} = 0$), and $\Phi_{\lambda,z} \equiv \sum \phi_{\lambda,k}$ is the number of useful spaxels at wavelength λ in the zone. The zone flux is thus N_z times the average flux over all non-flagged pixels. When none of the $F_{\lambda,k}$ fluxes are flagged, this equation simply sums all the fluxes in the zone, whereas when this is not the case, flagged entries are replaced by the average of non-flagged ones.

This scaling recipe is reasonable as long as the number of flagged pixels is not comparable to N_z . For example, in a zone of $N_z = 10$ spaxels, one would not like to take the resulting $F_{\lambda,z}$ seriously if eight of them are flagged. We chose to flag away entries whenever fewer than half of the spaxels in a zone have credible data at the given λ :

$$b_{\lambda,z} = \begin{cases} 0 & \text{if } \Phi_{\lambda,z} \geq N_z/2; \\ 1 & \text{if } \Phi_{\lambda,z} < N_z/2. \end{cases} \quad (2)$$

For our example galaxy, the fraction of flagged pixels in the 3800–6850 Å interval used in the spectral synthesis analysis ranges from 5 to 8%, with a median of 6% (see Fig. 1f).

The computation of the error in $F_{\lambda,z}$ follows a recipe similar to Eq. (1), but adding in quadrature:

$$\epsilon_{\lambda,z}^2 = \beta_z^2 \frac{N_z}{\Phi_{\lambda,z}} \sum_{k=1}^{N_z} \epsilon_{\lambda,k}^2 \phi_{\lambda,k}, \quad (3)$$

where β_z accounts for correlated errors (see below).

also produces the total spatially integrated spectrum, following these same prescriptions. This is useful to compare the analysis of the whole to the sum of the analysis of the parts (which we do in Sect. 5.9).

Finally, all the spectra are resampled to 2 Å. The resulting zone spectra are stored in ASCII and/or FITS files, with flux, error, and flag columns necessary for a careful spectral analysis. All the quality control images produced in this process are packed in a single FITS file, along with the technical parameters adopted in the different steps (S/N clipping, segmentation map, etc.).

3.3. Spatial binning and correlated errors

As mentioned, the datacubes have a spatial sampling of $1'' \times 1''$. Because of the three-fold dithering pattern used in the observations, each spaxel has a varying contribution from a number of fibers. Since one fiber can contribute to more than one spaxel, the noise in a given spaxel is partially correlated with that of its neighbors. This implies that when spectra from adjacent spaxels are added together the noise in the resulting spectrum has to be calculated taking spatial covariances into account. As an extreme example, consider N_z completely correlated (i.e., ~identical) spaxels in a zone. Clearly, co-adding their spectra would not result in the desired increase in the S/N as both signal

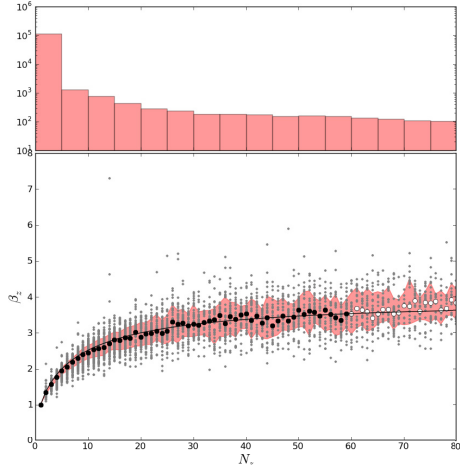


Fig. 2. Ratio of the measured over the idealized noise for Voronoi zones comprising N_z spaxels. The idealized noise is that derived under the assumption of uncorrelated errors, while the measured one is obtained from the detrended standard deviation of fluxes in a ± 45 Å range around 5635 Å. Gray dots represent β_z values for 99267 spaxels from 109 galaxies. Circles show the median β_z for each N_z , and the solid line shows Eq. (4). The top panel shows the histogram of N_z values (notice the logarithmic scale).

and noise scale linearly with N_z . Unless told otherwise, however, the zoning algorithm assumes that the spaxels are independent and hence that the noise in the zone is given by $\sqrt{\sum \epsilon_k^2}$, resulting in an improvement of the S/N of the co-added spectrum by $\sim \sqrt{N_z}$, whereas in fact it has not changed at all³.

An empirical correction was devised to account for the global behaviour of the spatial correlation of the signal in CALIFA data. We proceed by first defining initial Voronoi zones with the Cappellari & Copin (2003) algorithm. Because it assumes uncorrelated input, the code presumes the zone error is $\sqrt{\sum \epsilon_k^2}$. We then measure the “real” noise (e_z) in the resulting zone summed spectra from the (detrended) rms in the 5635 \pm 45 Å range. The ratio of these two numbers, which we call β_z , is represented versus the number of spaxels in each zone in Fig. 2. Small grey dots are β_z values for the individual zones, and circles represent the median value computed at each N_z , while the shaded region represents the 16 to 84 percentiles. There are nearly 10^5 points in this plot, obtained from 244 196 spaxels in 109 galaxies (all those observed with the V500 and V1200 setups up to May 2012). The top panel shows the histogram of N_z .

The rise and flattening of the $\beta_z - N_z$ relation reflects the expected behavior. Zones with small N_z group adjacent and highly correlated spaxels, producing the initial rise of β_z . As farther apart spaxels are aggregated, the errors become less correlated, leading to the flattening observed. The scatter in the relation is

³ ϵ_k denotes the noise in spaxel k , defined as the detrended rms in the same 5635 \pm 45 Å range used to define the signal for spatial binning purposes.

likely related to the way the Voronoi algorithm assemble spaxels. Also, the three-fold dithering pattern is not completely uniform, so the amount of correlation is not exactly the same across the face of the fiber bundle. Still, the $\beta_z(N_z)$ relation portrayed in Fig. 2 is tight enough to derive an excellent statistical correction.

The solid line represents the fit of the following function:

$$\beta_z(N_z) = \left(\frac{15N_z}{15 + N_z - 1} \right)^{1/2}, \quad (4)$$

where the fit was carried out considering only the filled circles. We can now apply this correction directly in the zoning code, replacing its idealized computation of the noise by

$$e_z = \beta_z(N_z) \sqrt{\sum_{k=1}^{N_z} \epsilon_k^2}, \quad (5)$$

which accounts for the effects of spatially correlated errors. This correction was applied λ by λ (cf. Eq. (3)). An independently derived correction very similar to Eq. (4) is presented in Husemann et al. (2013).

While this scheme naturally leads to larger zones than those obtained under the (erroneous) hypothesis of independent spaxels, it ensures that the target S/N of 20 is actually achieved in all but the outermost zones (when the algorithm runs out of spaxels to bin). Typically, we obtain 1000 zones per galaxy.

4. STARLIGHT runs and PyCASSO

is a spectral synthesis code which combines the spectra from a base in order to match an observed spectrum O_λ . The search for an optimal model M_λ and the coefficients of the population vector \mathbf{x} associated with the N_\star base elements also allows for reddening, a velocity off-set v_\star , and a stellar velocity dispersion σ_\star . The code was first introduced in Cid Fernandes et al. (2004) and substantially optimized by Cid Fernandes et al. (2005). The code, didactic introductions and a user manual are available at www.starlight.ufsc.br. We are using a new and yet to be documented version of `starlight`, but since most of the new features are not used in our analysis, the publicly available manual remains an accurate reference for the purposes of this paper.

The virtues and caveats of full spectral fits are discussed in a number of articles (e.g., Panter et al. 2003; Ocvirk et al. 2006; Cid Fernandes 2007; Tojeiro et al. 2007; McArthur et al. 2009; Sánchez-Blázquez et al. 2011). A general consensus in the field is that uncertainties in the results for individual objects average out for large statistical samples (Panter et al. 2007). With CALIFA, each galaxy is a statistical sample per se! Hence, even if the results for single spaxels (or zones) are not iron-clad, the overall trends should be robust (see Paper II for a detailed evaluation of the uncertainties in our `starlight`-based analysis of CALIFA data). It is also worth pointing out that despite the diversity of spectral synthesis methods, substantial changes in the results are more likely to come from revisions in the input data (as happened, for instance, with the recalibration of SDSS spectra between data releases 5 and 6) and from updates in the base models, the single most important ingredient in any spectral synthesis analysis.

The results reported in this paper rely on a spectral base of simple stellar populations (SSPs) comprising four metallicities, $Z = 0.2, 0.4, 1,$ and $1.5 Z_\odot$, and 39 ages between $t = 10^6$ and 1.4×10^{10} yr. This base (dubbed “GM” in Paper II) combines the Granada models of González Delgado et al. (2005) for

$t < 63$ Myr with those of Vazdekis et al. (2010; as updated by Falcón-Barroso et al. 2011) for larger ages. They are based on the Salpeter Initial Mass Function and the evolutionary tracks by Girardi et al. (2000), except for the youngest ages (≤ 3 Myr), which are based on Geneva tracks (Schaller et al. 1992; Schaerer et al. 1993a,b; Charbonnel et al. 1993). A comparison of results obtained with other bases and examples of the spectral fits are presented in Paper II.

The fits were carried out in the 3800–6850 Å interval. Reddening was modeled with the Cardelli et al. (1989) curve, with $R_V = 3.1$. As in Cid Fernandes et al. (2005), the main emission lines as well as the Na I D doublet (because of its sensitivity to ISM absorption) were masked. All runs were performed in the IAA-GRID, a network of computers which allows us to process 10^5 spectra in less than a day.

As documented in the user manual, `starlight` outputs a large array of quantities. In broad terms, these can be categorized as:

1. **Input data:** file names, configuration options, and other information provided either by the user explicitly or derived from the user-provided spectrum. Base-related data are also reported, including ages and metallicities of each component, the corresponding light-to-mass ratios (at the chosen normalization wavelength, λ_N), and a returned-mass correction factor.
2. **Fit results:** figures of merit (χ^2 , $\bar{\Delta}$), kinematic parameters (v_\star , σ_\star), the V -band extinction (A_V), total stellar masses and luminosities, and population vectors, expressed in terms of light (\mathbf{x}) and mass ($\boldsymbol{\mu}$) fractions.
3. **Spectral data:** the input (O_λ), best-model fit (M_λ), and weight spectra (w_λ , which equals ϵ_λ^{-1} , except for flagged, masked, and clipped pixels).

All these data are stored in a plain ASCII file, one for each fitted spectrum. The population vectors can be post-processed in a number of ways to obtain SFHs, compute the mass growth as a function of time, condense the results into first moments like the mean t and Z , etc. This scheme works fine for studies of independent objects, like SDSS galaxies or globular clusters.

IFS data, however, require a more structured level of organization, as it is cumbersome and inefficient to handle so many files separately. To handle datacubes we developed PyCASSO, which comprises three main parts:

1. A *writer* module, which packs the output of all fits of the individual zones of a same galaxy into a single (FITS or HDF5) file. This file also contains all information generated during the pre-processing steps (Sect. 3), as well as information propagated from the original datacube.
2. A *reader* module, which reads this file and structures all the data in an easy to access and manipulate format.
3. A *post-processing* module, which performs a series of common operations, such as mapping any property from zones to pixels, resampling and smoothing the population vectors, computing growth functions, and averaging in spatial, time or metallicity dimensions. All these functionalities are conveniently wrapped as python packages, easily imported into the user’s own analysis code.

PyCASSO will be the main workhorse behind a series of articles by our collaboration, so we dedicate the remainder of this paper to illustrating its main products.

5. Results

The Sb galaxy NGC 2916 (CALIFA 277) was chosen as a showcase. For the adopted distance of 56 Mpc, $1''$ (=1 CALIFA spaxel) corresponds to 270 pc. With an r -band absolute magnitude of -21.17 , $u-r = 2.18$ and $g-r = 0.54$ colors, and concentration index $C = 2.16$, NGC 2916 can be characterized as a blue-disk galaxy with an intermediate mass ($\sim 10^{11} M_{\odot}$). Rudnick et al. (2000) have shown that the galaxy presents some degree of lopsidedness, indicating a weak interaction (possibly with its irregular satellite $5'$ away, Gutiérrez et al. 2002) or a minor merger. Moorthy & Holtzman (2006) have obtained long-slit spectra and measured emission lines and Lick indices along the position angle $PA = -80^{\circ}$. They found that the nuclear spectrum is well within the AGN wing of the $[O \text{ III}]/H\beta$ vs. $[N \text{ I}]/H\alpha$ diagram, in a location close to what is now accepted as borderline between Seyfert and LINERs (Kewley et al. 2006).

Our Voronoi binning of the CALIFA datacube produces $N = 1638$ zones. The corresponding $N + 1$ spectra (the +1 corresponding to the spatially integrated spectrum) were fitted with PyCASSO and the results feed into PyCASSO . The following subsections describe how we handled the data and the products of the analysis.

5.1. Fit quality assessment

As with 1D spectra, the quality of the spectral fits should be examined before proceeding to interpretation of the results. This subsection describes some standard methods to do this, the caveats involved and strategies to circumvent them.

Figure 3a shows the map of the fit quality indicator

$$\bar{\Delta} = \frac{1}{N_{\lambda}^{\text{eff}}} \sum_{\lambda} \frac{|O_{\lambda} - M_{\lambda}|}{M_{\lambda}}, \quad (6)$$

where O_{λ} and M_{λ} are the observed and model spectra, respectively, and the sum is carried over the N_{λ}^{eff} wavelengths actually used in the fit, i.e., discarding masked, flagged, and clipped pixels⁴. For this galaxy $\bar{\Delta}$ spans the range between 1.0 and 5.6%, with a median value of 3.0%. It increases towards the outer regions, where the S/N is smaller (Fig. 1c). The $\chi^2 = \sum w_{\lambda}^2 (O_{\lambda} - M_{\lambda})^2$ map (Fig. 3b) shows the opposite behavior, since the errors also increase outwards. Because of its non-explicit reliance on the (often hard to compute, if not altogether unavailable) ϵ_{λ} spectrum, and because of its easily grasped meaning, $\bar{\Delta}$ is a more useful figure of merit to assess fit quality.

Inspection of the highest $\bar{\Delta}$ spectra often reveals non-masked emission lines or artifacts, like imperfect masking of foreground sources, slightly misplaced b_{λ} flags, or O_{λ} values that should have been clipped by m_{λ} but were not because of large ϵ_{λ} . We emphasize that such bugs are very rare in CALIFA. The median $\bar{\Delta}$ for the $\sim 10^5$ zone spectra analyzed so far is just 4% (corresponding to an equivalent S/N of 25), and in less than 2% of the cases $\bar{\Delta}$ exceeds 10%. This high rate of success is mainly due to the carefully derived errors and flags in the reduction pipeline and further refined in our pre-processing steps (Sect. 3).

⁴ We note that Eq. (6) is nearly, but not exactly, identical to what is called “adev” in PyCASSO ’s output, the difference being the use of M_{λ} instead of O_{λ} in the denominator. This avoids faulty (but not flagged) O_{λ} entries with very low flux affecting the statistics. This rarely occurs in CALIFA, and when it does the pixels invariably have large errors and so are irrelevant for the fit. They can, however, affect the value of $\bar{\Delta}$.

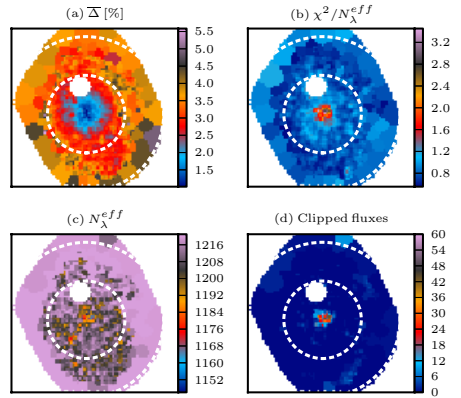


Fig. 3. Maps of spectral-fit quality indicators. **a)** Mean relative deviation $\bar{\Delta}$; **b)** χ^2 per fitted flux; **c)** number of fluxes used in the fit; and **d)** number of clipped fluxes.

One can use such maps to define spatial masks over which the spectral fits satisfy some quality threshold. Experiments with the whole data set suggest that a reasonable quality-control limit should be in the $\bar{\Delta} = 8$ to 10% range. Not surprisingly, the large residuals tend to be located in the outer regions of the galaxies. Generally speaking, results beyond 2–3 HLR should be interpreted with greater care. No $\bar{\Delta}$ -based cut is needed for our example galaxy. For the benefit of PyCASSO users, it is nevertheless worth making some further remarks on quality control.

5.1.1. Subtleties and caveats on quality control

In full spectral fitting methods, seemingly trivial operations like imposing a fit quality threshold often hide subtleties that can easily go unnoticed, particularly when processing tons of data. The paragraphs below (focused on PyCASSO but extensible to other codes) review some of these.

First, one should distinguish cases where $\bar{\Delta}$ is large because of bad data from those where large residuals arise because of the user’s failure to properly inform, through spectral masks (m_{λ}) or flags (b_{λ}), spectral regions that should be ignored in the fit. For instance, one can have an excellent spectrum of an HII region with several strong emission lines besides those included in a generic emission line mask feed into PyCASSO , causing an artificially large $\bar{\Delta}$. Large velocity offsets can have a similar effect, as emission lines get shifted out of fixed m_{λ} windows. Similarly, sky residuals and other artefacts missed out by the b_{λ} flags lead to large $\bar{\Delta}$, even when the overall spectrum is good. In short, not everything that fails a blind quality control is actually bad.

The clipping options implemented in PyCASSO help spot pixels that are too hard to fit and thus probably represent non-stellar or spurious features. Our fits use the “NSIGMA” clipping method and a conservative 4σ threshold, meaning that we only clip pixels when $|O_{\lambda} - M_{\lambda}| > 4\epsilon_{\lambda}$. Figure 3c maps the number of clipped points in CALIFA 277. One sees a peak in the central pixels, where the S/N is so high that our 4σ clipping does not forgive even small $O_{\lambda} - M_{\lambda}$ deviations (most often associated

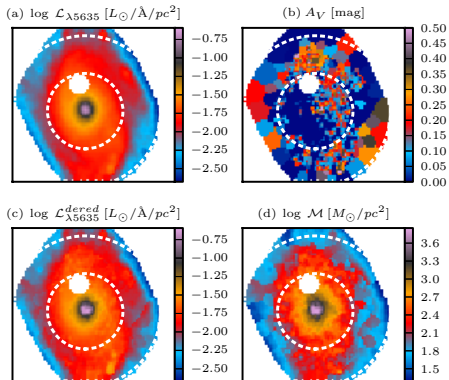


Fig. 4. a) Synthetic surface brightness at 5635 Å; b) stellar extinction map (A_V); c) dereddened \mathcal{L}_{5635} image; d) stellar mass surface density.

with problems with the base models rather than with the data). Elsewhere, very few pixels were clipped. The point to highlight here is that clipping only worked because we have a reliable ϵ_1 . Other clipping methods can be used when this is not the case, but in all cases the user should always carefully check the output, as it may easily happen that too many points are clipped.

Custom-made spectral masks also help. For instance, since Mateus et al. (2006), the analysis of SDSS spectra employs individual masks constructed by searching for emission lines in the $O_1 - M_1$ residual spectrum obtained from a first fit, and taking into consideration the local noise level. O_1 is then refitted with this tailor-made m_1 , circumventing some of the issues above. This refinement has not yet been implemented for CALIFA.

Errors, flags, and masks are, of course, secondary actors in any spectral synthesis analysis, but these general remarks illustrate that it is worthwhile to pay attention to them.

5.2. 2D maps: stellar light, mass, and extinction

One of the main products of spectral synthesis is to convert light to mass. Figure 4 illustrates the results for CALIFA 277. Its top-left panel shows the surface density of the luminosity at $\lambda_N = 5635$ Å, while the top-right panel shows the derived extinction map. The dust corrected image and the mass surface density are also shown.

While the effects of the Voronoi binning are present in all panels, they are much more salient in the A_V map. This is because the light and mass images were “dezonified” by scaling the value at each xy spaxel by its fractional contribution to the total flux in a zone (z). For instance, for the mass surface density (\mathcal{M}) this operation reads

$$\mathcal{M}_{xy} = \frac{M_{xy}}{A_{xy}} = \frac{M_z}{A_z} \times w_{xyz}, \quad (7)$$

where A_{xy} (A_z) denotes the area in a spaxel (zone), and

$$w_{xyz} = \frac{F_{xy}}{\sum_{xyz} F_{xy}}, \quad (8)$$

with F_{xy} as the mean flux in the 5635 ± 45 Å region, the same used in the Voronoi zoning (Sect. 3). This operation was applied

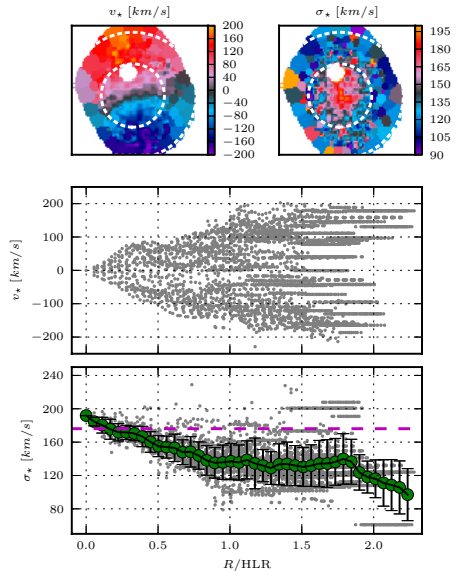


Fig. 5. Kinematical products of the spectral fitting. The σ_* values are *not* corrected for instrumental broadening, which dominates below 140 km s^{-1} . The horizontal stripes in the position-velocity and $\sigma_*(R)$ panels correspond to Voronoi zones.

to luminosity and mass related quantities, producing somewhat smoother images than obtained with $w_{xyz} = 1$. Intensive properties (like A_V , mean ages, σ_*), however, cannot be dezonified.

The stellar extinction map shows low values of A_V (of order 0.1–0.2 mag), with slight enhancements in the nuclear region and the arms. Overall, however, there is relatively little variation across the face of the galaxy (see also Fig. 10). The light and mass images have a similar structure, both showing the bulge at $R \lesssim 0.5$ HLR, and the disk beyond that. The spiral arms are less prominent in terms of mass than in light because of the higher L/M of stars in the arms.

The total stellar mass obtained from the sum of the zone masses is $M = 6.5 \times 10^{10} M_\odot$. This is the mass locked in stars nowadays. Counting also the mass returned by stars to the interstellar medium, $M' = 9.0 \times 10^{10} M_\odot$ were involved in star formation. These values ignore the mass in the masked region around the foreground star northeast of the nucleus. PyCASSO can fill in such holes with values estimated from (circular or elliptical) radial profiles. For CALIFA 277, this correction increases the masses quote above by 4%.

5.3. 2D maps: kinematics

Figure 5 shows the v_* and σ_* fields estimated by , as well as a position-velocity diagram and a radially averaged σ_* profile. The v_* field indicates a projected rotation velocity of $\sim 200 \text{ km s}^{-1}$. The V500 resolution prevents the determination of σ_* values below $\sim 150 \text{ km s}^{-1}$, and the flat $\sigma_*(R)$ profile beyond ~ 0.7 HLR reflects this resolution limit (we have not corrected the values for the instrumental resolution in this plot).

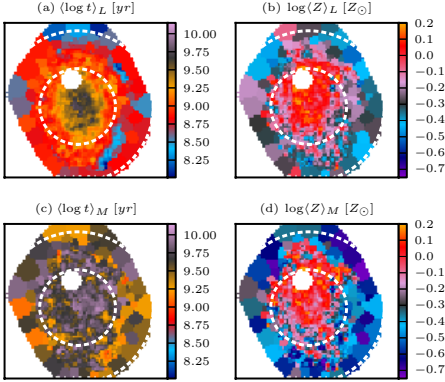


Fig. 6. Luminosity (top) and mass (bottom) weighted mean age (left) and metallicity (right) maps for CALIFA 277.

Only in the inner regions are the σ_* values reliable, reaching 200 km s^{-1} in the nucleus (equivalent to 140 km s^{-1} after correcting for instrumental broadening).

The kinematical information derived from our analysis will be superseded by studies based on the higher spectral resolution V1200 datacubes (Falcón-Barroso et al., in prep.). Eventually, one can envisage feeding the parameters derived from these more precise analyses back into the fits (using its fixed-kinematics mode). In fact, this feedback may well turn out to improve our stellar population analysis, given the potential degeneracy between σ_* and Z (decreasing the former while increasing the latter has the same global effect of making metal lines deeper; Koleva et al. 2009; Sánchez-Blázquez et al. 2011).

5.4. 2D maps: mean ages and metallicities

The crudest way to quantify the SFH of a system is to compress the age and metallicity distributions encoded in the population vectors to their first moments. For this purpose we will use the following definitions:

$$\langle \log t \rangle_L = \sum_{i,Z} x_{iZ} \log t \quad (9)$$

$$\langle Z \rangle_L = \sum_{i,Z} x_{iZ} Z, \quad (10)$$

where x_{iZ} is the fraction of light at λ_N due to the base population with age t and metallicity Z . The mass-weighted versions of these indicators, $\langle \log t \rangle_M$ and $\langle Z \rangle_M$, are obtained by replacing x_{iZ} by the mass fraction μ_{iZ} .

Figure 6 shows the light and mass-weighted mean (\log) age and metallicity maps. The $\langle \log t \rangle_L$ image shows a steady increase towards the center. Outside 1 HLR, traces of the spiral arms are noticeable as regions of lower age (as in the SDSS color image in Fig. 1a, the arms are brighter in the western half of the image). Because of the large weight of old populations, $\langle \log t \rangle_M$ spans a smaller dynamical range than $\langle \log t \rangle_L$, hence producing lower contrast maps, but the outwardly decreasing age is still visible. Negative gradients are also clearly present in metallicity, with indications of flattening within the bulge region. As in

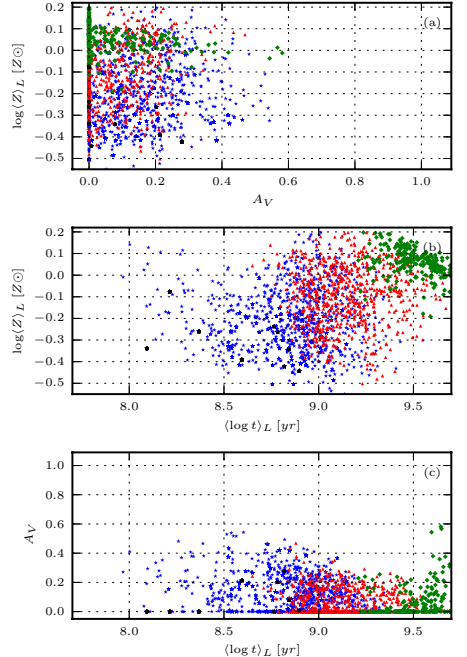


Fig. 7. Mean age versus mean metallicity versus extinction, coding zones by their distance to the nucleus. Green diamonds: $R < 0.5$ HLR. Red triangles: $0.5\text{--}1$ HLR. Blue stars: $1\text{--}2$ HLR. Black dots: > 2 HLR.

other 2D maps, the small-scale fluctuations towards the edges are at least in part due to the lower S/N.

The fact that t and Z grow in the same sense suggests that the results are not badly affected by the age-metallicity degeneracy. As shown by Sánchez-Blázquez et al. (2011), full spectral synthesis is much less sensitive to this than conventional index-based approaches. Figure 7 plots extinction versus mean age versus metallicity, the main properties involved in spectral synthesis. Points are color- and symbol-coded by their distance from the nucleus. One sees that the highest values of A_V are found for old central ($R < 0.5$ HLR) and young outer ($R > 1$ HLR) populations and that A_V bears no correlation with Z . The middle panel shows the positive $t\text{--}Z$ relation inferred from the 2D maps. Within 0.5 HLR (green diamonds), however, t anticorrelates with Z , most likely due to the age-metallicity degeneracy. The mean Z values in this central region straddle 1 and $1.5 Z_\odot$, the two highest metallicities in our base.

5.5. 2D maps: x_Y , x_I , x_O

Population synthesis studies in the past found that a useful way to summarize the SFH is to condense the age distribution encoded in the population vector into age ranges. This strategy comes from a time when the analysis was based on equivalent widths and colors (Bica 1988; Bica et al. 1994; Cid Fernandes et al. 2001, 2003), but it was also applied to full spectral fits (Gonzalez Delgado et al. 2004).

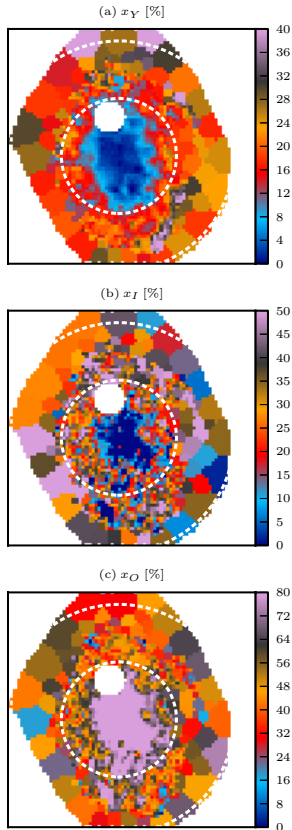


Fig. 8. Maps of the percentage contribution of young ($t < 0.14$ Gyr), intermediate age ($0.14 - 1.4$ Gyr), and old (> 1.4 Gyr) stars to the observed light at 5635 \AA .

Figure 8 presents images of the light fraction due to young, intermediate and old populations (x_Y , x_I , and x_O), defined as those with $t \leq 0.14$, $0.14 < t \leq 1.4$, and $t > 1.4$ Gyr, respectively. As usual, the choice of borderlines is somewhat subjective, constrained only by the underlying idea of grouping base elements covering relatively wide age ranges. For the base used in our runs, the Y, I, and O bins contain 4×20 , 4×10 , and 4×9 SSPs, respectively (where the $4 \times$ comes from the four metallicities).

The plots show that the spiral arms stand out more clearly in the x_Y map, specially in the western half of the galaxy, as also seen in the SDSS color composite (Fig. 1a). Very little of the light from $R < 1$ HLR comes from young stars. Intermediate age populations do contribute more, but the central ~ 0.5 HLR is completely dominated by old stars. Overall, however, despite the added informational content, these maps do not visibly add much to the $(\log t)_L$ image (Fig. 6).

5.6. 2D maps: Star formation rates and IFS-based variations over Scalo's b parameter

The base used in our fits comprises instantaneous bursts (i.e., SSPs). Thus, despite the large number of ages considered, our SFHs are not continuous and hence not derivable. Nonetheless, there are ways of defining star formation rates (SFR).

The simplest way to estimate a SFR is to cumulate all the stellar mass formed since a lookback time of t_{SF} and perform a mass-over-time average:

$$\overline{\text{SFR}}_{xy}(t_{\text{SF}}) = \frac{1}{t_{\text{SF}}} \sum_{t < t_{\text{SF}}} \mathcal{M}'_{txy}, \quad (11)$$

where \mathcal{M}'_{txy} is the mass (at xy and per unit area) of stars formed at lookback time t ⁵. Equation (11) gives the *mean* SFR surface density since $t = t_{\text{SF}}$. One can tune t_{SF} to reach different depths in the past, but as t_{SF} increases this estimator becomes increasingly useless, converging to the mass density divided by $t_{\infty} \equiv 14$ Gyr (the largest age in the base).

It is often more useful to consider SFRs in relation to some fiducial value instead of absolute units. The classical example is Scalo's birthrate parameter, b , which measures the SFR in the recent past ($t < t_{\text{SF}}$) with respect to its average over the whole lifetime of the system⁶. This is trivially obtained dividing $\overline{\text{SFR}}_{xy}(t_{\text{SF}})$ by its asymptotic value

$$b_{xy}^{\text{loc}}(t_{\text{SF}}) = \frac{\overline{\text{SFR}}_{xy}(t_{\text{SF}})}{\overline{\text{SFR}}_{xy}(t_{\infty})} = \frac{t_{\infty} \sum_{t < t_{\text{SF}}} \mathcal{M}'_{txy}}{t_{\text{SF}} \mathcal{M}'_{txy}}. \quad (12)$$

The superscript “loc” is to emphasize that the reference lifetime average SFR is that of the same spatial location xy . One should recall that while young stars in a spaxel were probably born there (or near it), old ones may have migrated from different regions. Thus, despite the identical definitions, the physical meaning of b_{xy}^{loc} is not really the same as for galaxies as a whole.

The IFS data allow for other definitions of b . For instance, one might prefer to compare $\overline{\text{SFR}}_{xy}(t_{\text{SF}})$ to the $\overline{\text{SFR}}(t_{\infty})$ of the galaxy as a whole, the bulge, the disk, or any general region. This variation measures the “present” ($t < t_{\text{SF}}$) “here” (at xy) to the “past” ($t \leq t_{\infty}$) in a spatial region \mathcal{R} :

$$b_{xy}^{\mathcal{R}}(t_{\text{SF}}) = \frac{\overline{\text{SFR}}_{xy}(t_{\text{SF}})}{\overline{\text{SFR}}_{\mathcal{R}}(t_{\infty})}. \quad (13)$$

A formally similar but conceptually different definition is obtained using for the reference value in the denominator the SFR surface density within the *same time-scale* but evaluated in a *different region*:

$$c_{xy}^{\mathcal{R}}(t_{\text{SF}}) = \frac{\overline{\text{SFR}}_{xy}(t_{\text{SF}})}{\overline{\text{SFR}}_{\mathcal{R}}(t_{\text{SF}})}, \quad (14)$$

i.e., to compare not “now versus then” but “now here versus now there”. Together with Eqs. (12) and (13), this definition covers

⁵ The stellar mass in this equation differs from that in Eq. (7), Fig. 4, and the definitions of $(\log t)_M$ and $\langle Z \rangle_M$. The latter are corrected by the mass returned to the medium by stars during their evolution (thus reflecting the mass currently in stars), while in the computation of SFRs this correction should not be applied. We distinguish the two types of stellar masses with the prime superscript (M versus M').

⁶ A related index is the so-called specific SFR, which differs from b just by the t_{∞} factor in Eq. (12).

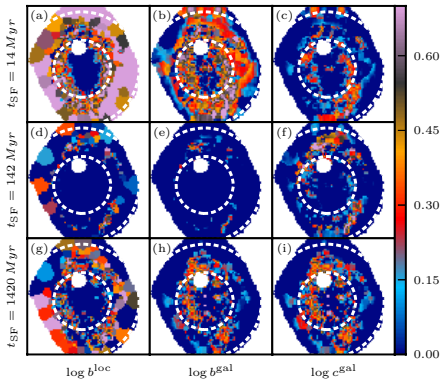


Fig. 9. Spatially resolved SFR surface density (Eq. (11)) on the last $t_{\text{SF}} = 14$ (top), 142 (middle), and 1420 (bottom) Myr in units of different reference values. The left panels compare $\overline{\text{SFR}}_{xy}(t_{\text{SF}})$ to $\overline{\text{SFR}}_{xy}(t_{\infty})$, i.e., the all-times average at xy , thus providing a local version of Scalo’s b parameter (Eq. (12)). Middle panels compare the local $\overline{\text{SFR}}$ to the all-times average over the whole galaxy (Eq. (13)). Panels on the right compare $\overline{\text{SFR}}$ to that of the galaxy as a whole over the same time scale (Eq. (14)). All images are on log scale from $\log 1$ to $\log 5$, such that only $\overline{\text{SFR}}_{xy}(t_{\text{SF}})$ values above the corresponding reference value are visible.

the different combinations of time and space enabled by the application of fossil methods to IFS data.

Figure 9 shows maps of b^{loc} (left panels), b^{R} (middle panels), and c^{R} (right panels) for three values of t_{SF} : 14 (top), 142 (middle), and 1420 Myr (bottom). In all panels the color scale is deliberately saturated to highlight regions where $\overline{\text{SFR}}(t_{\text{SF}})$ is larger than the chosen reference value; the dynamical range of the images goes from 1 to 5 (0 to 0.7 in log) in the corresponding relative units.

Panel a shows that spaxels that have formed stars over the past 14 Myr at a larger rate than their respective past average are all located in the outer regions. Nowhere within $R \leq 0.5$ HLR does one find $b^{\text{loc}}(14 \text{ Myr}) > 1$. Considering the past 142 Myr (panel d), the inner “deficit” covers as much as 1.2 HLR. On the longest time scale considered (g), one again sees that the inner spaxels have been less active than their lifelong average.

Maps look considerably different in the middle column of panels, where the local $\overline{\text{SFR}}$ is normalized to the past average over the whole galaxy (Eq. (13)). The spiral arms of CALIFA 277 appear better delineated in $b^{\text{gal}}(14 \text{ Myr})$ (panel b) than in any b^{loc} map. Interestingly, the b^{gal} map is practically featureless for $t_{\text{SF}} = 142 \text{ Myr}$ (e). This suggests that starformation is not continuous over this time scale but instead happens in a bursty mode. Over the past 1.4 Gyr (h), one again sees traces of the arms but with a lower amplitude than in panel b, which is qualitatively consistent with the cumulative effect of an intermittent sequence of short-duration bursts. (Due to the logarithmic age resolution of fossil methods, such short bursts can only be recognized as such at the very young ages sampled in panel b.)

The right column panels show our novel relative SFR index c (Eq. (14)), using the whole galaxy as reference region. Unlike Scalo’s b , this index does not compare present to past, but present to present elsewhere. Its 2D maps can be understood as “snapshots” of the SFR in the galaxy taken with an

“exposure time” t_{SF} . Keeping the “diaphragm” open for only the last 14 Myr (panel c) highlights the ongoing starformation in the galaxy. The spiral arms are clearly visible, and the structures are more focused than in the $b^{\text{gal}}(14 \text{ Myr})$ map (panel b). Integrating for 142 Myr (f), the inner parts of the arms fade, but their outer ($R > 1$ HLR) parts brighten up in terms of c^{gal} . Over the past 142 Myr, these regions have formed more stars than anywhere else in the galaxy, even though a comparison with panel e shows that only parts of the $c^{\text{gal}} > 1$ regions are forming stars at a rate per unit area larger than that of the galaxy as a whole through its entire life (i.e., $b^{\text{gal}} > 1$). For $t_{\text{SF}} = 1.4 \text{ Gyr}$ (panel i) the image becomes more blurred. Because of the long time scale, the $c^{\text{gal}}(1.4 \text{ Gyr})$ map is nearly indistinguishable from that obtained with b^{gal} for the same t_{SF} (panel h).

One thus sees that, despite some degree of redundancy (the numerator is always the same), these definitions offer different and complementary views of star formation in a galaxy.

5.7. 1D spatial maps: radial profiles

The information contained in 2D maps like the ones shown above can sometimes be hard to absorb. Azimuthal averaging is a useful way to compress and help digest 2D data. PyCASSO provides both circular and elliptical xy -to- R conversion tensors. The examples below are based on a circular mapping.

For quantities like \mathcal{M} , one can think of two types of radial averaging. The first is to add up all the stellar mass in xy spaxels within a given R -bin and then divide by the bin area (counting only non-empty spaxels). The second is to average the surface density values for each spaxel directly. The same applies to, for instance, $(\log t)_L$ (Eq. (9)): one can either add up the value of product $L_{xy} \times \log t$ for all spaxels at a given R and then divide by the corresponding $\sum L_{xy}$ or else simply average the $(\log t)_L$ values for each spaxel in the R -bin. The first method, which we call *area averaging*, effectively collapses the galaxy to 1D, but this kind of averaging cannot be applied to quantities which do not involve light or mass, like A_V and σ_* . For the sake of uniformity, in this subsection we chose the second type of radial averaging (henceforth *spaxel averaging*), noting that the two methods almost always give nearly identical results.

Figure 10 shows several PyCASSO products as a function of R . The grey points represent values for individual spaxels. The solid line and green circles show the mean value of the plotted quantity among the spaxels in the same R bin, and the error bars map the corresponding dispersion. (As discussed in Paper II, actual error bars in radial profiles are much smaller due to the large number statistics.) Several of the features discussed while describing the 2D images are clearly seen in these plots. The $(\log t)$ and $\langle Z \rangle$ gradients, in particular, are clearly depicted in these plots. As pointed out in Sect. 5.4, mean ages and metallicities increase ~simultaneously towards the nucleus, while A_V does not change much. This indicates that the classical degeneracies in stellar population studies do not play a strong role in shaping the results, with the possible exception of the central regions. As in Fig. 5, horizontal stripes of grey points in panels c, e, f, g, and h of Fig. 10 correspond to spaxels in the same Voronoi zones. The stripes disappear in panels a, b, and d because these extensive quantities were “dezonified” (cf. Eq. (7)).

5.8. 1D temporal maps: evolutionary curves

The main power of fossil record methods is to open the time domain, allowing evolutionary studies. The caveat is that it

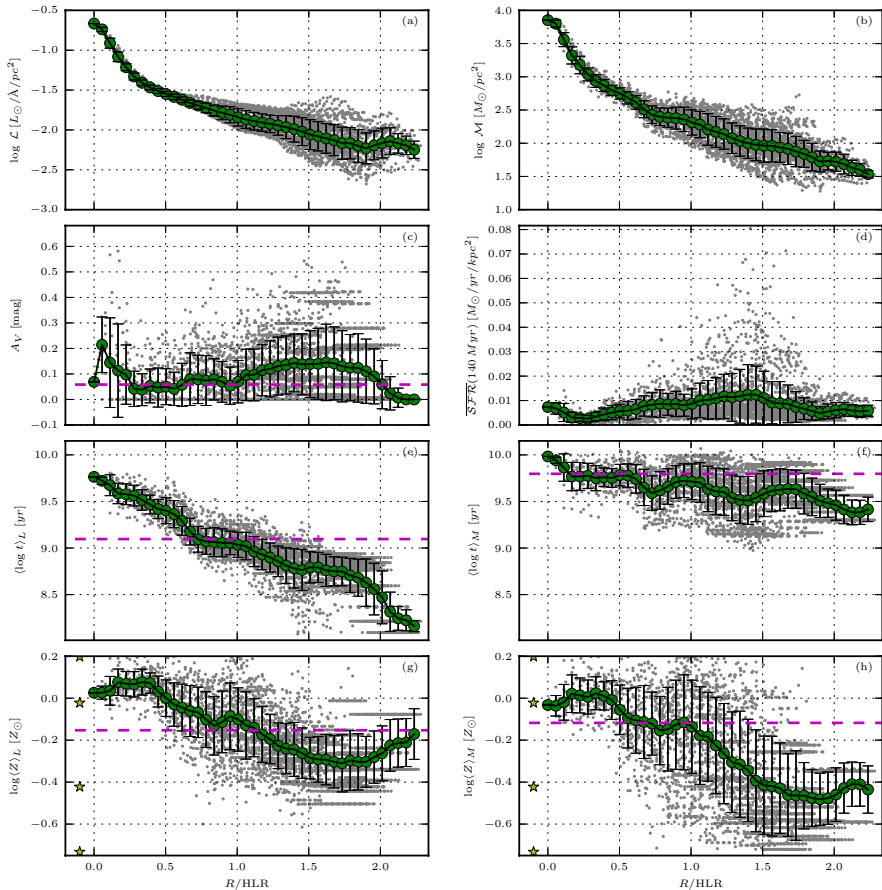


Fig. 10. Radial profiles of several properties. Grey points correspond to values in individual xy spaxels. The green circles and solid lines represent the average of the plotted quantity, while the error bars represent the dispersion in the R -bin. The dashed magenta horizontal line (only in the plots not involving surface densities) marks the value derived from the analysis of the integrated spectrum, i.e., collapsing the xy dimensions of the databube. The stars in the *bottom panels* mark the four metallicities in the base models.

does this with the typical logarithmic resolution inherent to stellar evolution, but several studies show that much can be learned about galaxy evolution despite this fundamental constraint. Because our 39 ages base is highly overdimensioned, some sort of SFH compression is necessary. As discussed by Asari et al. (2007), age resolutions between 0.5 and 1 dex are reasonable. We thus smooth the light and mass population vectors with a Gaussian of $FWHM = 0.5$ dex in $\log t$.

Figure 11 plots a number of our synthesis products against age. To keep an at least partial representation of the spatial information, we plot evolutionary curves derived for different radial regions: the nucleus, defined as the central pixel (plotted in grey dashed lines), $R \leq 0.5$ (dashed green), ≤ 1 (solid red), and > 1 HLR (solid blue).

The top panels show the growth of luminosity (Fig. 11a) and mass (b)⁷. Among other things, this plot illustrates the difference between light and mass, in the sense that regions inside and outside $R = 1$ HLR do not have the same mass, despite having (by definition) the same light. While $HLR = 4.8$ kpc, the radius containing half of the mass is 3.4 kpc. This is a direct consequence of the stellar population gradients in this galaxy. González Delgado et al. (in prep.) investigate the relation between light- and mass-based radii for different types of galaxies.

It is also seen that both light and mass grow at *different speeds for different regions*. This is better appreciated in panels c

⁷ For clarity, the cumulative mass is computed with the total mass that has participated in star formation, instead of the one corrected for returned mass. In other words, we cumulate M' instead of M .

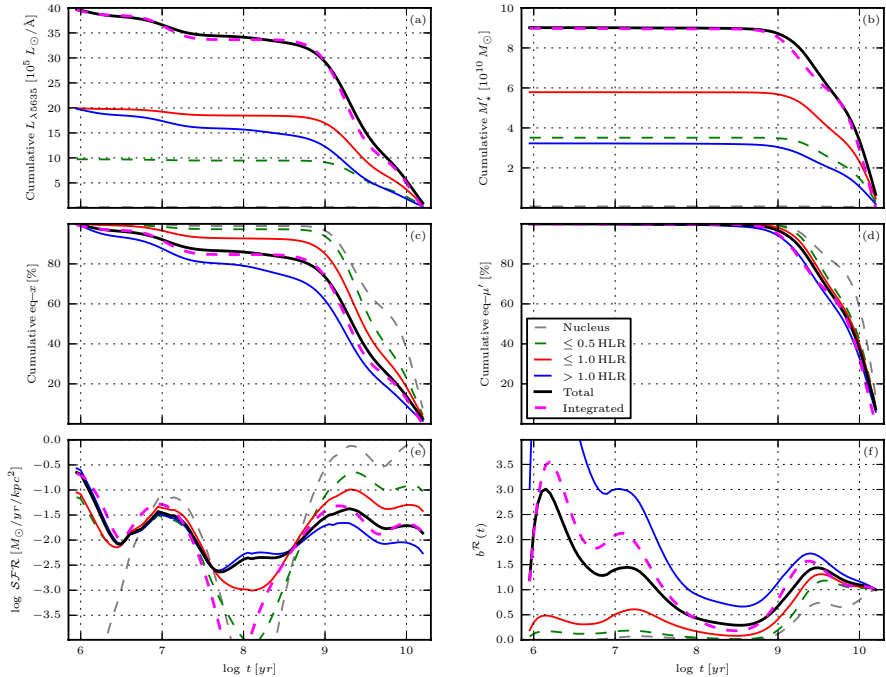


Fig. 11. Time evolution of light and mass representations of the SFH, as derived from the fits. The discrete $x_{i,Z_{\text{HI}}}$ and $\mu'_{i,Z_{\text{HI}}}$ population vectors involved in these curves were smoothed in $\log t$, marginalized in Z , and integrated over the spatial regions indicated. Dotted grey lines indicate the nucleus (central pixel). Green, red, and blue lines correspond to $R \leq 0.5$ HLR, $R \leq 1$ HLR, and $R > 1$ HLR regions, respectively. The black line represents the whole galaxy evolution as reconstructed from the sum of its parts, while (as in Fig. 10) the magenta dashed line is used to represent the results obtained for the spatially integrated spectrum.

and d, where each growth curve is plotted on a 0 to 1 scale, with 1 representing the present values (which tantamounts to cumulating the equivalent x_i and μ'_i vectors for each region). The nucleus reached 80% of its mass at $t = 8.5$ Gyr, while the $R > 1$ HLR region did so later, at $t = 1.9$ Gyr. As shown by Pérez et al. (2013), this inside-out ordering of the mass assembly history applies to essentially all massive galaxies.

Figure 11e shows $SFR(t)$. The SFR per unit area decreases from the nucleus outwards most of the time, but the trend is reversed in the last ~ 50 Myr. Notice that, because of the smoothing, $SFR(t)$ is now a continuous function of time, so that this panel represents the *instantaneous* SFR, as opposed to the mass-over-time definition in Eq. (11). Figure 11f shows Scalos's b parameter for each region, which does use the running mean $\overline{SFR}(t)$ of Eq. (11). This plot helps interpret Fig. 9, which opens up the radial regions into full 2D maps but compresses the time axis by stipulating fixed t_{SF} time scales.

5.9. The whole versus the sum of the parts

One of the applications of CALIFA is to assess the effects of the lack of spatially resolved information on the derivation of physical properties and SFHs from integrated-spectra surveys. The horizontal dashed magenta lines in Fig. 10 illustrate this point.

They represent the results obtained from the analysis of the spectrum of the datacube *as a whole*, that is, adding up all spaxels to emulate an integrated spectrum. Qualitatively, one expects that this should produce properties typical of the galaxy zones as a whole. This expectation is borne out in Fig. 10, where one sees that the extinction, mean ages, and metallicities marked by the dashed magenta line represent an overall average of the spatially resolved values. In this particular example, they all match quite well the values at 1 HLR. The stellar masses obtained from the whole and the sum of the parts are also in excellent agreement, differing by just 1%. Similarly, galaxy-wide luminosity and mass-weighted mean ages and metallicities computed in these two ways agree to within 0.05 dex.

But can one derive the SFH of a galaxy out of an integrated spectrum? Figure 11 says that, at least in CALIFA 277, the answer is yes. The dashed magenta and the black solid lines are very similar in all panels of this figure. As before, the former represents the results obtained from the analysis of the spatially compressed datacube, while the black curves are computed adding the results for each spaxel. We are thus comparing the whole against the sum of the parts, and they match.

This may seem a trivial result, but it is not. Formally, one only expects this to happen if A_V is the same at all positions, a condition which is approximately met in CALIFA 277. In

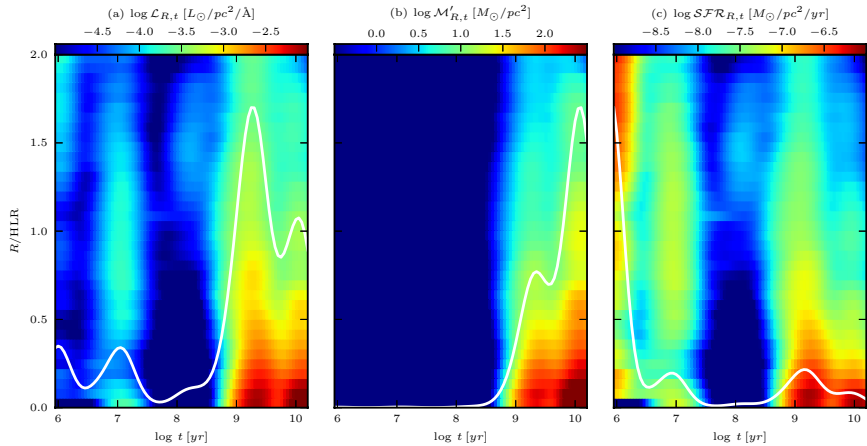


Fig. 12. R – t diagrams showing the radially averaged distribution of light, mass, and SFR as a function distance from the nucleus and age. *Left:* luminosity at $\lambda = 5635 \text{ \AA}$ per unit area. ($\mathcal{L}_{R,t}$). *Middle:* stellar mass formed per unit area ($M'_{R,t}$). *Right:* time-dependent SFR per unit area (SFR). The solid (white) lines represent the sum over all spaxels for a given age.

objects where dust has strong spatial variations, the spectral fitting of the global spectrum with a single A_V will inevitably operate compensations among the parameters, like increasing the age to compensate for an underestimated A_V and viceversa. Also, the combined effects of population gradients and kinematics (e.g., disk population contributing more to the wings of absorption lines than the ones from the bulge) are hard to predict. Since we are presenting results for a single example galaxy, it remains to be seen how general this “coincidence” is.

5.10. Space \times time diagrams: SFHs in 2D

One of the main challenges involved in the analysis of the multidimensional data built from the combination of the spatial dimensions with the t and Z dimensions opened by population synthesis is how to visualize the results. All examples shown so far project (or average over) two or more of these axes.

Figure 12 shows an attempt to visualize galaxy evolution as a function of both space and time. The trick is to compress xy into R and collapse the Z axis, producing a radially averaged SFH(R, t) map. The left panel shows the luminosity density \mathcal{L} at each radial position R and for each age t . As for the other panels in this figure, the original \mathcal{L}_{Zyx} array from which this map was derived was smoothed in $\log t$, marginalized over Z , and collapsed into one spatial dimension. Unlike in Fig. 10, we now use the area-averaging method discussed in Sect. 5.7, but the results do not depend strongly on this choice.

The $\mathcal{L}_{R,t}$ diagram shows that the light from old stars is concentrated in the bulge, while the youngest stars shine at all R . Also, $t \geq 1$ Gyr stars are more smoothly distributed in age in the disk than in the bulge, where they are concentrated in two populations, one at ~ 2.5 Gyr and the other older than 10 Gyr. Figure 12b shows the formed stellar mass surface density as a function of R and t . As usual, due to the highly non-linear relation between light and mass in stars, the young populations that show up so well in light practically disappear when seen in mass. Young stars reappear in the right panel, which shows the

evolution in time and space of the SFR surface density. As in Fig. 11g, these are obtained from the instantaneous SFR at each spaxel, computed as in Asari et al. (2007):

$$SFR(t) = \frac{M'_t}{\Delta t} = \frac{\log e M'_t}{\Delta \log t t}. \quad (15)$$

The age sampling is logarithmic ($\Delta \log t = \text{const.}$), so that the SFR is proportional to the stellar mass formed at t divided by t . The $SFR_{R,t}$ and $M'_{R,t}$ diagrams therefore carry the same information; it is the t^{-1} factor that makes them look so different.

When interpreting these or any other plot involving age, one should always keep in mind the logarithmic age resolution. For instance, taken at face value, the spatially integrated SFR of CALIFA 277 in the last few Myr is almost equal to its historical peak, ~ 2.5 Gyr ago (solid line in Fig. 12c). However, these two peaks span *vastly different time intervals*, roughly by a factor of Gyr/Myr = a thousand. The peak SFR around 2.5 Gyr ago, and indeed even well before that (at > 10 Gyr, when most of the mass was formed), were surely higher than the one we are now seeing at a few Myr but cannot be resolved in time. No fossil record method will ever be able to distinguish bursts much shorter than their current age. These limitations are well known in the field, but it is fit to recall them to avoid misinterpretation of the results.

Notwithstanding such age resolution issues, Fig. 12 represents a novel way of looking at galaxies both in time and space. It shows clear evidence in favor of an inside-out growth scenario in which the outer regions assemble their mass at a slower pace and over a more extended period. This behavior is not unique to this galaxy. Pérez et al. (2012) find just the same in a study of the first 105 galaxies observed by CALIFA.

5.11. Space vs. time “snapshots”

To go beyond the R – t diagrams of Fig. 12, one needs more dimensions than a sheet of paper can accommodate. An alternative is shown in Fig. 13, which shows t -slices through the cumulative \mathcal{M}'_{xyt} cube. Unlike the previous diagrams, which compressed the

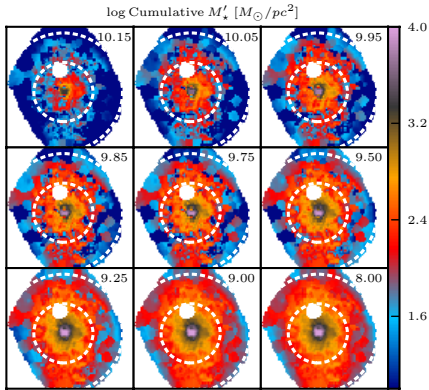


Fig. 13. “Pseudo snapshots” of the cumulative stellar mass surface density of CALIFA 277 at different ages: from $\log t$ [yr] = 10.15 to 8 (as labeled in each panel).

SFH in one way or another, these plots reveal the full 2D nature of the mass assembly history of CALIFA 277.

Age sequences like those in Fig. 13 can be constructed for several, but not all, properties inferred through or any other fossil method. One can, for instance, replace mass by intrinsic luminosity, SFR, or stellar metallicity in cumulative or differential form, but it is obviously impossible to reconstruct maps of A_V , σ_* , v_* as a function of t . It is also worth pointing out that the panels in Fig. 13 are *not* truly snapshots of a movie, that is, they are not pictures of the galaxy as it appeared at different look-back times. Instead, these are maps of where stars of a given age t are located nowadays.

Simulators should take notice of these simple facts. IFS data plus fossil methods provide a rich yet inevitably limited form of time travel. Illustrative and beautiful as they are, movies of stars and gas particles moving through time and space will never be directly compared to anything observational. In other words, simulations should be convolved through this “reality filter”. The observationally relevant predictions are the distribution of stellar ages and metallicities as a function of xy .

5.12. Emission line maps

Independent of the stellar population applications described throughout this paper, the fits provide a residual spectrum $R_\lambda = O_\lambda - M_\lambda$ that is, inasmuch as possible, free of stellar light. This is of great aid in the measurement of emission lines and hence in the derivation of a series of diagnostics of warm ISM properties, such as kinematics, nebular extinction, and chemical abundance. The complementarity of nebular and stellar analysis has been amply explored in studies of integrated spectra (e.g., Cid Fernandes et al. 2007; Asari et al. 2007; Pérez-Montero et al. 2010; García-Benito & Pérez-Montero 2012), and the addition of two spatial dimensions to this analysis holds great promise. Kehrig et al. (2012), for instance, combine analysis and nebular emission to study the impact of post-AGB populations on the ionization of the ISM in early-type galaxies.

Figure 14 shows a $R_{\lambda,xy}$ residuals cube with some of the main emission lines marked. The plot shows that emission lines are

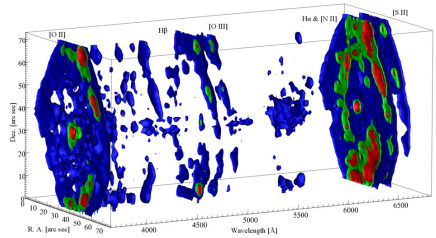


Fig. 14. Residual spectral cube in a 3D rendering.

brighter towards the outside, in particular over the spiral arms, as could be guessed from the distribution of actively star-forming regions traced by our SFH analysis (e.g., Fig. 9). Despite its active nucleus, the nuclear line fluxes are not particularly bright, implying a low-luminosity AGN.

6. Summary

This paper described a complete “analysis pipeline”, which processes reduced IFS data through the spectral synthesis code. Data for the spiral galaxy NGC 2916 (CALIFA 277) were used to illustrate the journey from (x, y, λ) datacubes to multidimensional maps of the synthesis products, focusing on the technical and methodological aspects. The three main steps in the analysis can be summarized as follows:

1. Pre-processing: this step comprises (a) construction of a spatial mask; (b) adjustments in the flag and error spectra; (c) rest-framing and resampling; (d) spatial binning. The last three stages were coded in a generic python package (), which can run in a fully automated fashion. Spatial binning was accomplished with a Voronoi tessellation scheme, which was tuned to produce zones with $S/N \geq 20$ spectra. In practice, because of the good quality of the data, no binning was necessary within $R \lesssim 1$ HLR. The issue of correlated errors in spatial binning was discussed and an empirical recipe to correct for it was presented. The output of these pre-processing steps are datacubes with fluxes, errors, and flags ready for a detailed λ -by- λ spectral analysis, as well as spatial masks, a zone map, and other ancillary products.
2. fits and organization of the synthesis results: Spectral fits for all spatial zones were performed using a base of SSP spectra from a combination of MILES and Granada models, spanning ages from 1 Myr to 14 Gyr and four metallicities between 0.2 and 1.5 solar. The results were packed in a coherent multilayered FITS (or HDF5) file with the Python Califa Starlight Synthesis Organizer (PyCASSO).
3. Post-processing tools: PyCASSO includes a reader module and a series of analysis tools to perform operations like zone-to-pixel image reconstruction; mapping the spectral and stellar population properties derived by into multidimensional time, metallicity, and spatial coordinates; averaging in spatial and temporal dimensions; manipulation of the stellar population arrays.

Some of the products of this whole analysis are standard in IFS work, like the kinematical field and emission line maps. The

real novelty resides in the spatially resolved stellar population products recovered from the fossil record of galaxy evolution encoded in the datacubes. The 2D products range from maps of the stellar extinction and surface densities of stellar mass to more elaborate products like mean ages and metallicities, time-averaged star formation rates, and b -parameters. These quantities are all normally used in the analysis of integrated spectra, but their application to IFS data raises some conceptual issues related to the unavoidable fact that not all stars in a given spaxel were born there. On the other hand, one can use spatially resolved data to construct diagnostics unapplicable to integrated data, such as indices comparing the present and past SFR in different regions or comparing the “present here” with the “present elsewhere”. These IFS-based variations of the traditional b parameter were shown to be useful to highlight different aspects of the spatially resolved SFH.

ID profiles in temporal or radial coordinates helped interpret the results. In our example galaxy, these compressed views of the (r, Z, x, y) manifold reveal clear age and metallicity negative gradients, as well as spatially dependent mass growth speeds compatible with an inside-out formation scenario. Finally, radius-age diagrams and snapshot sequences were introduced as further means of visualization.

Clearly, the application of spectral synthesis methods to IFS datacubes offers new ways of studying galaxies and their evolution. Future communications will use the tools laid out in this paper to explore the astrophysical implications of the results for galaxies in the CALIFA survey.

Acknowledgements. CALIFA is the first legacy survey performed at Calar Alto. The CALIFA collaboration would like to thank the IAA-CSIC and MPIA-MPG as major partners of the observatory and CAHA itself for the unique access to telescope time and support in manpower and infrastructure. We also thank the CAHA staff for their dedication to this project. R.C.F. thanks the hospitality of the IAA and the support of CAPES and CNPq. A.L.A. acknowledges support from INCT-A, Brazil. B.H. gratefully acknowledges the support by the DFG via grant Wi 1369/29-1. Support from the Spanish Ministerio de Economía y Competitividad through projects AYA2010-15081 (PI RGD), AYA2010-22111-C03-03 and AYA2010-10904E (SFS), AYA2010-21322-C03-02 (PSB) and the Ramón y Cajal Program (S.F.S., P.S.B. and J.F.B.) is warmly acknowledged. We also thank the Viabilidad, Diseño, Acceso y Mejora funding program ICTS-2009-10 for funding the data acquisition of this project.

References

Asari, N. V., Cid Fernandes, R., Stasińska, G., et al. 2007, *MNRAS*, 381, 263
Bell, E. F., Wolf, C., Meisenheimer, K., et al. 2004, *ApJ*, 608, 752

Bertin, E., & Arnouts, S. 1996, *A&AS*, 117, 393
Bica, E. 1988, *A&A*, 195, 76
Bica, E., Alloin, D., & Schmitt, H. R. 1994, *A&A*, 283, 805
Blanc, G. A., Gebhardt, K., Heiderman, A., et al. 2010, in *New Horizons in Astronomy*: Frank N. Bash Symposium 2009, 432, 180
Bruzual G., & Charlot S. 2003, *MNRAS*, 344, 1000
Cappellari, M., & Copin, Y. 2003, *MNRAS*, 342, 345
Cardelli, J. A., Clayton, G. C., & Mathis, J. S. 1989, *ApJ*, 345, 245
Charbonnel, C., Meynet, G., Maeder, A., Schaeller, G., & Schaerer, D. 1993, *A&AS*, 101, 415
Cid Fernandes, R. 2007, *IAU Symp.*, 241, 461
Cid Fernandes, R., Mateus, A., Sodré L., Stasińska, G., & Gomes, J. M. 2005, *MNRAS*, 358, 363
Falcón-Barroso, J., Sánchez-Blázquez, P., Vazdekis, A., et al. 2011, *A&A*, 532, A95
Folkes, S., Ronen, S., Price, I., et al. 1999, *MNRAS*, 308, 459
García-Benito, R., & Pérez-Montero, E. 2012, *MNRAS*, 423, 406
González Delgado, R. M., Cerviño, M., Martins, L. P., Leitherer, C., & Hauschildt, P. H. 2005, *MNRAS*, 357, 945
Gutiérrez, C. M., Azzaro, M., & Prada, F. 2002, *ApJS*, 141, 61
Ilbert, O., Capak, P., Salvato, M., et al. 2009, *ApJ*, 690, 1236
Kelz, C., Monreal-Ibero, A., Papaderos, P., et al. 2012, *A&A*, 540, A11
Kelz, A., Verheijen, M. A. W., Roth, M. M., et al. 2006, *PASP*, 118, 129
Koleva M., Prugniel P., & De Rijcke S. 2009, *Astron. Nachr.* 999, 1
Lilly, S. J., Le Fèvre, O., Hammer, F., & Crampton, D. 1996, *ApJ*, 460, 1
MacArthur, L. A., González, J. J., & Courteau, S. 2009, *MNRAS*, 395, 28
Madau, P., Ferguson, H. C., Dickinson, M. E., et al. 1996, *MNRAS*, 283, 1388
Moles, M., Benítez, N., Aguerri, J. A. L., et al. 2008, *AJ*, 136, 1325
Moorthy, B. K., & Holtzman, J. A. 2006, *MNRAS*, 371, 538
Ocvirk, P., Pichon, C., Lançon, A., & Thiébaud, E. 2006, *MNRAS*, 365, 46
Panter, B., Heavens, A. F., & Jimenez, R. 2003, *MNRAS*, 343, 1145
Panter, B., Jimenez, R., Heavens, A. F., & Charlot, S. 2007, *MNRAS*, 378, 1550
Pérez, E., Cid Fernandes, R., González Delgado, R. M., et al. 2013, *ApJ*, 764, L1
Pérez-González, P. G., Rieke, G. H., Villar, V., et al. 2008, *ApJ*, 675, 234
Pérez-Montero, E., García-Benito, R., Hägele, G. F., & Díaz, Á. I. 2010, *MNRAS*, 404, 2037
Roth, M. M., Kelz, A., Fechner, T., et al. 2005, *PASP*, 117, 62
Rudnick, G., Rix, H.-W., Kennicutt, R. C., Jr. 2000, *ApJ*, 538, 569
Sánchez, S. F., Kennicutt, R. C., Gil de Paz, A., et al. 2012, *A&A*, 538, A8
Sánchez-Blázquez, P., Ocvirk, P., Gibson, B. K., Pérez, I., & Peletier, R. F. 2011, *MNRAS*, 415, 709
Schaerer, D., Charbonnel, C., Meynet, G., Maeder, A., & Schaller, G. 1993a, *A&A*, 102, 339
Schaerer, D., Meynet, G., Maeder, A., & Schaller, G. 1993b, *A&AS*, 98, 523
Schaller, G., Schaerer, D., Meynet, G., & Maeder, A. 1992, *A&AS*, 96, 269
Tojeiro, R., Heavens, A. F., Jimenez, R., & Panter, B. 2007, *MNRAS*, 381, 1252
Vazdekis, A., Sánchez-Blázquez, P., Falcón-Barroso, J., et al. 2010, *MNRAS*, 404, 1639
Verheijen, M. A. W., Bershady, J. E., Andersen, D. R., et al. 2004, *Astron. Nachr.*, 325, 151
York, D. G., Adelman, J., Anderson, J. E., et al. 2000, *AJ*, 120, 1579
Walcher, J., Groves, B., Budavári, T., & Dale, D. 2011, *Ap&SS*, 331, 1

D.2 Resolving galaxies in time and space. II. Uncertainties in the
spectral synthesis of datacubes

Artigo por Cid Fernandes et al. (2014) (doi : [10.1051/0004-6361/201321692](https://doi.org/10.1051/0004-6361/201321692)).
Também disponível em *preprint* ([arXiv:1307.0562](https://arxiv.org/abs/1307.0562)).

Resolving galaxies in time and space

II. Uncertainties in the spectral synthesis of datacubes

R. Cid Fernandes^{1,2}, R. M. González Delgado², R. García Benito², E. Pérez², A. L. de Amorim^{1,2}, S. F. Sánchez^{2,3},
B. Husemann⁴, J. Falcón Barroso^{5,6}, R. López-Fernández², P. Sánchez-Blázquez⁷, N. Vale Asari¹, A. Vazdekis^{5,6},
C. J. Walcher⁴, and D. Mast^{2,3}

¹ Departamento de Física, Universidade Federal de Santa Catarina, PO Box 476, 88040-900 Florianópolis, SC, Brazil
e-mail: cid@astro.ufsc.br

² Instituto de Astrofísica de Andalucía (CSIC), PO Box 3004, 18080 Granada, Spain

³ Centro Astronómico Hispano Alemán, Calar Alto, (CSIC-MPG), C/Jesús Durbán Remón 2-2, 04004 Almería, Spain

⁴ Leibniz-Institut für Astrophysik Potsdam, innoFSPEC Potsdam, An der Sternwarte 16, 14482 Potsdam, Germany

⁵ Instituto de Astrofísica de Canarias, vía Lactea s/n, 38200 La Laguna, Tenerife, Spain

⁶ Departamento de Astrofísica, Universidad de La Laguna, 38205 Tenerife, Spain

⁷ Departamento de Física Teórica, Universidad Autónoma de Madrid, 28049 Madrid, Spain

Received 13 April 2013 / Accepted 28 June 2013

ABSTRACT

Aims. In a companion paper we have presented many products derived from the application of the spectral synthesis code to datacubes from the CALIFA survey, including 2D maps of stellar population properties (such as mean ages, mass, and extinction) and 1D averages in the temporal and spatial dimensions. Our goal here is to assess the uncertainties in these products.

Methods. Uncertainties associated to noise and spectral shape calibration errors in the data and to the synthesis method were investigated by means of a suite of simulations, perturbing spectra and processing them through our analysis pipelines. The simulations used 1638 CALIFA spectra for NGC 2916, with perturbation amplitudes gauged in terms of the expected errors. A separate study was conducted to assess uncertainties related to the choice of evolutionary synthesis models, the key ingredient in the translation of spectroscopic information into stellar population properties. We compare the results obtained with three different sets of models: the traditional Bruzual & Charlot models, a preliminary update of them, and a combination of spectra derived from the Granada and MILES models. About 10^5 spectra from over 100 CALIFA galaxies were used in this comparison.

Results. Noise and shape-related errors at the level expected for CALIFA propagate to uncertainties of 0.10–0.15 dex in stellar masses, mean ages, and metallicities. Uncertainties in A_V increase from 0.06 mag for random noise to 0.16 mag for spectral shape errors. Higher-order products such as star formation histories are more uncertain than global properties, but still relatively stable. Owing to the large number statistics of datacubes, spatial averaging reduces uncertainties while preserving information on the history and structure of stellar populations. Radial profiles of global properties, and star formation histories averaged over different regions are much more stable than those obtained for individual spaxels. Uncertainties related to the choice of base models are larger than those associated with data and method. Except for metallicities, which come out very different when fits are performed with the Bruzual & Charlot models, differences in mean age, mass, and metallicity are of the order of 0.15 to 0.25 dex, and 0.1 mag for A_V . Spectral residuals are of the order of 1% on average, but with systematic features of up to 4% amplitude. We discuss the origin of these features, most of which are present in both in CALIFA and SDSS spectra.

Key words. techniques: imaging spectroscopy – galaxies: evolution – galaxies: stellar content

1. Introduction

Large optical spectroscopic surveys have dominated the panorama of extra-galactic astrophysics over the last decade. Stellar population analysis of these data has produced information on stellar masses, mean stellar ages, abundances, dust content, and diagnostics of their star formation histories (SFHs), whose analysis per se and in relation to other properties (for instance, morphology or environment) has advanced the understanding of the physics of galaxies and their evolution through cosmic time. Yet, all this information is derived from spatially unresolved spectra, and thus reflects global averages over properties that are known to vary across the face of galaxies. Integral field spectroscopy (IFS) is a natural next step to move from

global properties to the internal physics of galaxies. Dissecting the different structural components will probably lead to a much more complete picture of galaxies, and to a clearer understanding of the results previously obtained in non-spatially resolved surveys. IFS has been around for over two decades, but has only recently been promoted to the scale of modern galaxy surveys. CALIFA, the Calar Alto Integral Field Area survey (Sánchez et al. 2012; Husemann et al. 2013), is a pioneer in this blooming field.

To harvest the full potential of IFS data one needs to adapt techniques developed for spatially unresolved galaxy spectra, folding in the information on the spatial structure. In a companion article (Cid Fernandes et al. 2013, hereafter Paper I) we have presented our method for extracting stellar population

properties out of CALIFA datacubes by means of the spectral-fitting software (Cid Fernandes et al. 2005). The packages developed to pre-process and partition the reduced datacubes (QBICK) and to post-process the results of the spectral synthesis (PyCASSO, the Python CALIFA Starlight Synthesis Organizer) were described in detail. The products of this work flow were exemplified using data for the nearby spiral NGC 2916 (CALIFA 277). Diagnostics such as 2D maps of physical properties (mean ages and metallicities, mass surface densities, star formation rates, etc.), 1D averages in the temporal and spatial dimensions, projections of the stellar light and mass growth onto radius-age diagrams, and cuts through the (x, y, age) cubes were presented to illustrate the potential of the combination of IFS data with spectral synthesis as a tool for studying galaxy evolution in time and space simultaneously.

Uncertainties in this whole process stem from (i) noise and calibration of the data; (ii) limitations of our spectral synthesis method; and (iii) evolutionary synthesis models, the key ingredient in the mapping of observed spectra to astrophysical information. These different sources of uncertainty, each one comprising a field of work by itself, intertwine and propagate in complex ways through our pipelines. Uncertainties in spectral synthesis products have been previously explored in the literature, such as the noise-effect simulations in Cid Fernandes et al. (2005), the model-impact study of Panter et al. (2007), and the suite of tests presented by Tojeiro et al. (2007), but never in the context of IFS.

This article complements Paper I by addressing the effects of these uncertainties. Our central goal is to provide quantitative and qualitative guidelines to allow an assessment of the robustness of results produced with the methods and tools explained in Paper I, which are being used in a series of publications by our collaboration. Pérez et al. (2013), for instance, analyzed the spatially resolved mass assembly history of 105 CALIFA galaxies, finding clear evidence for an inside-out growth for massive galaxies, and signs of outside-in growth for the less massive ones (see González Delgado et al. 2012 and 2013 for other results). Despite the focus on $\text{H}\alpha$ and CALIFA, the results reported here are also useful in the broader context of stellar population analysis of IFS data; for instance, experimental datacubes recently obtained by MaNGA run through our QBICK and PyCASSO pipelines without any modification.

The first part of this paper (Sects. 2 and 3) presents extensive simulations that explore the effects of uncertainties related to the data and spectral synthesis method. Random noise and shape-changing perturbations are added to both observed and synthetic spectra of all zones of the same galaxy analyzed in Paper I. These simulations are then used to evaluate uncertainties in global properties (mean ages, masses, etc.) and higher-order products such as SFHs. This is done both at the level of individual spectra and for spatial regions cut out from the datacube.

The second part (Sect. 4) is dedicated to experiments carried out to evaluate how our results are affected by different choices of evolutionary synthesis models for the spectra of simple stellar populations (SSP). This study uses ~ 100 thousand spectra from 107 galaxies observed by CALIFA, all of which were processed with three sets of SSP models used in the current literature. An inspection of the quality of the spectral fits and a comparison with results obtained for SDSS galaxies is also presented.

Section 5 summarizes our main results. Throughout this paper the notation and definitions established in Paper I are followed.

2. Uncertainties associated to the data and the method: description of the simulations

A drawback of $\text{H}\alpha$ is that it provides no error estimate on its output. The most straightforward (albeit computationally expensive) way to do so is to run the code several times perturbing the input data according to some realistic prescription of the errors involved. This section describes a set of extensive simulations tailored to match the characteristics of the CALIFA data. The simulations are designed to address the effects of

1. random noise,
2. shape-related calibration uncertainties, and
3. multiplicity of solutions,

upon the physical properties derived with $\text{H}\alpha$. Throughout these experiments we keep the set of SSPs fixed at the same set as used in Paper I, which is denoted “base GM” in Sect. 4, where the effects of this choice are investigated. This base comprises $N_* = 156$ elements with 39 ages between $t = 1$ Myr and 14 Gyr, and 4 metallicities from $Z = 0.2$ to 1.5 solar. The simulations are based on the data and $\text{H}\alpha$ fits of 1638 zone spectra¹ of CALIFA 277 studied in Paper I. Given the variety of properties found across this galaxy and the fact that all other datacubes in CALIFA were processed in the same way, the uncertainty estimates presented here are representative of CALIFA data in general.

Each spectrum was perturbed ten times for each of the R, C, and E error prescriptions discussed below and refitted. This data set is then used to evaluate uncertainties in the derived properties, both at the level of individual zones and for spatially averaged properties like those shown in Figs. 10 and 11 of Paper I. Observed as well as synthetic spectra were perturbed in the simulations. The first represent real-life conditions, while the latter are essentially a theoretical exercise which explores the sensitivity of the $\text{H}\alpha$ results to different types of perturbations.

2.1. Types of errors and simulations

The first type of error considered is that related to the variations on the derived properties induced by random fluctuations of the observed fluxes within the noise level. To study this, each zone spectrum was perturbed ten times with Gaussian noise with a λ -dependent amplitude given by the error spectrum ϵ_λ (hereafter OR1 runs, with O standing for observed, R for random, and 1 for the amplitude of the perturbation). Experiments were also conducted with perturbations of 2 and $3 \times \epsilon_\lambda$ (OR2 and OR3 runs, respectively) to emulate what would be obtained under conditions considerably worse than those in CALIFA².

A second set of simulations was carried to address the problem of the overall continuum shape calibration. $\text{H}\alpha$ relies on flux-calibrated input spectra, so it is relevant to access how much its solutions vary for spectra whose shapes vary within expected uncertainty ranges. Husseman et al. (2013) found that CALIFA synthetic $g-r$ colors typically differ by 0.05 mag from

¹ 1527 of the spectra come from single spaxels, while the remaining 111 correspond to Voronoi zones that typically comprise ten spaxels.

² Note that these simulations add noise to observed spectra, which already contains noise. Hence, OR1 spectra, which are nominally meant to represent variations at the level of $1\epsilon_\lambda$, effectively have errors of $\sqrt{2}\epsilon_\lambda$, i.e., 41% higher than intended. We nevertheless pretend these runs correspond to 1σ perturbations, which gives a safety margin in our analysis. Similarly, the OR2 and OR3 runs have errors 2.23 and 3.16 times larger than the original ones instead of factors of 2 and 3, respectively.

those obtained by SDSS photometry. We used this value to gauge the effects of continuum calibration uncertainty in each individual spectrum of CALIFA 277. For simplicity, but with no loss of generality, these simulations keep the flux at $\lambda_r = 6231 \text{ \AA}$ stable, such that the 0.05 mag variation in $g-r$ translates into a 0.02 dex uncertainty in the flux at $\lambda_g = 4770 \text{ \AA}$. To emulate the effects of such variations we produced ten versions of each spectrum by adding $A_g \times (\lambda_r - \lambda) / (\lambda_r - \lambda_g)$ to the original $\log F_{\lambda}$, with $A_g = \Delta \log F_{\lambda_g}$ sampled from a Gaussian distribution of zero mean and dispersion $\sigma(\log F_{\lambda_{4770}}) = 0.02$ (OC002 runs, where C stands for color). This produces both redder and bluer versions of the original spectrum. Experiments were also carried out for $\sigma(\log F_{\lambda_{4770}}) = 0.01$, and 0.04 dex (OC001 and OC004, respectively). We take OC002 runs as default for CALIFA, even though the spaxel-to-spaxel variations in the continuum calibration for a single galaxy are probably smaller than the $g-r$ dispersion quoted by Husemann et al. (2013), which was derived from the 100 galaxies in the CALIFA DR1 sample.

Finally, fits were also conducted without any perturbation at all (OE0 runs), the motivation for which is to quantify a qualitatively different source of uncertainty embedded in all other simulations. provides a single best-fit set of parameters out of typically many millions tried out during its likelihood-guided sampling of the parameter space. This single solution, however, is not meant to be mathematically unique. In fact, given the pseudo-random nature of its Markov chains, solutions depend on the input seed for the random-number generator. For large samples, and each CALIFA datacube is a large sample in itself, these variations have no relevant effect on the overall results of the analysis. For individual spectra, however, the multiplicity of solutions leads to uncertainties in the derived properties. The OE0 runs quantify these uncertainties, which ultimately reflect an intrinsic limitation of our spectral synthesis method.

2.2. Simulations based on synthetic spectra

The OE0, OR*, and OC* runs work upon the original observed spectra (hence the prefix O). A parallel set of simulations was carried out applying these same perturbation recipes to the synthetic spectra obtained in our fits of CALIFA 277. We label these runs as SE0, SR1, SR2, SR3, SC001, SC002, and SC004 (S for synthetic).

The S runs use exactly the same sampling, masks, flags, and ϵ_1 errors as in the O runs, thus following the pattern of CALIFA data in a realistic fashion. At the same time, these are idealistic simulations in the sense that the perturbations act upon perfect input spectra instead of on observed ones. This theoretical exercise therefore overlooks inadequacies in the SSP models (including problems such as potential flux calibration problems in the libraries, limited coverage of the stellar parameter space, missing or incorrectly modeled evolutionary phases) and other assumptions involved in the modeling (namely, extinction and kinematics).

The purpose of these runs is to evaluate to which extent recovers known input properties in the presence of perturbations. This kind of input versus output comparison is more commonly carried out by feeding the spectral fitting code with data generated with ad hoc parametric descriptions of the SFH (e.g., the so-called tau models), while our theoretical SFHs are inspired in those derived from actual observations. A valid criticism of these simulations is that the same base is used to generate and fit spectra. The alternative would be to generate models

Table 1. Notation for the simulations.

Run	Original spectra	Type of perturbation	Perturbation amplitude	Comments
(1)	(2)	(3)	(4)	(5)
OR1	observed	noise	$1 \times \epsilon_1$	Gaussian
OR2	observed	noise	$2 \times \epsilon_1$	Gaussian
OR3	observed	noise	$3 \times \epsilon_1$	Gaussian
OC001	observed	color	0.01 dex	at λ_g
OC002	observed	color	0.02 dex	at λ_g
OC004	observed	color	0.04 dex	at λ_g
OE0	observed	none	0	
SR1	synthetic	noise	$1 \times \epsilon_1$	Gaussian
SR2	synthetic	noise	$2 \times \epsilon_1$	Gaussian
SR3	synthetic	noise	$3 \times \epsilon_1$	Gaussian
SC001	synthetic	color	0.01 dex	at λ_g
SC002	synthetic	color	0.02 dex	at λ_g
SC004	synthetic	color	0.04 dex	at λ_g
SE0	synthetic	none	0	

Notes. (1) Nomenclature adopted to denote the different simulations. (2) The nature (observed or synthetic) of the spectra that are perturbed. (3) Type of perturbation. (4) Amplitude of the perturbations. For C runs, we list the amplitude of the variations at λ_g . Each of the 1638 spectra from CALIFA 277 were perturbed ten times according to each of these 14 recipes.

with some other set of t' s and Z' , but since our base is so large (39 ages and all four available metallicities), this would make very little difference in practice.

2.3. Notation

For clarity and quick reference, we summarize the notation and intended purpose of the simulations described above.

R runs (OR1, OR2, OR3, SR1, SR2, and SR3) explore the effect of noise by adding Gaussian perturbations scaled to have amplitudes 1, 2, or 3 times the nominal error ϵ_1 . C runs perturb the input spectra in their global shape by multiplying the original F_{λ} by a power law in λ , scaled such that the flux at λ_r remains fixed while that at λ_g differs by (on average over all realizations) 0.01 (OC001 and SC001), 0.02 (OC002 and SC002) and 0.04 (OC004 and SC004) dex with respect to the input flux. (In a $\log F_{\lambda} \times \lambda$ plot, these shape-perturbations correspond to straight lines anchored at λ_r and different slopes.) These runs are meant to emulate the effect of a flux calibration uncertainty in the data. E0 runs do nothing to the input spectra. They only differ in the random number seed feed to . The variance among these fits reflects the multiplicity of SSP combinations which lead to a similar total spectrum.

In all cases, a prefix O indicates that the perturbations act upon the observed spectra, while an S prefix means that synthetic spectra are perturbed. Table 1 summarizes the simulation-related nomenclature used throughout the paper.

3. Results of the simulations

The simulations described in Sect. 2 provide the material to evaluate uncertainties associated with the data and spectral synthesis method. We split the presentation of this material into an assessment of the errors in global properties (Sect. 3.1), radial profiles (Sect. 3.2), and SFHs (Sect. 3.3). We conclude this part of our investigation with a summary of the results of the simulations (Sect. 3.4).

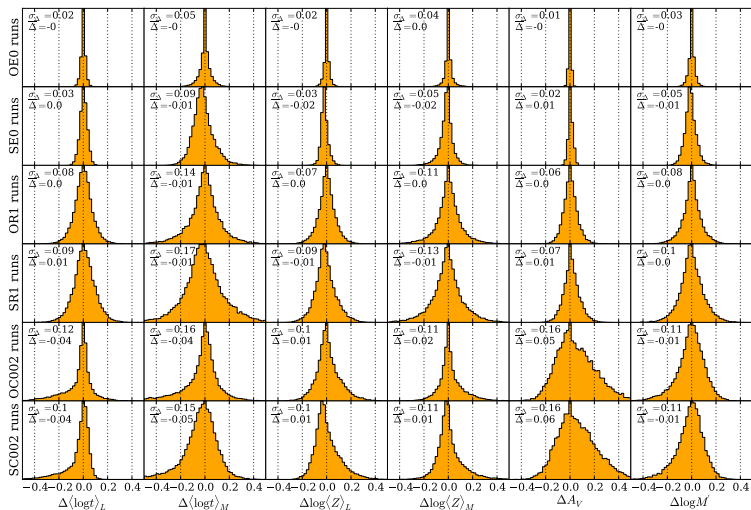


Fig. 1. Histograms of Δ (Δ = simulated minus original value) for the main scalar properties derived from the spectral synthesis: $(\log t)_L$, $(\log t)_M$, $\log(Z)_L$, $\log(Z)_M$, A_V and the initial stellar mass ($\log M'$). Each row corresponds to one set of simulations, alternating S and O runs (as labeled in the y -axis). Mean Δ s and their σ s are labeled in each panel. Except for the A_V column, each histogram is based on 16 380 values obtained from the 1638 zones in CALIFA 277 and ten Monte Carlo realizations of the perturbation. For clarity, the A_V histograms were drawn excluding the many $\Delta A_V = 0$ cases, which occur due to the $A_V \geq 0$ physical limit imposed on the spectral fits. Noise-free simulations (OE0 and SE0), which trace intrinsic degeneracies in spectral fits of composite stellar populations, are shown in the top two rows. Random-noise simulations (SRI and ORI, central rows) map the uncertainties caused by statistical fluctuations of the observed F_λ fluxes. C002-simulations, where the spectral-shape is changed to emulate calibration uncertainties, are shown in the bottom panels.

3.1. Uncertainties in global properties

The main scalar properties derived from the spectral synthesis are mean ages and metallicities (weighted by light or mass), extinction and stellar masses³. These first order products of the analysis convey enough information to draw a quite detailed sketch of the 2D distribution of stellar population properties in a galaxy. Before incorporating the spatial arrangement of the spectra, however, it is useful to assess uncertainties in the individual spectra as if they came from different galaxies.

Figure 1 shows histograms of the $\Delta \equiv$ simulation – original value (i.e., that obtained from the unperturbed spectrum) of each of these quantities, and for six different sets of simulations: E0, R1, and C002 runs for the O and S versions. Statistics for all runs are listed in Table 2.

3.1.1. E runs: noise-free simulations

The OE0 and SE0 panels show that variations due to the random number seed fed to Δ have a tiny effect on the derived properties, with no bias ($\Delta \sim 0$) and one σ uncertainty all in the second decimal place.

Intriguingly, SE0 runs have somewhat higher dispersions than OE0 runs. The mathematical reason for this behavior is subtle, but simple to grasp with the concepts developed by

³ Throughout this section we work with the initial stellar mass (M'), uncorrected for the mass expelled from stars back to the interstellar medium. Mass weighted ages and metallicities, however, do account for the returned mass.

Pelat (1997, 1998). By construction, SE0 spectra lie within the synthetic domain (SD), i.e., the space generated by convex combinations of the base spectra⁴. A point inside this space can be exactly fitted by at least one set of parameters. Even if the solution is mathematically unique, a whole range of other solutions produce nearly identical spectra. Because of the limitations of evolutionary synthesis models, observed spectra cannot possibly be fitted exactly even in the ideal limit of perfect calibration and $S/N = \infty$ signal-to-noise ratio, so OE0 spectra are inevitably outside the SD. Fits of OE0 spectra therefore have access to a smaller subspace of acceptable solutions than fits of SE0 spectra, which results in the lower dispersions observed in Fig. 1. This same interpretation applies to other runs. Even when the synthetic spectra are perturbed (for instance, in the SRI simulations), they remain closer to the SD than the corresponding O spectra, thus reaching a larger region of the solutions space.

3.1.2. R runs: random-noise simulations

Random noise at the nominal level (OR1 and SRI runs, middle rows in Fig. 1) lead to Δ -distributions with σ around 0.1 dex in ages, metallicities and masses, and 0.05 mag in A_V . As expected (and as also seen in the E0 runs), mass-weighted ages and metallicities have broader Δ distributions than their luminosity-weighted counterparts. In any case, these dispersions are all

⁴ In the case of Δ and other full spectral fitting codes this space is additionally enlarged by the extinction and kinematical dimensions, but we leave this aside to simplify the argument.

Table 2. Statistics of the simulations: $\bar{\Delta} \pm \sigma_{\Delta}$.

Property	OE0	OR1	OR2	OR3	OC001	OC002	OC004
$\langle \log t \rangle_L$	$-0.00 \pm \mathbf{0.02}$	$0.00 \pm \mathbf{0.08}$	$0.01 \pm \mathbf{0.13}$	$0.01 \pm \mathbf{0.16}$	$-0.00 \pm \mathbf{0.05}$	$-0.04 \pm \mathbf{0.12}$	$-0.09 \pm \mathbf{0.20}$
$\langle \log t \rangle_M$	$-0.00 \pm \mathbf{0.05}$	$-0.01 \pm \mathbf{0.14}$	$-0.02 \pm \mathbf{0.21}$	$-0.03 \pm \mathbf{0.26}$	$-0.00 \pm \mathbf{0.08}$	$-0.04 \pm \mathbf{0.16}$	$-0.10 \pm \mathbf{0.28}$
$\log(Z)_L$	$-0.00 \pm \mathbf{0.02}$	$0.00 \pm \mathbf{0.07}$	$-0.00 \pm \mathbf{0.12}$	$-0.00 \pm \mathbf{0.16}$	$0.00 \pm \mathbf{0.05}$	$0.01 \pm \mathbf{0.10}$	$0.03 \pm \mathbf{0.16}$
$\log(Z)_M$	$0.00 \pm \mathbf{0.04}$	$0.00 \pm \mathbf{0.11}$	$-0.00 \pm \mathbf{0.18}$	$0.00 \pm \mathbf{0.22}$	$0.00 \pm \mathbf{0.05}$	$0.02 \pm \mathbf{0.11}$	$0.05 \pm \mathbf{0.18}$
A_V	$-0.00 \pm \mathbf{0.01}$	$0.00 \pm \mathbf{0.06}$	$0.01 \pm \mathbf{0.10}$	$0.02 \pm \mathbf{0.14}$	$0.01 \pm \mathbf{0.06}$	$0.05 \pm \mathbf{0.16}$	$0.14 \pm \mathbf{0.29}$
$\log M'$	$-0.00 \pm \mathbf{0.03}$	$0.00 \pm \mathbf{0.08}$	$-0.00 \pm \mathbf{0.13}$	$0.00 \pm \mathbf{0.15}$	$-0.00 \pm \mathbf{0.05}$	$-0.01 \pm \mathbf{0.11}$	$-0.02 \pm \mathbf{0.21}$
Property	SE0	SR1	SR2	SR3	SC001	SC002	SC004
$\langle \log t \rangle_L$	$0.00 \pm \mathbf{0.03}$	$0.01 \pm \mathbf{0.09}$	$0.01 \pm \mathbf{0.14}$	$0.01 \pm \mathbf{0.18}$	$-0.01 \pm \mathbf{0.04}$	$-0.04 \pm \mathbf{0.10}$	$-0.10 \pm \mathbf{0.19}$
$\langle \log t \rangle_M$	$-0.01 \pm \mathbf{0.09}$	$-0.01 \pm \mathbf{0.17}$	$-0.02 \pm \mathbf{0.23}$	$-0.03 \pm \mathbf{0.27}$	$-0.02 \pm \mathbf{0.10}$	$-0.05 \pm \mathbf{0.15}$	$-0.11 \pm \mathbf{0.26}$
$\log(Z)_L$	$-0.02 \pm \mathbf{0.03}$	$-0.01 \pm \mathbf{0.09}$	$-0.01 \pm \mathbf{0.14}$	$-0.00 \pm \mathbf{0.18}$	$-0.01 \pm \mathbf{0.05}$	$0.01 \pm \mathbf{0.10}$	$0.02 \pm \mathbf{0.17}$
$\log(Z)_M$	$-0.02 \pm \mathbf{0.05}$	$-0.01 \pm \mathbf{0.13}$	$-0.00 \pm \mathbf{0.20}$	$0.01 \pm \mathbf{0.24}$	$-0.01 \pm \mathbf{0.06}$	$0.01 \pm \mathbf{0.11}$	$0.04 \pm \mathbf{0.19}$
A_V	$0.01 \pm \mathbf{0.02}$	$0.01 \pm \mathbf{0.07}$	$0.02 \pm \mathbf{0.11}$	$0.03 \pm \mathbf{0.15}$	$0.02 \pm \mathbf{0.06}$	$0.06 \pm \mathbf{0.16}$	$0.15 \pm \mathbf{0.30}$
$\log M'$	$-0.01 \pm \mathbf{0.05}$	$0.00 \pm \mathbf{0.10}$	$0.00 \pm \mathbf{0.14}$	$0.00 \pm \mathbf{0.16}$	$-0.01 \pm \mathbf{0.06}$	$-0.01 \pm \mathbf{0.11}$	$-0.03 \pm \mathbf{0.20}$

Notes. For each global property the table lists the mean simulated minus original difference ($\bar{\Delta}$) and its standard deviation (σ_{Δ}). This last, printed in bold, indicates the level of uncertainties under different circumstances. Each column denotes one set of simulations. The upper half of the table shows results of simulations based on variations of the original observed spectrum (O runs), whereas the bottom half corresponds to runs where the synthetic spectra were perturbed (S runs) and used as input.

relatively small. Indeed, they are smaller than those induced by the use of different SSP models (Sect. 4, Fig. 11).

Table 2 reports results for simulations with noise levels 2 and 3 times worse than ϵ_l . For the OR2 runs, for instance, the uncertainties in the properties plotted in Fig. 1 increase by roughly a factor of 2 with respect to those found in the OR1 simulations. The Δ distributions (not plotted) remain symmetric, without significant biases. We recall, however, that there is no reason to believe that the ϵ_l values produced by the CALIFA reduction pipeline are underestimated. On the contrary, Husemann et al. (2013) showed that, if anything, they are slightly overestimated.

3.1.3. C runs: shape perturbations

The bottom panels in Fig. 1 show the results for simulations where the continuum shape was perturbed to produce (on average) 0.02 dex variations in the flux at λ_g for a fixed flux at λ_r . The one σ variations in ages, metallicities, and masses for OC002 runs are larger than those obtained with the OR1 runs, but not as large as in OR2 (Table 2). Similar conclusions apply to the corresponding S runs. Predictably, A_V is more severely affected by these global shape perturbations, with $\sigma(\Delta A_V) \sim 2.5$ times higher than those in the OR1 runs.

Unlike in other simulations, the Δ distributions are skewed, particularly those for A_V and $\langle \log t \rangle_L$. This is a by-product of the $A_V \geq 0$ limit imposed upon the fits. 582 of the 1638 zones of CALIFA 277 were fitted with $A_V = 0$ (see Fig. 4 in Paper I). About half of the shape-perturbed versions of these spectra are bluer than the original ones. Since A_V was not allowed to decrease A_V to fit them, it gets stuck at $A_V = 0$, compensating the extra blueness with younger populations, which in turn produces the tail toward negative $\Delta \langle \log t \rangle_L$ seen in the bottom rows of Fig. 1. This is also the reason why there are more instances of $\Delta A_V > 0$ than < 0 , producing the positively skewed ΔA_V distributions.

Increasing the shape errors by a factor of 2 (C004 runs) leads to uncertainties roughly twice as large, biases of the order of -0.1 dex in ages, and $+0.15$ mag in A_V (Table 2), as well as larger skewness of the Δ distributions. Conversely, C001 runs result in uncertainties ~ 2 times smaller, with no bias nor much skewness.

3.1.4. Covariances

As usual in multivariate problems, variations in one property correlate with variations in others. In the context of spectral synthesis, such covariances are known as age-metallicity-extinction degeneracies: A_V affects colors while t and Z affect both absorption lines and colors. Previous work (e.g., Cid Fernandes et al. 2005; Sánchez-Blázquez et al. 2011) showed that λ -by- λ fits help in reducing these degeneracies, but do not eliminate them.

Figure 2 shows how the main scalar properties co-vary in our simulations. S runs were used in this plot—O runs produce similar plots, with slightly more compact contours. The first two columns (SR1 and SR2 runs) reveal the classical degeneracies of population synthesis, with mean ages increasing as mean metallicities decrease, and extinction variations also anti-correlated with variations in mean age. The bottom row shows how stellar masses increase as ages become older, and vice-versa.

In the R-runs, perturbations do not change the overall shape of the input spectrum. Hence, if a solution turns out to be somewhat older than the original one, its extinction and/or metallicity will decrease to compensate for the redder colors and stronger absorption lines of the older stars. C-runs, on the other hand, do change colors—that is, in fact, exactly what they are designed to do. This slightly changes the nature of “degeneracies”.

If the shape perturbation followed the same functional form of the extinction law, it would suffice to change A_V , leaving the population mixture essentially unchanged, varying t s and Z s at the level they would naturally vary without color perturbations (i.e., due to noise and the multiplicity of solutions). To first order, this is indeed what happens in the C-runs. Compare, for instance, the (SR1, SR2) and (SC001, SC002) pairs of $\Delta A_V \times \Delta \langle \log t \rangle_L$ panels in Fig. 2. In both pairs of plots the corresponding type of error changes by a factor of 2 in amplitude, yet one sees that the ΔA_V contours grow more from SC001 to SC002 than from SR1 to SR2. Furthermore, the ΔA_V contours are nearly vertically oriented in the C-runs, while in R-runs the anti-correlation with $\Delta \langle \log t \rangle_L$ is clear (the age-extinction degeneracy). We thus confirm the expectation that, to first order, continuum shape uncertainties primarily affect the A_V estimates.

There are still two second-order features to explain about the $\Delta A_V \times \Delta \langle \log t \rangle_L$ C-run maps in Fig. 2. First, the inner contours have a slightly positive slope, opposite to that expected from

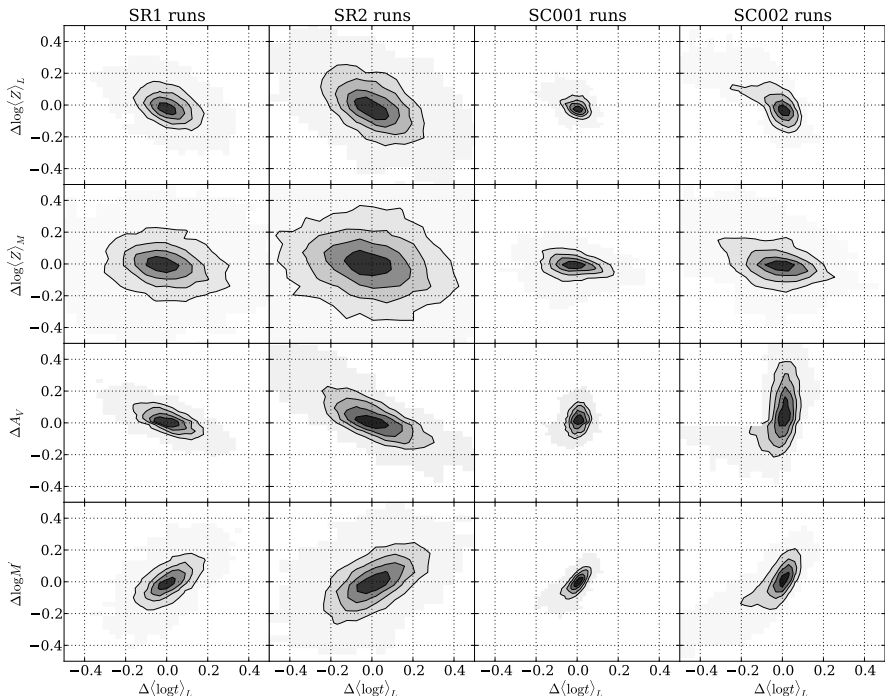


Fig. 2. Illustration of the correlated Δ variations of ages, metallicities, extinction, and masses. Each column corresponds to one set of simulations. Iso-density contours mark 20, 40, 60, and 80% of enclosed points.

the age-extinction degeneracy (clearly seen in the SR1 and SR2 panels). This behaviour arises because our shape-perturbations (where $\Delta \log F_\lambda$ changes linearly with λ) cannot be fully absorbed by the reddening curve used in the fits, because of the different functional forms. Since changing A_V alone is not quite enough to produce optimal spectral fits,

searches for other ways of making the synthetic spectrum redder or bluer (depending on the sign of the perturbation), and skewing the age mixture is the most effective one. In any case, the change in mean age is small: $\overline{\Delta(\log t)_L} = -0.04$ for SC002 runs (Table 2). Secondly, for SC002 runs, the outer contours, which contain about 20% of the points, are limited to $\Delta A_V \leq 0$ whenever simulated mean ages are more than 0.1 dex younger than the original ones ($\Delta(\log t)_L < -0.1$). Spectra along this odd-looking ridge were originally fitted with $A_V = 0$, and then perturbed to bluer colors. Since our fits do not allow $A_V < 0$, they were fitted with the same A_V (hence $\Delta A_V = 0$), but younger ages, leading to the pattern observed in this panel.

3.1.5. Checking the effects of imposing $A_V \geq 0$

As seen just above, the effects of a hypothetical systematic redness associated to spectroscopic calibration problems are almost entirely absorbed by biasing A_V upward, while an excessive blueness of the same nature stumbles upon the $A_V \geq 0$ constraint, leading to biases in the age mixture. An artificial way

of fixing this asymmetry is to allow for $A_V < 0$ in the spectral fits. A trivial statistical justification to allow for this unphysical possibility is that when A_V is truly = 0, unbiased estimates should oscillate around 0, including both negative and positive values. We also note that completely independent studies (different methods, different data) also allow for or deduce negative extinctions (e.g. Kauffmann et al. 2003, their Fig. 11).

An extra set of OE0-like simulations, but imposing $A_V > -1$, was run to investigate this issue. In practice what happens is that only zones that were originally fitted with $A_V \sim 0$ are systematically refitted with negative A_V . The 591 zones that result in $A_V < 0$ in these new fits include all the 582 for which we had originally found $A_V = 0$, and the remaining 9 had A_V very close to 0. The mean new A_V of these 591 zones was -0.12 mag, with a standard deviation of 0.08 mag. The lowest value reached was $A_V = -0.4$ mag, but in only 16% of the cases A_V went below -0.2 mag. The variations in other global properties (for these same 591 zones) were $\overline{\Delta(\log t)_L} = +0.12$, $\overline{\Delta(\log t)_M} = +0.12$, $\overline{\Delta \log(Z)_L} = -0.07$, $\overline{\Delta \log(Z)_M} = -0.04$, and $\overline{\Delta \log M'} = +0.03$ dex. Mean ages are the most affected property, but to an acceptably small degree, with biases of the same order as the one- σ variations produced by random and shape-related uncertainties at the nominal level (R1 and C002 simulations).

Zones originally fitted with $A_V > 0$ did not show systematic variations in their global properties in these extra runs.

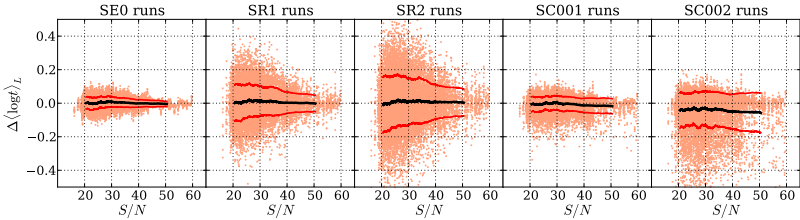


Fig. 3. $\Delta(\log t)_L$ variations for all 1638 zones \times 10 realizations plotted against the S/N of the corresponding original (observed) spectra. The different panels correspond to different sets of simulations, as labeled. The lines are the running mean of $\Delta(\log t)_L$ and the corresponding $\pm 1\sigma$ intervals.

3.1.6. The effect of S/N

The Δ histograms in Fig. 1 and the statistics in Table 2 represent the uncertainties of the CALIFA 277 data set as a whole, including zones of different S/N. The general expectation is that a lower S/N leads to larger uncertainties, such that the tails of the Δ distributions in Fig. 1 are dominated by the noisier spectra, while the cores (small Δ values) correspond to a higher S/N.

To verify this, Fig. 3 shows the $\Delta(\log t)_L$ variations against the S/N of the original spectra. The lines represent the mean $\pm 1\sigma$ range. Uncertainties do decrease with increasing S/N in the SE0, SR1, and SR2 runs, but not in the C-runs. This is in fact expected because the shape perturbations have the same amplitude for all spectra, independent of their S/N. The right-most panel illustrates the bias toward younger ages that results from the $A_V \geq 0$ barrier.

We note in passing that, as hinted in Fig. 3, the distribution of S/N values in CALIFA 277 is skewed toward the target minimum S/N of 20 stipulated in the spatial-binning scheme explained in Paper I. This same threshold was applied to all other datacubes, so the uncertainty estimates presented here should be representative of the CALIFA data in general, even though they are based on a single galaxy.

3.2. Exploring the statistics in IFS data: uncertainties in radial profiles

So far our error analysis has treated the datacube as a collection of unrelated spectra. Spectral synthesis does not care where a spectrum comes from, so the positional information provided by IFS has no effect on the uncertainties for individual zones. However, averaging results obtained for different zones brings obvious statistical benefits, reducing uncertainties in properties derived from individual spectra.

Figure 10 in Paper I shows azimuthally averaged profiles for a series of global properties. Despite the scatter at any given radius, gradients in age and metallicity were clearly detected in CALIFA 277. Figure 4 in this paper repeats that plot, but now showing the radial profiles derived from the simulated spectra, so that we can evaluate the uncertainties in azimuthal averages. The original profiles are plotted in solid black, while colored shades represent the ranges spanned by OR1 (blue) and C002 (red) runs. Each panel also shows an (arbitrarily shifted) simulation minus the original difference profile at its bottom.

As expected, random noise does not change the radial profiles significantly. A small bias of about 0.02 mag is seen in $\bar{A}_V(R)$ for radii beyond ~ 1 half light radius (HLR). This is again a side effect of the $A_V \geq 0$ constraint: when a spectrum originally fitted with $A_V \sim 0$ is perturbed, some will be refitted with

$A_V > 0$, but none will be refitted with $A_V < 0$. The resulting bias propagates to minor offsets in other properties, like slightly younger ages (panels e and f). Overall, however, these are all tiny effects.

Color perturbations (red-shaded regions) produce larger effects. The main effect is on the $A_V(R)$ profile (panel c), where the typical offset matches the expected $\bar{\Delta}(A_V) = 0.05$ mag reported in Table 2. Leaving aside this bias, the $\bar{A}_V(R)$ variations are much smaller than those in individual zones. For instance, considering all radial bins and all 10×1638 versions of the OC002 spectra, the rms in $\Delta(A_V)$ is only 0.05 mag, while individual zones are subjected to uncertainties of $\sigma(A_V) = 0.16$ mag (Fig. 1).

Larger than typical variations occur in the nucleus for the trivial reason that it comprises a single spaxel, so that no actual statistics is performed. More robust results for the nucleus require extending its definition to include more spaxels. For instance, Pérez et al. (2013) define the nucleus as the inner 0.1 HLR, which in the case of CALIFA 277 comprises the central-most nine spaxels. Uncertainties also increase in the outer regions ($R > 2$ HLR), induced by the lower S/N of the spectra and by the decrease in the number of zones compared with intermediate radii.

Figure 4 confirms the expected gain in dealing with averaged results. The simulations show that the uncertainties in the radial profiles are just too small to question the reality of the age and metallicity gradients in this galaxy. This conclusion holds even for our most pessimistic simulations (C004 and R3). This gain comes at the expense of a loss of spatial information—compressing the x, y plane to a single dimension (R) in the example presented here. Other forms of spatial averaging can be envisaged, such as isolating structural components (bulge, disk, bar, arms, inter-arm regions). From the results above, it is easy to see that as long as enough zones are involved in the statistics, any averaging scheme should lead to small uncertainties.

3.3. Uncertainties in star formation histories

outputs SFHs as population vectors: x and μ . The first gives the fractional contribution of each base element to the total flux at the chosen reference wavelength (5635 Å in our case), while the latter gives the corresponding mass fractions. The 39 ages in our base⁵ sample the 1 Myr to 14 Gyr interval with a mean $\log t$ separation of just 0.1 dex. Individually, the strength of each component is not reliable (see Fig. 1 in Cid Fernandes et al. 2004 for an example), given the many ways that spectrally

⁵ The base ages were chosen such that SSP spectra for ages in between t_j and t_{j+1} are adequately interpolated with the j and $j + 1$ SSPs (see Mateus et al. 2006 for more details).

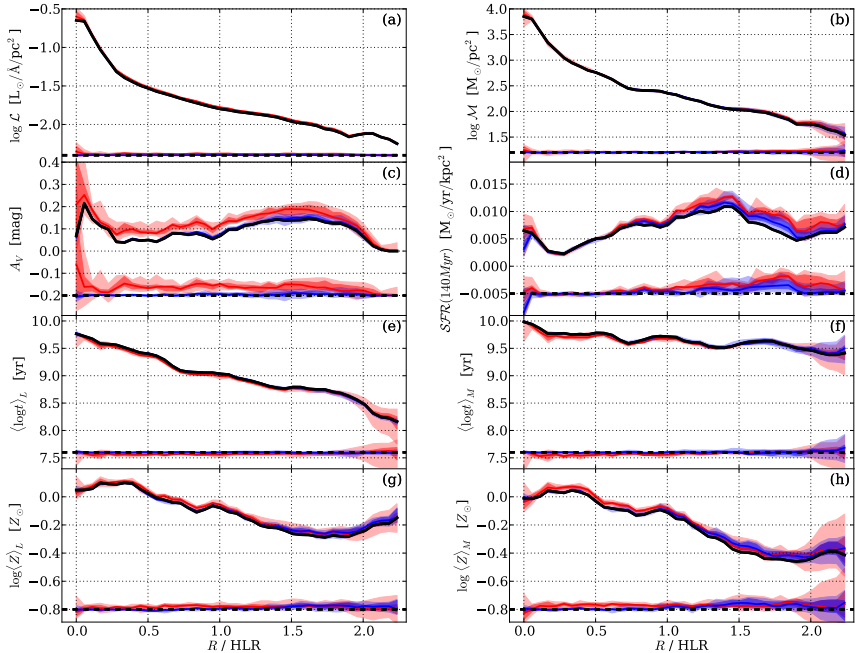


Fig. 4. Azimuthally averaged radial profiles of some global properties. **a)** Dereddened luminosity surface density at 5635 Å; **b)** stellar mass surface density; **c)** extinction; **d)** SFR surface density over the last 140 Myr; **e)** luminosity and **f)** mass-weighted mean log ages; **g)** luminosity and **h)** mass weighted mean metallicities. The original solution is shown as the solid black line, while those obtained from simulations are shown in colored shades. Light-blue shades show the full range of values found among the ten realizations of random noise (OR1 runs). The darker blue bands mark the range spanned by the six values closer to the median (marked with the blue solid line). OC002 simulations of color-change effects are plotted in red. The differences between the simulations and original profiles are shown at the bottom of each panel, with the zero level indicated by the dashed black line. The dispersion and offsets along these difference profiles give a measure of the uncertainties and biases involved in the radial profiles.

similar components can rearrange their x_j values to produce a similar total spectrum. Yet, their combination in indices such as $\langle \log t \rangle_L$ produces robust quantities, as shown by the simulations.

None of the properties studied in the previous sections relies heavily on the details of the spectral decomposition performed by [Bica et al. \(2004\)](#). Mean ages, for instance, are defined as the *first moment* of the age distributions encoded in \mathbf{x} and $\boldsymbol{\mu}$. By construction, however, SFHs do rely on higher-order descriptions of the age distribution. This section aims to evaluate the uncertainties in our SFHs. Before doing so, we digress on the actual meaning of the “H” in SFH.

There is no standard semantics for the meaning of “history” in spectral synthesis studies. On the contrary, the same term is used in very different ways in the literature, always qualitatively referring to some measure of the how star formation unfolded over time, but quantitatively varying from estimates of mean ages to measures of the “recent” star formation (where recent can mean anything between ~ 10 Myr and a few Gyr, depending on the tracers), and full t -by- t descriptions with varying age resolution. In addition to different timescales, different metrics can be used to quantify the SFH, such as luminosity or mass associated to stars in a given age range, in differential or cumulative forms, etc. This diversity is particularly natural

in the case of non-parametric codes such as [Pipetti et al. \(2013\)](#). Because no pre-established functional forms for $SFR(t)$ are imposed, one has plenty of freedom to design different indices and functions for characterizing the SFH. Paper I is itself an example of this diversity. We have presented there a series of SFH diagnostics obtained by manipulating the \mathbf{x} and $\boldsymbol{\mu}$ vectors in different ways, always with the underlying philosophy of compressing the overly-detailed output of [Pipetti et al. \(2013\)](#) into coarser but more robust descriptions of the SFH.

In short, there are numerous alternative ways to describe an SFH. In what follows we evaluate the uncertainties in a paper I-inspired selection of SFH-descriptions. Following the sequence of our analysis of global properties, we first present results for uncertainties in individual zones (Sect. 3.3.1) and then for spatially averaged SFHs (Sect. 3.3.2).

3.3.1. SFHs for individual zones

One way to characterize SFHs is to compress the population vectors into age ranges, an approach that dates back to the early days of spectral synthesis ([Bica 1988](#)). In the context of [Pipetti et al. \(2013\)](#), [Cid Fernandes et al. \(2004 and 2005\)](#) showed that a robust summary of the SFH can be obtained by binning \mathbf{x}

Table 3. Uncertainties in light fraction in age groups: $\overline{\Delta x} \pm \sigma_{\Delta x}$ [%].

log t range	OE0	OR1	OR2	OR3	OC001	OC002	OC004
6.0→8.2	0.0 ± 1.9	0.1 ± 3.3	-0.0 ± 4.9	-0.0 ± 6.0	0.1 ± 2.2	0.6 ± 2.7	1.6 ± 4.2
8.2→9.2	0.0 ± 4.5	-0.1 ± 9.3	0.7 ± 14.9	1.2 ± 18.9	0.7 ± 6.8	4.3 ± 14.7	9.4 ± 23.2
9.2→10.2	-0.1 ± 4.0	-0.2 ± 8.7	-1.0 ± 14.0	-1.7 ± 17.9	-0.8 ± 6.4	-5.0 ± 14.8	-11.6 ± 23.9
6.0→7.5	-0.0 ± 1.4	-0.2 ± 3.0	-0.4 ± 4.7	-0.6 ± 5.8	0.0 ± 1.6	0.3 ± 2.4	0.8 ± 4.0
7.5→8.5	-0.4 ± 3.1	-0.7 ± 5.9	-1.3 ± 8.4	-1.7 ± 10.1	-0.4 ± 3.5	-0.4 ± 4.8	-0.1 ± 7.2
8.5→9.3	0.0 ± 4.4	0.0 ± 9.4	0.6 ± 15.1	1.2 ± 19.2	0.7 ± 6.7	4.5 ± 14.7	9.8 ± 23.3
9.3→9.7	-0.1 ± 5.5	-0.7 ± 12.8	-2.3 ± 19.6	-4.0 ± 23.8	-0.6 ± 7.7	-3.2 ± 13.2	-7.4 ± 18.2
9.7→10.2	-0.1 ± 3.4	0.1 ± 10.4	0.4 ± 16.4	1.0 ± 20.1	-0.4 ± 5.6	-2.3 ± 11.0	-5.0 ± 15.4

Notes. As Table 2, but with the statistics of the light fractions in age groups for our different simulations. For each age group the table lists the mean simulated minus original difference (Δ) and its standard deviation (σ_{Δ} , in bold), both in percentages. The top part of the table corresponds to the young, intermediate and old groups description discussed in the text and Fig. 5, while the bottom one is for the five groups used in Fig. 6. The R1 and C002 columns are those applicable to CALIFA data.

into young (Y), intermediate (I) and old (O) groups. This $\mathbf{x} \rightarrow (x_Y, x_I, x_O)$ compression scheme was employed to produce the maps shown in Figs. 8 and 9 of Paper I, where these age groups were separated by frontiers placed at $t = 0.14$ and 1.4 Gyr.

We have used our simulations to assess the uncertainties in these fractions. The top three rows in Table 3 list the O-run statistics of Δx_Y , Δx_I and Δx_O , where, as before, $\Delta \equiv$ simulated – original value. The table shows that random noise at the one- σ level (R1 runs) induces uncertainties in x_Y , x_I and x_O of ~ 3 , 9 and 9% respectively⁶. Larger uncertainties ($\sim 15\%$) in x_I and x_O apply for shape-changing perturbations at the level expected for CALIFA (OC002 runs). Part of this increase is due to the aforementioned $A_V \geq 0$ effect, which forces low A_V zones that are perturbed to bluer spectra to become younger to compensate for the inability to reduce A_V below 0. This is also reflected in the biases, with $\overline{\Delta}(x_I) \sim -\overline{\Delta}(x_O) \sim +5\%$. At any rate, comparing these uncertainties with $(\overline{x}_Y, \overline{x}_I, \overline{x}_O) = (15, 25, 60)\%$, the average values over all zones in CALIFA 277, one concludes that this compact description of the SFH is reasonably robust.

Figure 5 show how the variations in these light fractions correlate with each other. Δx_O anti-correlates very strongly with Δx_I , which is not surprising given the $x_Y + x_I + x_O = 100\%$ constraint and the fact that these are the age groups that carry most of the light in CALIFA 277. The Y group, on the other hand, is roughly independent of the others.

Figure 6 shows OR1-based results for a finer-graded description using five age groups defined by $\log t[\text{yr}] = 6-7.5$, $7.5-8.5$, $8.5-9.3$, $9.3-9.8$, and $9.8-10.2$. The anti-correlations among adjacent age groups are visible along the diagonal. The $\sigma_{\Delta x}$ values are 3, 6, 9, 13, and 10% (Table 3) for mean fractions of $\overline{x}_i = 13, 3, 24, 34$ and 26%, respectively. This more detailed description shortens the difference between $\sigma_{\Delta x}$ values and the corresponding \overline{x}_i . The uncertainties are therefore larger, as expected, but these higher-resolution SFHs are still useful, especially if used in a statistical way.

As the name implies, μ fits light, so x -based SFH descriptions are the natural way to analyze its results. Yet, it is the stellar mass which carries the astrophysical information on the galaxy history. One can obviously group μ elements just as we did for \mathbf{x} , but while light fractions in different age groups can be directly intercompared, mass fractions cannot. With a factor of ~ 1000 decrease in light-to-mass ratio from the youngest to

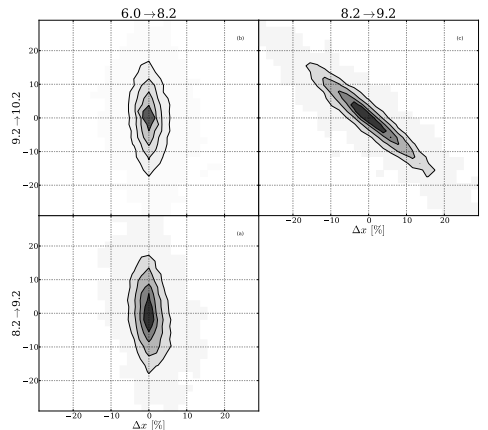


Fig. 5. Variations in the light fractions in young, intermediate, and old age groups (spanning $\log t = 6-8.2$, $8.2-9.2$ and $9.2-10.2$, respectively) for OR1 simulations. Contours are drawn at 20, 40, 60, and 80% of enclosed points.

the oldest elements in the base, wildly different mass fractions, say, $\mu_Y \sim 1\%$ and $\mu_O \sim 99\%$, can be equally relevant for the fits.

To evaluate uncertainties in the masses associated to different age groups it is better to use the masses themselves instead of mass fractions. Table 4 reports the uncertainties in $\log M'$, where the prime denotes the initial stellar mass, uncorrected for the mass returned to the interstellar medium by stellar evolution. The table reports the results of the simulations for both the (Y, I, O) and the five age groups descriptions of the SFH discussed above. Again, the fact that we are now exploring higher moments of the age distribution implies larger uncertainties than for global properties. A column-by-column comparison with the $\Delta \log M'$ statistics in Table 2 confirms this. For instance, while the total masses have uncertainties of just 0.08 dex in OR1 runs, the masses in age-groups are typically three times more uncertain, an unavoidable but still reasonable price to pay for a time-resolved description of results of the spectral synthesis.

Additional subdivisions lead to a quasi-continuous regime that is better handled in ways other than age-binning, such as

⁶ Note that % here does *not* mean a relative deviation, but the very units of the x_Y , x_I , and x_O fractions.

Table 4. Uncertainties in log mass in age groups.

log t range	OE0	OR1	OR2	OR3	OC001	OC002	OC004
6.0→8.2	0.00 ± 0.14	-0.00 ± 0.21	-0.02 ± 0.30	-0.03 ± 0.37	0.00 ± 0.16	0.02 ± 0.20	0.06 ± 0.29
8.2→9.2	0.00 ± 0.12	-0.01 ± 0.25	-0.00 ± 0.37	-0.00 ± 0.44	0.01 ± 0.18	0.08 ± 0.28	0.15 ± 0.36
9.2→10.2	-0.00 ± 0.05	-0.00 ± 0.12	-0.01 ± 0.19	-0.02 ± 0.24	-0.01 ± 0.08	-0.04 ± 0.20	-0.05 ± 0.33
6.0→7.5	-0.00 ± 0.11	-0.02 ± 0.18	-0.05 ± 0.27	-0.07 ± 0.32	-0.00 ± 0.12	0.01 ± 0.14	0.02 ± 0.18
7.5→8.5	-0.00 ± 0.22	-0.01 ± 0.35	0.06 ± 0.43	0.09 ± 0.49	0.00 ± 0.24	0.03 ± 0.29	0.12 ± 0.39
8.5→9.3	0.00 ± 0.12	-0.00 ± 0.24	0.01 ± 0.35	0.03 ± 0.41	0.01 ± 0.18	0.08 ± 0.28	0.16 ± 0.36
9.3→9.7	0.00 ± 0.14	-0.01 ± 0.25	-0.02 ± 0.34	-0.03 ± 0.39	-0.01 ± 0.17	-0.03 ± 0.24	-0.04 ± 0.31
9.7→10.2	-0.00 ± 0.11	-0.01 ± 0.24	-0.00 ± 0.34	0.02 ± 0.38	-0.01 ± 0.15	-0.03 ± 0.27	-0.00 ± 0.36

Notes. As Table 3, but for the (log) initial masses associated to stellar populations in different age groups. Each entry lists $\overline{\Delta \log M'} \pm \sigma_{\Delta \log M'}$ (in dex).

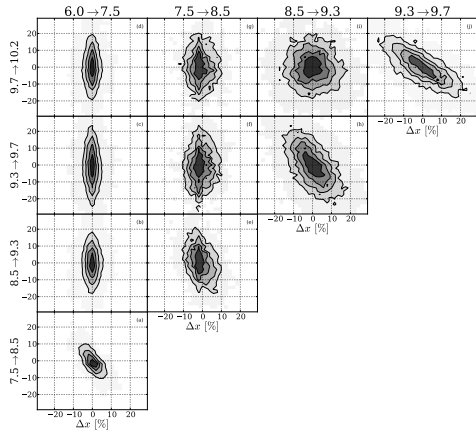


Fig. 6. As Fig. 5, but for a finer-graded description of the SFH in terms of five age groups.

cumulating x or μ . Figure 7 illustrates this. The left panels show the cumulative light fraction, shown after a cosmetic smoothing by a $FWHM = 0.2$ dex Gaussian in $\log t$. Six individual zones, including the nucleus (top) and the last one (bottom), were chosen to exemplify this alternative description of SFHs and its uncertainties. The thick solid line traces the original solution, while thin gray lines trace the solutions obtained for each of the ten OR1 perturbations, whose median is drawn as a dashed line. The red-shaded bands mark the range spanned by the six SFHs closer to the median at each t . The right panels show the corresponding mass assembly histories, all scaled to 100% at $t = 0$. The six zones in Fig. 7 cover different distances from the nucleus, S/N, and SFHs, thus providing representative examples of results for CALIFA data.

Except for the nucleus, where the perturbed spectra and the associated SFHs are nearly indistinguishable from the original ones because of the very high S/N, there is a clear spread in cumulative light and mass distributions. The dispersion is higher for ages older than a few Gyrs, which contain a substantial fraction of the light and most of the mass. The mild spectral evolution in this age range (Conroy 2013) explains the larger uncertainties, because components can be interchanged with relatively little variation in the total spectrum. Gauging the uncer-

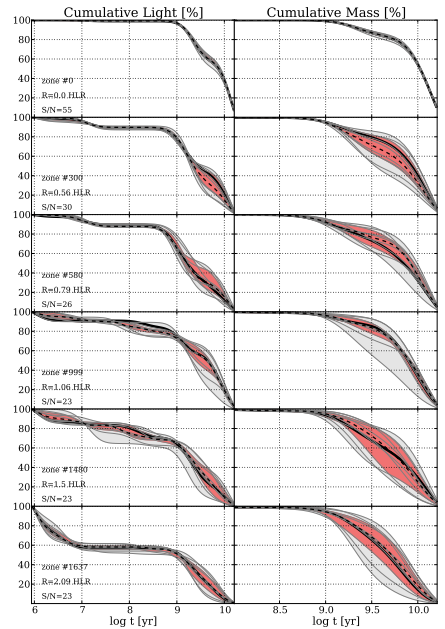


Fig. 7. SFHs of six different spatial zones, as represented by their cumulative light (left) and mass (right) distributions. Each panel shows 11 SFHs. The original one is plotted in thick black lines. Gray lines show the SFHs for the ten realizations of OR1 simulations, with a gray-shaded band tracing the full range of values. The median SFH is drawn as a dashed line, while the red band marks the range spanned by the six runs closer to the median. The zone number, distance to the nucleus, and the S/N are labeled in the left panels.

tainties in the cumulative SFHs by the width of the red band, we find it to be of the order of 10–20%, comparable to those reported in Tables 3 and 4 for age-grouped quantities.

Despite uncertainties, the example SFHs in Fig. 7 reveal a gradual shift toward younger ages for larger radii. This trend is the higher-order description of the clear mean age radial gradients previously shown in panels e and f of Fig. 4, where results for individual zones at same R were averaged.

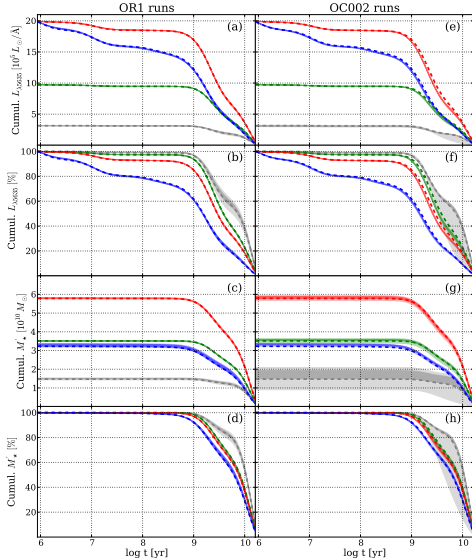


Fig. 8. Spatially averaged cumulative light and mass histories and their uncertainties for four regions: red, blue, green and grey colors correspond to regions $R > 1$, $R < 1$, $R < 0.5$ HLR and the nucleus, respectively. *Left and right panels* show OR1 and OC002 simulations, respectively. The *top four panels* show cumulative light distributions, in both absolute (a), (e) and relative (b), (f) units. Similarly, the bottom four panels show the corresponding mass distributions. In each panel and for each radial region the original solution is drawn as a dashed line, while results of the simulations are shown with shaded bands, hardly visible except for the nuclear curves (grey). Light shaded bands show the ranges spanned by all 10 perturbations, and darker shades indicate the range spanned by the 6 versions closer to the median. The nuclear curves in panels (a), (e) and (g) contain much less light and mass than the others, and so were multiplied by 20 for clarity.

3.3.2. Spatially averaged SFHs

In analogy with Sect. 3.2, uncertainties in the SFHs of individual zone spectra should be greatly reduced when averaging over spatial regions comprising many zones. This is confirmed in Fig. 8, which shows cumulative light and mass distributions (in both absolute and relative units) for four spatial regions: the nucleus (gray), $R < 0.5$ (green), $R < 1$ (red), and $R > 1$ HLR (blue). The smoothing here is by $FWHM = 0.5$ dex in $\log t$ for compatibility with Fig. 11 of Paper I. OR1 runs are shown in the left panels, OC002 in the right panels.

The statistical damping of the uncertainties is so strong that one can hardly notice that, as in Fig. 7, shaded bands are used to show the vertical ranges spanned by the simulations. The bands are so narrow that they look like thick lines. The exception is the nucleus (gray), where the uncertainties are visible for the simple reason that unlike for other regions, it does not involve any actual spatial averaging because it comprises a single spaxel.

Close inspection of the right panels reveals that the shape-changing simulations tend to have SFHs slightly skewed toward younger ages than SFHs inferred from spectral fits of the original data (marked by dashed lines). This is again the effect of some

perturbations making low A_V zones too blue to be fitted with $A_V \geq 0$, so ΔA_V compensates it with lower ages.

In conclusion, spatial averaging effectively eliminates the dispersions seen in the SFHs of individual zones. This remains valid even for simulations where the level of perturbations is higher than that expected for CALIFA spectra.

3.4. Summary of the simulations

The overall message from these experiments is that degeneracies inherent to stellar populations and uncertainties in the data have a limited impact upon our analysis. For the level of uncertainties expected in CALIFA, here represented by the R1 and C002 runs, the simulations yield acceptably small uncertainties in global properties. More precisely, mean ages and metallicities have one sigma variations of ~ 0.1 dex when weighted in luminosity and ~ 0.15 weighting by mass, while stellar masses are good to ~ 0.1 dex (round numbers), with negligible biases. Uncertainties in A_V are ~ 0.07 mag if only random noise is considered, increasing to 0.16 mag when shape-related uncertainties are accounted for. In the latter case, a bias of $\Delta A_V \sim 0.06$ mag appears as a side-effect of forbidding negative A_V . Because they are a higher-order product of the spectral synthesis, SFHs are naturally less strongly constrained than global properties, but the age-grouped and cumulative descriptions explored above were found to be relatively stable against random and spectral-shape perturbations.

It is a consensus in the field of spectral synthesis that the results are best used in a statistical sense (e.g., Panter et al. 2006), and the present study endorses this view. First, averaging reduces uncertainties, as confirmed by our experiments with radial profiles (Fig. 4) and spatially averaged SFHs (Fig. 8), which showed that the results are stable against the types of uncertainties studied here. Second, and more importantly, large samples allow for *comparative* studies, which can reveal astrophysically valuable trends while mitigating worries about data or method-related systematics affecting the absolute values. This point has been abundantly explored in spectral synthesis studies of SDSS galaxies, where unequivocal relations between, for instance, age, mass, and metallicity, have been identified in spite of the uncertainties in the properties derived for individual galaxies. The analogy with IFS data is clear. In IFS each galaxy is a large sample by itself, and the very goal of IFS is to compare properties in one place with those somewhere else.

This concludes our study of data- and method-related uncertainties. This whole study was based on a single set of SSP models, a fundamental prior in the analysis. We now turn to the uncertainties resulting from this choice.

4. Uncertainties associated to evolutionary synthesis models: an empirical evaluation

SSP spectra are the key astrophysical ingredient in any spectral synthesis analysis, the dictionary that translates stellar properties into spectroscopic information, which can then be compared with data through different methods to extract physical properties and SFHs. The computation of model SSP spectra combines an assumed initial mass function (IMF) with stellar evolution theory (isochrones) and a library to provide the spectra of stars with temperature, gravity, and chemical composition matching the values dictated by the evolutionary tracks. In practice, this algebraic exercise stumbles upon a series of problems that directly affect the predicted SSP spectra.

Table 5. Sets of SSP models used for spectral fitting.

Model-set	Code	Isochrones	IMF	Library	Metallicities	$N_Z \times N_t$	Ages [Gyr]
GM	SED@ + Vazdekis	Padova 2000	Salpeter	GRANADA + MILES	0.004, 0.008, 0.019, 0.033	4×39	0.001–14
CB	GalaxeV	Padova 1994	Chabrier	GRANADA + MILES	0.004, 0.008, 0.02, 0.05	4×40	0.001–14
BC	GalaxeV	Padova 1994	Chabrier	STELIB	0.004, 0.008, 0.02, 0.05	4×40	0.001–14

First, despite its (well-deserved) status as a founding stone of modern astrophysics, stellar evolution is still an open business. Rotation in massive stars (Levesque et al. 2012), rapid phases during the post-main-sequence evolution of intermediate-mass stars (Maraston 2005), and binarity (Li et al. 2013) are examples of phenomena that affect the radiative output of stellar populations, but are still at the forefront of research, and thus prone to uncertainties. A practical example of how incomplete treatment of evolutionary phases affects spectral synthesis analysis is discussed by Koleva et al. (2008), Cid Fernandes & González Delgado (2010), and Ocvirk (2010). Using different codes, these studies found that spectral synthesis of old Milky Way and LMC globular clusters suggests the presence of very young stellar populations accounting for some 10–20% of the optical light, an astrophysically absurd result that also happens in some old, “red and dead” galaxies (Cid Fernandes et al. 2011). These “fake young bursts” (Ocvirk 2010) are in fact by-products of inadequate modeling of the horizontal branch (and/or blue stragglers, Cenarro et al. 2008). Seeking for a best match, the spectral synthesis uses young hot stars to replace the old hot ones missing in the models.

Second, spectral libraries, whether empirical or theoretical, have their own limitations (Martins & Coelho 2007). The widely used Bruzual & Charlot (2003; BC03) models, for instance, are based on the STELIB library (Le Borgne et al. 2003), a major advance in its days, but limited to 249 stars, some of which have severe spectral gaps. Its relatively poor coverage of the stellar parameter space propagates to the predicted SSP spectra, with collateral effects on the results of a spectral synthesis analysis. Koleva et al. (2008), for instance, noticed that because of the lack of truly very metal-rich stars in the library, BC03 spectra for $2.5 Z_{\odot}$ SSPs behave like $\sim Z_{\odot}$ models of an older age. In short, this too is an evolving field, undergoing constant revisions.

In this unstable scenario, it is relevant to evaluate to which extent the results of our spectral synthesis analysis depend on the choice of SSP models. To this end, we performed spectral fits using three bases extracted from different sets of evolutionary synthesis models, listed in Table 5. We stress that this is by no means an exhaustive exploration of this matter, but it suits our goal of estimating uncertainties related to this choice. Section 4.1 describes the sets of models to be compared. The CALIFA data used in this study are described in Sect. 4.2. Comparisons of the properties obtained with different sets of SSPs are presented in Sect. 4.3. Fit-quality indicators and spectral residuals are discussed in Sect. 4.4, while Sect. 4.5 compares residuals in CALIFA and SDSS spectra.

4.1. SSP spectral models

Base GM is a combination of publicly available SSP spectra from Vazdekis et al. (2010)⁷, which start at an age of 63 Myr, with the González Delgado et al. (2005)⁸ models for younger ages. The former are based on stars from the MILES

library (Sánchez-Blázquez et al. 2006), while the latter relies on the synthetic stellar spectra from the library (Martins et al. 2005). Only minor adjustments were needed to match these two sets of models. First, we smoothed the models to the spectral resolution of MILES (2.5 \AA FWHM, cf. Beifiori et al. 2011 and Falcón-Barroso et al. 2011), and then multiplied them by a factor of 1.05, estimated from a direct comparison of the predicted spectra in the 63 Myr to 1 Gyr range, where these models agree very well in both continuum shape and absorption features. These independently derived SSP spectra complement each other, providing a base suitable for spectral fitting analysis of galaxies of all types.

The evolutionary tracks in base GM are those of Girardi et al. (2000), except for the youngest ages (1 and 3 Myr), which are based on Geneva tracks (Schaller et al. 1992; Schaerer et al. 1993a,b; Charbonnel et al. 1993). The specific subset of SSPs used in the spectral fits comprises 39 ages between 1 Myr and 14 Gyr. Four metallicities are included: $Z = 0.2, 0.4, 1,$ and 1.5 solar. The Salpeter IMF is adopted. Like the other bases discussed next, GM does not adequately cover the blue horizontal branch, both because it does not reach very low Z and because, as thoroughly discussed by Ocvirk (2010), these models perform poorly in this phase anyway.

Base CB is an updated version of the BC03 models (Charlot & Bruzual 2007, priv. comm.), replacing STELIB by spectra from the MILES and libraries. The IMF is that of Chabrier (2003), and the evolutionary tracks are those by Alongi et al. (1993), Bressan et al. (1993), Fagotto et al. (1994a,b), and Girardi et al. (1996), collectively labeled “Padova 1994” by BC03. $N_t = 160$ SSPs comprising 40 ages in the 1 Myr to 14 Gyr range and four metallicities (0.2, 0.4, 1, and $2.5 Z_{\odot}$) were chosen for the spectral fits.

Finally, base BC is built from the “standard” BC03 models, whose ingredients are identical to those of base CB except for the stellar library, which is STELIB. Base BC allows us to check whether differences between results obtained with bases GM and CB are associated to isochrones and/or IMF instead of stellar libraries.

These three bases cover the same age range, and all have the same number of metallicities. All bases start at $Z = 0.004$ ($0.2 Z_{\odot}$)⁹, but GM stops at $1.5 Z_{\odot}$, while both CB and BC extend to $2.5 Z_{\odot}$. Because they are both based on stars not far from the Sun, neither MILES nor STELIB actually contain many stars as metal-rich as $2.5 Z_{\odot}$, hence the latter models should be interpreted with care. On the other hand, the $Z \leq 1.5 Z_{\odot}$ limit of base GM may be too low to accommodate the metal-rich inner regions of galaxies, possibly leading to saturation effects. Base GM also differs from the others in IMF and isochrones. The differences in opacities and equation of state between Padova 2000 (GM) and 1994 (CB and BC) tracks produce somewhat warmer (hence bluer) stars in the red giant branch in the former than in the latter.

⁹ We excluded lower metallicity models to avoid SSPs that are not so well covered by the stellar libraries. Base GM base could include SSPs at $Z = 0.001$, but we chose not to do this because this metallicity is not available in the CB and BC models.

⁷ miles.iac.es

⁸ www.iaa.csic.es/~mcs/sed@

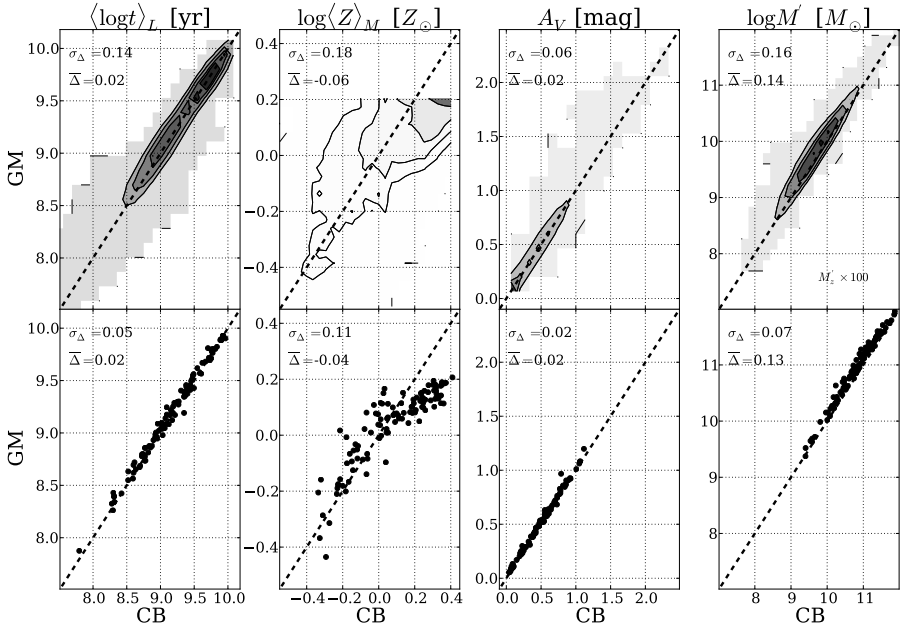


Fig. 9. Comparison of the global properties obtained with different bases GM (vertical axis) and CB (horizontal). The *top panels* compare luminosity-weighted ages ($\langle \log t \rangle_L$), mass-weighted metallicities ($\log \langle Z \rangle_M$), extinction (A_V), and initial stellar masses ($\log M'$) obtained for $\sim 10^5$ zones of 107 CALIFA galaxies, with contours drawn at every 20% of enclosed points. The *bottom panels* repeat the comparisons, but now for galaxy-wide values. A one-to-one line is drawn in all panels. Note that zone masses in the *top-right panel* are multiplied by 100 to put them on the same scale as the *bottom panel*.

In principle, one may thus expect to obtain older ages with GM than with CB and BC, but the differences in color are very small in the spectral range of our data, only becoming noticeable at longer wavelengths (see Fig. 2 of BC03).

4.2. Data: 98291 spectra from 107 CALIFA datacubes

The experiments described below were based on data with the same characteristics and pre-processed in the exact same way as the data for CALIFA 277. The difference with respect to the simulations presented in the first part of this paper is that we now use 107 galaxies, out of which a total of 98291 spectra corresponding to individual spaxels (or Voronoi zones) were extracted following the methodology outlined in Paper I.

Fits of these spectra were carried out using the three bases described above. Our interest here is to identify and quantify differences in the results obtained with different model SSPs, so we overlook the spatial information and treat each spectrum as an individual. We now use this massive dataset to compare the results obtained with bases GM, CB, and BC.

4.3. Comparison of global properties

Figure 9 compares results obtained with bases CB (horizontal axis) and GM (vertical). The top panels compare values of $\langle \log t \rangle_L$, $\log \langle Z \rangle_M$, A_V and $\log M'$ for all 98291 individual zones, grayscale-coding by the density of points. Note the wide ranges of values in all panels, illustrating the diversity of properties

spanned by the data. Each panel quotes the mean Δ and its standard deviation, where $\Delta = \text{property(GM)} - \text{property(CB)}$.

GM-based initial stellar masses are higher than CB ones by 0.14 dex on-average, reflecting their different IMFs¹⁰. Apart from this offset, the two masses agree to within 0.16 dex. Mean ages and extinctions also agree well, with dispersions of 0.14 dex in $\langle \log t \rangle_L$ and 0.06 mag in A_V , and insignificant offsets. Metallicities are obviously related, but with a substantial scatter due to a combination of the difference in evolutionary tracks and IMF, coarse Z grids, intrinsic difficulties in estimating metallicities, and the aforementioned difference in maximum Z.

To estimate the effect of this in-built difference we carried out experiments replacing the $2.5 Z_\odot$ SSPs in CB by models interpolated to $1.5 Z_\odot$, thus matching the Zs in GM. This modified CB base produces $\log \langle Z \rangle_M$ values that differ by $\sigma_\Delta \sim 0.15$ dex from the GM-based ones, slightly better than the 0.18 dex obtained with the original CB. Leaving aside caveats associated to the interpolation of SSP spectra, this result indicates that the difference in maximum Z between GM and CB has a relatively modest impact on the difference between $\log \langle Z \rangle_M$ values obtained with these two bases, so that differences in evolutionary tracks and IMF are also relevant.

The bottom panels repeat the comparison of the same four properties, but now for galaxy-wide values, so there are only

¹⁰ We recall that M' refers to the initial stellar mass. The difference between GM and CB masses increases to 0.27 dex when stellar mass loss is accounted for.

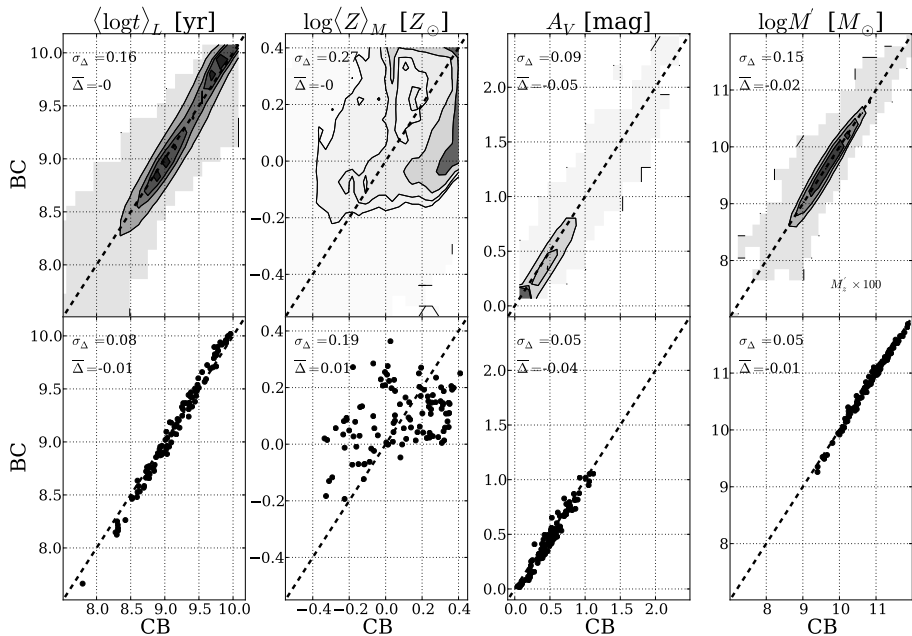


Fig. 10. As Fig. 9, but comparing results obtained with base CB (horizontal axis) and BC (vertical). Ages, extinction, and masses agree well, but BC-based mean metallicities differ significantly from both CB and GM-based estimates.

107 points¹¹. These cleaner plots confirm the results from the zone-by-zone comparison. Naturally, galaxy-wide averages are much more robust than values for individual zones, so the σ_{Δ} dispersions are significantly lower than those quoted in the top panels. $\langle Z \rangle_M$ estimates distribute around the identity line up to Z_{\odot} , where the relation bends down due to the differences in the maximum Z between the bases. In these cases all one can be sure of is that metallicities are over-solar.

Figure 10 compares results for bases BC (vertical axis) with CB (horizontal axis). Masses, ages, and extinctions agree to within 0.15 dex, 0.16 dex, and 0.09 mag, respectively, with a tendency of A_V to be 0.04 mag smaller in BC fits. This relatively good level of agreement does not apply to mass weighted metallicities, which differ substantially. Given that these two sets of models coincide in isochrones, IMF and evolutionary synthesis code, this disagreement must be related to the stellar libraries. Because of the several improvements in MILES over STELIB (Sánchez-Blázquez et al. 2006), metallicities from the CB and GM bases should be considered more reliable than those obtained with BC (see also Koleva et al. 2008). This is in line with previous empirical tests by González Delgado & Cid Fernandes (2010), who showed that MILES based SSP spectra perform better than STELIB-based ones in matching the metallicities of star clusters

derived from spectroscopy of individual stars or CMD analysis of the same systems.

Figure 11 shows histograms of the pair-wise Δ s: GM – CB (top), BC – CB (middle), GM – BC (bottom). The width of these histograms (the σ_{Δ} values listed in each panel) gives a measure of the uncertainties related to the choice of evolutionary synthesis models for the spectral fits. As usual, mass-weighted properties present larger uncertainties than luminosity-weighted ones. Metallicities, for instance, have dispersions in $\Delta \log \langle Z \rangle_L$ of 0.14 and 0.19 dex (GM versus CB, and BC versus CB, respectively), lower than the 0.18 and 0.27 dex found for $\Delta \log \langle Z \rangle_M$.

The overall conclusion of these comparisons is that from a statistical perspective, physical properties obtained from a spectral synthesis analysis do not depend strongly on the choice of SSP models. Mean ages and extinctions retrieved with the three models investigated here all agree to within relatively small margins, and the same is true for stellar masses once in-built differences in IMFs are accounted for. Metallicities are generally harder to estimate, and our experiments confirm this. Unlike other properties, mean Z s are sensitive to the choice of models. Base BC gives the most discrepant results, highlighting the influence of stellar libraries.

Rounding up numbers, we find that uncertainties related to the SSP models adopted in the analysis are about 0.15 dex in $\langle \log t \rangle_L$, 0.23 dex in $\langle \log t \rangle_M$, 0.15 dex in $\log M'$, and 0.1 mag in A_V . Excluding BC models, $\log \langle Z \rangle_L$ and $\log \langle Z \rangle_M$ have uncertainties of 0.14 and 0.18 dex, respectively.

¹¹ M' in this case is the sum of the M'_i values for each zone. The galaxy-wide $\langle \log t \rangle_L$ is obtained from $\sum_j \log t_j \sum_z L_{jz} / \sum_j \sum_z L_{jz}$, where j is the base age index and z is a zone index. $\langle Z \rangle_M$ is computed analogously. Lastly, the galaxy-wide A_V is defined as the mean A_{Vz} of all its zones.

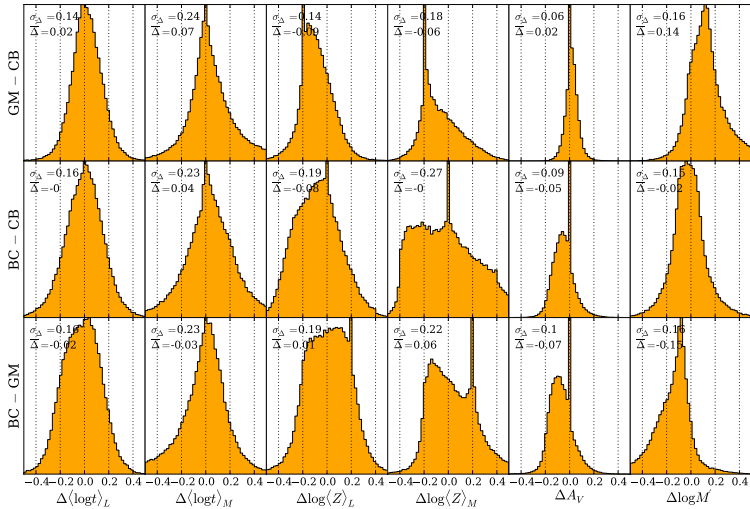


Fig. 11. Histograms of differences in global properties obtained with bases GM, CB and BC. Δ s are defined as GM – CB in the *top panels*, BC – CB in the *middle*, and BC – GM in the *bottom ones*. The horizontal scale is the same as in Fig. 1 to facilitate the comparison of data- and method-related uncertainties with the model-related ones.

4.3.1. Models versus data- and method- related uncertainties

How do these uncertainties compare with those related to the data and synthesis method derived in the first part of this article?

To answer this, we focus on the OR1 and OC002 simulations described in Sect. 2.1, because they represent random noise and shape-calibration errors in CALIFA. Comparing the σ_{Δ} values in Fig. 11 with those for the OR1 simulations in Fig. 1, we see that the former are roughly twice as high as the latter. In fact, the σ_{Δ} values in the top panels of Fig. 11 are closer to those obtained in the simulations where the noise was artificially amplified by a factor of 2 (OR2 runs in Table 2). Shape-related uncertainties also lead to uncertainties somewhat smaller than those found in this section, with the exception of A_V , whose uncertainty is 0.16 mag in the OC002 runs but 0.1 mag or less in ΔA_V histograms in Fig. 11. A visual comparison of Figs. 1 and 11 corroborates the conclusion that uncertainties related to differences among SSP models are larger than those related to data and method.

These comparisons, however, are not entirely fair, since model-related uncertainties were evaluated from $\sim 10^5$ zones of 107 galaxies, while data- and method- related uncertainty estimates were based on 1638 zones of a single galaxy, perturbed ten times in the simulations. Repeating Fig. 11 for CALIFA 277 alone, we still find σ_{Δ} values higher than those found in Sect. 3, but by a smaller margin. The important message, therefore, is not so much that variance among current SSP spectral models leads to larger uncertainties than those related to data and method, but that both types of uncertainties are of the same order.

4.4. Quality of spectral fits

In principle, one could use the quality of the spectral fits as a criterion to favor one base over another. In practice, however, all bases studied here provide \sim equally good fits to the data. This

is illustrated in Fig. 12, which shows the distributions of two figures of merit. Green, red, and blue correspond to bases GM, CB, and BC, respectively. The histograms are nearly identical. Considering all 98291 fits, the mean (median) values of the relative spectral deviation (Eq. (6) of Paper I) are $\bar{\Delta} = 4.33$ (3.92), 4.34 (3.93) and 4.37 (3.94) % for bases GM, CB, and BC respectively, while the corresponding mean (median) χ^2 per fitted flux are 1.14 (0.96), 1.15 (0.97), and 1.18 (0.99). Formally, this puts base GM in first place, with CB in second and BC in third, but these statistics reveal that it is clearly not possible to favour one or another model in terms of fit quality. Because of their more complete spectral libraries, we favor bases GM and CB over BC.

Figure 13 provides a more direct visualization of the quality of the spectral fits. The top panel shows (in black) the average of all zone spectra (for examples of fits to individual zones see González Delgado et al., in prep.). Each spectrum is first divided by the median flux in the 5590–5680 Å normalization window, such that all zones weight equally in the average. The average synthetic spectra are shown in green, red, and blue for fits with bases GM, CB, and BC, respectively, vertically offset for clarity. The corresponding residual spectra are shown in the bottom of the same panel, but can hardly be distinguished on this scale. This similarity persists even after zooming-in by a full order of magnitude in the flux scale, as shown in Fig. 13b. Gaps in this zoomed plot correspond to our generic emission line mask, i.e., λ -windows that were ignored in the fits. Note that, because of bad-pixel flags, augmented by windows around telluric features (Paper I), the number of spectra involved in these averaged residuals varies for each λ , as shown in the bottom panel.

4.5. Spectral residuals and comparison with SDSS

Clearly, the amplitude of the average spectral residuals is very small. Whereas the typical relative deviation for fits of individual

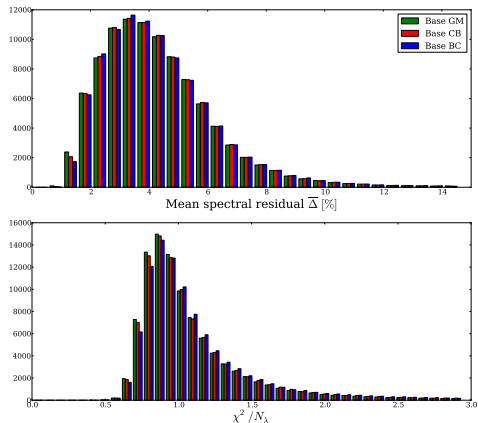


Fig. 12. *Top:* distribution of the mean percentual spectral deviation for fits with the GM (bars in green), CB (red) and BC (blue) bases. *Bottom:* as above, but for the distribution of χ^2 per fitted flux. In both cases the distributions are essentially identical, reflecting the fact that the three bases provide equally good spectral fits.

zones is $\bar{\Delta} \sim 4\%$ (Fig. 12), for the average spectra in Fig. 13 it is a tiny $\bar{\Delta} = 1\%$. This four-fold reduction indicates that random noise is responsible for a large share of the residuals in spectral fits of individual zones. Yet, if the residuals were truly random, this reduction should be by a factor of the order of $\sqrt{98\,291} \sim 300$, not just 4. Residuals may be small, but they are definitely real.

The systematics of the spectral residuals are visible in Fig. 13b. These deviations must be related to problems in the method, data, and/or models.

The narrow positive peaks in the average residual spectrum are due to our fitting method. They are in fact emission lines not included in our generic emission line mask. [NeIII] λ 3869, H8 λ 3889, [NI] λ 5199, and [OI] λ 6364 are the clearest ones in Fig. 13b, but weaker lines such as H9 λ 3835 and HeI λ 6678 are identified upon closer inspection. The conservative clipping parameters adopted in the fits (see Paper I) prevent from automatically clipping these lines completely. Other -based studies circumvented this problem by building emission line masks tailored for each spectrum individually (Mateus et al. 2006; Asari et al. 2007), a refinement that is yet to be implemented in our CALIFA pipelines.

The most noticeable features in Fig. 13b, however, are not the emission lines, but the broad $O_{\lambda} < M_{\lambda}$ trough around H β and the $O_{\lambda} > M_{\lambda}$ bumps in the 5800–6000 Å region. To understand whether these features are particular to CALIFA data, we compiled SDSS spectra for 50 galaxies in common with the current sample and analyzed them using the same masks, wavelength range, sampling, and configuration as used for CALIFA. These spectra were then averaged as in Fig. 13, and compared with the spectral statistics obtained from the nuclear CALIFA spectra of the same 50 galaxies. Figure 14 shows the results of this comparison. The figure follows the same layout as Fig. 13, with spectral statistics for the 50 CALIFA nuclei and the corresponding SDSS spectra plotted in the left and right panels, respectively. The spikier appearance of the SDSS residuals

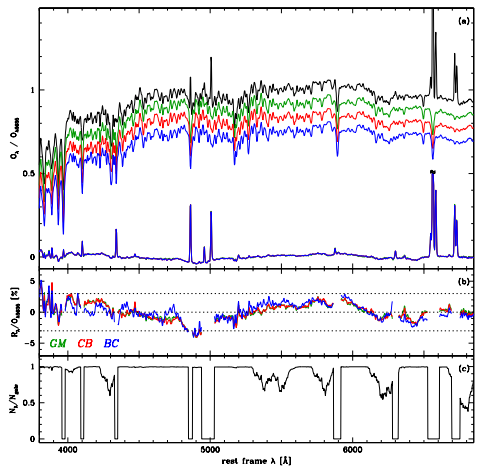


Fig. 13. **a)** Black line: mean (stacked) normalized spectrum of 98291 zones from 107 CALIFA galaxies, obtained by averaging O_{λ}/O_{15635} . Green, red, and blue lines (offset for clarity): mean synthetic spectra for bases GM, CB, and BC, respectively. The corresponding $(O_{\lambda} - M_{\lambda})/O_{15635}$ residual spectra are shown with the same colors, but they are hardly distinguishable. **b)** Zoom of the spectral residuals in the top panel, with emission lines removed for clarity. Dashed lines mark residuals of $-3, 0$, and $+3\%$. **c)** Fraction of the 98291 zones contributing to the spectral statistics in the *middle panel*.

is due to its higher spectral resolution (3 versus 6 Å FWHM), but this is irrelevant for the broad residual features discussed above.

The humps around the ~ 5800 Å region of CALIFA residuals are clearly absent in the SDSS. These features are seen as shallow slanted bands in Fig. 16 of Husseman et al. (2013), where residuals for 100 galaxies were sorted by redshift. We have tracked the origin of this feature to an imperfect removal of telluric NaI bands around 5900 Å in the observed frame. In analogy with what happened with the SDSS data releases, as CALIFA data are used imperfections like this will be identified and, when possible, corrected for in future updates of the data base.

The trough around H β , however, is present in both SDSS and CALIFA spectra. This problem has been noticed before (Cid Fernandes 2006; Panter et al. 2007; Walcher et al. 2009), but not satisfactorily explained to date. The fact that this feature appears in both data sets suggests that the models overpredict the continuum in a ~ 200 Å wide region centered around H β . On the other hand, the fact that the problem is present for both MILES- and STELIB-based models suggests that its origin is more likely related to data-calibration issues. This latter view is supported by studies such as the one by Ferré-Mateu et al. (2012), where fits of *William Herschel* Telescope long-slit spectra of massive compact galaxies with the Vazdekis et al. (2010) models (included in our GM base) did not reveal the H β trough seen in Fig. 13b. While a full investigation of this matter is beyond the scope of this paper, we note that the trough tends to be more pronounced in younger systems, as previously reported by Cid Fernandes (2006, see his Fig. 5).

The negative residual seen in the region of Mg lines near 5175 Å is almost as strong as the H β trough. This deficit is due

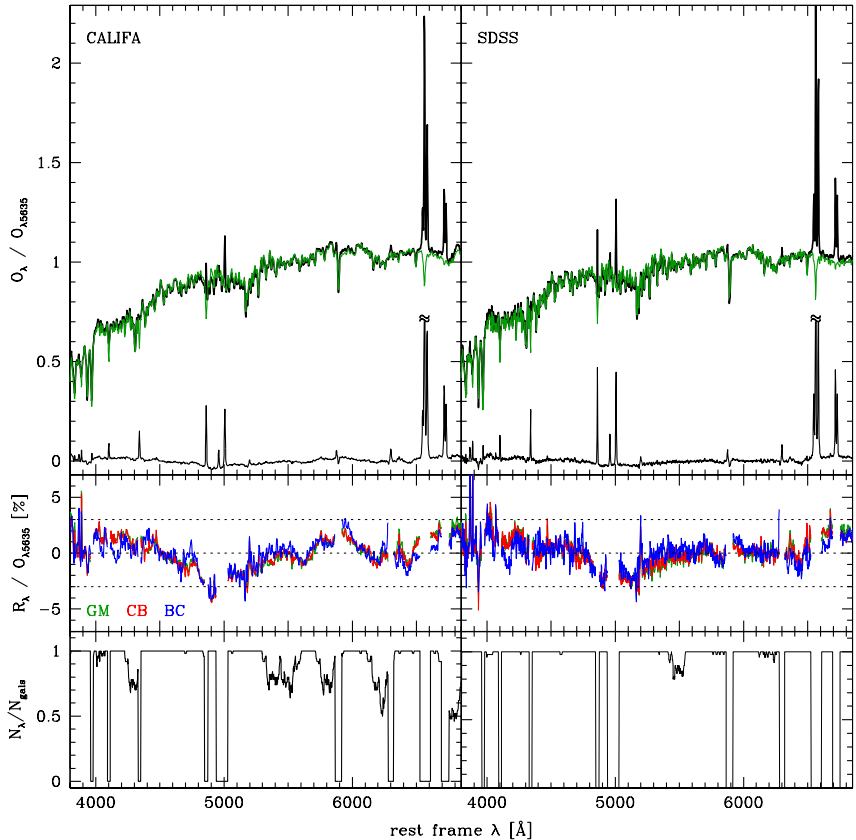


Fig. 14. As Fig. 13, but for a subset of 50 CALIFA galaxies for which SDSS spectra are available. Unlike in Fig. 13, however, the top panels show only results for GM-based spectral fits. Left panels show the spectral statistics for the nuclear extractions of CALIFA datacubes, whereas those on the right show results obtained from fits to the SDSS spectra.

to differences in the abundances of α elements between galaxies (particular the central regions of massive ones) and stars in the stellar libraries. That this residual is stronger in Fig. 14 (nuclear spectra) than in Fig. 13 (all zones) is most likely due to α /Fe gradients. Walcher et al. (2009) reported steps toward incorporating α /Fe in spectral synthesis analysis.

4.6. Public distribution of base GM spectra

Given the good performance of the GM base in the tests discussed in this section, we make these spectra available to the community¹². We stress that these models were produced by González Delgado et al. (2005) and Vazdekis et al. (2010), to whom all credit should be given. Our distribution just puts these two sets of models together.

5. Summary

We have performed an extensive study of the uncertainties in the stellar population properties derived from fits of optical integral field spectra from the CALIFA survey. In the first part of this investigation, Monte Carlo simulations were used to explore the effects of random noise, continuum-shape calibration uncertainties and degeneracies in the spectral synthesis. The simulations are based on the data and fits of 1638 zone spectra of the Sb galaxy CALIFA 277 (NGC 2916). Uncertainties in mean age, metallicity, extinction, stellar mass, and SFHs were evaluated both at the level individual zones (treating the datacube as a collection of unrelated spectra) and exploring the statistical power of IFS by means of radial profiles and other spatial averages. Second, we explored the variations in physical properties caused by using different sets of models for SSP spectra. We compared physical properties and spectral

¹² www.iaa.es/~rosa/AYA2010/AYA2010

residuals obtained from fits with three different SSP bases: (a) a combination of the Gonzalez Delgado et al. (2005) and Vazdekis et al. (2010) models (GM); (b) preliminary Charlot & Bruzual models using the and MILES libraries (CB); (c) the standard Bruzual & Charlot (2003) models with STELIB (BC). This comparison employed $\sim 10^5$ spectra from 107 CALIFA galaxies.

Our main results can be summarized as follows:

1. The level of noise in CALIFA spectra leads to one- σ uncertainties in mean ages and metallicities of ~ 0.08 dex when weighting in luminosity and ~ 0.15 dex weighting by mass. Stellar masses are uncertain at the ~ 0.08 dex level, while $\sigma(A_V)$ is about 0.06 mag.
2. Shape-related calibration uncertainties of 0.05 mag in $g-r$ produce uncertainties on the same order as those induced by random noise, except for A_V , which becomes uncertain at the level of $\sigma \sim 0.16$ mag and biased by $+0.05$ mag.
3. Time-resolved SFHs are higher-order products of the spectral synthesis, inevitably subjected to larger uncertainties than global properties. For instance, we found that, for individual zones, stellar masses formed in broad age ranges have uncertainties about three times larger than those of the mass formed over all times. While SFHs of individual zones do carry useful information, a statistical approach is more advisable.
4. Spectral synthesis results are best used in comparative studies involving large samples, and IFS data fit this requirement perfectly. Spatial averaging reduces uncertainties while preserving enough information on the history and structure of stellar populations. Radial profiles of mean ages, metallicities, mass density, and extinction are found to be very robust due to the large number statistics of datacubes. For instance, uncertainties in the data and limitations of the synthesis have a negligible impact upon the negative age and metallicity gradients detected in CALIFA 277. Similarly, SFHs averaged over different spatial regions are much more stable than those obtained for individual zones.
5. Mean ages, extinction, and stellar masses obtained with GM, CB, and BC models are reasonably consistent with one another, with one- σ differences in $(\log t)_L$, $(\log t)_M$, $\log M^*$, and A_V of ~ 0.15 , 0.24, 0.15 dex, and 0.08 mag, respectively. GM and CB produce luminosity- (mass-) weighted metallicities consistent to within 0.14 (0.18) dex rms, while BC-based metallicities hardly correlate with the others. The variations induced by the use of different SSP models are larger than uncertainties due to data and method by roughly a factor of 2, highlighting the important role of this ingredient in the whole analysis.
6. The quality of the spectral fits is very nearly the same whichever set of SSP models is used. Spectral residuals are on the order of 4% for individual zones and 1% when averaged over all zones and galaxies. The strongest feature in the residual spectra is a broad but shallow ($\sim 3\%$) trough around H β , also present in SDSS spectra, and its origin remains unidentified. Other systematic features in the residual spectra were tracked to incomplete masking of weak emission lines, imperfect removal of telluric features, and the lack of α enhanced models in the base.

These results, along with the tables and figures in this paper, fulfill our goal of assessing the uncertainties on the several products of applied to CALIFA datacubes presented in Paper I. The combination of these spatial and temporal diagnostics of stellar populations with the diversity of galaxy types

in the CALIFA survey offers new ways of studying galaxy evolution, that we aim to explore in other publications by our collaboration, and this paper provides quantitative and qualitative guidelines on how to interpret them appropriately.

Acknowledgements. CALIFA is the first legacy survey being performed at Calar Alto. The CALIFA collaboration would like to thank the IAA-CSIC and MPA-MPG as major partners of the observatory, and CAHA itself, for the unique access to telescope time and support in manpower and infrastructures. We also thank the CAHA staff for the dedication to this project. R.C.F. thanks the hospitality of the IAA and the support of CAPES and CNPq. A.L.A. acknowledges support from INCT-A, Brazil. BH gratefully acknowledges the support by the DFG via grant Wi 1369/29-1. Support from the Spanish Ministerio de Economía y Competitividad, through projects AYA2010-15081 (PI RGD), AYA2010-22111-C03-03 and AYA2010-10904E (SFS), AYA2010-21322-C03-02 (PSB) and the Ramón y Cajal Program (S.F.S., P.S.B. and J.F.B.), is warmly acknowledged. We also thank the Viabilidad, Diseño, Acceso y Mejora funding program, ICTS-2009-10, for funding the data acquisition of this project. Funding for the SDSS and SDSS-II has been provided by the Alfred P. Sloan Foundation, the Participating Institutions, the National Science Foundation, the U.S. Department of Energy, the National Aeronautics and Space Administration, the Japanese Monbukagakusho, the Max Planck Society, and the Higher Education Funding Council for England. The SDSS Web Site is <http://www.sdss.org/>. The SDSS is managed by the Astrophysical Research Consortium for the Participating Institutions. The Participating Institutions are the American Museum of Natural History, Astrophysical Institute Potsdam, University of Basel, University of Cambridge, Case Western Reserve University, University of Chicago, Drexel University, Fermilab, the Institute for Advanced Study, the Japan Participation Group, Johns Hopkins University, the Joint Institute for Nuclear Astrophysics, the Kavli Institute for Particle Astrophysics and Cosmology, the Korean Scientist Group, the Chinese Academy of Sciences (LAMOST), Los Alamos National Laboratory, the Max-Planck-Institute for Astronomy (MPIA), the Max-Planck-Institute for Astrophysics (MPA), New Mexico State University, Ohio State University, University of Pittsburgh, University of Portsmouth, Princeton University, the United States Naval Observatory, and the University of Washington.

References

- Alongi, M., Bertelli, G., Bressan, A., et al. 1993, *A&AS*, 97, 851
 Asari, N. V., Cid Fernandes, R., Stasińska, et al. 2007, *MNRAS*, 381
 Beifiori, A., Maraston, C., Thomas, D., & Johansson, J. 2011, *A&A*, 531, A109
 Bica, E. 1988, *A&A*, 195, 76
 Bressan, A., Fagotto, F., Bertelli, G., & Chiosi, C. 1993, *A&AS*, 100, 647
 Cenarro, A. J., Cervantes, J. L., Beasley, M. A., Marin-Franch, A., & Vazdekis, A. 2008, *Apl*, 689, L29
 Charbonnel, C., Meynet, G., Maeder, A., Schaeller, G., & Schaerer, D. 1993, *A&AS*, 101, 415
 Chabrier, G. 2003, *PASP*, 115, 763
 Cid Fernandes, R. 2006, *BAAA*, 49, 228
 Cid Fernandes, R., & González Delgado, R. M. 2010, *MNRAS*, 403, 780
 Cid Fernandes, R., Gu, Q., Melnick, J., et al. 2004, *MNRAS*, 355, 273
 Cid Fernandes, R., Mateus, A., Sodré, L., Stasińska G., & Gomes J. M. 2005, *MNRAS*, 358, 363
 Cid Fernandes, R., Stasińska, G., Mateus, A., & Vale Asari, N. 2011, *MNRAS*, 413, 1687
 Conroy, C. 2013 [[arXiv:1301.7095](https://arxiv.org/abs/1301.7095)]
 Fagotto, F., Bressan, A., Bertelli, G., & Chiosi, C. 1994a, *A&AS*, 104, 365
 Fagotto, F., Bressan, A., Bertelli, G., & Chiosi, C. 1994b, *A&AS*, 105, 29
 Falcón-Barroso, J., Sánchez-Blázquez, P., Vazdekis, A., et al. 2011, *A&A*, 532, A95
 Ferré-Mateu, A., Vazdekis, A., Trujillo, I., et al. 2012, *MNRAS*, 423, 632
 Girardi, L., Bressan, A., Chiosi, C., Bertelli, G., & Nasi, E. 1996, *A&AS*, 117, 113
 Girardi, L., Bressan, A., Bertelli, G., & Chiosi, C. 2000, *A&AS*, 141, 371
 González Delgado, R. M., Cerviño, M., Martins, L. P., Leitherer, C., & Hauschildt, P. H. 2005, *MNRAS*, 357, 945
 González Delgado, R. M., & Cid Fernandes, R. 2010, *MNRAS*, 403, 797
 González Delgado, et al. 2012, *Highlights of Astronomy*, Vol. 15, XXVIIIth IAU General Assembly
 González Delgado, R., Pérez, E., Cid Fernandes, R., et al. 2013, *The intriguing life of massive galaxies*, Proc. IAU Symp., 295
 Husemann, B., Jahnke, K., Sánchez, S. F., et al. 2013, *A&A*, 549, A87
 Kauffmann, G., Heckman, T. M., White, S. D. M., et al. 2003, *MNRAS*, 341, 33

- Koleva, M., Prugniel, P., Ocvirk, P., Le Borgne, D., & Soubiran, C. 2008, MNRAS, 385, 1998
- Le Borgne, J.-F., Bruzual, G., Pelló, R. et al. 2003, A&A, 402, 433
- Levesque, E. M., Leitherer, C., Ekstrom, S., Meynet, G., & Schaerer, D. 2012, ApJ, 751, 67
- Li, Z., Mao, C., Chen, L., Zhang, Q., & Li, M. 2013, ApJ, submitted [[arXiv:1302.0927](https://arxiv.org/abs/1302.0927)]
- Maraston, C. 2005, MNRAS, 362, 799
- Martins, L. P., & Coelho, P. 2007, MNRAS, 381, 1329
- Martins, L. P., González Delgado, R. M., Leitherer, C., Cerviño, M., & Hauschildt, P. 2005, MNRAS, 358, 49
- Mateus, A., Sodr , L., Cid Fernandes, R., et al. 2006, MNRAS, 370, 721
- Ocvirk, P. 2010, ApJ, 709, 88
- Panther, B., Heavens, A. F., & Jimenez, R. 2003, MNRAS, 343, 1145
- Panther, B., Jimenez, R., Heavens, A. F., & Charlot, S. 2007, MNRAS, 378, 1550
- P rez, E., Cid Fernandes, R., Gonz lez Delgado, R. M., et al. 2013, ApJ, 764, L1
- S nchez, S. F., Kennicutt, R. C., Gil de Paz, A. et al. 2012, A&A, 538, A8
- S nchez-Bl zquez, P., Peletier, R. F., Jim nez-Vicente, J., et al. 2006, MNRAS, 371, 703
- S nchez-Bl zquez, P., Ocvirk, P., Gibson, B. K., P rez, I., & Peletier, R. F. 2011, MNRAS, 415, 709
- Schaerer, D., Charbonnel, C., Meynet, G., Maeder, A., & Schaller, G. 1993a, A&A, 102, 339
- Schaerer, D., Meynet, G., Maeder, A., & Schaller, G. 1993b, A&AS, 98, 523
- Schaller, G., Schaerer, D., Meynet, G., & Maeder, A. 1992, A&AS, 96, 269
- Tojeiro, R., Heavens, A. F., Jimenez, R., & Panther, B. 2007, MNRAS, 381, 1252
- Vazdekis, A., S nchez-Bl zquez, P., Falc n-Barroso, J., et al. 2010, MNRAS, 404, 1639
- Walcher, C. J., Coelho, P., Gallazzi, A., & Charlot, S. 2009, MNRAS, 398, L44

D.3. The Evolution of Galaxies Resolved in Space and Time: A View of
Inside-out Growth from the CALIFA Survey

D.3 The Evolution of Galaxies Resolved in Space and Time: A
View of Inside-out Growth from the CALIFA Survey

Artigo por Pérez et al. (2013) (doi : [10.1088/2041-8205/764/1/L1](https://doi.org/10.1088/2041-8205/764/1/L1)). Também disponível em *preprint* (arXiv: [1301.1679](https://arxiv.org/abs/1301.1679)).

THE EVOLUTION OF GALAXIES RESOLVED IN SPACE AND TIME: A VIEW OF INSIDE-OUT GROWTH FROM THE CALIFA SURVEY

E. PÉREZ¹, R. CID FERNANDES^{1,2}, R. M. GONZÁLEZ DELGADO¹, R. GARCÍA-BENITO¹, S. F. SÁNCHEZ^{1,3}, B. HUSEMANN⁴,
D. MAST^{1,3}, J. R. RODÓN¹, D. KÜPKO⁴, N. BACKSMANN⁴, A. L. DE AMORIM², G. VAN DE VEN⁵, J. WALCHER⁴,

L. WISOTZKI⁴, C. CORTIJO-FERRERO¹, AND CALIFA COLLABORATION⁶

¹ Instituto de Astrofísica de Andalucía (CSIC), Glorieta de la Astronomía s/n, E-18008 Granada, Spain; eperez@iaa.es

² Departamento de Física, Universidade Federal de Santa Catarina, Florianópolis, Brazil

³ Centro Astronómico Hispano Alemán, Calar Alto, (CSIC-MPG), Jesús Durbán Remón 2-2, E-04004 Almería, Spain

⁴ Leibniz-Institut für Astrophysik Potsdam, An der Sternwarte 16, D-14482 Potsdam, Germany

⁵ Max-Planck-Institut für Astronomie, Königstuhl 17, D-69117 Heidelberg, Germany

⁶ CALIFA International Collaboration; <http://califa.caha.es>

Received 2012 October 23; accepted 2012 December 24; published 2013 January 22

ABSTRACT

The growth of galaxies is one of the key problems in understanding the structure and evolution of the universe and its constituents. Galaxies can grow their stellar mass by accretion of halo or intergalactic gas clouds, or by merging with smaller or similar mass galaxies. The gas available translates into a rate of star formation, which controls the generation of metals in the universe. The spatially resolved history of their stellar mass assembly has not been obtained so far for any given galaxy beyond the Local Group. Here we demonstrate how massive galaxies grow their stellar mass inside-out. We report the results from the analysis of the first 105 galaxies of the largest three-dimensional spectroscopic survey to date of galaxies in the local universe (CALIFA). We apply the fossil record method of stellar population spectral synthesis to recover the spatially and time resolved star formation history of each galaxy. We show, for the first time, that the signal of downsizing is spatially preserved, with both inner and outer regions growing faster for more massive galaxies. Further, we show that the relative growth rate of the spheroidal component, nucleus, and inner galaxy, which happened 5–7 Gyr ago, shows a maximum at a critical stellar mass $\sim 7 \times 10^{10} M_{\odot}$. We also find that galaxies less massive than $\sim 10^{10} M_{\odot}$ show a transition to outside-in growth, thus connecting with results from resolved studies of the growth of low-mass galaxies.

Key words: galaxies: bulges – galaxies: evolution – galaxies: fundamental parameters – galaxies: stellar content – galaxies: structure

Online-only material: color figures

1. INTRODUCTION

The stellar mass of a galaxy, M_* , is one of its most fundamental properties as it provides a measure of the galaxy evolution process. Elucidating how it evolves in space and time, and in relation to other galaxies is central to understanding the processes that govern the efficiency and timing of star formation in galaxies. Look-back time studies of galaxy evolution determine the spatially resolved star formation rate (SFR) at a range of redshifts as a proxy for the average history of a particular type of galaxy (Lilly et al. 1996; Madau et al. 1996; Folkes et al. 1999; York et al. 2000; Bell et al. 2004; Moles et al. 2008; Ilbert et al. 2009; Pérez-González et al. 2008; Nelson et al. 2012). A major handicap of this approach is the inability to follow the evolution of any one galaxy over time (Faber et al. 2007). In this work we follow an alternative approach. For a new set of integral field spectroscopic data of a large sample of galaxies in the local universe, we recover their spatially resolved individual star formation histories (SFH) by means of stellar population spectral synthesis.

Beyond the Local Group, where individual stars are not resolved, a powerful method to reverse engineer the SFH of a galaxy is to find the most plausible combination of evolved single stellar populations (SSPs) that matches its spectrum (Walcher et al. 2011 and references therein). This fossil record method has been applied to images (e.g., Brinchmann & Ellis

2000; Bell & de Jong 2000; Pérez-González et al. 2008; Hansson et al. 2012) with good spatial coverage but poor spectral resolution. It has also been applied to Sloan Digital Sky Survey (SDSS) spectra of many galaxies (Heavens et al. 2004; Brinchmann et al. 2004; Gallazzi et al. 2005; Cid Fernandes et al. 2005, 2011; Panter et al. 2007), although SDSS provides just a single spectrum per galaxy with varying spatial coverage with redshift. The CALIFA survey (Sánchez et al. 2012) provides a set of spectra that covers the extent of each galaxy with good spatial and spectral sampling. Here we report on the spatially resolved growth with cosmic time for 105 galaxies, which sample a wide range of properties in the color–magnitude diagram (CMD), drawn from the full CALIFA survey of 600 galaxies.

2. SAMPLE AND METHODS

Details of the CALIFA survey, sample selection, reduction and calibration methods, and analysis pipeline are provided by Sánchez et al. (2012), Husemann et al. (2012, 2013, CALIFA first public data release DR1), Cid Fernandes et al. (2013), and J. Walcher et al. (2013, in preparation). Here we use the spectral data cubes combining both setups, V500 and V1200 gratings, with median limiting sensitivity 1.0 and 2.2×10^{-18} erg s⁻¹ cm² Å⁻¹ arcsec⁻², spectral resolution ~ 6 Å in the range ~ 3650 – 7500 Å, median spatial resolution $3''.7$, and spectrophotometric calibration better than 15%.

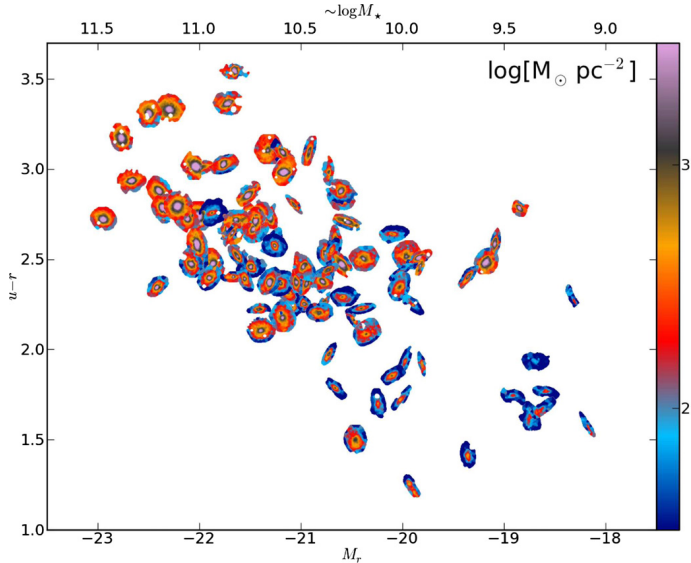


Figure 1. Stellar mass surface density ($M_{\odot} \text{pc}^{-2}$) in the galaxies CMD. Absolute magnitude in SDSS r , M_r , vs. SDSS $u-r$ color, where each galaxy is represented with its present-day stellar mass density distribution. Holes in some galaxies result from removing foreground stars. The upper horizontal axis indicates approximate values of the stellar mass, from a linear fit to the M_r - $\log(M_*)$ relation. The time evolution of the stellar mass buildup of each galaxy in this diagram can be seen in <http://www.iaa.es/~eperez/CALIFA/CMD>.

(A color version of this figure is available in the online journal.)

For each galaxy the data are spatially rebinned to a minimum signal-to-noise ratio of 20 in a continuum band at $5635 \pm 40 \text{ \AA}$ (Cid Fernandes et al. 2013). The stellar spectral synthesis code STARLIGHT (Cid Fernandes et al. 2005) is then used to recover the SFH, including a value for the stellar extinction, from each spectrum. Here we use a set of SSPs sampling the 1 Myr–14 Gyr age range with 40 age bins and four metallicities between 0.2 and 2.5 solar (S. Charlot & G. Bruzual 2007, private communication), assuming a Chabrier initial mass function. This method provides spatially resolved SFHs for ~ 200 –2000 regions per galaxy, which we use to derive a three-dimensional buildup of mass (with two spatial and one temporal coordinates).

3. RESULTS

Figure 1 shows the (M_r , $u-r$) CMD, where each galaxy is represented with its present-day distribution of stellar mass density (in logarithmic units of $M_{\odot} \text{pc}^{-2}$). Since the absolute magnitude M_r of galaxies is roughly proportional to their total $\log(M_*)$ (a main driver of galaxy physics) and the $u-r$ color works as a rough evolutionary clock, the CMD encapsulates galaxy evolution and the diversity of galaxies in a simple and observationally convenient form. Furthermore, given its widespread use in the literature (Faber et al. 2007; Blanton & Moustakas 2009) and the fact the CALIFA sample was defined to cover it as uniformly as possible, the CMD provides a natural framework to present and analyze our results. The general trend in Figure 1 shows more luminous galaxies to be redder, while the color coded mass density image of each galaxy shows that more

luminous ones have a higher central stellar surface density and steeper gradients;⁷ we now see these trends spatially resolved over a five magnitude range in M_r .

Spatially resolved mass distributions have been computed for some galaxies from broadband imaging (e.g., Zibetti et al. 2009; Wuyts et al. 2012). Since we have the spatially resolved SFH for each galaxy, we can also see the time evolution of the CMD. This is shown in the animation <http://www.iaa.es/~eperez/CALIFA/CMD>, with the 10,000–250 Myr age plotted in the top right-hand corner, stopping at a time when galaxies have most of their M_* in place. For clarity, and to emphasize the way M_* grows, galaxies are kept at their present location in the CMD, even though their luminosities and colors would actually change with time. The most luminous, redder, massive galaxies have transformed an important part of their mass into stars already 10 Gyr ago (e.g., Pérez-González et al. 2008), particularly in their central regions, while many of the less massive galaxies show a lower stellar surface density.

Although we can derive the time evolution of the stellar populations at their present-day location, it is not feasible to trace their spatial location at earlier epochs, i.e., we cannot follow the evolution of their motions. If the stars undergo major spatial shuffling over their lives, then our analysis would be hampered. Breaks in the exponential distribution of disk outer regions (e.g., Pohlen & Trujillo 2006; Erwin et al. 2008) have

⁷ With few exceptions, such as the outstanding low surface brightness galaxy at $(-21.87, 2.76)$.

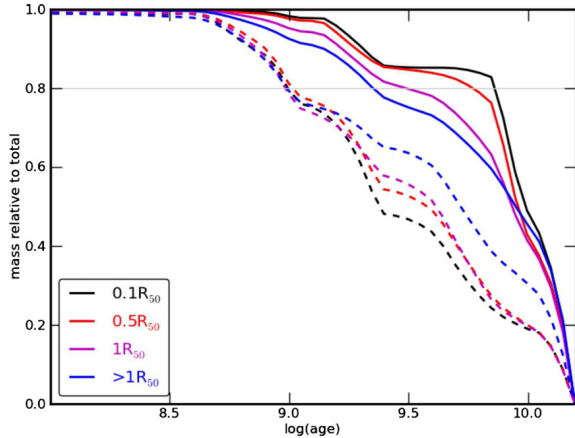


Figure 2. Relative stellar mass growth of four main spatial components (nucleus, inner $0.5 R_{50}$ and $1 R_{50}$, and outer $>1 R_{50}$) for two galaxy mass bins, the lowest (dashed, $\log M_* [M_\odot] \sim 9.58$) and an intermediate (full line, $\log M_* [M_\odot] \sim 10.83$). Each component is normalized to its final M_* . To compute a growth rate, a horizontal gray line at 0.8 marks when each component achieves 80% of its final M_* . At the lowest mass, galaxies’ outskirts grow faster (dashed blue line steeper), but at higher masses the growth proceeds inside-out (full black line steeper). (A color version of this figure is available in the online journal.)

been interpreted as evidence of radial migration, although there is no general consensus. Numerical simulations show that, for secular evolution, the consequences of radial migration are only significant in the outer parts of galaxies, beyond about 2–3 scale lengths (Figure 2 in Roškar et al. 2008; Figures 15 and 16 in Sánchez-Blázquez et al. 2009; Behroozi et al. 2012). Here we partition galaxies into four radial zones to compare their histories, so that the outer regions (at several effective radii) where radial migration may have an impact on the SFH do not have a significant contribution to the results in the analysis that follows.

3.1. Spatially Resolved Growth of Stellar Mass M_*

The animated CMD is a visually compelling tool, but lacks the quantitative information needed to probe the spatial growth of the stellar mass assembly. A more quantitative analysis in Figures 2–5 show the time evolution for four galaxy regions: the nucleus (left, defined as the central $0.1 R_{50}$ ⁸), the region inside $0.5 R_{50}$, the region inside $1 R_{50}$, and the region outside $1 R_{50}$. To make the growth of M_* more visible, galaxies are normalized to a common radial scale in units of R_{50} , and then stacked in seven equally populated bins (15 galaxies each) of increasing present-day galaxy M_* . Figure 2 shows the relative growth of the four spatial components for two M_* bins, the lowest (dashed, $\log M_* [M_\odot] \sim 9.58$) and an intermediate mass (full line, $\log M_* [M_\odot] \sim 10.83$). To compute the M_* growth rate, a gray line marks when each component achieves 80% of its final M_* . Clearly, at higher M_* the growth proceeds inside-out, while at the lowest M_* galaxies’ outskirts grow faster than their inner parts.

Figure 3 shows at a glance the trends for all mass bins. The horizontal axis represents log time (bottom) or redshift (top; $H_0 = 71$, $\Omega_M = 0.27$, $\Omega_\Lambda = 0.73$); the vertical axis

represents the present-day total M_* . Panels show gray scaled the relative growth of each of the four spatial components, normalized to its final stellar mass, so that all components grow up to mass unity (i.e., gray scale and contours in Figure 3 represent for all mass bins the growth curves shown for two example mass bins in Figure 2; the black contour line in each panel marks $0.8 M_*$). Thus, the relative growth of different parts of the galaxy can be assessed. Three M_* growth cuts are plotted corresponding to three mass bins (lowest, intermediate, and highest in blue, green, and red, as colored in their axis mass value). The right-hand side panel shows that outer reaches ($>1 R_{50}$) of less massive galaxies ($\log \text{mass}[M_\odot] \sim 9.58$, in the lower part of the plot) achieve $0.8 M_*$ about 1 Gyr ago, while more massive ones ($\log \text{mass}[M_\odot] \sim 11.26$) had $0.8 M_*$ already ~ 5 Gyr ago. The systematics of this outer galaxy M_* growth is clearly seen from the less massive up to the most massive galaxies in the sample. The central panels show a similar behavior for the inner regions ($1 R_{50}$ and $0.5 R_{50}$), but with a steeper growth at higher galaxy masses. The left panel shows a similar behavior for the nuclei, with an even steeper slope for galaxies more massive than $\log \text{mass}[M_\odot] \sim 10.5$. Thus there is a clear systematic sequence of M_* growth from the inside-out, where the mass is transformed into stars much earlier within $0.5 R_{50}$.

3.2. Spatially Resolved Mean Age of the Stellar Populations

To better understand this result, for each of the spatial regions we compute the age at $0.8 M_*$ (as indicated in Figures 2 and 3). These are represented color coded in Figure 4 (in Gyr, also shown in each box), with the present-day stellar mass of the galaxy in the vertical axis and the spatial zone in the horizontal. Arising from the number of galaxies, statistical errors in the age for each box amount to 0.23 dex, while systematic errors introduced by the choice of other SSP basis (González Delgado et al. 2005) are 0.05 dex (R. M. González Delgado et al. 2013, in

⁸ R_{50} is the circular half-light radius in $5635 \pm 40 \text{ \AA}$.

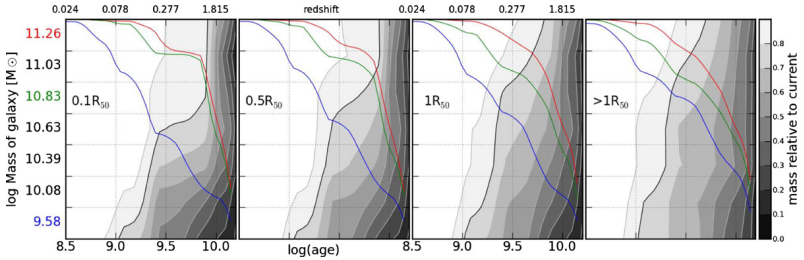


Figure 3. Inside-out stellar mass growth and spatially resolved downsizing. Panels show the normalized growth (gray scale in 10 intervals of 10%, with the 80% contour in black) in time in the four zones of Figure 2. To avoid number statistics biases, the galaxies are stacked in seven equally populated bins of 15 galaxies each, sorted by present-day total stellar mass; this implies that the vertical axis in Figures 3–5 is not uniform in log mass. For each spatial component, the growth is normalized to its total final stellar mass (i.e., the growth curves of Figure 2 are cuts for two of the mass bins through the gray scale and contours). For each zone, three example mass bins growth curves are plotted (lowest, intermediate, and highest in blue, green and red, respectively) showing how the signal of downsizing is spatially preserved (the four blue lines here correspond to the four dashed lines in Figure 2, while the four green lines here correspond to the four full lines in Figure 2); the axis corresponding to these cuts is the same as the gray scale, i.e., the scale 0.0–1.0 on the right-hand side. For a given galaxy mass, the progressive steepening of the growth from the outer ($>1 R_{50}$) toward the nucleus shows the inside-out growth trend with the total mass of a galaxy. At the same time, for a given galaxy region, more massive galaxies grow faster than less massive ones, and this is sustained systematically from the inner to the outer zones.

(A color version of this figure is available in the online journal.)

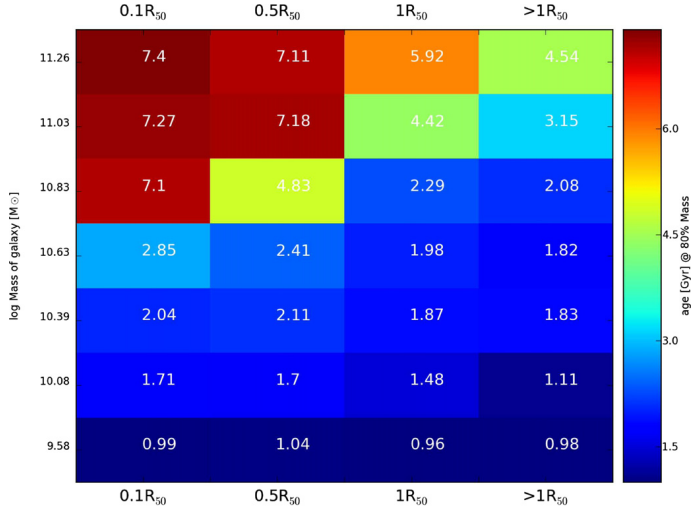


Figure 4. Inside-out stellar mass growth: ages. Using the same vertical axis as in Figure 3, this figure color codes the age at which each spatial component grows to 80% of its final stellar mass; the age (in Gyr) is shown within each box. For a given mass, the horizontal run of color gives the systematic aging from the outer (right) to the inner regions (left). Conversely, for a given galaxy region, the vertical run gives the systematic aging of that zone with increasing galaxy total stellar mass. There is a systematic change with both mass and location for all cases, with the exception of the very low mass galaxies (bottom row) for which there is no inside-out growth (the age at 80% growth is approximately the same in all four spatial components). These diagrams show clearly the differential inside-out growth and its explicit dependence on galaxy mass and galactocentric radius.

(A color version of this figure is available in the online journal.)

preparation). At a glance, it is clear that (1) running vertically for a given galaxy zone, older ages (red) correspond to more massive galaxies, and (2) running horizontally for a given galaxy mass, older ages (red) correspond to the central zones. The trends are clear for all masses and spatial regions, except for the lower mass bin, where there is no evidence of inside-out growth. In fact, the evidence at the lower masses is that galaxies do grow outside-in

(Figure 2), connecting with the behavior seen in studies of dwarf galaxies (e.g., Gallart et al. 2008; Zhang et al. 2012 and references therein).

The increase in mean stellar ages with increasing M_* reflects the downsizing phenomenon previously established on the basis of fossil record analyses of spatially unresolved data (Heavens et al. 2004; Pérez-González et al. 2008). Figures 3 and 4 show,

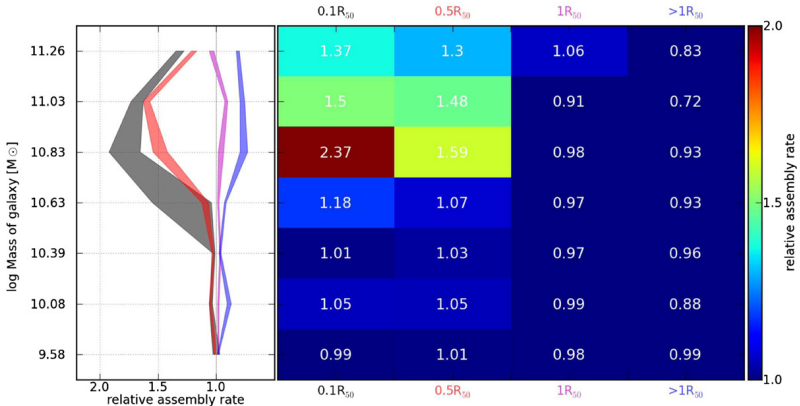


Figure 5. Stellar mass assembly rate. With the same axes of Figure 4, the right panel color codes the relative growth rate at 80% mass, for a given galaxy mass and zone, normalized to the total galaxy growth rate at 80%. The result indicates that for most of the galaxies, on average, the relative rate (within each galaxy) of transforming gas into stars is similar in all parts, except for the central regions ($<0.5 R_{50}$) of galaxies more massive than $\sim 5 \times 10^{10} M_{\odot}$, which are up to a factor of ~ 2 faster. The left panel shows vertical cuts through the four zones, including uncertainty bands computed in 1000 iterations of randomly removing five different galaxies at a time. (A color version of this figure is available in the online journal.)

for the first time, that the signal of downsizing is preserved in a radial fashion, with both inner and outer regions growing faster for more massive galaxies. At the same time, these figures show that different spatial regions in a galaxy grow at different paces.

3.3. Spatially Resolved Growth Rate of the Stellar Populations

To examine the relative growth of inner and outer regions more closely, we compute growth rates from the inverse of the cosmic time span corresponding to the buildup of $0.8 M_{*}$. This is done for each spatial component of each galaxy, and the resulting rates expressed in units of the growth rate of the galaxy as a whole, obtained by integrating over its full spatial extent. Thus we derive the relative growth rates shown in Figure 5. The right panel, with coordinates as in Figure 4, codes in color this relative growth rate. The left panel plots vertical cuts through the four locations within the galaxy, as a function of total present-day stellar mass. This figure shows at once that not only the inner parts of more massive galaxies grew M_{*} faster (as in Figure 4), but also that in galaxies more massive than $5 \times 10^{10} M_{\odot}$ the inner regions grew as much as 50%–100% faster than the galaxy-wide average. The relative growth rate for $1 R_{50}$ (magenta line) is close to unity, meaning that R_{50} best represents the stellar mass growth in the galaxy as a whole.

Although we have grouped 105 galaxies (105,123 spectra in total) in just a few mass bins to obtain robust results, when the complete CALIFA sample of 600 galaxies is observed and analyzed, these results will be established with a finer detail. The most striking aspect of Figure 5 is the peak at $M_{*} \sim 6\text{--}7 \times 10^{10} M_{\odot}$. At masses below this, the relative growth rates of inner and outer regions slowly converge to the galaxy average, becoming essentially indistinguishable at the lowest galaxy masses sampled. A convergence toward spatially uniform histories is also seen at masses above the critical mass, but the inner regions still grow faster than the outer ones at the highest

masses. The largest differences peak at $\sim 6\text{--}7 \times 10^{10} M_{\odot}$, where the nucleus grows about twice faster than the outer regions.

4. DISCUSSION AND SUMMARY

Previous studies have revealed a special mass or mass range (referred to as critical or pivotal) around $M_{*} \sim 6 \times 10^{10} M_{\odot}$ (Kauffmann et al. 2003; Mateus et al. 2006; Leauthaud et al. 2012, and references therein). Leauthaud et al. study the stellar-to-halo mass relation (SHMR) using COSMOS data and find that this mass marks where the accumulated stellar growth of the central galaxy has been the most efficient. On the modeling side, Shankar et al. (2006) discuss the shape of the SHMR as a change of dominance of two feedback mechanisms, with stellar winds and supernova (SN) efficiently removing the gas and quenching the star formation at lower galaxy masses, while active galactic nucleus (AGN) winds become more powerful in massive galaxies thus lowering star formation efficiency at higher masses. There is still much to be understood about the self-consistent combined effects of AGN and SN feedback (Stinson et al. 2013; Booth & Schaye 2012). Recent papers try to reproduce the observed SHMR from cosmological simulations (cf. Figure 14 in Behroozi et al. 2012), with values of $\sim 2\text{--}10 \times 10^{10} M_{\odot}$ in the peak efficiency of conversion of halo gas into stellar mass. Cosmological models of star formation with negative feedback do not allow yet for a more precise value of this critical mass for optimal growth (De Lucia & Borgani 2012).

In short, there is clear mounting evidence from a series of independent studies, both observationally and from numerical simulations, of a special galaxy mass range where the SFR reaches higher values faster. Our results, Figure 5, show that the physical process(es) responsible for this peak efficiency also leave a strong imprint in the *spatial* assembly of stars in galaxies. From our spatially resolved study, we can see that this is restricted to the inner reaches of galaxies with this pivotal mass. This would imply that the effect is seen in the spheroidal

component, which dominates the central mass distribution of galaxies at this stellar mass range, and that this happened 5–7 Gyr ago (a redshift ~ 0.5 –1; Figure 4).

We can also tentatively frame our results in the context of secular versus merger driven evolution. A possible scenario to interpret our findings is that galaxies with $M_* \gtrsim 5 \times 10^{10} M_\odot$ have grown quickly their inner part by means of a merger at ages 5–9 Gyr ago (such as M31), while lower mass galaxies are dominated by secular evolution (such as the Milky Way). Although we do not have the means to test this, it is compatible with the results obtained by Puech et al. (2012), and with the studies of M31 and the Milky Way (Hammer et al. 2007, 2010; Cignoni et al. 2006; Vergely et al. 2002; McMillan 2011).

Our analysis of the SFHs in 105 galaxies of the CALIFA survey provides a direct powerful probe of the rates and efficiency of spatially resolved stellar mass growth in galaxies, as derived from the information encoded in their present-day spectra. We demonstrate spatially resolved downsizing, with galaxies more massive than $M_* \sim 5 \times 10^9 M_\odot$ growing inside-out while lower mass galaxies grow outside-in. We find an optimal growth for the galaxy stellar mass around $\sim 7 \times 10^{10} M_\odot$.

This Letter is based on data obtained by the CALIFA survey (<http://califa.caha.es>), funded by the Spanish MINECO grants ICTS-2009-10, AYA2010-15081, and the CAHA operated jointly by the Max-Planck IfA and the IAA (CSIC). We benefited from discussions during the CALIFA busy weeks. The CALIFA Collaboration also thanks the CAHA staff for the dedication to this project.

REFERENCES

- Behroozi, P. S., Wechsler, R. H., & Conroy, C. 2012, *ApJ* (arXiv:1207.6105v1)
- Bell, E. F., & de Jong, R. S. 2000, *MNRAS*, 312, 497
- Bell, E. F., Wolf, C., Meisenheimer, K., et al. 2004, *ApJ*, 608, 752
- Blanton, M. R., & Moustakas, J. 2009, *ARA&A*, 47, 159
- Booth, C. M., & Schaye, J. 2012, *MNRAS* (arXiv:1203.3802v1)
- Brinchmann, J., Charlot, S., White, S. D. M., et al. 2004, *MNRAS*, 351, 1151
- Brinchmann, J., & Ellis, R. 2000, *ApJL*, 536, 77
- Cid Fernandes, R., Mateus, A., Sodré, L., et al. 2005, *MNRAS*, 358, 363
- Cid Fernandes, R., Stasińska, G., Mateus, A., et al. 2011, *MNRAS*, 413, 1687
- Cid Fernandes, R., et al. 2012, A&A, submitted
- Cignoni, M., Degl'Innocenti, S., Prada Moroni, P. G., & Shore, S. N. 2006, *A&A*, 459, 783
- De Lucia, G., & Borgani, S. 2012, *MNRAS*, 426, L61
- Erwin, P., Pohlen, M., & Beckman, J. E. 2008, *AJ*, 135, 20
- Faber, S., Willmer, C. N. A., Wolf, C., et al. 2007, *ApJ*, 665, 265
- Folkes, S., Ronen, S., Price, L., et al. 1999, *MNRAS*, 308, 459
- Gallart, C., Stetson, P. B., Meschin, I. P., et al. 2008, *ApJL*, 682, 89
- Gallazzi, A., Charlot, S., Brinchmann, J., et al. 2005, *MNRAS*, 362, 41
- González Delgado, R. M., Cerviño, M., Martins, L. P., et al. 2005, *MNRAS*, 357, 945
- Hammer, F., Puech, M., Chemin, L., Flores, H., & Lehnert, M. D. 2007, *ApJ*, 662, 322
- Hammer, F., Yang, Y. B., Wang, J. L., et al. 2010, *ApJ*, 725, 542
- Hansson, K. S. A., Lisker, T., & Grebel, E. K. 2012, *MNRAS*, 427, 2376
- Heavens, A., Panter, B., Jimenez, R., & Dunlop, J. 2004, *Natur*, 428, 625
- Husemann, B., Kamann, S., Sandin, C., et al. 2012a, *A&A*, 545, 137
- Husemann, B., et al. 2012b, *A&A*, 549, A87, CALIFA Data Release 1 (DR1)
- Ilbert, O., Capak, P., Salvato, M., et al. 2009, *ApJ*, 690, 1236
- Kauffmann, G., Heckman, T. M., White, S. D. M., et al. 2003, *MNRAS*, 341, 54
- Leauthaud, A., Tinker, J., Bundy, K., et al. 2012, *ApJ*, 744, 159
- Lilly, S., Le Fevre, O., Hammer, F., & Crampton, D. 1996, *ApJL*, 460, 1
- Madau, P., Ferguson, H. C., Dickinson, M. E., et al. 1996, *MNRAS*, 283, 1388
- Mateus, A., Sodré, L., Cid Fernandes, R., et al. 2006, *MNRAS*, 370, 721
- McMillan, P. J. 2011, *MNRAS*, 414, 2446
- Moles, M., Benítez, N., Aguerri, J. A. L., et al. 2008, *AJ*, 136, 1325
- Nelson, E. J., van Dokkum, P. G., Brammer, G., et al. 2012, *ApJL*, 747, 28
- Panter, B., Jimenez, R., Heavens, A. F., & Charlot, S. 2007, *MNRAS*, 378, 1550
- Pérez-González, P., Rieke, G. H., Villar, V., et al. 2008, *ApJ*, 675, 234
- Pohlen, M., & Trujillo, I. 2006, *A&A*, 454, 759
- Puech, M., Hammer, F., Hopkins, P. F., et al. 2012, *ApJ*, 753, 128
- Roškar, R., Debattista, V. P., Stinson, G. S., et al. 2008, *ApJL*, 675, 65
- Sánchez, S. F., Kennicutt, R. C., Gilde Paz, A., et al. 2012, *A&A*, 538, 1
- Sánchez-Blázquez, P., Courty, S., Gibson, B. K., & Brook, C. B. 2009, *MNRAS*, 398, 591
- Shankar, F., Lapi, A., Salucci, P., De Zotti, G., & Danese, L. 2006, *ApJ*, 643, 14
- Stinson, G. S., Brook, C., Macciò, A. V., et al. 2013, *MNRAS*, 428, 129
- Vergely, J.-L., Köppen, J., Egret, D., & Bienaymé, O. I. 2002, *A&A*, 390, 917
- Walcher, J., Groves, B., Budavári, T., & Dale, D. 2011, *Ap&SS*, 331, 1
- Wuyts, S., Förster Schreiber, N. M., Genzel, R., et al. 2012, *ApJ*, 753, 114
- York, D. G., Adelman, J., Anderson, J. E., Jr., et al. 2000, *AJ*, 120, 1579
- Zhang, H.-X., Hunter, D., Elmegreen, B. G., Gao, Y., & Schrubba, A. 2012, *AJ*, 143, 47
- Zibetti, S., Charlot, S., & Rix, H. W. 2009, *MNRAS*, 400, 1191

D.4 The star formation history of CALIFA galaxies: Radial structures

Artigo por González Delgado et al. (2014b) (doi : [10.1051/0004-6361/201322011](https://doi.org/10.1051/0004-6361/201322011)).
Também disponível em *preprint* ([arXiv:1310.5517](https://arxiv.org/abs/1310.5517)).

The star formation history of CALIFA galaxies: Radial structures^{*}

R. M. González Delgado¹, E. Pérez¹, R. Cid Fernandes^{1,2}, R. García-Benito¹, A. L. de Amorim², S. F. Sánchez^{1,3}, B. Husemann⁴, C. Cortijo-Ferrero¹, R. López Fernández¹, P. Sánchez-Blázquez⁵, S. Bekeraite⁴, C. J. Walcher⁴, J. Falcón-Barroso^{6,7}, A. Gallazzi^{8,16}, G. van de Ven⁹, J. Alves¹⁰, J. Bland-Hawthorn¹¹, R. C. Kennicutt, Jr.¹², D. Kupko⁴, M. Lyubenova⁹, D. Mast^{1,3}, M. Mollá¹³, R. A. Marino¹⁴, A. Quirrenbach¹⁵, J. M. Vilchez¹, L. Wisotzki⁴, and CALIFA collaboration^{**}

¹ Instituto de Astrofísica de Andalucía (CSIC), PO Box 3004, 18080 Granada, Spain
e-mail: rosa@iaa.es

² Departamento de Física, Universidade Federal de Santa Catarina, PO Box 476, 88040-900 Florianópolis, SC, Brazil

³ Centro Astronómico Hispano Alemán, Calar Alto, (CSIC-MPG), C/ Jesús Durbán Remón 2-2, 04004 Almería, Spain

⁴ Leibniz-Institut für Astrophysik Potsdam, innoFSPEC Potsdam, An der Sternwarte 16, 14482 Potsdam, Germany

⁵ Depto. de Física Teórica, Universidad Autónoma de Madrid, 28049 Madrid, Spain

⁶ Instituto de Astrofísica de Canarias (IAC), 38205 La Laguna, Tenerife, Spain

⁷ Depto. Astrofísica, Universidad de La Laguna (ULL), 38206 La Laguna, Tenerife, Spain

⁸ INAF – Osservatorio Astrofisico di Arcetri, Largo Enrico Fermi 5, 50125 Firenze, Italy

⁹ Max Planck Institute for Astronomy, Königstuhl 17, 69117 Heidelberg, Germany

¹⁰ University of Vienna, Turkenstanzstrasse 17, 1180 Vienna, Austria

¹¹ Sydney Institute for Astronomy, The University of Sydney, Sydney NSW 2006, Australia

¹² University of Cambridge, Institute of Astronomy, Madingley Road, Cambridge, CB3 0HA, UK

¹³ Departamento de Investigación Básica, CIEMAT, Avda. Complutense 40, 28040 Madrid, Spain

¹⁴ CEI Campus Moncloa, UCM-UPM, Departamento de Astrofísica y CC. de la Atmósfera, Facultad de CC. Físicas, Universidad Complutense de Madrid, Avda. Complutense s/n, 28040 Madrid, Spain

¹⁵ Landessternwarte, Zentrum für Astronomie der Universität Heidelberg, Königstuhl 12, 69117 Heidelberg, Germany

¹⁶ Dark Cosmology center, Niels Bohr Institute, University of Copenhagen, Juliane Mariesvej 30, 2100 Copenhagen, Denmark

Received 3 June 2013 / Accepted 21 October 2013

ABSTRACT

We have studied the radial structure of the stellar mass surface density (μ_*) and stellar population age as a function of the total stellar mass and morphology for a sample of 107 galaxies from the CALIFA survey. We applied the fossil record method based on spectral synthesis techniques to recover the star formation history (SFH), resolved in space and time, in spheroidal and disk dominated galaxies with masses from 10^9 to $10^{12} M_\odot$. We derived the half-mass radius, and we found that galaxies are on average 15% more compact in mass than in light. The ratio of half-mass radius to half-light radius (HLR) shows a dual dependence with galaxy stellar mass; it decreases with increasing mass for disk galaxies, but is almost constant in spheroidal galaxies. In terms of integrated versus spatially resolved properties, we find that the galaxy-averaged stellar population age, stellar extinction, and μ_* are well represented by their values at 1 HLR. Negative radial gradients of the stellar population ages are present in most of the galaxies, supporting an inside-out formation. The larger inner (≤ 1 HLR) age gradients occur in the most massive ($10^{11} M_\odot$) disk galaxies that have the most prominent bulges; shallower age gradients are obtained in spheroids of similar mass. Disk and spheroidal galaxies show negative μ_* gradients that steepen with stellar mass. In spheroidal galaxies, μ_* saturates at a critical value ($\sim 7 \times 10^2 M_\odot/\text{pc}^2$ at 1 HLR) that is independent of the galaxy mass. Thus, all the massive spheroidal galaxies have similar local μ_* at the same distance (in HLR units) from the nucleus. The SFH of the regions beyond 1 HLR are well correlated with their local μ_* , and follow the same relation as the galaxy-averaged age and μ_* ; this suggests that local stellar mass surface density preserves the SFH of disks. The SFH of bulges are, however, more fundamentally related to the total stellar mass, since the radial structure of the stellar age changes with galaxy mass even though all the spheroid dominated galaxies have similar radial structure in μ_* . Thus, galaxy mass is a more fundamental property in spheroidal systems, while the local stellar mass surface density is more important in disks.

Key words. galaxies: evolution – galaxies: stellar content – galaxies: structure – galaxies: fundamental parameters – galaxies: bulges – galaxies: spiral

1. Introduction

The separation of galaxies in a red sequence and a blue cloud according to their location in the color–magnitude diagram (CMD) has been well established since the work of

Strateva et al. (2001). This location correlates with stellar population properties (Kauffmann et al. 2003a,b; Baldrý et al. 2004; Bell et al. 2004; Brinchmann et al. 2004; Gallazzi et al. 2005; Mateus et al. 2006, 2007; Blanton & Moustakas 2009). Red galaxies are usually composed of metal rich and old stars, and have very little gas and recent star formation. In contrast, galaxies in the blue cloud are actively forming stars, and have a large gas fraction and a metal poor and young stellar population. This bimodal distribution of galaxy properties reflects the Hubble

^{*} Table 1 and appendices are available in electronic form at

<http://www.aanda.org>

^{**} <http://califa.caha.es>

sequence, because red galaxies are mainly spheroidal dominated systems, while blue galaxies are disk dominated systems. This distribution also depends on the galaxy stellar mass (M_*) which has become the most important parameter for galaxy evolution studies (e.g., Brinchmann & Ellis 2000; Dickinson et al. 2003; Fontana et al. 2006; Pérez-González et al. 2008), although environment can also play a relevant role (e.g., Peng et al. 2010).

Sorting galaxies by their stellar mass is a way to start to classify galaxies and to check if their properties scale among the different subsamples. Earlier results from the analysis of Sloan Digital Sky Survey (SDSS) data (Strateva et al. 2001) have reported the existence of a critical mass, $\sim 3 \times 10^{10} M_\odot$, that divides the local population of galaxies in two distinct families: lower mass galaxies with young stellar populations, low mass surface density and low concentration index typical of disks, and higher mass galaxies with old stellar populations, high mass surface density, and concentration index typical of bulges (Kauffmann et al. 2003a,b). This dependence of the galaxy properties on the stellar mass distribution points to morphology as a secondary parameter (Balogh et al. 2001; Boselli et al. 2001). Later works have also pointed out that μ_s is a more fundamental parameter than M_* . Kauffmann et al. (2006) found that there is also a critical $\mu_s \sim 3 \times 10^8 M_\odot \text{ kpc}^{-2}$ that divides galaxies in disk-dominated and bulge-dominated systems. Below this critical surface density, μ_s scales with the stellar mass, while above it μ_s is almost constant. These results suggest that the conversion of baryons into stars in low mass galaxies increases with their halo mass, but in massive galaxies the star formation efficiency decreases in the highest mass haloes, with little star formation occurring in massive galaxies after they have assembled.

These SDSS results were obtained by analyzing a single central spectrum per galaxy, with a 3 arcsec diameter covering from nuclear regions to not more than 70% of the total galaxy light, depending on distance. Because of the radial structure of galaxy properties, such as the mass-to-light (M/L) ratio, results based on SDSS spectroscopy can be greatly affected by aperture losses and fiber location within the galaxy (Ellis et al. 2005; Iglesias-Páramo et al. 2013).

Based on spatially resolved surface photometry, Bell & de Jong (2000) found that μ_s is a more fundamental parameter than M_* in driving the star formation history (SFH). They analyzed a sample of 121 nearby S0–Sd galaxies, and concluded that the SFH of a disk galaxy is primarily driven by its local surface density, with the total stellar mass as a secondary parameter that correlates with metallicity, but not with age. This suggests that galaxy mass dependent feedback is an important process in the chemical evolution of galaxies, as has also been suggested by the mass-metallicity relation (Tremonti et al. 2004), although recent works point out that this relation is a scaled-up integrated effect of a local μ_s – oxygen abundance relation (Rosales Ortega et al. 2012; Sánchez et al. 2013). We note, however, that Bell & de Jong (2000) use K -band surface brightness as a proxy of the stellar mass surface density, and their results are based on color gradients, which can be affected by spatial variation of the extinction, and even by emission lines contributing to optical bands.

In a pioneering work, Zibetti et al. (2009) carried out a detailed analysis of nine nearby galaxies using SDSS *ugriz* plus J , H , K images, devising a method to derive the spatially resolved H -band M/L ratio as a function of the $g-i$ color. Comparing the total stellar mass obtained from the spatially resolved μ_s map with the mass inferred from the integrated photometry, they find that the former can be up to 0.2 dex larger. However, because of the limited number of galaxies in their sample, they could not

study how the radial structure of μ_s changes with M_* or with galaxy type.

More recently, μ_s profiles have been obtained for individual galaxies at different redshifts, made possible by the high spatial resolution provided by WFC3 on board *Hubble* Space Telescope. Now it is possible to measure the rest frame optical emission of galaxies at redshift $z \sim 2$, and to obtain spatially resolved maps of the stellar mass by fitting the SED in each individual pixel (Wuys et al. 2012), or simply using an empirical relation between the rest-frame color and stellar M/L ratio (Szomoru et al. 2012). Stellar mass surface density radial profiles have been used to trace the mass distribution, concluding that galaxies at $z \sim 2$ are growing inside-out.

We note, however, that these works estimate not only μ_s but also the average age of the stellar population based on broad band photometry. The average age is a crude but robust way to represent the SFH of galaxies, and rest-frame optical colors are used extensively to obtain ages. Radial gradients of colors have been detected in bulges (Peletier et al. 1990; Silva & Bothun 1998; La Barbera et al. 2004; Menanteau et al. 2004; Wu et al. 2005; Moorthy & Holtzman, 2006; Roche et al. 2010) and disks (Peletier & Balcells 1996; de Jong 1996; Peletier & de Grijs 1998; Bell & de Jong 2000; MacArthur et al. 2004; Muñoz-Mateos et al. 2007; Tortora et al. 2010; Bakos et al. 2008). Usually, a color gradient is interpreted as due to radial variations in age or metallicity, but because of the age-metallicity-extinction degeneracy, color gradients can also be related to metallicity and/or extinction gradients that are certainly present in the disks and central regions of massive galaxies.

Spectroscopic data and measured line-strength stellar indices can help to break these degeneracies (Trager et al. 2000; Proctor & Sansom 2002; Sánchez-Blázquez et al. 2007; MacArthur et al. 2009). Pioneering three-dimensional spectroscopic surveys like SAURON (Bacon et al. 2001; de Zeeuw et al. 2002), and ATLAS3D (Capellari et al. 2011) have taken this approach to spatially resolve the stellar population properties of mainly early-type galaxies (Peletier et al. 1997; McDermid et al. 2006; Chilingarian 2009; Kuntschner et al. 2010; see also Ganda et al. 2007, for a few spiral galaxies). Unfortunately, the short spectral range in these works limits the analysis to a few spectral indices, with little leverage to trace extinction effects and to use long-range continuum shape to further constrain stellar populations properties. Surveys covering a larger spectral range exist (e.g., Chilingarian 2009; Blanc et al. 2013; Yoachim et al. 2012; Greene et al. 2012; Sil'chenko et al. 2012), but they are still based on a small number of galaxies.

It is clear from this summary that spatially resolved spectroscopy covering the whole optical wavelengths for a large homogenous sample is needed to better map the radial structure of the stellar population properties, and to ascertain the roles that μ_s and M_* play in the SFH of galaxies. The Calar Alto Integral Field Area (CALIFA, Sánchez et al. 2012; Husemann et al. 2013) is the largest 3D spectroscopic survey to date of galaxies in the local Universe, providing a unique set of data for galaxies covering a large range of masses (10^9 – $10^{12} M_\odot$) and morphological types (from E to Sc), spatially resolved up to three half-light radii (HLR).

We have already obtained the spatially resolved history of the stellar mass assembly for the first 105 galaxies of CALIFA. In Pérez et al. (2013) we applied the fossil record method of spectral synthesis to recover the spatially and time resolved SFH of each galaxy, finding that galaxies more massive than $10^{10} M_\odot$ grow inside-out. We also show that the signal of downsizing is spatially preserved, with both inner and outer regions growing

faster for more massive galaxies. Furthermore, we show that the relative growth rate of the spheroidal component, nucleus, and inner galaxy, which happened 5–7 Gyr ago, shows a maximum at a critical stellar mass of $\sim 7 \times 10^{10} M_{\odot}$.

We use the full spectral fitting technique because it has been proven to reduce the age-metallicity degeneracy (Sánchez-Blázquez et al. 2011). In addition, this technique, which has been extensively applied to single SDSS spectra of galaxies (e.g., Cid Fernandes et al. 2005, 2007; Asari et al. 2007), successfully produces the 2D distribution of the stellar population properties when applied to CALIFA data cubes (Cid Fernandes et al. 2013). Additionally, we have studied extensively the uncertainties associated with the estimation of the radial distribution of the stellar population properties (Cid Fernandes et al. 2014).

In this paper we extend our study of the spatially resolved stellar population properties of galaxies in the CALIFA survey; we obtain the radial structure of the stellar mass surface density and ages of the stellar population and their dependence on the galaxy stellar mass and morphology; we compare the averaged and integrated properties of the galaxies, and find out where and in which galaxies the total stellar mass and/or the local stellar mass surface density is more connected to their history.

This paper is organized as follows. Section 2 describes the observations and summarizes the properties of CALIFA galaxies and of the subsample studied here. In Sect. 3 we summarize the fossil record method of extracting the SFH, and the single stellar population models used as ingredients for the full spectral fitting. Section 4 presents the 2D maps of μ_* and age, as well as their radial structures. Section 5 deals with the total stellar mass. Section 6 compares the galaxy-averaged with the integrated stellar population properties, and links them with their values at one HLR. In Sect. 7 we obtain the mass weighted size, and we discuss the ratio of half-mass (HMR) to half-light radii as a function of galaxy mass and the spatial variation of the M/L ratio. Section 8 presents the radial structures of age and μ_* stacking galaxies according to their M_* , and concentration index, and we discuss the roles of M_* and μ_* in the history of disk and spheroidal galaxies. Finally, Sect. 9 summarizes the results obtained and presents our conclusions. Throughout we adopt a Salpeter IMF (Salpeter 1955), resulting in stellar masses a factor of 1.78 larger than in the case of a Chabrier IMF (Chabrier 2003).

2. Observations, data reduction, and sample

2.1. Observations and data reduction

The observations were carried out with the Potsdam Multi-Aperture Spectrophotometer (PMAS, Roth et al. 2005) in the PPak mode (Verheijen et al. 2004) at the 3.5 m telescope of the Calar Alto Observatory (CAHA); PPak is a fiber bundle of 382 fibers of 2.7" diameter each, covering a $74'' \times 64''$ field of view (FoV, Kelz et al. 2006).

Observations for CALIFA are obtained in two different spectral settings using the V500 and V1200 gratings. The V500 grating achieves a spectral resolution of $\sim 6 \text{ \AA}$ (FWHM) with a nominal wavelength coverage from 3745–7300 \AA , while the V1200 achieves a higher spectral resolution of $\sim 2.3 \text{ \AA}$, covering the 3650–4840 \AA range. However, the useful wavelength range is reduced by vignetting of the CCD corners which cannot be fully compensated with the three-dithering scheme. More extended explanations on the observational strategy, effects of vignetting,

the reduction pipeline, and data quality can be found in Sánchez et al. (2012) and Husemann et al. (2013).

To reduce the effects of the vignetting on the data, we combine the observations in both setups such that they fully cover the optical range from [OII] $\lambda 3727$ to [SII] $\lambda \lambda 6717, 6732$. To combine both spectral setups we first degraded the spectral resolution of the V1200 data set to match the V500 data. This is done within the standard CALIFA pipeline to ensure that the data handling and error propagation matches that of the V500 data. Spatial alignment of the V500 and V1200 datacubes requires only full pixel shifts because both datacubes have been reconstructed during the correction for differential atmospheric refraction such that the central surface brightness peak is centered on a certain pixel. The V500 and V1200 data are always observed under different observing conditions, so that the difference in the seeing will slightly affect the observed surface brightness for each spaxel. Thus, we scale all individual spectra of the V1200 data such that they match with surface brightness of the corresponding V500 data within the unvignetted wavelength range 4500–4600 \AA . Finally, a combined V1200 + V500 datacube is produced where the wavelength range shortward of 4600 \AA is taken from matched V1200 datacube and longward of 4600 \AA is taken from the original V500 datacube.

The combined V1200 + V500 datacubes were processed as described in Cid Fernandes et al. (2013). Briefly, spectra adequate for a full spectral synthesis analysis of the stellar population content were extracted in a way that ensures a signal-to-noise ratio $S/N \geq 20$ in a 90 \AA wide region centered at 5635 \AA (in the rest-frame). When individual spaxels do not meet this S/N threshold (typically beyond a couple of half-light radii from the nucleus), they were coadded into Voronoi zones (Cappellari & Copin 2003). On average, we analyzed ~ 1000 zones per galaxy (to be precise, the 107 galaxies studied in this paper were segmented into 98 291 zones). Pre-processing steps also include spatial masking of foreground/background sources and very low S/N spaxels, rest-framing, and spectral resampling. The whole process takes spectrophotometric errors (ϵ_i) and bad pixel flags (b_i) into account. The spectra were then processed through `y` (the Python CALIFA Synthesis Organizer), producing the results discussed throughout this paper.

2.2. The parent sample and the first 107 galaxies

A detailed characterization of the CALIFA sample will be presented by Walcher et al. (in prep.). Here we summarize its main properties and compare it to the subsample studied in this paper.

CALIFA's mother sample contains 939 galaxies selected from the SDSS DR7 photometric catalog (Abazajian et al. 2009). In addition to the restriction in declination to ensure good visibility from CAHA, the main selection criteria are: a) angular isophotal diameter in the SDSS r -band in the range $D_{25} = 45\text{--}80$ arcsec, to ensure that objects fill well the PPak FoV; and b) redshift range $z = 0.005\text{--}0.03$, guaranteeing that all relevant optical emission lines are covered. The sample includes a significant number of galaxies in the different areas across the CMD, ensuring that CALIFA spans a wide and representative range of galaxy types.

In this paper we present the results of the analysis of the first 107 galaxies observed by CALIFA. The observing order selection is random, but is this subset representative of the mother sample as a whole? To answer this question, Fig. 1 compares the distributions of galaxy properties in the mother sample (empty bars) and in our subsample. The plots show (scaled) histograms

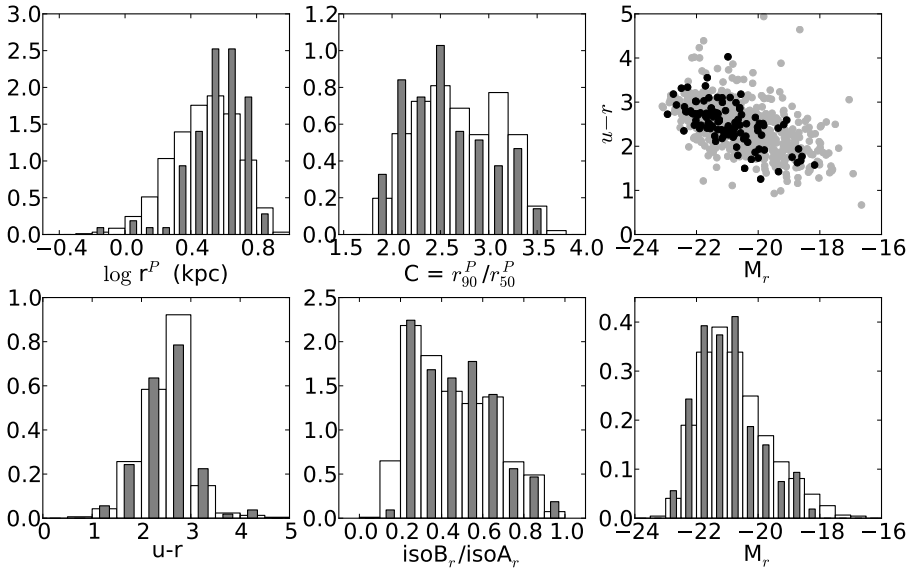


Fig. 1. Comparison of the distributions of the CALIFA mother sample (empty bars) and the 107 galaxies analyzed here (filled bars). From bottom up, and from left to right, we show the distributions of: $u-r$ color, the ratio between the semi-minor and semi-major axis, the absolute magnitude, the Petrosian 50% radius, r_{50}^P , and the concentration index (measured at the SDSS r band). The histograms are normalized to form a probability density, i.e. each bar scales with the ratio of the number of galaxies in each bin and the total number of galaxies \times bin width, so that we can directly compare the two distributions. The upper-right panel shows the CMD where galaxies of the mother sample are the gray points and the 107 galaxies analyzed here are marked as black points.

of the absolute magnitude, the ratio of the isophotal major-axis to minor-axis diameters, colors, the Petrosian radius, and concentration index (defined as the ratio of Petrosian radii r_{90}^P/r_{50}^P), as well as the $u-r$ vs. M_r CMD. All data were extracted from the SDSS photometric catalog for the CALIFA mother sample. The histograms are normalized to form a probability density, i.e. each bar scales with the ratio of the number of galaxies in each bin and the total number of galaxies multiplied by the bin width. A simple visual inspection shows that our subsample of 107 galaxies represents well the CALIFA sample. We thus expect that the results reported in this paper will remain valid once the full sample is observed. We note, however, that without applying a volume correction, these distributions do not represent the local galaxy population.

3. Methods, ingredients, and uncertainties

Our method of extracting stellar population information from the CALIFA data cubes is based on the full spectral synthesis approach. This section presents a summary of the method, ingredients, and tests that we have carried out (see also Appendix B).

3.1. The spectral synthesis method

Methods of extracting information on stellar populations encoded in galaxy spectra split into two broad categories: those which focus on spectral indices like equivalent widths and/or

colors (Bica 1988; Proctor et al. 2004; Gallazzi et al. 2005, 2006), and those which use the whole spectrum (Heavens et al. 2004; Cid Fernandes et al. 2005; Ocvirk et al. 2006; Koleva et al. 2009; Tojeiro et al. 2007; MacArthur et al. 2009). Both have pros and cons. The full spectral synthesis approach has boomed since the first generation of medium spectral resolution evolutionary synthesis calculations became available with the paper by Bruzual & Charlot (2003), and was one of the main tools employed in the mining of the SDSS spectroscopic database, leading to the derivation of physical properties and SFHs of galaxies (e.g., Panter et al. 2003, 2007; Mateus et al. 2007; Vale Asari et al. 2009; Tojeiro et al. 2009). Here, we use the full spectral fitting approach.

We analyze the stellar population properties of CALIFA galaxies with the `1` code (Cid Fernandes et al. 2005), which fits an observed spectrum (O_λ) in terms of a model (M_λ) built by a non-parametric linear combination of N_* simple stellar populations (SSPs) from a base spanning different ages (t) and metallicities (Z). Dust effects are modeled as a foreground screen with a Cardelli et al. (1989) reddening law with $R_V = 3.1$. Kinematical effects are also accounted for assuming a Gaussian line-of-sight velocity distribution. The fits were carried out in the rest-frame 3800–6850 Å interval, with a $\Delta\lambda = 2$ Å sampling. Windows around the main optical emission lines of [OI], [OII],

¹ Available at <http://www.starlight.ufsc.br> The version of used in this work differs from the publicly available, but mostly in aspects not related to the analysis performed here.

[OIII], [NII], HeI, and the Balmer series from H α to H ϵ were masked in all fits. Because of its interstellar absorption component, the NaI D doublet was also masked. A more detailed account of how we process CALIFA data cubes through is given in Cid Fernandes et al. (2013, 2014).

All spectral fits were performed using the cluster Grid-CSIC at the Instituto de Astrofísica de Andalucía. Example spectral fits are presented in Appendix B.

3.2. SSP spectral models

Simple stellar population models are the key ingredient in any spectral synthesis analysis, as it is through them that one transforms observed quantities to physical properties of the stellar populations in galaxies. The SSP spectra result from the combination of an initial mass function (IMF) with stellar isochrones and libraries that provide the spectra of stars with temperature, gravity, and metallicity demanded by the evolutionary tracks (e.g., Tinsley 1980; Bruzual & Charlot 1993; Leitherer et al. 1999; Walcher et al. 2011; Conroy 2013).

All these ingredients involve choices among different options (different IMFs, different tracks, different libraries, and different codes to put them all together), and for this reason we have performed spectral fits using three different sets of SSPs: (a) the *GM* base is a combination of the SSP spectra provided by Vazdekis et al. (2010) for populations older than 63 Myr and the González Delgado et al. (2005) models for younger ages; (b) base *CB* is an updated version of the Bruzual & Charlot (2003) models that replaces STELIB (Le Borgne et al. 2003) with a combination of the MILES (Sánchez-Blázquez et al. 2006; Falcón-Barroso et al. 2011b) and (Martins et al. 2005) spectral libraries; and (c) base *BC* comprises the standard Bruzual & Charlot (2003) models.

In Cid Fernandes et al. (2014) we compared the results of fitting the same 98 291 spectra studied here, and the main conclusions are that masses (or mass surface density), mean ages, and extinction are in very good agreement. Some discrepancies are, however, found in metallicity. Comparing *GM* and *CB*, the dispersion in luminosity weighted ages is 0.14 dex and the dispersion in A_V is 0.06 dex. *GM* stellar masses are 0.27 dex higher than *CB* due to the different IMFs (Salpeter vs. Chabrier), but apart from this offset, the two masses agree to within a dispersion of 0.16 dex. Similar conclusions are obtained when *GM* and *BC* results are compared. In short, the differences in mass, age, and extinction obtained with these three sets of SSP models are all relatively small. Uncertainties due to random noise variations and continuum shape errors associated to flux calibration were evaluated through simulations and found to be somewhat smaller than, but of the same order as those associated with the choice of SSP models.

For these reasons, here we present the results obtained with only one set of SSP models. We have chosen base *GM*, but a comparison of the results obtained with other bases for the most relevant galaxy properties analyzed here is presented in Appendix B. The *GM* base spans 39 ages from 1 Myr to 14 Gyr, and four metallicities ($Z = 0.2, 0.4, 1, 1.5 Z_\odot$). They are built with the Girardi et al. (2000) evolutionary tracks, except for the youngest ages (1 and 3 Myr), which are based on the Geneva tracks (Schaeller et al. 1992; Schaerer et al. 1993a,b; Charbonnel et al. 1993). We adopt a Salpeter initial mass function throughout.

4. Spatially resolved properties of the stellar population in galaxies

The spatial distributions of μ_* and the luminosity weighted mean stellar age ($\langle \log age \rangle_L$, defined in Eq. (9) of Cid Fernandes et al. 2013) are at the heart of the analysis carried out in this paper. For this analysis we prefer to use luminosity weighted ages for two reasons: first because luminosity is more sensitive than mass to age variations and thus provides a wider range of ages; second, because after comparing the ages estimated by μ_* for several galaxies with ages estimated using Lick indices, we find that luminosity weighted ages are more in agreement with Lick ages than mass weighted ones, so this choice facilitates comparison with this more traditional school of stellar population analysis in galaxies. This section presents the 2D maps and radial profiles of μ_* and $\langle \log age \rangle_L$. The results are presented in the framework of the CMD. Because absolute magnitude is related to M_* and color is a proxy for the stellar population age, the CMD is a convenient observational framework for studying the properties of different types of galaxies.

4.1. 2D maps: stellar mass surface density and age

Figures 2 and 3 both show the M_r vs. $(u-r)$ CMD for our sample². Each galaxy is represented by its 2D map of μ_* (Fig. 2) and $\langle \log age \rangle_L$ (Fig. 3), located at the position of their integrated M_r and $(u-r)$ values. In these plots the SFH of each galaxy is compressed into μ_* and $\langle \log age \rangle_L$, with μ_* representing the end product of the SFH and $\langle \log age \rangle_L$ a measure of the pace with which this end product was achieved.

Cid Fernandes et al. (2013) explain the processes that we follow to convert light into mass and the determination of the ages through the spatially resolved SFH, all included in our analysis pipeline γ . Effects of the spatial binning are visible in the mean age maps, where all pixels in a Voronoi zone have the same value. These effects are not noticeable in the μ_* images because the zoning effect was softened by scaling the value at each pixel by its fractional contribution to the total flux in the zone, thus producing smoother images.

Figures 2 and 3 show the results obtained with the *GM* template library. We note that our spectral synthesis analysis accounts for extinction, thus, to the extent that the simple foreground dust screen model works, our μ_* values and their radial variation are free of dust effects. This is an improvement compared to most works based on photometry, which estimate μ_* from the surface brightness typically assuming that color variations are entirely due to changes in M/L , and dust effects on colors compensate those on luminosity.

Figure 2 shows the stellar mass surface density maps of each of our 107 galaxies. One sees that spheroids are one or two orders of magnitude denser than disks. The gradient is steeper in the luminous and red galaxies than in faint and blue ones. The disk μ_* scales well with the luminosity of the galaxy.

Figure 3 shows that $\langle \log age \rangle_L$ is correlated both with color (as expected) and luminosity (due to the downsizing effect). Larger age gradients are seen in the galaxies in the green valley than in the more massive red galaxies. The fainter and bluer galaxies either do not show a clear age gradient or seem to have more of an inverted gradient, being younger in the center than in the outskirts.

² They are from SDSS tables and have been corrected for Galactic extinction.

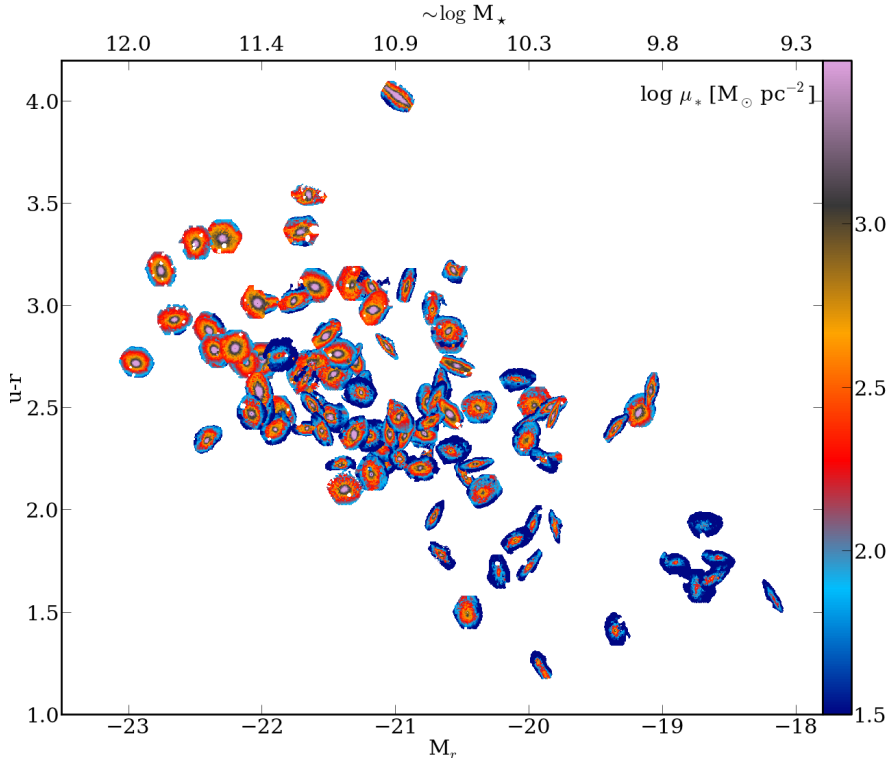


Fig. 2. 2D maps of the stellar mass density μ_* . Each galaxy is placed in its location in the $u-r$ vs. M_r diagram, where color and magnitude correspond to its global values. The stellar mass corresponding to M_r is shown in the top horizontal axis, following the fit $\log M_* = -0.45 - 0.54M_r$ (Fig. 5b). The 2D maps are shown with north up and east to the left.

4.2. Radial profiles of μ_* and $\langle \log age \rangle_L$

In order to study the radial variations with galaxy type, we compressed the 2D maps of μ_* and $\langle \log age \rangle_L$ in azimuthally averaged radial profiles. A common metric is needed to compare (and stack) the radial profiles, so we expressed the radial distance in units of HLR. Appendix A explains how we derived a_{50}^L , defined as the semi-major axis length of the elliptical aperture containing 50% of the light at 5635 \AA . There we also compared a_{50}^L with the Petrosian radius (r_{50}^P) and with the half-light radius obtained with circular apertures (R_{50}^L).

The `y` code provides two methods for computing radial profiles: area averaging and spaxel averaging (Cid Fernandes et al. 2013). The second method, which averages a property among all values in the same radial bin, is used here for both μ_* and $\langle \log age \rangle_L$, but area averaging yields very similar results.

We divide the CMD into 5×5 bins, covering the whole range in absolute magnitude ($-23 \leq M_r \leq -18$) and color ($1.25 \leq u-r \leq 4.25$). The individual radial profiles of galaxies located in the same bin are stacked, limiting the radial range to $R \leq 3$

HLR. The number of galaxies is shown in the top-right corner in each box.

Figure 4 shows the stacking results for $\log \mu_*$ and $\langle \log age \rangle_L$ as solid lines. Values for individual spaxels are shown in blue, intensity coded by the density of points. Unlike for μ_* , $\langle \log age \rangle_L$ images cannot be softened by the zone effects, so we assign the same age to all the spaxels that belong to a given Voronoi zone. Because these spaxels are at different distances within the galaxy, the radial structure of $\langle \log age \rangle_L$ shows horizontal stripes that are not seen in the radial profiles of $\log \mu_*$. The consequence is that the dispersion in $\langle \log age \rangle_L$ profiles is higher than in $\log \mu_*$, and the radial structure of $\langle \log age \rangle_L$ is more uncertain than that of $\log \mu_*$ beyond 2 HLR (where spatial binning becomes prevalent).

The mean stacked profile for all 107 galaxies is shown as the inset in the top-right of each figure. The horizontal and vertical scales of all panels is the same used in this plot. In addition to the mean stacked profile (solid line) in each CMD bin, we plot for reference the mean stacked profile of the 107 galaxies (dashed line), so that systematic trends in the radial structure are more clearly seen.

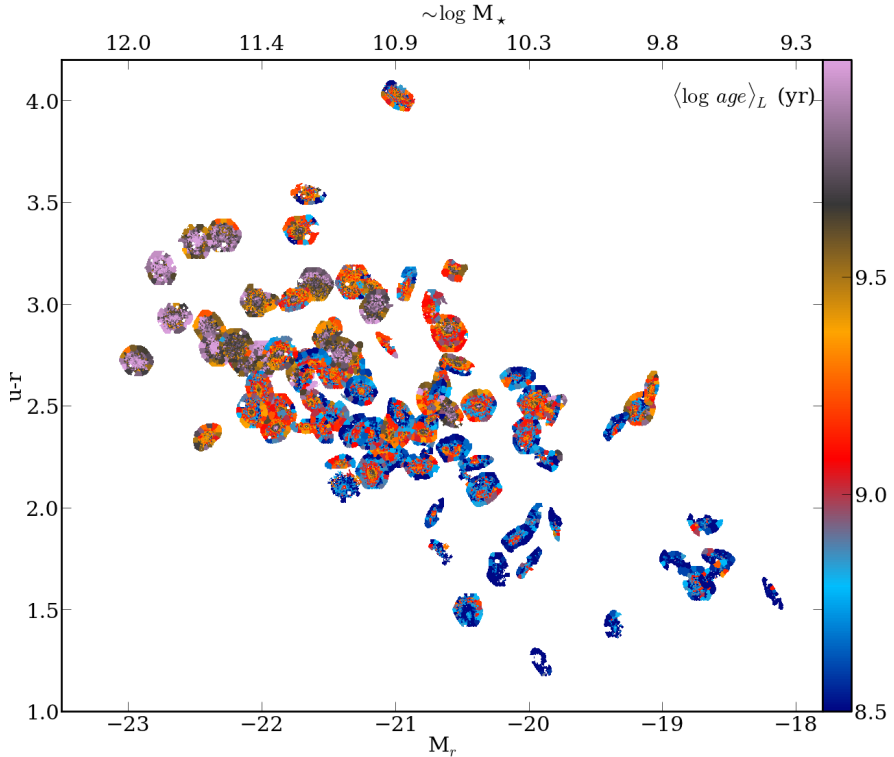


Fig. 3. As Fig. 2, but for images of the luminosity weighted mean age, $\langle \log \text{age} \rangle_L$ (in yr). Radial age gradients are visible in galaxies in the green valley ($-22 < M_r < -20$ and $2 < u-r < 3.5$), but not in the blue cloud or red sequence. CALIFA 853 ($u-r = 4.02$, $M_r = -20.98$) has ages similar to other galaxies of similar M_r , and its red color is mainly due to extinction ($A_V(1\text{HLR}) = 1.2$).

As expected, μ_* exhibits negative radial gradients in all cases. In the nuclei $2.5 \leq \log \mu_* (M_\odot \text{pc}^{-2}) \leq 4.5$, while in the outer radii $1.5 \leq \log \mu_* (M_\odot \text{pc}^{-2}) \leq 3$. A trend of $\log \mu_*$ with the magnitude and the color of the galaxy is found: red and luminous galaxies are denser than blue and faint galaxies throughout their extent. Disk galaxies show $\log \mu_*$ profiles that scale with M_r . A general trend is also found between the central value of $\log \mu_*$ of each galaxy (or the average $\log \mu_*$) and M_r , as expected since the magnitude correlates with the total mass.

Similarly, $\langle \log \text{age} \rangle_L$ shows negative gradients, but not for all CMD bins. A strong gradient is found for most of the disk galaxies in the green valley ($-22 \leq M_r \leq -19$ and $2 \leq u-r \leq 3.5$), with mean ages ranging from 5–6 Gyr at the galaxy center to 1 Gyr at $R = 1$ HLR in the disk. Galaxies in the blue cloud ($M_r \geq -20$ and $u-r \leq 2$) show less age gradient, with flat radial profiles at an age ≤ 1 Gyr beyond 1 HLR. Red galaxies are the oldest (~ 10 Gyr), not only at the core but also in the extended envelope, and they also show almost flat age gradients.

The CALIFA sample was chosen to cover most of the FoV of PPAK, which corresponds to sizes between 2 and 5 HLR; the typical size is 3 HLR. This is why the radial profiles in Fig. 4 are

represented up to 3 HLR, but the 2D maps in Fig. 3, are plotted up the maximum radius observed for each galaxy.

5. Stellar masses

The stellar mass is one of the most important physical properties for galaxy evolution. Armed with the results from our spectral synthesis analysis, we now present total stellar masses derived for the CALIFA subsample of 107 galaxies.

These masses are obtained by adding, for each galaxy, the masses of each zone, hence taking into account spatial variations of the stellar populations and extinction across the face of the galaxies. We take into account areas that were masked in the data cubes (see Appendix A), replacing the missing spaxels by the average of μ_* values at the same radial distance. On average, this correction amounts to just $\sim 5\%$, and for only 3% of the galaxies the correction reaches 0.05–0.1 dex in $\log M_*$. We have also verified that light outside the PPAK FoV does not add much to the stellar masses computed here. As explained in Appendix C, correcting for this effect would increase our masses by 8% on average.

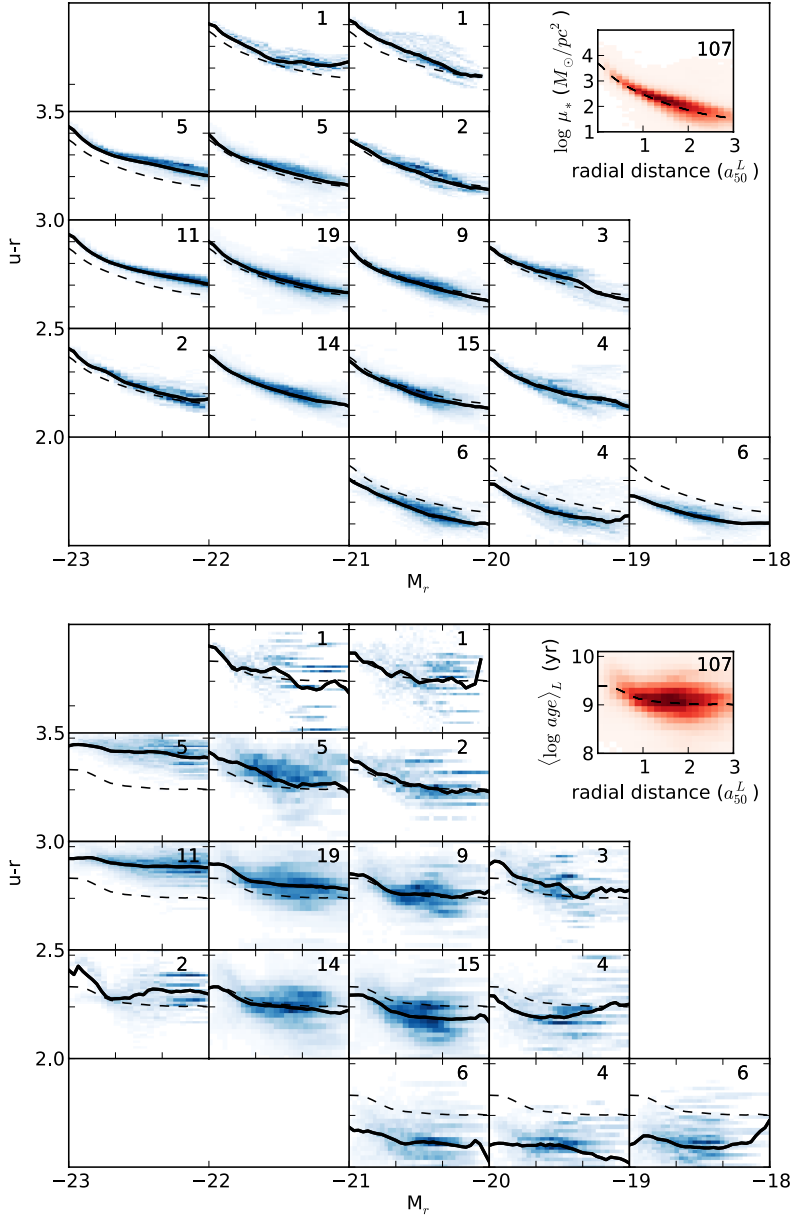


Fig. 4. Radial profiles (in units of HLR) of the stellar mass surface density ($\log \mu_*$, upper panel), and luminosity weighted mean age, ($\langle \log \text{age} \rangle_L$, bottom panel). Results are stacked in each CMD bin. Individual spaxels are shown in blue, while the mean profile in each CMD box is traced by a solid line. The dashed line is the averaged profile obtained with the 107 galaxies. This profile is also shown in the upper-right inset box that contains the whole spaxel distribution (in red). The number of galaxies in each bin is indicated in each panel.

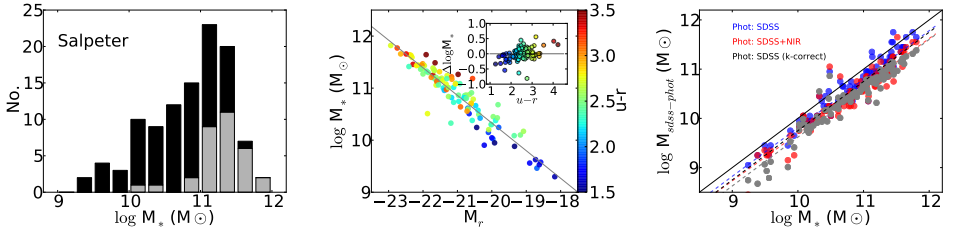


Fig. 5. *Left:* distribution of total stellar masses obtained from the spatially resolved spectral fits of each galaxy. Black bars mark galaxies with $C < 2.8$, gray bars those with $C \geq 2.8$. *Center:* correlation between the total stellar mass and SDSS r -band total magnitude. *Right:* comparison of the masses estimated from our analysis (horizontal axis), from SED fitting of integrated SDSS photometry (blue circles), and SDSS+2MASS (red) bands using the code explained in Walcher et al. (in prep.) gray points show the comparison with masses obtained fitting the SDSS photometry with the k -correct routine of Blanton & Roweis (2007). The photo-SED masses are obtained assuming a Chabrier IMF, while the masses are for a Salpeter IMF. The dashed blue, red, and gray lines show the best linear fits, while the solid black line is the one-to-one relation. The dashed black line is the one-to-one relation shifted by 0.25 dex to account for the expected offset due to IMF.

Figure 5a shows the distribution of M_* . The masses range between 10^9 and $10^{12} M_\odot$, with the peak at $\sim 10^{11} M_\odot$. Overall, our sample is dominated by galaxies in the $10^{10} - 3 \times 10^{11} M_\odot$ range, so CALIFA is successfully sampling Milky Way and M31-like galaxies. Using the concentration index, $C = r_{90}^p / r_{50}^p$, to divide the sample in spheroidal ($C \geq 2.8$) or disk ($C < 2.8$) dominated galaxies, we find a clear segregation in mass: galaxies with $C \geq 2.8$ are dominated by the most massive ones ($\geq 10^{11} M_\odot$), while disk galaxies are well distributed over the entire CALIFA mass range, with the peak at $10^{11} M_\odot$. This distribution in mass is not meant to be representative of the local universe, since the CALIFA sample is not complete for $M_r \geq -19.5$. Dwarf elliptical or irregular galaxies, for instance, are not sampled.

In the previous section the spatially resolved properties of galaxies were presented as a function of their location in the $(M_r, u-r)$ CMD (Figs. 2–4), where the absolute magnitude plays the qualitative role of galaxy mass. To calibrate this relation in quantitative terms, Fig. 5b shows our stellar masses against M_r . Results are shown for base GM , as are the results obtained with this set of SSP models adopted throughout this paper. As expected, a good correlation is found, but the dispersion in mass is ~ 0.19 dex with respect to a linear fit. The inset in Fig. 5b shows that residuals correlate with color, revealing the well-known relation between stellar mass and stellar population properties, with massive galaxies being older (and thus having larger M/L) than less massive ones, as previously shown in Fig. 4.

Figure 5c compares the masses estimated from our spatially resolved spectroscopic analysis with those obtained by Walcher et al. (in prep.) through SED fitting using just SDSS photometry (blue symbols) or 2MASS plus SDSS bands (red). Gray points represent photo-masses obtained by fitting the SDSS bands with the code (Blanton & Roweis 2007). Our GM -based masses correlate well with the photometric masses, but with systematic offsets: red, blue, and gray points in Fig. 5c are shifted from the one-to-one line by -0.20 , -0.33 , and -0.39 dex, respectively. Of this offset, a factor of -0.25 dex can be accounted for by the Salpeter IMF used in our spectral fits with base GM versus the Chabrier IMF adopted in the photo-masses. Also, the photo-masses are not corrected for extinction, so they are expected to be a factor of 0.16–0.2 dex lower than the values if we assume an average $A_V = 0.4$ –0.5 mag. Alternatively, the spectroscopic and photometric methods obtain SFHs that weight the contribution of old stellar populations in

different ways, resulting in M/L ratios larger in GM than obtained with SED fitting. The dispersion around the best linear fits (dashed lines in Fig. 5c) are 0.16–0.19 dex, which is of the same order as the dispersion between different photo-masses.

Table 1 lists the masses for all 107 galaxies obtained for the base GM . Figure B.2 shows the comparison of mass distributions for other SSP bases.

6. Spatially resolved properties vs. galaxy-averaged and integrated stellar population properties

In this section we take advantage of our spatially resolved information to address two inter-related questions: (a) what radial location can be considered typical of a galaxy as a whole in terms of its stellar population properties? and (b) how do properties derived from an integrated spectrum (obtained from the spatially collapsed data cube) relate to the typical (spatially averaged) properties within a galaxy?

The relevance of these questions resides in the fact that spatially unresolved spectra of galaxies will always be more abundant than IFS data like CALIFA. It is therefore important to understand precisely what it is that an integrated spectrum represents.

6.1. Galaxy-averaged stellar population properties

Let us define galaxy-wide average values for $\langle \log age \rangle_L$ and μ_* as follows:

- *Galaxy-averaged age:* the luminosity weighted mean value of $\langle \log age_{xy} \rangle_L$ over all spaxels is computed as

$$\langle \log age \rangle_L^{\text{galaxy}} = \frac{\sum_{xy} L_{xy} \langle \log age_{xy} \rangle_L}{\sum_{xy} L_{xy}}, \quad (1)$$

where L_{xy} is evaluated at our reference wavelength 5635 Å.

- *Galaxy-averaged stellar mass surface density:* we simply divide the total mass (summing the contributions from all the spaxels) by the total area of these spaxels to obtain the galaxy-averaged stellar mass density

$$\mu_*^{\text{galaxy}} = \frac{\sum_{xy} M_{xy}}{\sum_{xy} A_{xy}}. \quad (2)$$

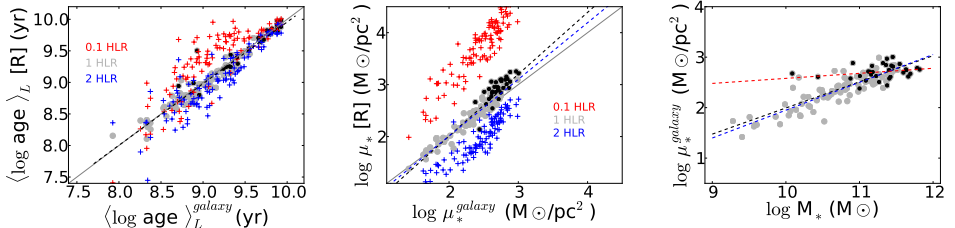


Fig. 6. *Left:* correlation between $\langle \log age \rangle_L$ at 1 HLR and the galaxy-averaged age $\langle \log age \rangle_L^{\text{galaxy}}$. Black dashed line shows the fit, which is almost equal to the one-to-one line. Black dots mark spheroidal galaxies, $C \geq 2.8$. Red and blue plus signs establish the relation between the nuclear (inner 0.1 HLR) and outer disk (2 HLR) ages as a function of $\langle \log age \rangle_L^{\text{galaxy}}$. *Center:* correlation between the stellar mass surface density at 1 HLR (gray circles) and $\log \mu_*^{\text{galaxy}}$. Black dashed line shows the fit to all the points, and dashed blue line the fit to the disk galaxies; plus signs like in the left plot. *Right:* correlation between the galaxy-averaged stellar mass surface density and galaxy stellar mass. Black points are spheroidal galaxies, $C \geq 2.8$. The dashed lines show the fits, for disk (blue) dominated galaxies and spheroidals (red). Black dashed line is the fit to all the galaxies.

Figure 6 compares these galaxy-wide averages with the corresponding values at $R = 0.1$ (red crosses), 1 (gray circles), and 2 HLR (blue crosses). The left panel shows a very good agreement between $\langle \log age \rangle_L$ at 1 HLR and the galaxy-wide average. The relations for other radii exhibit offsets and larger dispersions. As expected (see Fig. 4), the nuclei are older by an average of 0.2 dex than the galaxy-averaged age (red crosses). We note that because of the variation of the age gradient with the galaxy mass and Hubble type, the nuclei of spheroidal galaxies ($C \geq 2.8$) are only about 0.16 dex older than $\langle \log age \rangle_L^{\text{galaxy}}$, whereas for disk galaxies this difference increases to 0.23 dex. On the other hand, the outer 1–3 HLR of either disk or spheroidal galaxies are more similar to the average galaxy age (blue crosses), with an average offset of -0.08 dex.

Figure 6b repeats these comparisons, but now for the stellar mass surface density. Again, the galaxy-averaged values are well matched by the μ_* values at $R = 1$ HLR. For spheroidal galaxies (marked with black dots), μ_*^{galaxy} is slightly smaller than μ_* at 1 HLR, coinciding better with μ_* at 1.2 HLR. In nuclei μ_* is significantly larger than μ_*^{galaxy} , by typically 1.25 dex in disk galaxies and 1.43 in spheroidal galaxies.

In summary, the values of $\langle \log age \rangle_L$ and μ_* at 1 HLR represent remarkably well the galaxy-averaged age and stellar mass surface density, except that spheroidal galaxies are slightly denser at $R = 1$ HLR than their spatially averaged value.

Both $\langle \log age \rangle_L^{\text{galaxy}}$ and μ_*^{galaxy} correlate with the total stellar mass. The latter relation is shown in the right panel of Fig. 6, where one sees μ_*^{galaxy} increasing from $\sim 10^{1.5} M_\odot/\text{pc}^2$ for $M_* \sim 10^9 M_\odot$ to $\sim 10^3 M_\odot/\text{pc}^2$ for the most massive galaxies in the sample. The points are well fitted by a power law, $\mu_*^{\text{galaxy}} \propto M_*^{0.52 \pm 0.04}$. This relation was reported before by Kauffmann et al. (2003b) from the analysis of a much larger SDSS sample. They also reported a sharp change in the slope in the $\mu_* - M_*$ relation at a stellar mass of $\sim 3 \times 10^{10} M_\odot$, finding that below this mass μ_* increases as $M_*^{0.54}$, while above it μ_* is constant. Even though Fig. 6c does not show a clear change in slope, we can confirm that in the disk galaxies of our sample, $\mu_*^{\text{galaxy}} \propto M_*^{0.55 \pm 0.04}$, and in spheroid dominated galaxies (black symbols) the relation follows a much flatter slope, with $\mu_*^{\text{galaxy}} \propto M_*^{0.1 \pm 0.07}$. Similar results are obtained if we repeat the analysis replacing μ_*^{galaxy} by the surface density at 1 HLR, except that in this case the slope for early-type galaxies is 0.02 ± 0.11 , much closer to the Kauffmann et al. (2003) fit. The transition mass of $\sim 3 \times 10^{10} M_\odot$ reported

by Kauffmann et al. (2003) corresponds to $\sim 5\text{--}6 \times 10^{10} M_\odot$ for our IMF. Our sample does not yet allow us to precisely pinpoint a transition mass. Nonetheless, we will see below that all of the spheroid dominated galaxies in our sample with $M_* \geq 10^{11} M_\odot$ show radial variations of μ_* that are independent of the stellar mass.

6.2. Integrated vs. galaxy-averaged

Besides the 98291 spectra of all zones of all galaxies, we have also used to fit the 107 total spectra obtained by collapsing the data cube to a single spectrum per galaxy. These integrated spectra, which emulate the situation in integrated spectroscopy surveys, are fitted in the same way as the individual ones, adopting identical assumptions regarding the SSP templates, masks, etc. It is instructive to compare properties derived from the integrated spectra with those derived from our spatially resolved analysis.

Figure 7a compares the total stellar masses derived from the integrated spectra (on the vertical axis) with those obtained by adding the zone masses (horizontal). The two values agree very well. The mean difference in $\log M_*$ is in fact 0.00, and the dispersion is ± 0.07 dex.

Figure 7b compares the $\langle \log age \rangle_L$ values from the integrated spectra to the galaxy-average age (Eq. (1), gray circles). Again, the two values match each other, with no mean offset and a dispersion ± 0.1 dex. Extinction values also agree, as shown in Fig. 7c. The A_V values obtained from spectral fits of integrated spectra are on average only 0.02 mag larger than the mean A_V over all zones, with a dispersion of just ± 0.03 mag. The black symbols in Figs. 7b and c compare integrated ages and extinctions to those at 1 HLR. The integrated minus 1 HLR differences are 0.02 ± 0.12 dex for $\langle \log age \rangle_L$ and 0.06 ± 0.09 mag for A_V , only slightly worse than for galaxy-wide averages.

Overall, the total stellar mass, age and extinction estimated from integrated spectroscopy are remarkably robust when compared with those obtained from a spatially resolved analysis.

7. Mass weighted size: the half-mass radius and its relation to the half-light radius

While evolution of galaxies is nowadays characterized by their stellar mass more than their luminosity, galaxy sizes are still estimated from the way light, not mass, is distributed. Just as the

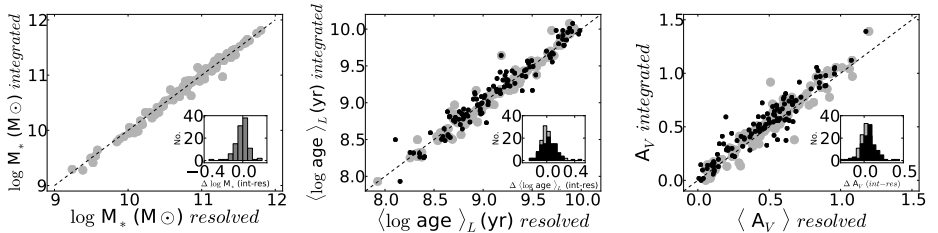


Fig. 7. Comparison of the averaged stellar population properties derived from the spatially resolved star formation history and the integrated properties derived from fitting the total galaxy spectrum; *left*: total stellar mass; *center*: luminosity weighted age; *right*: stellar extinction. The histograms in the insets show the distribution of the difference between the integrated and resolved properties. Black dots show the comparison between the integrated property and the value of the property at 1 HLR.

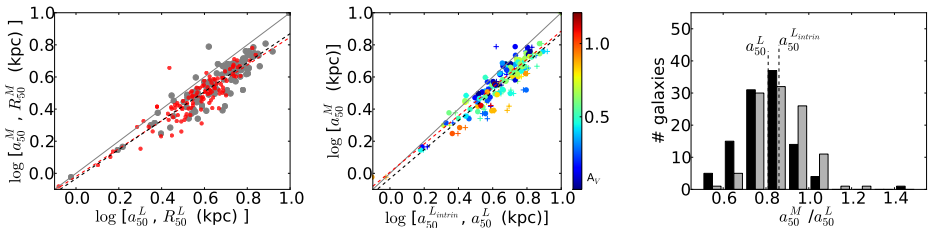


Fig. 8. *Left*: the a_{50}^M (gray points) vs. a_{50}^L and R_{50}^M (red points) vs. R_{50}^L estimated from the stellar mass integrating the stellar mass surface density profiles. Gray and red dashed lines show the fits. *Center*: relation between a_{50}^M and $a_{50}^{L_{\text{intrin}}}$ (dots) and a_{50}^M (cross). color bar codes A_V at a_{50}^L . *Right*: distribution of the ratio between half-mass and half-light ratio, corrected (gray bars) and un-corrected (black bars) by extinction. The dashed lines mark the averaged values of the distributions, $\log a_{50}^M/a_{50}^L = -0.096$ (std = 0.07) and $\log a_{50}^M/a_{50}^{L_{\text{intrin}}} = -0.071$ (std = 0.06).

stellar mass of a galaxy is a more fundamental property than its luminosity, at least when one considers galaxy evolution, the HMR is a more physical metric than the HLR. These two radii are only equivalent in the idealized case of a spatially uniform M_*/L ratio. Variations of the SFH and/or extinction within a galaxy produce a spatially dependent M/L ratio, and hence differences in their sizes estimated from mass and from light.

We take advantage of our spatially resolved SFH and extinction maps to investigate the relation between HLR and HMR. We use the 2D distribution of μ_* to define the HMR, for both circular (R_{50}^M) and elliptical (a_{50}^M) apertures, as the radius at which the mass curve of growth reaches 50% of its asymptote. Figure 8a shows how a_{50}^M and R_{50}^M relate to their luminosity based counterparts a_{50}^L and R_{50}^L . The following equations express the best fit relations between these radii (in kpc):

$$\log a_{50}^M = (0.90 \pm 0.04) \times \log a_{50}^L - (0.03 \pm 0.03), \quad (3)$$

$$\log R_{50}^M = (0.87 \pm 0.04) \times \log R_{50}^L - (0.02 \pm 0.03). \quad (4)$$

These fits and Fig. 8a show that the HMR is generally smaller than the HLR. The histogram of a_{50}^M/a_{50}^L for our 107 galaxies is shown in Fig. 8c (black bars). On average, $a_{50}^M/a_{50}^L = 0.80$ (std = 0.13), so galaxies are typically 20% smaller in mass than they appear to be in optical light. This number is only slightly smaller than the 25% reported by Szomoru et al. (2012) for a sample of high-redshift galaxies analyzed with multi-band photometry. This agreement gives us a preliminary indication that there is no significant cosmic evolution of the HMR/HLR ratio.

7.1. The relative roles of SFH and extinction gradients

Both SFH and extinction gradients induce differences between HMR and HLR. Our analysis provides a way to disentangle the relative roles of these two effects.

Unlike the HMR, the HLR is sensitive to extinction variations. When A_V increases inwards, which is generally the case, the excess dimming of the central regions with respect to outer ones produces HLR values larger than those which would be measured in the absence of extinction gradients. We use our -derived A_V maps to “dust off” the L_{15635} images and re-evaluate the HLR from the extinction corrected curve of growth, obtaining $a_{50}^{L_{\text{intrin}}}$. This allows us to quantify the role of dust in the observed difference between HMR and HLR.

Figure 8b compares a_{50}^M to both a_{50}^L (crosses) and $a_{50}^{L_{\text{intrin}}}$ (circles). Except for a slightly smaller scatter, the extinction correction brings the irregular galaxy NGC 3991 (CALIFA 475, the outlier cross with $a_{50}^M/a_{50}^L > 1$) to the one-to-one line. On average, however, $a_{50}^M/a_{50}^{L_{\text{intrin}}} = 0.85$ (std = 0.11) (Fig. 8c, gray histogram), corresponding to HMR 15% smaller than the extinction corrected HLR. Compared to the 20% difference found without this correction, we conclude that dust gradients play a relatively small role in explaining the difference between mass and light based sizes.

The main reason why HMR < HLR is thus that stellar populations produce less light per unit mass in the center than outside it. This is explicitly confirmed in Fig. 9, where $a_{50}^M/a_{50}^{L_{\text{intrin}}}$ is plotted against the difference in $\log M/L_{15635}^{\text{intrin}}$ (i.e., the extinction-corrected M/L ratio) between $R = 1$ HLR and the nucleus.

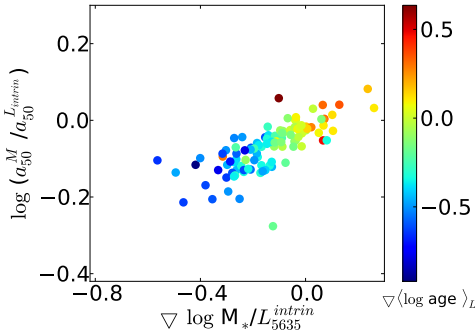


Fig. 9. Correlation between the $a_{50}^M/a_{50}^{L, intrin}$ and gradient of the M/L ratio. The color bar codes the gradient of the age of the stellar population in the inner 1 HLR.

Galaxies with small M_*/L gradients have $a_{50}^M/a_{50}^{L, intrin} \sim 1$, while those with the largest gradients can be up to a factor of two more compact in mass than in light. The points in Fig. 9 are color-coded by the corresponding $\nabla \langle \log age \rangle_L$, showing that age variations are the main factor behind the difference between HMR and HLR.

Therefore $HMR < HLR$ is ultimately a fingerprint of inside-out growth, previously found for this sample by Pérez et al. (2013). This result explains why effective radii derived in the near infrared are generally smaller than those obtained in optical bands (La Barbera et al. 2004, 2010; Falcón Barroso et al. 2011a). Besides being less sensitive to extinction effects, the near infrared is a better tracer of stellar mass than the optical.

7.2. Relation with galaxy properties

The dispersion in the HMR/HLR ratio is significant (Fig. 8c), which prompts the question of whether it correlates with some global galaxy property. Szomoru et al. (2012) were unable to identify any significant dependence of the ratio on the galaxy properties.

We investigated this issue by examining correlations between a_{50}^M/a_{50}^L (and $a_{50}^M/a_{50}^{L, intrin}$) with galaxy mass, luminosity, age, color, concentration index, central surface brightness, and size. Two distinct behaviors are identified: a_{50}^M/a_{50}^L decreases with color, surface brightness, central stellar age, and stellar mass surface density in galaxies that are bluer than $u-r \sim 2.5$, fainter than $M_r \sim -20.5$, younger than $\sim 1-3$ Gyr, and less dense than $\log \mu_* \leq 3.5 M_\odot/\text{pc}^2$ at their core. This trend can be seen in the relation between a_{50}^M/a_{50}^L and the stellar mass shown in Fig. 10. For galaxies with $M_* \leq 10^{11} M_\odot$, a_{50}^M/a_{50}^L decreases with increasing stellar mass, whereas this ratio is almost constant for more massive galaxies. This reflects the bimodal distribution of galaxies found in SDSS (Strateva et al. 2001): for spheroid dominated ($C \geq 2.8$), red, old massive galaxies, the ratio is almost constant, independent of the stellar mass, but for disk galaxies, the ratio changes significantly from 1 to 0.5 as galaxies go from the blue cloud to the red sequence through the green valley.

Galaxies with lower $a_{50}^M/a_{50}^{L, intrin}$ are those with larger M/L gradients and age gradients. These are galaxies dominated by a large

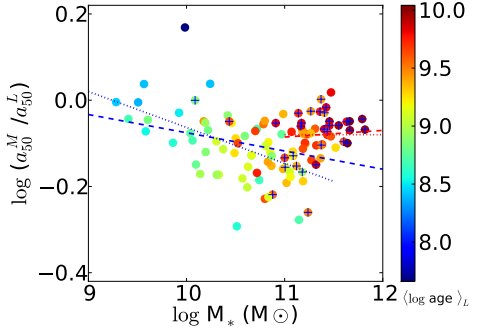


Fig. 10. Relation between a_{50}^M/a_{50}^L and the total stellar mass. Points are colored according to the luminosity weighted age of the stellar population at $R = 0.5 a_{50}^L$. Galaxies with concentration index $C \geq 2.8$ are marked with a cross. Dashed blue line shows the fit for all the galaxies with $\log M_* (M_\odot) \leq 11$, dashed red for $\log M_* (M_\odot) > 11$, and dotted blue and red lines are the fit for disk dominated galaxies and spheroidal galaxies, respectively.

central bulge surrounded by an extended luminous blue disk. These results point to the same conclusions obtained in Pérez et al. (2013), where we find that galaxies with $M_* \geq 10^{10} M_\odot$ grow their mass inside-out, and galaxies with a critical mass $\sim 6-8 \times 10^{10} M_\odot$ have been relatively more efficient growing their central regions. If galaxies grow inside-out, we expect that $a_{50}^M/a_{50}^L < 1$. In the proposed scenario by van Dokkum et al. (2010), galaxies more massive than $10^{10} M_\odot$ build their core via short violent bursts at high-redshift, and their envelope via accretion of material since $z = 2$. The SFH in the core, where half of the galaxy mass formed, results in a stellar population that is quite different from that of the extended envelope, giving $a_{50}^M/a_{50}^L < 1$. At intermediate masses, $\sim 10^{11} M_\odot$, disk galaxies have the lowest a_{50}^M/a_{50}^L , as expected if the central mass of these galaxies grow at a rate that is significantly larger than their extended envelope. However, for low mass galaxies ($M_* \leq 10^{10} M_\odot$), $a_{50}^M/a_{50}^L \sim 1$, as expected if they are not growing their mass inside-out, and the build up of their central mass is probably dominated by secular processes. Thus, HMR/HLR is a good probe of the variation of the SFH in the core with respect to extended envelope in galaxies.

8. Star formation histories in terms of stellar mass, surface density, and morphology

We now explore the dependence of the SFH (represented by the first moment of the age distribution, $\langle \log age \rangle_L$) with the total stellar mass (M_*), surface density (μ_*), and morphology (as encoded by the concentration index C). We inspect how the radial structure of $\langle \log age \rangle_L$ and μ_* varies with M_* and C . We discuss first the relation resulting from our spatially resolved analysis between μ_* and $\langle \log age \rangle_L$, then their gradients in the inner HLR, and radial profiles. The goal is to ascertain whether galaxies dominated by the spheroid or by the disk are well separated in their spatially resolved stellar population properties, where this takes place, and and which stellar mass or stellar mass

surface density is the main independent parameter that preserves the SFH of galaxies.

8.1. Stellar mass surface density – age relation

In a pioneering work, Bell & de Jong (2000) correlate the local surface brightness in the K band of a sample of spirals with the age of each region, derived from optical and near-infrared colors. They find that ages are much better correlated with their local surface brightness than with the galaxy absolute magnitude in the K band, and conclude that the surface density plays a more fundamental role in the SFH of disks than the mass of the galaxy. They suggest that the correlation can be explained through a dependence of the star formation law on the local density (see also Bell & Bowen 2000; Boissier & Prantzos 2000). They assume that colors trace age, and use surface brightness and total luminosity as proxies for μ_* and M_* , respectively. Furthermore, this conclusion was obtained only for spiral galaxies. In the light of this result, and armed with our spectroscopically derived properties, we ask whether this conclusion holds for all types of galaxies, and for all regions within galaxies.

We start by exploring the age-density relation for all regions of all galaxies in our sample. Figure 11 plots μ_* as a function of $\langle \log \text{age} \rangle_L$ for all our 98 291 individual spectra, color coded by the log density of points in the diagram. Large overplotted circles represent the galaxy-averaged $\langle \log \text{age} \rangle_L$ and $\log \mu_*$ obtained as explained in Sect. 6 (Eqs. (1) and (2)). The color of these circles code M_* (as labeled on the left-hand side legend). In this plane, our galaxies are divided into two distinct families that break at a stellar mass of $\sim 6\text{--}8 \times 10^{10} M_\odot$. Galaxies below this critical mass show a correlation between $\log \mu_*$ and $\langle \log \text{age} \rangle_L$, and are usually young disk galaxies. Above the critical mass, the relation is significantly flatter, and galaxies there are increasingly dominated by a spheroidal component. A similar result is found by Kauffmann et al. (2003b, 2006) who analyzed galaxy-averaged $\langle \log \text{age} \rangle_L$ and μ_* for 122808 SDSS galaxies. The critical mass reported by these works ($\sim 3 \times 10^{10} M_\odot$), is close to the one we find here once the differences in IMF are accounted for.

Galaxy-averaged values fall where a large fraction of the individual zone results are located because $\log \mu_*^{\text{galaxy}}$ and $\langle \log \text{age} \rangle_L^{\text{galaxy}}$ are well represented by values around 1 HLR, and most of the single spaxel zones are located between 1–1.5 HLR. Figure 11 shows that most of the individual zones follow the same general trend followed by the galaxy-averaged properties. Thus, local ages correlate strongly with local surface density. This distribution also shows that there is a critical value of $\mu_* \sim 7 \times 10^2 M_\odot/\text{pc}^2$ (similar to the value found by Kauffmann et al. 2006 once differences in IMF are factored in). Below this critical density, μ_* increases with age such that regions of low density formed later (are younger) than the regions of higher surface density, while above this critical density the dependence of μ_* on age is very shallow or altogether absent.

Since $\langle \log \text{age} \rangle_L$ reflects the SFH and it correlates with μ_* , the general distribution of galaxy zones in Fig. 11 suggests that the local mass density is linked to the local SFH, at least when $\mu_* \leq 7 \times 10^2 M_\odot/\text{pc}^2$. Since these densities are typical of disks (Fig. 7), this result is in agreement with the findings of Bell & de Jong (2000) that explain the correlation through a local density dependence in the star formation law. The large dispersion in the distribution for individual regions is caused mainly by the radial structure of the age and of the stellar mass surface density.

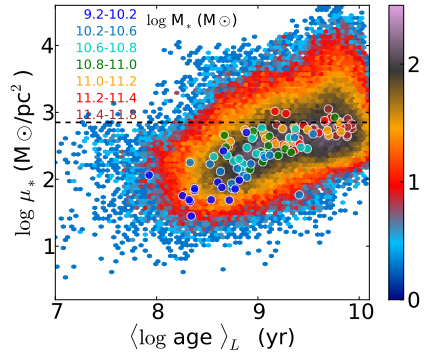


Fig. 11. The stellar mass surface density – age relationship resulting from fitting the 98291 spectra of 107 galaxies. The color bar shows the density of spectra per plotted point (red-orange are a few tens of spectra). Also plotted (as larger circles) are the averaged values for each galaxy, obtained as explained in Sect. 6. The colors of these circles code the galaxy mass (orange-red are galaxies more massive than $10^{11} M_\odot$); the dashed line marks $\mu_* = 7 \times 10^2 M_\odot/\text{pc}^2$.

8.2. Radial gradients of stellar mass surface density and age

We now investigate inner gradients in age and μ_* , and their relation with M_* . The gradient of $\log \mu_*$ in the inner HLR of each galaxy was computed as $\nabla \log \mu_* = \log \mu_*[1 \text{ HLR}] - \log \mu_*[0]$, and similarly for $\nabla \langle \log \text{age} \rangle_L$. Figure 12 shows these gradients as a function of the galaxy mass. Gray dots denote disk dominated galaxies ($C < 2.8$) and black dots mark spheroid dominated galaxies ($C \geq 2.8$). Colored symbols show mean values in eight equally populated mass bins³, with circles and stars representing spheroid and disk dominated systems, respectively.

A clear anti-correlation exists between $\nabla \log \mu_*$ and M_* . The stellar mass surface density profile becomes steeper with increasing galaxy mass. There does not seem to be a dependence on morphology, with both disk and spheroid dominated galaxies of similar mass having similar gradients $\nabla \log \mu_*$. Thus, at least for galaxies of $M_* \geq 10^{11} M_\odot$, $\nabla \log \mu_*$ is independent of the galaxy morphology. We note that this anti-correlation between $\nabla \log \mu_*$ and M_* holds only when the gradient is measured between the galaxy center ($\log \mu_*[0]$) and the galaxy-averaged stellar mass density ($\log \mu_*[1 \text{ HLR}]$), but that this result does not hold if the gradient is measured between the center and a fixed physical distance (e.g., 3 kpc) because a fixed distance represents a different position in each galaxy.

Age gradients show a different behavior with galaxy mass. While there is no correlation between $\nabla \langle \log \text{age} \rangle_L$ and M_* for the sample as a whole, a clear trend emerges when galaxies are separated by their concentration index (colored stars for disks and circles for spheroids). Overall, negative age gradients are detected, but low mass disk dominated galaxies (dark blue star) and high mass spheroidal galaxies (brown circles) have flat age profiles. High M_* disk galaxies show negative age gradients that steepen with increasing galaxy mass up to -0.5 dex/HLR for galaxies of $10^{11} M_\odot$, and then flatten towards the values of spheroidal galaxies of similar mass.

³ 15 galaxies per bin, except in the two bins with largest mass ($\log M_* > 11.4$) that add up to 17 galaxies.

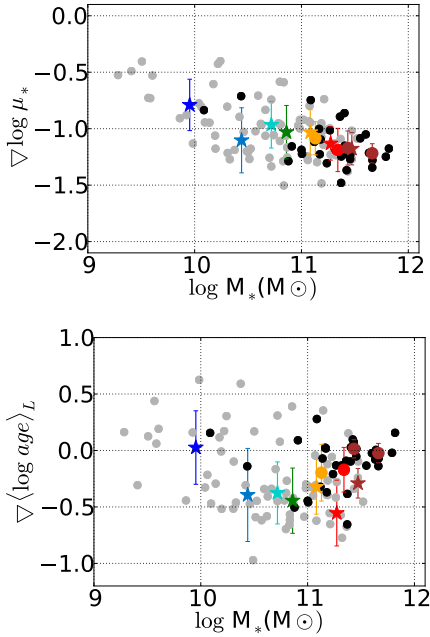


Fig. 12. Correlation between the inner gradient (calculated between the galaxy nucleus and at HLR) of $\log \mu_*$ (upper panel) and ages (bottom panel) and galaxy stellar mass. Black and gray points are galaxies with concentration index above (early-type galaxies) and below (late-type galaxies) 2.8, respectively. Median gradient value for different mass bins ($\log M_*$ (M_\odot) = 9.2–10.2, 10.2–10.6, 10.6–10.8, 10.8–11.0, 11.0–11.2, 11.2–11.4, 11.4–11.6, and 11.6–12.0) for early-type galaxies (dots) and late-type galaxies (stars) are shown. Stars and large colored dots are located at the mean value of $\log M_*$ of the galaxies that belong to the corresponding mass bin.

For early-type galaxies, we obtain an average $\nabla(\log age)_L$ of -0.11 and a dispersion ± 0.21 dex/HLR. Restricting to the more massive ones, even smaller gradients are obtained: $\nabla(\log age)_L = -0.02 \pm 0.08$ dex/HLR for $M_* > 2.5 \times 10^{10} M_\odot$. These values are in good agreement with the results obtained by fitting stellar indices of several small samples of ellipticals observed with long-slit (eg. Sánchez-Blázquez et al. 2007; Mehlert et al. 2003), or integral field spectroscopy (eg., Rawler et al. 2010; Kuntschner et al. 2006). These authors measure age gradients compatible with zero, ranging from -0.09 to 0.02 dex per effective radius, also in agreement with some of the results obtained from color gradients (Wu et al. 2005). Some of the CALIFA spheroidal galaxies show a positive central gradient (cf. Fig. 13), but these are certainly smaller than those derived from color gradients recently reported (e.g., Tortora et al. 2010; La Barbera et al. 2012) or from stellar indices (Greene et al. 2012).

For spirals we find that age gradients become increasingly negative for masses up to $\sim 10^{11} M_\odot$. In amplitude, these $\nabla(\log age)_L$ values are in agreement with results previously

reported by MacArthur et al. (2004) based on color maps of several samples of spiral galaxies. However, our trend with M_* and the age-gradient values are not in agreement with those reported by Tortora et al. (2010). They use SDSS radial color profiles to find a bimodal distribution with galaxy mass, negative gradients of ~ -0.2 dex per effective radius for galaxies less massive than $10^{10} M_\odot$, going through 0 and turning positive for high mass ($10^{11} M_\odot$) spirals. There are several possible reasons for this discrepancy, one of which is dust, which is not considered in their analysis. Furthermore, their fits compare colors of galaxy disks to single SSPs, an unrealistic approximation for the SFH of spirals, which are better represented by composite stellar population models such as those we use, or by τ models as in MacArthur et al. (2004).

In summary, we find that there is a good correlation between the μ_* gradient and M_* , and a trend of the age gradient with the mass that breaks at $M_* \sim 10^{11} M_\odot$, which is also approximately where the M_* - μ_* correlation breaks (Fig. 7c; Kauffmann et al. 2003b). In the next section we inspect if the trend of the age gradient with stellar mass is a consequence of the $M_* - \mu_*$ relation.

8.3. Radial profiles as a function of stellar mass and concentration index

A first glance at how the radial profiles of μ_* and $(\log age)_L$ change with stellar mass is shown in Fig. 4 since M_* scales with the galaxy mass. In more detail, Fig. 13 shows the result of stacking $\log \mu_*$ (left column) and $(\log age)_L$ (right column) radial profiles sorting the galaxies in seven M_* bins, chosen so as to have a similar number of 15 galaxies in each one. The mean radial profiles are obtained by co-adding $\log \mu_*$ or $(\log age)_L$ in each of the following intervals in $\log M_*(M_\odot)$: 9.2–10.2, 10.2–10.6, 10.6–10.8, 10.8–11.0, 11.0–11.2, 11.2–11.4, and 11.4–11.8.

The top row in Fig. 13 shows that the radial profiles of $\log \mu_*$ and $(\log age)_L$ scale well with the total stellar mass. Both $\log \mu_*$ and $(\log age)_L$ show negative gradients, which are flatter in the outskirts, except for the galaxies in the lowest mass bin (blue) which also have a flatter $(\log age)_L$ gradient in the inner 1 HLR. These negative gradients are also observed if mass weighted age is used instead of luminosity weighted age. This trend confirms again that galaxies more massive than $\sim 10^{10} M_\odot$ grow inside-out (Pérez et al. 2013). More massive galaxies are denser than lower mass ones, not only in their core but all along their extent. There is also a clear trend of the age profile with the mass. More massive galaxies are older along most of their radial extent. There is some overlapping in the ages at radii between 1 and 2 HLR in galaxies of a few $10^{11} M_\odot$ (red and orange). The mean age shows radial structure, with a generally steeper gradient in the inner HLR. This depends on M_* , with the largest inner gradient occurring in galaxies of intermediate mass (light blue to red curves). The most massive galaxies of the sample studied here (brown) also show negative age gradients but flatter than those of galaxies that belong to the intermediate mass bins, even though they have the largest $\log \mu_*$ gradient. Thus, the age gradient does not seem to be correlated with the central stellar mass surface density.

To check whether M_* is the only galaxy property that determines the radial structures of age and μ_* , or whether these depend on structural properties like the morphological type, we divide the sample into two subclasses according to the galaxy concentration index.

First, we divide the sample into spheroidal ($C \geq 2.8$) and disk ($C < 2.8$) dominated galaxies, and then co-add the radial profiles of galaxies in the same M_* bin. The central and bottom

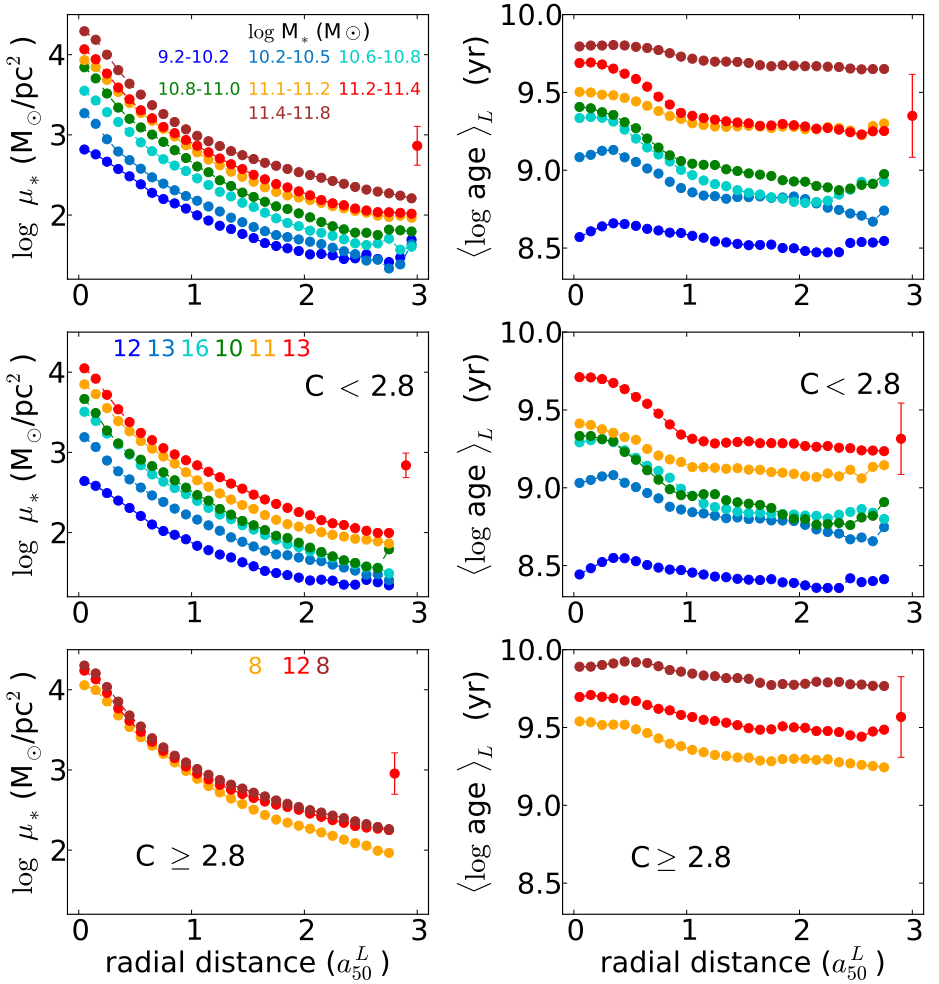


Fig. 13. The radial profiles of the stellar mass surface density and ages stacked in seven bins of galaxy stellar mass. In each bin $\log M(M_\odot)$ is: 9.2–10.2, 10.2–10.6, 10.6–10.8, 10.8–11.0, 11.0–11.2, 11.2–11.4, and 11.4–11.8. *Upper panel:* all the galaxies. *Middle panel:* disk dominated galaxies. *Lower panel:* spheroidal dominated galaxies ($C \geq 2.8$). Here, we show only the profiles in the mass bins with at least two galaxies. Numbers in the *middle and lower panels* indicate the number of galaxies in each mass bin. In the *upper panel* the number of galaxies in each mass bin is 15, except in the highest mass bin which has 17 galaxies. The error bars in all panels indicate the typical dispersion at any given distance in the mass bin $\log M(M_\odot) = 11.2\text{--}11.4$; it is similar for other mass bins and radial distances.

rows of Fig. 13 show the results. Now the number of galaxies in each mass bin is smaller and uneven (i.e. there is not the same number of galaxies in each mass bin), and that the highest M_* bin (brown) is not populated by disk galaxies. Conversely, there are no spheroidals in the low mass bins (see also Fig. 5a)⁴. The

$\log \mu_*$ and $\langle \log \text{age} \rangle_L$ radial structure of disk galaxies (central panels in Fig. 13) is similar to that for the whole sample for galaxies with mass below $10^{11} M_\odot$. There is a steep age gradient in the inner part of disk galaxies more massive than a few $10^{10} M_\odot$ (cyan to red), and $\log \mu_*$ scales with the galaxy mass. The difference in the $\log \mu_*$ radial structure of galaxies with $M \geq 10^{11} M_\odot$ (orange and red) is very small in comparison with

⁴ The CALIFA mother sample does not include dwarf ellipticals, so this analysis lacks low mass spheroidals.

the difference in the $\langle \log age \rangle_L$ radial structure between these same two mass bins. Thus, for similar μ_* , the more massive disk galaxies have older disks and bulges. Also, the difference in bulge ages is larger than the difference between disk ages for these two high mass bins. This is also clearly shown in Fig. 12, where the largest mass bins show age gradients larger for the late-type than for the early-type galaxies.

Spheroidal galaxies (bottom panels in Fig. 13) show $\langle \log age \rangle_L$ and $\log \mu_*$ profiles that clearly differ from disk galaxies. Because low mass bins are not well populated, we concentrate first on comparing the three highest mass bins. The most remarkable result is that, as seen in the bottom-right panel, the SFH of spheroidal galaxies changes with stellar mass, while $\log \mu_*$ shows little variation⁵. In addition, for the same galaxy mass, the extended envelopes of early-type galaxies are denser than in disk galaxies, and formed earlier than the disks, although the bulge of the most massive disk galaxies can be as old as the core of spheroids. It is not only that the average μ_* of early-type galaxies is almost constant, but also that the inner gradient of $\log \mu_*$ is independent of the stellar mass (see also Fig. 12).

In summary, we see that stellar mass surface density and total stellar mass play a significant role in determining the ages, and their radial variations, but for most of the early-type galaxies, the age at the core, and the galaxy-averaged age change with the total stellar mass, even though they have similar stellar mass surface density, and similar μ_* gradients in the inner HLR. These empirical results imply that, for early-type galaxies, total mass is a more important property than mass surface density to shape the age radial profiles, which in principle reflect the spatial variation of the SFH of galaxies.

8.4. The role of stellar mass in the inner regions of galaxies

Throughout this section we have shown a series of relations between stellar age and mass density, local or galaxy-wide averaged, and their mass stacked radial dependencies, as illustrated in Figs. 11–13. These results show that in early-type galaxies $\langle \log age \rangle_L$ scales with M_* but *not* with μ_* , while in disk dominated systems $\langle \log age \rangle_L$ scales with μ_* as well as with M_* . Furthermore, we found that μ_* and $\langle \log age \rangle_L$ for many of the individual regions in the galaxies follow the same relation found for the galaxy-averaged age and mass density (Fig. 11). These findings indicate that μ_* is correlated with the stellar ages, and is thus linked to the SFH. Yet, the apparent disconnection between μ_* and age at high masses, coupled to the $\langle \log age \rangle_L - M_*$ relation (implicit in the right panels of Fig. 13) suggests that M_* is more related to the SFH than μ_* is.

If μ_* is the main parameter defining the mean stellar population age, one would expect that the relation between them holds for any region of any galaxy. However, Fig. 11 shows that there is a large dispersion around the global $\log \mu_*^{\text{galaxy}} - \langle \log age \rangle_L^{\text{galaxy}}$ relation, a dispersion that reflects the spatial variations of μ_* and $\langle \log age \rangle_L$ within galaxies. The scatter is larger for ages older than 2–3 Gyr, which is where the global relation between $\log \mu_*^{\text{galaxy}}$ and $\langle \log age \rangle_L^{\text{galaxy}}$ starts to flatten. Figure 14 sheds light on the nature of this dispersion. The figure is analogous to Fig. 11, except that now the color of the small dots indicates M_* (upper panel) or the distance to the nucleus (lower panel). As in Fig. 11, the large circles plot the global $\log \mu_*^{\text{galaxy}} - \langle \log age \rangle_L^{\text{galaxy}}$ relation, and their colors code for M_* .

⁵ The coincidence of the radial profiles for early-type galaxies is a consequence of combining the radial profiles scaled in HLR units.

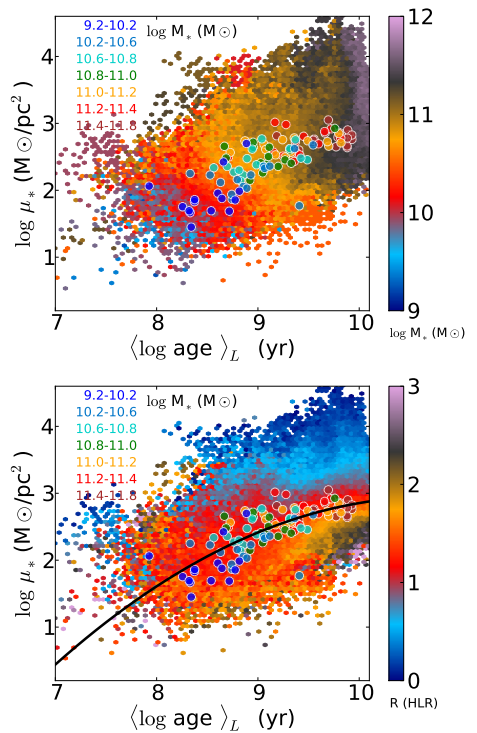


Fig. 14. Stellar mass surface density – age relationship for all of the 98291 individual zones in the 107 galaxies. Small points are color coded by the stellar mass of the galaxy to which they belong (*upper panel*) and by the distance of each zone to the nucleus of the galaxy in units of HLR (*bottom panel*). The circles are color coded by galaxy mass and represent the global μ_*^{galaxy} and $\langle \log age \rangle_L^{\text{galaxy}}$ relation. The line in the *bottom panel* shows the result of a second-order polynomial fit.

These plots show that regions that are older than a few Gyr belong to massive galaxies ($M_* \geq 7 \times 10^{10} M_\odot$) and/or they are located in the inner 1 HLR of the galaxies. These inner regions are denser than those at 1 HLR (which approximately represent the galaxy-wide average) and the outer ones, even though they all formed in a similar epoch (bottom panel of Fig. 14).

To quantify how much the inner regions are overdense with respect to the galaxy-averaged μ_* , we have fitted a second-order polynomial to the $\log \mu_*^{\text{galaxy}} - \langle \log age \rangle_L^{\text{galaxy}}$ relation⁶, shown as a black line in the bottom panel of Fig. 14. If μ_* is the main property that determines the local SFH, this fit predicts the expected stellar mass density given the age. Deviations from the relation trace deviations from this assumption, so it is interesting to correlate the residuals with other properties, M_* being the obvious contender.

This is done in Fig. 15, where we plot the difference with respect to the fit ($\Delta \log \mu_*$) as a function of M_* . The plot contains

⁶ $\log \mu_*^{\text{galaxy}} = -0.18 \times (\langle \log age \rangle_L^{\text{galaxy}})^2 + 3.9 \times \langle \log age \rangle_L^{\text{galaxy}} - 17.94$.

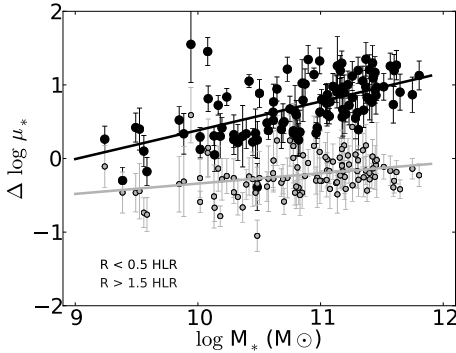


Fig. 15. The stellar mass surface density excess ($\Delta \log \mu_*$, see text) as a function of the galaxy stellar mass. Gray points and “error” bars are galaxy-by-galaxy averages and dispersions obtained for points located outside $R = 1.5$ HLR, while black points are for inner regions ($R < 0.5$ HLR).

two sets of 107 points each. The gray points and their error bars represent the mean and ± 1 sigma values of $\Delta \log \mu_*$ for all zones located at $R \geq 1.5$ HLR in each of the 107 galaxies in our sample. These points are scattered around $\Delta \log \mu_* = 0$, with a small shift towards a negative residual. This residual would be even smaller if we used only points around 1 HLR (which, as shown in Fig. 6, match the galaxy-averaged properties very well). More importantly, the residuals show little, if any, correlation with M_* . Black points, however, do correlate strongly with M_* . These are obtained considering only regions inside $R = 0.5$ HLR, where (as seen in the bottom panel of Fig. 14) μ_* values are generally well above the critical μ_* of $\sim 7 \times 10^2 M_\odot/\text{pc}^2$. The inner regions show an excess μ_* which grows for increasing M_* , particularly so for galaxies more massive than $10^{10} M_\odot$. In the inner regions of the most massive systems the $\log \mu_*^{\text{galaxy}} - (\log \text{age})_L^{\text{galaxy}}$ relation fails by about an order of magnitude, confirming our earlier conclusion that μ_* is basically unrelated to the stellar population age in these cases.

To sum up, we find that the ages and their spatial variations in the inner parts (< 1 HLR) of galaxies more massive than $10^{10} M_\odot$ are primarily related to the total stellar mass, and to the mass surface density in the outer parts (> 1 HLR).

9. Summary

We have analyzed the stellar population properties of the first 107 galaxies observed by CALIFA with the V500 and V1200 gratings to investigate the trends in the star formation history with radial distance as a function of the galaxy stellar mass and morphology, as traced by the concentration index. This CALIFA sub-sample is well distributed in the CMD ($-23 \leq M_r \leq -18$) covering from the blue cloud to the red sequence. In terms of concentration index, our sample contains a fair representation of early-type (spheroidal) dominated galaxies and late-type (disk) dominated galaxies. A full spectral fitting analysis was performed comparing combinations of SSP spectra with those of our sample galaxies using the `code`. The fitting results are processed with our pipeline `y` allowing us to resolve the galaxies in time and space. Here, the time information

is collapsed to produce 2D maps of the stellar mass surface density and light weighted ages, azimuthally averaged to produce radial profiles. Throughout we adopt a Salpeter IMF, resulting in stellar masses a factor of 1.78 (0.25 dex) larger than in case of a Chabrier IMF.

Our main conclusions are:

1. **Total stellar mass:** the sample is distributed between 10^9 – $10^{12} M_\odot$ with a peak $\sim 10^{11} M_\odot$ similar to MW and M31. Masses obtained from the integrated spectra match well those obtained from the spatially resolved SFH. This makes integrated masses a robust result. SDSS photometric masses are also well correlated with spectroscopic masses, but the former can be underestimated if the photo-SED fit does not account for stellar extinction.
2. **Spatially averaged vs. integrated galaxy properties:** the luminosity weighted age $(\log \text{age})_L$ and the stellar surface mass density μ_* , averaged over the whole galaxy, and from integrated spectra, correlate well with the age and local surface density measured at 1 HLR. These results show that the properties of a galaxy at 1 HLR are representative of the integrated and of the averaged galaxy properties.
3. **Mass weighted size:** half-mass radii are on average 20% smaller than the half-light radii, with spatial variations in the extinction accounting only for 1/4 of this difference. Thus, galaxies are intrinsically more compact in mass than in light. This average size difference shows a dual dependence on stellar mass, in the sense that in disk dominated galaxies the ratio of the half-mass to half-light radii decreases with stellar mass, but in spheroidal systems, the ratio is independent of total stellar mass. Differences between HLR and HMR arise because of radial variations in the SFHs, reflected in M/L gradients. In spheroidal systems and low mass spirals, where the spatial variation of the SFH are small, the ratio is smaller than in massive spirals. These massive spirals, that are mainly disk-like systems with large central bulges, can be up to a factor of 2 more compact in mass than in luminosity.
4. **Stellar mass surface density:** the local stellar mass surface density scales with the total mass in disk dominated galaxies; the more massive galaxies are more compact than galaxies of lower mass, and this result is preserved radially at any given distance. Spheroidal systems saturate at a critical stellar mass surface density of $\sim 7 \times 10^2 M_\odot/\text{pc}^2$ (measured at 1 HLR) which is almost independent of the galaxy stellar mass.
5. **Luminosity weighted age:** the radial run of $(\log \text{age})_L$ shows inner regions older than outer ones, changing with the galaxy stellar mass and with concentration index. There is no *correlation* between the gradient and the total stellar mass, but there is a clear trend with galaxy mass when they are separated in early-type and late-type systems. Low mass disk galaxies (usually the galaxies with lowest galaxy mass) and high mass spheroidals (usually galaxies in the highest mass bins) have relatively flat age profiles. The larger inner gradients are detected in massive disk galaxies. The presence of a massive bulge in spirals imprints a large spatial variation of the age in the inner HLR. This suggests that the SFH of building a massive bulge is quite different to the process in low mass disk dominated galaxies.
6. **Stellar local mass surface age-density relation:** the SFH of the regions located beyond 0.5-1 HLR are well correlated with their local μ_* . They follow the same relation as the galaxy-averaged age and μ_* . This suggests that it is the local stellar mass surface density that preserves the SFH in disks. However, the radial structure of the age in spheroidal

galaxies changes significantly with galaxy mass even if all these galaxies show a similar radial structure in μ_* . This implies that the SFH of spheroids is more fundamentally related to the stellar mass. Thus, galaxy mass is a more fundamental property in spheroidal systems, while the local stellar mass surface density is more important in disks.

Acknowledgements. CALIFA is the first legacy survey carried out at Calar Alto. The CALIFA collaboration would like to thank the IAA-CSIC and MPIA-MPG as major partners of the observatory, and CAHA itself, for the unique access to telescope time and support in manpower and infrastructures. We also thank the CAHA staff for the dedication to this project. Support from the Spanish Ministerio de Economía y Competitividad, through projects AYA2010-15081 (PI RGD), AYA2010-22111-C03-03 and AYA2010-10904E (SFS), AYA2010-21322-C03-02 (PSB), AYA2010-21322-C03-02 (JFB), AIB-2010-DE-00227 (JFB), the Ramón y Cajal Program (SFS, PSB and JFB), and FP7 Marie Curie Actions of the European Commission, via the Initial Training Network DAGAL under REA grant agreement number 289313 (JFB, GvdV) are warmly acknowledged. We also thank the Viabilidad, Diseño, Acceso y Mejora funding program, ICTS-2009-10, for funding the data acquisition of this project. RCF thanks the hospitality of the IAA and the support of CAPES and CNPq. ALA acknowledges support from INCT-A, Brazil. BH gratefully acknowledges the support by the DFG via grant WI 1369/29-1. AG acknowledges funding from the FP7/2007-2013 under grant agreement n. 267251 (AstroFit). R.A. Marino was also funded by the Spanish programme of International Campus of Excellence Moncloa (CEI). RGD acknowledges the support of CNPq (Brazil) through Programa Ciência sem Fronteiras (401452/2012-3). We also thank the referee for her/his suggestions and comments.

References

- Abazajian, K. N., Adelman-McCarthy, J. K., Agüeros, M. A., et al. 2009, *ApJS*, 182, 543
- Asari, N. V., Cid Fernandes, R., Stasińska, G., et al. 2007, *MNRAS*, 381, 263
- Baldry, I. K., Balogh, M. L., Bower, R. G., Glazebrook, K., & Nichol, R. C. 2004, *AIP Conf. Proc.*, 743, 106
- Balogh, M. L., Charlot, D., Zabludoff, A. I., & Zaritsky, D. 2001, *ApJ*, 557, 117
- Bacon, R., Copin, Y., Monnet, G., et al. 2001, *MNRAS*, 326, 23
- Bakos, J., Trujillo, I., & Pohlen, M. 2008, *ApJ*, 683, L103
- Bell, E. F., & Bower, R. G. 2000, *MNRAS*, 319, 235
- Bell, E. F., & de Jong, R. S. 2000, *MNRAS*, 312, 497
- Bell, E. F., Wolf, C., Meisenheimer, K., et al. 2004, *ApJ*, 608, 752
- Bica, E. 1988, *A&A*, 195, 76
- Blanc, G. A., Weinzirl, T., Song, M., et al. 2013, *AJ*, 145, 138
- Blanton, M. R., & Moustakas, J. 2009, *ARA&A*, 47, 159
- Blanton, M. R., & Roweis, S. 2007, *AJ*, 133, 734
- Boissier, S., & Prantzos, N. 2000, *MNRAS*, 312, 398
- Boselli, A., Gavazzi, G., Donas, J., & Scodreggio, M. 2001, *AJ*, 121, 753
- Brinchmann, J., & Ellis, R. S. 2000, *ApJ*, 536, 77
- Brinchmann, J., Charlot, S., Heckman, T. M., et al. 2004, *MNRAS*, 351, 1151
- Bruzual, G., & Charlot, S. 1993, *ApJ*, 405, 538
- Bruzual, G., & Charlot, S. 2003, *MNRAS*, 344, 1000
- Cappellari, M., & Copin, Y. 2003, *MNRAS*, 342, 345
- Cappellari, M., Emsellem, E., Krajnovic, D., et al. 2011, *MNRAS*, 413, 813
- Cardelli, J. A., Clayton, G. C., & Mathis, J. S. 1989, *ApJ*, 345, 245
- Chabrier, G. 2003, *PASP*, 115, 763
- Charbonnel, C., Meynet, G., Maeder, A., Schaeffer, G., & Schaefer, D. 1993, *A&AS*, 101, 415
- Chilingarian, I. V. 2009, *MNRAS*, 394, 1229
- Cid Fernandes, R. 2007, *IAU Symp.*, 241, 461
- Cid Fernandes, R., Mateus, A., Sodré, L., Stasińska, G., & Gomes, J. M. 2005, *MNRAS*, 358, 363
- Cid Fernandes, R., Pérez, E., García Benito, R., et al. 2013, *A&A*, 557, A86
- Cid Fernandes, R., González Delgado, R. M., Pérez, E., et al. 2014, *A&A*, 561, A130
- Conroy, C. 2013, *ARA&A*, 51, 393
- de Jong, R. S. 1996, *A&A*, 313, 377
- De Zeeuw, P. T., Bureau, M., Emsellem, E., et al. 2002, *MNRAS*, 329, 513
- Dickinson, M., Papovich, C., Ferguson, H. C., & Budavári, T. 2003, *ApJ*, 587, 25
- Ellis, S. C., Driver, S. P., Allen, P. D., Liske, J., & Bland-Hawthorn, J. 2005, *MNRAS*, 363, 1257
- Falcón-Barroso, J., Sánchez-Blázquez, P., Vazdekis, A., et al. 2011a, *A&A*, 532, A95
- Falcón-Barroso, J., van den Ven, G., Peletier, R. F., et al. 2011b, *MNRAS*, 417, 1787
- Fontana, A., Salimbeni, S., Grazian, A., et al. 2006, *A&A*, 459, 745
- Gallazzi, A., Charlot, S., Brinchmann, J., White, S. D. M., & Tremonti, C. A. 2005, *MNRAS*, 362, 41
- Gallazzi, A., Charlot, S., Brinchmann, J., & White, S. D. M. 2006, *MNRAS*, 370, 1106
- Ganda, K., Peletier, R. F., & McDermid, R. M. 2007, *MNRAS*, 380, 506
- Girardi, L., Bressan, A., Bertelli, G., & Chiosi, C. 2000, *A&AS*, 141, 371
- González Delgado, R. M., Cerviño, M., Martins, L. P., Leitherer, C., & Hauschildt, P. H. 2005, *MNRAS*, 357, 945
- Greene, J. E., Murphy, J. D., Comerford, J. M., Gebhardt, K., & Adams, J. J. 2012, *ApJ*, 750, 32
- Heavens, A., Panter, B., Jimenez, R., & Dunlop, J. 2004, *Nature*, 428, 625
- Husemann, B., Jahnke, K., Sánchez, S. F., et al. 2013, *A&A*, 549, A87
- Iglesias-Páramo, J., Vilchev, J. M., Galbany, L., et al. 2011, *A&A*, 553, L7
- Kauffmann, G., Heckman, T. M., White, S. D. M., et al. 2003a, *MNRAS*, 341, 33
- Kauffmann, G., Heckman, T. M., White, S. D. M., et al. 2003b, *MNRAS*, 341, 54
- Kauffmann, G., Heckman, T. M., De Lucia, G., et al. 2006, *MNRAS*, 367, 1394
- Kelz, A., Verheijen, M. A. W., Roth, M. M., et al. 2006, *PASP*, 118, 129
- Koleva, M., Prugniel, P., & De Rijcke, S., et al. 2009, *Astron. Nachr.*, 330, 960
- Kuntschner, H., Emsellem, E., Bacon, R., et al. 2006, *MNRAS*, 369, 497
- Kuntschner, H., Emsellem, E., Bacon, R., et al. 2010, *MNRAS*, 408, 97
- La Barbera, F., Merluzzi, P., Busarello, G., Massarotti, M., & Mercurio, A. 2004, *A&A*, 425, 797
- La Barbera, F., de Carvalho, R. R., de la Rosa, I. G., et al. 2010, *MNRAS*, 408, 1313
- La Barbera, F., Ferreras, I., de Carvalho, R. R., et al. 2012, *MNRAS*, 426, 2300
- Le Borgne, J. F., Bruzual, G., Pellé, R., et al. 2003, *A&A*, 402, 433
- Leitherer, C., Schaerer, D., Goldader, J. D., et al. 1999, *ApJS*, 123, 3
- MacArthur, L. A., Courteau, S., Bell, E., & Holtzman, J. A. 2004, *ApJS*, 152, 175
- MacArthur, L. A., González, J. J., & Courteau, S. 2009, *MNRAS*, 395, 28
- Martins, L. P., González Delgado, R. M., Leitherer, C., Cerviño, M., & Hauschildt, P. 2005, *MNRAS*, 358, 49
- Mateus, A., Sodré, L., Cid Fernandes, R., et al. 2006, *MNRAS*, 370, 721
- Mateus, A., Sodré, L., Cid Fernandes, R., & Stasińska, G. 2007, *MNRAS*, 374, 1457
- McDermid, R. M., Emsellem, E., Shapiro, K. L., et al. 2006, *MNRAS*, 373, 906
- Menanteau, F., Ford, H. C., Illingworth, G. D., et al. 2004, *ApJ*, 612, 202
- Mehlert, D., Thomas, D., Saglia, R. P., Bender, R., & Wegner, G. 2003, *A&A*, 407, 423
- Moorthy, B. K., & Holtzman, J. A. 2006, *MNRAS*, 371, 538
- Muñoz-Mateos, J. C., Gil de Paz, A., Boissier, S., et al. 2007, *ApJ*, 658, 1006
- Ocvirk, P., Pichon, C., Lançon, A., & Thiébaud, E. 2006, *MNRAS*, 365, 46
- Panter, B., Heavens, A. F., & Jimenez, R. 2003, *MNRAS*, 343, 1145
- Panter, B., Jimenez, R., Heavens, A. F., & Charlot, S. 2007, *MNRAS*, 378, 1550
- Peletier, R., Davies, R. L., & Illingworth, G. 1990, in *International Conference on dynamics and Interactions of Galaxies*, 267
- Peletier, R. F., & Balcells, M. 1996, *AJ*, 111, 2238
- Peletier, R. F., & de Grijs, R. 1998, *MNRAS*, 300, L3
- Peletier, R. F., Prada, F., Arribas, S., et al. 1997, *IEEEES*, 15, 16
- Peng, Y., Lilly, S. J., Kovac, K., et al. 2010, *ApJ*, 721, 193
- Pérez, E., Cid Fernandes, R., González Delgado, R. M., et al. 2013, *ApJ*, 764, 1L
- Pérez-González, P. G., Rieke, G. H., Villar, V., et al. 2008, *ApJ*, 675, 234
- Proctor, R. N., & Sansom, A. E. 2002, *MNRAS*, 333, 517
- Proctor, R. N., Forbes, D. A., & Beasley, M. A. 2004, *MNRAS*, 355, 1327
- Rawler, T. D., Smith, R. J., & Lucey, J. R. 2010, *MNRAS*, 401, 852
- Roche, N., Bernardi, M., & Hyde, J. 2010, *MNRAS*, 407, 1231
- Rosales-Ortega, F. F., Sánchez, S. F., Iglesias-Páramo, J., et al. D. 2012, *ApJ*, 756, L31
- Roth, M. M., Kelz, A., Fechner, T., et al. 2005, *PASP*, 117, 62
- Saltper, E. E. 1955, *ApJ*, 121, 161
- Sánchez, S. F., Kennicutt, R. C., Gil de Paz, A., et al. 2012, *A&A*, 538, A8
- Sánchez, S. F., Rosales-Ortega, F. F., Jungwiert, B., et al. 2013, *A&A*, 554, A58
- Sánchez-Blázquez, P., Peletier, R. F., Jiménez-Vicente, J., et al. 2006, *MNRAS*, 371, 703
- Sánchez-Blázquez, P., Forbes, D. A., Strader, J., Brodie, J., & Proctor, R. 2007, *MNRAS*, 377, 759
- Sánchez-Blázquez, P., Ocvirk, P., Gibson, B. K., Pérez, I., & Peletier, R. F. 2011, *MNRAS*, 415, 709

- Schaerer, D., Charbonnel, C., Meynet, G., Maeder, A., & Schaller, G. 1993a, *A&A*, 102, 339
- Schaerer, D., Meynet, G., Maeder, A., & Schaller, G. 1993b, *A&AS*, 98, 523
- Schaller, G., Schaerer, D., Meynet, G., & Maeder, A. 1992, *A&AS*, 96, 269
- Sil'chenko, O. K., Proshina, I. S., Shulga, A. P., & Kopusov, S. E. 2012, *MNRAS*, 427, 790
- Silva, D. R., & Bothun, G. D. 1998, *AJ*, 116, 2793
- Stoughton, C., Lupton, R. H., Bernardi, M., et al. 2002, *AJ*, 123, 485
- Strateva, I., Ivezić, Z., Knapp, G. R., et al. 2001, *AJ*, 122, 1861
- Szomoru, D., Franx, M., & van Dokkum, P. G. 2012, *ApJ*, 749, 121
- Tinsley, B. 1980, *Fundamentals of Cosmic Physics*, 5, 287
- Tojeiro, R., Heavens, A. F., Jimenez, R., & Panter, B. 2007, *MNRAS*, 381, 1252
- Tojeiro, R., Wilkins, S., Heavens, A. F., Panter, B., & Jimenez, R. 2009, *ApJS*, 185, 1
- Tortora, C., Napolitano, N. R., Cardone, V. F., et al. 2010, *MNRAS*, 407, 144
- Trager, S. C., Faber, S. M., Worthey, G., & González, J. J. 2000, *AJ*, 119, 1645
- Tremonti, C. A., Heckman, T. M., Kauffmann, G., et al. 2004, *ApJ*, 613, 898
- Vale Asari, N., Stasińska, G., Cid Fernandes, R., et al. 2009, *MNRAS*, 396, L71
- van Dokkum, P. G., Whitaker, K. E., Brammer, G., et al. 2010, *ApJ*, 709, 1018
- Vazdekis, A., Sánchez-Blázquez, P., Falcón-Barroso, J., et al. 2010, *MNRAS*, 404, 1639
- Verheijen, M. A. W., Bershad, M. A., Andersen, D. R., et al. 2004, *Astron. Nachr.*, 325, 151
- Walcher, J., Groves, B., Budavári, T., & Dale, D. 2011, *Ap&SS*, 331, 1
- Wu, H., Shao, Z., Mo, H. J., Xia, X., & Deng, Z. 2005, *ApJ*, 622, 244
- Wuyts, S., Forster Schreiber, N. M., Genzel, R., et al. 2012, *ApJ*, 753, 114
- Yoachim, P., Roskar, R., & Debattista, V. P. 2012, *ApJ*, 752, 97
- Zibetti, S., Charlot, S., & Rix, H. W. 2009, *MNRAS*, 400, 1181

Table 1. Stellar population properties.

CALIFA ID#	Name NED	log Mass M_{\odot}	log μ_{\ast} [0] M_{\odot}/pc^2	log μ_{\ast} [HLR] M_{\odot}/pc^2	$\langle \log \text{age}[0] \rangle_L$ (yr)	$\langle \log \text{age}[HLR] \rangle_L$ (yr)	HLR pc	HLR ^{DeRed} pc	HMR pc	C
001	IC 5376	10.88	4.10	2.72	9.76	9.25	4039	3938	2441	3.3
003	NGC 7819	10.37	3.28	1.98	8.43	9.03	5612	4902	4305	2.1
004	UGC 00029	11.40	3.87	2.85	9.85	9.81	4897	4509	4141	3.1
007	UGC 00036	11.23	4.18	3.05	9.50	9.42	4071	3885	3402	2.7
008	NGC 0001	11.00	4.17	2.86	9.31	8.80	2778	2594	1945	3.0
010	NGC 0036	11.31	3.95	2.72	9.74	9.14	6010	6103	5117	2.5
014	UGC 00312	9.92	2.74	1.73	8.17	8.35	5298	4931	4937	2.1
039	NGC 0444	10.04	2.74	1.85	8.94	8.60	5937	5597	4939	2.3
042	NGC 0477	10.87	3.51	2.21	9.38	8.93	6242	5942	4415	2.2
043	IC 1683	10.85	3.93	2.75	8.67	9.14	3636	2747	2755	2.6
045	NGC 0496	10.72	2.99	2.12	8.62	8.98	6354	5458	5460	2.0
053	UGC 01057	10.62	3.38	2.29	9.29	8.65	4979	4336	3135	2.4
073	NGC 0776	11.19	4.14	2.50	9.29	8.98	5062	4598	3293	2.1
088	UGC 01938	10.83	3.47	2.64	9.49	8.87	5687	5067	4546	2.5
100	NGC 1056	10.09	4.01	3.05	8.84	8.98	955	791	954	3.2
119	NGC 1167	11.47	4.32	2.93	9.81	9.77	4433	4555	4634	2.8
127	NGC 1349	11.43	4.22	2.76	9.81	9.46	5126	5326	4215	2.6
133	UGC 03107	11.02	3.71	2.59	9.39	9.05	6989	5957	4509	2.5
146	UGC 03253	10.80	3.88	2.61	9.52	9.14	3656	2754	2149	2.3
147	NGC 2253	10.33	3.39	2.02	9.09	8.66	3606	3280	2422	2.1
151	NGC 2410	11.12	4.03	2.72	9.54	9.21	4392	4097	3085	3.1
152	UGC 03944	10.14	3.03	1.96	9.08	8.77	3853	3430	2611	2.2
155	UGC 03995	11.26	4.22	2.77	9.67	9.32	5479	5488	4021	2.4
156	NGC 2449	11.18	4.04	2.88	9.59	9.24	4181	3941	3570	2.7
208	UGC 04461	10.51	3.52	2.09	8.99	8.12	4766	3978	2430	2.4
213	NGC 2623	10.74	3.67	2.44	8.69	8.75	3385	2520	2204	2.6
273	IC 2487	10.63	3.41	2.31	9.44	8.99	6283	5591	4392	2.5
274	IC 0540	10.18	3.53	2.82	9.31	9.43	2202	2061	1981	2.7
277	NGC 2916	10.83	3.81	2.37	9.73	9.02	5398	5488	3903	2.2
306	UGC 05358	9.58	2.41	1.57	8.54	8.60	4093	3772	3571	2.4
307	UGC 05359	10.98	3.42	2.27	9.55	9.17	8231	7855	5692	2.4
309	UGC 05396	10.59	3.06	2.20	9.10	8.79	6077	5584	5042	2.1
319	NGC 3160	11.07	3.75	2.68	9.82	9.74	5303	4807	4480	2.7
326	UGC 05598	10.67	3.51	2.37	8.88	8.48	5056	4912	3837	2.5
364	UGC 06036	11.36	4.10	3.11	9.78	9.70	5076	5439	4771	3.4
387	NGC 3615	11.63	4.44	3.10	9.93	9.81	4167	4034	3728	3.3
388	NGC 3614	10.46	3.42	2.23	9.50	9.01	3652	3583	3240	2.2
475	NGC 3991	9.99	2.99	1.77	7.41	8.13	3946	5140	5843	1.8
479	NGC 4003	11.38	4.09	2.76	9.58	9.70	5269	4381	4141	2.8
486	UGC 07012	9.86	3.02	1.98	8.75	8.26	2847	2785	2252	2.7
489	NGC 4047	10.97	3.81	2.71	9.23	8.64	3534	3292	2938	2.3
500	UGC 07145	11.08	3.56	2.52	9.75	9.07	7107	6578	5363	2.3
515	NGC 4185	10.99	3.48	2.43	9.72	9.40	6088	6213	5657	2.0
518	NGC 4210	10.49	3.69	2.32	9.95	8.92	3749	3696	2813	1.9
528	IC 0776	9.40	1.99	1.38	8.62	8.29	3615	3719	3260	2.0
548	NGC 4470	10.24	2.92	2.45	8.25	8.59	2795	2793	3063	2.0
577	NGC 4676	11.09	3.49	2.63	9.15	9.43	6073	4707	4515	2.8
607	UGC 08234	11.40	4.19	2.92	9.37	9.40	3940	3737	3685	3.3
609	UGC 08250	10.22	2.63	2.19	8.56	8.79	5866	5477	5091	2.3
610	UGC 08267	11.07	3.60	2.67	9.28	8.90	5862	5093	4377	2.4
657	UGC 08733	9.60	2.33	1.69	8.54	8.71	3522	3410	3151	2.1
663	IC 0944	11.47	4.02	2.85	9.71	9.45	6792	6294	5631	2.8
676	NGC 5378	10.70	3.86	2.44	9.69	9.47	3441	3798	2932	2.4
758	NGC 5682	9.51	2.35	1.95	8.18	8.36	2387	2211	2362	2.6
764	NGC 5720	11.32	3.85	2.50	9.97	9.17	7079	7536	5510	2.4
769	UGC 09476	10.42	3.15	2.17	9.05	8.79	4413	4236	4071	1.8
783	UGC 09665	10.10	3.55	2.47	9.16	8.66	2481	2315	1762	2.4
797	UGC 09873	10.31	3.20	1.86	8.86	8.81	5489	4665	3725	2.4
798	UGC 09892	10.57	3.42	2.27	9.37	8.72	6313	6140	4164	2.5
802	ARP 220	11.15	3.88	2.40	8.38	8.83	4906	3252	2603	2.3
806	NGC 5966	11.16	4.10	2.96	8.06	9.85	3693	3483	3247	2.8
820	NGC 6032	10.50	3.51	2.22	8.94	9.05	5947	5486	4822	2.0
821	NGC 6060	11.05	3.99	2.61	9.40	8.97	5787	5576	3971	2.2
823	NGC 6063	10.30	3.16	2.23	9.37	8.85	3757	3617	3021	1.9
826	NGC 6081	11.32	4.37	3.06	9.83	9.68	3539	2968	2507	3.4

Table 1. continued.

CALIFA ID#	Name NED	log Mass M_{\odot}	log $\mu_{\ast}[0]$ M_{\odot}/pc^2	log $\mu_{\ast}[\text{HLR}]$ M_{\odot}/pc^2	$\langle \log \text{age}[0] \rangle_L$ (yr)	$\langle \log \text{age}[\text{HLR}] \rangle_L$ (yr)	HLR pc	HLR ^{DeRed} pc	HMR pc	C
828	UGC 10331	10.06	2.79	1.90	8.81	8.65	4239	4046	3460	2.4
829	NGC 6125	11.46	4.41	3.10	9.91	9.90	3343	3168	2974	3.2
832	NGC 6146	11.82	4.39	3.07	9.83	9.98	5586	5057	4788	3.4
845	UGC 10693	11.66	4.22	2.84	9.93	9.86	6347	6362	5469	3.3
847	UGC 10710	11.38	3.85	2.13	9.68	8.97	9430	12147	9366	2.8
848	NGC 6310	10.78	3.89	2.85	9.77	9.32	4025	4057	3538	2.3
850	NGC 6314	11.27	3.98	2.86	9.44	9.30	4867	4601	4593	3.3
851	NGC 6338	11.78	4.30	2.94	9.92	9.88	6948	6574	6248	2.8
852	UGC 10796	9.57	2.47	1.64	7.95	8.39	3352	3345	3715	2.4
853	NGC 6361	11.26	4.21	3.08	9.55	9.18	4237	4062	3522	2.6
854	UGC 10811	11.19	3.71	2.58	9.65	9.28	7712	7482	6407	2.7
856	IC 1256	10.80	3.58	2.49	9.18	8.97	4885	4536	3815	2.2
857	NGC 6394	11.21	3.53	2.71	9.77	9.11	6759	6575	5331	2.1
858	UGC 10905	11.60	4.19	2.96	9.52	9.51	5489	5011	4453	3.5
859	NGC 6411	11.14	4.08	2.94	9.72	9.64	3328	3308	3093	3.0
860	NGC 6427	10.91	4.53	3.24	9.75	9.82	1669	1551	1463	3.3
863	NGC 6497	11.21	3.93	2.65	9.86	9.20	5435	5853	4330	2.7
864	NGC 6515	11.42	4.25	2.77	9.69	9.77	4811	4586	4645	3.1
866	UGC 11262	10.20	3.02	1.71	9.24	8.65	5315	5062	4054	2.2
867	NGC 6762	10.43	3.87	3.06	9.70	9.54	1581	1538	1411	2.9
869	NGC 6941	10.52	3.11	1.80	9.70	9.24	6675	6787	5329	2.1
872	UGC 11649	10.72	3.88	2.43	9.80	9.22	3524	3665	2373	2.1
873	UGC 11680NED01	11.52	4.03	2.78	9.68	9.18	5744	5338	4369	2.5
874	NGC 7025	11.45	4.65	3.22	9.84	9.72	3131	3223	2739	3.3
877	UGC 11717	11.23	4.12	2.54	9.71	9.50	5929	6137	3263	2.9
878	MCG-01-54-016	9.28	2.30	1.70	8.26	8.40	2827	2719	2800	2.3
879	UGC 11740	10.80	3.15	2.51	9.64	8.78	5341	5718	4746	2.4
880	UGC 11792	10.66	3.71	2.72	9.31	8.98	4190	3684	3200	2.4
881	NGC 7194	11.64	4.48	3.10	10.01	9.99	4372	4113	3409	3.3
883	UGC 11958	11.55	4.15	2.94	9.97	9.81	4936	4772	4367	2.8
886	NGC 7311	11.37	4.60	3.25	9.64	9.25	3268	3491	2580	3.1
887	NGC 7321	11.37	3.99	2.69	9.59	8.91	6275	5914	4580	2.4
888	UGC 12127	11.69	4.20	2.84	10.00	9.91	6285	6378	5498	3.1
890	UGC 12185	11.00	3.96	2.66	9.73	9.24	4516	4540	3312	2.8
896	NGC 7466	11.06	3.89	2.44	9.31	8.95	6212	5505	4093	2.7
900	NGC 7550	11.43	4.36	3.01	9.56	9.69	3732	3305	3170	2.9
901	NGC 7549	10.87	3.84	2.44	9.06	8.58	4182	4288	3102	2.1
902	NGC 7563	11.17	4.50	3.15	9.81	9.83	2338	2141	2073	3.5
904	NGC 7591	11.18	4.12	2.89	9.24	8.84	3838	3398	2639	3.0
935	UGC 12864	10.19	3.03	1.89	8.69	8.70	5396	4466	4752	2.4
938	NGC 5947	10.83	3.78	2.12	9.32	8.76	5280	5076	3143	2.4
939	NGC 4676B	11.19	3.99	2.89	9.66	9.49	3769	3305	2918	2.4

Appendix A: Structural parameters: Half-light radius

To compare the spatial distribution of any given property in galaxies which are at different distances, the 2D maps need to be expressed in a common metric. We chose the half-light radius (HLR). To compute the HLR, we collapse the spectral cubes in the rest-frame window $5635 \pm 45 \text{ \AA}$, derive the isophotal ellipticity and position angle, and then integrate a curve of growth from which we derive the HLR. In some galaxies, the integrated image may contain masked regions at the position where the original cube contains foreground stars or some other artifacts (see Cid Fernandes et al. 2013 for further explanations) which may affect the estimation of the different parameters, including the HLR. To correct for these missing data, we build an average surface brightness radial profile for each galaxy using circular apertures. This profile is used to estimate the surface brightness of the spaxels masked in the original cube, assuming a smooth change of surface brightness between the missing data and the averaged values of their near neighbors at the same distance. This reconstructed flux image is used to derive the ellipticity and position angle of the aperture, and to obtain the average azimuthal radial profiles of the stellar population properties. These structural parameters are defined and obtained as follows:

- *Galaxy center*: we take as the galaxy center the peak flux position. This definition is correct for most of the galaxies, except for the irregular galaxy CALIFA 475 (NGC 3991), where the maximum flux is well outside of the morphological center.
- *Ellipticity and position angle*: the flux-weighted moments of the 5635 \AA image are used to define the ellipticity and position angle (Stoughton et al. 2002). The reconstructed flux image is used to calculate the so-called Stokes parameters in order to obtain the ellipticity and position angle at each radial distance. The values, however, are kept constant beyond 2 HLR, which are taken to define a unique elliptical aperture for each galaxy. The final values do not change significantly after an iteration, filling the missing data with the surface brightness profile resulting from adding the flux with the derived elliptical aperture, and then estimating again the Stokes parameters.
- *Half-light radius (HLR)*: for each galaxy, the reconstructed flux image is used to build the flux curve of growth and to obtain the half-light radius. The flux is integrated in elliptical apertures with a position angle and ellipticity defined as explained above. The semi-major axis length at which the curve of growth reaches 50% of its maximum value is defined as the half-light radius, a_{50}^L .

For the sample analyzed here, $1 \leq a_{50}^L \leq 8 \text{ kpc}$, with a mean value of 4.6 kpc . These values are higher than the Petrosian radius r_{50}^P (obtained from the SDSS data archive), as shown in Fig. A.1. However, the circularized size, defined as $a_{50}^L \times \epsilon^{1/2}$, where ϵ is the ellipticity, follows well the one-to-one line, as does the HLR obtained through curve of growth integrating in circular rings, R_{50}^L . The linear fit, in fact, deviates from the one-to-one line, giving circular HLR that are on average 5% lower than r_{50}^P . The outlier in the correlation is CALIFA 886 (NGC 7311), the central galaxy of a compact group. Given the morphology of the system, r_{50}^P is probably overestimated.

Table 1 lists a_{50}^L values obtained for our sample. In this paper we will use HLR to refer generally to this metric, whether it is

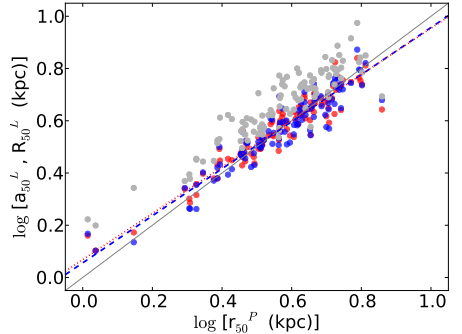


Fig. A.1. The Petrosian radius r_{50}^P versus a_{50}^L (gray) the semi-major axis length of the ellipse that contains half of the flux estimated from the CALIFA data cube through the curve of growth at 5635 \AA ; the radius ($a_{50}^L \times \epsilon^{1/2}$) of the circle with equivalent flux to the ellipse (blue points); the half-light radius, R_{50}^L (red points). The black line is the one-to-one line, while the dotted blue line is the fit to $(a_{50}^L \times \epsilon^{1/2})$ and r_{50}^P , and the dashed red line the fit to R_{50}^L .

computed in circular or elliptical geometry, unless the specific results depend on the actual definition (as in Sect. 7).

Appendix B: Quality of the spectral fits and uncertainties associated with evolutionary synthesis models

B.1. Quality of the spectral fits

All stellar population information used throughout this work comes from the fits of the 98 291 individual spectra from 107 CALIFA data cubes. Here we illustrate these spectral fits with example spectra extracted from the nucleus and from a spaxel at 1 HLR for three different galaxies.

The top panels in Fig. B.1 show the nuclear spectra (black) of CALIFA 001 (IC 5376), CALIFA 073 (NGC 776), and CALIFA 014 (UGC 00312). The respective fits are shown by the red line. Each panel also shows the $O_\lambda - M_\lambda$ residual spectrum. Examples of fits for regions 1 HLR away from the nucleus are shown in the bottom panels.

As customary in full spectral fitting work, the fits look very good. In these particular examples the figure of merit $\bar{\Delta}$, defined as the mean value of $|O_\lambda - M_\lambda|/M_\lambda$ (Eq. (6) in Cid Fernandes et al. 2013), is $\bar{\Delta} = 1.3\%$ (5.8%) for the nucleus (at 1 HLR) of IC 5376, 1.3% (5.8%) for NGC 776, and 1.6% (5.0%) for UGC 00312. The median values for the 107 galaxies are $\bar{\Delta} = 1.6\%$ at the nucleus and 5.1% at $R = 1 \text{ HLR}$. The SSP models used in these examples are from the *GM* base, built from evolutionary synthesis models by González Delgado et al. (2005) and Vazdekis et al. (2010), as summarized in Sect. 3. Very similar results are obtained with bases *CB* and *BC*.

B.2. Uncertainties associated with using different SSP models

To evaluate to what extent the results of our spectral synthesis analysis depends on the choice of SSP models, we now compare properties derived with bases *GM*, *CB*, and *BC*. Since

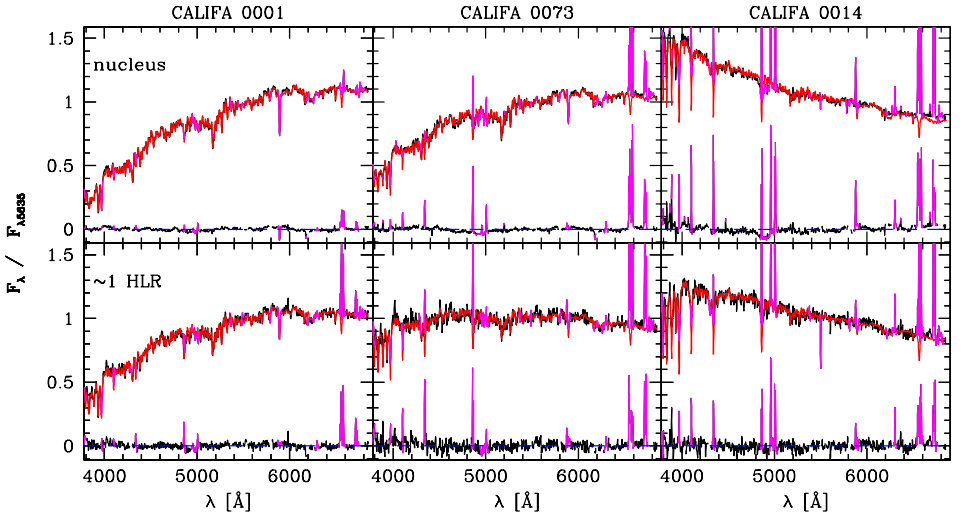


Fig. B.1. Example fits for IC5376 (CALIFA 001, *left*), NGC 776 (CALIFA 073, *middle*), and UGC00312 (CALIFA 014, *right*). The *top panels* show the nuclear spectrum, while the *bottom panels* are for spaxels located at 1 HLR from the nucleus. Observed and synthetic spectra are shown in black and red lines, respectively. Masked regions (mostly emission lines) are plotted in magenta, and bad pixels are not plotted. Emission line peaks in the residual spectra were clipped for clarity.

Cid Fernandes et al. (2014) have already performed this comparison for the same data analyzed here, we focus on comparisons related to specific points addressed in this paper.

First, we compare the results obtained for M_* . Figure B.2 shows the galaxy stellar mass distribution obtained with the *CB* and *BC* bases. The *GM* mass distribution (see Fig. 5a) is shifted to higher masses than *CB* and *BC* by ~ 0.27 dex, as expected because of the different IMFs (Salpeter in *GM* and Chabrier in *CB* and *BC*). The Salpeter IMF used in *GM* models has more low mass stars than the Chabrier function used in *CB* and *BC*, implying larger initial masses for the same luminosity. In addition, for the Salpeter IMF about 30% of this mass is returned to the ISM through stellar winds and SNe, while for a Chabrier IMF this fraction is 45%. These effects end up producing differences of a factor of ~ 1.8 in the total mass currently in stars.

In the context of this paper, it is useful to compare the results for μ_* and $(\log age)_L$ at the nucleus and at 1 HLR, as these allow us to estimate the uncertainties associated with the stellar mass surface density and age gradient due to the choice of SSP models. This is done in the top two rows of Fig. B.3, where values obtained with *GM* bases are plotted in the vertical axis, while *CB*- and *BC*-based estimates are in the horizontal. In all panels the labels Δ and σ_Δ denote the mean and rms of the difference of values in the *y*- and *x*-axis, and the histogram of these differences is shown in the inset panels.

The $\mu_*(0)$ and $\mu_*(1 \text{ HLR})$ values show the same 0.27 dex IMF-induced systematic differences seen in Fig. B.2. The dispersions in $\log \mu_*$ values are ~ 0.1 dex, much smaller than the $\nabla \log \mu_*$ gradients seen in Fig. 12. IMF factors shift $\log \mu_*(0)$ and $\log \mu_*(1 \text{ HLR})$ by the same amount. We thus conclude that SSP model choice has no significant impact on the μ_* gradients discussed in this work.

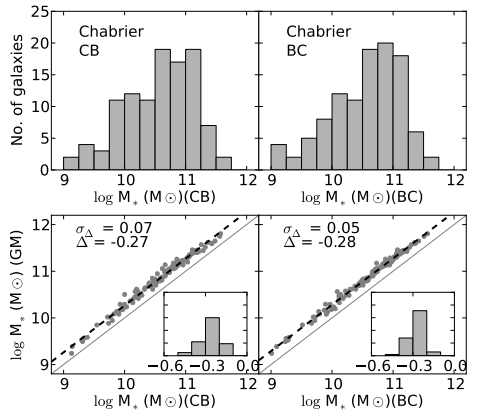


Fig. B.2. The galaxy stellar mass distributions obtained from the spatially resolved star formation history. The histograms show the results obtained with the bases *GM*, *CB*, and *BC*, from *left to right*, *upper panels*. The *lower panels* show the comparison of the galaxy stellar mass obtained with *GM* (vertical axis) and *CB* or *BC* (horizontal axis) for the 107 CALIFA galaxies. A one-to-one line is drawn in all the panels, as well as the best fit (dashed lines). The histogram inserted in each panel shows the differences in the $\log M_*$ obtained with the base *CB* or *BC* with respect to *GM*. In the top-left corner of the panel, Δ is defined as $CB - GM$ or $BC - GM$, and their dispersions are labeled.

Dispersions in the $(\log age)_L$ values are also of the order of 0.1 dex. One sees a small bias whereby the nuclei of mainly

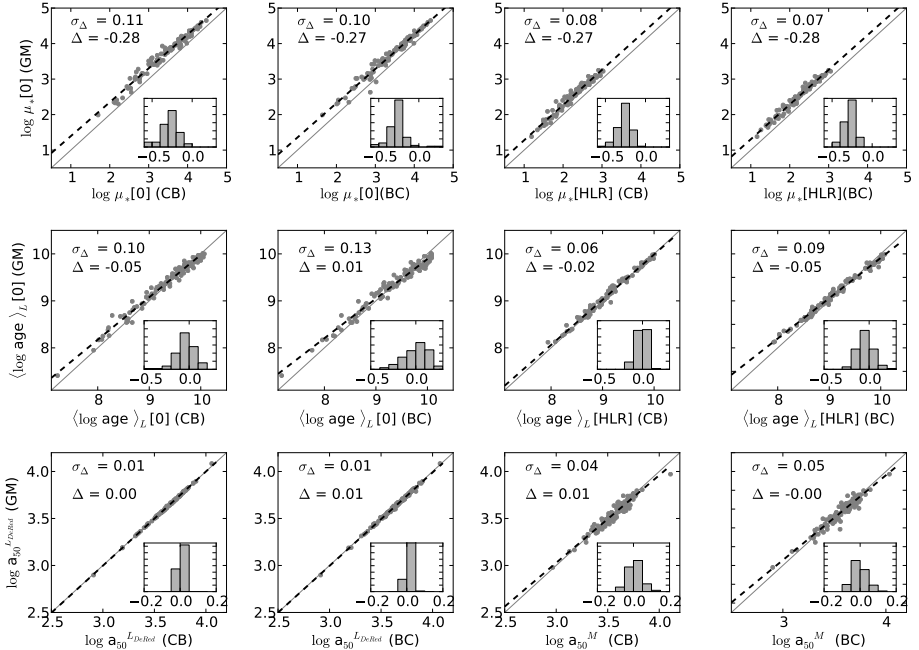


Fig. B.3. Comparison of stellar population properties obtained with bases *GM* (vertical axis) and *CB* or *BC* (horizontal axis) for the 107 CALIFA galaxies. A one-to-one line is drawn in all panels, as well as the best fit (dashed lines). The histogram inserted in each panel shows the differences in the property obtained with the base *CB* or *BC* with respect to *GM*. In the top-left corner of each panel, Δ is defined as the mean *CB* – *GM* (or *BC* – *GM*) difference, and σ_{Δ} is the corresponding standard deviation.

low mass galaxies are older with *GM* than *CB* by 0.05 dex, whereas the difference at 1 HLR is 0.02 dex. This would make $\langle \log age \rangle_L \sim 0.03$ larger (i.e. a smaller gradient) with *CB* than with *GM*, a small effect which does not affect our conclusion that low mass galaxies show flat age radial profiles. The same small effect is found when comparing *GM* and *BC* ages.

Finally, we evaluate the effect of SSP choice on the half-mass and half-light radii discussed in Sect. 7. We note that a_{50}^M depends on the spatial variation of the SFH (through the M/L ratio), while a_{50}^{min} also depends on the radial variation of the stellar extinction. The bottom panels of Fig. B.2 show that the choice of SSP base has no significant impact upon the estimates of either HLR or HMR. Light-based sizes derived from *GM*, *CB*, and *BC* fits agree with each other to within ± 0.01 dex, while HMR have dispersion of 0.05 dex or less.

Appendix C: Missing mass in the CALIFA FoV

The main constraint in the sample selection for the CALIFA survey is a size⁷ $\text{isoA}_r < 79.2''$, only 7% larger than the PPAK FoV of $74''$. This implies that while some galaxies are completely enclosed within the FoV, others are somewhat larger. The question arises of how much stellar mass is left out of our stellar

population synthesis analysis because it is out of the FoV. To estimate this “missing mass”, we proceed in the following manner, depicted in Fig. C.1 for the case of CALIFA 003. We use a $3' \times 3'$ copy of the SDSS *r*-band image to compute and subtract the background around the galaxy; the distribution of the background residual is used to compute the edge of the galaxy as that enclosed above 1σ of the background (red contour in the figure). The missing flux (light blue in the top-right panel) is that contained within this contour and outside the CALIFA image; the points corresponding to this missing flux are represented in green in the radial profile in the bottom-left panel. From our population synthesis analysis of the CALIFA data cube, we compute the M/L ratio as a function of distance from the center of the galaxy (gray points in the bottom-right panel of the figure). The mean M/L value between 1.5 and 2.5 HLR is then used together with the missing flux to compute the missing mass outside the PPAK FoV. This is an approximate method, because we assume a constant value for the M/L in the outer parts of the CALIFA FoV, but the results are quite reliable, given that M/L has generally little or no gradient in these outer reaches, as can be seen in the bottom panels for the case of CALIFA 003.

The overall results for the missing mass are shown in the histogram of Fig. C.2; with a mean value of 8.63%, it shows a lognormal-type shape with a peak at $\sim 5\%$.

⁷ The semi-major axis length corresponding to the isophote 25 mag/arcsec² in the *r* band.

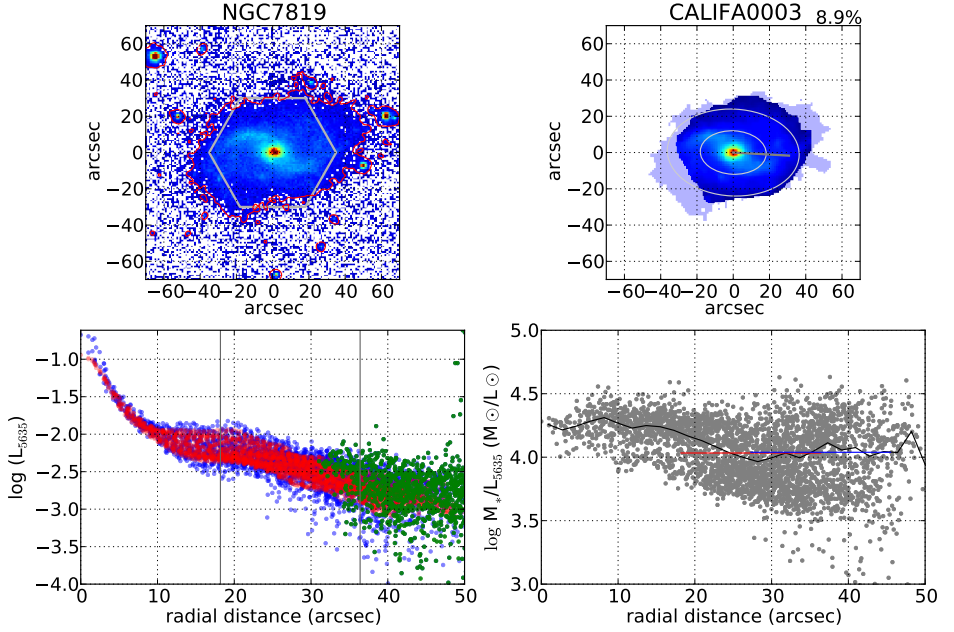


Fig. C.1. *Upper-left panel:* r -band SDSS image of NGC 7819 (CALIFA 003); a hexagon indicates the PPAk FoV, and a red contour shows the 1σ background. *Upper-right panel:* CALIFA image at 5635 Å; light blue shows the area of the galaxy outside the PPAk FoV, taken as that enclosed within the red contour in the left image minus the CALIFA image. The ellipses show the positions of 1 HLR and 2 HLR (a_{50}^L), and the gray line shows r_{90}^p . *Bottom-left panel:* (blue points) SDSS r -band surface brightness profiles scaled to (red points) CALIFA surface brightness profiles at 5635 Å; the green points are those red points that fall outside PPAk FoV, and are the ones used for the computation of the missing stellar mass. The position of 1 HLR and 2 HLR are marked by vertical lines. *Bottom-right panel:* mass-luminosity ratio derived from our spectral fits obtained pixel to pixel (gray points) and the averaged radial profile (black line). Horizontal lines are the mass-to-luminosity ratio averaged for points that are between 1 and 2 HLR (red) and 1.5–2.5 HLR (blue).

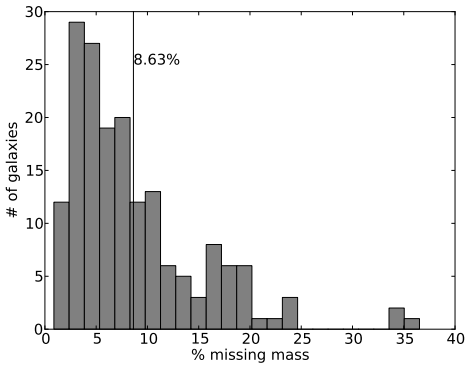


Fig. C.2. Histogram of the fraction of mass that is outside of the CALIFA FoV. The average value is marked by a vertical line.

Referências Bibliográficas

- Abazajian K. N., Adelman-McCarthy J. K., Agüeros M. A., Allam S. S., Allende Prieto C., An D., Anderson K. S. J., Anderson S. F., Annis J., Bahcall N. A., et al., 2009, *ApJS*, 182, 543
- Asari N. V., Cid Fernandes R., Stasińska G., Torres-Papaqui J. P., Mateus A., Sodré L., Schoenell W., Gomes J. M., 2007, *MNRAS*, 381, 263
- Bershady M. A., Verheijen M. A. W., Swaters R. A., Andersen D. R., Westfall K. B., Martinsson T., 2010, *ApJ*, 716, 198
- Bian W., Gu Q., Zhao Y., Chao L., Cui Q., 2006, *MNRAS*, 372, 876
- Binney J., Tremaine S., 2011, *Galactic Dynamics: (Second Edition)*, Princeton Series in Astrophysics. Princeton University Press
- Bruzual G., Charlot S., 2003, *MNRAS*, 344, 1000
- Bryant J. J., Owers M. S., Robotham A. S. G., Croom S. M., Driver S. P., Drinkwater M. J., Lorente N. P. F., Cortese L., Scott N., Colless M., Schaefer A., Taylor E. N., Konstantopoulos I. S., Allen J. T., Baldry I., Barnes L., Bauer A. E., Bland-Hawthorn J., Bloom J. V., Brooks A. M., Brough S., Cecil G., Couch W., Croton D., Davies R., Ellis S., Fogarty L. M. R., Foster C., Glazebrook K., Goodwin M., Green A., Gunawardhana M. L., Hampton E., Ho I.-T., Hopkins A. M., Kewley L., Lawrence J. S., Leon-Saval S. G., Leslie S., McElroy R., Lewis G., Liske J., López-Sánchez Á. R., Mahajan S., Medling A. M., Metcalfe N., Meyer M., Mould J., Obreschkow D., O'Toole S., Pracy M., Richards S. N., Shanks T., Sharp R., Sweet S. M., Thomas A. D., Tonini C., Walcher C. J., 2015, *MNRAS*, 447, 2857
- Bundy K., Bershady M. A., Law D. R., Yan R., Drory N., MacDonald N., Wake D. A., Cherinka B., Sánchez-Gallego J. R., Weijmans A.-M., Thomas D., Tremonti C., Masters K., Coccato L., Diamond-Stanic A. M., Aragón-Salamanca A., Avila-Reese V., Badenes C., Falcón-Barroso J., Belfiore F., Bizyaev D., Blanc G. A., Bland-Hawthorn J., Blanton M. R., Brownstein J. R., Byler N., Cappellari M., Conroy C., Dutton A. A., Emsellem E., Etherington J., Frinchaboy P. M., Fu H., Gunn J. E., Harding P., Johnston E. J., Kauffmann G., Kinemuchi K., Klaene M. A., Knapen J. H., Leauthaud A., Li C., Lin L., Maiolino R., Malanushenko V., Malanushenko E., Mao S., Maraston C., McDermid R. M., Merrifield M. R., Nichol R. C., Oravetz D., Pan K., Parejko J. K., Sanchez S. F., Schlegel D., Simmons A., Steele O., Steinmetz M., Thanjavur K., Thompson B. A., Tinker J. L., van den

Referências Bibliográficas

- Bosch R. C. E., Westfall K. B., Wilkinson D., Wright S., Xiao T., Zhang K., 2015, *ApJ*, 798, 7
- Calzetti D., Kinney A. L., Storchi-Bergmann T., 1994, *ApJ*, 429, 582
- Cappellari M., Copin Y., 2003, *MNRAS*, 342, 345
- Cappellari M., Emsellem E., Krajnović D., McDermid R. M., Scott N., Verdoes Kleijn G. A., Young L. M., Alatalo K., Bacon R., Blitz L., Bois M., Bournaud F., Bureau M., Davies R. L., Davis T. A., de Zeeuw P. T., Duc P.-A., Khochfar S., Kuntschner H., Lablanche P.-Y., Morganti R., Naab T., Oosterloo T., Sarzi M., Serra P., Weijmans A.-M., 2011, *MNRAS*, 413, 813
- Cardelli J. A., Clayton G. C., Mathis J. S., 1989, *ApJ*, 345, 245
- Cid Fernandes R., González Delgado R. M., García Benito R., Pérez E., de Amorim A. L., Sánchez S. F., Husemann B., Falcón Barroso J., López-Fernández R., Sánchez-Blázquez P., Vale Asari N., Vazdekis A., Walcher C. J., Mast D., 2014, *A&A*, 561, A130
- Cid Fernandes R., Mateus A., Sodr e L., Stasińska G., Gomes J. M., 2005, *MNRAS*, 358, 363
- Cid Fernandes R., Pérez E., García Benito R., González Delgado R. M., de Amorim A. L., Sánchez S. F., Husemann B., Falcón Barroso J., Sánchez-Blázquez P., Walcher C. J., Mast D., 2013, *A&A*, 557, A86
- Cid Fernandes R., Stasińska G., Mateus A., Vale Asari N., 2011, *MNRAS*, 413, 1687
- Croom S. M., Lawrence J. S., Bland-Hawthorn J., Bryant J. J., Fogarty L., Richards S., Goodwin M., Farrell T., Miziarski S., Heald R., Jones D. H., Lee S., Colless M., Brough S., Hopkins A. M., Bauer A. E., Birchall M. N., Ellis S., Horton A., Leon-Saval S., Lewis G., López-Sánchez Á. R., Min S.-S., Trinh C., Trowland H., 2012, *MNRAS*, 421, 872
- Curtis H. D., 1918, *Publications of Lick Observatory*, 13, 9
- de Souza R. E., Gadotti D. A., dos Anjos S., 2004, *ApJS*, 153, 411
- de Vaucouleurs G., 1948, *Annales d'Astrophysique*, 11, 247
- , 1977, in *Evolution of Galaxies and Stellar Populations*, Tinsley B. M., Larson D. Campbell R. B. G., eds., p. 43
- Driver S. P., Norberg P., Baldry I. K., Bamford S. P., Hopkins A. M., Liske J., Loveday J., Peacock J. A., Hill D. T., Kelvin L. S., Robotham A. S. G., Cross N. J. G., Parkinson H. R., Prescott M., Conselice C. J., Dunne L., Brough S., Jones H., Sharp R. G., van Kampen E., Oliver S., Roseboom I. G., Bland-Hawthorn J., Croom S. M., Ellis S., Cameron E., Cole S., Frenk C. S., Couch W. J., Graham A. W., Proctor R., De Propriis R., Doyle I. F., Edmondson E. M., Nichol R. C., Thomas D., Eales S. A., Jarvis M. J., Kuijken K., Lahav O., Madore B. F., Seibert M., Meyer M. J., Staveley-Smith L., Phillipps S., Popescu C. C., Sansom A. E., Sutherland W. J., Tuffs R. J., Warren S. J., 2009, *Astronomy and Geophysics*, 50, 12
- Erwin P., 2015, *ApJ*, 799, 226
- Freeman K. C., 1970, *ApJ*, 160, 811
- García-Benito R., Zibetti S., Sánchez S. F., Husemann B., de Amorim A. L., Castillo-

- Morales A., Cid Fernandes R., Ellis S. C., Falcón-Barroso J., Galbany L., Gil de Paz A., González Delgado R. M., Lacerda E. A. D., López-Fernandez R., de Lorenzo-Cáceres A., Lyubanova M., Marino R. A., Mast D., Mendoza M. A., Pérez E., Vale Asari N., Aguerri J. A. L., Ascasibar Y., Bekeraite S., Bland-Hawthorn J., Barrera-Ballesteros J. K., Bomans D. J., Cano-Díaz M., Catalán-Torrecilla C., Cortijo C., Delgado-Inglada G., Demleitner M., Dettmar R.-J., Díaz A. I., Florido E., Gallazzi A., García-Lorenzo B., Gomes J. M., Holmes L., Iglesias-Páramo J., Jahnke K., Kalinova V., Kehrig C., Kennicutt R. C., López-Sánchez Á. R., Márquez I., Masegosa J., Meidt S. E., Mendez-Abreu J., Mollá M., Monreal-Ibero A., Morriset C., del Olmo A., Papaderos P., Pérez I., Quirrenbach A., Rosales-Ortega F. F., Roth M. M., Ruiz-Lara T., Sánchez-Blázquez P., Sánchez-Menguiano L., Singh R., Spekkens K., Stanishev V., Torres-Papaqui J. P., van de Ven G., Vilchez J. M., Walcher C. J., Wild V., Wisotzki L., Ziegler B., Alves J., Barrado D., Quintana J. M., Aceituno J., 2015, *A&A*, 576, A135
- González Delgado R. M., Cerviño M., Martins L. P., Leitherer C., Hauschildt P. H., 2005, *MNRAS*, 357, 945
- González Delgado R. M., Cid Fernandes R., García-Benito R., Pérez E., de Amorim A. L., Cortijo-Ferrero C., Lacerda E. A. D., López Fernández R., Sánchez S. F., Vale Asari N., Alves J., Bland-Hawthorn J., Galbany L., Gallazzi A., Husemann B., Bekeraite S., Jungwiert B., López-Sánchez A. R., de Lorenzo-Cáceres A., Marino R. A., Mast D., Mollá M., del Olmo A., Sánchez-Blázquez P., van de Ven G., Vilchez J. M., Walcher C. J., Wisotzki L., Ziegler B., Collaboration920 C., 2014a, *ApJ*, 791, L16
- González Delgado R. M., García-Benito R., Pérez E., Cid Fernandes R., de Amorim A. L., Cortijo-Ferrero C., Lacerda E. A. D., López Fernández R., Vale-Asari N., Sánchez S. F., Mollá M., Ruiz-Lara T., Sánchez-Blázquez P., Walcher C. J., Alves J., Aguerri J. A. L., Bekeraite S., Bland-Hawthorn J., Galbany L., Gallazzi A., Husemann B., Iglesias-Páramo J., Kalinova V., López-Sánchez A. R., Marino R. A., Márquez I., Masegosa J., Mast D., Méndez-Abreu J., Mendoza A., del Olmo A., Pérez I., Quirrenbach A., Zibetti S., CALIFA collaboration, 2015, *ArXiv e-prints*
- González Delgado R. M., Pérez E., Cid Fernandes R., García-Benito R., de Amorim A. L., Sánchez S. F., Husemann B., Cortijo-Ferrero C., López Fernández R., Sánchez-Blázquez P., Bekeraite S., Walcher C. J., Falcón-Barroso J., Gallazzi A., van de Ven G., Alves J., Bland-Hawthorn J., Kennicutt R. C., Kupko D., Lyubanova M., Mast D., Mollá M., Marino R. A., Quirrenbach A., Vilchez J. M., Wisotzki L., 2014b, *A&A*, 562, A47
- Häußler B., Bamford S. P., Vika M., Rojas A. L., Barden M., Kelvin L. S., Alpaslan M., Robotham A. S. G., Driver S. P., Baldry I. K., Brough S., Hopkins A. M., Liske J., Nichol R. C., Popescu C. C., Tuffs R. J., 2013, *MNRAS*, 430, 330
- Hubble E., 1926, *Contributions from the Mount Wilson Observatory / Carnegie Institution of Washington*, 324, 1
- Hubble E., 1936, *The Realm of the Nebulae*, Mrs. Hepsa Ely Silliman memorial lec-

- tures. Yale University Press
- Hubble E. P., 1927, *The Observatory*, 50, 276
- Husemann B., Jahnke K., Sánchez S. F., Barrado D., Bekerait*error*è S., Bomans D. J., Castillo-Morales A., Catalán-Torrecilla C., Cid Fernandes R., Falcón-Barroso J., García-Benito R., González Delgado R. M., Iglesias-Páramo J., Johnson B. D., Kupko D., López-Fernandez R., Lyubenova M., Marino R. A., Mast D., Miskolczi A., Monreal-Ibero A., Gil de Paz A., Pérez E., Pérez I., Rosales-Ortega F. F., Ruiz-Lara T., Schilling U., van de Ven G., Walcher J., Alves J., de Amorim A. L., Backsmann N., Barrera-Ballesteros J. K., Bland-Hawthorn J., Cortijo C., Dettmar R.-J., Demleitner M., Díaz A. I., Enke H., Florido E., Flores H., Galbany L., Gallazzi A., García-Lorenzo B., Gomes J. M., Gruel N., Haines T., Holmes L., Jungwiert B., Kalinova V., Kehrig C., Kennicutt R. C., Klar J., Lehnert M. D., López-Sánchez Á. R., de Lorenzo-Cáceres A., Mármol-Queraltó E., Márquez I., Mendez-Abreu J., Mollá M., del Olmo A., Meidt S. E., Papaderos P., Puschignig J., Quirrenbach A., Roth M. M., Sánchez-Blázquez P., Spekkens K., Singh R., Stanishev V., Trager S. C., Vilchez J. M., Wild V., Wisotzki L., Zibetti S., Ziegler B., 2013, *A&A*, 549, A87
- Johnston E. J., Aragón-Salamanca A., Merrifield M. R., Bedregal A. G., 2012, *MNRAS*, 422, 2590
- Kauffmann G., Heckman T. M., White S. D. M., Charlot S., Tremonti C., Peng E. W., Seibert M., Brinkmann J., Nichol R. C., SubbaRao M., York D., 2003, *MNRAS*, 341, 54
- Kelvin L. S., Driver S. P., Robotham A. S. G., Hill D. T., Alpaslan M., Baldry I. K., Bamford S. P., Bland-Hawthorn J., Brough S., Graham A. W., Häussler B., Hopkins A. M., Liske J., Loveday J., Norberg P., Phillipps S., Popescu C. C., Prescott M., Taylor E. N., Tuffs R. J., 2012, *MNRAS*, 421, 1007
- Kelz A., Verheijen M. A. W., Roth M. M., Bauer S. M., Becker T., Paschke J., Popow E., Sánchez S. F., Laux U., 2006, *PASP*, 118, 129
- King I. R., 1966, *AJ*, 71, 64
- Kirkpatrick S., Gelatt C. D., Vecchi M. P., 1983, *Science*, 220, 671
- Knox-Shaw H., 1915, *Helwan Institute of Astronomy and Geophysics Bulletins*, 15, 129
- La Barbera F., de Carvalho R. R., 2009, *ApJ*, 699, L76
- Lara-López M. A., Bongiovanni A., Cepa J., Pérez García A. M., Sánchez-Portal M., Castañeda H. O., Fernández Lorenzo M., Pović M., 2010, *A&A*, 519, A31
- Lara-López M. A., Cepa J., Bongiovanni A., Pérez García A. M., Castañeda H., Fernández Lorenzo M., Pović M., Sánchez-Portal M., 2009, *A&A*, 505, 529
- Lawrence A., Warren S. J., Almaini O., Edge A. C., Hambly N. C., Jameson R. F., Lucas P., Casali M., Adamson A., Dye S., Emerson J. P., Foucaud S., Hewett P., Hirst P., Hodgkin S. T., Irwin M. J., Lodiou N., McMahon R. G., Simpson C., Smail I., Mortlock D., Folger M., 2007, *MNRAS*, 379, 1599
- Levenberg K., 1944, *Quart. Applied Math.*, 2, 164

- Liang Y. C., Hammer F., Yin S. Y., Flores H., Rodrigues M., Yang Y. B., 2007, *A&A*, 473, 411
- Lintott C. J., Schawinski K., Slosar A., Land K., Bamford S., Thomas D., Raddick M. J., Nichol R. C., Szalay A., Andreescu D., Murray P., Vandenberg J., 2008, *MNRAS*, 389, 1179
- Marquardt D. W., 1963, *Journal of the Society for Industrial and Applied Mathematics*, 11, 431
- Mateus A., 2006, PhD thesis, Instituto de Astronomia, Geofísica e Ciências Atmosféricas da Universidade de São Paulo
- Mateus A., Sodré L., Cid Fernandes R., Stasińska G., 2007, *MNRAS*, 374, 1457
- Méndez-Abreu J., Aguerri J. A. L., Corsini E. M., Simonneau E., 2008, *A&A*, 478, 353
- Metropolis N., Rosenbluth A. W., Rosenbluth M. N., Teller A. H., Teller E., 1953, *J. Chem. Phys.*, 21, 1087
- Moffat A. F. J., 1969, *A&A*, 3, 455
- Moles M., Benítez N., Aguerri J. A. L., Alfaro E. J., Broadhurst T., Cabrera-Caño J., Castander F. J., Cepa J., Cerviño M., Cristóbal-Hornillos D., Fernández-Soto A., González Delgado R. M., Infante L., Márquez I., Martínez V. J., Masegosa J., del Olmo A., Perea J., Prada F., Quintana J. M., Sánchez S. F., 2008, *AJ*, 136, 1325
- Möllenhoff C., Popescu C. C., Tuffs R. J., 2006, *A&A*, 456, 941
- Nelder J. A., Mead R., 1965, *The Computer Journal*, 7, 308
- Peeples M. S., Pogge R. W., Stanek K. Z., 2009, *ApJ*, 695, 259
- Peng C. Y., Ho L. C., Impey C. D., Rix H.-W., 2002, *AJ*, 124, 266
- , 2010, *AJ*, 139, 2097
- Pérez E., Cid Fernandes R., González Delgado R. M., García-Benito R., Sánchez S. F., Husemann B., Mast D., Rodón J. R., Kupko D., Backsmann N., de Amorim A. L., van de Ven G., Walcher J., Wisotzki L., Cortijo-Ferrero C., CALIFA Collaboration, 2013, *ApJ*, 764, L1
- Racine R., 1996, *PASP*, 108, 699
- Ricci T. V., Steiner J. E., Menezes R. B., 2014, *MNRAS*, 440, 2419
- Rosales-Ortega F. F., Kennicutt R. C., Sánchez S. F., Díaz A. I., Pasquali A., Johnson B. D., Hao C. N., 2010, *MNRAS*, 405, 735
- Roth M. M., Fechner T., Wolter D., Sandin C., Kelz A., Bauer S. M., Popow E., Monreal-Ibero A., Kehrig C., Streicher O., 2010, Commissioning of the ccd231 4k x 4k detector for pmas
- Roth M. M., Kelz A., Fechner T., Hahn T., Bauer S.-M., Becker T., Böhm P., Christensen L., Dionies F., Paschke J., Popow E., Wolter D., Schmoll J., Laux U., Altmann W., 2005, *PASP*, 117, 620
- Saha P., Williams T. B., 1994, *AJ*, 107, 1295
- Sánchez S. F., Kennicutt R. C., Gil de Paz A., van de Ven G., Vílchez J. M., Wisotzki L., Walcher C. J., Mast D., Aguerri J. A. L., Albiol-Pérez S., Alonso-Herrero A., Alves J., Bakos J., Bartákóvá T., Bland-Hawthorn J., Boselli A., Bomans D. J.,

- Castillo-Morales A., Cortijo-Ferrero C., de Lorenzo-Cáceres A., Del Olmo A., Dettmar R.-J., Díaz A., Ellis S., Falcón-Barroso J., Flores H., Gallazzi A., García-Lorenzo B., González Delgado R., Gruel N., Haines T., Hao C., Husemann B., Iglesias-Páramo J., Jahnke K., Johnson B., Jungwiert B., Kalinova V., Kehrig C., Kupko D., López-Sánchez Á. R., Lyubenova M., Marino R. A., Mármol-Queraltó E., Márquez I., Masegosa J., Meidt S., Mendez-Abreu J., Monreal-Ibero A., Montijo C., Mourão A. M., Palacios-Navarro G., Papaderos P., Pasquali A., Peletier R., Pérez E., Pérez I., Quirrenbach A., Relaño M., Rosales-Ortega F. F., Roth M. M., Ruiz-Lara T., Sánchez-Blázquez P., Sengupta C., Singh R., Stanishev V., Trager S. C., Vazdekis A., Viironen K., Wild V., Zibetti S., Ziegler B., 2012, *A&A*, 538, A8
- Sandage A., Sandage M., Kristian J., 1975, *Galaxies and the universe*, Stars Stellar Syst. Chicago Univ. Press, Chicago, IL
- Scoville N., Aussel H., Brusa M., Capak P., Carollo C. M., Elvis M., Giavalisco M., Guzzo L., Hasinger G., Impy C., Kneib J.-P., LeFevre O., Lilly S. J., Mobasher B., Renzini A., Rich R. M., Sanders D. B., Schinnerer E., Schminovich D., Shopbell P., Taniguchi Y., Tyson N. D., 2007, *ApJS*, 172, 1
- Sérsic J. L., 1963, *Boletín de la Asociación Argentina de Astronomía La Plata Argentina*, 6, 41
- Simard L., Willmer C. N. A., Vogt N. P., Sarajedini V. L., Phillips A. C., Weiner B. J., Koo D. C., Im M., Illingworth G. D., Faber S. M., 2002, *VizieR Online Data Catalog*, 214, 20001
- Stasińska G., Vale Asari N., Cid Fernandes R., Gomes J. M., Schlickmann M., Mateus A., Schoenell W., Sodr e Jr. L., Seagal Collaboration, 2008, *MNRAS*, 391, L29
- Storn R., Price K., 1997, *J. of Global Optimization*, 11, 341
- Sánchez S. F., 2014, in *Proceedings of the International Astronomical Union*, Vol. 10, *Galaxies in 3D across the Universe*, pp. 85–92
- Tatarskii V. I., 1961, *Wave Propagation in Turbulent Medium*. McGraw-Hill
- Vazdekis A., Sánchez-Blázquez P., Falcón-Barroso J., Cenarro A. J., Beasley M. A., Cardiel N., Gorgas J., Peletier R. F., 2010, *MNRAS*, 404, 1639
- Vika M., Bamford S. P., Häußler B., Rojas A. L., Borch A., Nichol R. C., 2013, *MNRAS*, 435, 623
- Walcher C. J., Wisotzki L., Bekerait e S., Husemann B., Iglesias-Páramo J., Backsmann N., Barrera Ballesteros J., Catalán-Torrecilla C., Cortijo C., del Olmo A., García-Lorenzo B., Falcón-Barroso J., Jilkova L., Kalinova V., Mast D., Marino R. A., Méndez-Abreu J., Pasquali A., Sánchez S. F., Trager S., Zibetti S., Aguerri J. A. L., Alves J., Bland-Hawthorn J., Boselli A., Castillo Morales A., Cid Fernandes R., Flores H., Galbany L., Gallazzi A., García-Benito R., Gil de Paz A., González-Delgado R. M., Jahnke K., Jungwiert B., Kehrig C., Lyubenova M., Márquez Pérez I., Masegosa J., Monreal Ibero A., Pérez E., Quirrenbach A., Rosales-Ortega F. F., Roth M. M., Sanchez-Blazquez P., Spekkens K., Tundo E., van de Ven G., Verheijen M. A. W., Vilchez J. V., Ziegler B., 2014, *A&A*, 569, A1

- Willett K. W., Lintott C. J., Bamford S. P., Masters K. L., Simmons B. D., Casteels K. R. V., Edmondson E. M., Fortson L. F., Kaviraj S., Keel W. C., Melvin T., Nichol R. C., Raddick M. J., Schawinski K., Simpson R. J., Skibba R. A., Smith A. M., Thomas D., 2013, MNRAS, 435, 2835
- Wolf M., 1908, Publikationen des Astrophysikalischen Instituts Koenigstuhl-Heidelberg, 3, 109
- York D. G., Adelman J., Anderson Jr. J. E., Anderson S. F., Annis J., Bahcall N. A., Bakken J. A., Barkhouser R., Bastian S., Berman E., Boroski W. N., Bracker S., Briegel C., Briggs J. W., Brinkmann J., Brunner R., Burles S., Carey L., Carr M. A., Castander F. J., Chen B., Colestock P. L., Connolly A. J., Crocker J. H., Csabai I., Czarapata P. C., Davis J. E., Doi M., Dombek T., Eisenstein D., Ellman N., Elms B. R., Evans M. L., Fan X., Federwitz G. R., Fiscelli L., Friedman S., Frieman J. A., Fukugita M., Gillespie B., Gunn J. E., Gurbani V. K., de Haas E., Haldeman M., Harris F. H., Hayes J., Heckman T. M., Hennessy G. S., Hindsley R. B., Holm S., Holmgren D. J., Huang C.-h., Hull C., Husby D., Ichikawa S.-I., Ichikawa T., Ivezić Ž., Kent S., Kim R. S. J., Kinney E., Klaene M., Kleinman A. N., Kleinman S., Knapp G. R., Korienek J., Kron R. G., Kunszt P. Z., Lamb D. Q., Lee B., Leger R. F., Limmongkol S., Lindenmeyer C., Long D. C., Loomis C., Loveday J., Lucinio R., Lupton R. H., MacKinnon B., Mannery E. J., Mantsch P. M., Margon B., McGehee P., McKay T. A., Meiksin A., Merelli A., Monet D. G., Munn J. A., Narayanan V. K., Nash T., Neilsen E., Neswold R., Newberg H. J., Nichol R. C., Nicinski T., Nonino M., Okada N., Okamura S., Ostriker J. P., Owen R., Pauls A. G., Peoples J., Peterson R. L., Petravick D., Pier J. R., Pope A., Pordes R., Prosapio A., Rechenmacher R., Quinn T. R., Richards G. T., Richmond M. W., Rivetta C. H., Rockosi C. M., Ruthmansdorfer K., Sandford D., Schlegel D. J., Schneider D. P., Sekiguchi M., Sergey G., Shimasaku K., Siegmund W. A., Smee S., Smith J. A., Snedden S., Stone R., Stoughton C., Strauss M. A., Stubbs C., SubbaRao M., Szalay A. S., Szapudi I., Szokoly G. P., Thakar A. R., Tremonti C., Tucker D. L., Uomoto A., Vanden Berk D., Vogeley M. S., Waddell P., Wang S.-i., Watanabe M., Weinberg D. H., Yanny B., Yasuda N., SDSS Collaboration, 2000, AJ, 120, 1579